

Characterization of Lower Eocene Reservoirs in the LL-652 Area, Lagunillas Field

Draft Report to
Lagoven, S.A., Caracas, Venezuela

by

Noel Tyler, William A. Ambrose,
Shirley P. Dutton, Fred Wang, and Joseph S. Yeh
Bureau of Economic Geology

Eulise Ferrer, Antonio Padron, and Williams Carrasquel
Lagoven, S.A.

Bureau of Economic Geology
W. L. Fisher, Director
The University of Texas at Austin
Austin, Texas 78713-7508

October 1993

CONTENTS

I.	Executive Summary.....	1
II.	Introduction.....	3
	Objective.....	4
	Study Area, Methods, and Database.....	5
III.	General Geological Setting	11
	Structural Setting.....	11
	Regional Setting.....	11
	Study Area.....	12
	Stratigraphic Setting.....	13
	Regional Setting.....	13
	Study Area.....	14
	Seismic Stratigraphy.....	15
IV.	Structural Interpretation.....	17
	Fault-Surface.....	17
	Paleostructural Map and C-3-X Structural-Top Marker.....	17
	Structural Cross Sections.....	18
	Cross Section A.....	18
	Cross Section B.....	19
	Cross Section D.....	19
	Cross Section F.....	19
	Cross Section G.....	20
	Cross Section 4.....	20
	Cross Section 6.....	20
	Cross Section 7.....	21
	Cross Section 8.....	21
	Cross Section 9.....	22
	Cross Section 12.....	22
	Cross Section 16.....	22
	Seismic Sections.....	23
	Seismic Line CO-90B-28.....	23
	Seismic Line CO-90B-30.....	24
	Seismic Line CO-87B-27.....	24
	Seismic Line CO-87B-72.....	25
	Seismic Line CO-87B-76.....	25

Dipmeter Analysis.....	25
LL-1310 Well.....	26
LL-1293 Well.....	26
VLA-724 Well.....	26
LL-1095 Well.....	27
Fieldwide Structural Maps.....	27
Fault Analysis.....	29
Net Thickness Map of C-3-X Member.....	29
Subcrop Map.....	30
Fault Characteristics.....	31
Tectonic Features in Cores.....	31
Fault-Seal Analysis.....	32
Middle C-3-X Submember.....	33
Upper C-4-X Submember.....	33
Upper C-5-X Submember.....	33
Fault Compartment Geometries.....	36
Structural Style.....	37
V. Depositional Systems.....	39
Facies Model.....	39
Facies.....	41
Distributary Channel.....	41
Channel-Mouth Bar.....	42
Delta Front.....	42
Distal Delta Front.....	43
Tidal Channel and Tidal Flat.....	43
Transgressive Sand Shoal and Shelf.....	44
Fluvial-Estuarine Channel.....	44
Facies Summary and Comparisons.....	45
Three-Dimensional Architecture.....	45
Permeability and porosity characteristics.....	48
VI. Depositional and Sandstone Architectural Trends of C Member Reservoir Intervals.....	50
Introduction.....	50
C-7-X Member.....	51
Sandbody Geometry.....	51
Lithology and Depositional Systems.....	51
Reservoir Development.....	52

Lower Lower C-6-X Submember.....	52
Sandbody Geometry.....	52
Lithology and Depositional Systems.....	52
Reservoir Development.....	53
Upper Lower C-6-X Submember.....	53
Sandbody Geometry.....	53
Lithology and Depositional Systems.....	53
Reservoir Development.....	54
Lower Upper C-6-X Submember (21-22 Interval).....	54
Lower 21-22 Interval.....	54
Sandbody Geometry.....	54
Lithology and Depositional Systems.....	54
Reservoir Development.....	55
Upper 21-22 Interval.....	55
Sandbody Geometry.....	55
Depositional Systems.....	56
Reservoir Development.....	56
Upper Upper C-6-X Submember.....	56
Sandbody Geometry.....	56
Depositional Systems.....	57
Reservoir Development.....	57
Lower C-5-X Submember.....	58
Sandbody Geometry and Depositional Facies.....	58
Reservoir Development.....	58
Lower Lower C-5-X Submember.....	58
Sandbody Geometry.....	58
Lithology and Depositional Systems.....	58
Reservoir Development.....	58
Upper Lower C-5-X Submember.....	59
Sandbody Geometry.....	59
Lithology and Depositional Systems.....	59
Reservoir Development.....	59
Middle C-5-X Submember.....	60
Sandbody Geometry.....	60
Lithology and Depositional Systems.....	60
Reservoir Development.....	60

Lower Middle C-5-X Submember.....	61
Sandbody Geometry.....	61
Lithology and Depositional Systems.....	61
Reservoir Development.....	61
Middle Middle C-5-X Submember.....	62
Sandbody Geometry.....	62
Lithology and Depositional Systems.....	62
Reservoir Development.....	62
Upper Middle C-5-X Submember.....	63
Sandbody Geometry.....	63
Lithology and Depositional Systems.....	63
Reservoir Development.....	63
Upper C-5-X Submember.....	64
Sandbody Geometry.....	64
Lithology and Depositional Systems.....	64
Reservoir Development.....	64
Lower C-4-X Submember.....	65
Reservoir Development.....	65
Middle C-4-X Submember.....	65
Reservoir Development.....	66
Upper C-4-X Submember.....	66
Sandbody Geometry.....	67
Lithology and Depositional Systems.....	67
Reservoir Development.....	67
#4 Unit in Upper C-4-X Submember.....	69
Sandbody Geometry.....	69
Lithology and Depositional Systems.....	69
Reservoir Development.....	69
Lower C-3-X Submember.....	70
Sandbody Geometry.....	70
Lithology and Depositional Systems.....	70
Reservoir Development.....	71
Middle C-3-X Submember.....	71
Sandbody Geometry.....	71
Lithology and Depositional Systems.....	71
Reservoir Development.....	72

Upper C-3-X Submember.....	73
Sandbody Geometry.....	73
Reservoir Development.....	73
VII. Petrography of Misosa Sandstones Compositional, Textural, and Diagenetic Controls on Porosity Distribution and Evolution	74
Methodology.....	74
Texture.....	76
Framework Mineralogy.....	76
Detrital Clay Matrix.....	77
Cements.....	78
Quartz.....	79
Authigenic Clays.....	80
Carbonate Cements.....	81
Porosity.....	82
Diagenetic Controls on Reservoir Quality.....	83
Conclusions.....	85
VIII. Production Analysis.....	86
Kh production.....	86
Oil-Water Contacts.....	87
Middle C-3-X Submember.....	88
Upper C-4-X Submember.....	89
Low-Resistivity Sandstones.....	89
IX. Petrophysics.....	91
Data Integration.....	91
Petrophysical Models and Key Well Evaluation.....	92
Model for Calculating Shale Volume (V_{sh}).....	92
Porosity Model (V_{sh} -Porosity Transforms).....	93
Permeability Model (Permeability-Porosity Transform).....	94
Water Saturation Model.....	96
Formation Water Salinity and R_w Determination.....	96
Cementation and Saturation Exponents.....	96
Water Saturation Model Selection.....	96
Fieldwide Formation Evaluation and Validation by Mapping.....	97
Net-Pay Determinations.....	98
X. Volumetrics.....	100
Calculation of OOIP and Remaining Oil Volumes.....	100

Net oil sandstone.....	101
C-7-X Member.....	101
C-6-X Member.....	101
C-5-X Member and Lower Middle C-5-X Submember.....	102
C-4-X Member and Upper C-4-X Submember.....	102
C-3-X Member and Middle C-3-X Submember.....	102
C-1-X and C-2-X Members.....	103
Porosity.....	103
C-6-X and C-7-X Members.....	103
C-5-X Member and Lower Middle C-5-X Submember.....	104
C-4-X Member and Upper C-4-X Submember.....	104
C-3-X Member and Middle C-3-X Submember.....	104
Permeability.....	105
C-7-X and C-6-X Member.....	105
C-5-X Member and Lower Middle C-5-X Submember.....	105
C-4-X Member and Upper C-4-X Submember.....	105
C-3-X Member and Middle C-3-X Submember.....	106
C-2-X Member.....	106
Water saturation.....	106
C-6-X Member.....	107
C-5-X Member.....	107
C-4-X Member.....	107
C-3-X Member.....	108
C-2-X and C-1-X Member.....	108
Porous hydrocarbon volume.....	108
C-7-X Member.....	108
C-6-X Member.....	109
C-5-X Member.....	109
C-4-X Member.....	109
C-3-X Member.....	110
Original Oil in Place.....	110
C-6-X Member.....	110
C-5-X Member.....	111
C-4-X Member.....	111
C-3-X Member.....	111
Remaining oil.....	112

C-6-X Member.....	112
C-5-X Member.....	113
C-4-X Member.....	113
C-3-X Member.....	113
Reservoir Boundaries.....	114
Vertical Communication.....	114
Horizontal Communication.....	115
Production.....	115
C-6-X Member.....	116
Lower Lower C-6-X Submember.....	116
Upper Lower C-6-X Submember.....	116
Lower Upper C-6-X Submember.....	117
C-5-X Member.....	117
Lower C-5-X Submember.....	117
Combined Middle and Upper Middle C-5-X Submember.....	117
3. C-4-X Member.....	118
a. Middle C-4-X Submember.....	118
b. Upper C-4-X Submember.....	118
C-3-X Member.....	119
Lower C-3-X Submember.....	119
Middle C-3-X Submember.....	119
XI. Opportunities and Strategies for Recovery Optimization and Reserve Growth	121
New Extended-Development Locations.....	122
Deepened, Recompleted, and Redrilled Wells.....	122
Resource-Targeted Infill Wells.....	123
Secondary Recovery.....	123
XII. Conclusions	126
XIII. References.....	133

I. EXECUTIVE SUMMARY

Lower Eocene reservoirs (C Members) in the LL-652 area will contain substantial volumes of remaining mobile oil (923 million barrels [MMbbl]) after primary development. This resource exists in poorly drained or undrained reservoir compartments defined by a combination of complex structure and the heterogeneous tide-dominated deltaic facies geometry. The product of this combined structural and depositional complexity are reservoirs that have a high degree of geologic heterogeneity, considerable variation in reservoir quality, and therefore a low recovery efficiency.

The tide-dominated deltaic depositional model of the C Members in the LL-652 area captures a system of dip-elongate distributary-channel sandstones that merge northeastward with extensive, dip-parallel delta-front sandstones. These two facies compose most of the reservoir sandstones and therefore contain most of the remaining oil. Permeability range and average are similar for the major facies. However, there are significant permeability contrasts (up to three orders of magnitude) locally between distributary-channel and tidal-flat, fluvial-estuarine channel and distal delta-front, and distributary-channel and delta-front facies where the base of the distributary-channel facies contains clay clasts that may retard vertical fluid flow.

Diagenesis, not depositional environment, is the main control on porosity and permeability distribution in the C Members. Porosity and permeability in the C Members decrease with increasing depth. In particular, the volume of quartz cement is the main influence on reservoir quality, and because the volume of quartz cement increases significantly with depth, reservoir quality decreases with depth.

The original-oil-in-place (OOIP) resource base of the C Members in the LL-652 area has been increased by 867 MMbbl (60 percent) to 2,318.2 MMbbl. This increase is mainly in the C-3-X and C-4-X Members through documenting additional reservoir area and through improved quantification of petrophysical parameters such as porosity. Extended development through continued pattern infill with 97 new wells will increase reserves from 127 MMbbl to 302 MMbbl. However, an additional 116 MMbbl can be produced from 102 geologically based infill wells strategically targeted to tap areas of high remaining oil saturation by contacting narrow sandbodies that pinch out over distances less than the current 80-acre (1,968 ft [600 m]) well spacing.

A pilot waterflood in the Upper C-4-X Submember in the eastern part of the LL-652 area can recover an additional 70 MMbbl of oil. Expansion of waterflood operations to the entire

field could increase recovery by as much as 20 percent of the OOIP, representing a secondary-recovery resource of approximately 460 MMbbl.

The LL-652 area is divided into five main and two minor structural compartments. The central structural compartment is the largest production area in the field and includes 76 wells with a cumulative production of 85.8 MMbbl. Seventy-seven percent (66.1 MMbbl) of this production comes from the C-4-X.01 reservoir.

II. INTRODUCTION

Many oil reservoirs contain substantial volumes of unrecovered mobile oil trapped in poorly drained compartments after primary and secondary development. For example, of the nearly 500 billion barrels (Bbbl) of oil that have been discovered in the United States, approximately 300 Bbbl in existing fields will remain unproduced after primary and secondary recovery with existing technology (Fisher 1987; Tyler 1988). Of this 330 Bbbl, 80 to 100 Bbbl is mobile oil that can be recovered at low cost through conventional infill exploration and development strategies that target untapped compartments and optimize existing waterfloods (fig. II 1). Three-dimensional facies architecture and structural complexity exert a strong control over the distribution and continuity of reservoir compartments and paths of fluid flow, and therefore the areas of reservoir that have been swept. Reservoirs with complex internal architecture contain large volumes of remaining mobile oil whereas those with simple internal architecture are efficiently drained.

Although oil reservoirs are internally complex and commonly contain undrained or partially drained compartments, traditional infill strategies, based on the assumption that all reservoirs are homogeneous and almost perfectly continuous, have simply maintained geometric grid patterns of well spacing. These infill strategies have missed numerous untapped or ineffectively swept compartments and have resulted in many nonproductive or poorly productive wells that increase the average cost per infill well.

A more efficient means of recovering mobile oil is through a geologically based infill-development strategy that targets compartments defined by large-scale, depositional-facies geometry and structure. Tyler (1988) demonstrated a relationship between original depositional environment, drive mechanism, and recovery efficiency (fig. II 2). This relationship is based on a review of 450 major Texas oil reservoirs that together account for almost 75% of Texas production and provide examples of oil production from a wide variety of depositional environments (Galloway and others, 1983).

The recovery efficiency of reservoirs vary tremendously according to depositional type (fig. II 2). Homogeneous barrier-island and wave-dominated deltaic reservoirs typically have strong water drives and have high mobile-oil recovery, whereas internally complex fluvial-deltaic reservoirs have moderate drive energies and exhibit recovery efficiencies ranging from approximately 20 to 50 percent. By comparison, lower Eocene tidally influenced deltaic reservoirs in the C members of the Misoa Formation in Lagunillas field, which are the focus of this study, are expected to have an ultimate recovery of only 20 percent at the end of primary recovery operations. A resource of 1160 million barrels of oil will remain including perhaps as much as 750 million barrels (MMbbl) of unrecovered mobile oil at the current well spacing of

approximately 80 ac. This report demonstrates that the structural complexity and depositional heterogeneity of these reservoirs has resulted in enormous potential for reserve growth from the remaining recoverable mobile oil. For example, the complex, multistage tectonic history of Lake Maracaibo has created many structural compartments between intersecting faults of different age. Additionally, sandbody trends, as a result of the tidally influenced deltaic depositional system of the reservoirs in the C members, are strongly linear and are consistently oriented northeastward. These sandstone trends impart a preferred pathway for fluid flow in the reservoir. Importantly, the sandstone bodies are narrow, typically less than the distance between wells, and are bounded laterally by low-permeability siltstones and mudstones resulting in laterally discontinuous, or compartmentalized, reservoirs. This report documents the volume of oil remaining in the C reservoirs and will identify, on a between-well scale, the location of the remaining oil so that cost-effective, geologically targeted recovery strategies can be implemented to recover a large part of this resource. Specifically, this report targets selected reservoir zones for infill drilling, strategic recompletions, and water flooding to maximize oil recovery.

Objective

The primary objective of this study was the geological characterization of the C members in the Eocene in the LL-652 area of Lake Maracaibo in order to better estimate hydrocarbon reserves, identify potential areas for secondary recovery projects and to establish a field-depletion plan to evaluate advanced recovery opportunities and extended development. This objective was met by conducting an integrated study that included a structural, stratigraphic, petrophysical, and production-engineering analysis from well logs, cores, seismic, thin-section, and petroleum engineering data. Thirteen specific tasks were designed to complete the study:

- (1) Correlating and subdividing the major depositional cycles (stratigraphic sequences) of the C members.
- (2) Determining the geometry (lateral and vertical continuity) of sandstone bodies in the depositional cycles.
- (3) Describing and analyzing whole cores in order to interpret depositional environments, calibrate log responses, and to construct a depositional model.
- (4) Determining original and current fluid contacts from log analysis, production data, and core information.
- (5) Establishing reservoir limits from structural and stratigraphic maps.

- (6) Producing a structural model by analyzing sealing and non-sealing faults and preparing structural maps of marker tops and fault planes.
- (7) Extending the geological interpretation into the Maraven block for a better evaluation of the structurally complicated western part of the LL-652 area.
- (8) Conducting a petrophysical study for each reservoir based on core information, well logs, production data, and petrophysical parameters (porosity, permeability, V_{cl} , m , n , a , capillary pressure, S_{wirr} , and grain density), supporting the calculation of original oil in place (OOIP) and recoverable reserves through primary development methods, and estimating the rock-quality characteristics.
- (9) Producing isopach maps of net oil sandstone, porosity, permeability, water saturation, and porous hydrocarbon volume.
- (10) Estimating OOIP, remaining mobile oil, and delineating reservoir boundaries.
- (11) Identifying potential areas for secondary recovery projects and development locations.
- (12) Evaluating diagenetic processes and type and distribution of clay that may affect the production performance of reservoirs in areas or potential intervals for secondary recovery projects.
- (13) Creating a data bank with information gathered from the study for incorporation into existing data bases.

Study Area, Methods and Database

The LL-652 area, located in the Maracaibo Basin in northwestern Venezuela, is considered to be one of the most important oil-producing basins in the world. The LL-652 area covers an area of about 54 mi² (140 km²) and is bounded on the north by the western Tia Juana area, on the west by the Maraven Block 1 concession, on the east by the LL-370 area, and on the south and southeast by the LL-453 area (figs. II 3 and II 4). The LL-652 area was discovered in 1953. It is one of the most prolific hydrocarbon-producers in the Misosa formation in the C-1-X to C-6-X Members (fig. II 5). With an official OOIP of 1.5 Bbbl, the LL-652 area has produced more than 170 MMbbl of mainly light oil during the last 40 years. Production comes from ten reservoirs contacted by a total of 150 Lagoven wells. The main production and development problems in the LL-652 area include: (1) undefined variations in reservoir quality throughout the area, particularly in the low-permeability C-5-X, C-6-X, and C-7-X Members, (2) high water production in high-resistivity zones in the C-6-X and C-7-X Members, (3) structural complexity in the northern, west-central, and southwestern parts of the field, (4) poorly documented net-

sandstone thickness trends and their influence on reservoir drainage, (5) unknown or poorly understood reservoir boundaries in the northern, western (Maraven boundary), and southern parts of the field, and (6) discrepancies between or poor information on oil-water contacts in the C-3-X through C-6-X Members.

The research was systematically conducted in phases or steps. In phase 1, a detailed study plan was made for all the stages of the project to determine research activities, priorities, critical phases, objectives, limitations and to estimate man power required to finish the project.

Phase 2 consisted of data collection and review. The collection and preparation of data was an important step and required as much effort as possible to select good-quality data, ensuring the timely development of all the stages of the project. A new base map was updated to assure the accuracy and completeness of all well locations. Geological, engineering and geophysical data were collected from Lagoven S.A. and Maraven S.A. and cataloged and organized into files. Data were updated and new files generated as needed. Digitized tapes of well log data were transferred into the computer system. Previous studies of Lagunillas field and the Maracaibo Basin were obtained from Lagoven and Maraven company reports and published articles from general literature. Official and operational maps were reviewed in order to better define the limits of the study area and to incorporate production data in the reservoir models.

Phase 3 included log correlations. Initial log correlations were at a regional scale and used wells with the most complete and thickest stratigraphic sections. Ten major shale marker beds were identified as regional markers across the area. The LL-2942 well (fig. II 5) was selected as the type log because it contacts a complete unfaulted interval in the entire lower Eocene. An initial study area in the east-central part of Lagunillas field was selected for initial correlations because it is (a) structurally less complex, (b) located in an area where most of the cored wells are present, and (c) where the well control is greater. Detailed correlations with 10 major shale and 25 other, less-continuous shale marker beds in the B and C members were made in the initial area and extended away to the 150 wells in the LL-652 area and 40 wells of Maraven Block 1 (fig. II 4). Correlations of each well were made with a minimum of three other wells within a loop beginning and ending with the same log, reducing correlation errors to a minimum. Correlations were extended across the study area in a grid of 27 stratigraphic cross sections (14 dip and 13 strike) to verify the correlations, faults, and to identify wells with unresolved discontinuities and thickness changes in stratigraphic units. All well logs were included in at least one of the 27 cross sections. The general structural framework, initially established by well-log correlations, was checked and revised through structural maps of tops of each C member as well as on the Eocene unconformity. Additionally, twelve structural cross sections were constructed to check and verify the existence of faults, structural dip, and folds. Twelve seismic cross sections (six dip and six strike) were interpreted to further verify the

structural framework and to correlate and demonstrate the stratal geometry of major stratigraphic sequences.

In phase 4, sedimentology and stratigraphy, whole cores from 8 wells (LL-846, LL-2425, LL-2850, LL-3074, LL-3075, LL-3080, LL-3140, and LL-3282) (fig. II 4), which together contain a total of 3,266 ft (995.7 m) of section, were described in detail to interpret depositional environments, calibrate log responses, develop a depositional model, and provide a framework for thin-section sampling. These cores were described graphically on a form that depicts grain-size trends, nature of contacts, sedimentary structures, rock type, degree of calcite cement, as well as other important features such as clay clasts, burrows, and organic fragments (see appendix E for examples). In addition to these graphically depicted data, relative percentages of stratification types and accessory features (degree of induration [consolidation], shells, burrows, organics, clay clasts, graded beds, sorting, roundness, fractures, visual porosity, and soft-sediment deformation) were indicated by relative width of filled-in columns. Close-up photographs were taken of important features in the core to document the lithofacies.

A method for determining net-sandstone thickness from well logs was established by calibrating the core descriptions to the gamma-ray curve. This was done by comparing the core descriptions to the gamma-ray curve at the same scale, measuring net-sandstone thickness from the core descriptions, and then adjusting a vertical cutoff line of the gamma-ray curve to match the amount of net-sandstone thickness determined from the core descriptions. Based on this procedure, a 33-percent of greatest leftward gamma-ray deflection from a normalized shale baseline was used as a cutoff for counting net-sandstone thickness in the C-3-X and C-4-X Members. For the C-5-X, C-6-X, and C-7-X Members, this cutoff was 28 percent. For logs without the gamma-ray curve, resistivity and SP curves were used to measure net-sandstone thickness.

A depositional model was developed by integrating information from core descriptions and maps of net-sandstone thickness, percent sandstone, and log facies. Percent-sandstone values were determined by dividing thickness of stratigraphic unit by net-sandstone thickness. Log-facies maps, showing distribution of gamma-ray or SP responses for an individual stratigraphic unit or the most common log response in a thick stratigraphic unit containing several sandstone beds, were prepared for selected submembers. The types of log responses mapped included upward-coarsening, upward-fining, blocky, serrate, and baseline deflections.

Phase 5 consisted of petrographic description of the C members. Seventy-six thin sections were selected from the cores for analysis. If possible, these thin sections were selected at the same depths as core plugs so that the petrographic description could be calibrated against permeability, porosity, and other data derived from previous core analyses. The types of features described in the petrographic study included mineral composition of grains and clays, cement

types, estimates of each type of porosity (primary, secondary, or microporosity), volume of total clay, and diagenetic sequence. Scanning electron microscopy (SEM) was conducted to evaluate calcite-cement dissolution and to assess differences in pore types among different sandstones and facies. The effects of the diagenetic processes and type and distribution of clay that may influence the production performance of reservoirs was assessed in areas of potential secondary recovery projects.

Phase 6 was a structural interpretation of the LL-652 area, beginning with the construction of accurate fault-surface maps for all recognized faults. These maps were checked for three-dimensional geometric validity and integrated with structure maps. Compilation of the fault data commenced with identification of fault-cut points that represent the intersection of a drilled well with a fault surface. The thickness of missing or repeated section (magnitude of the fault measured in an electric log by correlation) was recorded in order to measure the vertical separation. An estimate of the subsea depth was also required for each fault-cut point.

Fault-trace positions were difficult to define without the use of the fault-structure map integration technique. Also, the width of a fault gap was documented, which is a function of the angle and direction of dip of the fault, as well as the dip of strata (Tearpock, 1991). Therefore, the width of a fault gap for any given fault on a structure map could not be intuitively determined. Finally, fault maps were not finalized until a later stage of the structural interpretation when fault positions were fully documented with new data.

A paleostructural map was made of the C-3-X Member to define and compare the general tendency of the Eocene structure. To define the paleostructure map, it was necessary to document (1) the total thickness between the Eocene unconformity and the top of the C-3-X Member (2) distribution of faulted wells and (3) changes or anomalies in structure. The paleostructural map of the C-3-X Member showed the structure on the top of the C-3-X Member at the time when the La Rosa Formation was deposited on the Eocene unconformity, with the assumption that the paleotopography of the unconformity was almost horizontal. In the LL-652 area the La Rosa Formation has few thickness changes (average thickness 190 ft [57.9 m]). In the Maracaibo Basin, the average thickness is 195 ft (60 m) (Bot and Perdomo, 1987).

Structural cross sections across the LL-652 area were prepared in order to interpret the structural framework and solve problems related to faulting, dip of strata, and folds. Cross sections were oriented perpendicular, parallel and oblique to the structural strike, and perpendicular to fault strike. Evaluation of the structure and fault geometry required 22 structural cross sections at exaggerated vertical scales to permit legible detail (see fig. IV 5). The sections were later used in conjunction with structure maps to provide a three-dimensional analysis of the LL-652 area. Finally, special detailed sections were prepared to evaluate the continuity of individual reservoir sandstones.

Twelve seismic cross sections were analyzed to visualize the structure, to prepare accurate structure maps, and to document the continuity of large-scale stratigraphic sequences. Most of these sections were oriented perpendicular to the strike of the fold areas and faults. Well data were tied to seismic sections with synthetic seismograms of 5 selected wells with high-quality sonic and bulk-density logs. The Eocene-Miocene unconformity, top of C-3-X Member, Guasare Formation and Socuy Member were selected for correlations, as they correspond to the most prominent and most continuous seismic reflectors in the area. Finally, fault trends were projected from electric-log cross sections to the seismic sections.

Dipmeter logs were interpreted to resolve local structural anomalies and complexities. Forty-seven dipmeter logs in the Lagoven area and 32 in the Maraven area (see appendix A) were analyzed to estimate the direction of dip and strike and apparent changes in thickness of stratigraphic intervals. Sixty percent of the dipmeter data were presented in tabular form, showing only selected levels that were used in the structural map of some level. Vectorial diagram (arrows) presentations composed the remaining 40 percent of the dipmeter data, showing a graphic presentation of direction and magnitude of dip versus the depth of the well at the correlation point (Western Atlas, 1974). We used these either for interpretation of the structural maps or for use in interpretation of major dip change on transverse sections, faults, and folds.

Structural-top data were tabulated for all members and submembers in 195 wells (150 Lagoven and 45 Maraven) in the study area (see appendix A). The test of the fault and structural framework was whether interpretations fit on a series of horizons at various depths. Multiple-horizon mapping was essential to support the integrity of structural interpretations, to provide an accurate and reasonable interpretation, and to validate the three-dimensional framework. Eight stratigraphic levels were selected, including the Miocene-Eocene unconformity and tops of C-1-X through C-7-X Members. Eight structure maps were based on structural-tops data, fault-surface map, structural cross sections, seismic sections, dipmeter analysis and the preliminary structural marker map, mapped on the top of the C-3-X Member.

The objective of the fault analysis was to characterize all 17 of the principal faults in the field and consisted of the following steps: (1) analysis of the net-thickness map of the C-3-X Member, with the objective of determining controls on thickness variations across faults possibly related to syndepositional tectonism, (2) subcrop map analyzing the intensity of the faulting and determining the relative age of faults, used in combination with the Miocene-Eocene unconformity structural map, and (3) analysis of fault characteristics, with the final objective of documenting the basic elements (dip, strike, and displacement) of the faults and fault type and seal. Horizontal separation of faults was determined to evaluate reservoir connectivity as an important factor in the evaluation of the potential hydrocarbon accumulation. This analysis was

conducted in conjunction with investigation of pressure variations across faulted blocks. Fault-compartment geometries were delineated to document structural compartmentalization.

Phase 7 was a production and pressure analysis conducted for each member and submember. These data were analyzed against a background of structural and stratigraphic maps to infer controls on anomalous production histories and pressures. The stratigraphic horizon of each perforated interval was identified and producing wells in each member and submember were plotted on structural and stratigraphic maps. Fluid contacts were inferred from production and structural maps.

Phase 8 included construction of a petrophysical model by integrating core information, digitized well logs, production data, and key parameters such as porosity, permeability, V_{cl} , m , n , a , capillary pressure, S_{wirr} , and grain density. Permeability-porosity crossplots were prepared for major facies recognized from cores, with the objective of characterizing the fluid-flow potential. A transform function relating log response to rock and fluid properties was developed in order to make isopach maps of net oil sandstone, porosity, permeability, water saturation, porous hydrocarbon volume, original oil in place and remaining mobile oil.

In phase 9, three reservoirs were selected for detailed analysis and identification of potential areas for secondary recovery projects and development locations. A set of eight structural cross sections (four dip and four strike) presented detailed correlations of all sandstones and mudstones in the C-3-X and C-4-X Members in the C-4-X.01 and C-4-X.03 reservoirs. Six cross sections were selected for similar analysis of the C-5-X.02 reservoir. The objectives of these cross sections were to document the vertical and lateral continuity of sandstones and to construct a three-dimensional model to predict probable fluid-flow paths for proposed waterflood operations and to identify reservoir compartments to be contacted by infill wells.

In phase 10, areas favorable for infill-well development were delineated for each reservoir by comparing maps of hydrocarbon volumetrics and production to structural and stratigraphic maps. Specific recommendations for extended development wells, recompletions and geologically targeted infill locations were made on the basis of these comparisons, and the potential for secondary oil recovery for each member and submember was evaluated.

III. GENERAL GEOLOGIC SETTING

Structural Setting

Regional Setting

Five main structural trends exist in the Maracaibo basin (fig. III 1, Lugo, 1991) as follows: (1) North-northeast-trending major faults are mainly represented by the Icotea fault, the largest fault in the Lake Maracaibo area, extending for more than 80 mi (130 km). West of the LL-652 area, it is a positive flower structure (Lugo, 1991). The Icotea fault is left-lateral-strike-slip (Krause, 1971, Lugo 1991), having associated minor faults in flower and horsetail patterns, and locally having abrupt, alongstrike increases in throw (scissor or trap-door structures). (2) North-northeast-trending folds are slightly oblique to the main north-northeast-trending faults; the LL-652 area is located in this trend (fig. III 1). (3) Northwest-trending normal faults that trend from N30°W to N50°W have generally normal displacement. Most of these faults offset Upper Eocene units and are truncated by the Eocene-Miocene unconformity. (4) North-trending thrust faults represent the youngest faulting events in the Maracaibo basin and offset all stratigraphic units. They are associated with regional east-west compression in late Pliocene to Holocene time. (5) Northwest-trending thrust faults are located in the Central Lago, Lagunillas, and Bachaquero areas (fig. III 1). The southwest movement of these faults indicate a tectonic transport from the northeast during early to middle Eocene time.

The structural framework evolved in discrete stages. The north-northeast trend is pre-Cretaceous, and was repeatedly reactivated during Cretaceous and Cenozoic tectonic episodes (Lugo, 1991). Additionally, the transpressive regime in the Maracaibo Basin is subdivided into four periods: firstly, middle to late Eocene transpression occurred, in which the main structural features, such as the Icotea fault, were delineated. The structural interpretation for the post-late-Eocene and pre-middle-Miocene (fig. III 2) is based on the observation that all Eocene strata are cut by faults that are, in turn, truncated by the Eocene-Miocene unconformity. Secondly, during late Eocene-early Miocene transpression quiescence, the Maracaibo Basin was exposed to regional erosion. This event has been interpreted as a tectonic uplift that produced the tilting of the basin to the west-southwest (Zambrano and others, 1971). The structural map of the Eocene-Miocene unconformity (fig. III 3) shows that post-unconformity deformation increases to the

north-northeast, particularly along the Icotea fault, where the unconformity gently dips southward at 4 degrees. Also, almost all the en-echelon, northwest-trending normal faults terminate below the unconformity. Thirdly, middle Miocene to Pliocene transpression, rejuvenation, and fault rotations occurred in the late Eocene to early Miocene erosional episode. The basin was subjected to renewed transpression during the middle Miocene, but this time the compressive component was larger and the main faults were reactivated, offsetting the unconformity. Fourthly, the last important event that affected the Maracaibo basin occurred in the Pliocene to Pleistocene and consisted of east-west compression exemplified by north-trending thrust faults principally along the eastern flank of the La Sierra de Perijá and near the eastern coast of Lake Maracaibo. This compressional event reactivated the northern part of the Icotea fault. Tectonic episodes from Paleocene to Pliocene in Figure III 4 summarize the main late Tertiary tectonic events in the Maracaibo Basin.

Study Area

Structure of the LL-652 area is a north-northeast-trending, elongate anticline with a steeply dipping (25 to 45 degrees) western and northwestern limb and a relatively gently dipping (5 to 10 degrees) east and southeast flank. In the Maraven area the structure is a monocline with a gentle 3- to 8 degree -dip to the east (Maraven internal report).

The structure of the study area is complex because it was affected by multiple tectonic events that generated three trends of normal faults and one trend of reverse faults, representing the local scale of all the major trends defined by Lugo (1991) in the regional setting in the Maracaibo Basin. North-northeast-trending major faults are represented by a master normal fault located in the eastern part of the Maraven area. Maraven reports a "flank east fault" with an east dip and 500 ft (152 m) of throw. In the current study we interpreted 1200 ft (366 m) of throw in the south that decreases to 800 ft (244 m) toward the north. This fault represents a geological boundary between the Maraven Block-I and Lagoven LL-652 area; the fault runs slightly oblique to the boundary between the two concessions. Also, this master fault was reactivated after the Eocene-Miocene unconformity that is offset by 80 ft (24 m). North-northeast-trending folds are represented by an elongate anticline that is slightly oblique to the main north-northeast-trending fault. The northern area of the fold, where well LL-2946 is located, is on the crest of an anticline. High dips (47 degrees) occur in the LL-1293 well on the northwest limb and 54 degrees in the well LL-827 on the east limb. The LL-827 well is located near the intersection of a reverse fault and the master normal fault. The southern area of the fold represents 80 percent of the LL-652 area. Three normal faults trend N20°-35°W, N40°-45°W, and N50°-60°W with

multiple occurrences of missing section (vertical separation) ranging from 50 to 1,200 ft (15.2 to 366 m). Most of these faults offset the entire Eocene section and are truncated by the Eocene-Miocene unconformity (fig. III 3). A major normal fault is located northeastward with 400 to 800 ft (122 to 244 m) of throw. Northeast-trending normal faults are represented by two antithetic faults in the northern part of the field. They are located within 1,968 ft (600 m) of each other and have 550 ft (167 m) and 500 ft (152 m) of throw, respectively. Additionally, north-northeast-trending thrust faults cut across the older normal faults and represent the youngest deformation in the Maracaibo Basin (Lugo, 1991). Other evidence from the paleostructural and subcrop analysis shows that these faults were reactivated along other normal faults (Lugo, 1991). Seismic interpretation, as described in a later section "structural interpretation", shows evidence of reactivation along the western master fault in the Maraven area.

The principal reservoirs (C-4-X.01, C-5-X.02 and C-6-X.01) are separated from the C-4-X.03, C-5-X.08 and C-6-X.16 reservoirs on the southwest by a major normal fault that trends N60°W with 300 ft (91.5 m) of throw, extending to the northwest and being offset by reverse faults. The master normal fault in the east is the boundary of the C-4-X.01, C-5-X.02 and C-6-X.01 reservoirs. The southwest limit of the C-4-X.03, C-5-X.16 and C-6-X.08 reservoirs is a normal fault trending N35°W with 600 ft (183 m) of throw.

The north-northeast-trending reverse faults are on the ridge-crestal area in the western part of the main reservoirs, and are subparallel to the strike of the steeply dipping west limb of the reservoir. Several wells from the south to the north across the main reservoirs intersect faults with repeat section ranging from 60 to 150 ft (18 to 45.7 m) thick. These faults may internally divide the principal reservoirs (C-4-X.01, C-4-X.03, C-5-X.01, C-5-X.15, C-6-X.01, and C-6-X.08).

Stratigraphic Setting

Regional Setting

The Maracaibo Basin is centered on the southwest margin of Lake Maracaibo and is approximately 19,300 mi² (50,000 km²) in area (fig. II 3). The Cretaceous platform of the basin consists of carbonates and marine mudstones of the Rio Negro to Mito Juan Formations (fig. III 5) (Zambrano and others, 1972; Gonzalez de Juana and others, 1980). At the end of the Paleocene with deposition of the Guasare Formation, thick Eocene fluvial-deltaic sediments, derived from the southwest, were deposited on the platform. The Eocene fluvial facies tract is

represented by the Mirador Formation and the deltaic facies tract is the Misoa Formation (fig. III 5). The Lower Eocene, informally referred to as the "C" Sands (Walton, 1967), is composed of a progradational cycle at the base (C-6-X and C-7-X Members) and two other progradational cycles in a net retrogradational sequence (Bot and Perdomo, 1987; Graves and others, 1987) (fig. III 5).

Maximum transgressive conditions in the Maracaibo Basin occurred during deposition of the C-1-X Member and regressive conditions returned with subsequent deposition of major progradational clastic wedges of the Upper Eocene "B" Sands (Gonzalez de Juana and others, 1980). The Eocene is truncated by a major angular unconformity (Eocene Unconformity). In the region of Lagunillas field the Misoa Formation is directly overlain by the Miocene La Rosa Formation (fig. III 5).

Study Area

The bulk of the oil production in the Lower Eocene in the LL-652 area (135 MMbbl) is from the combined C-3-X and C-4-X Members (fig. II 5). The C-5-X Member has produced approximately 18 MMbbl and the C-6-X Member accounts for 7.5 MMbbl. The sandstone-poor C-2-X Member has produced 1 MMbbl, the C-1-X Member has produced 0.8 MMbbl, and no oil has been produced from the C-7-X Member.

The Lower Eocene in the LL-652 area is approximately 4,000 ft (1,220 m) thick and contains multiple regressive-transgressive cycles in a net-retrogradational sequence (fig. II 5). The C-1-X through C-7-X Members, informally subdivided into two to three submembers, are bounded by laterally continuous shale marker beds that mark transgressive surfaces. The submembers range from 50 to 200 ft (15.2 to 61 m) thick and correspond to one or several paragenetic sequences that are each 50 to 80 ft (15.2 to 24.4 m) thick. Informal shale marker beds, numbered from 1 to 27 in the Lower Eocene section, were correlated throughout the LL-652 area.

The C-7-X Member represents a major progradational wedge truncated by an unconformity inferred to be caused by sea-level fall. Lower C-6-X progradational cycles above this unconformity are overlain by muddy Upper C-6-X retrogradational deposits. The C-5-X Member and the lower part of the C-4-X Member contain minor progradational cycles bounded by transgressive shales. In contrast, the Upper C-4-X Submember represents a major deltaic advance northeast of the LL-652 area. The Upper C-4-X Submember consistently exhibits excellent gamma-ray and resistivity responses, reflecting good reservoir quality and high oil saturation. Beginning with the C-3-X Member, there was a major retrogradational phase that

continued throughout deposition of the Lower Eocene. The sandstone-rich Middle C-3-X Submember represents a brief phase of deltaic offlap, but the majority of the sequences in the C-3-X, C-2-X, and C-1-X Members are shale-dominated, highstand-systems tracts.

Four stratigraphic cross sections (appendix D) across the LL-652 area exhibit lateral variability in stratigraphic sequences, continuous shale marker beds, and missing section due to faults. Large-scale stratigraphic sequences (for example, the Upper C-4-X Submember) and bounding shale markers are continuous across the field. However, there is much variability in individual sandstone thickness and log response reflecting facies variation within the sequences. Stratigraphic dip section E-E' (appendix D) shows up to 2,000 ft (610 m) of relief on the Eocene unconformity, which progressively truncates older section southwestward. In the northeast part of the LL-652 area, the lowermost B members and the C-1-X Member are preserved below the unconformity, whereas in the Maraven concession the unconformity truncates the C-2-X and C-3-X Members. There are multiple occurrences of missing section ranging from 150 to 550 ft (45.7 to 167.7 m) in the C-3-X and C-4-X Members in the LL-652 area.

Stratigraphic dip section J-J' (appendix D) shows only 800 ft (244 m) of relief on the Eocene unconformity and up to 200 ft (61 m) of the C-1-X Member is preserved below the unconformity in the Maraven concession.

Stratigraphic strike section 4-4' (appendix D) includes five wells that penetrate the C-7-X Member and shows the lateral extent of the unconformity at the base of the Lower C-6-X Submember. Additionally, the C members are also apparently thicker in the northwestern part of the section, but this is due to steeply dipping strata in the LL-1695 well and the deviated LL-1316 well. Because this strike section is proximal and parallel to a major northwest-trending fault in the eastern part of the LL-652 area, there is a continuous zone of approximately 1,000 ft (305 m) of missing section in the Lower B members and C-1-X Member. The Eocene unconformity also shows considerable relief and truncates more strata in the northwest than in the southeast, where strata as young as the B-6-X Member are preserved. Relief along this unconformity is much less (only 600 ft [182.9 m]) on stratigraphic strike section 11-11' (appendix D).

Seismic Stratigraphy

The C members contain three major seismic stratigraphic units (lower, middle, and upper) that correspond approximately to the C-5-X to C-7-X, C-3-X and C-4-X, and C-1-X and C-2-X Members, respectively (table III 1). Correlation of stratigraphic horizons to seismic reflectors

was in part based on projections between prominent seismic reflectors (Eocene unconformity, Guasare Formation) identified by Lugo (1991), and by use of synthetic seismograms.

The lower seismic unit consists of a 0.1- to 0.3-s zone of low- to moderate-amplitude reflectors that are irregular, wavy and discontinuous (fig. III 6). The lower unit represents multiple regressive/transgressive couplets in the C-5-X and C-6-X Members that are individually too thin to be resolved seismically. These reflectors overlie a high-amplitude, continuous pair of prominent reflectors that correspond to the Guasare Formation (Lugo, 1991), deposited on a mixed carbonate/clastic shelf (Gonzalez de Juana and others, 1980). The lower unit is overlain by a pair of moderate- to high-amplitude, semicontinuous reflectors that forms the base of the middle seismic unit (fig. III 6).

The middle seismic unit is defined as an upper pair of high-amplitude, continuous and parallel reflectors 0.15 to 0.20 s above a lower pair of moderate-amplitude, semicontinuous reflectors. Between these reflector pairs are low-amplitude, commonly inclined, and irregular reflectors (fig. III 6). The middle seismic unit corresponds roughly to the C-3-X and C-4-X interval, and represents a regressive/transgressive couplet (table III 1). The pair of high-amplitude, continuous reflectors that forms the upper bounding surface of the middle unit is the most distinctive seismic marker in the lower Eocene and is interpreted to represent a zone of high velocity contrast between the shaly C-3-X Member and the sandy Upper C-4-X Submember (figs. III 6 and III 7). The upper reflector in this pair represents an onlapping, marine-flooding surface that marks the onset of a major retrogradational sequence in the upper C members (fig. II 5). The marine onlapping surface merges updip (southwestward) with underlying low-amplitude clinoforms of a deltaic offlapping wedge in the C-4-X Member (fig. III 6).

The upper seismic unit (upper C members) represents a major retrogradational highstand-systems tract that onlaps southwestward over the regressive progradational cycles of the C-4-X Member. The Upper seismic unit consists of several, moderate-amplitude reflectors in a zone that is 0.20 to 0.25 s thick (table III 1 and figs. III 6-7). These reflectors have good continuity but are not as continuous as those in the middle seismic unit. The high-amplitude reflection in the upper seismic unit may correspond to widespread sandstones at the top of upward-coarsening sequences that represent a relatively high-velocity contrast with mudstones.

The Eocene unconformity is represented by a continuous, high-amplitude pair of parallel reflectors (table III 1) that merge with and are inferred to truncate underlying reflectors in the westward and southwestward direction (fig. III 6). In the LL-652 area, the lower B members are present below the unconformity but are absent west of the main fault along the concession boundary.

IV. STRUCTURAL INTERPRETATION

Fault-Surface Maps

Fault and folds play a significant role in the trapping of hydrocarbons in the LL-652 area and define reservoir boundaries. The preparation of accurate fault-surface maps required the integration of fault-surface maps with maps of several key structural horizons to determine the structural style.

The fault-surface map (fig. IV 1) was used to (1) aid in solving three-dimensional structural problems, especially to delineate complex fault patterns in the area, (2) define the location of the faults in both the horizontal and vertical dimensions, (3) supplement structure maps to accurately delineate the upthrown and downthrown fault traces in order to delineate the correct width of the fault gap or overlap, and (4) estimate the dip and strike (table IV 1) at any location along twelve normal faults and two trends of reverse faults in the study area. Neither minor faults, with displacement of 70 ft (21 m) or less, nor the two antithetic normal faults are included in this map because of poorly documented, fault-intersection data.

Paleostructural Map and C-3-X Structural-Top Marker

The net-thickness map of the interval between the Eocene-Miocene unconformity and the top of the C-3-X Member (fig. IV 2), shows 5 major and 8 minor thickness anomalies in the LL-652 area. The strongest anomaly is located along the Maraven boundary, and there are three others in the northern and northeastern part of the field as well as one in the south. This tendency is consistent with regional patterns where the number of anomalies increase northward, subparallel to the Icotea fault. Additionally, this map represents local scale variation and is consistent with the unrestored total isopach map (fig. IV 3) of the Eocene, although both show a strong anomaly on the east side of the Icotea and Block-1 master faults.

To further interpret thickness anomalies in the net-thickness map we constructed a paleostructural map (fig. IV 5). This represents the "structural map" or topography on the top of the C-3-X Member at the time of deposition of the La Rosa Formation. This map does not reflect any structural feature that affected the area after formation of the unconformity. The northern part of the field was persistently a complex structural area. There is also an elongate

anticline with a relatively high-dipping (20 degrees) northern and western limb and a gently dipping (6 degrees) southeastern flank.

The crest of the anticline is oriented subparallel to the eastern master fault, from the Maraven area in the southwest throughout the Lagoven concession in the north-northeast. The northern part has a crest with a N22°E strike and is offset 0.9 mi (1.5 km) from the main crest (N12°E).

Structural Cross Sections

Twenty-two structural cross sections were completed (fig. IV 5). All cross sections have a vertical exaggeration of 2:1 and do not represent the true attitude of the structure. However, they provide significant information to verify the existence of faults, relative changes in structural dip, stratigraphic discontinuities, folds and other important structural features.

After several stages of revision to improve the accuracy of the interpretation, the final cross sections agreed with the completed structural maps and seismic interpretation and conformed to the structural style of the LL-652 area. Twelve cross sections are included in this report to document the interpretation. These cross sections show that the youngest reverse faults offset the unconformity and truncate the oldest normal faults. The master fault also cuts the Eocene-Miocene unconformity. All the normal faults die below the unconformity, except the master fault, and some block rotation is associated with reverse faults.

Cross Section A

This cross section is located in the northern part of the field and shows the LL-1695 well in the downthrown block (high-dip zone) of the reverse fault (fig. IV 6). The LL-3250 well is located between two reverse faults in the upthrown block, and is intersected by the left reverse fault and has a repeat section of 190 ft (58 m). The LL-827 well is located in a structurally high position and has a repeat section of 120 ft (36.6 m) at the reverse fault. The lower part of the LL-827 well is in the downthrown block and shows a rotation and 54 degree dip from the dipmeter log.

The main normal fault located between the LL-827 and LL-2981 wells shows a throw of 400 ft (122 m); this fault may have offset Paleocene strata. The LL-2981 well is located in an isolated block and is separated from the LL-637 well by a fault that offsets the Guasare Formation. The C members are truncated progressively westward from the LL-627 well.

Cross Section B

Cross section B contains the VLA-744 well, with 300 ft (91.5 m) faulted out at the bottom of the C-2-X Member and top of the C-3-X Member (fig. IV 7). West of the VLA-89 well is the master fault with a throw of 800 ft (244 m). The LL-1089 well is faulted 150 ft (45.7 m) by the reverse fault at the level of the B-9-X Member. This well is located in the downthrown block in a high-dip zone. The LL-3144 well is located in an upthrown block bounded by the reverse fault in the east and a normal antithetic fault on the west. The LL-3141 well shows a missing section of 900 ft (274 m) in the B-8-X, B-9-X and C-1-X Members. The LL-1166 well is located eastward and is intersected by the main fault in the C-5-X Member and in the lower C-1-X Member by a secondary fault.

Cross Section D

Cross section D is a dip section that crosses the anticline from the west flank (VLA-598 and LL-857 wells, high-dip zone) to the east flank (LL-3249 well) where there is a gentle dip of only 5 degrees (fig. IV 8). The VLA-90 and VLA-931 wells are located in the upthrown block of the master fault; on the downthrown side the VLA-598 well is bounded by a reverse fault on the east. The B members are preserved in this well. The LL-857 well is intersected by the reverse fault in the C-1-X Member. The downthrown block is in the high-dip (38 degrees) zone, as interpreted from the dipmeter log of this well.

The LL-1803 and LL-3279 wells are intersected by minor faults and are located in the upthrown block bounded by two reverse faults. The LL-3267 well is intersected by a normal fault that cuts the top of the C-3-X Member and terminates in the shaly section of the C-2-X Member. The LL-3249 well is intersected by the master fault with a missing section of 1180 ft (360 m) in the B-8-X, B-9-X and part of C-1-X Members. The downthrown block of the main fault (on the east, LL-3249 well) and master fault (on the west, VLA-598) contains the important, oil-bearing B-6-X Member.

Cross Section F

This cross section contains the VLA-751 and VLA-28 wells that are located in the upthrown block of the master fault (north horst, Maraven reports) (fig. IV 9). The relative dip is low (6 degrees in the VLA-28 well) toward the east. The LL-917 well is located in an upthrown

block, bounded by two reverse faults. One of these faults cuts the well at the base of the C-5-X Member (8420 ft) with a repeat section of 110 ft (33.5 m). This well is also intersected by a normal fault in the C-2-X Member and exhibits 80 ft (24.4 m) of missing section.

The LL-1310 well is faulted in the Upper C-4-X Submember at 7580 ft with 80 ft (24.4 m) of missing section. The LL-866, LL-1106 and LL-1310 wells are located in a relatively undisturbed structural block with a low dip angle. The LL-1310 well is intersected by the central fault at 7580 ft at the top of the C-4-X Member with a missing section of 180 ft (55 m).

Cross Section G

Cross section G is located in the southern part of the field and includes the VLA-281 and VLA-724 wells (faulted in the Lower C-4-X Submember) that are located in the upthrown block of the master fault (fig. IV 10). The VLA-96 well is located in the upthrown block and is bounded by two reverse faults and is also cut by a reverse fault. The LL-1196 well is intersected by a reverse fault in the Upper C-2-X Member. The log response in this well clearly illustrates the reverse fault as it shows a good contrast in the repeat section. This well also is intersected by a normal fault at 7460 ft with a missing section of 60 ft (18 m).

Cross Section 4

(Fig. IV 11) illustrates a faulted anticline with the crest located in the LL-1095 well. In the northwest there is a relatively high dip and on the southeast a gentle dip. Between the LL-3204 and LL-3144 wells there is a trough associated with a fault. The LL-975 well is located in another fold towards the northwest. The LL-3204, LL-3144 and LL-1095 wells are bounded by two reverse faults. Both the LL-3204 and LL-1095 wells are intersected by these faults. The central part of the section shows the C-1-X Member truncated by the Eocene-Miocene unconformity, which shows a high degree of angularity. Toward the southeast the truncation is less and the B-9-X Member is present. The LL-1276, LL-847, LL-2942, LL-1198 and LL-1986 wells are located in the structurally simple part of the southeast limb of the anticline.

Cross Section 6

Cross section 6 (fig. IV 12) is important because it includes the LL-3282 cored well that shows a repeat section in the Lower Middle C-5-X Submember associated with the reverse fault.

Also, the LL-3301 well has a textbook example of a 90-ft (27.4-m) repeat section in the Middle C-3-X Submember. Figure IV 13 shows detailed correlations between this well and the LL-1782 well, located approximately 450 ft (137 m) southeastward from the LL-3282 well. The identical log response of this section is also present. The VLA-613 (fig. IV 13) well is one of two wells (the other is VLA 13) with missing section (± 1100 ft [335 m]) due to the eastern master fault in the Maraven area. Cross section 6 also shows a transverse view of the anticline, with the high-dip zone on the northwest flank and the gently dipping southeast flank. The VLA-564 well shows the B members preserved in the downthrown block of the master fault. The western reverse fault intersects the LL-857 well in the B-9-X Member, and the LL-3282, LL-1169, LL-3301 and LL-1782 wells are intersected by the eastern reverse fault with an average of 90 ft (27.4 m) of repeat section. The LL-852 and LL-2197 wells are located in the downthrown block of the reverse fault.

Cross Section 7

This cross section includes the VLA-90, VLA-862, VLA-882, and VLA-874 wells, located in a structural block on the upthrown side of the master fault (fig. IV 14). This simple structural block dips 6 degrees eastward and is bounded southeastward by the master fault. The VLA-534 well is located in a downthrown block between the master fault and a reverse fault. The LL-917 and LL-1303 wells are intersected by the reverse fault and located in the upthrown block between two other reverse faults. The LL-1245, LL-3074 and LL-833 wells are located in an undisturbed, 5 degree -dipping block (LL-833 dipmeter log).

Cross Section 8

This cross section shows the VLA-96 well in a upthrown block of the reverse fault. The LL-946 well has a repeat section (70 ft [21.3 m]) in the Middle C-3-X Submember (fig. IV 15). The LL-3260, LL-1124, and LL-1010 wells are located in a 6 degree -dipping block with a minor fold. The best evidence of the unconformity offset by a reverse fault is shown between the LL-946 and LL-3260 wells.

Cross Section 9

Cross section 9 is located in the northern fold and shows the VLA-105 and LL-975 wells in the southwest flank of the fold, dipping 25 degrees (LL-975 dipmeter log) in the same direction (fig. IV 16). The LL-3250 and LL-2946 wells are located in upthrown block, bounded by two reverse faults. This block is the structurally highest in the field. The LL-846 and LL-450 wells are located in the same adjacent structural block, where the LL-846 well has a 20-degree dip, indicated from the dipmeter log. This block is extremely important for new well locations, as will be discussed in a latter section of this report (production and new development opportunities).

Cross Section 12

Cross section 12 shows a general picture of the structural complexity in the whole study area (fig. IV 17). It spans an area from the southwest in the Maraven area, that includes the VLA-281, VLA-66, VLA-777 and VLA-28 wells, bounded by a minor fault in the upthrown block of the master fault to the LL-907, VLA-534, LL-3186, LL-103 and LL-3056 wells associated with several normal and reverse faults. It also includes the LL-1095 well located on the crest of the anticline and intersected by the reverse fault, and the LL-1209 well, intersected by two faults. It also shows downthrown B members preserved from erosion in the northeast block.

Cross Section 16

This cross section shows the main fault (fig. IV 18). On the southwest the LL-3235, LL-971, and LL-2425 wells are located in the upthrown block of the fault. This block shows an apparently high dip in the section, but the real dip is 6 degrees to the southeast (dipmeter log of LL-895 well). The LL-2191 well is offset 1,000 ft (305 m) by a fault in the C-1-X and C-2-X Members. The LL-1258 well is located in the downthrown block and shows, in correlation with LL-2191 well, preservation of the B members (from B-9-X to B-5-X) whereas in the upthrown block the B-5-X, B-6-X, and B-7-X Members are eroded and the B-8-X Member is truncated.

Seismic Sections

In the LL-652 area, seismic data were used to further delineate the major faults and folds and provided general support for projection of the structural framework into areas with poor well control in the northern part of the field. Five seismic sections were selected (fig. IV 5) for structural analysis. Four seismic reflectors (Eocene unconformity, Guasare formation, Socuy Member and C-3-X/C-4-X interval) were selected to document the regional structural framework. The Eocene-Miocene unconformity is represented by two continuous, high-amplitude parallel reflectors that truncate underlying reflectors in the B and C Members. The Guasare Formation is represented by a high-amplitude, continuous pair of prominent reflectors. One high-amplitude, continuous reflector corresponds to the Socuy Member, which is overlain by three (0.15 s thick) moderate- to high-amplitude, semicontinuous reflectors that represent the Cretaceous limestone that overlies the uncommercial basement. The middle seismic unit in the Eocene (between the unconformity and the Guasare Formation) corresponds to the C-3-X and C-4-X Members and represents a pair of high-amplitude, continuous reflectors. These reflectors are the most distinctive seismic markers in the Eocene, and represent a zone of high-velocity contrast between the shaly Lower C-3-X Submember and the sandstone-rich Upper C-4-X Submember.

Seismic Line CO-90B-28

The northwest part of this line shows the typical profile of the Icotea fault (fig. IV 19). It is an elongate anticline bounded longitudinally by upward- and outward-divergent strands of a wrench fault that has mostly reverse separation (Harding, 1985 and 1990). The fault splays upward from the basement, deforming the Cretaceous to Eocene section below the unconformity. The lower part of the post-unconformity sequence is also offset, but is related to later reactivation that also deformed the LL-652 area (Lugo 1991).

At SP-345 (central part of the line) there is a normal fault with 0.25 s of throw. This fault offsets the whole section and represents the master fault in the study area. A low-angle reverse fault at SP-330 offsets the basement and has associated secondary reverse faults that offset mainly Cretaceous and Paleocene strata. There is a reverse fault that offsets only the Eocene at SP-270.

The LL-450 well is located at SP-260 on line CO-90B-28. This well was drilled to the C-2-X Member. However, underneath there is a closed fold that disrupts the C-3-X/C-4-X reflectors. This interpretation is also supported by structural cross section A (fig. IV 6), which

shows a fold between the LL-846 and LL-450 wells. Both elements of interpretation coincide and confirm this as is the continuation of the north fold. Structural heterogeneity in the northern part of the field caused by this fold should justify further development.

Seismic Line CO-90B-30

This line is parallel to the CO-90B-28 line (fig. IV 19) and also shows a profile of the positive flower structure in the Icotea fault, where the unconformity is most deformed (fig. IV 20). At SP-320 the master fault cuts the entire sequence. The LL-1293 well (SP-235) is located on the downthrown side of the reverse fault that offsets the basement (where there is a detachment surface) up to the Eocene sequence. This is confirmed by the dipmeter of the same well that shows a 47-degree dip in the C-4-X Member. The LL-2946 well (SP-260) is located westward of the structure and is bounded by two reverse faults. The LL-2981 well (SP-235) is located in the downthrown block of a reverse fault. This block shows an apparent dip toward the LL-637 well (projected at SP-185), which is located down-structure in the southwest. This line is subparallel to structural cross section A (fig. IV 6). Two minor normal faults bound the LL-2981 well in the structural cross sections. However, the presence of these faults is questionable because of the poor vertical resolution of the seismic data, especially of faults of small throw.

Seismic Line CO-87B-27

This line is a north-northwest (Maraven area) to south-southwest section that shows the VLA-534 well (SP-85), located on the downthrown side of the master fault that offsets the whole section from the basement to the unconformity (fig. IV 21). At SP-80 there is a reverse fault. The LL-917 well (SP-125) is located in an upthrown block bounded by two reverse faults. This area contains several splinter reverse faults. For example, well LL-917 is intersected by a normal fault in the C-2-X Member and a reverse fault in the C-6-X Member. The LL-1303 well (projected to SP-140) is intersected by the reverse fault that was earlier recognized in log correlations where 130 ft (39.6 m) of repeat section was noted in the C-3-X Member. The LL-1245 and LL-2547 wells are located in an area where the seismic resolution is poor. Between SP-190 and SP-260 there are two thrust faults that offset Lower Eocene, Paleocene and Cretaceous strata. This seismic line is parallel to structural cross section No. 7 (fig. IV 14) where there are several major structural features that include reverse faults intersecting the LL-917 and LL-1303 wells. In contrast, the LL-2547 well is in an unfaulted block.

Seismic Line CO-87B-72

This line (fig. IV 22) is a southwest-northeast seismic profile that transversely crosses the southern part of the master fault and terminates at the main fault in the east. The VLA-761 well is located in the upthrown block of the master fault. A reverse fault that offsets the entire sequence is located at SP-940. To the right are two reverse faults that cut only Paleocene and Eocene strata. The LL-1001 well (SP-890) is also cut by a reverse fault that has 180 ft (54.9 m) of repeat section. The LL-833 well is located in a structural block, bounded by a fault (probably the central fault) toward the northeast. Cretaceous strata in this area are offset by reverse faults. The LL-895 well (SP-650) is located on the upthrown block of the main fault.

Seismic Line CO-87B-76

This section (fig. IV 23) is intersected by lines CO-87B-27 (SP-635) and CO-90B-30 (SP-435) (fig. IV C1). The VLA-751 well is located in the south horst of the Maraven area (Maraven reports). The VLA-53 well (SP-85) is located in a downthrown block, between the master fault on the southwest and a reverse fault on the northeast in a structurally complex zone. The LL-1169 well (SP-590) is located in the area of reverse faults. This well has a repeat section of 60 ft (18 m) in the C-4-X Member. The LL-2937 and LL-2942 wells have a repeat section of 60 ft (18 m) in the C-4-X Member. The LL-2937 and LL-2942 wells are located in the upthrown block of the main fault (SP-520). This fault intersects the LL-2901 well (1180 ft [360 m] of missing section in B and C Members).

Dipmeter Analysis

The 47 dipmeter logs available in the Lagoven area and 32 in the Maraven area (fig. IV 5) provided a large data base for dipmeter analysis. All the dipmeter interpretations (appendix XIII A) were incorporated in the seven structural maps (see figs. IV 29 through 35 presented later in this chapter), however, no dipmeter data were available for the C-7-X Member. The dipmeter analysis was of major importance in the calculation of dip and strike, in helping to identify areas with major dip changes in the northwest part of the field, and in the quantification of fault and fold attributes.

Identification of folded and faulted areas is useful for targeting sites for further field development. For example, the LL-827 well in structural cross section A (fig. IV 6) is in a

structurally complicated zone that has a 54-degree southeast dip associated with the reverse fault and another minor normal fault. The LL-1169 well is located in section 6 (fig. IV 12); the dipmeter log of this well indicates dip changes in all members along the crest of a small fold near reverse faults that intersect the C-4-X Member.

LL-1310 Well

The LL-1310 well (fig. IV 24) exhibits a missing section of 180 ft (54.9 m) in the C-4-X Member. The dipmeter log of this well shows a normal-trending dip of 3 degrees (azimuth 80°) in the Upper C-3-X Submember. Dip gradually changes in the Middle C-3-X Submember and finally reaches the highest value of 12 degrees (azimuth 210 degrees) in the drag zone, below which the fault zone is present. Below is the normal dip of 3 degrees (azimuth 85 degrees) where this well is located.

LL-1293 Well

Figure IV 25 shows part of the Lagunillas and La Rosa Formations having an average dip of 4 degrees. Below, separated by the Eocene unconformity, the B-9-X and C-1-X Members have an average dip of 28 degrees. The correlation between the LL-1293 and LL-3250 wells (fig. IV 26) in the C-4-X Member illustrates the use of a dipmeter log to aid in determining true stratigraphic thickness compared to true vertical thickness (LL-1293 in high-dip [45°] zone). Figure IV 26 also illustrates the difficulty in correlating the high-dip zone in structurally complex areas.

VLA-724 Well

This well is faulted in the Lower C-4-X Submember at 6800 ft and has 100 ft (30.5 m) of missing section (fig. IV 27). The dipmeter log of this well shows a structural dip that increases from 6 degrees to 12 degrees adjacent to the fault in the footwall block, an erratic distribution in the faulted zone at 6800 ft and the drag zone of the other block, and finally the normal dip of ± 5 degrees. The transverse section shows the interpretation and the drag zone in the upthrown (6850-6950 ft) block, the drag zone in the downthrown block (6650-6775 ft), and in the faulted zone (6775-6850 ft).

LL-1095 Well

Figure IV 28 illustrates the correlation in the Middle to Lower C-4-X Submembers and C-5-X Member between the LL-1095, LL-3286 and LL-3055 wells. Below the top of the C-5-X Member there are few thickness changes. The LL-1095 well shows a slightly thicker section in the C-4-X Member as well as a repeat section (± 90 ft [27.4 m]) by reverse faulting at the top of the C-5-X Member. Above the top of this member the dipmeter log shows dips over 35 degrees, and below, average dips of only 6 degrees.

Another well with the same dipmeter response to a reverse fault is the LL-946 well that is faulted in the C-3-X Member and exhibits a maximum dip of 53 degrees in the upthrown block and 10 degrees in the downthrown block. This is a typical dipmeter response in the LL-652 area in beds cut by reverse faults where the dip of the beds reaches a maximum dip on the upthrown block, indicating a drag zone and drop to lowest values in the downthrown block.

Fieldwide Structural Maps

Structure plays a significant role in the trapping of hydrocarbons in the advanced stages of development and depletion of the field, especially in the C-4-X Member, which includes the main reservoir. The integration of all the previous structural data as fault-surface maps, structural cross sections, paleostructural maps, seismic interpretations, dipmeter analyses and structural tops allowed the mapping of the important horizons that include the Eocene-Miocene unconformity, and tops of the C-1-X, C-2-X, C-3-X, C-4-X, C-5-X, C-6-X, and C-7-X Members (figs. IV 29 to IV 36).

The structural map of the Eocene-Miocene unconformity indicates a gentle dip to the south-southwest (3 to 8 degrees). The western part of the study area shows that post-unconformity deformation increases slightly northward and was caused by the northwest-southeast compression after the unconformity, reflected by the north-northeast-trending reverse faults.

From the C-1-X to the C-7-X Member the maps show similar trends in the central and southern parts of the field. The main north-northeast-trending, elongate anticline has a steeply dipping (25-degree) west-northwest limb and a gently dipping (5-degree) southeast limb. The crest of the anticline is deformed by subparallel reverse faults. The reverse faults have a N12°E strike in the central part and N5°E in the southern part of the field. The anticlinal crest in the central part of the area is in the vicinity of the LL-1095 well (concession A-225).

The crest of the "north fold" has a strike of N40°E, with a northwest-dipping flank and 7-degree dipping flank to the southeast. The crest of this fold is located between the LL-2946 and LL-827 wells and is offset 0.9 mi (1.5 km) from the crest of the main anticline. The area between the two crests (fig. IV 31) is the most structurally complex in the field because (1) local structures are discontinuous and untraceable across the reverse faults, (2) it is associated with a reactivation zone between the main fault and the reverse fault, (3) three fault patterns are present in this area, where some displacement was transferred to other faults or folds at terminations against other faults, (4) abrupt dip increases occur in the upthrown block of the reverse fault, and (5) it is associated with the two antithetic faults.

The structure maps, supported by seismic lines CO-90B-28 (fig. IV 19), CO-90B-30 (fig. IV 20) and structural cross section 9 (fig. IV 16) clearly show that the "north fold" continues to the north-northeast. In areas affected by the reverse fault the dipmeter response is erratic, with dips in several directions.

The C-1-X Member (fig. IV 30) shows a continuously steep slope toward the crestral high with flattening of dip, indicating that this member was deeply eroded over the whole area, especially on the crest of the main anticline and the north fold. In the Maraven area the C-1-X Member is absent in the central and southern part and is truncated in the north. The C-2-X Member is eroded in the southern part of the Maraven area. A mapping problem with the construction of the reverse fault overlap is overlap in structure contours. Confusion is eliminated by dashing a line parallel to the fault on the upthrown block, indicating a zone of fault overlap.

Several normal faults and one zone of reverse faults are present in maps of C-1-X to C-7-X Members. The study area was divided into 8 fault-bounded zones (fig. IV 30). Zone I is located in the northeast part of the study area in the downthrown block of the north reverse fault and the main fault. This zone is in part the continuation of the "north fold" toward the northeast. Zone II is the upthrown block between two reverse faults in the north crest of the "north fold". Zone III is located in the western, high-dip flank in a downthrown block between a reverse fault on the east and the master fault on the west. Zone IV is the central part of the area bounded by two reverse faults in the east and west, an antithetic fault in the north and the central fault in the south. Zone V is located in a structurally simple area, bounded by the main fault in the north, central fault on the south and a reverse fault on the west. Zone V is the largest and most productive area in the field. Zone VI is located in the southwestern part of the field and is associated with the reverse fault and the master fault. Zone VII is located in the southeastern part of the study and is bounded by the central fault to the north, the south fault to the south and the reverse fault to the west. Zone VIII is located in the Maraven area and can be divided into several subzones because it is so large. However, it was not divided into subzones because it is west of the LL-652 area.

Fault Analysis

The LL-652 area contains multiple fault patterns that reflect a multistage tectonic history. Because of the structural complexity, all available data were used to characterize the field. Net-thickness maps of key intervals as well as subcrop maps were made to best evaluate the structural heterogeneity and fault history.

Net Thickness of C-3-X Member

Net-thickness of the C-3-X Member was mapped to evaluate syndepositional tectonism because (1) the C-1-X and C-2-X Members were truncated on the western side of the master fault, and (2) forty percent of the wells are not deep enough to entirely penetrate the C-4-X Member. The net-thickness map of the C-3-X Member (fig. IV 37) reflects the general northeast-trending depositional patterns. East of the master fault is a constant increase in thickness toward the north, from less than 500 ft (152 m) in the south to more than 650 ft (198 m) in the north. On the western side of the master fault thickness varies from less than 500 ft (152 m) in the south to 590 ft (180 m) in the central part of the field, and less than 500 ft (152 m) in the north. These two net-thickness trends are different on either side of the master fault, reflected by an abrupt increase in interval thickness along the downthrown side of this fault, especially in the north part of the field. These variations can be explained by either deposition controlled by syntectonic growth faults or strike-slip fault movement. Syntectonic deposition could have produced a rollover anticline associated with a normal listric growth fault as a result of bending of the hanging-wall fault block as it conformed to the curve of the fault (Harding, 1979). However, this theory is problematic in that the majority of growth faults dip toward the basin and are parallel or subparallel to the coastline. The master fault is also associated with net-thickness changes in the northern part of the field, away from the southern depocenter where such net-thickness changes would be expected. Strike-slip movement could also have occurred, because lateral displacements may juxtapose dissimilar stratigraphic sequences as observed in the LL-652 area. Strike-slip tectonics can also be inferred from anomalous variations in the amount of stratigraphic separation across the fault profile (Harding, 1985). A credible identification of strike-slip faults requires several combinations of profile and map criteria in regional areas (Harding, 1990) and should be confirmed with other criteria that refute alternative interpretations, but they are beyond the scope of this study.

Subcrop Map

A subcrop map of stratigraphic intervals below the Miocene unconformity (fig. IV 38) exhibits erosion of the B Members along the crest of the anticline in the north fold and in the main anticline to the south fault. On the limbs of the anticline there is a gradual truncation of the C-1-X Member, and the B members appear away from the crest. On the downthrown side of the main fault the B-9-X to B-4-X Members were not eroded. Also in the high-dip zone, the B Members were preserved downthrown of the master fault in the central and northern parts of the fields.

In the Lagoven concession erosion was controlled by normal faults. Greatest erosion occurred in the Maraven area. The degree of erosion increases from north to south; in the north, only the B-9-X Member is preserved and in the south the C-3-X Member is truncated. On the east side of the master fault all the normal faults control the degree of erosion and truncation between individual blocks, but on the west side, the normal faults do not control the degree of erosion and truncation between blocks.

The reverse faults represent the youngest deformation in the area and do not control the degree of truncation between individual blocks. This is evident in the southern and central part of the study area, where there are few important differences between the downthrown and upthrown block of the fault, where normally the same member is present. However, in the north fold there is a marked difference in thickness of preserved section between the central upthrown block where the C-1-X Member is truncated and the downthrown block, where normally the same member is present. This is an important indication of reactivation of two reverse faults along the previous normal faults. The paleostructural map of the C-3-X Member (fig. IV 4) reinforces this interpretation and shows that the main fault is continuous northward, where it changes strike in concession A-224 and formed a reactivation surface for the eastern reverse faults.

Fault Characteristics

Tectonic Features in Cores

The structure map on top of the C-3-X Member (fig. IV 32) shows the location of the 8 cored wells in the LL-652 area. Tectonic features from cores are summarized in table IV 2. Tectonic features include microfaults, fractures, fault breccia, and faulted zones.

Microfaults are present in the C-3-X to C-7-X Members in all the cored wells, except in the LL-846 well, which contains most disrupted core in this study. Figures IV 39a and b show an example of a normal microfault (8826 ft) and a reverse microfault (8952.5 ft), respectively, in the LL-3080 well. Another example of a normal microfault is at 7737.5 ft in the LL-3074 well (fig. IV 39d).

There are excellent examples of fractures in the C-3-X to C-7-X Members in the LL-2850, LL-3074, LL-3075, LL-3080, LL-3140 and LL-3282 wells. The LL-3282 well has the greatest abundance of fractures, followed by the LL-3140 well. Figure IV 40 shows examples of fractures in the LL-3140 well (9,075 ft and 8,902 ft), LL-3074 well (7,752 ft), and multiple combinations of fractures and microfaults at 7,429 ft in the LL-2425 well.

Zones of fault breccia occur at 9,036 ft and 9,168 ft in the LL-3140 well (fig. IV 39c). The breccia may be associated with minor faults not recognized from well correlation. There are also tectonically disrupted beds at 9,175 ft in this well.

The LL-3282 well represents the best example of a faulted zone (45 ft [13.7 m] thick) in the C-5-X Member (fig. IV 41). The log response is anomalous, showing a 90-ft (27.4-m) trend (from 8090 ft) of low resistivity with a reading of 6 ohm-m (shallow) and 10 ohm-m (deep) resistivity as an excellent example of fluid invasion in a fracture zone, with indications of pervasive fractures. The GR log shows an average, almost unvarying trend of 75 API, caused by an effect that reflects nearly vertically tilted beds associated with a reverse fault (fig. IV 41). The cored section in the LL-3282 well has other zones with tectonic features such as beds tilted 30 degrees (8,095 to 8,170 ft), 10-15 degrees (8,074 to 8,078 ft) and an intensely fractured zone (8,115 to 8,134 ft). The zone may represent post-depositional tectonism where a reverse and normal fault intersect in the area of the LL-3282 well.

Fault-Seal Analysis

Criteria for analyzing fault seals are based mainly on theoretical studies of rock types juxtaposed at faults, as illustrated in Figure IV 43 (Smith, 1980). Additionally, Bouvier and others (1989) empirically derived the variation in clay-smear potential across the fault surface by relating clay source-bed thickness and position of clay source-beds to the displacement at a given point on the fault surface, thereby extending fault-sealing characteristics beyond simple sand-to-shale juxtaposition. Field studies indicate that complete smearing on fault surfaces may extend down fault planes from shale footwall-cutoffs for distances equivalent to at least six times the thickness of the shale source layer. Lehner and Pilaar (1974, personal communication with Bouvier) observed that clay gouges in shear zones of faults (1) originated from both the upthrown and downthrown sides of shale source beds, (2) decreased in thickness away from source beds, and (3) coalesced from separate source beds to form one multilayered clay gouge. Additionally, thick shale source beds provided longer, more continuous clay gouges than thin source beds.

Two variables must be assessed when evaluating fault-plane seal: (1) juxtaposition of lithology, and (2) clay smear. Figure IV 43b is a diagrammatic illustration of these variables showing sandstone juxtaposition but separation by a clay-filled fault zone about 3 ft (0.9 m) wide. These variables for the evaluation of fault seals in hydrocarbon traps, as outlined by Smith (1980) and Bouvier and others (1989), are static geometric criteria (Harding and Tuminas, 1989). However these criteria are limited because dynamic phenomena such as the relative rates of migration into a trap versus rates of leakage out of the trap or production were not considered.

The probability of faults acting as pressure barriers is important in infield development and production, where fault-bounded compartments may not be in pressure communication. The best way to verify communication between individual blocks is with pressure data. Knott (1993) presented criteria for identifying whether a fault is sealing, based on pressure and fluid (hydrocarbon type and hydrocarbon-water contact) data from the North Sea.

The pattern of map-scale faults is known in the LL-652 area, but data are sparse on rock material in fault zones and associated features in cores near faults. To determine local pressure-sealing versus non-sealing cutoff values, individual pressure values must be calibrated against known trapped hydrocarbons in sandstone-to-sandstone windows along fault planes. The repeat-formation-tester (RFT) pressures measured in the seven development wells (table IV 3) provides calibration and pressure evaluation and is a test for the presence of differential pressures across fault planes.

In the LL-652 area seven RFT's (table IV 3) were run between March 1991 and May 1992 in the LL-3141, LL-3173, LL-3186, LL-3195, LL-3260, LL-3261, and LL-3263 wells to

identify possible stratigraphic controls on pressure values. The RFT device provides a resolution of 1 psi, with a 2-percent error (Schlumberger, 1980). The most-productive three intervals (Middle C-3-X, Upper C-4-X and Upper C-5-X Submembers) were analyzed in conjunction with facies and permeability maps. All RFT data were set for the same datum (7300 ft for the C-3-X and C-4-X Members and 7900 ft for the C-5-X Member) to make a direct comparison between values. As a result of these comparisons, 130 psi was determined as the minimum pressure differential between two wells in the same zone to infer reservoir compartments.

Middle C-3-X Submember

The LL-3173 (fig. IV 44) well is not in complete communication with the LL-3195 well because it contacts a tidal-ridge deposit lateral to a distributary-channel deposit (see also fig. VI 26). Figure IV 44 shows a cross section between the LL-3173 and LL-3195 wells where the log response is upward-coarsening to serrate in the LL-3173 well and the permeability is 39 md and the average pressure is 2314 psi. The LL-3195 well in the Middle C-3-X Submember has an upward-fining to serrate log response and 192 md permeability and 2196 psi pressure. The contrast in log response and permeability is reflected in a 118-psi difference in pressure between the wells.

Upper C-4-X Submember

In the Upper C-4-X Submember the LL-3173 and LL-3195 wells contact different dip-elongate tidal-ridge sandstones that are separated by a narrow (less than 500 ft [152 m]) band of muddy interr ridge deposits (see also fig. VI 22). The permeability values are similar between the LL-3195 well (180 md) and the LL-3173 well (140 md), but they have a 206-psi pressure difference (fig. IV 44). Thus, even though both wells encounter permeable sandstones in the Upper C-4-X Submember, there are interwell heterogeneities (interridge clay laminae) that reduce interwell hydraulic communication.

Upper C-5-X Submember

Three wells (LL-3186, LL-3195, and LL-3261) contact tidal-ridge sandstones in the Upper C-5-X Submember (see fig. VI 30). The LL-3195 and LL-3261 wells intersect axial parts of a tidal-ridge sandstone, whereas the LL-3186 well is in a muddy interr ridge area. Figure IV 45

shows a cross section incorporating these wells, where the log character indicates two upward-coarsening to serrate sandstones in the LL-3261 well with 4.6 md of permeability (fig. IV 45) and 1915 psi of average pressure. The log response in the LL-3195 well is also upward-coarsening in 5 md permeability sandstone and 1767 psi pressure, with 148 psi of pressure differential between the two wells.

The low value of differential pressure (118 psi) in the Middle C-3-X Submember was expected because of good lateral continuity of sandbodies in this interval. In contrast, the high pressure differential (206 psi) in the Upper C-4-X Submember (fig. IV 44) is due to lateral restriction in hydraulic communication between the LL-3173 and LL-3195 wells, which are separated along depositional strike by interr ridge mudstones.

Figure IV 45 shows the fault between the LL-3261 and LL-3195 wells. The LL-3261 well is located on the downthrown side of the fault and tested 1702 psi in the Upper C-4-X Submember, which is juxtaposed at the fault surface against the Middle C-4-X Submember in the upthrown block of the fault. The Middle C-4-X Submember was measured at 1503 psi in the LL-3165 well. Also the Lower C-3-X Submember was measured at 2314 psi in the LL-3261 well. This zone is juxtaposed against the Upper C-4-X Submember in the LL-3195 well with a pressure of 1575 psi; there is a difference of 739 psi between these two zones. We conclude that both pressures are high enough to consider sealing in this area.

The LL-3186 and LL-3261 wells are separated by two reverse faults (fig. IV 45); both wells are located in downthrown blocks. The individual pressures between juxtaposed sandstones show sealing in these two faults in the C-3-X and C-4-X Members. Figure IV 46 shows a structural cross section between the LL-3263 and LL-3141 wells. The LL-3286 well was also included to document the relative dip in this area. The reverse fault (#13) in this area has 80 ft (24.4 m) of throw. The Upper Middle C-5-X Submember in the LL-3263 well, located on the upthrown side of the fault, has 2787 psi average pressure and is juxtaposed at the fault surface against the Upper Middle to Upper C-5-X Submembers in the LL-3141 well that was tested with an average pressure of 2358 psi, indicating that there is 428 psi of pressure difference between the two blocks. The LL-3263 well has a pressure of 1752 psi in the Upper C-4-X Submember and the LL-3141 well has a pressure of 1960 psi. This represents a 208-psi difference and therefore we conclude that the fault is sealing.

Another method to evaluate fault seal is to compare historical trends in pressure between fault blocks. As shown in Figure IV 47, this was made by selecting three wells (LL-1310, LL-3038 and LL-866) in the downthrown block (C-4-X.01 reservoir) of the central fault and three wells (LL-1245, LL-1103 and LL-1176) in the upthrown block (C-4-X.03 reservoir) of the fault. The pressure data for the C-4-X.01 reservoir prealigned on a linear trend while in the C-4-X.01 reservoir the distribution is more erratic. However, the pressure-decline trend, although parallel

between the two reservoirs, is offset by 1100 psi in pressure, implying no communication across the fault seal.

Three sealing faults have been identified in the LL-652 area: the reverse #13 (fig. IV 33), the central fault (#6) and fault #4. To extrapolate to the rest of the field, we applied a parameter used by Knott (1993) for reservoirs in the Brent Group in the North Sea. This parameter is called "maximum fault throw versus reservoir thickness." Knott (1993) demonstrated that sealing is proportional to fault throw, normalized as a fraction of reservoir thickness. He also concluded that with faults with throws greater than reservoir thickness, there is a better-than-90-percent probability of sealing (fig. IV 48). These types of faults were interpreted as extrareservoir faults, and the seal is primarily by juxtaposition of different rock types. For example, because the C-3-X Member is 560 ft (171 m) thick, the C-4-X Member is 600 ft (183 m) thick, and the C-5-X Member is 550 ft (168 m) thick, therefore in the LL-652 area there are probably only three extrareservoir faults, as shown in table 4.

The relation of member thickness to fault throw was plotted for each member (table IV 4). In comparison with the C Members, the Brent Group is thinner. As was expected, the three faults have a 90-percent probability of being sealed. Structural cross section 16 (fig. IV 18) shows an excellent example where the LL-1258 well, located in the downthrown block of the main fault, shows a shaly section (± 700 ft [213 m] thick) of the C-2-X Member juxtaposed against the Middle and Lower C-3-X Submembers. The Upper C-4-X Member, located in the upthrown block that includes the LL-2191 well, has a missing section (main fault) of 1000 ft (305 m) in the C-2-X Member.

For other faults, a method based on part b of Figure IV 48 (intrareservoir faults) was used where the fault throw is less than the average thickness 570 ft (174 m) of the C members. The results are in the table IV 4, along with an estimate of the probability of the fault providing a seal. The three faults inferred to be sealing by pressure analysis show a fault-seal probability (FSP) between 28 and 33 percent. A major conclusion that can be drawn from this observation is that different fault-sealing mechanisms are present and that it is difficult to determine the relative importance of each with only static geometric criteria like clay-smear potential (Bourier 1989) instead of dynamic pressure measurements. Finally, the most probable sandbody architecture for combined vertical and lateral seal is a top seal formation that is thicker (shaly section of C-1-X/C-2-X Members) than the magnitude of the fault displacement to provide both vertical and lateral seals.

Fault Compartment Geometries

The LL-652 area is divided into several fault-sealed compartments that in conjunction with structural closure provide the trapping mechanism. For example, the paleostructural map (fig. IV 4) shows that the north fold is structurally complex and separated from the main anticline, and structural cross section 12 (fig. IV 17) shows the intensity of compartmentalization due to faulting. The division of the field into eight zones (fig. IV 30) is defined by the fault-sealing probability and the pressure analysis.

Compartment I is isolated from other compartments by the northeast-trending reverse fault (90 percent fault seal probability), and the main fault (90 percent FSP). On the northeast this compartment is bounded by fault no. 1, which has a 33 percent probability of being a seal. Southeastward, the limit is an oil-water contact, whereas the northern limit is unknown.

Compartment II is bounded on the east and west by reverse faults (each 90 percent FSP) and on the south by the number 8 fault (49 percent FSP). In contrast, the northern limit is unknown.

Compartment III is located in the high-dip limb of the anticline and is bounded by two sealing faults—the master fault (90 percent FSP) and the northwest reverse fault (90 percent FSP). Internally, this zone is divided into three smaller compartments.

Compartment IV is bounded by two reverse faults—a northwest reverse fault with 90 percent FSP and the east-central reverse fault with 28 percent FSP. This fault was analyzed with RFT pressure data and was inferred to be sealing. The southern boundary of this compartment has only a 33 percent probability of FSP but is sealing according to the pressure history in both fault blocks. To the north the limit is an antithetic fault (8) with 49 percent probability FSP. Also, this compartment occurs on the crest of the main anticline.

Compartment V is located in an unfaulted area and represents the best zone of production and reserves. This area, recommended for a pilot waterflood project, is bounded by three sealing faults—the main fault, fault 13, and the central fault. Internally this compartment has two minor faults that pinch out downstructure.

Compartment VI is located in the ridge-crestal area south of the anticline and is bounded by the master fault, the central fault, the south fault, and fault 16. Half of this compartment is located in the Maraven concession and the other in the Lagoven concession and represents the only compartment where C Members have been tested and produced on the downthrown side of the master fault (VLA-96 and VLA-68 wells). This compartment is very complex because it is intersected by several reverse faults.

Compartment VII is bounded by the central fault (33 percent FSP), the southeast reverse fault (28 percent FSP) and the southern fault (90 percent FSP). This compartment is divided by fault no. 7 (28 percent FSP) in two smaller compartments.

Compartment VII is in the Maraven concession and consists of several smaller compartments in the upthrown block of the master fault. The reverse faults control reservoir compartmentalization in the LL-652 area, as they define these seven compartments. Compartments II, III, IV and V occur in the C-4-X.01, C-5-X.02, and C-6-X.01 reservoirs. Compartments VI and VII are in the C-4-X.03, C-5-X.08 and C-6-X.16 reservoirs. Distribution of these compartments is crucial to the viability of prospects. However, seals along normal faults are more variable and commonly less effective than seals along reverse or strike-slip faults, which may be a consequence of the more common formation of fault-parallel extension fractures associated with normal faults (Harding, 1989). The best examples of fractures in cores in the LL-652 area are associated either with normal faults (LL-3140 well) or reverse faults (LL-3282 well). This means that fluid flow may occur along a temporary sealing fault as the result of increased pressure differential from production on one side of a fault block.

Structural Style

The differentiation of structural styles in local areas can be difficult and imprecise because a particular structural characteristic may have several tectonic origins. Often the most reliable and direct basis for identifying the styles is to determine the type of slip (reverse, normal, or strike) of the dominant faults (Harding, 1985). Identification includes the recognition of key structural elements such as en echelon folds and faults, trap-door blocks, critical differences in local trends, and regional structural patterns.

It was also necessary in the analysis to consider both cross section and map characteristics, especially of the master fault and reverse faults where styles appeared similar in profile, but where their structures had distinctly different areal distributions. This provided a clue for the configuration of the assemblage style.

The style of faulting in the LL-652 area is complex because of the combination of strike-slip movements, and major extensional, compressional, and transpressional events. The master fault, main fault, northwest-trending normal faults, north fold, and main anticline are structures associated or related with the wrench system of the Icotea fault. The north-northeast-trending reverse faults make up a structural style associated with the regional east-west compression in late Pliocene to Holocene time (Lugo, 1991). Finally, the overprints of several structural styles in the area, especially in the northern part of the field, resulted in complex patterns a second-

order or antithetic fault system having a transverse orientation with respect to the normal style of the area.

V. DEPOSITIONAL SYSTEMS

This section presents and discusses the tide-dominated deltaic facies model of the C Members in the LL-652 area. Tide-dominated deltaic reservoirs differ from fluvial- and wave-dominated types of deltaic reservoirs in that (1) the geometry of delta-front sandstones is both dip-elongate and dip-parallel, (2) the sandstones are extremely heterogeneous because of the high degree of interbedded mudstone, and (3) as a consequence of (1) and (2), tide-dominated deltaic reservoirs typically have a low recovery efficiency and therefore a high potential for secondary oil recovery.

Facies Model

The depositional model of the C Members in the LL-652 area consists of dip-elongate, distributary- and tidal-channel sandstones that merge northeastward with extensive, dip-parallel delta-front sandstones in a tide-dominated (fig. V 1). Channel-mouth bar sandstones, volumetrically unimportant compared to distributary-channel and delta-front sandstones, occur at the distal (northeast) terminii of the distributary-channel sandstones.

Muddy, non-framework facies separating reservoir sandstones consist of (1) lower delta plain (tidal-flat) deposits that encase distributary- and tidal-channel sandstones and (2) inner-shelf, transgressive mudstones that encase delta-front sandstones; seaward (northeastward), delta-front sandstones grade into thinner, distal delta-front sandstones interbedded with mudstones.

Criteria for the definition of the tide-dominated delta model for the LL-652 area were derived from two main sources; (1) maps of net-sandstone thickness and log-facies and (2) cores (table V 1). Although these criteria are individually not conclusive, their combined occurrence strongly support the model.

The deltaic nature of these deposits is inferred from consistent trends in upward-fining and blocky, northeast-trending and -bifurcating framework sandstones. These sandstones pinch out downdip (northeastward) into sandy mudstones with upward-coarsening log responses inferred to be marine in origin from burrow types (Ophiomorpha, Planolites, Asterosoma, Teichichnus) and from accessory sedimentary structures such as symmetrical wave ripples and hummocky cross bedding.

The main criteria in distinguishing tide-dominated deltaic deposits from other types of deltaic deposits from maps is in the geometry of the delta-front sandstones. Although vertical profiles through fluvial- and tide-dominated deltaic deposits are similar (for example, both

upward-coarsening, burrowed delta front), the delta-front sandstones in the C Members are strongly dip-elongate and dip-parallel (figs. V 2 and V 3). In wave-dominated deltaic systems, delta-front sands are reworked by waves into strike-elongate sheets (fig. V 2a), whereas in fluvial-dominated, wave-modified deltas, the delta-front sands are only slightly reworked into lobate patterns (fig. V 2b). Delta-front sands in fluvial-dominated deltas are primarily dip-elongate (fig. V2c) as well as in fluvial- and tide-dominated deltas (fig. V 2d), but commonly the delta-front sands in fluvial-dominated deltas are not parallel and are instead flanked by point-sourced, lobate crevasse-splay deposits that fill muddy interdistributary areas. In tide-dominated deltaic systems, flood-and ebb-tidal currents rework delta-front deposits into parallel upward-coarsening sand ridges (Off, 1963; Klein, 1970). However, elongate and dip-parallel delta-front sandstones can also occur in fluvial-dominated deltaic systems where distributaries prograde into lacustrine/interdistributary-bay areas (Tye and Coleman, 1989), but these types of delta-front deposits (1) are confined to small, discrete areas in the lower delta plain, (2) comprise only a fraction of the total delta-front deposits in the system, and (3) have a dip-parallel geometry partly controlled by the shape of the oblong lacustrine receiving basin and the bathymetry of the lake floor. Additionally, delta-front deposits of the C Members have a strong marine association, as inferred from burrow types, whereas the modern Achafalaya lacustrine delta is in a lower-delta-plain setting where marine processes are weak to absent (Tye and Coleman, 1989).

Other criteria supporting the interpretation of the tide-dominated deltaic model are numerous clay clasts and clay-draped reactivation surfaces. Abundant clay clasts result from repetitive, episodic scouring of a mud-rich substrate by flood- and ebb-tidal currents. Although they are most abundant in distributary- and tidal-channel deposits, clay clasts are also scattered throughout tidal sand-ridge deposits in the delta front (Meckel, 1975; Maguregui, 1991; Maquregui and Tyler, 1991). Mud-draped reactivation surfaces that consist of flaser ripples and multiple, thin mud layers draping clean, moderately to well-sorted sand, indicate alternating high- and low-energy conditions that correspond to different phases of the tidal cycle (Reineck and Wunderlich, 1968; Reineck and Singh, 1973). Reactivation surfaces, although not restricted to tidal settings, commonly result from reworking of bedforms by the relatively weak reversing tidal current (Klein, 1970; de Mobraay and Visser, 1984). Flaser ripples vary according to relative amounts of mud and sand. In sandy deposits, mud occurs as thin upward-concave lenses (Clifton, 1982); if mud and sand are in equal abundance, mud occurs as complex layers around sandy ripples; if mud is dominant as in the C Members, sand occurs as isolated "starved" ripples.

Another important criterion for tidal conditions is bi-directionality of sedimentary structures such as ripples and crossbeds. In cores of the C Members, bi-directional ripples are present but uncommon. However, in many settings in tide-dominated deltaic systems, there is a

dominant tidal current that commonly results in unidirectional bedforms being preferentially preserved.

The presence of burrows does not exclusively support a tide-dominated deltaic interpretation, as they are common in all deltaic systems. However, the consistent and recurring presence of a wide variety of burrows in all major facies in the C Members, especially lower-delta-plain, such as Ophiomorpha, Asterosoma, Planolites and Chondrites indicates a strong marine influence from tidal currents.

Facies

Distributary Channel

Distributary-channel deposits in the C Members individually range from 5 to 20 ft (1.5 to 6 m) thick, are erosionally based and upward-fining, contain festoon crossbeds, clay clasts and burrows, and exhibit a dip-elongate sandstone geometry (table V 2). An example from the Middle C-5-X Submember shows an individual distributary channel deposit, 13 ft (4 m) thick, that truncates tidal-flat and tidal-channel deposits (fig V 4). This distributary-channel deposit consists of fine sandstone capped by siltstone and very-fine sandstone. The lower 9 ft (2.7 m) is extensively crossbedded (fig. V 5), whereas the upper 4 ft (1.2 m) contains inclined beds and asymmetrical ripples. Organic fragments, burrows, and very-coarse to gravel-size clay clasts are present throughout the section. This distributary-channel deposit is part of a narrow (550 to 3,000 ft [168 to 915 m] wide), northeast-trending belt of more than 20 ft (6 m) of mostly upward-fining sandstone bounded by muddy deposits with either upward-coarsening or serrate log responses (see fig. VI 16). These muddy deposits are interpreted to have been formed in a lower-delta-plain (tidal-flat) setting transected by a network of distributary channels. The distributary-channel facies commonly truncate delta-front facies. An example from the Middle C-3-X Submember in the LL-3074 well (fig. V 6) shows a 13-ft (4-m) upward-fining distributary-channel sandstone that truncates a 21-ft (6.4-m) section of upward-coarsening, burrowed delta-front mudstones and sandstones (fig. V 7a). The distributary-channel sandstone is pervasively rich in gravel-size clay clasts (fig. V 7b), and exhibits a succession of low-angle inclined beds at the base to plane beds at the top. There are multiple erosional reactivation surfaces throughout the lower half of the sandstone and a 2.5-ft (0.8-m) zone of calcareous cement at the base that may have resulted from dissolution of shell lag at the base of the channel. This distributary-channel deposit differs from the previous example in figure V 4 in that it is composed of

multiple, thin (commonly less than 1-ft [0.3-m]) sandstone beds with clay clasts and reactivation surfaces instead of one main sandstone bed. These numerous, thin sandstone beds reflect a more distal setting of the distributary and deposition by episodic tidal currents instead of fluvial processes.

Channel-Mouth Bar

Channel-mouth bar deposits, which occur at the terminii of the distributary-channel facies (fig. V 1), are uncommon in cores of the C Members. This facies is distinguished by very clean, wavy bedded and tabular crossbedded medium sandstone at the top of a burrowed, upward-coarsening sequence (table V 3 and fig. V 8). The crest of the channel-mouth bar, the coarsest part of the deposit, is only 3 ft (0.9 m) thick in this example and consists of oil-stained, crossbedded medium sandstone with minor clay clasts (fig. V 9), representing some of the best reservoir-quality rock in the C Members. However, this facies is volumetrically insignificant as it commonly occurs as eroded remnants between younger distributary-channel deposits.

Delta Front

The delta-front and distal-delta front are collectively the most volumetrically significant facies in the C Members (fig. V 1). The delta-front facies is distinguished by (1) upward-coarsening grain size trend, (2) stratification consisting of plane beds and ripples at the base and small crossbeds and inclined laminations at the top, (3) clay clasts and shell debris at the top, and most significantly, (4) a strong dip-elongate and parallel sandstone geometry (table V 4).

The proximal delta-front is relatively coarse, with an average grain size of fine sandstone in a range of siltstone at the base to medium sandstone at the top (fig. V 10). Sedimentary structures consist of asymmetric ripples in the lower one-third and small-scale crossbedding and planar bedding in the upper two-thirds (fig. V 11). Clay clasts are common throughout and the upper 6 ft (1.8 m) contains abundant Ophiomorpha burrows and shell debris.

In contrast to the proximal delta-front, the medial delta-front facies, averages from fine to very-fine sandstone (fig. V 12). Sedimentary structures range from bi-directional, asymmetrical ripples in the lower one-half (fig. V 13a) to inclined beds and symmetrical ripples at the top (fig. V 13b). Clay clasts are most common at the top of the section. Most medial delta-front deposits are thinner than proximal delta-front deposits and are also well-burrowed (figs. V 14, 15a, 15b), attesting to a strong marine influence. The most common burrow types are Planolites

(fig. V 15a) and Ophiomorpha (fig. V15b), which tends to be more common at the top of the delta-front section.

Distal Delta Front

Individual distal delta-front deposits in the C Members are only 5 to 10 ft (1.5 to 3 m) thick and exhibit a spiky log response (table V 5). Additionally, the distal delta-front facies may include load structures and slump deposits (figs. V 16 and V 17). Other common features are bi-directional asymmetric ripples (figs. V 18 and V 19). The distal delta-front facies in the C Members commonly occurs in multiple, upward-coarsening sequences, each no more than 6 ft (1.8 m) thick (fig. V 20). These deposits typically have a dip-parallel net-sandstone thickness trend (see fig. VI 25).

Tidal Channel and Tidal Flat

Tidal channels are essentially small-scale creeks that transect the muddy tidal flat (fig. V 1). In the C Members, tidal-channel deposits are typically only 5 to 10 ft (1.5 to 3 m) thick, have an upward-fining or blocky grain-size trend, and are erosionally based (table V 6). Tidal-flat deposits in the C Members commonly have a slight upward-fining grain-size trend, reflecting progradation of the muddy tidal flat over the high-energy intertidal sand bar. Tidal-flat deposits are complexly stratified, with asymmetrical flaser and symmetrical ripples and plane beds in sandstone interbedded with mudstone (table V 7).

An example of a tidal-channel deposit shows a 9-ft (2.7-m), erosionally based section of upper-fine sandstone overlain by upper very-fine sandstone (fig. V 21). Stratification in the lower part of the deposit is poorly preserved, owing to incorporation of channel-margin, bank-collapse deposits (fig. V 22). Other important features are microfaults toward the base and clay clasts which decrease in size upward.

A complete tidal-channel/tidal-flat sequence consists of a 15-ft (4.5-m), upward-fining section containing 9 ft (2.7 m) of erosionally based, crossbedded and rippled fine to very-fine sandstone overlain by 6 ft (1.8 m) of rippled siltstone (fig. V 23). The ripples are primarily shale-draped, lenticular flaser ripples with minor reactivation surfaces (fig. V 24), reflecting fluctuating depositional energy.

Transgressive Sand Shoal and Shelf

The transgressive sand-shoal facies represents destructional delta-front deposits overlain by marine shelf deposits. Many of these sand-shoal deposits record autocyclic deltaic abandonment and subsidence, whereas others resulted from a general rise in sea level. The transgressive sand-shoal facies is distinguished by thin (2- to 10 ft [0.6- to 3-m]), upward-coarsening sandstones with numerous internal erosion surfaces and thin, calcareous zones (table V 8). The shelf facies is distinguished by (1) fine grain size, (2) marine burrows, (3) high degree of lateral continuity, and (4) its stratigraphic position (commonly directly overlies the transgressive sand-shoal facies) (table V 9).

An example of a transgressive sand-shoal/shelf facies couplet (fig V 16) is a 16-ft (4.9-m) complex of multiple upward-coarsening, calcareous sandstones overlain by a 6-ft (1.2-m) section of siltstone with thin (approximately 6-in [2.4-cm]) sandstone interbeds. The lower section of sandstones contains large, irregular gravel-size clay clasts, shell fragments, and numerous internal scour surfaces (fig. V 25). A similar transgressive sand-shoal/shelf facies couplet (fig. V 26) consists of a pair of two upward-coarsening sandstones, each 5 to 7 ft (1.5 to 2.1 m) thick, overlain by a 4-ft (1.2-m) section of burrowed silty mudstone. One calcite-cemented zone contains cone-in-cone structures and stylolitic horizons (fig. V 29a). The burrowed silty mudstones (shelf facies) contain numerous, thin lenses of very fine sandstone and siltstone (fig. V 27b).

Fluvial-Estuarine Channel

The fluvial-estuarine channel facies, present in the Lower C-6-X Submember, consists of non-marine, valley-fill channel sandstones deposited during periods of sea-level fall. The diagnostic features of the fluvial-estuarine channel facies are (1) thick, massively crossbedded sandstones, (2) erosional base that commonly truncates marine shale, and (3) few or no marine burrows in the lower part of the section (table V 10).

With subsequent rise in sea level, the narrow (less than 5 mi [8 km] wide) paleovalley carved by the entrenched, low-stand fluvial system became the locus of deposition for tidally influenced deltas in an embayed receiving basin (fig. V 28). The fluvial-estuarine channel-fill sandstones are thickest in a northeast-trending belt in the LL-652 area (see figs. VI 2 and VI 3 and occupy paleotopographic low areas above an angular unconformity).

Examples of fluvial-estuarine, channel-fill sandstones (figs. V 29 and V 30) show a 30-ft (9-m) or more section of erosionally based, upward-fining sandstone in the Lower C-6-X

Submember that truncates burrowed marine shale in the underlying C-7-X Member. The unburrowed sandstone contains large tabular crossbeds at the base; higher in the section there are small tabular crossbeds overlain by ripples and plane beds. Clay clasts and organic fragments (fig. V 31), which decrease in size upward, are abundant in the lower 14 ft (4.3 m) of section. A similar succession of rock types and bedforms is present in a Middle Jurassic valley-fill sequence in Northeastern England (Ravenne and others, 1991), where the basal valley fill consists of massively crossbedded, erosion-based fluvial sandstone overlain by thinner and lenticular, mixed fluvial-tidal sandstones that are overlain by estuarine sand-flat deposits and transgressive shales.

Facies Summary and Comparisons

Three-dimensional architecture

Reservoirs in the C Members are extremely heterogeneous as a result of the three-dimensional sandstone architecture, a function of deposition in a tide-dominated deltaic system. Sandstone architecture is dominated by a system of narrow (less than 2,000 ft [610 m] wide), dip-elongate and dip-parallel, northeast-trending sandbodies (fig. V 1). As will be fully discussed later in this report, the strong northeast-trending grain of the sandbodies may result in anisotropic reservoir drainage patterns and must be considered in new infill well locations, recompletions, and waterflood programs in the LL-652 area.

The primary facies that together comprise the bulk of the C reservoirs are (1) delta-front, (2) distal delta-front, and (3) distributary-channel (table V 11). Other facies that comprise smaller volumes are (4) tidal-channel, (5) channel-mouth bar, and (6) fluvial-estuarine channel. The other facies, (7) transgressive sand-shoal, (8) shelf, and (9) tidal-flat are either poor-quality reservoir facies because of diagenetic heterogeneities (complex, calcite-cemented zones) or high mudstone content.

The tide-dominated deltaic facies tract in the LL-652 area forms a strongly dip-elongate system. However, within this system there are specific changes in sandstone geometry and in sandstone partitioning in the system (figs. V 32, V 33 and V 34). Net- and percent-sandstone patterns in the lower delta plain are typically complex and reticulated, whereas these patterns in the transition between lower delta plain and proximal delta-front (distributary-channel and channel-mouth bar facies) are dip-elongate and bifurcating (fig. V 32). Both the proximal and distal delta-front facies contain dip-parallel sandstone bodies that are progressively thinner downdip.

In progradational sequences the sandiest parts of the deltaic system are the delta-front and distributary-channel/channel-mouth bar facies (figs. V 33b and V 33c), whereas the distal delta-front and lower delta-plain are relatively muddy (figs. V 33a and V 33d). Examples of progradational sequences in the LL-652 area are the Middle C-5-X Submember and the Upper C-3-X Submember (table V 12). These submembers are sandstone-rich, averaging a maximum of 50 to 70 percent sandstone in distributary-channel and delta-front facies. However, the upper part of the Middle C-4-X Submember (fig. II 5), which represents mainly interdistributary, tidal-flat deposits in the LL-652 area, is relatively muddy.

In retrogradational sequences the sandiest part of the deltaic system is the distributary-channel/channel-mouth bar, whereas both the proximal and distal delta-front are sandstone-poor (fig. V 34). Examples in the LL-652 area include the Upper 21-22 interval in the Lower Upper C-6-X, Lower C-5-X, Lower C-4-X, and Lower C-3-X Submembers (table V 12). Delta-front deposits in these submembers typically contain only 20 to 30 percent sandstone, in contrast to the relatively sandstone-rich, distributary-channel system.

In aggradational sequences where deposition was sufficient to keep pace with rising sea level, the dominant preserved facies are distributary-channel, channel-mouth bar, and proximal delta-front (table V 12). However, the distributary-channel facies is sandier than the delta-front facies. In the Middle C-3-X Submember, the distributary-channel facies correspond to relatively thick belts of more than 50 percent sandstone but delta-front deposits contain only 30 to 40 percent sandstone. In the Lower 21-22 interval in the Lower Upper C-6-X Submember and the Upper C-3-X Submember the proximal delta-front deposits contain only 20 to 30 percent sandstone.

In sequences with base-level fall and extreme offlap northeast of the LL-652 area, net- and percent-sandstone patterns are dominated by linear, fluvial sandstone belts that locally contain more than 60 percent sandstone (table V 12). Sandstones, locally more than 70 ft (21.3 m) thick, were deposited in a coarse-grained fluvial system that incised into older delta-front deposits (fig. V 28). These belts are separated by sandstone-poor, interfluvial areas that escaped channel incision.

The infield development potential of reservoirs in the C Members, based on net-sandstone distribution of the different deltaic facies, varies between the different types of sequences. Distributary-channel and channel-mouth bar facies are excellent targets, especially in progradational sandstones that were deposited during periods of net retrogradation, because in these types of sequences there is a great net-sandstone and permeability contrast between these facies and the sandstone-poor, delta-front facies. Intrareservoir stratigraphic traps are favorable in these areas of permeability contrasts, whereas progradational sequences deposited during

periods of offlap may contain fewer permeability contrasts between the distributary-channel and delta-front facies that are both sandstone-rich.

In contrast, there is little variation in relative sandiness in the interdistributary/tidal-flat facies (lower-delta-plain) between progradational and retrogradational cycles in the LL-652 area. This part of the deltaic facies tract was an area of sediment bypass in progradational cycles when sediment was stored in the delta-front and channel-mouth bar facies. During retrogradation, relatively more sediment was stored in the distributary channels than in the delta front, but interdistributary areas were relatively muddy. Therefore, the lower-delta-plain facies tract is heterogeneous in the C Members and is inferred to contain multiple sites of high-permeability contrasts that may represent numerous but small stratigraphic traps for remaining mobile oil. Excellent examples of genetic depositional episodes (submembers) with high reservoir-quality sandstone encased in muddy interdistributary deposits are the Upper C-4-X and Middle C-3-X Submembers. These two submembers together account for most of the production in the combined C-3-X/C-4-X Members and yet still contain a high potential for mobile oil production.

In both the volumetrically significant and less significant facies, the dominant sandbody trends and shapes are ribbons and belts, whereas in the other facies, the sandbodies occur as sheets with no dominant trend (table V 11). Each facies contains component heterogeneities that limit internal reservoir sandstone continuity. The most homogeneous facies is channel-mouth bar; however, it is uncommon in the C Members. Facies with moderate internal heterogeneities—delta-front, distributary-channel, tidal-channel, and fluvial-estuarine channel—differ slightly in where these internal heterogeneities occur. For example, in the delta-front facies, maximum reservoir-quality sandstone is at the top of the upward-coarsening section, where silt and mud were winnowed out by wave and tidal processes. Distributary-, tidal-, and fluvial-estuarine channel facies contain the best reservoir-quality sandstone toward the base (for example, fig. V 30), where the grain size of the sandstone is maximum, but the lower part of the channel facies also commonly contain clay clasts, organic fragments and intraformational channel-margin, bank-collapse material that limit reservoir quality. The distal delta-front facies, although volumetrically significant, contain numerous internal heterogeneities (multiple shale interbeds) that limit vertical reservoir communication. The remaining facies (transgressive sand-shoal, shelf, tidal-flat) are internally heterogeneous or muddy, and may be difficult to develop efficiently.

The tide-dominated deltaic facies architecture and diagenetic history together control reservoir permeability (fig. V 32 and table V 11). Field-wide unconformities associated with sequence boundaries (base-level changes) and phases of deltaic abandonment (ravinement surfaces) may constitute significant permeability barriers. Additionally, local permeability barriers that extend over short distances (2,000 ft [610 m] or less) are controlled by facies

pinchouts such as distributary- and tidal-channel sandstone into tidal-flat mudstone and superposition of distributary-channel onto delta-front deposits. The detailed facies maps in this report may be used as a guide in delineating areas of potential reservoir traps controlled by permeability barriers in conjunction with faults and folds.

For example, lateral pinchouts of sandy tidal-channel deposits into the muddy tidal flat are expected to form permeability barriers, but superposition of sand-rich distributary-channel deposits onto delta-front sandstones may only constitute permeability barriers if the base of these distributary-channel deposits contain abundant clay clasts and organic fragments that can retard vertical fluid flow along the facies contact. Similarly, the seaward (northeastward) transition from distributary channel, channel-mouth bar, delta front, to distal delta-front is gradational, with inferred permeability loss over only great distances northeastward along these sandbodies.

Permeability and Porosity Characteristics

The main control on reservoir quality (permeability and porosity) in the C Members is depth. The median permeability of coreplug samples in each member decreases from 30.4 md in the C-3-X Member to 0.61 md in the C-7-X Member (figs. V 35 and V 36). The cumulative-frequency curves of the C-3-X and C-4-X Members differ substantially from those of C-5-X through C-7-X Members. However, this may be partly due to sampling bias: the depth differential between the Middle and Lower C-3-X Submembers and the Upper C-4-X Submember is commonly only 250 ft (76 m). In contrast, the depth differential between the Upper C-4-X Submember and Middle to Upper C-5-X Submembers is commonly as much as 600 ft (182.9 m).

A cumulative-frequency plot of permeability of different facies in the combined C-3-X to C-7-X Members shows great similarity in the volumetrically important distributary-channel, delta-front, and distal delta-front facies (fig. V 37). However, the volumetrically less important facies show clear departures from the trend of the main facies. For example, the transgressive shelf facies is the most permeable; however, this facies was sampled only in the shallow C-3-X Member, where permeability values in almost all facies are high. Likewise, the fluvial-estuarine channel facies in the C-6-X Member has a low-permeability trend because of the great depth at which it was sampled. The two volumetrically unimportant facies that may have realistic permeability trends are tidal-flat and shelf; these facies are mudstone-rich and are therefore expected to have low permeability values. Furthermore, the tidal-flat and shelf facies were sampled throughout the C-3-X to C-7-X Members, thereby removing the effects of sample depth from the permeability trends of these facies. In virtually all cases, permeability and porosity

values in each facies decrease with depth from the C-3-X to C-6-X Members (figs. V 38-44), whereas differences between facies in the same member are only slight to non-existent (figs. V 45-48). For example, there are no significant differences in permeability and porosity between the distributary-channel and delta-front facies, except in the C-5-X Member (fig. V 45). Likewise, few differences exist between delta-front and distal delta-front facies (fig. V 46), although a clear difference is noted between distributary-channel and tidal-flat facies in the C-3-X and C-4-X Members (fig. V 47), as well as a slightly higher average porosity in tidal-channel compared to the tidal-flat facies in the C-4-X Member (fig. V 48a).

The permeability-porosity distribution data, although indicating great similarity in facies, do not assess the importance of permeability and porosity contrasts along facies boundaries. For example, there is an order-of-magnitude difference in permeability across the distributary-channel/delta-front facies boundary in the LL-2850 well in the Middle C-3-X Submember, although the average permeability for each of these facies is virtually the same (fig. V 49). In addition, there is up to a two order-of-magnitude difference in permeability across the distributary-channel/tidal-flat facies boundary in this well.

Permeability differences also exist along certain segments of the unconformity associated with the fluvial-estuarine channel facies; for example, there is a two to three order-of-magnitude difference in permeability across the fluvial-estuarine channel/tidal-flat facies boundary in the LL-3080 well (fig. V 50). However, where the fluvial-estuarine channel facies truncates the distributary-channel facies, there is no permeability contrast.

The permeability-porosity crossplots (figs. V 45-48) also ignore differences in reservoir quality that exist over short intervals within individual facies. For example, the permeability varies from less than 1 md to almost 1,000 md over 5-ft (1.5-m) intervals within individual distal delta-front and distributary-channel deposits in the LL-2850 well in the Upper C-4-X Submember (fig. V 51). These small-interval permeability variations reflect the depositional style, which in turn controls the rock fabric (sedimentary structures) and degree of shaly interbeds, clay clasts, and burrows. Another control on these small-interval permeability variations is diagenesis (calcite-cemented zones, clay type, etc.). These permeability variations caused by both depositional and diagenetic factors can be integrated to formulate an improved model of reservoir heterogeneity.

VI. DEPOSITIONAL AND SANDSTONE ARCHITECTURAL TRENDS OF C MEMBER RESERVOIR INTERVALS

Introduction

Depositional trends of the tide-dominated deltaic sandstones of the C Members exerts a strong control over reservoir heterogeneity and consists of a system of narrow (less than 2,000 ft [610 m] wide), dip-parallel sandbodies that are commonly not contacted at the current well spacing of approximately 80 ac. Most of the framework distributary-channel and delta-front sandbodies are northeast-trending and may preferentially influence reservoir drainage in this direction, a factor to be considered in future infield development.

The C members in the LL-652 area were deposited in multiple progradational and retrogradational stages in a net-retrogradational megasequence (fig. II 5). The C-7-X Member was deposited as a major offlapping progradational clastic wedge; the upper, aggradational part of the C-7-X Member was eroded by fluvial systems associated with a major fall in sea level. Valley-fill, fluvial-estuarine sandstones of the Lower C-6-X Submember were deposited in northeast-trending bands along axes of maximum fluvial incision.

The Middle C-6-X Submember, not mapped in this study, consists of a series of progradational wedges bounded by marine flooding surfaces, whereas the sandstone-poor Upper C-6-X Submember represents a backstepping, retrogradational system (fig. II 5). Marine highstand conditions persisted during deposition of the mudstone-dominated Lower C-5-X Submember, but with deposition of the Middle C-5-X Submember, regressive conditions returned with an offlapping deltaic wedge. The top of the C-5-X Member is marked by a marine-dominated, retrogradational system.

The Lower C-4-X Submember, deposited during highstand conditions, is overlain by two progradational deltaic wedges of the Middle C-4-X Submember (fig. II 5). Deposition of the C-4-X Member culminated in a major progradational wedge in the Upper C-4-X Submember that extended northeastward well beyond the LL-652 area in a phase of maximum offlap in the lower Misoa Formation. However, within the Upper C-4-X Submember, the net sequence was backstepping. The Upper C-4-X Submember consistently exhibits the greatest gamma-ray and resistivity deflections, reflecting high-reservoir-quality sandstones deposited in a delta-front and lower delta-plain setting.

The C-3-X Member marks the beginning of a major retrogradational phase that continued with deposition of the C-2-X and C-1-X Members (fig. II 5). The base of the C-3-X Member,

defined by a laterally continuous marine flooding surface, is overlain by distal delta-front deposits of the Lower C-3-X Submember. The thin (approximately 100-ft [30.5-m]) but sandstone-rich Middle C-3-X Submember represents a short-lived phase of offlap during this extended period of net retrogradation. The sandstone-poor Upper C-3-X Submember records a possible reorganization of the basin as indicated by anomalous southeast-trending and lobate net-sandstone thickness patterns.

C-7-X Member

Sandbody Geometry

The C-7-X Member is the basal stratigraphic unit in the lower Misoa Formation and is a 150- to 300-ft (45.7- to 91.4-m), upward-coarsening interval truncated by the C-6-X Member (fig. II 5). Sandbody geometry of the C-7-X Member is sheetlike (table VI 1), except in a northeast-trending band of less than 80 ft (24.4 m) of net sandstone, 2,000 to 6,000 ft (610 to 1,829 m) wide, centered on the LL-3140 well (fig. VI 1). This band corresponds to a zone of relatively deep erosion by the overlying C-6-X Member. Net-sandstone thickness in the C-7-X Member is commonly over 100 ft (30.5 m), except in the zone of deep erosion, where it is locally less than 30 ft (9 m) (figs. V 50 and VI 1).

Lithology and Depositional Systems

Deposits of the C-7-X Member consist of thin (individual beds less than 2 ft [0.6 m] thick), finely laminated, upward-coarsening sandstones interbedded with moderately burrowed shale (appendix E, LL-3140 well, 9,164-9,202 ft). Load structures, slump deposits, and microfaults are common in the lower part of the section, whereas multiple, erosion-based clay-clast beds overlain by shale drapes are present in the upper part of the section. These shales and sandstones were deposited in distal delta-front and delta-front settings; the distal delta-front is the lower upward-coarsening section with load structures and slumps and the delta front contains multiple clay-clast beds that represent frontal-splay deposits.

Reservoir Development

Three wells (LL-1803, LL-2942, and LL-3056) have been perforated in the C-7-X Member (fig. VI 1). However, there has been no oil production from any of these wells, due to high water saturation in the C-7-X Member.

Lower Lower C-6-X Submember

Sandbody Geometry

The Lower Lower C-6-X Submember consists of a northeast-trending belt of mainly upward-fining sandstone, 90 to 130 ft (27.4 to 39.6 m) thick and 2,500 to 3,500 ft (762 to 1,067 m) wide, bounded by areas of less than 80 ft (24.4 m) of mainly upward-coarsening sandstone (table VI 2 and figs. VI 2 and VI 3). This northeast-trending belt is a the zone of relatively deep incision by the C-6-X Member into the C-7-X Member (see fig. VI 1).

Lithology and Depositional Systems

The Lower Lower C-6-X Submember in the LL-3140 well consists of approximately 130 ft (39.6 m) of net sandstone in a sequence with a lower 50-ft (15.2-m) upward-fining sandstone overlain by an upper 50-ft (15.2-m) sandstone with blocky to upward-coarsening log responses. A third, 30-ft (9-m) sandstone caps the sequence (fig. V 50). The lower sandstone is massively crossbedded and erosionally based, containing abundant clay clasts and organic fragments (figs. V 29, V 31, and appendix E, LL-3140 well, 9,118 to 9,164 ft). This sandstone is overlain by a 23-ft (7-m), poorly burrowed shale with thin (1- to 2-ft [0.3- to 0.6-m]), interbedded sandstones (appendix E, LL-3140 well, 9,095 to 9,118 ft). The overlying sandstone is crossbedded and also contains erosional surfaces.

Thickest sandstones in the Lower Lower C-6-X Submember represent valley-fill deposits deposited after an inferred sea-level fall; the lower sandstone was deposited by fluvial channels that occupied the valley floor, incising into older delta-front deposits of the C-7-X Member. With subsequent sea-level rise and drowning of the valley, estuarine mudstones and thin sandstones were deposited over the fluvial section (fig. V 28). The upper sandstones represent distributary-channel and delta-front deposits of an estuarine deltaic system. These sandstones are

in turn overlain by retrogradational, estuarine-fill and shelf mudstones that mark the maximum transgression of the incised valley (fig. V 50).

Reservoir Development

Drilling activity in the Lower Lower C-6-X Submember has been limited mainly to the central part of the LL-652 area. Of the seven wells perforated in this zone, only two have intersected the relatively thick fluvial-estuarine facies (figs. VI 2 and VI 3).

Upper Lower C-6-X Submember

Sandbody Geometry

The Upper Lower C-6-X Submember consists of one main northeast-trending belt of upward-fining sandstone in the northern part of the field, locally more than 80 ft (24.4 m) thick, bounded laterally by upward-coarsening sandstones less than 50 ft (15 m) thick (table VI 3 and fig. VI 4). There are other northeast-trending sandstone remnants in the southern part of the field (fig. VI 4).

Lithology and Depositional Systems

The Upper Lower C-6-X Submember consists of a lower upward-coarsening interval, approximately 80 ft (24.4 m) thick (fig. V 50), overlain by a thick (approximately 75-ft [22.9-m]), upward-fining sandstone, which in turn is overlain by a thin (20-ft [6-m]) laterally continuous silty shale. The lower upward-coarsening interval consists of burrowed delta-front sandstones truncated by a 12-ft [3.7-m] section of crossbedded distributary-channel sandstones (appendix E, LL-3140 well, 8,987 to 9,036 ft). The upper section is a thick, multistoried succession of upward-fining, erosionally based, crossbedded and unburrowed sandstones of a fluvial-estuarine channel complex that truncates older marine strata (appendix E, LL-3140 well, 8,880 to 8,935 ft). This fluvial-estuarine channel complex is similar to that of the underlying Lower Lower C-6-X Submember (fig. V 50). The uppermost 20 ft (6 m) of silty mudstone are transgressive deposits that cap the sequence.

Reservoir Development

The Upper Lower C-6-X Submember has been developed mainly in the central part of the LL-652 area, with minor activity toward the southwest (fig. VI 4). As in the Lower Lower C-6-X Submember, most of the perforated wells have been away from the main depositional axis, with three wells perforated with less than 50 ft (15.2 m) of net sandstone.

Lower Upper C-6-X Submember (21-22 Interval)

The Lower Upper C-6-X Submember is an upward-fining interval, 150 to 200 ft (45.7 to 61 m) thick (fig. II 5); it is composed of a lower sandstone-rich unit (lower 21-22 interval) and an upper sandstone-poor unit (upper 21-22 interval) that together constitute a retrogradational, transgressive sequence.

Lower 21-22 Interval

Sandbody Geometry

The Lower 21-22 interval in the LL-652 area is defined as two main dip-elongate and digitate upward-fining sandbodies more than 40 ft (12 m) thick and approximately 2,000 ft (610 m) wide (table VI 4 and figs. VI 5 and VI 6). These sandbodies thin laterally into muddy areas with less than 30 ft (9 m) of net sandstone (fig. VI 5).

Lithology and Depositional Systems

The lower two-thirds of the lower 21-22 interval, cored in the LL-3080 well, consist of a lower 33-ft (10-m) upward-coarsening section of burrowed mudstone interbedded with thin (0.5- to 2.5-ft [0.2- to 0.8-m]) rippled sandstones that increase upward in thickness (appendix E, LL-3080 well, 8,677 to 8,710 ft). The upper section of the lower 21-22 interval is a 42-ft (12.8-m) sandstone-rich unit with a 17-ft (5.2-m) sharp-based, crossbedded and rippled organic-rich sandstone overlain by a 12-ft (3.7-m) rippled and crossbedded, calcite-cemented sandstone that is

capped by a thin, 10-ft (3-m) zone of rippled siltstone and very-fine sandstone (appendix E, LL-3080 well, 8,634 to 8,677 ft).

This cored segment represents a single regressive-transgressive couplet composed of a lower offlapping, progradational deltaic wedge (distal delta-front, delta-front, and distributary channel) overlain by an upper retrogradational, transgressive sandstone. Two regressive-transgressive couplets, each no more than 60 ft (18 m) thick, comprise the lower 21-22 interval. Across a 1.7-mi (2.8-km) dip section (fig. VI 7) along the axis of a deltaic depocenter in the central part of the LL-652 area, a lower offlapping deltaic wedge, approximately 60 ft (18 m) thick, thins eastward to less than 5 ft (1.5 m). This wedge is overlain by a retrogradational sandstone that thins westward from 25 ft (7.6 m) to only 3 ft (0.9 m). The upper offlapping deltaic wedge is separated from the lower wedge by a continuous, 5-ft (1.5-m) shale inferred to be a marine flooding surface. In contrast to the lower deltaic wedge, the upper wedge contains a retrogradational unit that pinches out in the LL-652 area.

Reservoir Development

Development of the Lower 21-22 interval has been fairly uniform throughout the central part of the LL-652 area (figs. VI 5 and VI 6). However, there are no perforated wells in the northern and only limited development in the southwest parts of the field. There is no correspondence between net-sandstone thickness, log-facies, and location of perforated wells in the Lower 21-22 interval.

Upper 21-22 Interval

Sandbody Geometry

The Upper 21-22 interval is a muddy unit that is composed of multiple northeast-trending, dip-elongate sandstones that range in thickness from 30 to 45 ft (9 to 15 m) and in width from 1,500 to 2,500 ft (457 to 762 m) (table VI 5 and fig. VI 8). These sandstones pinch out into extensive muddy areas of less than 15 ft (4.5 m) of net sandstone.

Depositional Systems

Although there are no cores in the Upper 21-22 interval in the LL-652 area, net-sandstone thickness trends and the overall mudstone-rich nature of this unit suggest a distal delta-front or inner-shelf setting. All of the sandstones in the Upper 21-22 interval have upward-coarsening or serrate log responses, except for the thick (more than 40-ft [12-m]) upward-fining sandstones in the southwest part of the LL-652 area, near the Maraven concession boundary. These upward-coarsening and serrate log responses are consistent with progradational, offlapping sandbodies located distally from the deltaic platform.

Reservoir Development

Development of the shaly Upper 21-22 interval is extremely limited. In the three areas where the Upper 21-22 interval has been penetrated, there have been no perforations in the northern, two in the central, and only three in the southern part of the LL-652 area (fig. VI 8). In the central area, sandstone-poor areas have been perforated rather than sandstone-rich depositional axes. In the southern area, only one well (LL-946) has been perforated in a depositional axis, which is projected to extend northeastward into the southeastern corner of the central area.

Upper Upper C-6-X Submember

Sandbody Geometry

The Upper Upper C-6-X Submember is a thin (average 70-ft [21.3-m]), typically upward-coarsening interval at the top of the C-6-X Member (fig. II 5). This unit is composed of dominantly upward-coarsening, northeast-trending, dip-elongate sandstones, 40 to 50 ft (12 to 15.2 m) thick and 500 to 3,500 ft (150 to 1,067 m) wide (table VI 6 and fig. VI 9). A major depocenter exists in the southwestern part of the LL-652 area, near the Maraven concession, where there is a single dip-elongate trend of more than 40 ft (12 m) of net sandstone.

Depositional Systems

The Upper Upper C-6-X Submember, dominated by upward-coarsening sandstones, represents delta-front deposits throughout most of the LL-652 area. However, in the southwestern part of the LL-652 area, there is a single dip-elongate trend of distributary-channel sandstones that represent the updip equivalent of these delta-front sandstones.

Reservoir Development

The Upper Upper C-6-X Submember is only moderately developed; there are extensive undeveloped areas in the LL-652 area, particularly in the north and southeast. Of the main depositional axes defined by more than 40 ft (12 m) of net sandstone, only one well (LL-946) has been perforated.

Lower C-5-X Submember

Sandbody Geometry and Depositional Facies

The Lower C-5-X Submember, which is divided into lower and upper intervals, is a sandstone-poor, approximately 250-ft (76-m) thick interval composed of multiple, thin sandstones interbedded with mudstones (fig. II 5). These sandstones form semi-continuous, narrow (1,500 to 3,000 ft [457 to 915 m] wide) belts more than 70 ft (21.3 m) thick (table VI 7 and fig. VI 10) in a system of inferred upward-coarsening tidal sand-ridge deposits in a distal delta-front setting.

Reservoir Development

The Lower C-5-X Submember has been moderately developed, although there are some areas in the LL-652 area that have not been tested. For example, there are virtually no perforations in the north and in the southwest, except for four wells close to the Maraven-Lagoven concession boundary. The pattern of perforations is random, with little or no correspondence to depositional axes (fig. VI 10).

Lower Lower C-5-X Submember

Sandbody Geometry

The Lower Lower C-5-X Submember is defined as the 100- to 150-ft (30.5- to 45.7-m) interval between the 20 shale marker and the top of the C-6-X Member (fig. II 5). Sandbodies in this interval are inferred to be dip-elongate, discontinuous belts, 40 to 55 ft (12 to 16.8 m) thick and 1,000 to 2,000 ft (305 to 610 m) wide (table VI 8 and fig. VI 11).

Lithology and Depositional Systems

Sandstones in the Lower Lower C-5-X submembers are thin (1 to 3 ft [0.3 to 0.9 m]) and interbedded with burrowed mudstone (appendix E, LL-3075 well, 8,330 to 8,452 ft). Sedimentary structures in the sandstones consist of asymmetrical starved ripples, plane beds, and minor inclined beds. These thin sandstones represent distal delta-front deposits located seaward (northeastward) from an inferred distributary-channel system in the Maraven concession.

Reservoir Development

Development in the Lower Lower C-5-X Submember is limited to four wells in a 0.58-mi² (1.5-km²) area in the central part of the field and two wells in the southwest part of the field (fig. VI 11). In the central area, almost all of the wells have been perforated in shaly locations away from the main depocenter of more than 30 ft (9 m) of net sandstone. Likewise, the depocenter in the north has not been developed.

Upper Lower C-5-X Submember

Sandbody Geometry

The Upper Lower C-5-X Submember, defined as the interval from the 19 to the 20 shale markers (fig. II 5) is 100 to 150 ft (30.5 to 45.7 m) thick and consists of a system of east-trending, dip-parallel sandstones, 40 to 60 ft (12 to 18 m) thick and 2,000 to 5,000 ft (610 to 1,524 m) wide (table VI 9 and fig. VI 12). The most common log responses are upward-coarsening to serrate.

Lithology and Depositional Systems

As in the Lower Lower C-5-X Submember, the Upper Lower C-5-X Submember contains multiple sandstones interbedded with mudstone. However, individual sandstones are up to 5 ft (1.5 m) thick and are separated by comparatively thinner mudstones (appendix E, LL-3075 well, 8,177 to 8,330 ft). The sandstones are also more commonly crossbedded, although asymmetrical ripples and plane beds are abundant. The two intervals in the Lower C-5-X Submember (upper and lower) together represent the distal facies tract of a deltaic system; the lower unit is distal delta-front and the upper unit is delta-front. No distributary-channel deposits are inferred in either of the units in the LL-652 area, as the deltaic system had not prograded very far eastward.

Reservoir Development

The Upper Lower C-5-X has undergone a moderate level of development: ten wells have been perforated in the north-central part of the field in an area that covers approximately 0.97 m² (2.5 km²) (fig. VI 12). However, there has been no development in two sandy depositional axes in the northern part of the field and none toward the southwest, except for three wells near the Maraven lease.

Middle C-5-X Submember

The Middle C-5-X Submember consists of all strata between the 18 and 19 shale markers and is typically 250 ft (76 m) thick (fig. II 5). It is a composite of three units (lower, middle, and upper) that are each 50 to 100 ft (15.2 to 30.5 m) thick.

Sandbody Geometry

The Middle C-5-X Submember is composed of multiple, east- and northeast-trending belts of sandstone, 80 to 110 ft (24.4 to 33.5 m) thick and 2,000 to 8,000 ft (610 to 2,439 m) wide (table VI 10 and fig. VI 13). In the northern part of the LL-652 area, the sandstone trends are east-to southeast-trending, whereas in the southwest they trend northeastward.

Lithology and Depositional Systems

Individual units in the Middle C-5-X Submember consist of (1) a lower upward-coarsening unit, (2) a middle unit composed of mudstone and erosion-based sandstones, and (3) an upper sandstone-rich unit (appendix E, LL-3075 well, 7,993 to 8,177 ft). These units correspond to (1) delta-front, (2) proximal delta-front and lower delta-plain, (3) and inner estuarine bay-fill units, respectively, overlain by a retrogradational, marine-dominated interval. These three units together make up an offlapping progradational wedge. A stratigraphic strike section that displays log-facies responses (fig. VI 24) shows the (1) lower system of mainly upward-coarsening tidal sand ridge deposits overlain by the (2) middle unit consisting of proximal delta-front (upward-coarsening log response) and tidal-flat deposits (upward-fining and serrate log responses), and (3) the upper estuarine bay-fill with thick (more than 35-ft [11-m]) distributary-channel deposits capped by transgressive deposits. An upward increase in upward-fining sandstones in the Middle C-5-X Submember reflecting progradation of the delta plain over the delta front in the LL-652 area.

Reservoir Development

The Middle C-5-X Submember has been extensively developed, especially in the north and north-central parts of the LL-652 area. Much of the southwest part of the field, near the Maraven concession, has also been perforated. However, since the Middle C-5-X Submember is

a complex of three depositional subunits, these perforations are distributed among different stratigraphic horizons, resulting in numerous opportunities for additional infield development.

Lower Middle C-5-X Submember

Sandstone Geometry

This basal unit in the Middle C-5-X Submember is typically a 100-ft (30.5-m), upward-coarsening section (fig. II 5). The sandstone geometry is strongly dip-parallel throughout most of the LL-652 area (table VI 11 and fig. VI 15). The sandstones range from 30 to 45 ft (9.1 to 13.7 m) thick and from 1,000 to 6,000 ft (305 to 1,829 m) wide.

Lithology and Depositional Systems

The Lower Middle C-5-X Submember is composed of upward-coarsening sandstones, 5 to 12 ft (1.5 to 3.7 m) thick, interbedded with burrowed siltstone and mudstone (appendix E, LL-3075 well, 8,128 to 8,177 ft). These sandstones have a succession of bedforms that range from asymmetric ripples at the base to clay-clast-rich, inclined beds and crossbeds at the top. Each sandstone is a tidal-ridge deposit in a delta-front setting and contains maximum reservoir quality at the top.

Reservoir Development

Greatest development of the Lower Middle C-5-X Submember has been in the central part of the LL-652 area (fig. VI 15). All of the thickest sandstone bodies in this area have been perforated by at least two wells. However, there are sites in each of these sandstones that can still be targeted for additional development. Other areas where the current perforation density is sparse includes the far northern part of the field and selected areas in the updip (southwestern) part of the facies tract in the vicinity of the LL-3062 well.

Middle Middle C-5-X Submember

Sandstone Geometry

The Middle Middle C-5-X Submember is a thin (50- to 100-ft [15.2- to 30.5-m]) interval that consists of narrow (550 to 3,000 ft [168 to 915 m] wide), northeast-trending bands of upward-fining sandstones more than 20 ft (6 m) thick pinching out laterally into mudstones (table VI 12 and fig. VI 16). These sandstones have northeast-bifurcating trends in the northern part of the LL-652 area.

Lithology and Depositional systems

The Middle Middle C-5-X Submember (appendix E, LL-3075 well, 8,058 to 8,128 ft) consists of a lower section of thick (20-ft [6-m]) mudstone and thin (1- to 1.5-ft [0.3- to 0.5-m]) sandstones truncated by a crossbedded, upward-fining 12-ft (3.7-m) sandstone. The upper part of the section contains several upward-coarsening, rippled and crossbedded sandstones interbedded with burrowed mudstone. The base of this sequence is composed of muddy tidal-flat deposits truncated by a single distributary-channel deposit; the upper part of the section is composed of progradational bay-fill deposits.

Reservoir Development

The Middle Middle C-5-X Submember has been extensively developed. Most of the major sandstone bodies in this stratigraphic unit have been perforated. However, as in the Lower Middle C-5-X Submember, these sandstone bodies have been incompletely developed and contain locations for additional wells or recompletions. There are opportunities in the southwest and extreme northern part of the field. Additionally, the thickest parts of the dip-elongate sandstone body in the central part of the field have not been contacted, especially where this sandstone has been intersected by the northeast-trending zone of partly-sealing reverse faults.

Upper Middle C-5-X Submember

Sandbody Geometry

The Upper Middle C-5-X Submember represents the last stage in the offlapping progradational wedge in the Middle C-5-X Member and consists of a system of dip-elongate and digitate sandbodies, more than 40 ft (12 m) thick with a complex geometry (table VI 13 and fig. VI 17). In the southern part of the LL-652 area, the sandstone bodies are simple, northeast-trending belts that extend across the field, whereas in the northern part they are northeast-bifurcating pods that pinch out downdip (northeastward).

Lithology and Depositional Systems

The lower part of the Upper Middle C-5-X Submember (appendix E, LL-3075 well, 7,995 to 8,088 ft) consists of a 15-ft (4.6-m) interval of rippled, burrowed sandstones overlain by another 15-ft (4.6-m) interval of erosion-based, crossbedded and clay-clast rich sandstone. The upper 24 ft (7.3 m) contains two intensely burrowed, upward-coarsening sandstones, each 5 to 7 ft (1.5 to 2.1 m) thick; burrow types include Ophiomorpha, Skolithos, and Planolites. This stratigraphic succession includes a basal delta-front deposit truncated by distributary-channel deposits. The upper part of the sequence consists of transgressive-shoreface (reworked delta-front) deposits, indicated by clean, upward-coarsening sandstones with marine burrows and symmetrical wave ripples.

Reservoir Development

Although the Upper Middle C-5-X Submember has been intensely perforated in the central part of the LL-652 area, there are still areas where thick sandstones have not been tested or developed. For example, the distributary-channel sandstone in the northeast part of the LL-652 area, centered on the LL-2729 well, has not been perforated. The southern belt of sandstone (more than 40 ft [12 m] thick) between the LL-946 and LL-1001 wells has been incompletely perforated.

Upper C-5-X Submember

Sandbody Geometry

The Upper C-5-X Submember is the uppermost 50 to 100 ft (15.2 to 30.5 m) of the C-5-X Member (fig II 5) and features an east-trending system of interconnected belts of more than 30 ft (9 m) of net sandstone, 2,000 to 3,500 ft (610 to 1,067 m) wide in the northern part of the LL-652 area (table VI 14 and fig. VI 18). These sandstones have dominantly upward-coarsening or serrate log responses.

Lithology and Depositional Systems

The Upper C-5-X Submember (appendix E, LL-3282 well, 7,920 to 8,028 ft and appendix E, LL-3075 well, 7,905 to 7,995 ft), consists mostly of multiple upward-coarsening sandstones interbedded with burrowed mudstone. Individual upward-coarsening sequences range from 3 to 8 ft (0.9 to 2.4 m) thick in the LL-3282 well and 5 to 16 ft (1.5 to 4.9 m) thick in the LL-3075 well, along the depositional axis of one of the dip-elongate sandbodies (fig. VI 18). The sandstones commonly have asymmetrical ripples and plane beds at the base and crossbeds and clay clasts at the top, although clay clasts are also abundant throughout most of the sandstones. Large, symmetrical ripples are present at the top of some of the upward-coarsening sequences. The multiple upward-coarsening sandstones of the Upper C-5-X Submember were deposited in delta-front and distal delta-front settings. The lack of upward-fining and blocky log responses indicates that the delta-plain facies tract was not present in the LL-652 area, and is inferred to have been westward in the Maraven area.

Reservoir Development

The Upper C-5-X Subunit has been intensely developed (fig. VI 18). However, the northern dip-elongate sandstone body has not been perforated, and as this is an area of complex structure, may present an opportunity for development.

Lower C-4-X Submember

The Lower C-4-X Submember includes all strata from the 16 shale marker to the top of the C-5-X Member and is approximately 250 ft (76 m) thick in the LL-652 area (fig. II 5). Sandstones in the Lower C-4-X Submember occur in northeast-trending, dip-elongate belts that merge into a broad, 2-mi (3.2-km) wide area toward the north (table VI 15 and fig. VI 19). These sandstones have upward-coarsening and serrate log responses and were deposited in delta-front and distal delta-front environments. Although there is an absence of upward-fining and blocky log responses that indicate distributary-channel deposits, a depocenter is inferred in the northern part of the Maraven concession, west of the broad, relatively sandstone-rich area in the northern part of the field.

Reservoir Development

The Lower C-4-X Submember has been perforated throughout the central and north-central part of the LL-652 area, where it contains more than 20 ft (6 m) of net sandstone (fig. VI 20). However, the thinner (15-ft [4.5-m]) belt of northeast-trending sandstone between the LL-1310 and LL-1162 wells has not been perforated, as well as the entire belt of 15 ft (4.5 m) of sandstone in the extreme southern part of the field.

Middle C-4-X Submember

The Middle C-4-X Submember includes all strata from the 14 to 16 shale markers and is typically 200 ft (61 m) thick (fig II 5). This submember is a composite of two separate depositional units: the lower unit is bounded below by the 16 shale marker and above by the 15 shale marker, and the top of the upper one is the 14 shale marker. Each depositional unit is composed of lower delta-plain (tidal-flat, distributary-, and tidal-channel) deposits overlying delta-front deposits. The two units together contain north- to northeast-trending belts of sandstone more than 40 ft (12 m) thick and 2,000 to 7,500 ft (610 to 2,287 m) wide. Locally, these sandstones are as much as 60 ft (18 m) thick (table VI 16 and fig. VI 20).

Most of the Middle C-4-X Submember is cored in the LL-2850 well (appendix E, 7,770 to 7,898 ft). Five main facies, in ascending order in the core, (1) tidal-channel, (2) tidal-flat, (3) delta-front, (4) distributary-channel, and (5) distal delta-front make up the submember. The tidal-channel deposits are defined by multiple, erosion-based and upward-fining sandstones, each

2 to 4 ft (0.6 to 1.2 m) thick and stacked into two composite intervals 12 to 16 ft (3.7 to 4.9 m) thick. A 7-ft (2.1-m) tidal-flat section overlies the upper tidal-channel sequence from 7,846 to 7,854 ft and is composed of slightly upward-fining siltstone with burrows and flaser ripples (figs. V 23 and V 24). The delta-front deposit that forms the basal part of the Upper Middle C-4-X Submember (14 to 15 interval) extends from 7,825 to 7,839 ft and is an upward-coarsening interval of fine and very-fine sandstone interbedded with burrowed and rippled siltstone and mudstone. A 15- to 20-ft (4.6- to 6.1-m) distributary-channel deposit directly overlies the delta-front sequence. This distributary-channel deposit consists of crossbedded and plane-bedded fine to upper-fine sandstone with organic fragments and minor burrowing. Some of the crossbeds are oversteepened and have been distorted by soft-sediment deformation. The uppermost part of the section is a 15-ft (4.6-m), distal delta-front deposit that contains three 2- to 3-ft (0.6- to 0.9-m), very-fine sandstone beds interbedded with burrowed mudstone and siltstone.

Reservoir Development

The Middle C-4-X Submember is in an advanced stage of development. Virtually every major sandstone in this interval has been perforated, especially in the east-central part of the LL-652 area (fig. VI 20). However, some of these sandstones can still be contacted in less-developed areas. For example, the narrow (less than 600 ft [182.9 m] wide), northeast-trending sandstone body more than 40 ft (12 m) thick, located in the southwestern part of the LL-652 area, has not been tested south of the LL-1245 well and may contain remaining mobile oil, especially in the zone of the reverse faults.

Upper C-4-X Submember

The Upper C-4-X Submember consists of all strata from the 14 shale marker to the top of the C-4-X Member (fig. II 5). The Upper C-4-X Submember is composed of four main, dominantly upward-coarsening units that represent a depositional parasequence as part of the major progradational cycle that makes up the C-4-X Submember (fig. VI 21). Of these four main units, the lowest (#4) is the thickest, unit and was mapped separately; the others (#1, 2, and #3) are thinner, are partly bounded by thin (typically less than 10-ft [3-m]) discontinuous shales, and could not be mapped separately.

Sandbody Geometry

The Upper C-4-X Submember is composed of northeast-trending, dip-elongate sandbodies with a combined thickness of 90 to 140 ft (27.4 to 42.7 m), separated by sandstone-poor areas with as little as 40 to 50 ft (12 to 15.2 m) of net sandstone (table VI 17 and fig. VI 22). The trends of thickest net sandstone (more than 100 ft [30.5 m]) occur in four main belts in the LL-652 area.

Lithology and Depositional Systems

Each of the four main units that compose the Upper C-4-X Submember consist of multiple, upward-coarsening sandstones (appendix E, LL-3074 well, 7,650 to 7,775 ft). The #4 unit, incompletely cored in this well, consists of upward-coarsening and upward-thickening, wavy-bedded sandstones separated by thin (less than 5-in [12.7-cm]) mudstones. The upper 3 ft (0.9 m) is medium, oil-stained, sandstone with clay clasts (figs. V 8 and V 9).

The #3 unit consists of two upward-coarsening sandstones, each 6 to 10 ft (1.8 to 3 m) thick (appendix E, LL-3074 well, 7,719 to 7,749 ft). Maximum grain size in the lower sandstone is fine, whereas it is lower medium in the upper sandstone. Sedimentary structures in each sandstone range from plane and wavy beds at the base to inclined laminations and ripples at the top; Planolites burrows are common in the lower sandstone and clay clasts are present in the upper sandstone, also oil-stained at the top.

The #2 unit is a complex, 39-ft (11.9-m) interval of at least four heterogeneous, upward-coarsening sandstones finely interbedded with siltstone and mudstone (appendix E, LL-3074 well, 7,680 to 7,719 ft). Each sandstone is 4 to 10 ft (1.2 to 3 m) thick and contains clay clasts, organic fragments, and burrows. These units have an average grain size of very fine to fine, whereas the #3 and #4 units have an average grain size of fine sandstone.

The #1 unit, different from the other sandstones in the Upper C-4-X Submember, contains several 0.5- to 1-ft (0.15- to 0.3-m), calcite-cemented zones associated with erosional surfaces and shell fragments (appendix E, LL-3074 well, 7,650 to 7,680 ft). These sandstones, which range in thickness from 5 to 8 ft (1.5 to 2.4 m), are also rich in large (cobble- to gravel-size), irregular clay clasts.

The main four units of the Upper C-4-X Submember compose successive progradational wedges in a net retrogradational, backstepping clastic wedge (fig. V 51). The #4 unit represents proximal delta-front and lower delta-plain deposits in an initial advance of a delta in the LL-652 area. Deltaic progradation was from the southwest to the northeast and individual units in the

Upper C-4-X Submember thicken slightly northeastward, reflecting the direction of deltaic progradation. Delta-front sandstones of the #1, #2 and #3 units are progressively shalier northwestward due to increasing amounts of thin mudstone interbeds. An exception is the #4 unit that features a channel-mouth-bar remnant updip (southwest) of a distributary-channel complex in the LL-2850 core (fig. V 51). This channel-mouth-bar remnant is approximately 1,500 ft (457 m) from a major depositional axis composed of distributary-channel sandstones that had cannibalized associated channel-mouth bar deposits (fig. VI 22). The #1 unit (fig. V 51) differs slightly from the two underlying units in that the upper sandstones represent retrogradational deposits associated with the laterally extensive marine flooding surface at the top of the Upper C-4-X Submember (fig. V 51).

Reservoir Development

The Upper C-4-X Submember is in a mature stage of development, has been perforated extensively throughout the LL-652 area (fig. VI 22), and is currently undergoing rapid pressure depletion. Although the sandstone geometry of the Upper C-4-X Submember is dominantly northeast-trending, a rapidly north- to northwest-advancing zone of water encroachment is present just south of the LL-2850 well. The reason why the water encroachment is north- to northwest-trending is because the thick sandstones in the Upper C-4-X Submember together have a great net-sandstone thickness in this part of the field (fig. VI 22) and the structural gradient is up toward the northwest.

Because of the high number of previous perforations in the field, the Upper C-4-X Submember is a primary target for a strategic waterflood program. Areas north of the LL-2850 well that are relatively shalier and stratigraphically heterogeneous in the Upper C-4-X Submember can be efficiently swept with water-injection wells located along axes of narrow, northeast-trending sandbodies that may feature anisotropic reservoir drainage patterns because of the strong depositional geometry.

#4 Unit in Upper C-4-X Submember

Sandbody Geometry

The #4 Unit, representing the initial and furthest advance of a deltaic system in the Upper C-4-X Submember, consists of a system of multiple, northeast-trending and -bifurcating upward-fining sandstones defined by more than 70 percent (30 ft [9 m]) of net sandstone (table VI 18 and fig. VI 23). In the southern part of the LL-652 area, these sandstone belts extend across the map area, but in the north they pinch out into muddy areas with less than 40 percent sandstone that have serrate and upward-coarsening log responses (figs. VI 23 and VI 24).

Depositional Systems

The #4 Unit in the LL-652 area and the eastern part of the Maraven concession represents a system of mainly distributary-channel sandstones grading downdip (northeastward) into sandy channel-mouth bar deposits and pinching out into muddy delta-front deposits. Interdistributary areas consist of either channel-mouth bar remnants or tidal-flat mudstones. The #4 Unit is an excellent example of depositionally controlled heterogeneity; percent sandstone values range from less than 10 percent in interdistributary areas to as much as 100 percent along narrow (only 1,000 ft [305 m] wide) distributary-channel axes (fig. VI 23).

Reservoir Development

Although the #4 Unit has been perforated throughout the field and is part of a thick (150-ft [45.7-m]) package of sandstones composing a potential target for a secondary-recovery waterflood program, it also contains numerous opportunities for strategic infill drilling or recompletion. For example, the dip-elongate, northeast-bifurcating distributary-channel sandbody in the northern part of the A-188 concession (north and south of the LL-1089 well) has not been perforated, even though it is in a structurally complex area (fig. VI 23). Thick (locally more than 80 ft [24.4 m] of net sandstone) areas of high-reservoir-quality, channel-mouth bar deposits, may be excellent targets for recompletion (fig. VI 23). Additionally, the southern segment of this distributary-channel system, centered on the LL-3186 well, is poorly developed and could be a target for infill drilling.

Lower C-3-X Submember

Sandbody Geometry

The Lower C-3-X Submember is a 250- to 300-ft (76- to 91.5-m), sandstone-poor interval (fig. II 5). Two depocenters in the Lower C-3-X Submember are defined by more than 70 ft (21.3 m) of net sandstone in the Maraven concession; the main depocenter is located in the east-central part of the Maraven concession, and a minor depocenter exists in the extreme southern part of the area (table VI 19 and fig. VI 25). These depocenters are connected to narrow (500 to 2,000 ft [152 to 610 m] wide), continuous bands of sandstone more than 50 ft (15.2 m) thick in the LL-652 area. The log responses in the depocenters are blocky and upward-fining with numerous variations, whereas the log responses of the narrow bands are upward-coarsening and serrate.

Lithology and Depositional Systems

The Lower C-3-X Submember is extremely heterogeneous. Virtually all of the sandstone beds are very-fine and are interbedded with mudstone (appendix E, LL-3074 well, 7,535 to 7,645 ft). The thickest individual sandstone bed is only 5 ft (1.5 m) thick; most sandstone beds are only 1 ft (0.3 m) thick. Most of the sandstones in the Lower C-3-X Submember occur in multiple, upward-coarsening sequences that range in thickness from 1.5 to 10 ft (0.5 to 3 m). Each upward-coarsening sequence typically exhibits a succession of bedforms that range from plane beds and asymmetrical ripples at the base to inclined beds and symmetrical ripples at the top. Marine burrows, including Planolites, Teichichnus, and Rhizocorallium are common, and clay clasts are present at the top of some upward-coarsening sequences. The lowest 18 ft (5.5 m) contains slump deposits and thin (1- to 2-ft [0.3- to 0.6-m]), sharp-based and upward-fining sandstones with very-coarse and small-gravel clay clasts.

The basal part of the Lower C-3-X Submember was deposited in an inner-shelf setting following the transgression that marked the end of deposition of the C-4-X Member. Thin, sharp-based and upward-fining sandstones in this interval were deposited as frontal splays on the inner shelf. Multiple, upward-coarsening sequences in the Lower C-3-X Submember represent distal delta-front deposits downdip (eastward and northeastward) of deltaic depocenters in the Maraven concession; these delta-front deposits were reworked by tidal currents along

depositional dip into narrow (commonly less than 1,000 ft [305 m] wide), parallel tidal sand ridges (fig. VI 25).

Reservoir Development

The Lower C-3-X Submember is an aggregate of numerous, thin (individual units less than 10 ft [3 m]) sandstone beds that are interbedded with thin, low-permeability shaly zones. These sandstone beds have a combined thickness of more than 50 ft (15.2 m) in multiple, dip-elongate belts with greater-than-average net-pay thickness. Therefore, these belts are areas of potential infill wells. In particular, infill locations or recompletions could be considered where tidal-ridge sandstones have a combined thickness of more than 50 ft (15.2 m) in areas distant from previously perforated wells.

Middle C-3-X Submember

Sandbody Geometry

The Middle C-3-X Submember is a thin, 70- to 100-ft (21.3- to 30.5-m) sandstone-rich interval (fig. II 5). The sandstone geometry consists of northeast-trending patterns of more than 50 ft (15.2 m) of net sandstone in dip-parallel bands, 1,500 to 3,500 ft (457 to 1,067 m) wide (table VI 20 and fig. VI 26). The log-facies map of the Middle C-3-X Submember also exhibits northeast-trending patterns in a system of upward-coarsening and serrate log responses transected by a system of upward-fining and blocky log responses in the southern part of the area (fig. VI 27). The majority of the dip-elongate belts of upward-fining and blocky log responses are approximately 2,000 ft (610 m) wide. The trend of blocky log responses approximately coincides with more than 50 ft (15.2 m) of net sandstone (fig. VI 26).

Lithology and Depositional Systems

The Middle C-3-X Submember, cored in the LL-2425, LL-2850, and LL-3074 wells, contains a lower upward-coarsening section of delta-front deposits, 14 to 20 ft (4.3 to 6.1 m) thick, commonly truncated by 8- to 14-ft (2.4- to 4.3-m) upward-fining, distributary-channel

sandstones (fig. V 49). The upper part of the section contains a variety of different types of sandbodies, including upward-coarsening, interbedded overbank deposits (LL-3074 well), very-fine and fine, rippled tidal-flat sandstones with no grain-size trends (LL-2425 and LL-2850 wells), and erosion-based, upward-fining tidal-channel sandstones (LL-2850 well). The Middle C-3-X Submember is bounded by a 10-ft (3-m) laterally continuous, mainly upward-coarsening zone of irregularly calcite-cemented, transgressive sand-shoal deposits that are in turn overlain by a 4- to 6-ft (1.2- to 1.8-m) laterally continuous, burrowed mudstone representing a marine flooding surface.

A stratigraphic strike section that cuts across the grain of the sandbodies in the Middle C-3-X Submember shows the deltaic facies architecture (fig. VI 28). Lenticular distributary-channel sandbodies, individually about 2,000 ft (610 m) wide, locally truncate an extensive system of delta-front sandstones. These distributary-channel sandstones are bounded laterally by muddy tidal-flat deposits that have an irregular sheet geometry. This paragenetic sequence is bounded below by a laterally extensive shelf mudstone and above by an irregular transgressive sandsheet and associated shelf mudstone. Areas where high permeability and porosity contrasts are expected are along (1) distributary channel-delta front contacts, particularly at the base of channel deposits where clay clasts and organic fragments may comprise flow barriers and (2) lateral pinchouts of distributary-channel sandstones into tidal-flat mudstones. Other flow barriers may exist in the transgressive sand shoal/sheet facies between numerous thin and impermeable, calcite-cemented zones. However, these zones are not easily recognized from electric logs and their lateral continuity is difficult to predict.

Reservoir Development

The Middle C-3-X Submember has been perforated throughout the LL-652 area (figs. VI 26 and VI 27). However, this submember continues to be an active producer and is experiencing a pressure decline less severe than that of the Upper C-4-X Submember. Therefore, undrained or partly drained compartments may exist in this unit and recompletions, infill wells, or even strategically implemented waterfloods may be necessary to most efficiently produce the remaining mobile oil. Areas in the field where this oil could be targeted by recompletions and infill wells are defined by structurally and stratigraphically complex areas distant from previously existing completions.

A limited waterflood may be appropriate in the central, unfaulted part of the LL-652 area that has been extensively perforated, where it may be able to sweep remaining mobile oil that

remains along facies contacts between distributary-channel and delta-front facies, or tidal-channel and tidal-flat facies.

Upper C-3-X Submember

Sandbody Geometry

The sandstone-poor Upper C-3-X Submember makes up the upper 200 ft (61 m) of the C-3-X Member (fig. II 5). Unlike the Lower C-3-X Submember that is also sandstone-poor, the sandstone geometry of the Upper C-3-X Submember is east- and southeast-trending and -bifurcating; these trends are defined by more than 40 ft (12 m) of net sandstone or more than 20 percent sandstone and are 700 to 1,600 ft (213.4 to 487.8 m) wide (table VI 21 and fig. VI 29). The sandbodies define the depositional axes of a system of inferred distributary-channel deposits that pinch out into interdistributary-bay deposits and delta-front mudstones. Because of the lobate and digitate nature of the sandstones, the Upper C-3-X Submember is interpreted as having been deposited in a fluvial-dominated setting with low tidal influence.

Reservoir Development

Despite the shallow depth of the Upper C-3-X Submember, there are many areas in the LL-652 area where reservoir development has been minimal. One reason for this lack of development is because the Upper C-3-X Submember is shaly and contains only a few sandstones that individually are up to 10 ft (3 m) thick. Areas of relatively thick net sandstone (20 ft [6 m] or more) that correspond to distributary-channel and channel-mouth bar deposits exist with few or no perforations. For example, all perforations in the extreme northern part of the field have missed the thickest sandstone bodies (fig. VI 29). Although the density of perforations is greater in the southern part of the field, there still exist certain areas that can be targeted for development.

VII. PETROGRAPHY OF MISOA C SANDSTONES: COMPOSITIONAL, TEXTURAL, AND DIAGENETIC CONTROLS ON POROSITY DISTRIBUTION AND EVOLUTION

The goal of the petrographic study was to identify the main influences on porosity and permeability distribution in the Misoa C sandstones. Original porosity and permeability of Misoa sandstones were determined by their grain size and sorting, which were controlled, in turn, by depositional environment. However, diagenesis has significantly altered reservoir characteristics since deposition by the processes of compaction and cementation. This study indicates that diagenesis, not depositional environment, is the main control on porosity and permeability distribution in Misoa sandstones. In particular, the volume of quartz cement is the main influence on reservoir quality, and because the volume of quartz cement increases significantly with depth, reservoir quality decreases.

Methodology

A key to our approach is to conduct petrographic analyses in the context of the stratigraphic framework. The composition of Misoa sandstones was determined from 76 thin sections made from representative samples of the different members (C-3-X through C-6-X) and facies. It was then possible to quantify the petrographic characteristics of each sandstone and facies—grain size, detrital mineralogy, authigenic cements, and porosity. Matrix-free (clean) sandstones were sampled preferentially because most reservoirs are in clean sandstones. Many of the chips used to make the thin sections were taken immediately adjacent to core-analysis plugs so that petrographic parameters could be compared to porosity and permeability. The plugs themselves were not available for this study, but in general it is preferable to make thin sections from end trims off the core-analysis plugs. Composition of Misoa sandstones was determined by standard thin-section petrography and scanning electron microscopy (SEM) with an energy dispersive X-ray spectrometer (EDX).

Sampling concentrated on the five key wells, LL-2850, LL-3074, LL-3075, LL-3080, and LL-3140, from which a total of 66 thin sections were made. Thin sections also were made from two other wells, LL-846 and LL-2425, in order to sample the facies they contained, but these wells had no core-analysis data that could be compared with petrographic data. All sample depths in this report have been converted to log depths so that petrographic data can be directly compared to log response.

Point counts were done on all 76 thin sections chosen as representative of the range of Misoa sandstones. A total of 200 counts were made on each thin section. This number of counts

allows reasonable statistical accuracy compared with counting 300 points, but because each sample takes less time, more samples can be completed. Counting error varies with the percentage of the constituent. For a sample in which 200 points are counted, a constituent that composes 50 percent of the sample has an error of ± 3.6 percent, whereas a constituent that is 10 percent has an error of ± 2.1 percent and one that is 2 percent of the sample has an error of ± 0.9 percent (Folk, 1974). In comparison, if 300 points were counted, a constituent that composes 50% of the sample has an error of $\pm 3.0\%$, one that is 10 percent has an error of ± 1.7 percent, and a constituent that is 2% of the sample has an error of $\pm 0.7\%$.

Framework grain size was estimated by comparing the thin sections to standardized grain-size charts. Grain size estimated from viewing thin sections averages only 85% of grain size measured by sieving (Folk, personal communication, 1975), so raw values of grain size should be divided by 0.85 to give actual grain size. All values of grain size reported in text and tables in this report are the raw values determined from thin section and should be divided by 0.85 if the sieve-equivalent size is desired.

Point counts recognize four major categories of rock volume: detrital framework grains, matrix, authigenic cements and replacive minerals, and pores. Framework grains are subdivided by composition. The essential framework grains are those used to classify the sandstone: quartz, feldspar, and rock fragments, including chert. Other framework grains, such as biotite or tourmaline, are counted but are excluded from the calculation of sandstone type.

Detrital clay matrix is defined as grains too small to be identified in thin section. Detrital clay was distinguished from authigenic clay by using many of the criteria summarized by Wilson and Pittman (1977), including the following: 1) detrital clay commonly fills primary pores and occurs at grain-to-grain contacts; 2) it may form distinct laminae; 3) it has been compacted and does not contain porosity visible in thin section between clay particles, and 4) crystal size is generally smaller than that of authigenic clays. Where sand-size detrital clay clasts were recognized, they were counted separately from clay matrix. However, where clay clasts were deformed by compaction and no longer recognizable as distinct grains, they were counted as matrix.

Authigenic cements were categorized by composition and location, that is, whether they filled intergranular pores or occurred within secondary pores that formed by dissolution of a framework grain. It is necessary to make this distinction in order to calculate "minus-cement porosity," which is the sum of primary porosity plus the volume of cements that occur in primary pores. Minus-cement porosity provides an indication of the relative amount of porosity lost by compaction, and the total volume of cements in primary pores provides an estimate of the amount of porosity lost by cementation.

Porosity is identified during point counting as primary, intergranular porosity or secondary porosity that formed by dissolution of a framework grain or cement. It is difficult to recognize intergranular pores that were filled with carbonate cement that has subsequently completely dissolved. Unless the cement enlarged the intergranular pore space by dissolving adjacent framework grains or overgrowths, cement-dissolution porosity generally cannot be recognized except in places where part of the cement remains.

The point count data from each of the thin sections in this study are tabulated in Appendix C in tables 1-7. Each sample is identified by well number and core depth. The values listed in the tables are in percent of total rock volume, including porosity. Thus, mineral percentages listed in these tables and mentioned throughout the report refer to percent of whole-rock volume, as distinct from the percent of the solid-rock volume. The data for each sample continue on two pages; detrital minerals and detrital clay matrix are on one page and authigenic minerals and porosity are on the second page. Mean grain size is also listed on the second page.

Texture

Most Misoa sandstone samples viewed in this study are very fine grained (3.0 to 4.0 phi [0.062 to 0.125 mm]) or fine grained (3.0 to 2.0 phi [0.125 to 0.25 mm]). They are well sorted (0.35 to 0.5 phi) to moderately sorted (0.5 to 1.0 phi), according to the definition of Folk (1974). Differences in grain size are slight among the C-3-X to C-6-X sandstones (table VII 1) and among facies (table VII 2). C-6-X sandstones are the coarsest grained of the sandstone intervals, having an average grain size of 0.14 mm, and C-3-X sandstones are the finest, averaging 0.11 mm. The reason that the C-6-X sandstones are somewhat coarser than the other sandstones probably is because many C-6-X sandstones were deposited in a fluvial-estuarine channel environment, which is the coarsest grained facies (table VII 2).

Framework Mineralogy

Misoa sandstones are sublitharenites (fig. VII 1), and the average composition is Q₈₂F₆R₁₂. C-3, C-4, and C-6-X sandstones are slightly more quartz-rich than are C-5-X sandstones. Detrital quartz composes an average of 58 percent of the total rock volume and forms between 61 and 97 percent of the essential constituents. Plagioclase, the most abundant type of feldspar, has an average volume of 3.5 percent; orthoclase, which is rare, has an average volume of only 0.04 percent. Some feldspar was dissolved during diagenesis, and the volume is now occupied by secondary pores or secondary pores filled with kaolinite or calcite cement. If

we assume all the open secondary pores and all the secondary pores filled by calcite or kaolinite were originally feldspar grains, the original detrital sandstone was a subarkose with composition Q76F13R11.

Rock fragments range from 1 to 30 percent of the essential framework grains. Metamorphic rock fragments, which are composed predominantly of muscovite and quartz, are the most common lithic grains (average = 3.9 percent). Most of the metamorphic rock fragments are of low-rank rocks such as slate, phyllite, and slightly metamorphosed chert grains. Sedimentary rock fragments (average = 3.6 percent) include detrital grains of sandstone, siltstone, shale (many of which may be contemporaneous mud rip-up clasts), and chert. Minor volumes of plutonic rock fragments (average = 0.6 percent) composed of quartz and plagioclase occur in most sandstones. Most rock fragments in the Misoa sandstones are ductile and deform during compaction. Ductile grain deformation, a form of mechanical compaction, is an important cause of porosity loss in these sandstones (Plate VII 1a and b).

Other framework grains in Tirrawarra sandstones include biotite and muscovite, which are each present in volumes of ≤ 1.0 percent in most samples. Tourmaline, zircon, glauconite, leucoxene (altered ilmenite), and hematite (altered magnetite) occur in many samples in volumes of ≤ 0.5 percent. Organic matter is present in volumes ranging from 0 to 8 percent and averaging 0.6 percent.

Framework-grain composition of Misoa sandstones varies among facies (fig. VII 2). The most quartz-rich samples occur in the fluvial/estuarine channel facies in the C-6-X member. The transgressive-sand-shoal, distal-delta-front, and delta-front facies have intermediate framework-grain compositions, and the distributary-channel and tidal-channel facies contain the greatest volume of rock fragments (fig. VII 2). Delta-front and transgressive-sand-shoal sandstones probably contain a higher percentage of detrital quartz because wave and current abrasion removed more of the mechanically unstable rock fragments and because differences in hydraulic properties allowed wave and current action to winnow quartz from rock fragments. Distributary- and tidal-channel sandstones contain more abundant rock fragments because they were not winnowed. The high percentage of quartz in the fluvial/estuarine-channel deposits cannot be explained by depositional processes, and it is likely that these incised channels tapped a different, more quartz-rich source area.

Detrital Clay Matrix

Detrital clay matrix composes only 0 to 6 percent of the volume of Misoa sandstones in the samples chosen for this study. However, these samples were particularly chosen to emphasize

clean sandstones and thus do not accurately represent the average volume of detrital clay in all Missoa sandstones. In many cases it is difficult to distinguish detrital and authigenic clays, so some of the volume of clay reported as authigenic may actually be detrital (table VII 1). No X-ray diffraction analyses of matrix were done for this study, but previous X-ray work by Ghosh and others (1988) indicates that kaolinite, chlorite, illite, and mixed-layer illite-smectite (MLIS) with 70 to 80 percent illite layers occur in varying proportions in Missoa "C" sandstones. Ghosh and others did not specify whether the X-ray samples contained detrital clay, but their data suggest that the Missoa matrix is composed of a mixture of clay mineral types. Clay-size quartz probably also is a component of matrix.

Cements

Cements and replacive minerals constitute between 9 and 49 percent of the sandstone volume in Missoa samples. Cement is most abundant in clean sandstones that contain little detrital clay matrix. Because clean sandstones were preferentially sampled for this study, the average volume of 18 percent cement may not accurately represent the average volume of cement in all Missoa sandstones. It should, however, be representative of the volume of cement in reservoir sandstones. The highest average volume of cement is in the C-5-X sandstones (table VII 1), which contain particularly abundant carbonate cements—calcite, ankerite, and siderite. The facies with the highest average volumes of total cement are tidal channel, transgressive sand shoal, and distal delta front, all of which have abundant carbonate cement (table VII 2). The volume of quartz cement is 8 to 10 percent in all facies, with the exception of the fluvial/estuarine-channel samples, which have an average of 12 percent.

Quartz, carbonates, and clay minerals are the most common cements in Missoa sandstones. The relative proportion of these cements varies in the different sandstone intervals, with the C-6-X sandstones containing the greatest proportion of quartz cement and the C-3-X sandstones containing the most carbonate cements (fig. VII 3a). The relative proportions of cement types by facies are quite similar among all the facies except for the fluvial/estuarine channel sandstones, which contain the highest proportion of quartz cement (fig. VII 3b). Thus, the reason for the relatively abundant quartz cement in the C-6-X sandstones is that many of them were deposited in fluvial/estuarine-channel environments.

The only other authigenic mineral observed in the Missoa sandstones was pyrite, which is uncommon and generally occurs in volumes of <0.5 percent. Reservoir bitumen ("dead oil"), a solid hydrocarbon residue that occurs in some sandstones, is also considered a cement in this study, although it is not a mineral.

On the basis of petrographic evidence, the relative order of occurrence of the major events in the diagenetic history of the Misoa sandstones was found to be (1) precipitation of siderite rims and nodules, (2) formation of illite, and minor chlorite, rims, (3) mechanical compaction by grain rearrangement and deformation of ductile grains, (4) precipitation of quartz overgrowths, (5) precipitation of calcite cement, (6) generation of secondary porosity by dissolution of feldspars, rock fragments, and calcite cement, (7) precipitation of kaolinite and minor illite and chlorite in secondary pores, (8) precipitation of ankerite cement, (9) precipitation of additional quartz cement, and (10) migration of hydrocarbons into the reservoirs. Many of these events overlapped in time (fig. VII 4).

Quartz

Quartz is volumetrically the most abundant cement in the Misoa sandstones; the volume ranges from 0 to 19 percent and averages 10 percent. Quartz cement increases with depth, from an average of 7.8 percent at 7,200 ft to 12.5 percent at 9,200 ft (fig. VII 5; plate VII 1c and d and VII 2a and b); the relationship is significant at the 99-percent confidence level. (Four outliers were omitted from the calculation of the linear regression equation relating quartz cement and depth. Some of these atypical samples have low volumes of quartz cement because they were extensively cemented by early siderite, others because they have such abundant ductile grains and organics that they lost all porosity by compaction.) The reason for the high average volume of quartz cement in fluvial/estuarine-channel sandstones is that their average depth is 9,100 ft, considerably deeper than the other facies (table VII 2). Quartz-cement volume is the main control on porosity and permeability in C-3-X through C-6-X sandstones in the study area, as will be discussed further in the section Diagenetic Controls on Reservoir Quality.

Weak positive correlations (significant at the 90-percent confidence level) exist between volume of quartz cement and (1) the volume of detrital quartz ($r = 0.36$) and (2) grain size ($r = 0.27$). Inverse correlations exist between quartz cement and (1) volume of detrital clay ($r = -0.33$) and (2) volume of rock fragments ($r = -0.26$). Grain size and detrital-quartz content both increase with depth in this set of Misoa sandstone samples. Thus, one explanation for the increasing volume of quartz cement with depth is that quartz cement precipitated preferentially in the coarser-grained, more detrital-quartz-rich sandstones, and these occur in the deeper part of the stratigraphic section. The trend of quartz cement with depth in this case would simply be a consequence of the fact that the coarsest, most quartz-rich sandstones are oldest.

Alternatively, the volume of quartz cement may increase with depth because the deeper sandstones have higher thermal maturities, and more quartz cement precipitated in them during

their longer, hotter burial. A correlation between increased quartz cement and higher thermal maturity has been noted in other basins (for example, the East Texas Basin [Dutton and Diggs, 1990] and the Green River Basin [Dutton, 1993]). The increase of quartz cement with depth suggests that quartz cementation occurred throughout the burial history of the Misoa sandstones, probably during discrete episodes (fig. VII 4). Later episodes of quartz cementation apparently enlarged existing quartz overgrowths in optical continuity and without dust lines or other inclusions, making it difficult to distinguish different generations of quartz cement. If this hypothesis is correct, then the correlation of quartz cement with grain size and detrital-quartz content is simply a consequence of the fact that the coarsest, most detrital-quartz-rich sandstones occur in the part of the section with the highest thermal maturity. Because quartz cement has been observed to increase with thermal maturity in other formations and basins, we favor this second hypothesis to explain the increase in quartz cement with depth in the Misoa sandstones.

Authigenic Clays

Authigenic kaolinite and illite were identified by thin-section and SEM examination of Misoa sandstones. Illite and mixed-layer illite-smectite (MLIS) cannot be distinguished by these techniques, but on the basis of previous X-ray analyses (Ghosh and others, 1988) some of the clays identified as illite probably included MLIS as well. Some illite and MLIS occurs as rims of tangentially oriented flakes that developed around detrital grains early in the diagenetic history (plate VII 2c). In some places the illite rims apparently were thick enough to inhibit the precipitation of quartz cement. Other illite and MLIS has a flaky to fibrous morphology and extends into and across primary pores (plate VII 2d). The distribution and morphology of the illite and MLIS bridging and lining intergranular pores and pore throats causes a reduction in permeability in samples with abundant illite. Authigenic illite is most abundant in the tidal-channel and transgressive-sand-shoal sandstones (table VII 2), which each contain an average of 2 percent illite. All of the other facies contain an average of 1 percent illite.

Kaolinite is a reaction product of feldspar dissolution, and it is found mainly within secondary pores (plate VII 2c). Kaolinite probably has less impact on permeability in Misoa sandstones because it is somewhat isolated within secondary pores. However, much of the kaolinite appears loosely packed and thus may be susceptible to being dislodged during production, creating a mobile fines problem.

Chlorite is less abundant than either illite or kaolinite. It was tentatively identified in thin sections as coating some detrital grains and occurring in secondary pores. However, no chlorite

was observed in the SEM samples, so perhaps most of what was called chlorite in thin section is actually illite or kaolinite.

Carbonate Cements

Siderite, iron-bearing calcite, and ankerite all occur in Misoa C sandstones. Textural relations indicate that siderite was one of the first cements to precipitate (fig. VII 4; Plate VII 3a and b). Most Misoa sandstones contain only a few percent siderite cement (average volume = 3 percent), but a wide range of volumes, from 0 to 30 percent, were observed. Five samples contain more than 10 percent siderite—one sample each from delta-front, distal-delta-front, tidal-channel, transgressive-shelf, and transgressive-sand shoal facies. On average, siderite is most common in the distal-delta-front, tidal-channel, and transgressive-sand-shoal facies, but this may simply reflect the relatively small sample sizes of these facies (table VII 2) and the presence of one extensively cemented zone in each. The extensively siderite-cemented layers have very low porosity and permeability and may compartmentalize reservoirs, but their distribution and lateral extent cannot be predicted with current information.

Iron-bearing calcite cement precipitated after quartz (Plate VII 3c). The average volume of calcite cement is 2 percent, but its distribution is highly variable, ranging from 0 to 46 percent. A few samples are extensively cemented by calcite (5 samples contain >10 percent calcite and 10 samples contain 0.5 to 10 percent), but most samples (61) contain no calcite. Of the 5 samples with >10 percent calcite, two are from distributary-channel, two from delta-front, and one from tidal-channel facies. As with siderite, the controls on distribution of calcite cement could not be determined.

Dissolution of calcite cement was recognized as an important mechanism of porosity enhancement in the shallower Misoa B sandstones in this area (Ghosh and others, 1988; Maguregui, 1993). Dissolution of calcite cement is interpreted to have taken place during post-Eocene uplift, when meteoric water penetrated the formation (Ghosh and others, 1988). On the basis of thin-section and SEM observations of Misoa C samples in this study, it does not appear that calcite cement dissolution was as important in the C sandstones as in the B sandstones. Most calcite in Misoa C sandstones shows no evidence of dissolution when it is viewed in thin section or SEM. Most detrital quartz grains and overgrowths observed in SEM lack the calcite-replacement textures described by Burley and Kantorowicz (1986) and Bloch (1991), although abundant authigenic clay may obscure these features. However, dissolution of pore-filling and grain-replacing calcite did open up pores in some C sandstones. The former presence of calcite cement is inferred from remnants of calcite, enlarged intergranular pores, and irregular, corroded

margins of detrital grains (Plate VII 3d). Oversize secondary pores may or may not represent framework grains that were replaced by calcite at one time. Therefore, it seems likely that calcite dissolution occurred in the C sandstones but was relatively restricted, and most secondary pores were not previously cemented by calcite. Instead, secondary pores probably formed directly by dissolution of feldspars and other framework grains, without going through an intermediate stage of being replaced by calcite cement. However, zones of particularly abundant secondary porosity and enlarged intergranular pores probably represent porosity enhancement by dissolution of grain-replacing and pore-filling calcite.

The C sandstones are deeper than the B sandstones, which probably explains the difference between them in the importance of calcite dissolution. In the LL-3074 well, which was the shallowest well in the study area at the time of the post-Eocene uplift, the C-3-X sandstone was still 1,500 ft deep at maximum uplift. This depth was probably too great for significant meteoric water penetration and calcite dissolution in the C sandstones.

Precipitation of ankerite cement was a late diagenetic event (fig. VII 4) that apparently followed feldspar dissolution. The average volume of ankerite is 0.6 percent, and the range is 0 to 6 percent. Because of the uniformly low volume of ankerite cement, it has little impact on porosity distribution in Missoa sandstones.

Porosity

Porosity in Missoa C sandstones observed in thin section ranges from 0 to 19 percent; porosimeter-measured porosity for the equivalent samples ranges from 6.9 to 25.4 percent. Average porosimeter porosity in the Missoa sandstones that were included in the petrographic study is 15.5 percent, compared with an average of 10.3 percent thin-section porosity. In general, thin-section porosity is lower than porosimeter porosity because accurately identifying the volume of microporosity in thin section is difficult. When the microscope cross hair lands on authigenic illite or kaolinite, it is counted as the clay mineral, but abundant microporosity actually exists between the clay flakes (Plate VII 1c, d). The two measures of porosity in Missoa C sandstones are related by the following equation: porosimeter porosity = $10 + 0.5 \times (\text{thin-section porosity})$ ($r = 0.62$).

Thin-section porosity was divided into (1) primary, intergranular pores and (2) secondary pores that result from dissolution of framework grains or cements. On the basis of thin-section identification, average primary porosity has been found to be 4.9 percent, and average secondary porosity, 5.1 percent. Most secondary pores formed by the dissolution of framework grains, particularly feldspar and rock fragments. Some secondary pores contain remnants of the original

detrital grains and the reaction product kaolinite. Both primary and secondary porosity identified in thin section correlate significantly with porosimeter porosity ($r = 0.59$ and 0.50 , respectively).

Microporosity, defined as pores having pore-aperture radii $<0.5 \mu\text{m}$ (Pittman, 1979), is moderately abundant in Misoa sandstones. Microporosity cannot be accurately quantified by routine thin-section point counts, but an estimate of the volume of microporosity can be obtained by taking the difference between porosimeter-measured porosity and thin-section porosity. This method is predicated on the fact that pores that cannot be distinguished in thin section are micropores. The average volume of microporosity in Misoa C sandstones estimated by this method is 5.2 percent. The different sandstone intervals and facies of the Misoa sandstones vary in their relative proportions of primary, secondary, and microporosity (fig. VII 6). Primary porosity is relatively most abundant in C-4-X sandstones, whereas microporosity is relatively most abundant in C-3-X sandstones (fig. VII 6a). The reason for the large difference between porosimeter and thin-section porosity in the C-3-X sandstones is unknown, but it is this difference that results in the estimate of a large volume of microporosity in C-3-X sandstones. The high average permeability in C-3-X sandstones (table VII 1) suggests that most porosity is actually effective and interconnected and that for some reason the measurements of thin-section porosity in the C-3-X sandstones are too low. The fluvial/estuarine-channel facies has the highest proportion of macroporosity (primary + secondary porosity), and microporosity is most common in the transgressive-sand-shoal and distal-delta-front facies (fig. VII 6b).

Much of the depositional porosity in Misoa sandstones was lost by mechanical compaction, such as reorientation of competent grains and deformation of ductile grains (Houseknecht, 1987). Many of the sedimentary and metamorphic rock fragments in Misoa C sandstones are ductile and have been deformed during compaction, causing a reduction of primary porosity. Minus-cement porosity, which is a measure of the amount of porosity remaining after compaction, averages 19 percent in Misoa sandstones. At the time of deposition, moderately well sorted Misoa sandstones probably had a porosity of about 40 percent (Pryor, 1973; Atkins and McBride, 1992). Thus, about 21 percent porosity (53 percent of the original porosity) was lost by compaction. Much of the remaining intergranular porosity was occluded by precipitation of an average of 14 percent primary-pore-filling cement, leaving an average of about 5 percent intergranular porosity.

Diagenetic Controls on Reservoir Quality

By comparing point-count data of thin sections with core analyses, the influence of parameters such as grain size, compaction, detrital mineralogy, volume of authigenic cements,

and pore type (primary versus secondary) on porosity and permeability were analyzed (table VII 3). Only 57 of the thin-section samples were taken directly adjacent to core-analysis plugs, so only those samples were used to compare petrographic and petrophysical parameters. These samples were mostly chosen from sandstones with the best reservoir quality within each C interval, thus, the petrographic samples are not representative of the entire range of porosity and permeability in each sandstone.

When the Misoa sandstone petrographic data base is taken as a whole, combining samples from all sandstones, two parameters emerge as having the major control on porosity: depth and volume of quartz cement. Although depth is not a petrographic property of the rocks, it is the best predictor of porosity in Misoa sandstones (fig. VII 7). Porosity decreases with increasing depth in the 57-sample petrographic data base, from an average of 21 percent at 7,200 ft to 11 percent at 9,200 ft (fig. VII 7). Porosity shows the same significant decrease with depth when samples from only one facies are considered. Distributary channel samples have an average porosity of 20 percent at 7,200 ft and 10 percent at 9,200 ft. Differences in average porosity among facies are mainly a function of the depth from which the samples were taken. Thus, delta-front and transgressive-sand-shoal samples have high average porosity because those samples are from relatively shallow depths, whereas fluvial/estuarine channel samples have low average porosity because they are from greater depths (table VII 2).

The other parameter that correlates strongly with porosity is volume of quartz cement (fig. VII 8). Because quartz-cement volume increases with depth (fig. VII 5), porosity decreases. The scatter in the relationship between quartz-cement volume and porosity (fig. VII 8) indicates that quartz cement is not the only control on porosity, although it is the single most important petrographic factor (table VII 3). Thus, the decrease in porosity with depth is explained mainly by the increase of quartz cement with depth.

Relationships between permeability and various textural and mineralogic parameters in Misoa sandstones also were quantified by least-squares linear regression (table VII 3). As is true for porosity, permeability in the petrographic data base decreases significantly with depth (fig. VII 9). Average permeability at 7,200 ft is 136 md, compared with 2.8 md at 9,200 ft.

Porosity is the best predictor of permeability (fig. VII 10), and there is a good linear trend between porosity and log permeability when data from all sandstone intervals are combined. Both primary and secondary porosity contribute to permeability (table VII 3), which indicates that secondary pores are not isolated but are connected to the flow paths by primary pores. Porosity and permeability decrease systematically from the C-3-X to the C-6-X sandstones (fig. VII 10). Although the C-4-X and C-5-X sandstones have the same average porosity, average permeability is higher in the C-4-X sandstones because they contain a higher proportion of macroporosity than do the C-5-X sandstones (fig. VII 6a).

Porosity is not an independent variable but is in turn controlled by other factors. The independent petrographic parameters that correlate significantly with permeability are volume of (1) ductile grains, (2) quartz cement, and (3) authigenic illite (table VII 3). Ductile grains are defined in this study as metamorphic rock fragments, sedimentary rock fragments (sandstone, siltstone, and shale, but not chert), biotite, muscovite, and organic matter. All of these grains are easily deformed during burial, resulting in a loss of porosity and permeability by mechanical compaction. Thus, as the volume of ductile grains increases, permeability decreases (table VII 3). Quartz and illite volume also correlate significantly (at the 99-percent confidence level) with permeability (table VII 3). Grain size is not an important control on permeability in Misoa sandstones. The coarsest grains occur in the C-6-X sandstone, but they have low permeability because of deep burial and resulting abundant quartz cement.

Conclusions

Misoa C sandstones are fine to very fine grained sublitharenites. Quartz, plagioclase, and metamorphic and sedimentary rock fragments are the most abundant detrital grains. Quartz overgrowths, siderite, calcite, illite, and kaolinite are the major cements in these sandstones. An average of 5 percent primary porosity remains in these sandstones even after compaction and cementation. Porosity is further enhanced by dissolution of feldspar, rock fragments, and some calcite cement to form secondary pores.

The main control on porosity in Misoa C sandstones in the study area is the volume of quartz cement; because quartz cement increases significantly with depth, porosity decreases. Variations in average porosity among facies are a function of the average depth from which the samples were taken. Thus, delta-front and transgressive-sand-shoal samples have high average porosity because those samples are from relatively shallow depths, whereas fluvial/estuarine channel samples have low average porosity because they are from greater depths. The main parameters that influence permeability are volume of ductile grains, quartz cement, and illite cement; grain size is not an important control on permeability. Permeability decreases significantly with increasing depth because of the increase in quartz cement with depth.

In these Misoa C sandstones, diagenesis, specifically the precipitation of quartz cement, is the main control on reservoir quality. More deeply buried sandstones contain more quartz cement and thus have lower permeability than do shallower sandstones, no matter what their grain size or depositional environment. Original variations in permeability that resulted from differences in depositional energy have been overwhelmed by the subsequent diagenetic overprint.

VIII. PRODUCTION ANALYSIS

Kh Production

Cumulative production to March 1993 in 130 active wells in the LL-652 area was 165.5 MMbbl of oil (table VIII 1), mainly 37° API, and 8.3 MMbbl of water. Eighty-two percent (135.8 MMbbl) of the oil production comes from the C-3-X and C-4-X Members with an average of 1.5 MMbbl of cumulative production per well and average of 155 barrels of oil per day (BOPD). Twelve percent (20.5 MMbbl) comes from the C-5-X Member, which as an average of 0.6 MMbbl of cumulative oil per well and 215 BOPD of 41° API. The C-6-X Member has 5 percent (8.4 MMbbl) of cumulative production with an average of 0.4 MMbbl per well and 80 BOPD of 40° API. The C-2-X Member has only 1 percent (0.8 MMbbl) with an average of 109 BOPD of 37° API.

The LL-652 area is divided in seven structural compartments (fig. IV 30). Each compartment produces from multiple reservoirs. For example, compartment V has produced from the C-4-X.01 reservoir (C-3-X and C-4-X Members), the C-5-X.02 reservoir (C-5-X Member), and the C-6-X.01 reservoir (C-6-X Member). Compartment I has produced from 9 wells with a cumulative production of 17 MMbbl and 1.9 MMbbl average production per well. The LL-851 well has the best cumulative production (table P2) in this compartment with 5.3 MMbbl. The LL-1066, LL-1209, and LL-3273 wells are producing more than 200 BOPD and the LL-2981 well is producing 432 BOPD. Compartment II has a cumulative production of 5.7 MMbbl from 10 wells. The LL-652 well has the best cumulative production with 4.2 MMbbl and the LL-1316 well is producing 238 BOPD. Compartment III, located in the steeply dipping flank of the anticline in the north, is being drained by just 2 wells that have a cumulative production of 5.10 MMbbl. The LL-1293 well has produced 2.6 MMbbl and the LL-1695 has produced 2.5 MMbbl and is still producing 201 BOPD. Compartment I has produced from 8 wells with 4.5 MMbbl of cumulative production. The LL-1169 well has produced 2.1 MMbbl and the LL-3186 well is the best producer in the entire field with 635 BOPD and only 33 barrels of water per day (BWPD). Compartment V (central structural block) has the biggest production area of the field and includes 76 wells with a cumulative production of 85.8 MMbbl. Seventy-seven percent (66.1 MMbbl) of this production comes from the C-4-X.01 reservoir. The LL-852, LL-971 and LL-1106 wells have produced more than 4 MMbbl each and 7 wells are currently producing more than 200 BOPD and 4 wells are producing more than 320 BOPD. The LL-3238 well is the best producer, with 480 BOPD (table VIII 4). Compartment VI has produced from 11

wells with a cumulative production of 14.5 MMbbl. This compartment has also produced in the Maraven area from the VLA-68 and VLA-96 wells which have 2.4 MMbbl and 1.2 MMbbl of cumulative production, respectively. The best cumulative production in the Lagoven area in this compartment is from the LL-1006 well with 5.3 MMbbl. Compartment VII has produced from 28 wells with a cumulative production of 32.9 MMbbl of oil and 1.2 MMbbl of water. The LL-833 and LL-900 wells have produced 6.1 MMbbl and 4.2 MMbbl, respectively. Four wells are currently producing more than 230 BOPD and the LL-3059 and LL-3155 wells are excellent producers with more than 460 BOPD.

It was impossible to evaluate production maps at the level of submembers because open intervals in each well commonly include several submembers. We therefore had to compare production logs, but only 6 good production logs from the LL-2938, LL-2089, LL-1876, LL-3074, LL-3156 and LL-3062 wells were available. These wells are located in different blocks and produce from different members. Figures VIII 4 and VIII 5 show an example of production logs in the LL-3156 and LL-3074 wells.

The combined C-3-X/C-4-X Members account for 82 percent of oil production in the LL-652 area. The C-5-X Member has produced 12 percent and the C-6-X Member has produced 5 percent. The productivity is directly related to the average kh calculated by pressure (table VIII 3) that is highest in the C-3-X/C-4-X Members (590 md-ft), C-5-X Member (490 md-ft), and C-6-X Member (155 md-ft).

Oil-Water Contacts

An aquifer exists in the southeastern flank of compartments I, V, and VII. The movement of this aquifer is partially active as inferred from production and pressure data. Water is moving laterally along and subparallel to structural contours, also parallel with sandstone bodies. There are also multiple oil-water contacts in each member and submember that are poorly defined as a single surface because of high degree of sandstone and mudstone interbedding. Also, irregular production and lateral stratigraphic changes introduce barriers to the normal movement of the oil-water contacts not parallel with the structure. Therefore, in the absence of data, we assumed that the oil-water contacts are parallel to the structure.

Positions of oil-water contacts were estimated from (1) production history, (2) log analysis (resistivity and density log response by well), (3) water saturation from petrophysical evaluation (maps), and (4) structure and stratigraphy. Original oil-water contacts were revised from interpretations of the log response in older wells located downstructure and from production data. These contacts were also validated from the results of the petrophysical study. Table VIII 4

shows the depths where the original oil-water contacts were interpreted in compartments I, V and VII. Current oil-water contacts were estimated from log response from new wells and production-history analysis.

The Middle C-3-X and Upper C-4-X Submembers contain the best examples in the field of multiple oil-water contact analysis because they are thick and sandstone-rich and are well-documented with cores and production data.

Middle C-3-X Submember

In compartment V the original oil-water contact in the Middle C-3-X Submember was estimated at 8200 ft because the LL-1060 well (A-253) is located downstructure and contains 70 ft (21.3 m) of net pay from the petrophysical evaluation. The LL-895 well (A-254) shows the lowest oil-saturated sandstone at 8200 ft. This well has a cumulative production of 1.7 MMbbl in the C-3-X Member and was recompleted with low production. Also, the old LL-866 and LL-971 wells produced 2.7 and 4.1 MMbbl, respectively, from the C-3-X Member. The current oil-water contact in compartment V was defined at 7850 ft. The production history of the LL-895 well showed the oil-water contact was below 7800 ft. Also, the newer LL-3235 well (A-254) was drilled 120 ft (36.6 m) upstructure of the LL-895 well and was opened only in the Middle C-3-X Submember (fig. VIII 6) with more than 180 BOPD and only 8 percent water production (BWPD). The LL-1799 well, located in concession A-271, is still producing with moderate potential and shows an oil-water contact at 7850 ft.

Another good example in the Middle C-3-X Submember is in compartment VII A (table VIII 4). The original oil-water contact was defined at 7850 ft from the LL-900 well (A-274), which has a cumulative oil production of 4.1 MMbbl and is still producing from the C-3-X Member. Also, the LL-1748 well, located 220 ft (67.1 m) downstructure from the LL-900 well, has produced from the Middle C-3-X Submember in low-resistivity sandstones. The current oil-water contact was defined at 7880 ft from the new LL-3306 well, perforated in low-resistivity sandstones (± 10 ohm-m) (fig. VIII 10) and is producing more than 200 BOPD with only 4 percent water. The LL-3306 well is located at the same level of the LL-900 well, which is still producing without water and is 150 ft (45.7 m) downstructure of LL-833 well which has a cumulative production of 6.0 MMbbl and is still producing oil. Also, the production log of the LL-3156 well (fig. VIII 5) shows that this submember is producing only oil.

Upper C-4-X Submember

The original oil-water contact in compartment V in the Upper C-4-X Submember was defined at 8120 ft because the LL-1060 well (A-253) is wet and the LL-895 well (concession A-254) contained original residual oil at 8150 ft, inferred from the log response and petrophysical evaluation. The current oil-water contact in compartment V was defined at 7800 ft mainly from the production history of the high-producing LL-1987, LL-866, LL-1876, LL-2089 and LL-2191 wells, but the water contact has reached these wells, especially the LL-1987 well located downstructure at 7800 ft. The original oil-water contact in compartment VII A (north) was defined at 7980 ft because the LL-900 well (A-274) is totally wet in this member, and the top of the lowest oil sandstone was interpreted at 7950 ft. The LL-833 well also shows a wet zone below 7950 ft. The current oil-water contact is irregular but is interpreted at an average depth of 7950 ft, because the newer LL-3149 well shows a contact at this level. The LL-3156 well (A-273) shows different internal levels of oil-water contacts in this submember that were interpreted at an average of 7950 ft.

An additional area in the C-4-X.01 and C-5-X.02 reservoirs (compartment V) is now recognized because the original (official) oil-water contact was estimated too shallow. The Middle C-3-X Submember (part of the C-4-X.01 reservoir) has the old contact interpreted at 7800 ft and with the new interpretation it is at 8200 ft (cf. fig. VIII 6 with fig VIII 8). However, the Upper-Middle C-5-X.02 original oil-water contact is at 8090 ft and with the reinterpretation it is at 8300 ft. Also, we recognize an additional area in the C-4-X.03 and C-5-X.16 reservoirs (compartment VII). For example, the original (official) oil-water contact was estimated in the Middle C-3-X Submember at 7720 ft and with the new interpretation it is at 7950 ft.

Low-Resistivity Sandstones

As part of the production analysis, a general review of wells producing from low-resistivity sandstones was made as a preliminary step for the petrophysical evaluation and consisted of identifying the open low-resistivity interval in each member with water production less than 5 percent to ascertain which intervals are producing oil. Table VIII 5 is a summary of all producing wells with low-resistivity sandstones. The resistivity cutoff in the C-3-X and C-4-X Members was determined to be 10 ohm-m and in the C-5-X Member it was determined to be 10-12 ohm-m. The resistivity cutoff in the C-6-X Member (14 ohm-m) was calculated from production logs. Also, the C-3-X, C-4-X and C-5-X Members were validated by production logs. The LL-900 well (fig. VIII 9) is an example of an old well of open intervals in low-

resistivity (less than 10 ohm-m) sandstones in the C-3-X Member. The LL-3306 well (fig. VIII 10) is a new example that shows open intervals with 10 ohm-m in the Upper and Middle C-3-X Member. This well is producing 220 BOPD with only 4 percent water (7 BWPD).

IX. PETROPHYSICS

Petrophysical characterization of the LL-652 area was accomplished through integrating core and log data, quantifying petrophysical properties from wireline logs, validating petrophysical properties by net-sandstone thickness and facies maps, all ultimately leading to the calculation of reservoir volumetrics (fig. IX 1). One of the major obstacles in this petrophysical characterization was the limited number of good porosity logs due to severe borehole washouts. This difficulty was successfully resolved by developing transforms between porosity and shale volumes determined from gamma-ray and resistivity logs.

Data Integration

Data integration consisted of building a core and log database and data normalization. TerraStation, a log analysis software package from Terra Science was used to store the database and to perform well-log analysis. One hundred and forty-five digitized well logs were transferred from Lagoven into TerraStation in BEG computers. After a review of the digitized data, forty-seven wells were eliminated because of missing or anomalous curves. Among the remaining 98 well logs, 65 wells have complete electric and porosity log suites including SP, GR, caliper, neutron, density, and shallow- and deep-resistivity curves while the other 33 wells have only the electric logs including SP, and short and long normal curves. Core data were available in six key wells: LL-2850, LL-3074, LL-3075, LL-3080, LL-3140 and LL-3282.

Standardization of log data and depth adjustment were required to normalize data. The sources of differences in logs were tool malfunction, inconsistent shop and field calibration, and different operator and logging companies. Moreover, in the LL-652 area, wells were logged by five different companies over a period of forty years resulting in major differences in gamma-ray data (fig. IX 2). After a review of histograms of gamma-ray logs, we determined that differences were mainly caused by inconsistent tool calibration rather than by different company approaches. Moreover, when the volume of shale was used, the GR log was normalized on an individual well basis and the fieldwide standardization of gamma-ray logs became unnecessary.

Standardization of density-log data was not attempted because the variability in histograms of density data (fig. IX 3) could have been caused by complex depositional facies in the C Members. However, density-log data in the LL-2850 well was abnormally high. Core data from this well were used to correct the density-log data. A grain density of 2.9 gm/cc was required to match core porosity while the mean grain density of 2.67 gm/cc from core data (as shown in fig. IX 4) was the same as from other cored wells. The abnormal density-log data were

caused by over correction of the borehole effect. Therefore, a correction was made by subtracting 0.1 gm/cc from the original density-log values.

Depth adjustments were necessary because of differences in data depths from logging suites and core depth. Because of severe borehole washouts, porosity logs could not be used for depth shifting. Depth shifting between porosity and electric logs were done by mainly matching GR and SP curves, or in some cases by matching GR and resistivity logs with high-quality SP logs. In the cored wells, depth shifting of core data versus log data was accomplished by comparing GR logs between core and log (table IX 1). For the LL-3140 well the core depth was shifted by 54 ft (16.5 m) due to differences in the core-gamma and GR logs (fig. IX 5).

Petrophysical Models and Key Well Evaluation

The objective in petrophysical characterization was to develop field-specific models for evaluating petrophysical properties from wireline logs. For shaly-sand log analysis, factors such as availability of porosity logs and core data, formation-water salinity and its variability, type and distribution of clay, and volume of shale and heavy minerals were determined as important parameters for selecting and developing petrophysical models for calculating porosity, permeability and water saturation. Petrophysical models were determined by calibrating log with core data. The lack of good porosity logs as a consequence of severe borehole washouts made petrophysical characterization of LL-652 area especially difficult. Porosity, the key parameter required in petrophysical characterization, was derived indirectly from non-porosity logs such as GR, SP and resistivity. The petrophysical models of LL-652 area were developed from a total of approximately 1,500 core data points and wireline logs in six key wells.

Model for Calculating Shale Volume (V_{sh})

The V_{sh} model was important for water saturation and porosity calculations for LL-652 area. Figure IX 6 shows the models for calculating shale volume from gamma-ray index (Hilchie, 1989). The gamma-ray index of shale volume (I_{GR}) is defined as

$$I_{GR} = (GR - GR_{min}) / (GR_{max} - GR_{min}) \quad (IX.1)$$

where GR, GR_{min} , and GR_{max} are the gamma-ray values at well log depth, clean sandstone and shale. The linear model is $V_{sh} = I_{GR}$ and the Johnson and Linke's model (1978) for Tertiary deposits is non-linear. Johnson and Linke's model (1978) was developed by calibrating I_{GR}

with total V_{sh} values estimated from thin sections. In this study, thin sections were taken only in clean sandstones and hence estimated V_{sh} values were not available in shaly intervals. The linear model was selected because both porosity and water saturation derived from linear model have a better match to core-derived porosity, permeability and water saturation.

Porosity Model (V_{sh} -Porosity Transforms)

Shale volume is solely a function of gamma-ray index. However, in the C Members, there is a general trend of decreasing porosity with depth as a result of compaction and diagenesis (an increase in quartz overgrowths with depth). To account for this depth effect, the V_{sh} -porosity transforms were developed for each member.

We used both core porosity and density porosity to develop the V_{sh} -porosity transforms. Core porosity is biased towards clean sandstones and density porosity is affected by borehole washouts. Since washouts are more serious in shaly intervals than in sandy intervals, good porosity data, obtained after filtering density porosity from caliper and porosity cutoffs, are also biased towards clean sandstones. Crossplots of V_{sh} versus core porosity and density porosity for the C-3-X to C-7-X Members are shown in figures IX 7 to IX 10 and IX 11 to IX 15 respectively. Although the data points are scattered, there is a trend of increasing porosity with decreasing V_{sh} . Because both core and density porosities are biased towards the sandstones, the relationships between V_{sh} and porosity (fig. IX 16) were determined initially by linear regression from the Reduced-Major-Axes (RMA) method and subsequently by matching foot-by-foot core porosities and permeabilities in six key wells. Permeability was highly sensitive to the error in porosity estimation and porosity, obtained from the V_{sh} -porosity transforms, as well as GR_{min} and GR_{max} values. The final equations developed for the V_{sh} -porosity transforms are

$$f = (1.20 - V_{sh}) / 4.5 \quad (IX.2)$$

for the C-1-X to C-3-X Members,

$$f = (1.20 - V_{sh}) / 5 \quad (IX.3)$$

for the C-4-X Member,

$$f = (1.211 - V_{sh}) / 6 \quad (IX.4)$$

for the C-5-X Member,

$$f = (1.17 - V_{sh}) / 7.5 \quad (IX.5)$$

for the C-6-X Member and

$$f = (1.01 - V_{sh}) / 7.57 \quad (IX.6)$$

for the C-7-X Member.

The shale porosity (microporosity) also decreases with depth. As shown in track 3 of figure IX 17 in the LL-2850 well (7,285 to 7,315 ft) and in figure IX 18 in the LL-3080 well (9,057-9,070 ft) in zones of good density-log response, porosity derived from the GR log with V_{sh} -porosity transforms matches both density and core porosity within about two porosity units, while in washed-out intervals (9,000 to 9,056 ft and 9,071 to 9,200 ft), porosity derived from the GR log from V_{sh} -Porosity transforms matches core porosity within two porosity units. These transforms work well for all members in key wells in track 4 (appendix H). The shaded areas are washed-out intervals. With reliable porosity estimates, water saturation and permeability were then calculated. Another merit of V_{sh} -porosity transforms is that we used V_{sh} calculated from other logs such as SP or resistivity. Although density-log data were not reconstructed, they were calculated from porosity values derived from V_{sh} -porosity transforms.

Permeability Model (Permeability-Porosity Transforms)

Permeability of shaly sandstones is a function of porosity, pore type, particle size, sorting, clay type and distribution, and degree of cementation. However, only porosity can be derived from conventional logs and permeability is then calculated by permeability-porosity transforms obtained from core data. The ranges of scatter in permeability and porosity crossplots were of two to three orders of magnitude. These wide scatters were caused by factors other than porosity. Many efforts have been attempted to understand the effect of each factor on permeability (Beard and Weyl, 1973; Neasham, 1977; Herron and others, 1987; Panda and Lake, 1992). Neasham (1977) showed that pore-bridging clays reduce permeability more effectively than pore-filling and pore-lining clays by an order of magnitude. The recent development of geochemical logs, which provide foot-by-foot information about cement and clay types, is designed to improve permeability estimates (Herron and others, 1987).

There is a great difference between average permeability values in the C-3-X, C-4-X Members versus the C-5-X, C-6-X, and C-7-X Members (fig. V 35). The average permeabilities are 30 md in the C-3-X and C-4-X Members, and only 1 md in the C-5-X, C-6-X and C-7-X Members. These differences suggest depth control on permeability. Permeability varies greatly by member because of decrease in average porosity with depth.

This is a good porosity-permeability correlation of each C Member in each well. However, in combining all porosity-permeability data (fig. IX 19), the range of scatter in data points is significantly increased to two orders of magnitude. The range of scatter reduces significantly when these data are grouped by C Member. The scatter is caused by differences in degree of cementation and other factors that cannot be differentiated. The scatter can be reduced slightly

by grouping porosity-permeability data by facies (fig. V 37) because many factors such as particle size, degree of sorting, and clay fraction and distribution can be better differentiated by facies than by members.

For the same porosity, permeability increases with depth (fig. IX 20). A similar trend exists in the Wilcox Formation in the Gulf of Mexico (Archie, 1950). For a given porosity value, the degree of quartz cementation increases with depth while shale volume decreases with depth. Clean quartz-cement lined pores more prominent at depth have a higher permeability than the shallower, mud-rich sediments with clay-lined pores. Pore-bridging clay can reduce permeability by an order of magnitude more than pore-filling cement. The equations for the porosity-permeability transforms are obtained by RMA fit as:

$$k = 10^{-3.473 + 27.3 f} \quad (\text{IX.7})$$

for the C-1-X to C-3-X Members,

$$k = 10^{-3.696 + 31.1 f} \quad (\text{IX.8})$$

for the C-4-X Member,

$$k = 10^{-4.05 + 31.4 f} \quad (\text{IX.9})$$

for the C-5-X Member,

$$k = 10^{-4.736 + 43.8 f} \quad (\text{IX.10})$$

for the C-6-X Member, and

$$k = 10^{-5.048 + 51.0 f} \quad (\text{IX.11})$$

for the C-7-X Member, where k (permeability) is in millidarcys and ϕ (porosity) is percent. Equation IX.9 for the C-5-X Member tends to underestimate permeability because core data in this member are limited.

The comparisons between permeability, calculated by these transforms, to core permeability are shown in track 5 in Figures IX 17 and IX 18. The permeability values are consistent in most intervals. The transforms for the C-5-X, C-6-X and C-7-X Members tend to underestimate the high permeability from core data. The gamma ray curve does not adequately record thin sandstones and consequently permeability is underestimated. Detailed comparisons between calculated and measured core permeabilities of the key wells are shown in appendix H.

Water Saturation Model

Water saturation is difficult to determine in shaly sandstones. The effect of shaly-sandstone models on water saturation calculations was beyond the scope of this study. However the parameters (1) water salinity, (2) V_{sh} , and (3) clay type were incorporated into the water-saturation model.

Formation Water Salinity and R_w Determination

Water salinity was selected from the frequency histogram (fig. IX 21) that shows ranges in salinity from laboratory water analysis. The variation in water salinity in the C Members is not significant. For example, some wells have slightly higher salinity in the C-4-X Member than in the C-5-X Member. The water-salinity values used in the water-saturation model were 11,000 ppm NaCl that corresponds to 0.50 ohm-m at 77° F.

Cementation and Saturation Exponents

The predominant clays in the C Members are kaolinite, chlorite and illite. The effect of clays is to increase conductivity and in turn to reduce cementation exponent (m) and saturation exponent (n). Overburden pressure affects both cementation and saturation exponents slightly. Data from special core analysis of the LL-3282 well (fig. IX 22) indicates that m increases from about 1.8 without overburden pressure to 1.90 with 4,600 or 6,000 psi overburden pressure. Similarly, n increases from about 1.48 without overburden pressure to 1.70 with 4,600 psi overburden pressure. After correcting the shaliness using the Waxman-Smits equation, both m and n were adjusted to 2.0 (fig. IX 23), which is the value used in the well log analysis.

Water Saturation Model Selection

Petrophysical parameters used in log analysis, listed in table IX 2, were used to calculate water saturation in each key well from the Archie, Simandoux, Indonesia, and Waxman-Smits models. As shown in track 4 in Figure IX 17, the Archie equation always calculates too high water saturation and the Simandoux model matches water saturations measured from cores well. On track 2 of figure IX 24, Indonesian, Simandoux, and Waxman and Smits model are compared. The Waxman and Smits equation tends to calculate too high water saturation while

the Simandoux and Indonesian equations match the correlation well. The Simandoux model related resistivity to the total (laminated and dispersed) volume of shale:

$$S_w = (0.5 R_w / f^2) ([4 f^2 / R_w R_t])^{1/2} + (V_{sh} / R_{sh})^2 - (V_{sh} / R_{sh}) \quad (IX.12)$$

where R_w , R_{sh} and R_t are the resistivities of water, shale and formation respectively, ϕ is the porosity, and V_{sh} is the volume of shale.

Finally, the petrophysical model was used to evaluate and validate the six key wells validate in the C-3-X to C-7-X Members. Water saturations calculated by the Simandoux equation were matched to water saturations from core (fig. IX 17 to IX 18 and appendix H). There is a general trend of water saturations both measured from core and derived from log decrease with depth. As listed in table IX 6, the average water saturation is about 40 percent in the C-3-X and C-4-X Members and about 30 percent for the C-5-X, C-6-X and C-7-X Members. This may be due to the shale effect being more pronounced in the C-3-X and C-4-X Members, as well as the cement effect being more pronounced in the C-5-X, C-6-X and C-7-X Members. Microporosity associated with shale causes high capillary-trapped water saturation and high apparent water saturation. The water saturation in sandstone is actually much lower than the apparent water saturation. This may explain why there was a negligible amount of water produced from most wells in the C-3-X and C-4-X Members although the apparent water saturations were high.

The water salinity around 11,000 ppm and the water saturation calculated by the Simandoux equation are highly sensitive to the value of saturation exponent but not to the value of porosity. Water saturation values calculated by Simandoux equation with n values of 2.00, 2.02 and 2.04 were compared to water saturation values from core at 9,000 to 9,200 ft in the C-6-X Member in the LL-3080 well. The n values of 2.00, 2.02 and 2.04 are within limits of measurement error. However, the calculated water saturation varies by more than 20 percent in many intervals, especially at 9,090 to 9,170 ft. Water saturations calculated with $n = 2.00$ indicate that these intervals are greatly oil-saturated, while those calculated with $n = 2.02$ and 2.04 indicate that these intervals are wet. It is recommended to use $n = 2.00$ in the future for porosity greater than 12 percent, and to use $n = 2.02$ for porosity less than 12 percent.

Fieldwide Formation Evaluation and Validation by Mapping

All petrophysical models were validated with core and production (initial, current, and cumulative) data by well, and validated by mapping net-sandstone thickness, net pay, V_{sh} , ϕ , k ,

S_w , and kh . Map anomalies indicated problems in input parameters. The results of all wells were iteratively checked and re-evaluated during mapping to resolve inconsistencies. After petrophysical models were developed from key-well data, we applied them to sixty-five control wells with GR logs and thirty-nine wells without GR logs, using procedures listed in Figure IX 26 V_{sh} was derived from SP or resistivity logs in thirty-four other wells without density or GR curves and was calculated from the SP log.

$$V_{sh} = (SP - SP_{min}) / (SP_{max} - SP_{min}) \quad (IX.13)$$

where SP is log value, SP_{min} is SP of clean sandstone and SP_{max} is SP of shale. Base line shifting and selection of clean-sandstone values were major problems in using the SP log to calculate V_{sh} . Calculations were done in sections with shifted baselines. If SP logs could not be used, resistivity logs were used to estimate V_{sh} as

$$V_{sh} = [(R_{sh}/R_t) ((R_{max} - R_t) / (R_{max} - R_{sh}))]^{1/b} \quad (IX.14)$$

where R_{sh} is resistivity of adjacent shale, R_t the measured resistivity, R_{max} is the maximum resistivity of the clean pay zone, and b is an empirical exponent (Terra Science, 1992). The uncertainties in V_{sh} calculated by resistivity were much higher than those calculated by GR or SP. A trial and error method was used to select R_{max} and b . V_{sh} is very sensitive to the value of the b exponent. The value of b ranged from 2.0 to 3.5 and increased with the mean porosity of each member. Porosity, calculated from resistivity logs agrees with porosity calculated from density and GR logs (fig. IX 27).

Net-Pay Determinations

Net-sandstone and net-pay thickness values were determined with cutoff values of V_{sh} , water saturation and porosity. Only the V_{sh} cutoff values were used for calculating net-sandstone thickness. The relationship of V_{sh} to net-sandstone thickness for each member was determined from net-sandstone thickness counted from cores.

Net-pay thickness was determined with cutoff values for both V_{sh} , S_w and porosity. S_w cutoff was determined from resistivity logs. For the C-1-X to C-4-X Members, the resistivity cutoff was determined to be 10 ohm-m, for the C-5-X Member 12 ohm-m, and 14 ohm-m for the C-6-X Member. For the C-7-X Member, porosity and permeability are too low for this interval.

to be productive, but is still considered prospective in sandstones with resistivity greater than 25 ohm-m and porosity greater than 8 percent.

Production data were also used to validate the results of petrophysical evaluation and cutoff values. Twelve production logs from the LL-1001, LL-1156, LL-1876, LL-2010, LL-2089, LL-2187, LL-2938, LL-3062, LL-3074, LL-3075, LL-3155 and LL-3156 wells were used. Open intervals with less than 8 percent porosity and more than 55 percent water saturation were considered non-productive (see figs. VIII 4 and VIII 5). Cutoff values of V_{sh} and S_w (table IX 3) for net-sandstone and net-pay thicknesses were further modified during mapping. They were determined to be 55 percent for the C-1-X to C-4-X Members, and 50 percent for the C-5-X to C-7-X Members. The higher cutoff in water saturation for the C-3-X and C-4-X Members reflected a shale effect that is more pronounced in the C-3-X and C-4-X Members and a cement effect that is more pronounced in the C-5-X, C-6-X and C-7-X Members. The final results of net-sandstone thickness, net pay, S_w , porosity, permeability, kh, and Øh by member and submember in each well are summarized in tables IX 4 to IX 10.

X. VOLUMETRICS

Calculation of OOIP and Remaining Oil Volumes

The first step in the procedure of calculating OOIP and remaining oil volumes was to prepare computer-generated maps of net pay, S_w , ϕ , k , kh , and $S_o\phi h$ for each reservoir submember. These maps were then hand-contoured to reflect trends in net-sandstone thickness and log-facies maps and were later digitized for volumetric calculation. The digitized maps were converted to grids with Zycor's PCMS mapping software (PC mapping system) on 328-ft (100-m) spacing to preserve geological information such as faults, compartment boundaries, and net-sandstone thickness trends.

Hydrocarbon pore volume ($S_o\phi h$) maps were constructed by multiplying oil saturation (S_o), porosity (ϕ), and net-pay (h) values at each grid point. Original oil in place (OOIP) was calculated for each submember and structural compartment by integrating the gridded $S_o\phi h$ data with area.

Values and spatial distribution of remaining oil volume were determined in a three-step process. First, OOIP per 80-acre well spacing was calculated by scaling up the 328-ft (100-m) grids to 1,968-ft (600-m) grids. Second, well-by-well production at the submember level, apportioned from kh , was partitioned among adjacent grids by the reverse-distance weighting method. Third, maps of remaining oil in place for individual submembers were prepared by subtracting oil production from oil-in-place values for each 80-acre spacing grid.

The volumetrics analysis has resulted in an increase in the original-oil-in-place resource base of 867 MMbbl (60 percent) to 2,318.2 MMbbl (table X 1). This increase was mainly in the C-3-X and C-4-X Members by documenting additional reservoir areas and by using more appropriate and carefully validated petrophysical parameters. For example, the official porosity value used to calculate OOIP for these members was 15 percent, but this study determined a more appropriate value of 18 percent. In contrast, the OOIP estimate in the C-6-X Member was decreased by 31 percent (table X 1) as a result of adjusting the average porosity value of 13.2 percent to 11 percent.

This study applied a recovery factor of 20.2 percent for reservoirs in the C Members, the same value also previously used by Lagoven. Based on this recovery factor and the volumetric analysis, the estimated ultimate recovery (EUR) of oil at current technology is 468 MMbbl, an increase of 175 MMbbl (60 percent) (table X 2). Additionally, the estimated amount of reserves has increased by 137 percent (175 MMbbl) from 127.5 to 302.5 MMbbl (table X 2).

Net Oil Sandstone

Net-oil-sandstone (net-pay) maps of the C members and submembers (figs. X 1 to X 8 and appendix F) exhibit northeast-trending patterns, reflecting depositional influence on reservoir geometry. Net-pay contours extend across the field in most members and submembers, although in some intervals (for example, the Lower Upper C-6-X Submember, C-5-X Member, Lower C-5-X Submember, combined Middle and Upper Middle C-5-X Submembers, and C-2-X Member), net-pay thickness decreases northeastward, reflecting seaward (northeastward) pinchout of delta-front sandstones. Structural influences are indicated by abrupt changes in net-pay values across faults, particularly in the southwestern and northeastern parts of the field. Net-pay contours are closely spaced and bounded by zero values due to oil-water contacts on the southern and southeastern limbs of the field. Net-pay distribution varies tremendously across the field for each member and submember but tends to be greater in the northern part of the field due to steeply dipping strata.

C-7-X Member

The C-7-X Member is nonproductive due to high (>55%) water saturation. However, the net-pay map indicates a theoretical net-pay maximum of more than 60 ft (18 m) in an irregular, northeast-trending band that includes the LL-2942 and LL-3173 wells (fig. X 1). These theoretically high values may reflect high net-sandstone thickness values in a deltaic depocenter. A structurally complex, prospective area exists northward where no wells have yet penetrated the C-7-X Member.

C-6-X Member

The C-6-X Member contains up to 350 ft (106.7 m) of net pay in the northern and central parts of the field (fig. X 2). In contrast, the extreme southwestern part of the field commonly contains less than 200 ft (61 m) of net pay. The area of more than 250 ft (76.2 m) of net pay in the central part of the field is northeast-trending, whereas there is no apparent trend in the northern part of the field.

C-5-X Member and Lower Middle C-5-X Submember

The C-5-X Member contains the lowest net pay per foot of the C-3-X through C-6-X Members. The net-pay thickness map of the C-5-X Member exhibits four bands of more than 100 ft (30.5 m), of which only one band centered on the LL-1782 and LL-1130 wells, extends across the field (fig. X 3). The low net-pay thickness of the C-5-X Member is partially controlled by the sandstone-poor, distal-deltaic nature of the Lower and Upper C-5-X Submembers (figs. VI 10 and VI 18), reflected by pinchout of net-pay patterns (fig. X 3).

Net-pay distribution in the Lower Middle C-5-X Submember is strongly controlled by net-sandstone thickness (figs. X 4 and VI 24, respectively). Net pay exists as parallel, narrow (commonly less than 2,000 ft [610 m]) belts of 20 ft (6 m) or more in the central part of the field, corresponding to dip-parallel, delta-front sandstones. Because of the heterogeneous pay distribution, multiple infill well opportunities exist in the Lower Middle C-5-X Submember in this part of the field, particularly where relatively thick net-pay trends intersect the zone of sealing and partly sealing reverse faults.

C-4-X Member and Upper C-4-X Submember

Net pay in the C-4-X Member is strongly dip-oriented and is greatest (up to 280 ft [85.4 m]) in the northern part of the field (fig. X 5). The Upper C-4-X Submember contains the greatest pay of the three submembers in the C-4-X Member, with up to 200 ft (61 m) of net pay in the northern part of the field (fig. X 6). There is good correspondence between net-pay thickness and net-sandstone thickness in the Upper C-4-X Submember (fig. VI 22), suggesting a strong depositional control on reservoir geometry. However, high net-pay thickness in the northern part of the field is partly controlled by steeply dipping strata in a structurally complex area.

C-3-X Member and Middle C-3-X Submember

The C-3-X Member contains less net pay (fig. X 7) than the C-4-X Member because most of the C-3-X Member is sandstone-poor, except for the Middle C-3-X Submember, in which net pay is distributed in multiple bands of more than 40 ft (12 m) of varying width that mostly extend across the field (fig. X 8). The majority of the thicker net-pay bands correspond to depositional axes of more than 50 percent sandstone (fig. VII 26), although the band of thick net

pay that includes the LL-866 and LL-1176 wells is slightly north of the corresponding zone of more than 50 percent sandstone. Multiple infill targets exist in the Middle C-3-X Submember because this interval is sandstone-rich and also internally heterogeneous, reflected in great net-pay contrast that ranges from 20 to 60 ft (6 to 18 m) (fig. X 8).

C-1-X and C-2-X Members

The C-1-X and C-2-X Members are relatively unimportant targets for additional development because they each contain relatively thin net pay (commonly less than 20 and 40 ft [6 and 12 m], respectively) distributed in small, discrete areas in the field (appendix F). These discontinuous areas of net pay may represent thin, shaly delta-front or inner-shelf sandstones with moderate to poor reservoir quality.

Porosity

As with net pay, porosity in the C members and submembers is distributed in narrow (commonly less than 3,000 ft [915 m] wide), northeast-trending belts (figs. X 9 to X 12 and appendix F). However, there is a consistent decrease in maximum porosity from the C-3-X Member to the C-6-X Member (20 to 12 percent) related to burial diagenesis rather than to depositional control.

C-6-X and C-7-X Members

Porosity in the C-6-X and C-7-X Members is typically distributed in 2,000- to 3,000-ft (610- to 915-m) wide bands of 12 percent or more, bounded laterally by wide (more than 6,000-ft [1,829-m]) areas of 9 to 11 percent porosity (appendix F). The Lower Lower C-6-X Submember is representative of these stratigraphic intervals and contains one, northeast-trending band of more than 12 percent porosity (fig. X 9) that coincides with the zone of deep incision inferred to be thick (90 to 130 ft [27.4 to 39.6 m]) fluvial-estuarine sandstones (fig. VI 2).

C-5-X Member and Lower Middle C-5-X Submember

Porosity in the C-5-X Member ranges from 11 to 17 percent (appendix F), with maximum porosity typically confined to discontinuous, northeast-trending pods of more than 16 percent that occur within multiple belts of 14 to 16 percent porosity, 1,000 to 4,000 ft (305 to 1,220 m) wide. In the shalier submembers (for example, the Lower and Upper C-5-X Submembers), these belts of 14 to 16 percent porosity pinch out downdip (northeastward). The sandstone-rich Lower Middle C-5-X Submember contains four belts of 14 to 16 percent porosity that extend across the field (fig. X 10). The dip-parallel nature of these high-porosity belts reflects a system of dip-elongate tidal-ridge sandstones that correspond to multiple, parallel belts of 20 ft (6 m) or more of net pay (fig. X 4).

C-4-X Member and Upper C-4-X Submember

Porosity in the C-4-X Member ranges from 13 to 19 percent and is distributed in multiple, northeast-trending belts (appendix F and fig. X 11). The Upper C-4-X Submember contains the highest porosity in the C-4-X Member, which occurs in dip-elongate pods in the southwestern and northwestern parts of the field (fig. X 11). The great variability and spatial complexity in porosity in the Upper C-4-X Submember impart a high degree of heterogeneity to this submember, making it an excellent candidate for infield development. Remaining oil may be stratigraphically trapped in isolated, high-porosity (more than 18-percent) pods in the central part of the field and may also be structurally trapped in the north-northeast-trending zone of reverse faults.

C-3-X Member and Middle C-3-X Submember

Porosity in the C-3-X Member reaches a maximum of just over 20 percent (appendix F) and is best developed in the Middle C-3-X Submember (fig. X 12). The porosity distribution in each submember strongly reflects the net-sandstone and net-pay distribution. For example, in the Lower C-3-X Submember there are numerous, northeast-trending and narrow (commonly less than 1,200 [366 m] wide) belts of 18 to 20 percent porosity that correspond to tidal-ridge sandstones (appendix F), whereas in the Middle C-3-X Submember the relatively wide belts of high porosity are related to thick (more than 40-ft [12-m]) multilateral distributary-channel sandstone bodies (fig. X 12). Additionally, the east- and southeast-trending belts of high

porosity in the Upper C-3-X Submember are controlled by the east- and southeast-trending depositional fabric of fluvial-dominated, distributary-channel sandstones.

Permeability

Average permeability in the C-3-X to C-7-X Members ranges from more than 200 md in the C-3-X Member to less than 10 md in the C-7-X Members (figs. X 13 to X 17 and appendix F). Average permeability trends are similar to those of net-pay and porosity and consist of northeast-trending belts that extend over large distances (typically over 4 mi [6.4 km]) across the field.

C-7-X and C-6-X Members

Greatest average permeability in the C-7-X Member occurs in a single, northeast-trending belt centered on the LL-2940 well. This belt contains 4 md or more of average permeability and ranges from 2,000 to 4,000 ft (610 to 1,220 m) wide (fig. X 13). Average permeability in the C-6-X Member is low and reaches a maximum only 16 md in the Lower Lower and Lower Upper Submembers (appendix F). Permeability trends in the C-6-X Member are mostly simple, dip-parallel or bifurcating belts, reflecting the dominance of delta-front facies (appendix F).

C-5-X Member and Lower Middle C-5-X Submember

Average permeability in the C-5-X Member is just as low as in the C-6-X Member, and is commonly less than 8 md (appendix F). The Lower Middle C-5-X Submember has the greatest average permeability in the C-5-X Member, distributed in four belts of more than 6 md (fig. X 14). These belts are 1,600 to 4,000 ft (488 to 1,220 m) wide with the central two bifurcating and pinching out northeastward.

C-4-X Member and Upper C-4-X Submember

Average permeability in the C-4-X Member (appendix F) is significantly higher than in the C-5-X, C-6-X, and C-7-X Members and reaches a maximum of over 250 md in the Upper C-4-X Submembers, which contains three continuous and two discontinuous belts of more than 150

md permeability, 1,600 to 3,200 ft (488 to 976 m) wide (fig. X 15). Average permeability in the Upper C-4-X Submember is highest in the central and north-central parts of the field, where the belts of high permeability are more continuous. Permeability contrast in the Upper C-4-X Submember is also higher than in the other C-4-X submembers, which may indicate a higher average potential for unswept mobile oil in areas of abrupt change in permeability.

C-3-X Member and Middle C-3-X Submember

The C-3-X Member contains the greatest differences in permeability trends between individual submembers than in any other member in the LL-652 area (appendix F and fig. X 16). Highest average permeability in the Lower C-3-X Submember occurs in two discontinuous, northeast-trending belts of more than 150 md in widely separated areas (appendix F), whereas the Middle C-3-X Submember contains a major, continuous northeast-trending belt of more than 200 md in the southern part of the field, as well as scattered pods of more than 150 md elsewhere (fig. X 16). In contrast, average permeability distribution in the Upper C-3-X Submember occurs in discontinuous and narrow (less than 2,000 ft [610 m] wide) southeast-trending pods of more than 100 md (appendix F).

C-2-X Member

Average permeability in the C-2-X Member is significantly lower than in either the C-3-X and C-4-X Members. Greatest permeability occurs in isolated patches of more than 60 md (fig. X 17). The low average permeability of the C-2-X Member is primarily related to low net-sandstone content and irregular sandstone geometry.

Water Saturation

Water saturation in the C-1-X to C-6-X Members ranges from approximately 25 to 55 percent inside the reservoir limits (appendix F and fig. X 18). Because the productive limit for the C members is 55 percent or less water saturation, the entire C-1-X to C-6-X interval produces oil (fig. II 5). Water-saturation trends reflect structural control, although some members and submembers contain anomalous trends that may reflect depositional control.

C-6-X Member

Minimum water saturation (approximately 25 percent) in the C-6-X Member is present on the western edge of the LL-652 area in the Lower Lower and Upper Lower C-6-X Submembers (appendix F). This area corresponds to 35 percent water saturation in the other C-6-X submembers (appendix F). Water-saturation trends in most C-6-X submembers are structurally controlled. However, the lower C-6-X submembers differ from the upper C-6-X submembers in the northern part of the field in that contours are southward-deflected and oriented orthogonally to the main anticlinal structure.

C-5-X Member

Water-saturation values in the C-5-X Member are lowest (25 percent or less) in the Lower and Lower Middle C-5-X Submembers in the northwestern part of the LL-652 area (appendix F). In the Upper and combined Middle and Upper Middle C-5-X Submembers, these areas correspond to 30 and 40 percent water saturation, respectively (appendix F). Although the southern limb of the reservoir contains structurally controlled water-saturation contours, the central part of the field, particularly in the Upper and combined Middle and Upper Middle C-5-X Submembers, features podlike, northeast-trending contours that may correspond to the depositional fabric (see also figs. VI 15, VI 16, VI 17, and VI 18). These contours cut across structurally high areas, and exhibit northeastward pinchouts consistent with net-sandstone thickness trends.

C-4-X Member

Water-saturation values in the C-4-X Member are lowest (less than 40 percent) in the northern and western parts of the field (appendix F). However, the Upper C-4-X Submember contains two northeast-trending belts of less than 40 percent water saturation that are 3,000 to 6,000 ft (915 to 1,820 m) wide and which extend across the field (fig. X 18). These belts are depositionally influenced and correspond to sandstone-rich, distributary-channel and delta-front depositional axes (fig. VI 22). Additional oil resources may exist in these belts of low water saturation where reservoir drainage may be partly controlled by the depositional architecture.

C-3-X Member

Average water saturation in the C-3-X Member is higher than in the C-4-X to C-7-X Members and is typically 40 to 45 percent throughout most of the field (appendix F and fig. X 19). Trends of water saturation in the C-3-X submembers are poorly related to net-sandstone thickness trends, except in the Middle C-3-X Submember where there are northeast-trending bands of low water saturation (less than 40 percent) that mimic net-sandstone thickness (fig. VI 26). In contrast, most water-saturation trends in the shaly Lower and Upper C-3-X Submembers are nearly at right angles to net-sandstone thickness trends, suggesting that the shaly nature and numerous but thin sandstones in these submembers (individually commonly less than 5 ft [1.5 m]) are not sufficient to control water saturation except only on a local scale.

C-2-X and C-1-X Member

Water saturation in the C-2-X and C-1-X Members is high, with values commonly greater than 45 percent (appendix F). There are few distinctive water-saturation trends in these members, except for small, scattered pods of anomalously high or low values of water saturation in the C-2-X Member in the northern part of the field (appendix F).

Porous Hydrocarbon Volume

Porous hydrocarbon volume ($S_o\emptyset h$), measured in feet, is distributed in five structural compartments in the LL-652 area (figs. X 20 to X 27). Northeast trends of $S_o\emptyset h$ in the LL-652 area strongly reflect net-pay distribution, which in turn is dominated by the northeast-trending depositional fabric. The greatest $S_o\emptyset h$ values in the C Members occur in the sandstone-rich Upper C-4-X and Middle C-3-X Submembers.

C-7-X Member

Porous hydrocarbon volume ($S_o\emptyset h$) in the C-7-X Member reaches a maximum of 5.48 ft (1.67 m) (fig. X 20). Greatest values of $S_o\emptyset h$ are northeast-trending and correspond to maximum net-pay thickness (fig. X 1).

C-6-X Member

The Lower Lower C-6-X Submember contains the greatest value of $S_o\emptyset h$ (9.54 ft [2.91 m]) of all submembers in the C-6-X Member, with a northeast-trending band of more than 7 ft (2.1 m) centered on the LL-1172 and LL-1126 wells (fig. X 21). This band of high $S_o\emptyset h$ values is controlled by the belt of thick (more than 90-ft [27.4-m]) fluvial-estuarine sandstone in a zone of relatively deep incision of the C-6-X Member into the C-7-X Member (figs. VI 2 and VI 3).

All other submembers in the C-6-X Member exhibit strong northeast-trending $S_o\emptyset h$ patterns (appendix F), reflecting the predominant northeast-trending grain of net-sandstone thickness. Consistently higher $S_o\emptyset h$ values in the northern structural blocks reflect dipping strata.

C-5-X Member

The Lower C-5-X and combined Middle and Upper Middle C-5-X Submembers contain the greatest $S_o\emptyset h$ values (up to 9.60 ft [2.93 m] (fig. X 22) and 8.57 ft [2.61 m] (fig. X 23), respectively) in the C-5-X Member. High $S_o\emptyset h$ values in the Lower C-5-X Submember are controlled by the relatively great thickness (approximately 250 ft [76 m]) of this submember (fig. II 5) which is sandstone-poor (fig. VI 10). In contrast, high $S_o\emptyset h$ values in the combined Middle and Upper Middle C-5-X Submembers is primarily controlled by thick distributary-channel and proximal delta-front sandstones (figs. VI 16 and VI 17), particularly in the central and southern structural blocks (fig. X 23).

C-4-X Member

Submembers in the C-4-X Member contain the greatest $S_o\emptyset h$ values in the entire C section, particularly in the Upper C-4-X Submember, where $S_o\emptyset h$ values reach a maximum of 26.6 ft (8.1 m) (fig. X 24). These high $S_o\emptyset h$ values primarily reflect thick net-pay values (fig. X 6) associated with a major sandstone-rich, progradational deltaic wedge (figs. II 5 and VI 22). Greatest $S_o\emptyset h$ values (more than 10 ft [3 m]) correspond to thick depositional axes of more than 100 ft (30.5 m) of net sandstone (fig. VI 22), particularly in the area of the LL-2089 well and LL-3186 wells in the central structural block and the LL-3262 well in the north-central structural block (fig. X 24).

The Lower and Middle C-4-X Submembers both feature prominent northeast-trending $S_o\emptyset h$ patterns (appendix F). In contrast to the Upper C-4-X Submember, the Middle C-4-X Submember contains highest $S_o\emptyset h$ values is (more than 5 ft [1.5 m]) in one 2,000-ft (610-m) wide, northeast-trending band in the north-central part of the field (fig. X 25).

C-3-X Member

Greatest $S_o\emptyset h$ values in the Lower and Middle C-3-X Submembers are similarly high (12.44 ft [3.79 m] [fig. X 26] and 9.62 ft [2.93 m] [fig. X 27] respectively). The reasons why these greatest $S_o\emptyset h$ values are similar is that even though the Lower C-3-X Submember is thicker than the Middle C-3-X Submember (fig. II 5), it is much shalier than the Middle C-3-X Submember (figs. VI 25 and VI 26). Additionally, whereas high $S_o\emptyset h$ values are widely distributed across the field in the Middle C-3-X Submember (fig. X 27), they are confined to narrow (less than 1,500-ft [457-m]) belts in the Lower C-3-X Submember (fig. X 26). The difference in the $S_o\emptyset h$ geometry between these submembers is controlled by the different depositional system and sandstone architecture: the Lower C-3-X Submember in the LL-652 area consists of narrow, distal delta-front, tidal-ridge sandstones (fig. VI 25) whereas the Middle C-3-X Submember is composed of sandstone-rich, distributary-channel and proximal delta-front sandstones (fig. VI 26).

Original Oil in Place

Original oil in place (OOIP) in the C Members in the LL-652 area is strongly related to net-pay and net-sandstone thickness and is therefore commonly distributed in northeast-trending patterns. The Upper C-4-X and Middle C-3-X Submembers contain the greatest volumes of OOIP, with locally up to 16 MMbbl and 6.2 MMbbl per 80 acres, respectively. As a result of the volumetric analysis and use of improved petrophysical parameters, the net value of OOIP has been greatly increased for the C Members in the LL-652 area (table X 1).

C-6-X Member

All submembers in the C-6-X Members have prominent, northeast-trending OOIP patterns (fig. X 28 and appendix F). The Lower Lower C-6-X Submember contains the greatest OOIP values (up to 8 MMbbl per 80 acres) in an area of northeast-trending contours centered on the

LL-1172 and LL-847 wells (fig. X 28), which corresponds to thick (more than 90-ft [27.4-m]) fluvial-estuarine deposits (figs. VI 2 and VI 3).

C-5-X Member

The Lower and combined Middle and Upper Middle C-5-X Submembers contain the greatest values of OOIP (locally more than 5 MMbbl per 80 acres [fig. X 29 and X 30, respectively]). Due to sparse well control, OOIP contours are poorly defined in the Lower C-5-X Submember in the southern structural block (fig. X 29). However, contours are well-defined in the central structural block and they consist of east- and northeast-trending pods of more than 1 MMbbl per 80 acres. These pods correspond to narrow (less than 2,000 ft [620 m]) distal delta-front, tidal sand-ridge deposits encased in inner-shelf mudstone (fig. VI 10). In contrast, OOIP contours in the combined Middle and Upper Middle C-5-X Submember in the central structural block consist of wide (more than 3,000 ft [915 m]), eastward- and northeastward-bifurcating pods that reflect the depositional geometry of distributary-channel sandstones in the Middle Middle C-5-X Submember (fig. VI 26).

C-4-X Member

The Lower and Middle C-4-X Submembers contain moderate volumes of OOIP (locally more than 4 MMbbl per 80 acres [appendix F]), whereas the Upper C-4-X Submember contains high volumes of OOIP (commonly more than 6 MMbbl per 80 acres in the central and more than 10 MMbbl per 80 acres in the northern structural blocks [fig. X 31]). Thick pods of more than 7 MMbbl per 80 acres of OOIP approximately correspond to thick (more than 80-ft [24.4-m]) distributary-channel and proximal delta-front sandstones (fig. VI 22) in the central structural block (fig. X 31). The northern structural blocks commonly contain more than 10 MMbbl per 80 acres of OOIP and coincide with dipping strata in a northern deltaic depocenter of more than 100 ft (30.5 m) of net sandstone (fig. VI 22).

C-3-X Member

Greatest values of OOIP (more than 6 MMbbl per 80 acres) in the C-3-X Member occur in the northern structural blocks in the Lower C-3-X Submember (fig. X 32) and in the eastern part of the central structural block in the Middle C-3-X Submember (fig. X 33). These high values of

OOIP in the eastern part of the central structural block roughly correspond to thick (more than 50-ft [15.2-m]) distributary-channel sandstones (figs. VI 26 and VI 27). Although the Lower C-3-X Submember locally contains higher OOIP values than the Middle C-3-X Submember, average OOIP values in the Middle C-3-X Submember in the central structural block are higher than average OOIP values in the Lower C-3-X Submember (figs. X 33 and X 32, respectively), reflecting sandstone-rich, distributary-channel and proximal delta-front deposits in the Middle C-3-X Submember (fig. VI 26) as contrasted against muddy, distal delta-front deposits in the Lower C-3-X Submember (fig. VI 25).

Remaining Oil

Maps of remaining oil of the C Submembers (figs. X 34 to X 40) have similar to identical trends to maps of original oil in place (figs. X 28 to X 33). Sites for each submember where values of remaining oil are identical or nearly identical to those of original oil in place indicate areas of undrained or poorly drained reservoir compartments that can be targeted for additional oil recovery.

C-6-X Member

The Lower Lower C-6-X and the Upper Lower C-6-X Submembers contain the greatest volumes of remaining oil in the C-6-X Member (up to 6 MMbbl and 4.4 MMbbl per 80 acres [figs. X 34 and X 35], respectively). These volumes of remaining oil are depositionally controlled. As with S_oØh (fig. X 21), greatest volumes of remaining oil in the Lower Lower C-6-X Submember occur in a northeast-trending band of more than 4 MMbbl per 80 acres, centered on the LL-1172 and LL-847 wells (fig. X 34). This band also corresponds to the belt of thick (more than 90-ft [27.4-m]) fluvial-estuarine sandstones in the zone of relatively deep incision of the C-6-X Member into the C-7-X Member (figs. VI 2 and VI 3). Greatest volumes of remaining oil (more than 3.60 MMbbl per 80 acres) in the Upper Lower C-6-X Submember also occur in a northeast-trending band that corresponds to a northeast-trending belt of more than 70 ft (21.3 m) of fluvial-estuarine sandstones (fig. VI 4).

Remaining oil in other C-6-X submembers is distributed in also northeast-trending patterns, reflecting the depositional fabric of distributary-channel and delta-front sandstones (appendix F). Volumes of remaining oil in the Middle and Upper C-6-X Submembers are less than in the Lower C-6-X Submembers as a result of these submembers having been deposited in a sandstone-poor, net-retrogradational sequence (fig. II 5).

C-5-X Member

The Lower and combined Middle and Upper Middle C-5-X Submembers contain the largest volumes of remaining oil in the C-5-X Member (figs. X 36 and X 37). The Lower C-5-X Submember contains high volumes of remaining oil per unit area in the southern and northern structural blocks (locally more than 3.6 MMbbl per 80 acres) but relatively less per unit area (typically 1 to 2 MMbbl per 80 acres) in the central structural block (fig. X 36), reflecting the combined effects of sandstone thickness (fig. VI 10) and dipping strata in the structurally complex, northern part of the LL-652 area.

In contrast to the Lower C-5-X Submember, the combined Middle and Upper Middle Submembers features eastward- and northeastward-trending, lobate trends of remaining oil (more than 1.8 MMbbl per 80 acres), reflecting depositional control by distributary-channel and channel-mouth bar deposits in the Upper Middle C-5-X Submember (fig. VI 17).

C-4-X Member

The Upper C-4-X Submember (fig. X 38) contains more remaining oil than the Lower and Middle C-4-X Submembers combined (appendix F). Many areas, particularly in the northern part of the field, contain nearly as much remaining oil as original oil in place (cf. fig. X 31), indicating that the Upper C-4-X Submember has a high potential for secondary oil recovery. Other areas with great volumes of remaining oil are in the western, northern, and eastern parts of the central structural block (more than 8 MMbbl per 80 acres) that coincide with thick (more than 80-ft [24.4-m]) delta-front and distributary-channel sandstones (fig. VI 22).

C-3-X Member

High volumes of remaining oil in the Lower C-3-X Submember (more than 4 MMbbl per 80 acres) occur in the northern part of the field (fig. X 39), coincident with high values of original oil in place (fig. X 32). High volumes of remaining oil in the Middle C-3-X Submember also occur in the eastern part of the central structural block (more than 4 MMbbl per 80 acres) and in the northern part of the three northern structural blocks (more than 3 MMbbl per 80 acres) (fig. X 40). Volumes of remaining oil in the Middle C-3-X Submember are quite similar to those of original oil in place (fig. X 33), indicating that this submember has an excellent potential for secondary oil recovery.

Reservoir Boundaries

Criteria for analyzing reservoir boundaries were mainly based on the degree of communication between faulted blocks and the architecture of individual sandstones, extremely important in the LL-652 area where the structural style and stratigraphic complexity combine to produce reservoir heterogeneity. Reservoir boundaries were determined by analyzing the vertical and horizontal communication assessing (1) RFT data, previously used in the fault-seal analysis, (2) permeability data from special analysis in the six cored wells, and (3) integration with petrophysical parameters and stratigraphy.

Vertical Communication

Vertical communication was estimated from RFT data in 7 wells (table IV 3). This tool can resolve a pressure difference of 50 psi between two overlying sandstones, a value which is sufficient to indicate poor reservoir communication. In the LL-652 area there is no communication between members and submembers because almost 98 percent of the pressure data (figs. IV 43, IV 44, and IV 45) showed an average of more than 50 psi. For example, the LL-3195 well (fig. IV 43) has a 625-psi difference between the C-3-X (2200 psi) and C-4-X (1575 psi) Members, and a 190-psi difference (fig. IV 44) between the C-4-X and C-5-X (1760 psi) Members. The LL-3186 well (fig. IV 44) has a 500-psi difference between the C-3-X (2513 psi) and C-4-X (2010 psi) Members. The LL-3141 well (fig. IV 45) has 1950 psi in the Upper C-4-X Submember and an average of 2480 psi in the Middle C-4-X Submember, a 530-psi difference. Also, the LL-3195 well (fig. IV 47) has a 255-psi difference between the Upper C-5-X (1767 psi) and Upper Middle C-5-X Submembers. Finally, most of the RFT tests showed that between individual sandstones in submembers, there is poor or restricted vertical communication. For example, the LL-3173 well (fig. IV 43) has a 135-psi difference between the upper sandstone (1720 psi) and lower sandstones in the Upper C-4-X Submember.

Permeability data from the LL-2850, LL-3074, LL-3075, LL-3080, LL-3140 and LL-3282 were used to verify vertical communication between subjacent sandstones. Permeability is a measurement of the ability of the filling fluid to move through the pore space and reflects the interconnectivity of pores in the rock. The low-quality reservoirs in the LL-652 area have a correlation line on the porosity-permeability crossplot (fig. IX 19) that plots lower along the permeability axis with respect to that of good-quality reservoirs. In particular, the LL-652 reservoirs are low-permeability more than they are low-porosity. the vertical variation of permeability from core was also a good indicator of interbedded, complexly stratified reservoirs.

For example, the horizontal versus vertical permeabilities for the LL-2850 well, shown in figure X 41, indicate that horizontal permeabilities are always higher than vertical permeabilities for the same depth. For average samples, horizontal permeabilities are approximately 400 higher than vertical (at $k_h=50$ md, $k_v=10$ md).

Finally, the RFT and permeability data showed that the vertical permeability is extremely poor or nonexistent between subjacent sandstones in the C-3-X, C-4-X, C-5-X and C-6-X Members.

Horizontal Communication

RFT and pressure data indicated strong stratigraphic controls on pressure values in conjunction with complex fault patterns. The boundaries of reservoir compartments were inferred from the pressure analysis.

By using fault-seal--probability data (table IV 4) we recognized 4 faults that form reservoir boundaries. The Master fault, located in the Maraven area represents the western limit of the LL-652 area and for engineering models should be considered a geological boundary. The main fault and the northeast reverse fault (#11) combine to isolate compartment I (fig IV 49) which is located on the downthrown side of these faults. This fault separates other reservoirs (C-4-X.01, C-5-X.02 and C-6-X.01) that are located on the upthrown block of these two faults. The south fault forms the southern limit of the C-4-X.03, C-5-X.08 and C-6-X.16 reservoirs. The central fault bounds the C-4-X.01, C-5-X.02 and C-6-X.01 reservoirs from the C-4-X.03, C-5-X.08 and C-6-X.16 reservoirs.

Another reservoir boundary is formed by the northwest reverse fault, but due to the small area west of this fault in the high-dip zone, it is recommended that the reserves in this area be assigned to the C-4-X.01 and C-05-X.02 reservoirs. The southeastward boundary is defined by an aquifer (individual oil-water contacts by submembers) previously described in the production-analysis section. The northern limit is unknown due to the sparse well control, but it was defined for each of the C-3-X, C-4-X, C-5-X and C-6-X Members for the structurally lowest oil-saturated sandstone interpreted by petrophysical analysis and was estimated with the equivalent structure depth of the oil-water contact from the southeastern flank of the field.

Production

Cumulative production, apportioned by k_h in each C Submember, varies greatly across the LL-652 area. Reasons for this variability include (1) differences in age of producing well, in

which old wells have had time to produce larger quantities of oil than young wells, (2) greater-than-average production in areas of repeat section and inferred great fracture-permeability in zones of reverse faults, (3) greater-than-average production in areas of thick net pay and net sandstone along depositional axes, and (4) differences in net thickness of intervals perforated in each submember.

General areas of opportunity for optimizing oil recovery were determined by comparing cumulative production values with those of $S_o\phi h$ and remaining mobile oil. Numerous areas exist for infill wells, particularly in the sparsely developed northern part of the LL-652 area. These areas have little or no cumulative production, and yet are inferred to contain great volumes of OOIP and remaining oil.

C-6-X Member

Lower Lower C-6-X Submember

Production from the Lower Lower C-6-X Submember is sparse, with greatest cumulative production (85,216 bbl) in the LL-3056 well and 76,806 bbl in the LL-1276 well (fig. X 42). However, none of these wells have contacted the northeast-trending zone of greatest remaining oil (more than 5 MMbbl) (fig. X 34) that coincides with thick (more than 90-ft [27.4-m]) fluvial-estuarine sandstones (figs. VI 2 and VI 3). Additionally, there is no production from the northern part of the LL-652 area, where remaining oil values are up to 3 MMbbl (fig. X 34).

Upper Lower C-6-X Submember

Most production from the Upper Lower C-6-X Submember is from the LL-1061 well (961,228 bbl), the LL-1095 well (475,249 bbl), and the LL-3056 well (204,519 bbl) (fig. X 43). Other production is from 7 wells to the south and east of these wells. However, all of these wells have not contacted the northeast-trending band of highest remaining mobile oil (more than 3.6 MMbbl) (fig. X 35) that corresponds to thick (more than 70-ft [21.3-m]) fluvial-estuarine sandstones (fig. VI 4).

Lower Upper C-6-X Submember

Nineteen wells have produced from the Lower Upper C-6-X Submember (fig. X 44). Of the six wells that have produced more than 100,000 bbl, four intersect the zone of reverse faults. Areas of high potential for incremental oil recovery are in the north, where there is only one producing well in an area where remaining oil exceeds 2 MMbbl (appendix F). Additionally, the area of the LL-2424 well contains relatively thick (more than 40-ft [12-m]) distributary-channel and delta-front sandstones, has not been produced, and is in an area of more than 1.6 MMbbl. Other promising sites exist along the zone of reverse faults in areas distant from the previously producing wells.

C-5-X Member

Lower C-5-X Submember

The Lower C-5-X Submember has been produced from 21 wells, of which four (LL-904, LL-1001, LL-1005, and LL-111) have each produced more than 800,000 bbl (fig. X 45). The LL-1001 and LL-1005 wells are located in the zone of reverse faults, whereas the LL-904 and LL-1111 wells occur in a northeast-trending band of more than 70 ft (21.3 m) of net sandstone (fig. VI 10). Additionally, the LL-904 well is in an area of approximately 1.6 MMbbl of remaining oil (fig. X 36) and is expected to produce large volumes of additional oil. In general, the west-central belt of high net-pay thickness is greater than 40 ft (12 m) (appendix F) controls high-producing wells in the center of the field. Also, the northern area has been untapped in the Lower C-5-X Submember, where there are alternating bands of high and low net-sandstone thickness (fig. VI 10) and $S_o\phi_h$ (fig. X 22).

Combined Middle and Upper Middle C-5-X Submember

Twenty-eight wells have produced from the combined Middle and Upper Middle C-5-X Submember (fig. X 46). The best producer, the LL-847 well, accounts for more than 2 MMbbl near a zone of high net pay (appendix F) that also corresponds to intermediate $S_o\phi_h$ values (appendix F). Two of the three northern structural blocks, where high net-pay values have not been developed and therefore can be targeted for additional oil recovery.

C-4-X Member

Middle C-4-X Submember

The Middle C-4-X Submember has produced from 51 wells (fig. X 47). However, only one well (the LL-1130) has produced more than 1 MMbbl. A group of superior wells in the central part of the field correspond to axes of high net pay (more than 30 ft [9 m]), whereas poorer wells are in low net-pay zones (appendix F). Additionally, a belt of three wells of more than 750,000 bbl (LL-827, LL-1066, LL-1209) of cumulative oil production in the northern part of the field is in a high net-pay zone.

Areas of development opportunities exist in the southeastern part of the field area near the LL-1387 and LL-2094 wells where there are moderate $S_o\phi h$ values (fig. X 25) and high net-pay values (appendix F). Also, there is a linear, high- $S_o\phi h$ belt (fig. X 25) that cuts across the area of the LL-1095 and LL-3056 wells that has not yet been produced (fig. X 47).

Upper C-4-X Submember

The Upper C-4-X Submember is the most productive interval in the C Members and has produced from 14 wells each with cumulative production more than 1.5 MMbbl and 11 wells each with 1.0 to 1.5 MMbbl (fig. X 48). Despite the high production in the Upper C-4-X Submember, there are numerous sites in the LL-652 area where high volumes of remaining oil coincide with little or no production. For example, high values of remaining oil (more than 10 MMbbl) (fig. X 38) occur in the area of the LL-1095 and LL-3263 wells, where there has been no previous production. In addition, the extreme northern part of the field also has high values of projected remaining oil where there has been no production. There are also areas of more than 7 MMbbl of remaining oil in the western part of the central structural block that coincide with no production (LL-997 well) or limited production (LL-1803 and LL-3186 wells) (fig. X 48).

High values of net pay (more than 180 ft [54.9 m]) (fig. X 6) occur in the extreme northern, non-produced part of the field. Also, high values of net pay (more than 120 ft [39.6 m]) occur in the area of the LL-1095 and LL-3056 wells where there is no production (fig. X 48).

A final consideration in infield development of the Upper C-4-X Submember is locating infill wells in the northeast-trending zone of reverse faults. Some wells in this fault zone (LL-852, LL-946, LL-1001, and LL-1196) have produced more than 1 MMbbl. However, there are

numerous segments of other reverse faults in the Upper C-4-X Submember that have not been contacted, particularly in the western part of the LL-652 area.

C-3-X Member

Lower C-3-X Submember

Eight wells have each produced more than 500,000 bbl in the Lower C-3-X Submember (fig. X 49). The leading two wells (LL-851 and LL-1124) have produced approximately 2.09 and 1.55 MMbbl of oil, respectively.

Although the Lower C-3-X Submember is composed of multiple, thin sandstones with limited lateral extend (table VI 19 and fig. VI 25), it still has good potential for incremental oil recovery because it is a thick (more than 250-ft [76-m]) interval (fig. II 5) that locally contains more than 80 ft (24.4 m) of net pay (appendix F) and 4 MMbbl of remaining oil (fig. X 32). Additionally, there are several areas in the field where there has been none or limited production that coincide with high volumes of remaining oil. For example, high volumes (more than 6 MMbbl) of remaining oil are projected in the extreme northern part of the field, beyond areas of previous production. Additionally, a broad (more than 4,000 ft [1,200m] wide), east-trending swath of no production cuts across the north-central part of the field and is centered on the LL-1095 well (fig. X 49). This area coincides with values of remaining oil that range from 2.8 to 4.2 MMbbl (fig. X 32).

The north-northeast-trending zone of reverse faults also contains numerous sites where either recompletions or infill wells can tap additional remaining oil resources. Virtually no wells have been perforated in the Lower C-3-X Submember along these faults, where as a result of repeat section and fractures, kh values and permeability are inferred to be significantly higher.

Finally, as a result of the extremely limited lateral extent of distal delta-front, tidal-ridge sandstones that compare most of the Lower C-3-X Submember (fig. VI 25), opportunities for infill wells still exist even in the extensively developed central structural block. For example, up to 3.6 MMbbl of remaining oil exists in narrow (less than 2,000 ft [620 m] wide) uncontacted tidal-ridge sandstones between the LL-1198 and LL-2896 wells that are separated by 3,000 ft (915 m) (fig. X 32).

Middle C-3-X Submember

The Middle C-3-X Submember has produced oil from 60 wells (fig. X 50). Seventeen of these wells have each produced more than 500,000 bbl. Most production is from southern and central areas, with limited production in the north. Although the Middle C-3-X Submember is sandstone-rich throughout the entire LL-652 area (fig. VI 26), there are broad areas in the western, extreme northern, and north-central part of the field that have no production (fig. X 50). Each of these three unexploited areas contain large volumes (typically 3 MMbbl per 80 ac) of remaining oil (fig. X 40). In addition, the eastern part of the central structural block still contains large volumes of remaining oil (more than 3 MMbbl per 80 ac) (fig. X 40) in permeable (fig. X 16) distributary-channel and proximal delta-front sandstones (fig. VI 26), despite the fact that it contains 6 wells each with more than 500,000 bbl of cumulative production (fig. X 50).

The Middle C-3-X Submember has also been poorly developed along the north-northeast-trending zone of reverse faults (fig. X 50). Several opportunities exist for infill wells or recompletion in this fault zone, especially in areas of high volumes of remaining oil. Examples include the area of the LL-857, LL-997, LL-1218, and LL-1782 wells in the western part of the central structural block and the area of the LL-1061 to LL-3140 wells in the northern part of the central structural block (figs. X 40 and X 50).

XI. OPPORTUNITIES AND STRATEGIES FOR RECOVERY OPTIMIZATION AND RESERVE GROWTH

The potential for oil field reserve additions is a function of the oil volumes originally in place, level of development of the reservoir, and importantly, the degree of internal geologic complexity of the field. Reservoirs in the C Members in LL-652 area contain a high degree of depositional and structural variability. The product of this combined structural and depositional complexity are reservoirs that have a high degree of geologic heterogeneity, considerable variation in reservoir quality, and hence, relatively low recovery efficiency. The poor recovery efficiency is a function of the weak solution-gas drive mechanism and, more importantly, well spacing that is greater than the size of the reservoir compartments that collectively compose the main reservoir sandstones.

In addition to relatively low permeabilities, detailed well-log correlations indicate that considerable between-well variability is also responsible for the low recovery efficiency of the LL-652 area. Wells from the same reservoir yield widely varying amounts of oil, further demonstrating even smaller scale heterogeneity. These reservoirs have a current well spacing of 80 ac and a primary recovery efficiency of 20 percent (468 MMbbl). The 923 MMbbl of unrecovered oil (fig. XI 1) compose a major target for reserve additions and increased production.

Reservoir rock-quality analysis focused on petrophysical and diagenetic factors (e.g. pore scale distribution and clay mineralogy) that currently influence oil production and which could be critical in future advanced oil recovery projects. Together with stratigraphic and structural complexity, rock-property variation emphasizes the fact that targeted strategies must be defined for increasing ultimate recovery. Maps of porous hydrocarbon volume ($S_o\phi h$) and remaining oil were indispensable in planning strategies for additional recovery and reserve growth. These maps were interpreted in the planning of optimum new well locations; for continued conventional development, targeted off-pattern infill-drilling; well-recompletion programs, and a waterflood pilot.

The maps of remaining oil in the LL-652 area represent the integration of geological, petrophysical and production studies and showed that most of the remaining oil occurs in areas with high cumulative production. These areas have the highest permeability-ft (kh) and the greatest original oil in place. Infill-drilling, new locations, and recompletion strategies were based on comparison of the mutual occurrence of remaining resources, kh values, and current production.

New Extended-Development Locations

New development well locations were primarily directed toward the recovery of proved-hydrocarbon resources that could not be recovered by existing wells. In some cases, development wells were proposed as alternate wells or to accelerate production. Well-location maps (figs. XI 2 to XI 7) show 97 recommended new well locations. In the C-3-X and C-4-X Members, most of the new locations for extended development are in the sparsely drilled, northern and northeastern parts of the LL-652 area (figs. XI 2 and XI 3). However, other locations are targeted for the reverse fault in the eastern part of the central structural compartment, as well as the southern limb of the field in the southern structural compartment. The southern structural compartment. The eastern and south-central parts of the central structural compartment contain areas where delta-front and distributary-channel sandstones of the C-3-X and C-4-X Members have been incompletely contacted. The majority (more than 20) of extended-development locations in the C-5-C Member are in the northern and central structural blocks, whereas only six are targeted in the southern structural block, principally along the zone of reverse faults (figs. XI 4 and XI 5). In contrast, virtually all of the extended-development locations in the C-6-X Member are in the central structural block and target relatively high volumes of remaining oil in delta-front sandstones (figs. XI 6 and XI 7).

Table XI 1 has the total number of well locations by reservoir and preliminary potential (high >250 BOPD, moderate 150 to 250 BOPD, and low <150 BOPD) for each reservoir and table XI 2 shows names of these new well locations. The C-4-X.01 reservoir has the highest number (30) of locations of the area and the C-4-X.New has the highest number (8) of high-potential locations. From 97 new locations in 9 reservoirs, 34 have high preliminary potential, 55 have moderate, and 8 have low preliminary potential. These wells are projected to have an average recovery of 1.5 MM barrels of oil in C-3-X and C-4-X members, and 1.0 MM barrels of oil in C-5-X and C-6-X Members. In total, it is projected that the wells will add 97 MMbbl of oil.

Deepened, Recompleted, and Redrilled Wells

Twelve wells are recommended for evaluation of mechanical condition (table XI 3) in order to propose deepening, recompletion or redrilling. The mechanical condition of each well will determine the type of workover required. Wells with poor mechanical conditions require a new (twinned) well location.

Resource-Targeted Infill Wells

Resource-targeted, or strategic infill drilling is required to tap remaining mobile oil in uncontacted compartments of heterogeneous reservoirs. The LL-652 area epitomizes a highly complex or heterogeneous reservoir system with a high potential for drilling successful, off-spacing infill wells. Experience has shown (Tyler and others, 1986; Bebout and others, 1987) that strategic infill-well locations in mature fields are often located in parts of the reservoir with superior reservoir quality. Typically, these are the most productive areas of conventional primary production as delineated by early development wells. Clearly, optimum advanced recovery through deployment of targeted infill drilling in the LL-652 area should focus on areas of superior reservoir quality and high productivity.

Depositional trends govern the location of areas of the reservoir with high remaining mobile oil. The sandstone trends are strongly linear and consistently oriented northeastward reflecting deposition in dip-elongate distributary channel and tidal sand ridge facies tracts. Though partially drained by the existing production infrastructure, these sand-rich trends offer numerous sites for strategic infill well locations. Volumes of the remaining oil resource and its residency (as displayed by $S_o\phi$ h and remaining oil maps) has been addressed in the previous chapter. It is estimated that deployment of infill wells will increase recovery efficiency by an incremental five percent of the OOIP.

One hundred and two infill well locations have been targeted to contact remaining mobile oil in the C-3-X and C-4-X Members (figs. XI 2 and XI 3) and 50 locations for the C-5-X Member (figs. XI 4 and XI 5). These infill well locations are based on the occurrence of large volumes of remaining mobile oil established through comparison of production, volumetrics, structural, and depositional-facies maps and do not conform to the traditional grid spacing. These wells are projected to have an average recovery of 830,000 barrels of oil in C-3-X and C-4-X members and 500,000 barrels of oil in C-5-X Members. In total, it is projected that the wells will add 110 MMbbl of oil produced from the C-3-X, C-4-X, and C-5-X Members to the LL-652 reserve base.

Secondary Recovery

It is recommended that a pilot waterflood be considered for implementation in the structurally uncomplicated parts of the LL-652. These complexly stratified C-member reservoirs have large vertical and lateral variations in permeability that result in great volumes of unswept

mobile oil locally occurring in poorly drained reservoir compartments. Because reservoirs in the C Members are so complexly stratified, more detailed geologic modeling and pilot waterflood simulations will be necessary to predict fluid-flow pathways to most effectively sweep remaining mobile oil.

The Upper C-4-X Submember was chosen for the pilot waterflood. The pilot area covers about 2.3 mi² (5.9 km²) and includes 18 wells (fig. IV 33). The Upper C-4-X Submember in the east-central structural compartment was selected because (1) initial geologic studies suggest lateral discontinuities in the pilot area and (2) the reservoir pressure in the pilot area is declining faster than in other reservoirs and (3) it is in a structurally simple area. For example, in well LL-3195 (located in fig. II 4), repeat formation test results show an average reservoir pressure in the upper C-4-X Submember to be 1600 psi while the average reservoir pressure in the Middle C-3-X Submember is 2200 psi.

Geologic and engineering assessment of the pilot waterflood should include three overlapping and integrated tasks. Task one would construct a detailed, high-resolution geologic framework showing the three-dimensional distribution of the complexly stratified reservoir sandstones of the Upper C-4-X Submember. Task two would quantify this framework petrophysically using available core data, wireline logs, pressure data, and production history and geostatistical techniques to interpolate petrophysical data between wells. Task three would simulate recovery in a three-dimensional numerical simulator to test various water-injection patterns to evaluate production performance. Methods of scaling up reservoir parameters should be investigated in preparation for simulation studies of larger areas.

Sandstones in the Upper C-4-X Submember were deposited in northeast-trending deltaic progradational wedges in a net retrogradational sequence, resulting in the lower part of the sequence containing thick (commonly more than 30-ft [9-m]) distributary-channel and lower-delta-plain sandstones and the upper part containing numerous but thin (commonly 5- to 15-ft [1.5- to 4.5-m]) delta-front and prodelta sandstones (fig. VI 21). As a result of strong tidal processes, the deltaic sands were reworked into narrow (600- to 1,500-ft [183- to 457-m]), northeast-trending, dip-parallel belts (fig. XI 8) that may control anisotropic reservoir drainage patterns.

The pilot study area is located in a 4.6-mi² (12-km²) structurally simple area between a major northwest-trending, sealing normal fault and a minor non-sealing normal fault to the southwest. (fig. IV 33). This pilot study area is on the northern limb of a rapidly north- to northwest-advancing zone of water encroachment that may be halted or slowed by a relatively shaly area defined by a northeast-trending band of less than 70 ft (21.3 m) of net sandstone that bisects the pilot study area (fig. XI 8). The project could be expanded beyond the pilot area to

include the entire fault block, providing a larger area in which different water-injection patterns can be tested.

All sandstones and shales in the Upper C-4-X Submember must be correlated in the study area to document the geometry and lateral extent of the reservoirs and to predict the pathways of injected water in each zone. Additionally, vertical connectivity of sandstones should be documented to construct a three-dimensional model of the Upper C-4-X Submember. The detailed geologic model will then be integrated with petrophysical data to more accurately simulate the projected waterflood.

Simulation studies must critically evaluate the effectiveness of waterflooding in the Upper C-4-X Submember reservoir. The important parameters to be addressed are (1) geometry of lithofacies, (2) injection patterns, (3) hysteresis effect on gas flow, (4) vertical communication, (5) gascap-pressure maintenance, and (6) methods of scaling up reservoir parameters for fieldwide simulation. Water channeling through the lower thick sandstone and oil flowing into the gas cap will be the most serious problems for waterflooding. Optimizing injection patterns and strategies to minimize these problems must be critically assessed.

The potential of secondary recovery to add to the LL-652 reserve base will be quantified through this detailed simulation exercise. However, an indication of the volume of reserves that may be added can be gained by comparison with analogous reservoirs in Texas.

Fluvial deltaic reservoirs under secondary recover in Texas have recovery efficiencies that average 40 percent. These reservoirs are typically more densely drilled than the LL-652 area with 20- to 4-acre well spacings as compared to the 80-acre spacing in the LL-652 area. Also the styles of reservoir architecture differ. However, by comparison with the maturely drilled U.S. field, there is the potential to add as much as 20 percent of the OOIP to the LL-652 reserve base by deployment of secondary recovery technology. Over 460 million barrels of oil is the possible reward for application of waterflooding to the LL-652 area.

XII. CONCLUSIONS

The LL-652 resource base has been substantially increased as a result of this study. Rigorously established field limits, together with careful petrophysical analysis have documented the OOIP resource to be 2.3 Bbbl. Extended development through continued pattern infill can increase reserves from 127 MMbbl to 302 MMbbl (fig. XI 1). Substantial volumes of mobile oil (923 MMbbl) will remain in the LL-652 area following recovery of proved and extended-development reserves. This mobile oil is targeted through deployment of geologically optimized infill wells that are projected to recover 116 MMbbl of oil and a pilot waterflood that could recover almost 70 MMbbl. Expansion of waterflood operations to the entire field could increase recovery by as much as 20 percent of the OOIP. Other significant results include:

- A 137-percent increase in oil resources (175 MMbbl) and a 60-percent increase in OOIP (POES) have been estimated for the LL-652 area from volumetrics analysis of the C Members.
- 97 new well locations to continue the field development have been identified in the LL-652 area to contact additional remaining oil.
- There is a 60-percent increase in expected ultimate recovery (175 MMbbl) in the C Members in the LL-652 area. Most of the remaining mobile oil exists in the combined C-3-X and C-4-X Member.
- The primary control on reservoir quality in the C Members is diagenetic: porosity loss is controlled by increasing quartz cement with increasing depth.
- A 2.3-mi² (5.9-km²) area has been selected in the eastern part of the LL-652 area for a pilot waterflood simulation in the prolific Upper C-4-X Submember to maximize secondary oil recovery by predicting between-well fluid-flow pathways.
- 102 geologically targeted infill well locations have been selected to contact remaining oil in the C-3-X and C-4-X Members and 50 locations have been selected for the C-5-X Member.

Poorly drained or undrained reservoir compartments in the LL-652 area are defined by a combination of structure and depositional-facies geometry. The complex, multistage tectonic

history of Lake Maracaibo has created many structural compartments between faults of different ages. Sandbody trends, as a result of the tide-dominated deltaic depositional system, are linear, parallel, and consistently oriented northeastward, imparting a preferred pathway for reservoir drainage. Because the sandbodies are narrow, typically less than the distance between wells (1,968 ft [600 m]), and are bounded laterally by low-permeability mudstones, they contain uncontacted oil that can be produced with cost-effective, geologically targeted recovery strategies.

The structure of the LL-652 area is a north-northeast-trending, elongate anticline with a steeply dipping (25° – 45°) western and northwestern limb and a relatively gently dipping (5° – 10°) east and southeast limb. Multiple tectonic events generated three trends of normal faults and one trend of younger reverse faults, representing the local scale of five major structural trends in the Maracaibo Basin (Lugo, 1991). The principal reservoir areas (C-4-X.01, C-5-X.02 and C-6-X.01) are separated from the C-4-X.03, C-5-X.08 and C-6-X.16 reservoir areas by a major northwest-trending normal fault in the northeast part of the LL-652 area. Other northwest-trending normal faults bound the reservoirs. A north-northeast-trending zone of partly sealing reverse faults with repeat section ranging from 60 to 150 ft (18 to 45.7 m) internally divides the principal reservoirs and provides additional compartments for remaining oil.

A net-thickness map of the interval between the Eocene unconformity and the top of the C-3-X Member indicates anomalies along the Maraven boundary as well as areas in the northern, northeastern, and southern parts of the field. The most persistently complex structural area is inferred to have been in the northern part of the field. A grid of 22 structural cross sections shows that the young reverse faults offset the unconformity and truncate the oldest normal faults. All of the normal faults, except the master fault, terminate below the unconformity. Minor block rotation is associated with the reverse faults. Strata are locally tilted up to 54° along faults, as indicated by dipmeter logs.

The net-thickness map of the C-3-X Submember shows different trends on either side of the master fault that may be due to either syntectonic growth faulting or strike-slip fault movement. Additionally, erosion associated with the Eocene unconformity was controlled by normal faults in the LL-652 area. The degree of erosion increases from north to south. However, in the Maraven area, normal faults do not control the degree of erosion.

Tectonic features such as microfaults, fault breccia, fractures, and faulted zones are common in cores in the LL-652 area. The best example of a faulted zone in core is from the LL-3282 well. In this core there is a 45-ft (13.7-m) faulted zone that includes vertically tilted beds with anomalous resistivity and GR log responses.

Fault-seal analysis indicates that there are at least seven compartments in the LL-652 area bounded faults. These faults vary in degree of sealing probability from 28 to 90 percent. Four

compartments occur in the C-4-X.01, C-5-X.02, and C-6-X.01 reservoirs and two are in the C-4-X.03, C-5-X.08, and C-6-X.16 reservoirs. One compartment is isolated from other compartments by the zone of northeast-trending reverse faults.

The Lower Eocene in the LL-652 area is approximately 4,000 ft (1,220 m) thick and contains multiple regressive-transgressive cycles in a net-retrogradational sequence. Individual deltaic cycles are 50 to 80 ft (15.2 to 24.4 m) thick. The C-7-X Member is a major progradational wedge truncated by an unconformity inferred to have been caused by fall in sea level. Lower C-6-X progradational deposits above this unconformity are overlain by muddy Upper C-6-X retrogradational deposits. The C-5-X Member and the Lower C-4-X Submembers contain minor progradational cycles, whereas the Upper C-4-X Submember, although a net retrogradational sequence, contains deltaic wedges that off lapped northeast of the LL-652 area. Sandstones in the Upper C-4-X Submember consistently exhibit excellent gamma-ray and resistivity responses, reflecting good reservoir quality and high oil saturation. A major retrogradational phase commenced with deposition of the C-3-X Member. The sandstone-rich Middle C-3-X Submember represents a brief period of deltaic offlap, but the majority of sequences in the C-3-X, C-2-X, and C-1-X Members are sandstone-poor, highstand-systems tracts and contain only minor volumes of hydrocarbons.

The C Members contain three major seismic stratigraphic units (lower, middle, and upper) that correspond approximately to the C-7-X to C-5-X, C-4-X to C-3-X, and C-2-X to C-1-X Members, respectively. The lower seismic unit is a 0.1- to 0.3-s zone of low- to moderate-amplitude reflectors that are irregular, wavy, and discontinuous. These reflectors represent multiple regressive/transgressive couplets. The middle seismic unit encompasses a 0.15- to 0.20-s zone bounded below by a pair of moderate-amplitude, semicontinuous reflectors and above by a pair of high-amplitude, continuous and parallel reflectors that corresponds to a zone of high velocity contrast between the shaly C-3-X Member and the sandy Upper C-4-X Submember. This boundary is an onlapping, marine-flooding surface that marks the onset of a major retrogradational sequence in the Upper C Members. The upper seismic unit represents a major retrogradational highstand-systems tract that onlaps southwestward over the regressive, progradational cycles of the C-4-X Member. The upper seismic unit consists of multiple, moderate-amplitude reflectors in a 0.20- to 0.25-s zone that is bounded above by the Eocene unconformity, represented by a continuous, high-amplitude pair of parallel reflectors that merge with and are inferred to truncate underlying reflectors westward and southwestward.

The tide-dominated deltaic depositional model of the C Members in the LL-652 area contains a system of dip-elongate distributary- and tidal-channel sandstones that merge northeastward with extensive, dip-parallel delta-front sandstones. The distributary-channel and delta-front facies comprise most of the reservoir sandstones and therefore contain most of the

remaining oil. Minor facies are tidal-channel, tidal-flat, channel-mouth bar, transgressive sand-shoal, shelf, and fluvial-estuarine channel. The dominant reservoir geometry consists of narrow (commonly less than 2,000 ft [610 m] wide), northeast-trending sandstones, reflecting strong inferred tidal processes that redeposited channel-mouth bar and proximal delta-front deposits into linear tidal sand ridges.

Thickest sandstone in progradational sequences in the LL-652 area occur in delta-front, channel-mouth bar, and distributary-channel facies. In contrast, thickest sandstones in retrogradational sequences occur in distributary-channel facies, whereas the delta-front facies is relatively muddy. In sequences with base-level fall and extreme offlap northeast of the LL-652 area, thickest sandstones occur locally in thick fluvial belts bounded by wide, muddy areas.

Permeability in the C Members in the LL-652 area is mainly a function of depth and is similar for major facies. However, there are significant permeability contrasts (up to three orders of magnitude) locally between distributary-channel and tidal-flat, fluvial-estuarine channel and distal delta-front, and distributary-channel and delta-front facies where the base of the distributary-channel facies contains clay clasts that may retard vertical fluid flow.

Diagenesis, not depositional environment, is the main control on porosity and permeability distribution in the C Members. In particular, the volume of quartz cement is the main influence on reservoir quality, and because the volume of quartz cement increases significantly with depth, reservoir quality decreases with depth. Quartz, plagioclase, and metamorphic and sedimentary rock fragments are the most abundant detrital grains. Quartz overgrowths, siderite, calcite, illite, and kaolinite are the major cements in the sandstones. An average of 5 percent primary porosity remains in these sandstones even after compaction and cementation. Porosity is enhanced by dissolution of feldspar, rock fragments, and calcite cement to form secondary pores.

Cumulative production to March 1993 in 130 active wells in the L-652 area was 165.5 MMbbl of oil, mainly 37 degree API, and 8.3 MMbbl of water. Eighty-two percent (135.8 MMbbl) of the oil production comes from the C-3-X and C-4-X Members, whereas the C-5-X Member accounts for only 12 percent (20.5 MMbbl). The C-6-X Member has 5 percent (8.4 MMbbl) and the C-2-X Member has only 1 percent (0.8 MMbbl) of cumulative oil production. The LL-652 area is divided into five main and two minor structural compartments. The central structural compartment is the largest production area in the field and includes 76 wells with a cumulative production of 85.8 MMbbl. Seventy-seven percent (66.1 MMbbl) of this production comes from the C-4-X.01 reservoir compartment.

Multiple oil-water contacts exist in each reservoir because of the high degree of sandstone and mudstone interbedding. Irregular production and lateral stratigraphic changes introduce barriers to the normal movement of the oil-water contacts not parallel with structural contours, particularly in the C-3-X and C-4-X Members.

V_{sh} -porosity and permeability-porosity transforms were developed for each C Member rather than for each facies, in recognition of depth control on reservoir quality. The Simandoux model of water saturation best matches water-saturation values measured from cores. There is a general trend of decreasing water saturation with increasing depth in the C Members in the LL-652 area.

Net-sandstone and net-pay thickness values were determined with cutoff values of V_{sh} , water saturation, and porosity. For the C-1-X to C-4-X Members, the resistivity cutoff is 10 ohm-m, for the C-5-X Member it is 12 ohm-m, and for the C-6-X Member it is 14 ohm-m. Cutoff values of water saturation, further modified during mapping, were determined to be 55 percent for the C-1-X to C-4-X Members and 50 percent for the C-5-X to C-7-X Members.

As a result of volumetric analysis the original-oil-in-place resource base was increased by 867 MMbbl (60 percent) to 2,318.2 MMbbl. This increase was mainly from the C-3-X and C-4-X Members by documenting additional reservoir areas and by using improved petrophysical parameters. For example, the official porosity value used to calculate OOIP for the C-3-X and C-4-X Members was 15 percent, but this study determined a more appropriate value of 18 percent. In contrast, the OOIP value for the C-6-X Member was decreased by 31 percent as a result of adjusting the average porosity value of 13.2 percent to 11 percent.

Maps of net-pay, porosity, permeability, $S_o\phi h$, OOIP, and remaining-oil in the C Members and submembers exhibit northeast-trending patterns, reflecting depositional influence on reservoir geometry. Values of these volumetric parameters commonly decrease downdip (northeastward) and are commonly controlled by pinchout of delta-front sandstones. Structural influences are indicated by abrupt changes in values across faults, particularly in the southwestern and northeastern parts of the LL-652 area. Net-pay, $S_o\phi h$, OOIP, and remaining oil contours are closely spaced and bounded by zero values due to oil-water contacts on the southern and southeastern limbs of the field and tend to be greater toward the north due to steeply dipping strata. In contrast, water-saturation trends reflect structural control, although some members and submembers contain anomalous trends that may reflect depositional control.

Maps of remaining oil in the C Members have similar to nearly identical trends to maps of OOIP, indicating that the reservoirs contain areas of undrained or poorly drained compartments that can be targeted for advanced oil recovery. The Lower Lower C-6-X and Upper Lower C-6-X Submembers contain the greatest volumes of remaining oil in the C-6-X Member (locally up to 6 MMbbl and 4.4 MMbbl per 80 acre area, respectively). In the C-5-X Member, the Lower and combined Middle and Upper Middle C-5-X Submembers contain the greatest volumes of remaining oil (up to 3.6 MMbbl per 80 acres). The Upper C-4-X Submember contains more remaining oil than the Lower and Middle C-4-X Submembers combined. Areas of more than 8 MMbbl per 80 acres of remaining oil in the Upper C-4-X Submember coincide with thick (more

than 80-ft [24.4-m]) delta-front and distributary-channel sandstones as well as steeply dipping strata. High volumes of remaining oil in the Lower C-3-X Member (locally more than 4 MMbbl per 80 acres) principally occur in the northern part of the field and in the Middle C-3-X Member areas of more than 4 MMbbl per 80 acres occur in the eastern part of the central structural block.

Vertical communication between C reservoir sandstones is poor. RFT data indicate average pressure differences of more than 50 psi between subjacent sandstones. However, horizontal communication in sandstones is better than vertical communication, except in faulted areas such as the master fault and the zone of reverse faults.

Cumulative production, apportioned by kh in each C Submember, varies greatly across the LL-652 area. Reasons for this variability include (1) differences in age of producing well, (2) greater-than-average production in areas of repeat section and inferred great fracture permeability in zones of reverse faults, and (3) differences in net thickness of intervals perforated in each submember.

In the Lower Lower and Upper Lower C-6-X Submembers, few wells have been perforated in thick fluvial-estuarine sandstones in the north-central part of the field. These sandstones locally contain up to 3 MMbbl of remaining oil per 80 acres that could be contacted through recompletions.

The Lower and combined Middle and Upper Middle C-5-X Submembers contain numerous areas that have not been produced, particularly in the northeast-trending zone of reverse faults and in narrow, elongate delta-front and distributary-channel sandstones. In the combined Middle and Upper Middle C-5-X Submember, two of the three northern structural blocks with high net-pay values have not been developed and therefore can be targeted for secondary oil recovery.

There are substantially more producing wells in the C-4-X Member than in the C-5-X Member. For example, the Middle C-4-X Submember has been produced from 51 wells, whereas the combined Middle and Upper Middle C-5-X Submember has produced from only 28 wells. The Upper C-4-X Submember is the most productive interval in the C Members and fourteen wells in the Upper C-4-X Submember have each produced more than 1.5 MMbbl and 11 have each produced between 1.0 and 1.5 MMbbl. However, there are numerous sites in the LL-652 area in the Upper C-4-X Submember where high volumes of remaining oil (more than 6 MMbbl per 80 acres) coincide with little or no production, especially in the north-central and extreme northern parts of the field.

The most productive submember in the C-3-X Member is the Middle C-3-X Submember, which has been contacted in 60 wells. Seventeen wells have each produced more than 0.5 MMbbl. Most of the production is from southern and eastern areas, with limited production in the north. Despite the intense level of development, there are areas in the Middle C-3-X Submember that have no production, particularly in the zone of reverse faults and in thicker

segments of distributary-channel and proximal delta-front sandstones in the central structural block.

XIII. REFERENCES

- Allan, U.S., 1989, Model for hydrocarbon migration and entrapment within faulted structures: American Association of Petroleum Geologists Bulletin, V. 73, No. 7, P. 803-811.
- Allen, G. P., and Posamentier, H. W., 1993, Sequence stratigraphy and facies model of an incised valley fill: the Gironde Estuary, France: Journal of Sedimentary Petrology, v. 63, no. 3, p. 378-391.
- Añez, M.E., 1989, Estrategias de explotación para el área LL-652 (segregaciones: Liviano y condensado): Lagoven, S.A., Internal Report, 34 p.
- Añez, M.E., 1990, Estrategias de explotación en zonas poco desarrolladas del área LL-652: Lagoven, S.A., Internal Report 20 p.
- Añez, M.E., 1990, Resultados de la estrategia de explotación de yacimiento to C-4-X.01: Lagoven, S.A., Internal Report 22 p.
- Archie, G. E., 1950, Introduction to Petrophysics of reservoir rocks: American Association of Petroleum Geologists Bulletin, vol. 34, p. 943-961.
- Asquith, George, 1985, Log evaluation of shaly sandstone reservoirs: a practical guide: American Association of Petroleum Geologists, Methods in Exploration Series, 59 p.
- Bjoraker, R., 1980, A Geological Study of the C-4-X.01 reservoir: Lagoven, S.A., Internal Report, 15 p.
- Beard, D. C., and Weyl, P. K., 1973, Influence of texture on porosity and permeability of unconsolidated sand: American Association of Petroleum Geologists Bulletin, vol. 57, p. 349-369.
- Bebout, D.G., Lucia, F.J., Hocott, C.R., Fogg, G.E., and Vanderstoep, G.W., 1987, Characterization of the Grayburg reservoir, University Lands Dune field, Crane County, Texas: The University of Texas at Austin, Bureau of Economic Geology Report of Investigations, no. 1678, 68 p.
- Bouvier, J.D., Kaars-Sijpesteijn, C.H., and others, 1989, Three-dimensional seismic interpretation and fault sealing investigation Nun River field, Nigeria: American Association of Petroleum Geologists Bulletin, V. 73, No. 11, P. 1397-1414.
- Bot, P., and Perdomo, J. L., 1987, Analisis sismoestratigrafico del Eoceno y evolucion tectonica en la Cuenca del Lago de Maracaibo: Lagoven, S. A., Caracas, Internal Report, 98 p.
- Clifton, H. E., 1982, Estuarine deposits, in Scholle, P. A., and Spearing, Darwin, eds., Sandstone Depositional Environments: American Association of Petroleum Geologists Memoir 31, p. 179-189.
- Coleman, J. M., and Prior, D. B., 1982, Deltaic Environments of deposition, in Scholle, P. A., and Spearing, Darwin, eds., Sandstone Depositional Environments: American Association of Petroleum Geologists Memoir 31, p. 139-178.

- Core Laboratories, 1984, Análisis especiales de núcleos en el pozo LL-2850, preparado para Lagoven, S.A., Internal Report, 70 p.
- Core Laboratories, 1984, Análisis convencionales de núcleos en el pozo LL-2850, preparado para Lagoven, S.A., Internal Report, 51 p.
- Core Laboratories, 1989, Análisis convencionales de núcleos en el pozo LL-3074, preparado para Lagoven, S.A., Internal Report, 46 p.
- Core Laboratories, 1989, Análisis especiales del núcleos en el pozo LL-3074, preparado para Lagoven, S.A., Internal Report, 65 p.
- Core Laboratories, 1991, Propiedades avanzado de la roca en el pozo LL-3140, preparado para Lagoven, S.A., Internal Report, 100 p.
- Core Laboratories, 1991, Análisis convencionales de núcleos en el pozo LL-3140, preparado para Lagoven, S.A., Internal Report, 46 p.
- Core Laboratories, 1992, Propiedades basicas soterramiento de la roca en el pozo LL-3282, preparado para Lagoven, S.A., Internal Report, 96 p.
- Core Laboratories, 1992, Propiedades avanzada de la roca en el pozo LL-3282, preparado para Lagoven, S.A., Internal Report, 90 p.
- Dalrymple, R. W., Zaitlin, B. A., and Boyd, Ron, 1992, Estuarine facies models: conceptual basis and stratigraphic implications: *Journal of Sedimentary Petrology*, v. 62, no. 6, p. 1130-1146.
- De Mowbray, Tessa, and Visser, M. J., 1984, Reactivation surfaces in subtidal channel deposits, Oosterschelde, southwest Netherlands: *Journal of Sedimentary Petrology*, v. 54, no. 3, p. 811-824.
- Delgado, I., 1985, Estudio geológico de los miembros C-2, C-3 y C-4- Pilar norte, Bloque I: Maraven S.A., Caracas, Internal Report, 75 p.
- Downey, M.W., 1984, Evaluating seals for hydrocarbon accumulations: *American Association of Petroleum Geologists Bulletin*, V. 68, No. 11, P. 1752-1763.
- Egep-Consultores, S.A., 1985, Evaluación para la explotación futura del yacimiento C-4-X.01, preparado para Lagoven, S.A., Internal Report, 8 Volumes of 120 p. each.
- Fisher, W. L., Brown, L. F., Jr., Scott, A. J., and McGowen, J. H., 1969, Delta systems in the exploration for oil and gas: The University of Texas at Austin, Bureau of Economic Geology Special Publication, 78 p.
- Fisher, W. L., 1987, Can the U. S. oil and gas resource base support sustained production?: *Science*, v. 236, p. 1631-1636.
- FLSTP, 1989, Análisis especiales, pozo LL-3080, preparado para Lagoven, S.A., Internal Report, 133 p.
- FLSTP, 1989, Análisis convencionales, pozo LL-3080, preparado para Lagoven, S.A., Internal Report, 54 p.

- FLSTP, 1989, Análisis convencionales, pozo LL-3075, preparado para Lagoven, S.A., Internal Report, 25 p.
- FLSTP, 1990, Analisis especiales, pozo LL-3075, preparado para Lagoven, S.A., Internal Report, 101 p.
- Galloway, W. E., Ewing, T. E., Garrett, C. M., Jr., Tyler, Noel, and Bebout, D. G., 1983, Atlas of major Texas oil reservoirs: The University of Texas at Austin, Bureau of Economic Geology Special Publication, 139 p.
- Ghosh, S., Di Crole, J., Isea, A., and González, C., 1988, Relación entre los ambientes de sedimentación, diagénesis y profundidad de en areniscas del Eoceno, Cuenca de Maracaibo Intevp, S.A., Los Teques, Internal Report, 376 p.
- Gómez, M.E. y Guzmán, T., 1984, Distribución de fluidos remanentes en el yacimiento C-4-X.01 (Area LL-652): Lagoven, S.A., Internal Reprot, 34 p.
- Gómez, M.E., 1987, Comportamiento de producción del yacimiento C-4-X.03 area LL-652: Lagoven, S.A., Maracaibo, Internal Report, 29 p.
- Gonzalez de Juana, C., Iturraide, J., and Picard, X., 1980, Geología de Venezuela y sus cuencas petrolíferas: Caracas, Foninves, 1031 p.
- González, M., Ochoa, E., and Sampson, E., 1983, Estudio geológico de las anenas "C" Formacion Misoa area LL-652, Lago de Maracaibo: Lagoven, S.A., Internal Report, 28 p.
- González, G., 1985, Estudio geologico del miembros C-5 (Eoceno Inferior)-Pilar norte Bloque I: Maraven, S.A., Caracas, Internal Report, 70 p.
- Graves, G. R., Adams, G. E., Guzman, J. I., Seijas, F., Petzal, C. de, Furrer, M., and Meyer, R., 1987, Estudio del Eoceno del Lago de Maracaibo, Parte Norte y Este: Lagoven, S. A., Caracas, Internal Report, 197 p.
- Harding, T.P., 1985, Seismic characteristic and indentification of negative flower structures, positive flower structures, and positive structural inversion: American Association of Petroleum Geologists Bulletin, V. 69, No. 4, P. 582-600.
- Harding, T.P., and Lowell, J.D., Structural styles, their plate-tectonic habits, and hydrocarbon traps in petroleum provinces: American Association of Petroleum Geologists Bulletin, V. 63, No. 7, P. 1016-1058.
- Harding, T.P., and Tuminas, A.C., 1989, Structural interpretation of hydrocarbon traps sealed by basement normal block faults at stable flank of foredeep basins and at Rift basins: American Association of Petroleum Geologists Bulletin, V. 73, No. 7, P. 812-840.
- Harding, T.P., 1990, Identification of wrench faults using subsurface structural data: criteria and pitfalls: American Association of Petroleum Geologists Bulletin, V. 74, No. 10, P. 1590-1609.
- Herron, M. M., 1987, Estimating the intrinsic permeability of clastic sediments from geochemical data: Transactions, Society of Professional Well Log Analysts, 28th Annual Logging Symposium, paper HH.

- Hilchie, D. W., 1989, Advanced well log interpretation: D. W. Hilchie Inc., Boulder, Co., pp. 496.
- Johnson, , and Linke, , 1978, Some practical applications to improve formation evaluation in Mackenzie Delta: Transactions, Society of Professional Well Log Analysts, 19th Annual Logging Symposium, paper C.
- Klein, G. de V., 1970, Depositional and dispersal dynamics of intertidal sand bars: Journal of Sedimentary Petrology, v. 40, p. 1095-1127.
- Knott, S.D., 1993, Fault seal analysis in the North Sea: American Association of Petroleum Geologists Bulletin, V. 77 No. 5 p. 778-792.
- Kreisa, R. D. and Moiola, R. J., 1986, Sigmoidal tidal bundles and other tide-generated sedimentary structures of the Curtis Formation, Utah: Geological Society of America Bulletin, v. 97, p. 381-387.
- Levey, R. A., 1991, Infield gas reserve growth potential: Gulf Coast sandstone reservoirs (Frio, Vicksburg, Wilcox): The University of Texas at Austin, Bureau of Economic Geology, short course prepared for the Gas Research Institute under contract no. 5088-212-1718, unpaginated.
- Lugo, J., 1991, Cretaceous to Neogene tectonic control on sedimentation: Maracaibo Basin, Venezuela: PhD dissertation, The University of Texas at Austin, 219 p.
- Maguregui, J. A., 1990, Evolution and reservoir properties of Middle-Eocene tide-dominated deltaic sandstones in eastern Lagunillas field, Maracaibo Basin, Venezuela: Master's thesis, The University of Texas at Austin, 171 p.
- Meckel, L. D., 1975, Holocene sand bodies in the Colorado delta area, northern Gulf of California, in Broussard, M. L., ed., Deltas: Models for Exploration: Houston Geological Society, p. 239-265.
- Neasham, J. W., 1977, The morphology of dispersed clay in sandstone reservoirs and its effect on sandstone shaliness, pore space and fluid flow properties: SPE paper 6858 presented at the 52nd Annual Technical Conference, Denver, Colorado.
- Off, Theodore, 1963, Rhythmic linear sand bodies caused by tidal currents: American Association of Petroleum Geologists Bulletin, v. 47, no. 2, p. 324-341.
- Panda, M. N. and Lake, L. W., 1992, Estimation of single-phase permeability from parameters of particle-size distribution: presented at annual meeting of the American Association of Petroleum Geologists, Calgary, Canada.
- Reineck, H. E., and Wunderlich, F., 1968, Classification and origin of flaser and lenticular bedding: Sedimentology, v. 11, p. 99-104.
- Reineck, H. E., and Singh, I. B., 1973, Depositional Sedimentary Environments: Springer-Verlag, Berlin, 439 p.
- Smith, D.A., 1980, Sealing and nonsealing faults in Louisiana gulf coast salt basin: American Association of Petroleum Geologists Bulletin, V. 64, No. 2, p. 145-172.
- Tearpock, D.J., and Bischke, R.E., 1991, Applied subsurface geological mapping, 610 p.

Terra Science, 1992, Manual for TerraStation v.5.4, Terra Science Inc., Denver, Co.

Tye, R. S., and Coleman, J. M., 1989, Depositional processes and stratigraphy of fluvially dominated lacustrine deltas: Mississippi delta plain: *Journal of Sedimentary Petrology*, v. 59, no. 6, p. 973-996.

Tyler, Noel, Galloway, W. E., Garrett, C. M., Jr., and Ewing, T. E., 1984, Oil accumulation, production characteristics, and targets for additional recovery in major oil reservoirs of Texas: The University of Texas at Austin, Bureau of Economic Geology Geological Circular No. 84-2, 31 p.

Tyler, Noel, Gholston, J.C., and Ambrose, W.A., 1986, Genetic stratigraphy and oil recovery in an Upper Cretaceous wave-dominated deltaic reservoir, Big Wells (San Miguel) field, South Texas: The University of Texas at Austin, Bureau of Economic Geology Report of Investigations no. 153, 38 p.

Tyler, Noel, 1988, New oil from old fields: *Geotimes*, v. 33, p. 8-10.

Walton, W. M., 1967, The informal units of the subsurface Eocene: *Asociacion Venezolana de Geologia, Minería y Petróleo Boletín*, v. 10, no. 1, p. 21-30.

Worthington, P. E., 1985, The evolution of shaly-sand concepts in reservoir evaluation: *The Log Analyst*, v. 25, no. 1, p. 23-40.

Zambrano, E., Vasquez, E., Duval, B., Latreille, M., and Confineres, B., 1972, Paleogeographic and petroleum synthesis of Western Venezuela: 27, Rue Ginoux, Paris 15e, Editions Technip, 62 p.

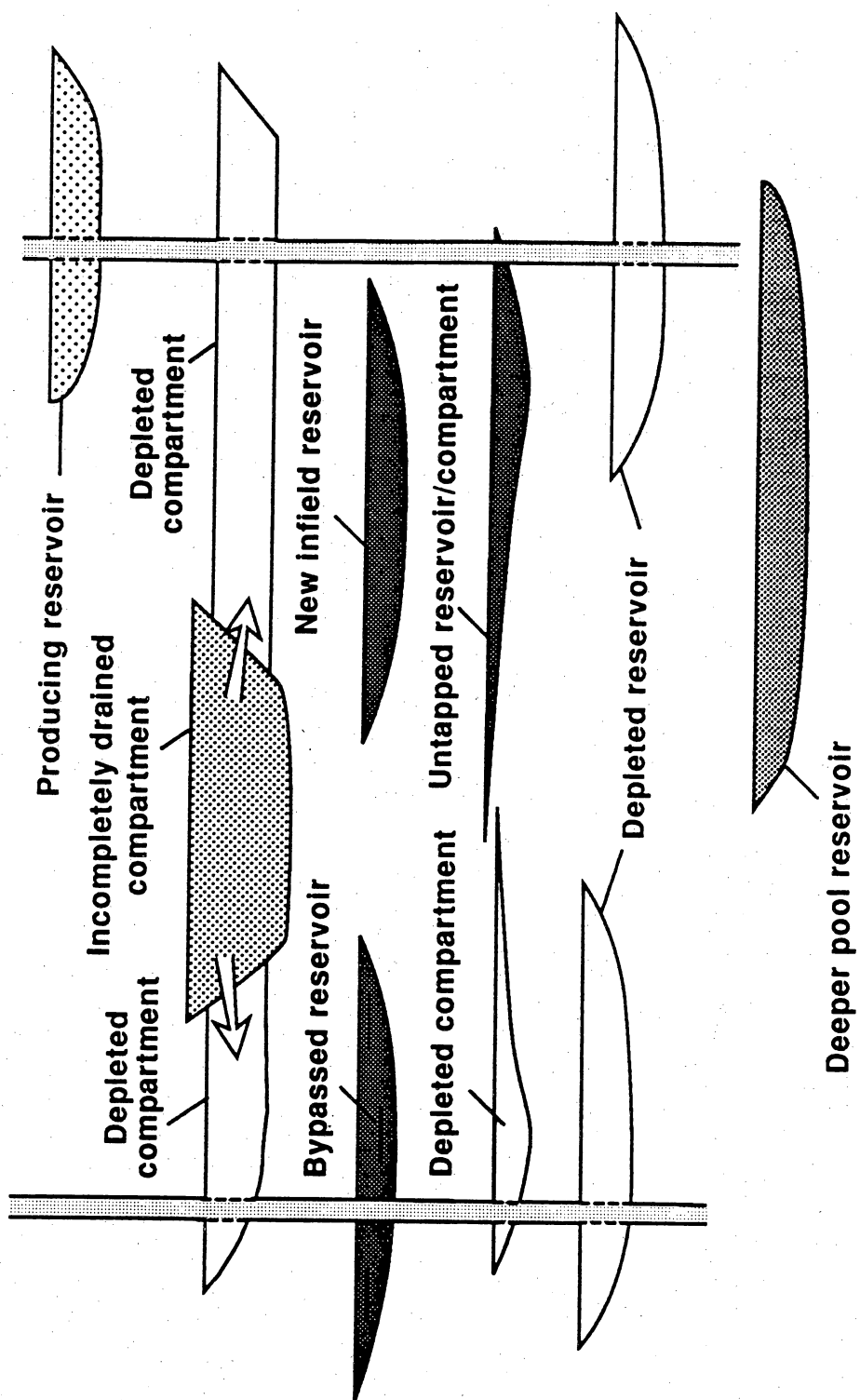


Figure II 1. Major types of reservoir compartments. From Levey (1991).

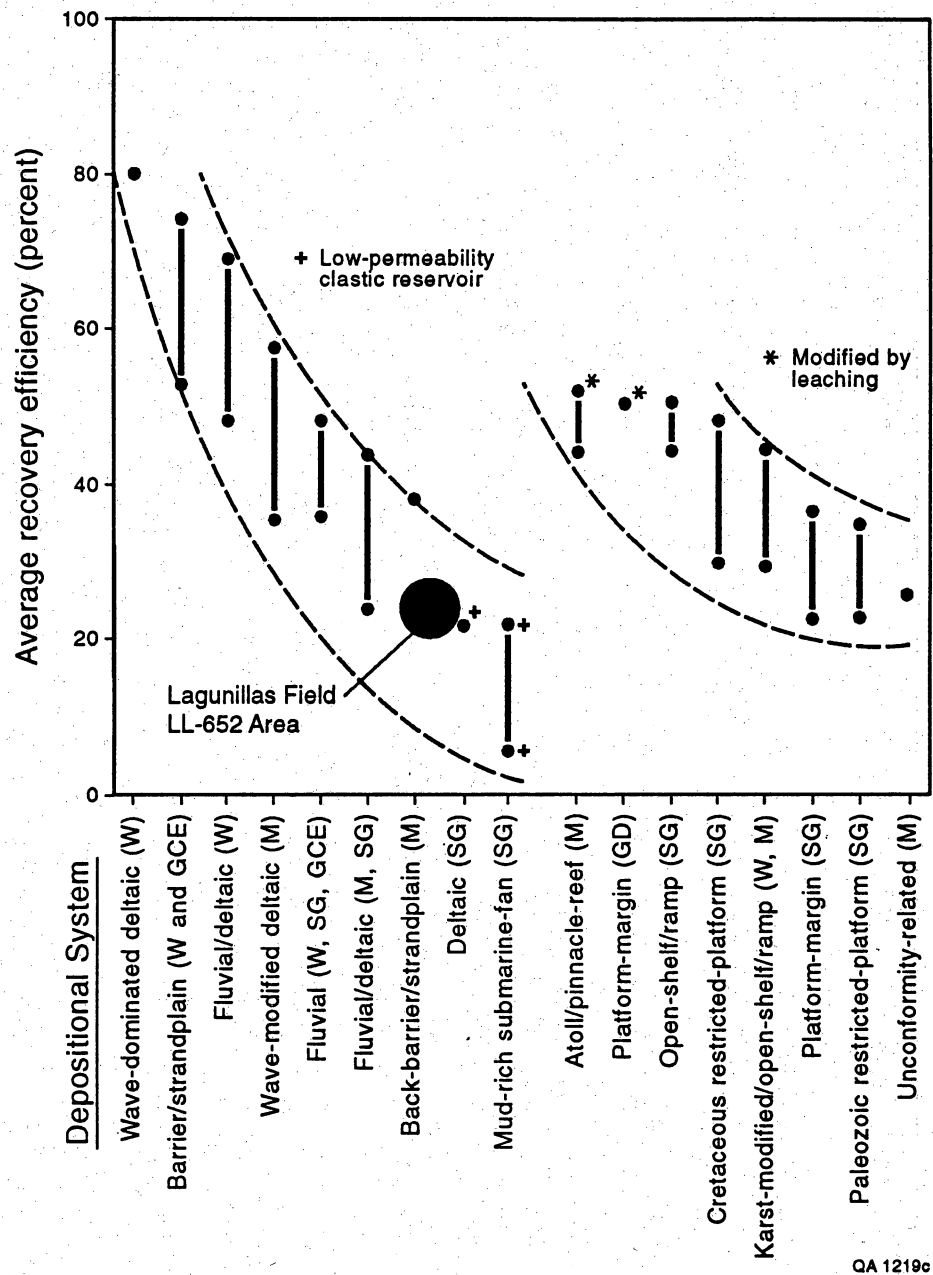
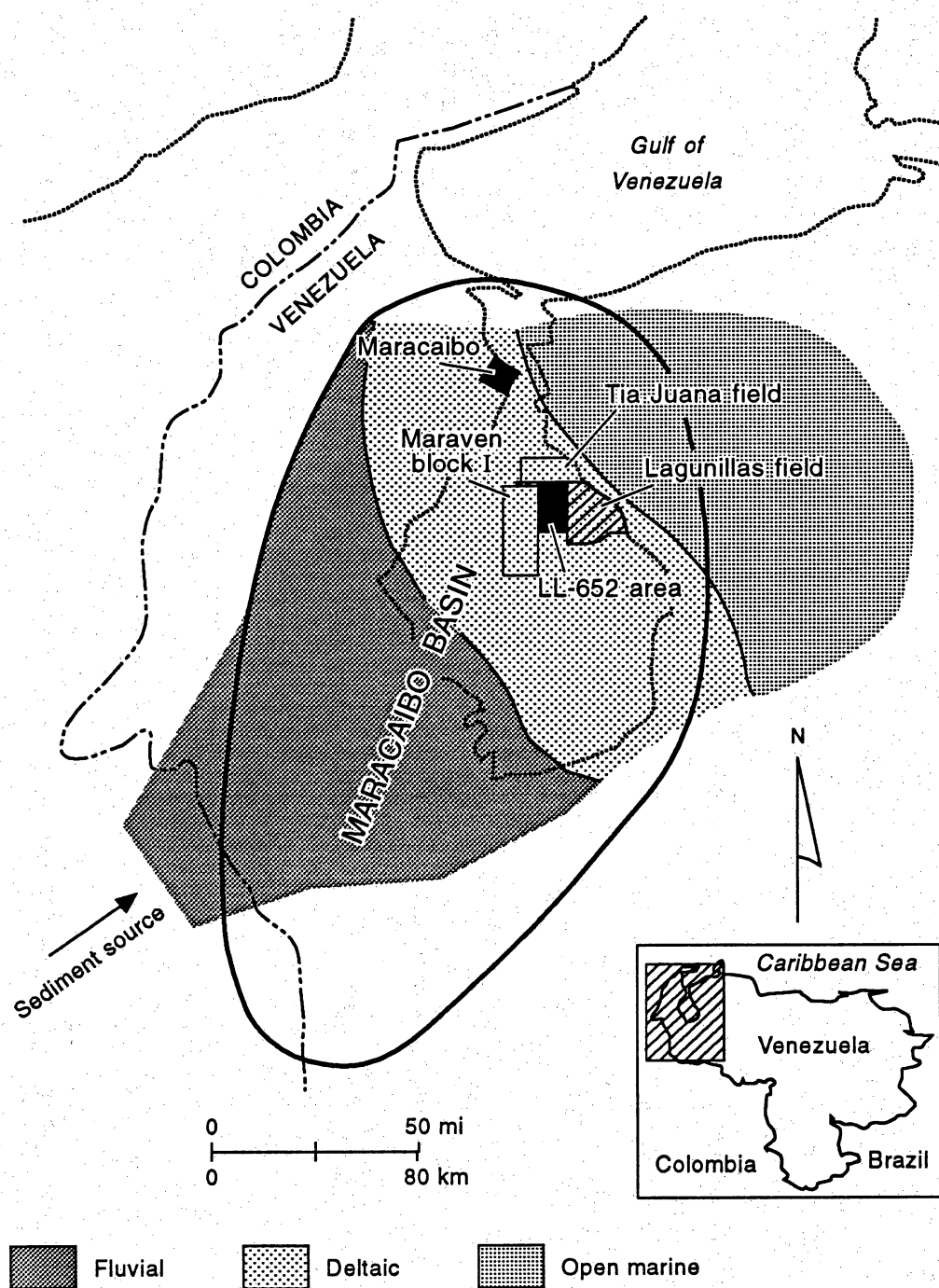


Figure II 2. Average recovery efficiency of oil reservoirs versus depositional system. Tide-dominated deltaic reservoirs at Lagunillas field have an expected ultimate recovery of only 22 percent after primary development.



From Maguregui and Tyler (1991)

QAa4418c

Figure II 3. Location of the LL-652 area and Lagunillas field in the Maracaibo Basin.

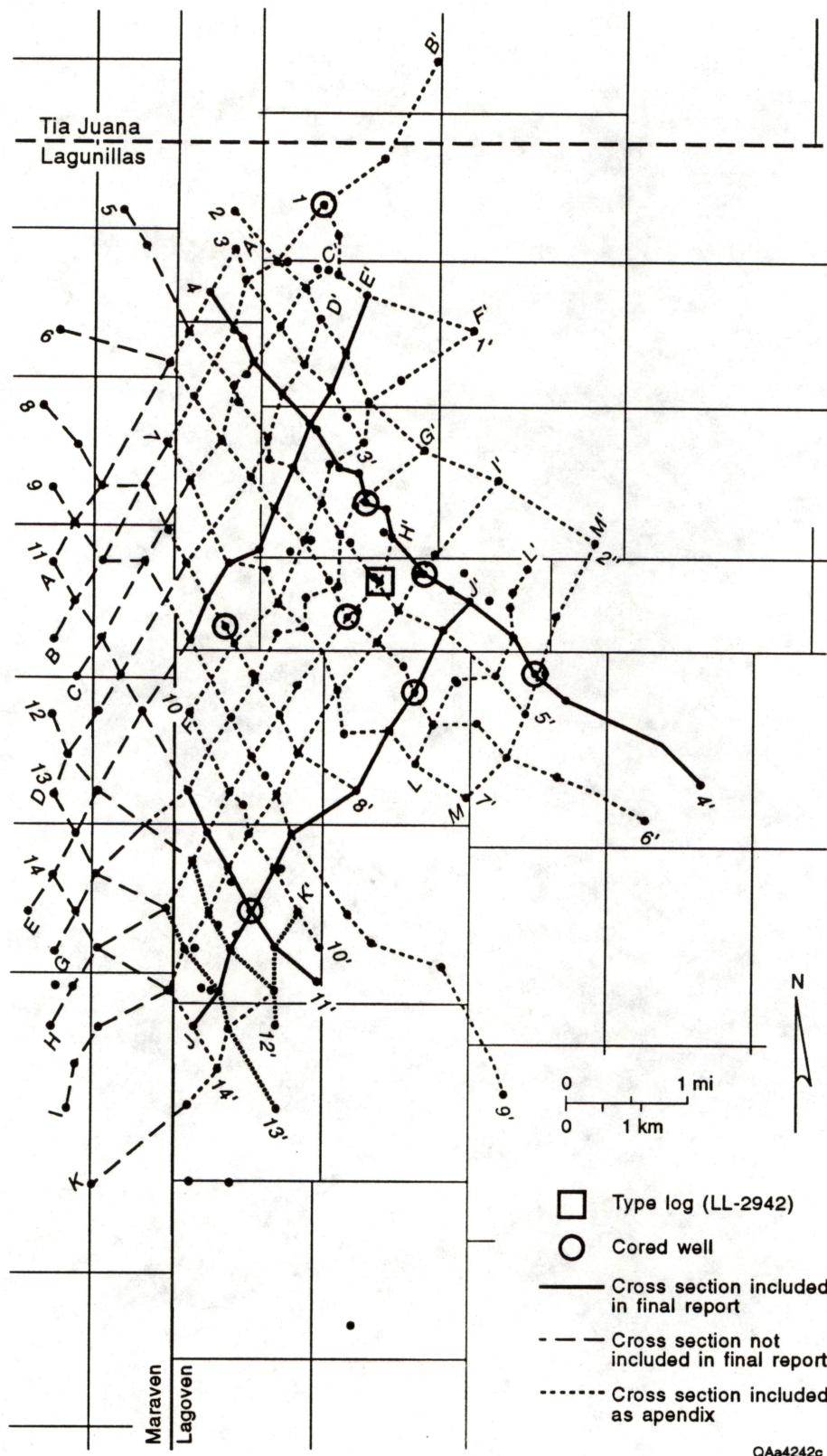


Figure II 4. Well control in the LL-652 area, Lagunillas field.

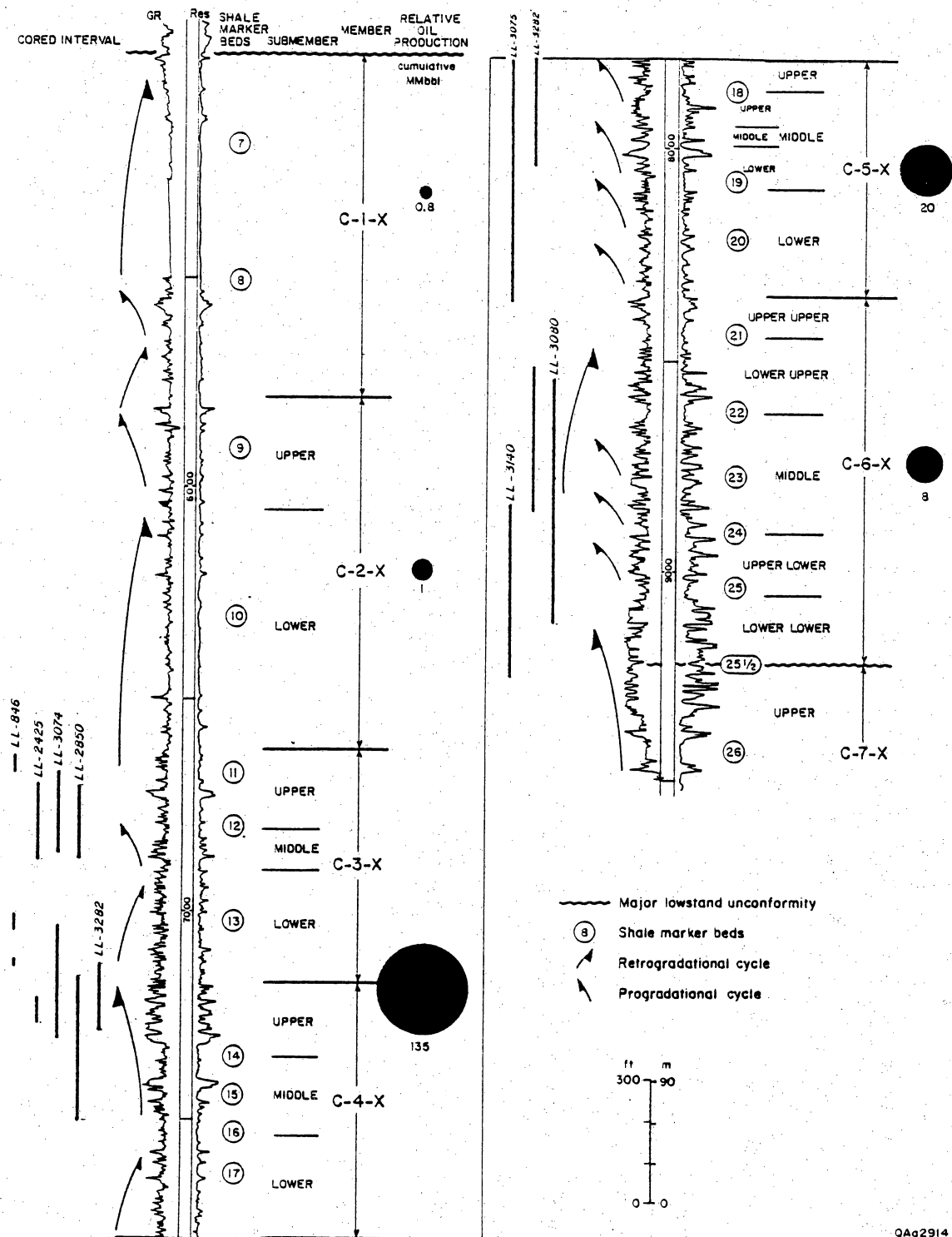


Figure II 5. Type log (LL-2942) in the LL-652 area, showing stratigraphic units, major depositional sequences, cored intervals, and cumulative oil production. Type log is located in figure II 4.

Table II 1. Summary of faulted wells in the LL-652 area.

Well	Conc.	Depth (ft)	Missing Section (ft)	Repeat Section (ft)	Member	Dipmeter Yes	Dipmeter No	Comments
LL-601	A-253	5550	600	-	B-X		x	
LL-827	A-224	5550	-	120	C-2	x		
LL-851	A-224	7490	480	-	C-4	x		
LL-851	A-229	6150	-	140	C-2	x		
LL-857	A-188	5500	-	200	B-9	x		
LL-857	A-188	5500	-	200	B-9	x		
LL-904	A-229	5900	-	120	C-2	x		
LL-917	A-272	8410	-	110	C-6	x		
LL-917	A-272	6450	80	-	C-2	x		
LL-946	A-273	7150	-	70	C-3	x		
LL-962	A-226	8170	350	-	C-5	x		
LL-997	A-188	5970	-	160	C-1		x	
LL-1001	A-276	8290	-	180	C-5	x		
LL-1005	A-273	6790	160	-	C-3	x		Major dip change by fault
LL-1005	A-273	7780	-	90	C-5		x	
LL-1022	A-262	8630	200	-	C-4	x		
LL-1023	A-273	6470	-	80	C-2	x		
LL-1060	A-253	7200	450	-	C-2	x		
LL-1061	A-229	7310	150	-	C-4	x		
LL-1061	A-229	5700	-	90	C-2	x		
LL-1066	A-224	6650	180	-	C-3	x		
LL-1066	A-224	5650	200	-	C-1	x		
LL-1089	A-188	6150	-	150	C-1		x	
LL-1095	A-225	550	-	90	C-5	x		The dip angle increase affected by reverse fault
LL-1126	A-225	5840	1200	-	C-1/C-2		x	
LL-1129	A-271	7470	80	-	C-4		x	
LL-1159	A-229	5370	1150	-	B-X/C-1		x	
LL-1166	A-224	6490	180	-	C-3	x		
LL-1166	A-224	8600	450	-	C-5	x		

Table II 1. Table continued.

LL-3059	A-273	6270	300	-	C-2		x	
LL-3060	A-225	5240	900	-	C-1		x	
LL-3075	A-229	5370	1150	-	B-X/C-1		x	
LL-3140	A-225	5310	1200	-	B-X		x	
LL-3141	A-225	5250	900	-	B-X/C-1		x	
LL-3144	A-225	6280	80	-	C-2		x	
LL-3149	A-273	8070	120	-	C-4		x	
LL-3155	A-272	7300	260	-	C-4		x	
LL-3173	A-225	6650	50	-	C-3		x	
LL-3204	A-188	8260	-	180'	C-5		x	
LL-3238	A-225	5200	800	-	B-X/C-1		x	
LL-3249	A-225	5670	1180	-	B-X/C-1		x	
LL-3250	A-187	7690	-	190	C-5		x	
LL-3261	A-229	7650	120	-	C-4		x	
LL-3263	A-188	6840	100	-	C-4		x	
LL-3267	A-225	6480	50	-	C-3		x	
LL-3274	A-225	7080	800	-	C-3/C-4		x	
LL-3279	A-225	7360	140	-	C-4		x	
LL-3282	A-188	*	*	-	C-5			*Faulted Zone 8090-8180 (90')
LL-3284	A-273	6490		70	C-2			
LL-3286	A-225	6350	100	-	C-3		x	
LL-3301	A-272	7080		90	C-3			
VLA-13	LAC-25	7500	920	-	C-3	x		
VLA-68D	LAC-21	8450		80	C-5			
VLA-93	LAC-13	6410	150	-	C-4		x	
VLA-96D	LAC-17	9180		100	C-6		x	
VLA-200	LAC-21	6220	150	-	C-3	x		
VLA-613	LAC-5	5300	1100	-	B-X/C-1	x		
VLA-724	LAC-17	6800	100	-	C-4	x		Major dip change by fault
VLA-744	LAC-5	6200	300	-	C-3	x		
VLA-758	LAC-5	6380	320	-	C-3	x		
VLA-860	LAC-13	6110	120	-	C-3	x		

Table II 1. Table continued.

LL-1172	A-229	6925	100	-	C-3		x	
LL-1176	A-273	7520	350	-	C-4		x	
LL-1196	A-273	7470	60	-	C-3		x	
LL-1196	A-273	6100	-	140	C-2		x	
LL-1209	A-224	5540	300	-	C-1	x		
LL-1209	A-224	6350	180	-	C-2	x		
LL-1218	A-272	6940	180	-	C-2		x	
LL-1218	A-272	6590	-	140	C-2		x	
LL-1218	A-272	7590	-	60	C-4		x	
LL-1303	A-273	6960	-	130	C-3		x	
LL-1307	A-273	7700	100	-	C-4		x	
LL-1310	A-272	7580	180	-	C-4	x		Good dipmeter example in a faulted zone
LL-1312	A-225	5520	1190	-	C-1		x	
LL-1339	A-229	5580	900	-	B-X/C-1		x	
LL-1679	A-277	7560	650	-	C-2		x	
LL-1748	A-274	5950	180	-	C-1		x	
LL-1782	A-272	6410	-	80	C-2		x	
LL-1803	A-188	6970	200	-	C-3	x		
LL-2038	A-272	7135	140	-	C-3		x	
LL-2039	A-229	6040	1150	-	B-X/C-1		x	
LL-2187	A-271	7490	50	-	C-3		x	
LL-2191	A-228	6540	1000	-	C-2		x	
LL-2280	A-272	6900	70	-	C-2		x	
LL-2729	A-224	7240	550	-	C-4		x	
LL-2896	A-229	5890	1000	-	B-X/C-1		x	
LL-2901	A-225	5670	1180	-	B-X/C-1		x	
LL-2938	A-229	7070	140	-	C-3		x	
LL-2940	A-225	6530	50	-	C-3		x	
LL-2981	A-2274	6510	150	-	C-2		x	
LL-3055	A-225	5220	800	-	C-1		x	
LL-3056	A-225	6890	100	-	C-3		x	
LL-3056	A-225	7150	-	50	C-4		x	
LL-3059	A-273	6270	300	-	C-2		x	

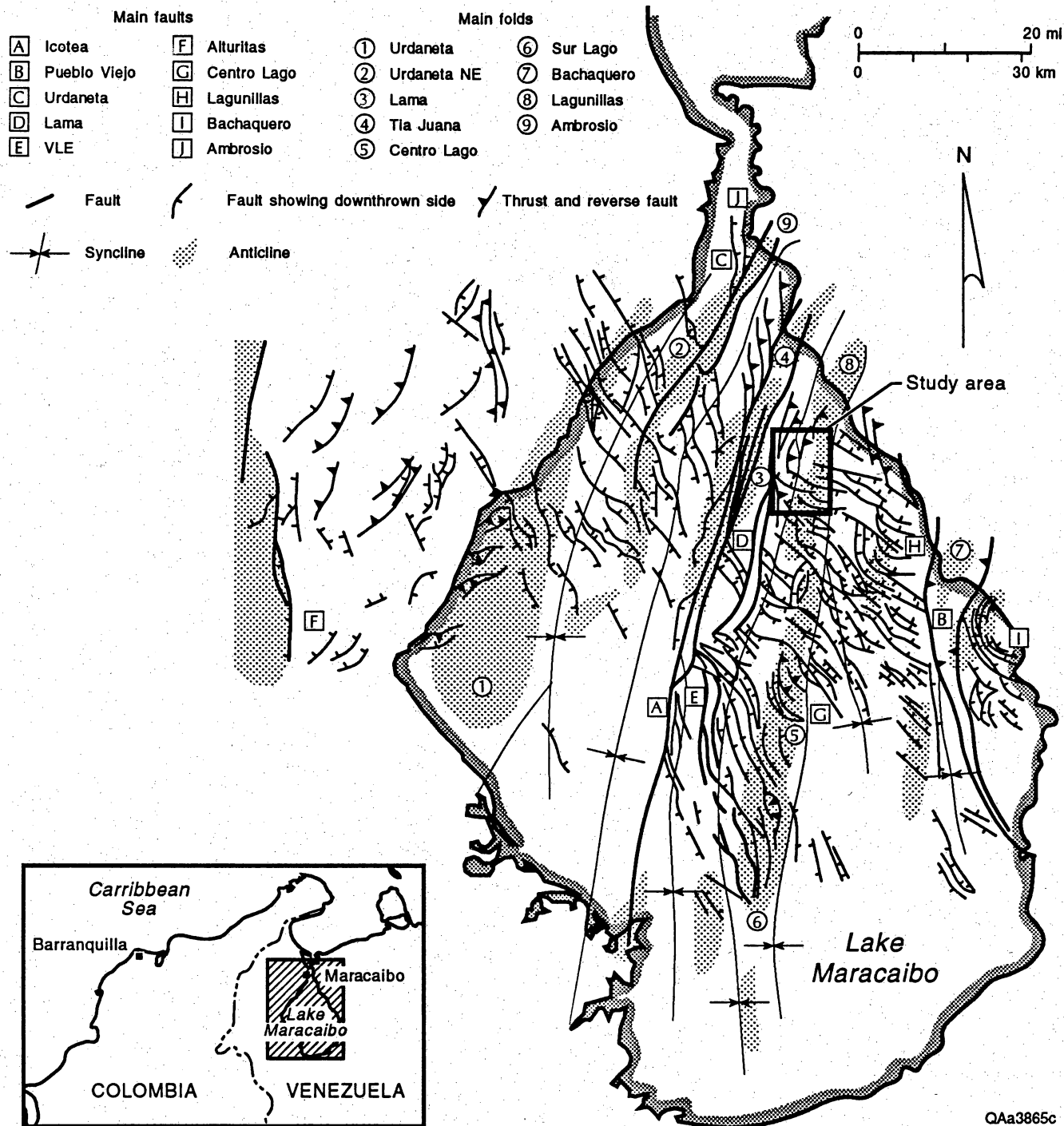


Figure III 1. Present structural styles in the Maracaibo Basin. Modified from Lugo (1991).

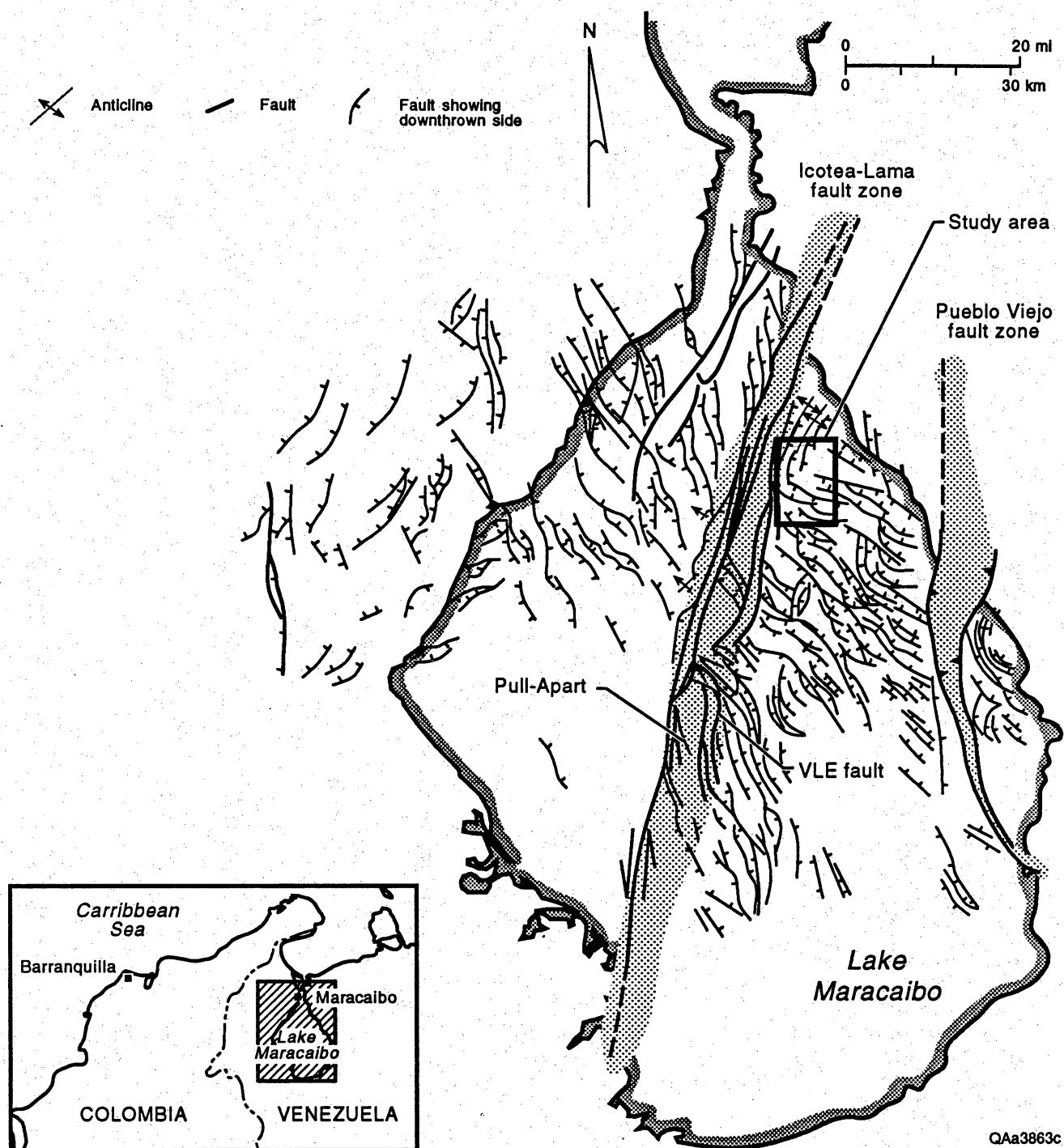


Figure III 2. Fault maps of post-Middle Eocene and pre late-Eocene to Oligocene unconformity. From Lugo (1991).

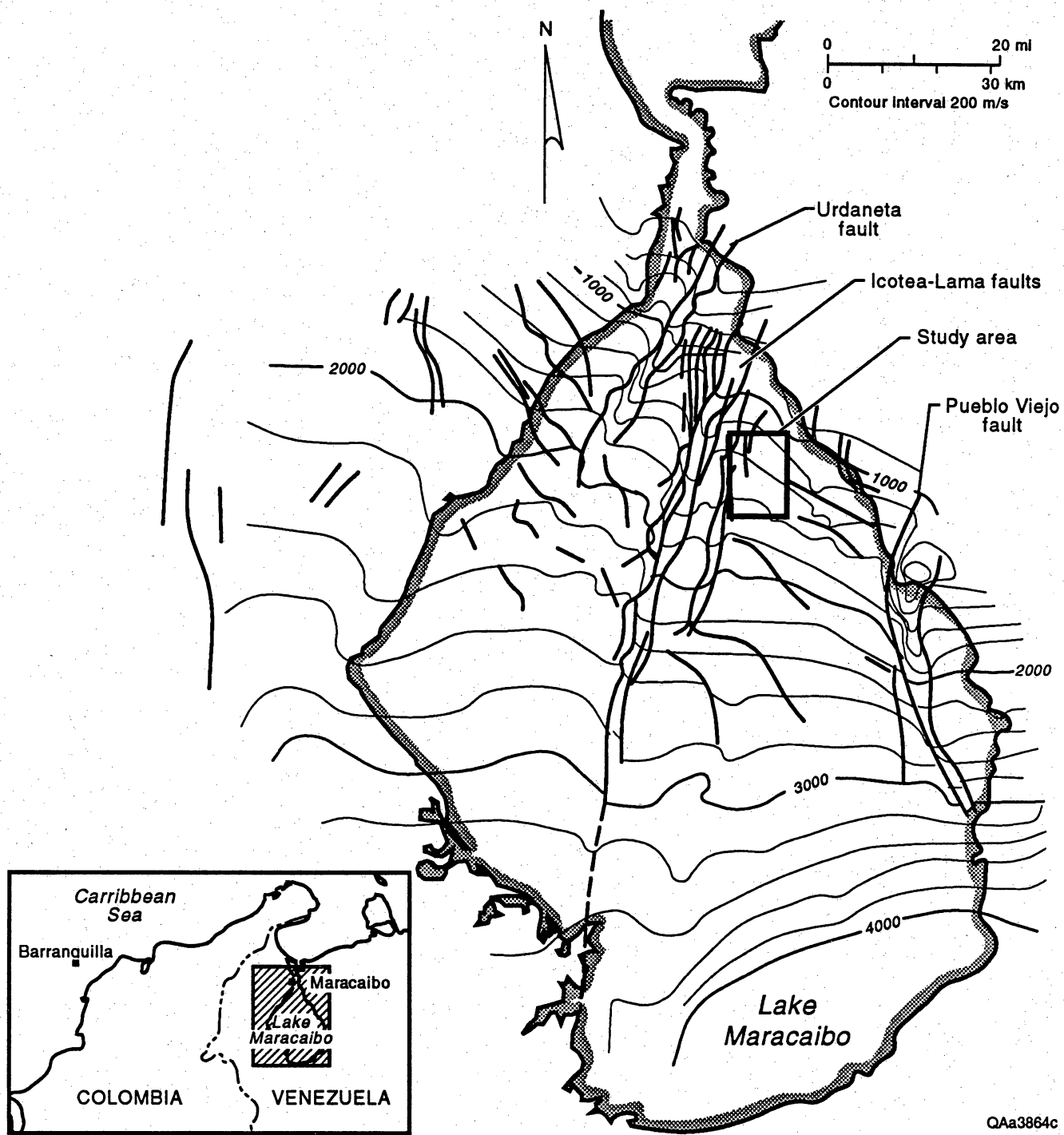
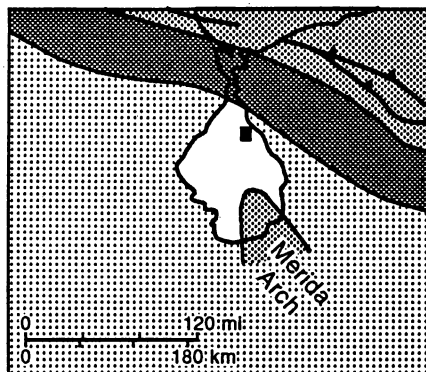


Figure III 3. Structural map of the Eocene-Miocene unconformity. From Lugo (1991).

Late Paleocene

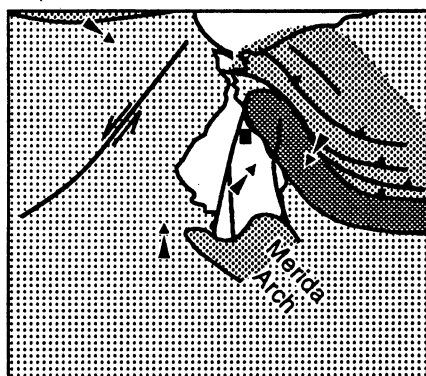


Early Eocene

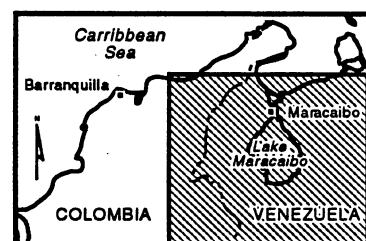
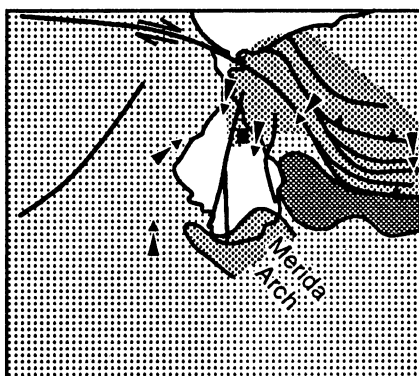


- Study area
- ↖ Sediment provenance
- Fault
- ▨ Orogens
- Main depocenter

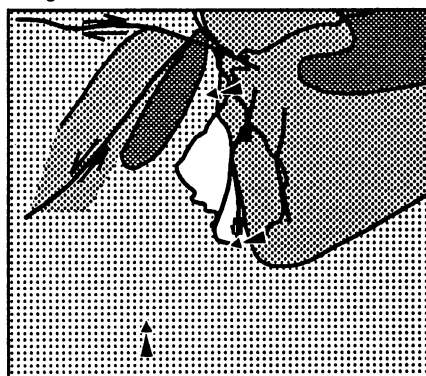
Middle Eocene



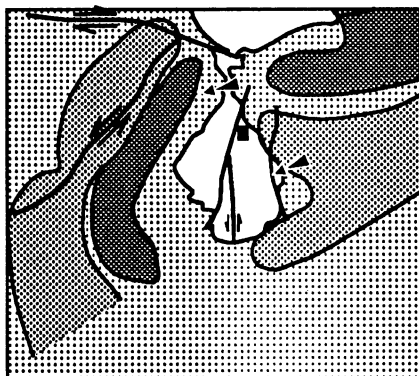
Middle-Late Eocene



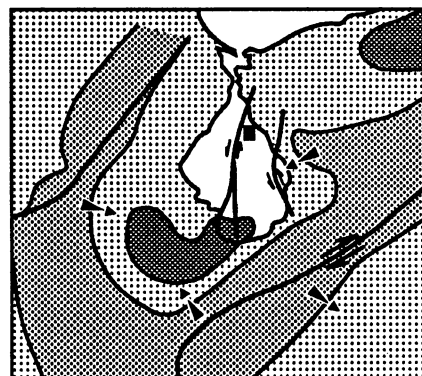
Oligocene



Middle Miocene



Pliocene



QAa3862c

Figure III 4. Paleotectonic maps showing chronology of tectonic episodes that affected the Misoa Formation. Modified from Lugo (1991).

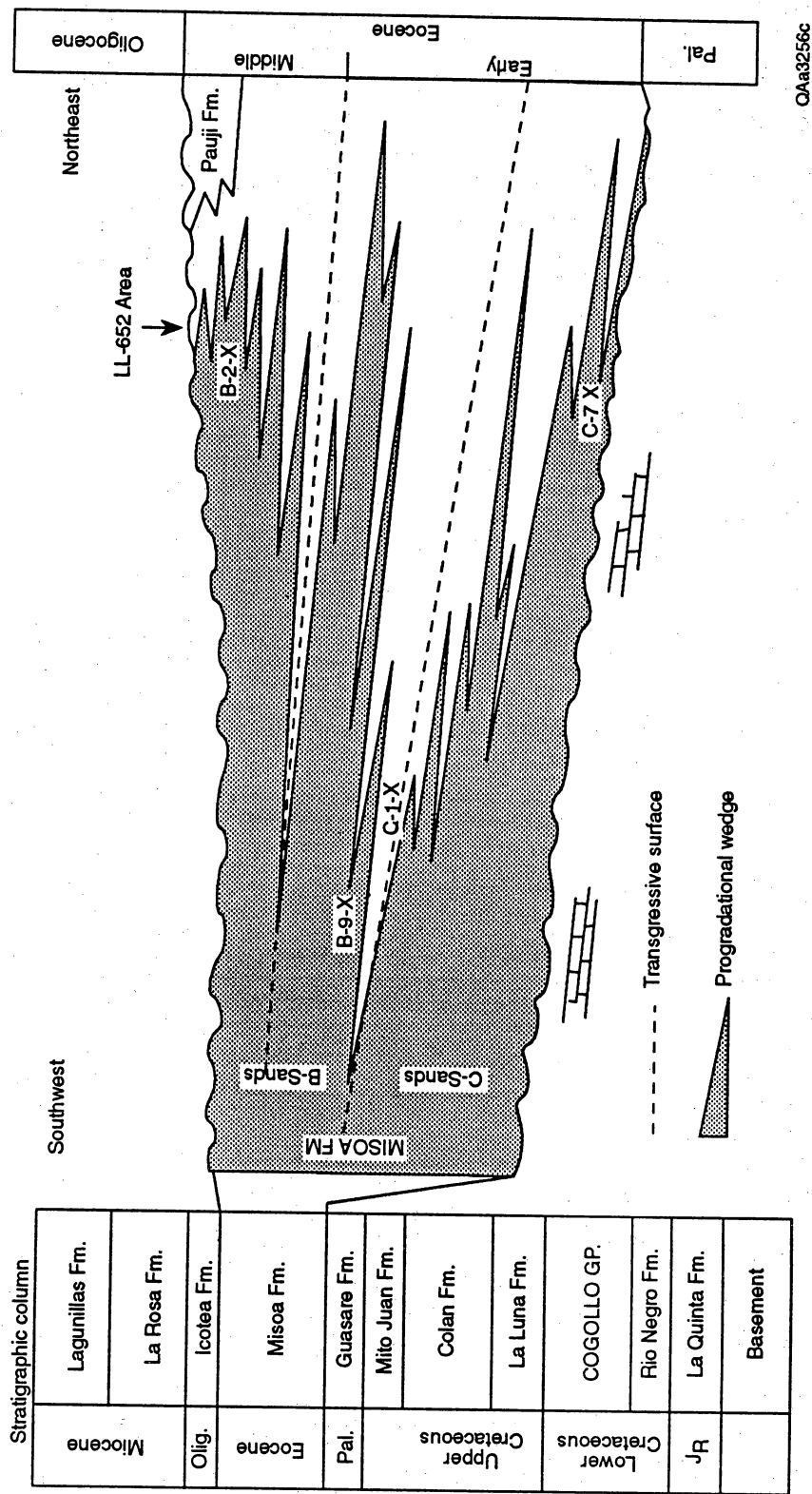


Figure III 5. Major Eocene stratigraphic sequences in the Maracaibo Basin. Modified from Maguregui (1991) after Bot and Perdomo (1987) and Graves and others (1987).

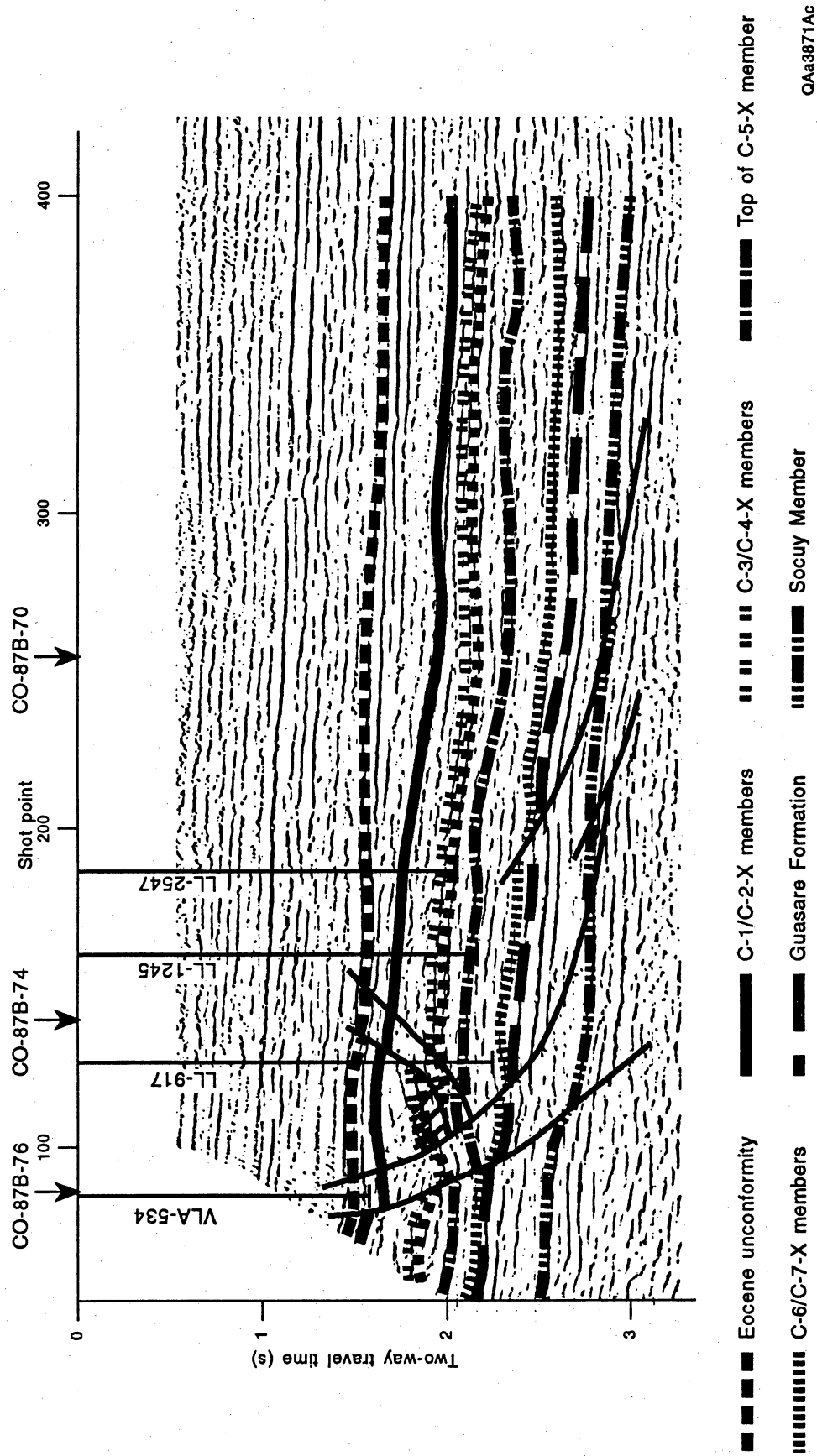


Figure III 7. Seismic strike section, showing seismic-stratigraphic units and multiple faults in the northwest part of the LL-652 area.

Table III 1. Eocene and Paleocene seismic facies in the LL-652 area. Seismic-stratigraphic units shown in figures III 6 and III 7.

<u>STRATIGRAPHIC UNITS</u>	<u>SEISMIC RESPONSES</u>	<u>INTERPRETATION</u>
Eocene Unconformity	Strong pair of westward-dipping, continuous and parallel reflectors	Angular unconformity
Upper C Members (C-1-X/C-2-X)	Moderate to moderately strong reflectors with good to fair continuity	Retrogradational, highstand systems tract
Middle C Members (C-3-X/C-4-X)	Strong, continuous pair of parallel reflectors	Regressive/transgressive couplet
Lower C Members (C-5-X to C-7-X)	Poorly-defined zone of irregular, weak to fair reflectors with poor continuity	Multiple regressive/transgressive couplets overlying low-stand unconformity (C-6-X/C-7-X boundary)
Guasare Formation	Strong, continuous pair of reflectors	Mixed carbonate/clastic shelf

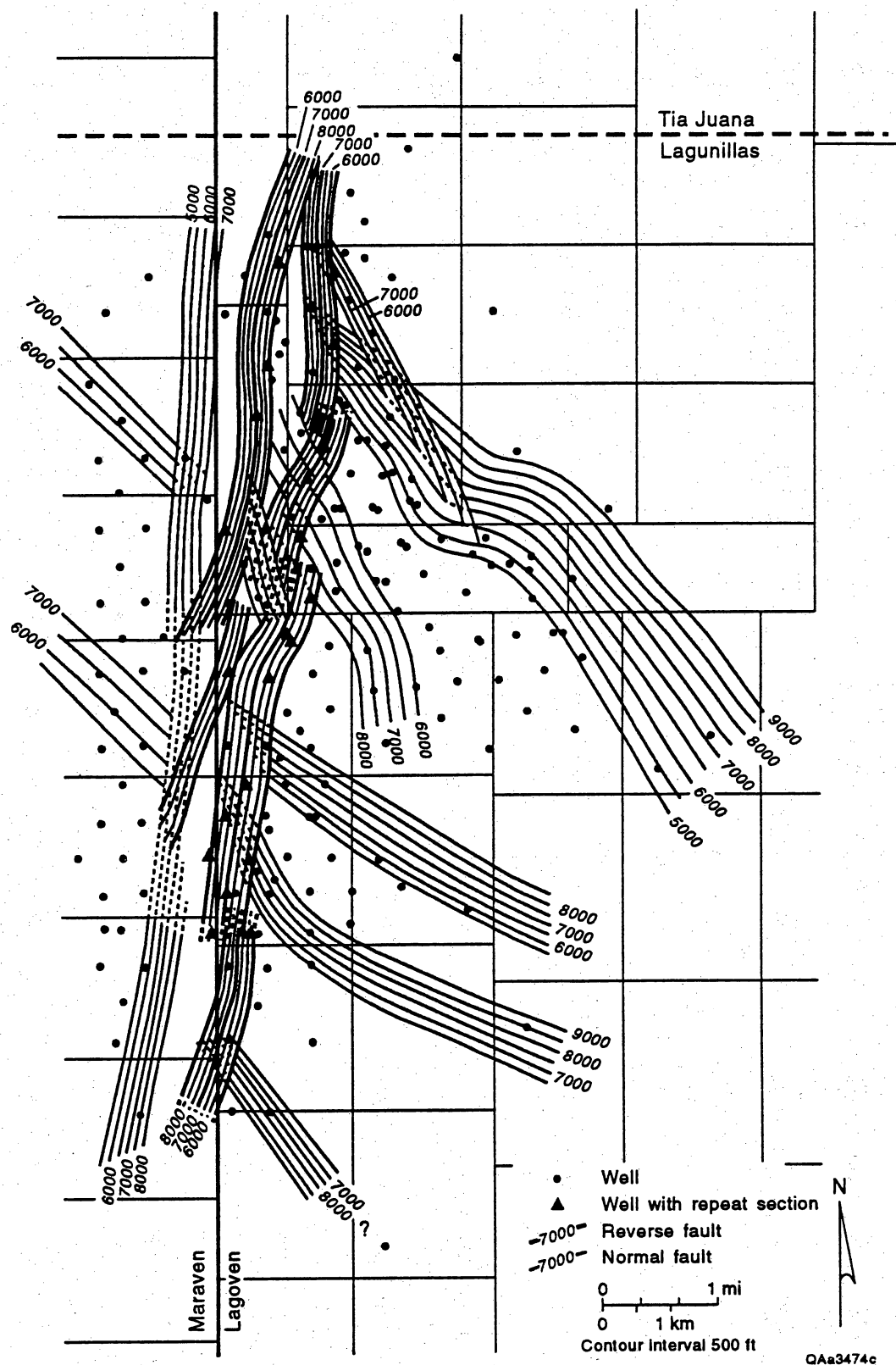


Figure IV1. Fault-surface map of the LL-652 area.

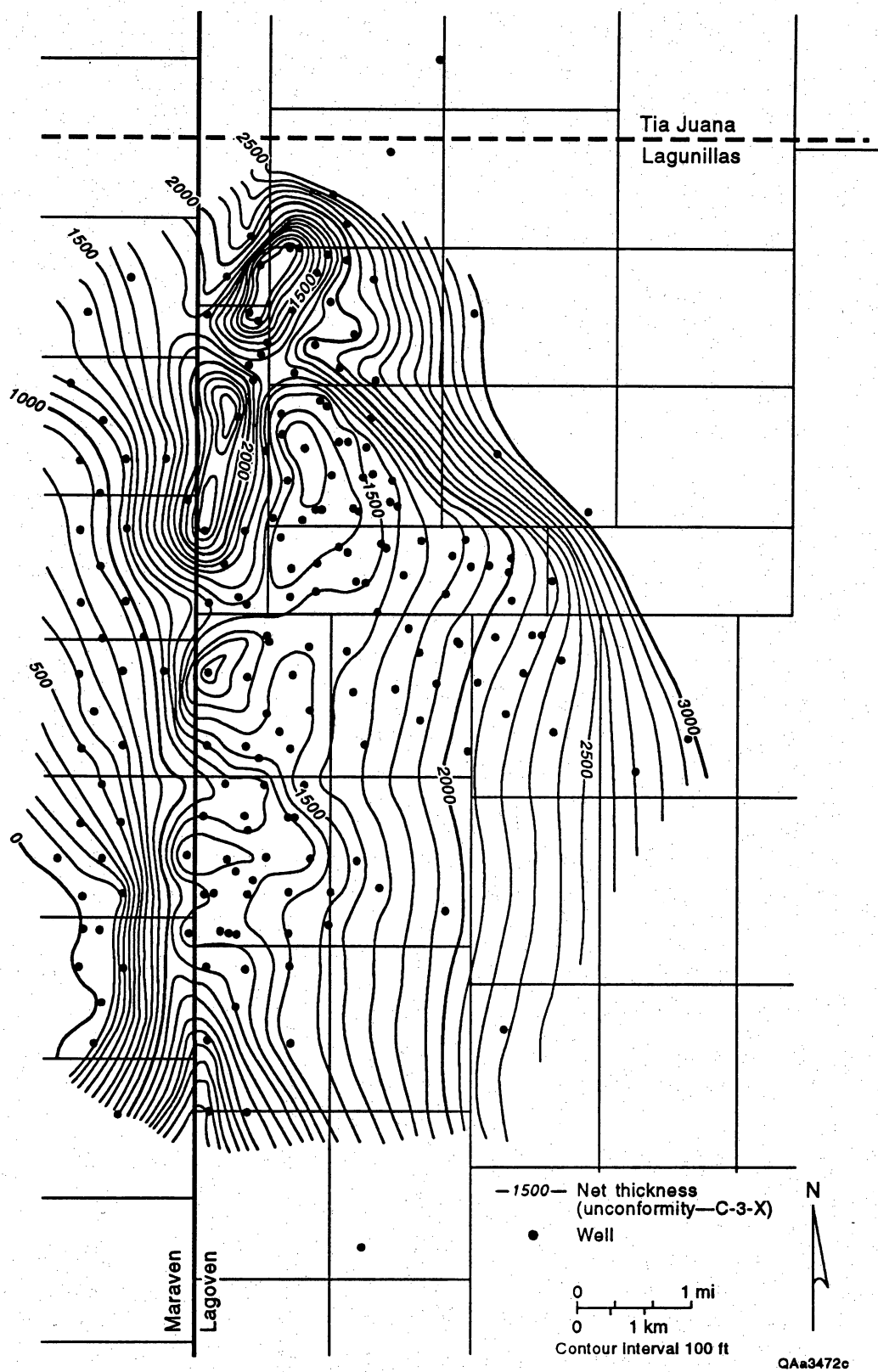


Figure IV 2. Net-thickness map of the interval between the Eocene-Miocene unconformity and the top of the C-3-X Member.

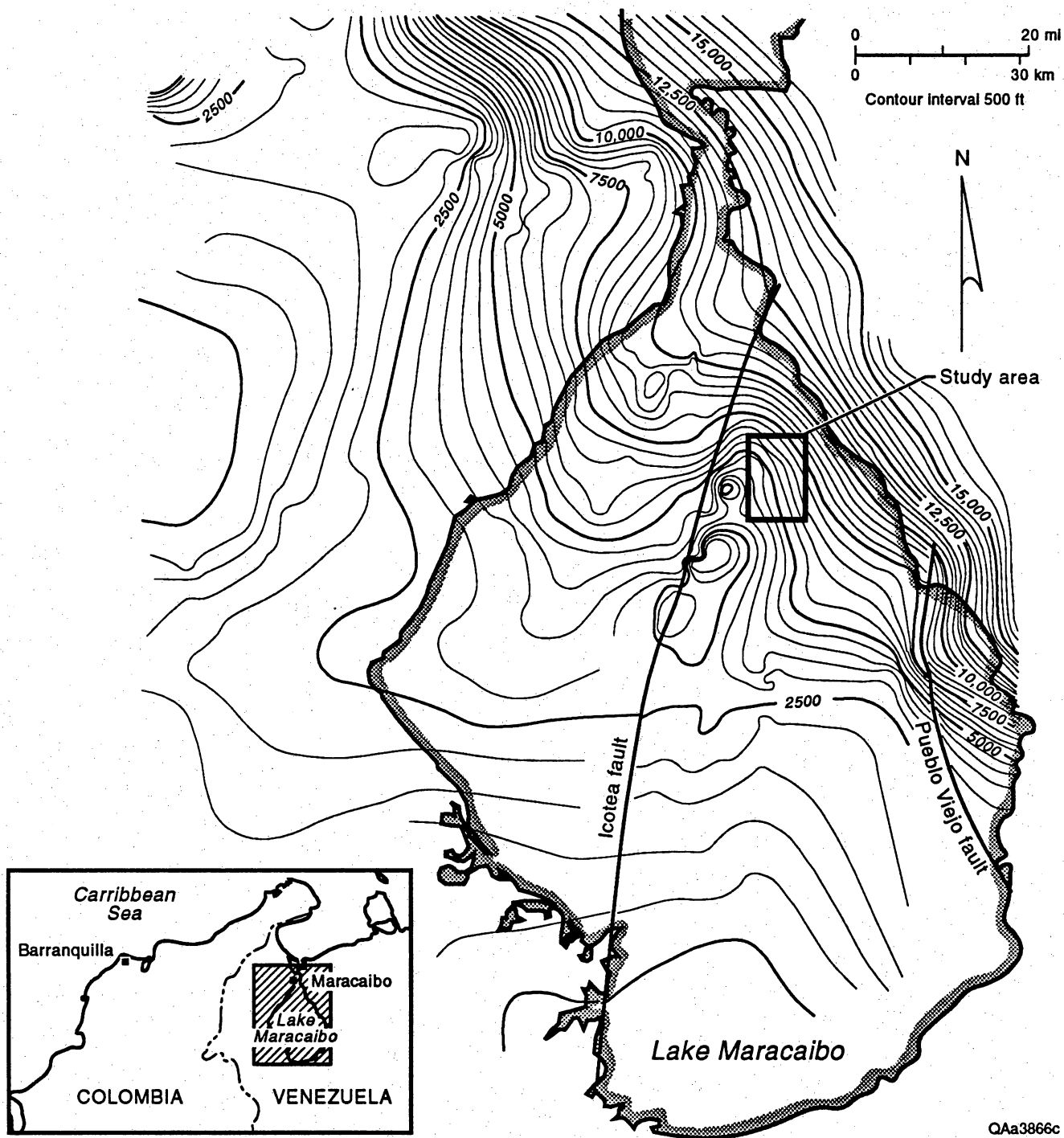
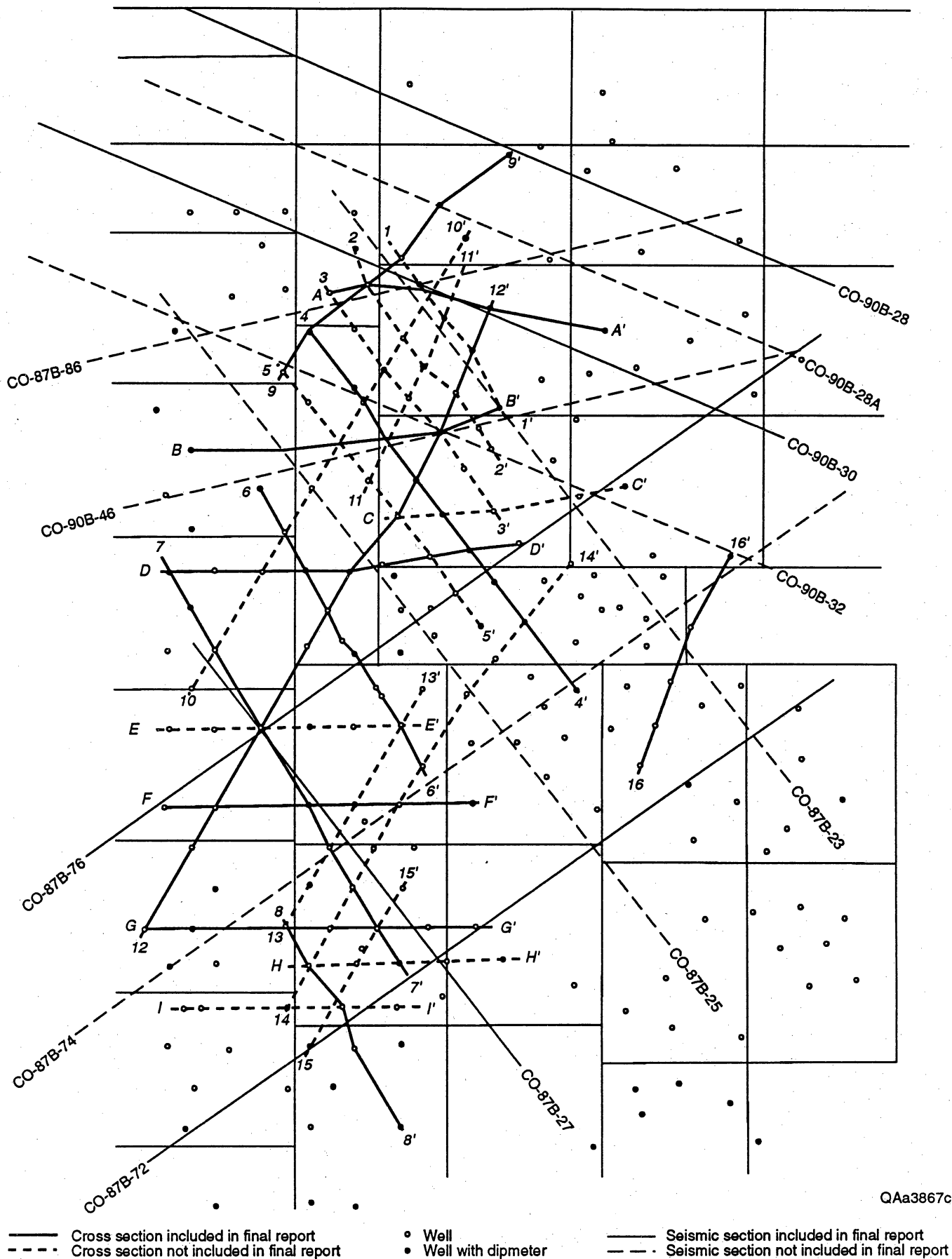
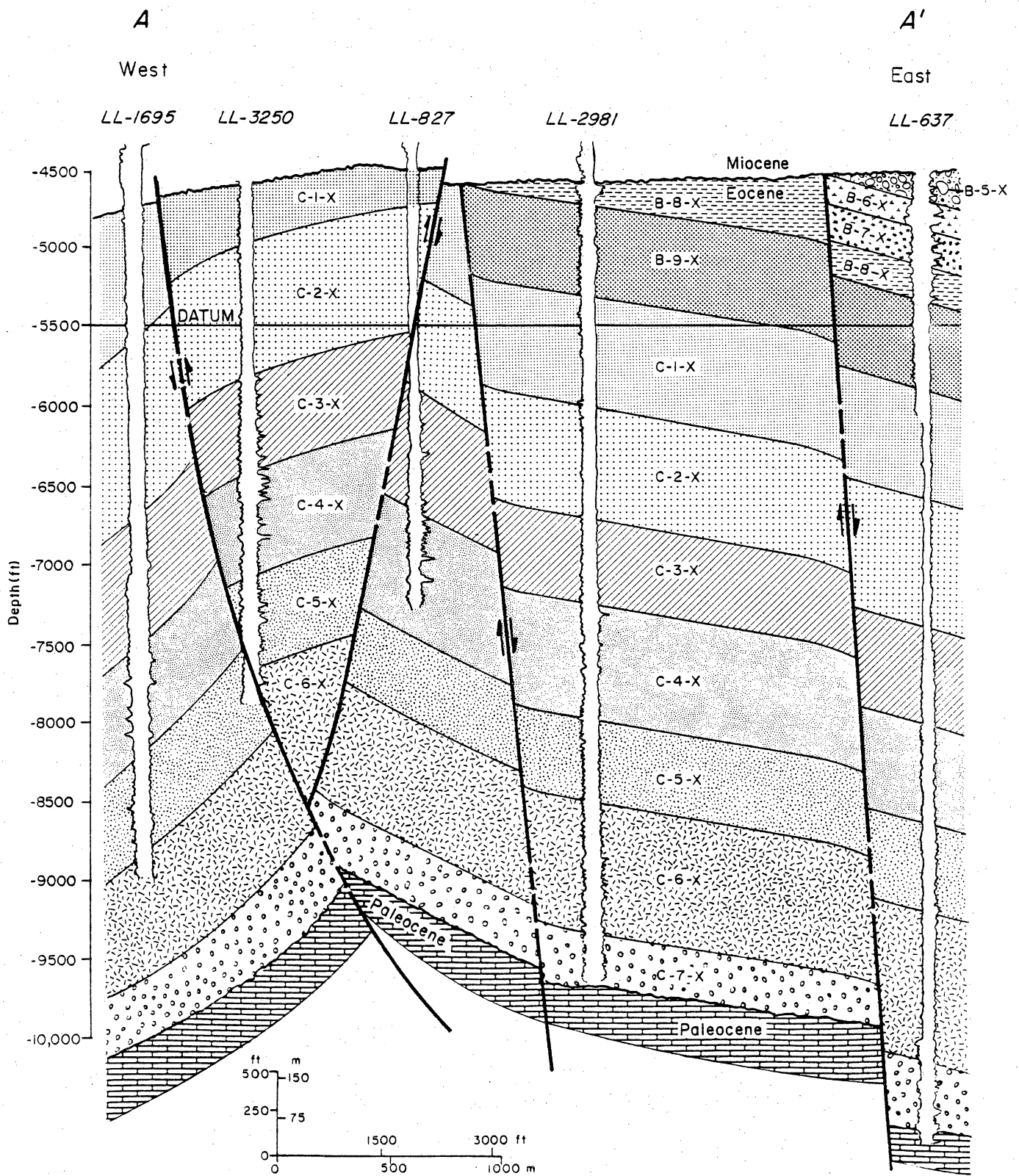


Figure IV 3. Unrestored total isopach map for the Eocene. From Lugo (1991).



QAa3867c

Figure IV 5. Structural cross section and seismic section grid.



QAa3467

Figure IV 6. Structural cross section A-A'.

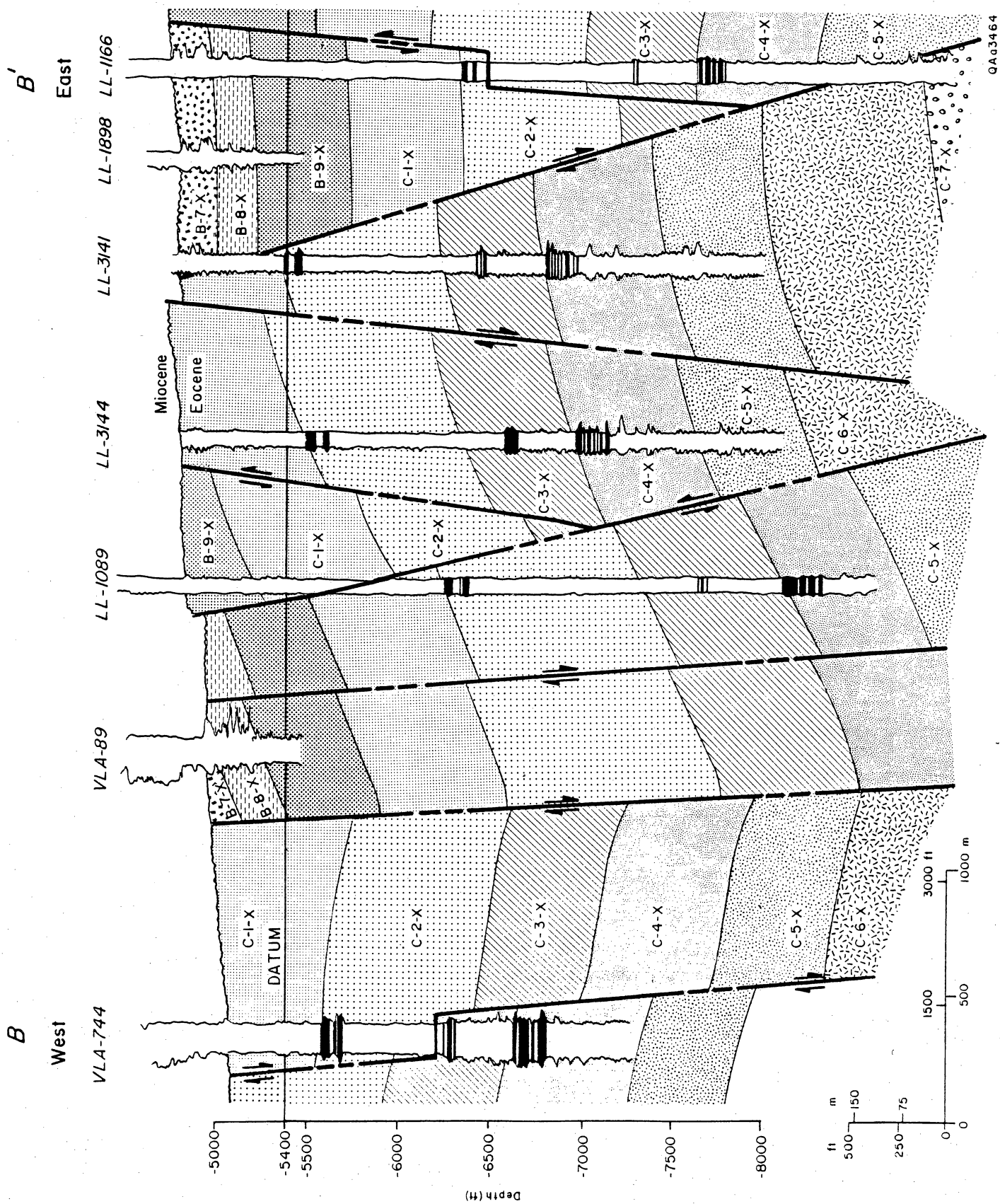
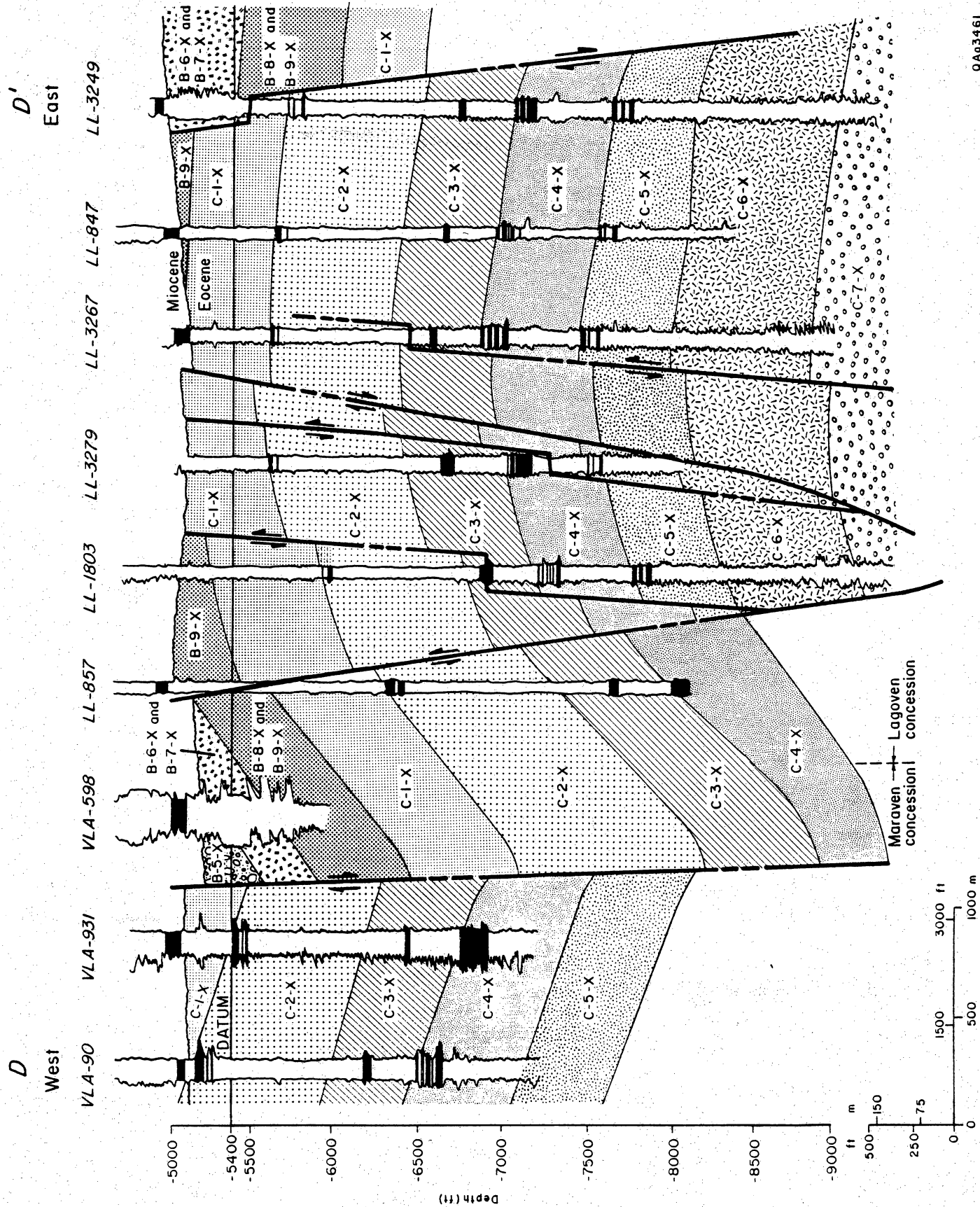


Figure IV 7. Structural cross section B-B'.



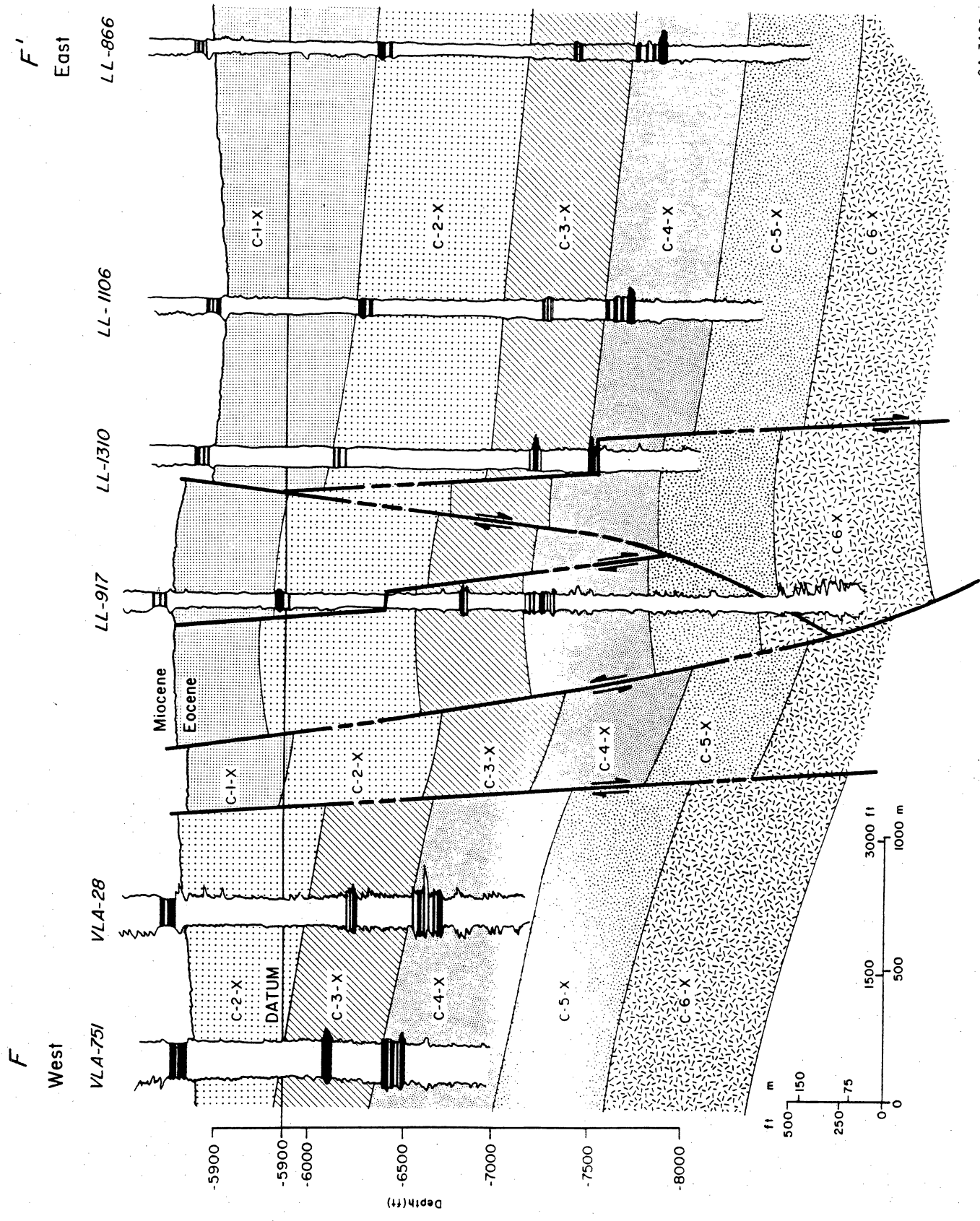


Figure IV 9. Structural cross section F-F'.

G

West

VLA-281

VLA-724

VLA-96

LL-1196

LL-3074

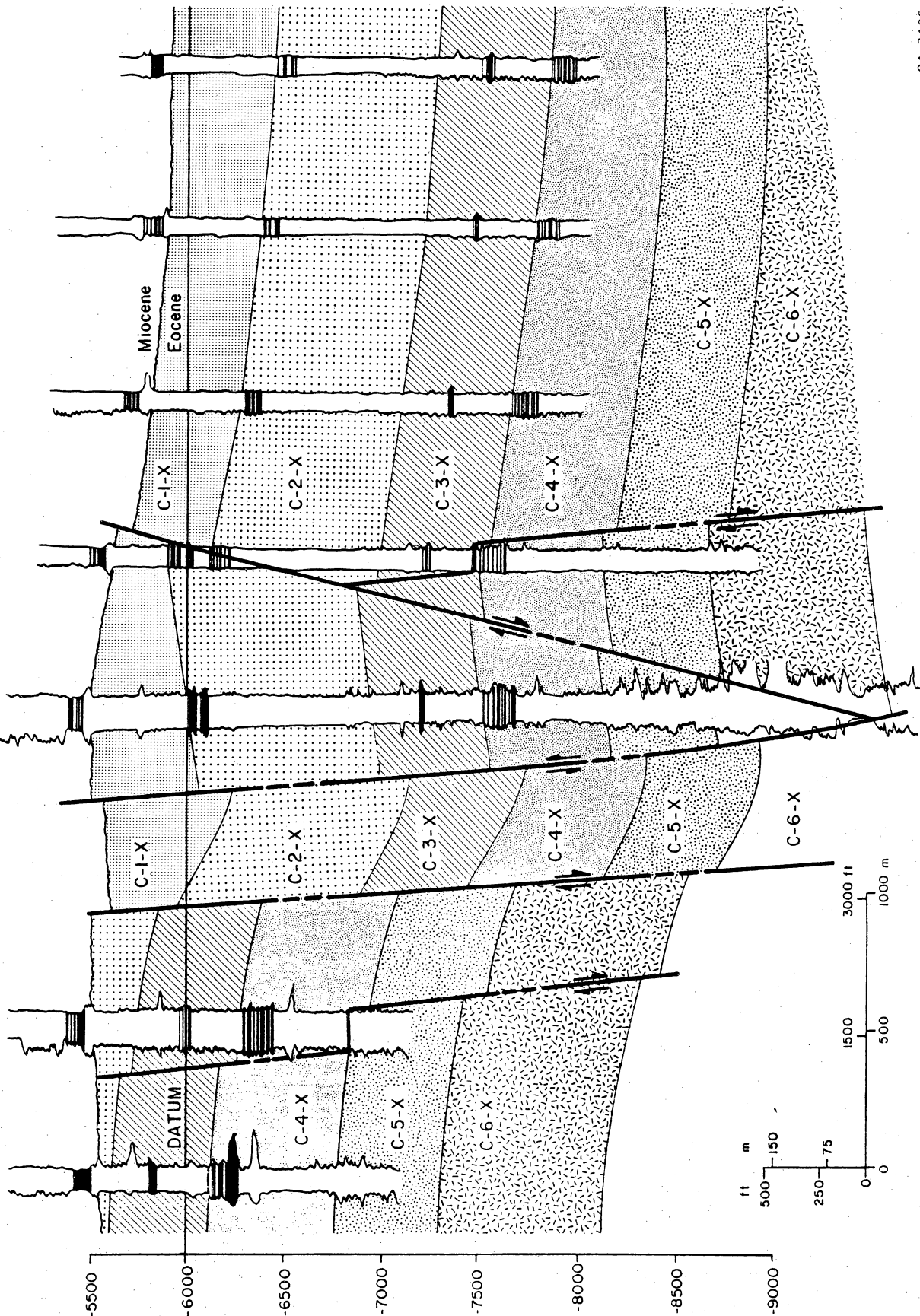
LL-2547

LL-3097

East

Depth(ft)
-5500
-6000
-6500
-7000
-7500
-8000
-8500
-9000

ft m
500 150
250 75
0 0
3000 ft
1000 m



QA03465

Figure IV 10. Structural cross section G-G'.

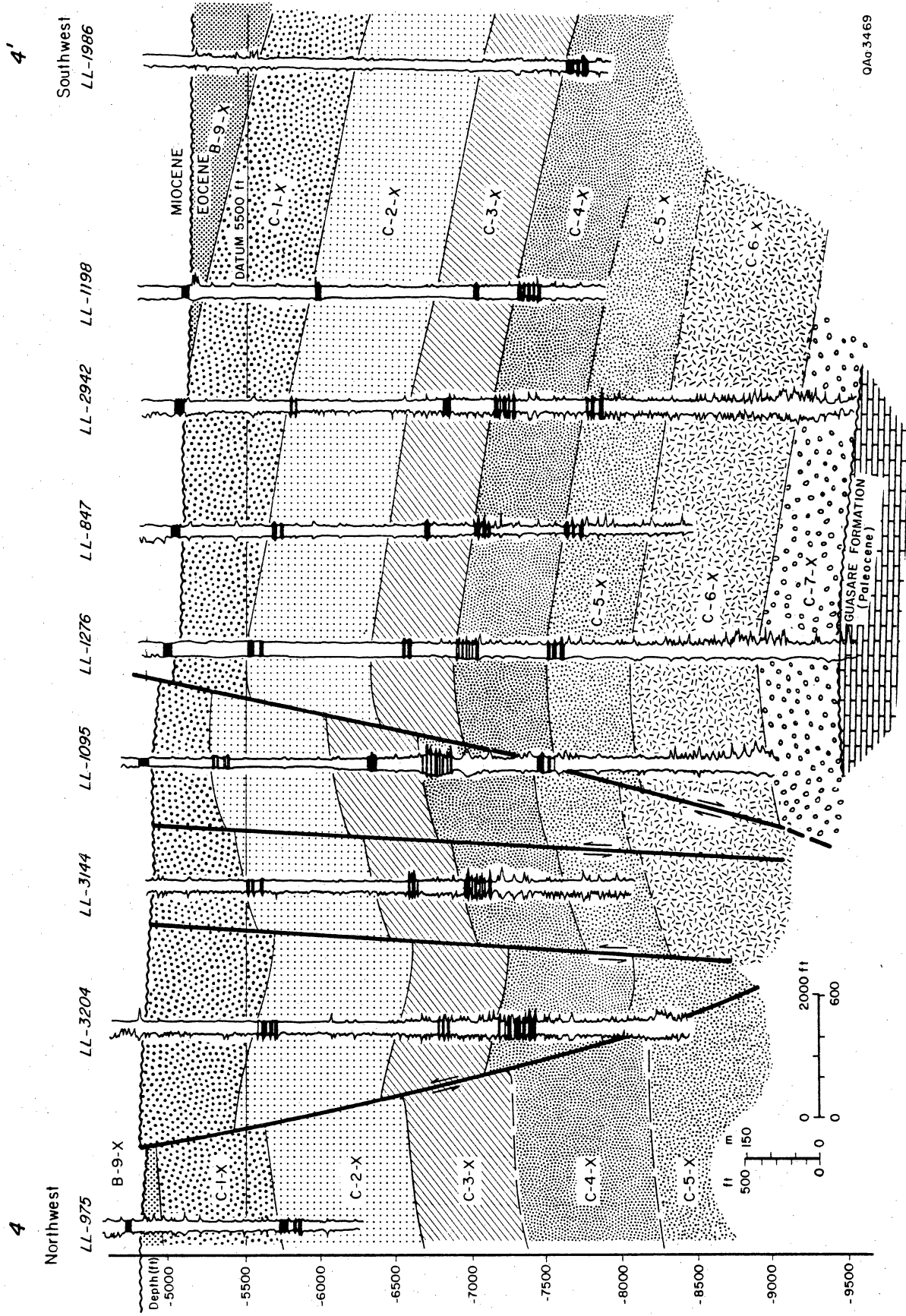


Figure IV 11. Structural cross section 4-4'.

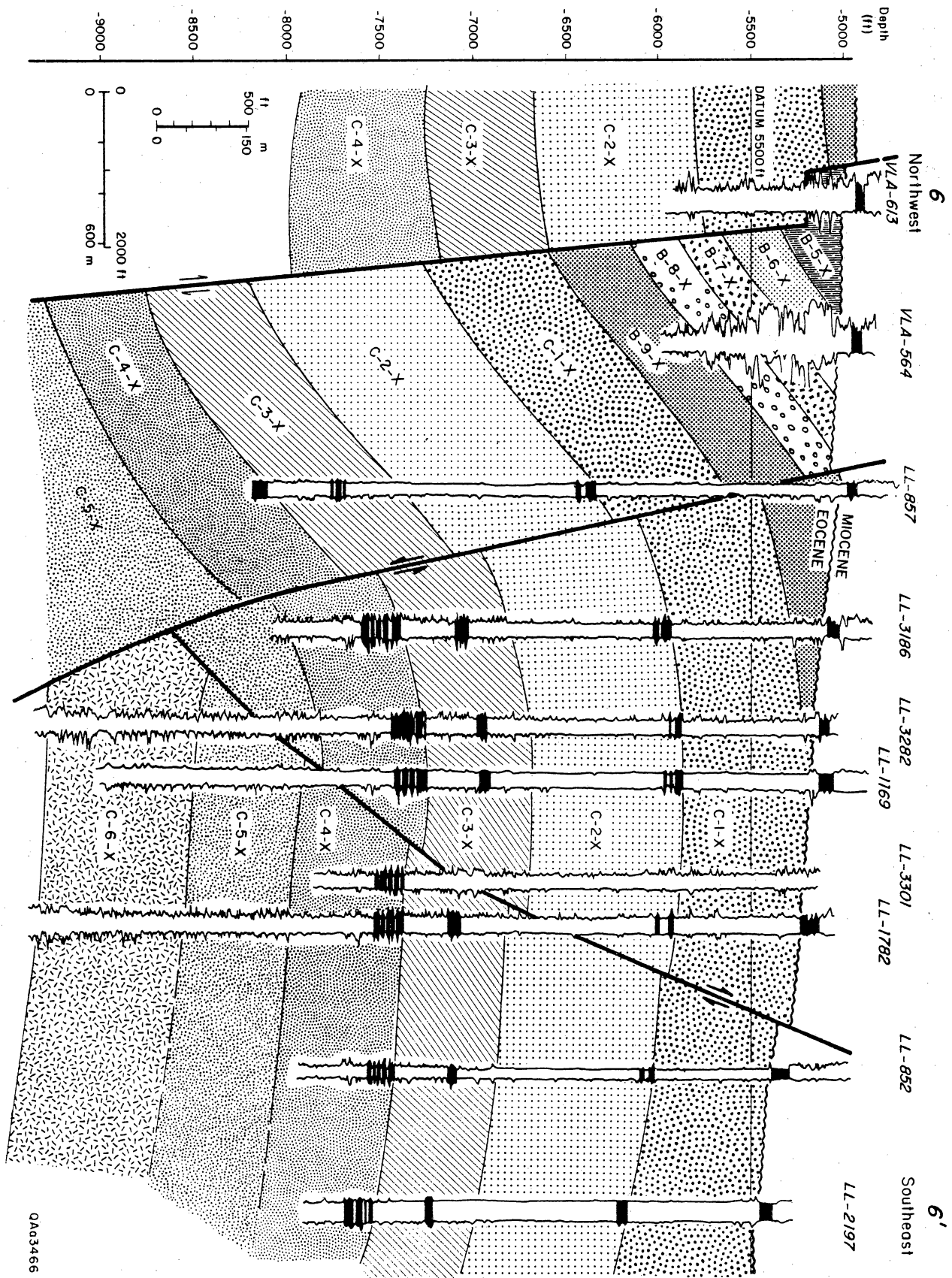
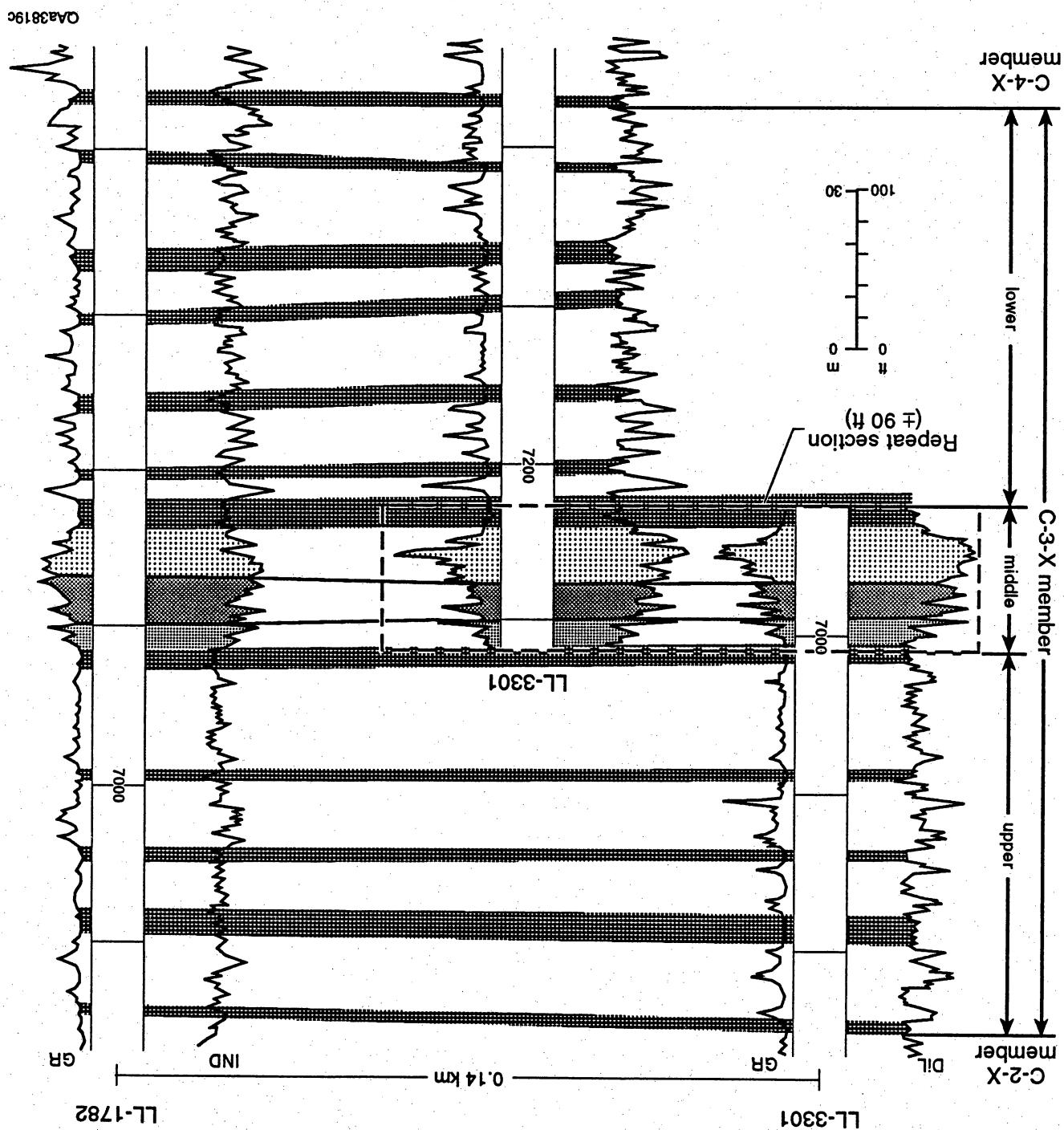


Figure IV 12. Structural cross section 6-6'.

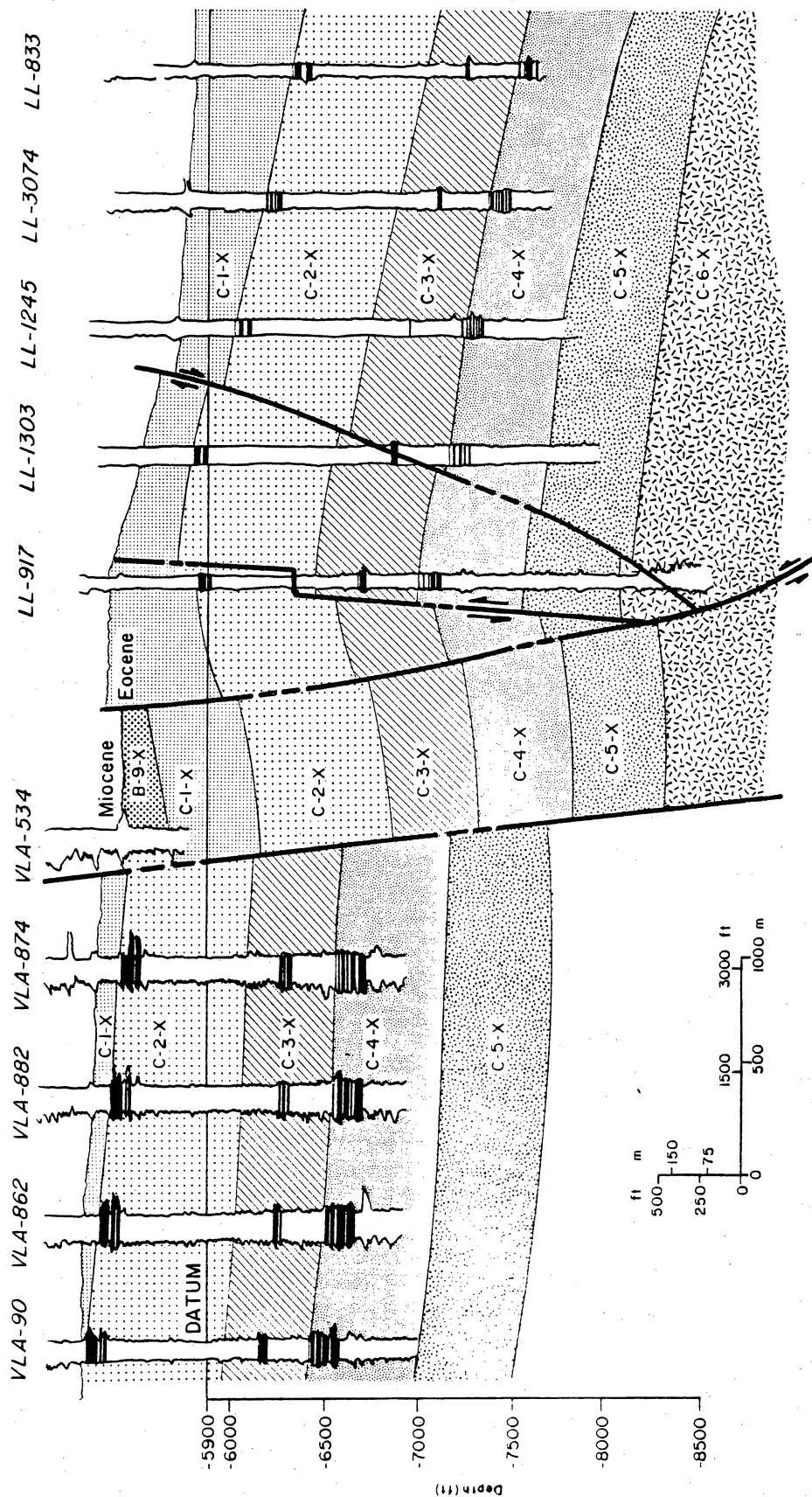
0A03466

Figure IV 13. Detailed correlation between the repeat section in the LL-3301 and LL-1782 wells.



Northwest

Southeast



QA03468

Figure IV 14. Structural cross section 7-7'.

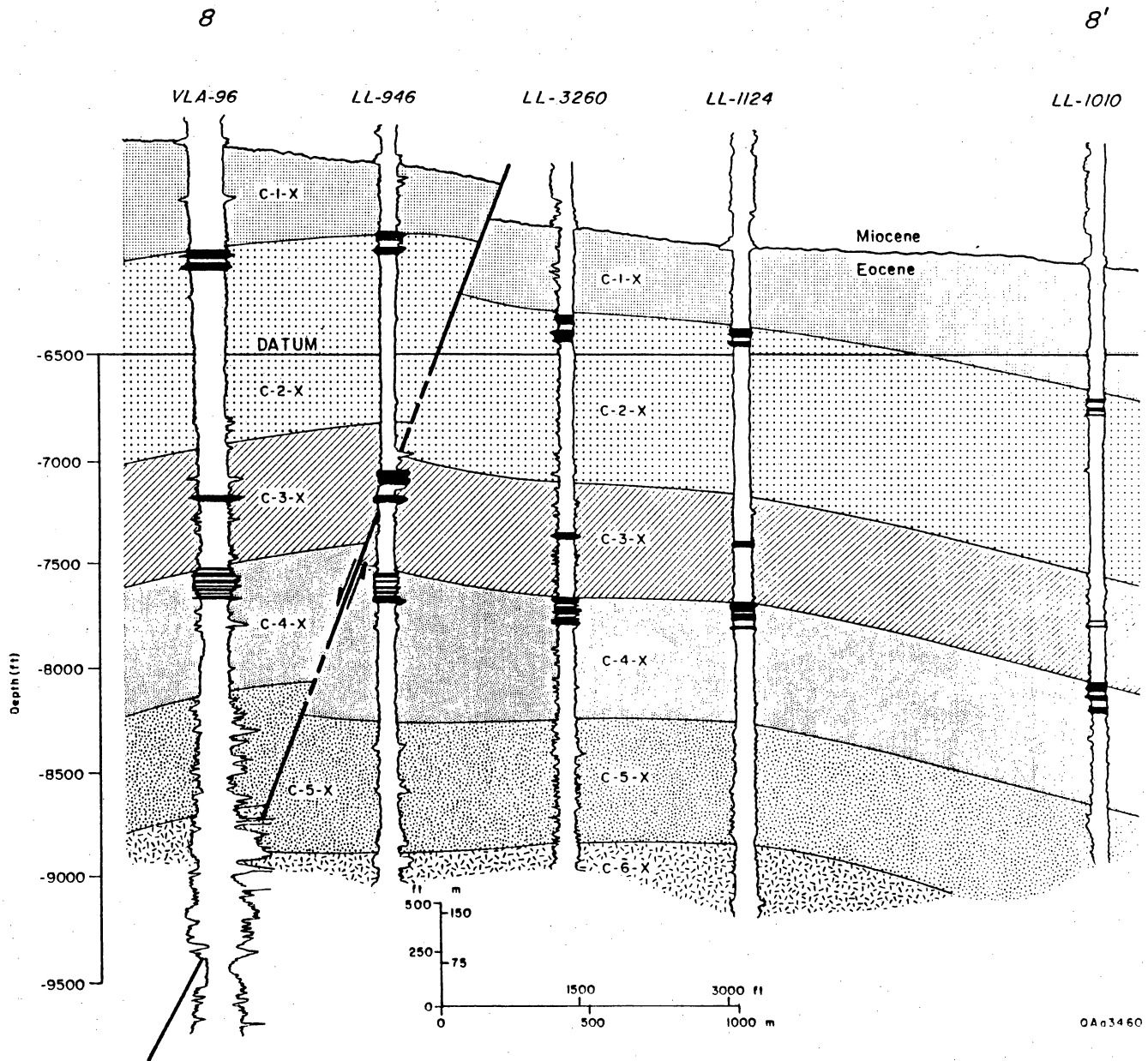


Figure IV 15. Structural cross section 8-8'.

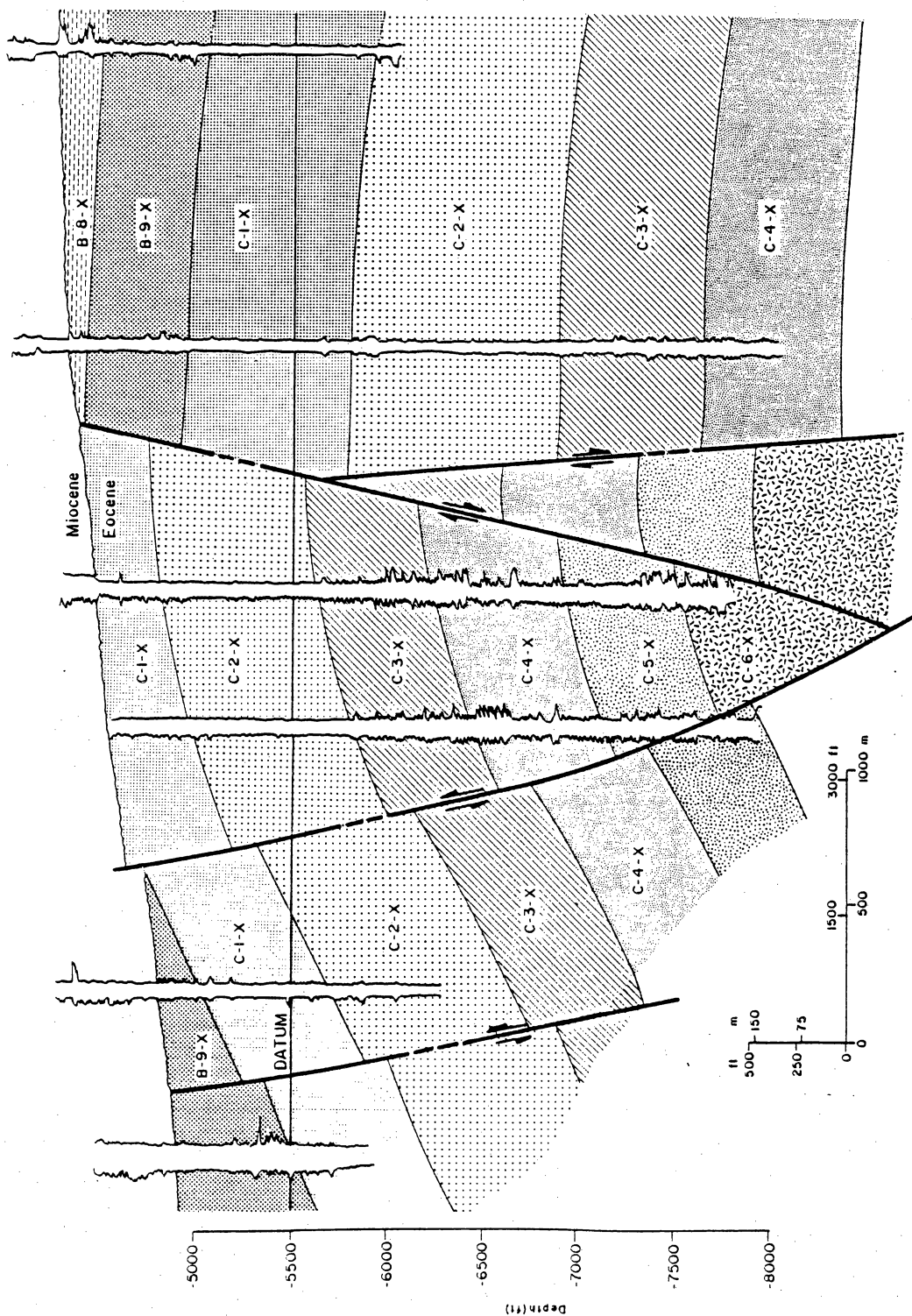


Figure IV 16. Structural cross section 9-9'.

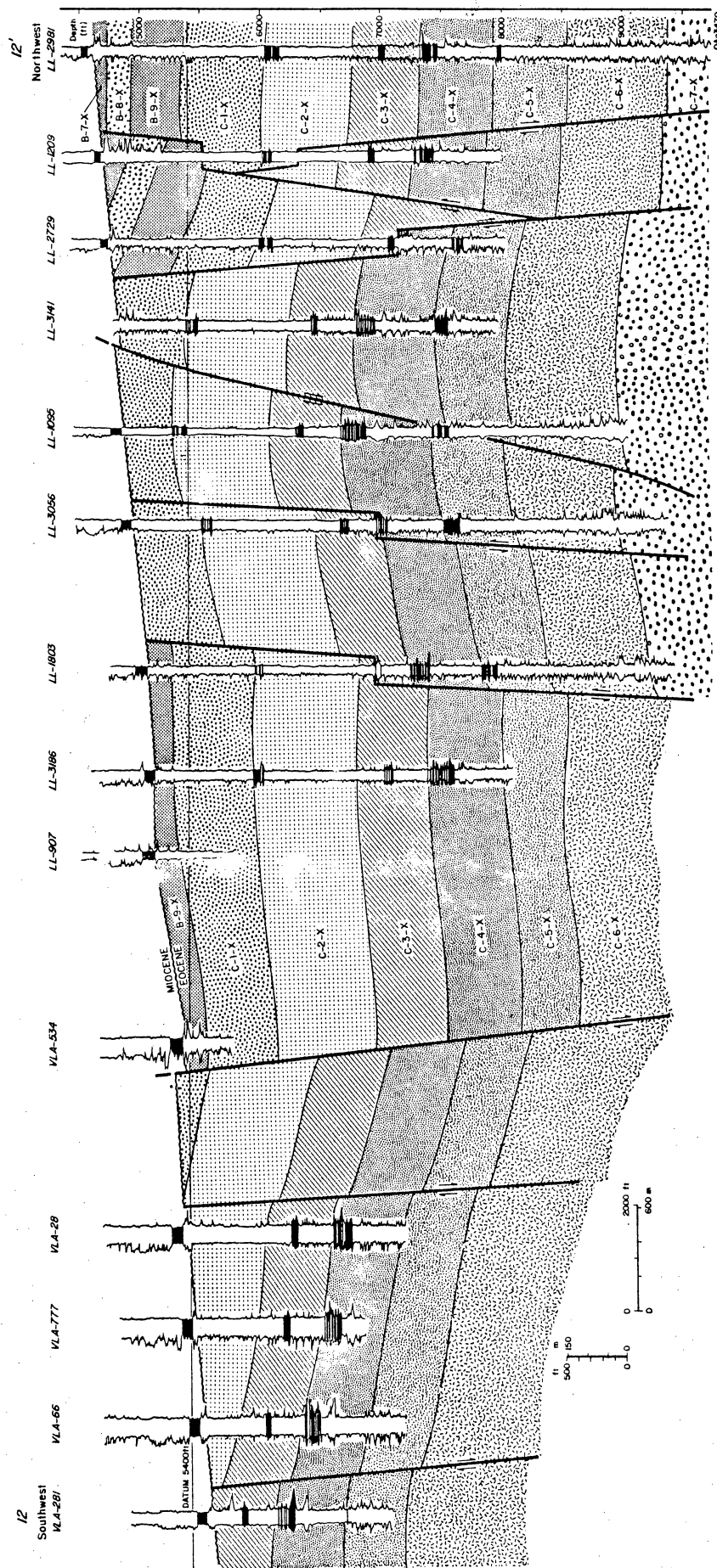


Figure IV 17. Structural cross section 12-12'.

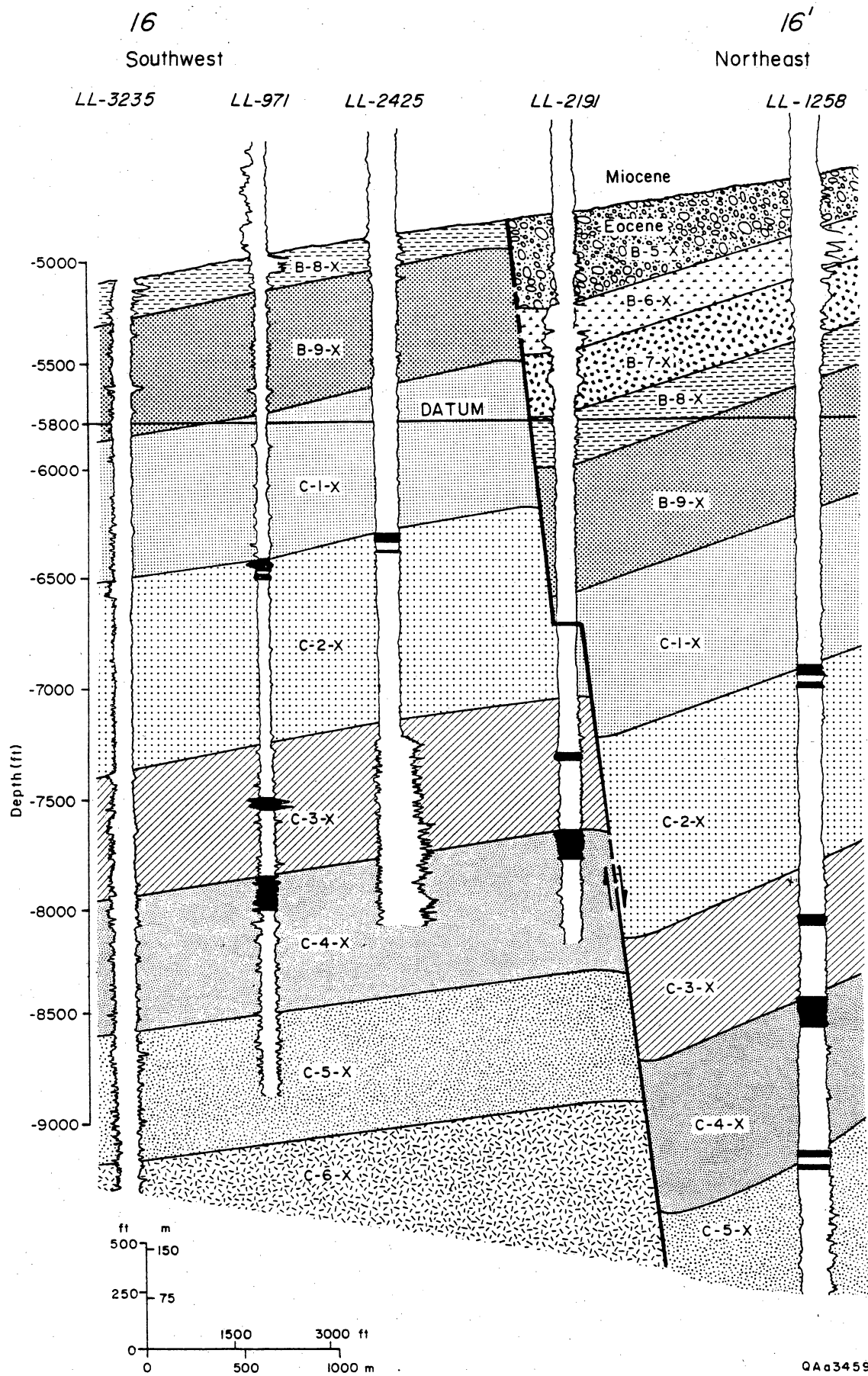


Figure IV 18. Structural cross section 16-16'.

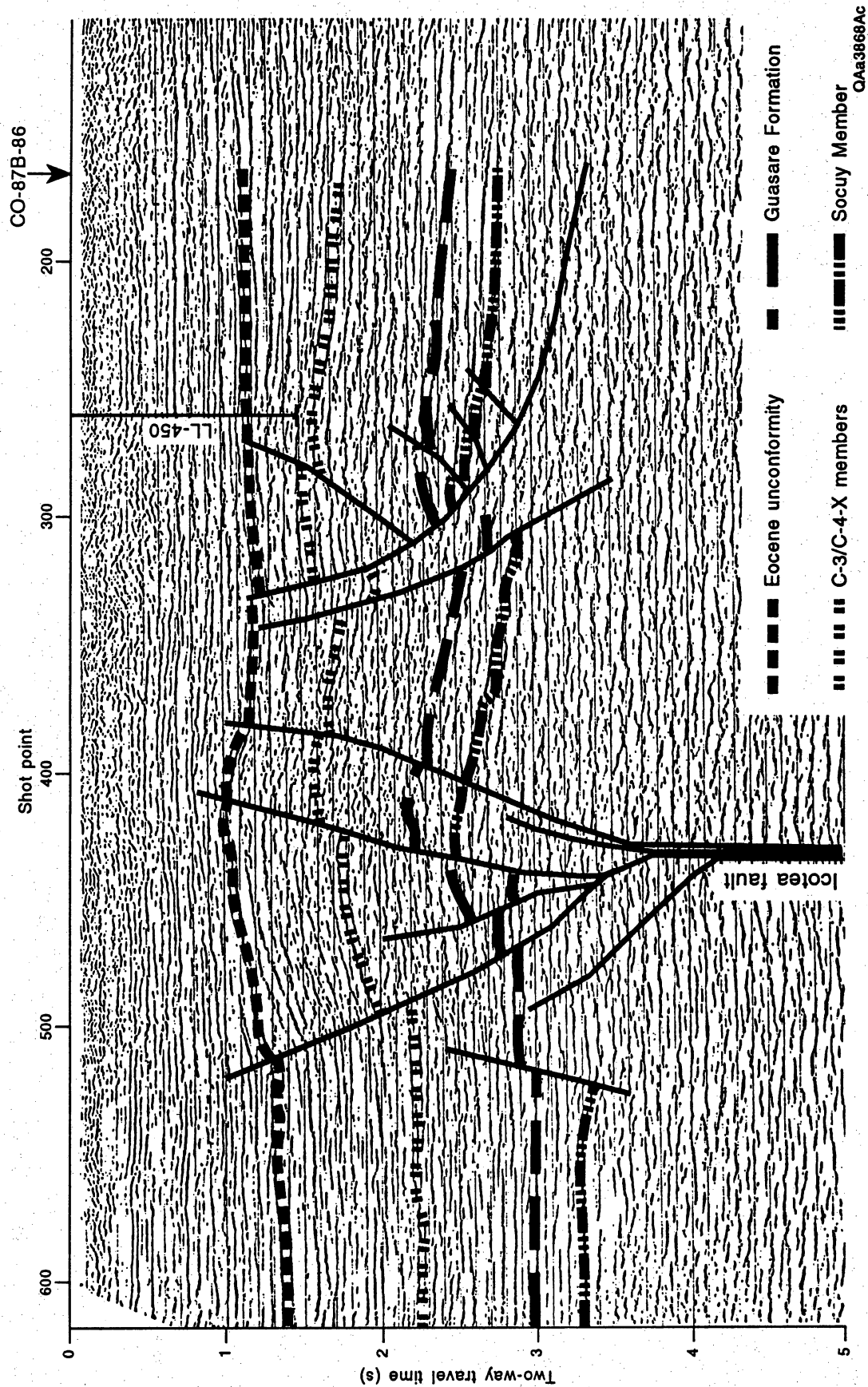


Figure IV 19. Seismic line CO-90B-28.

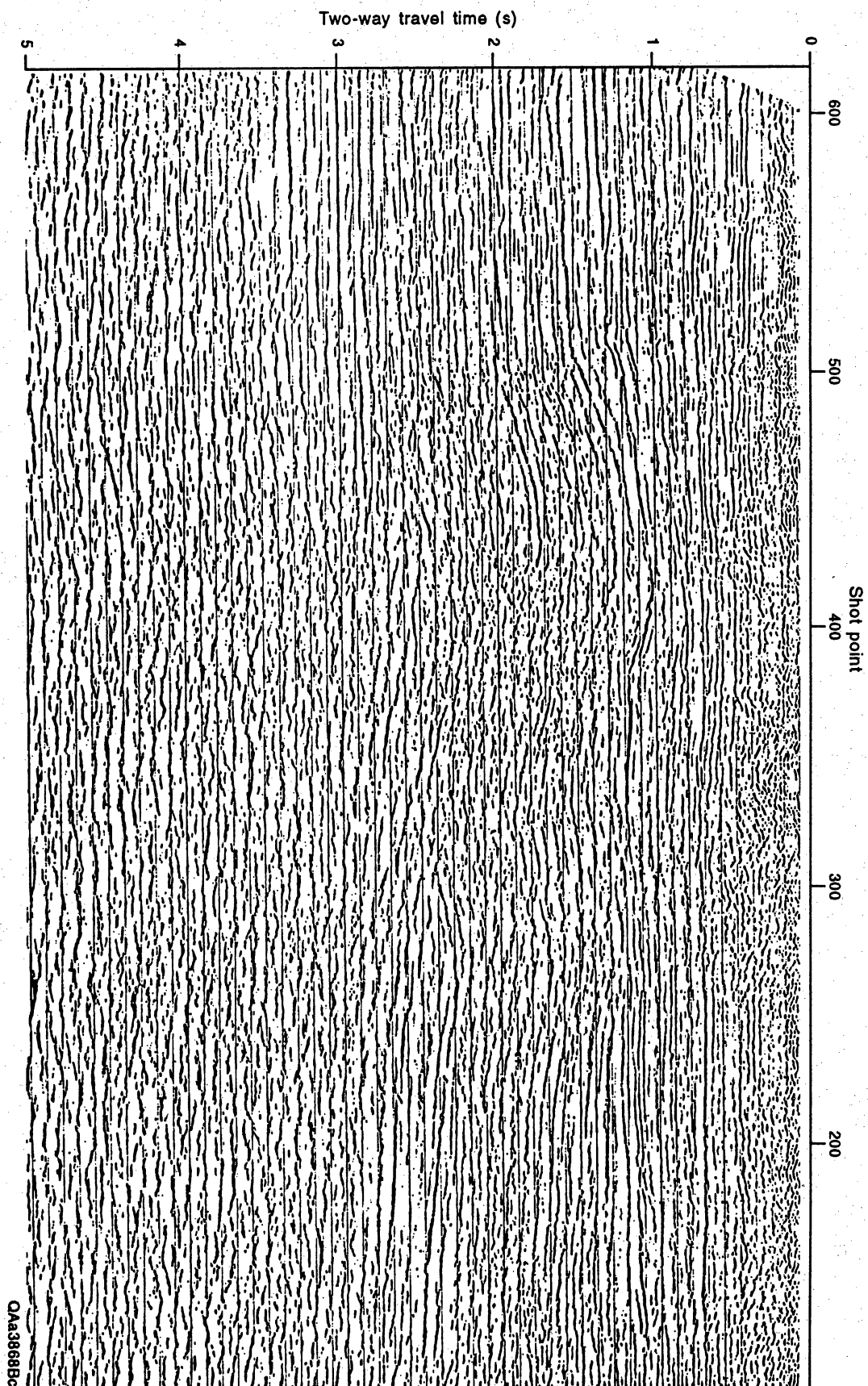


Figure IV 19 (continued). Uninterpreted seismic line CO-90B-28.

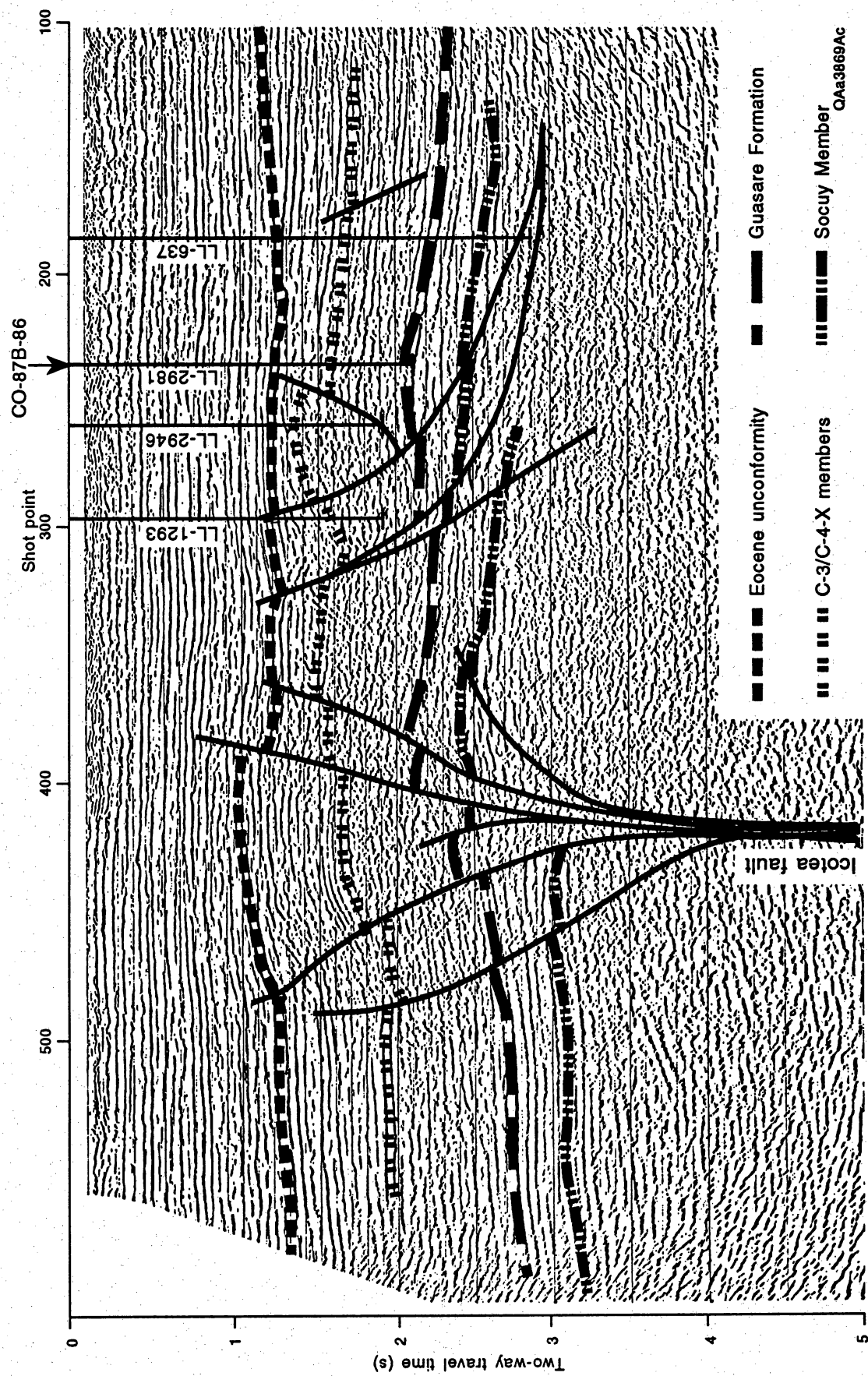


Figure IV 20. Seismic line CO-90B-30.

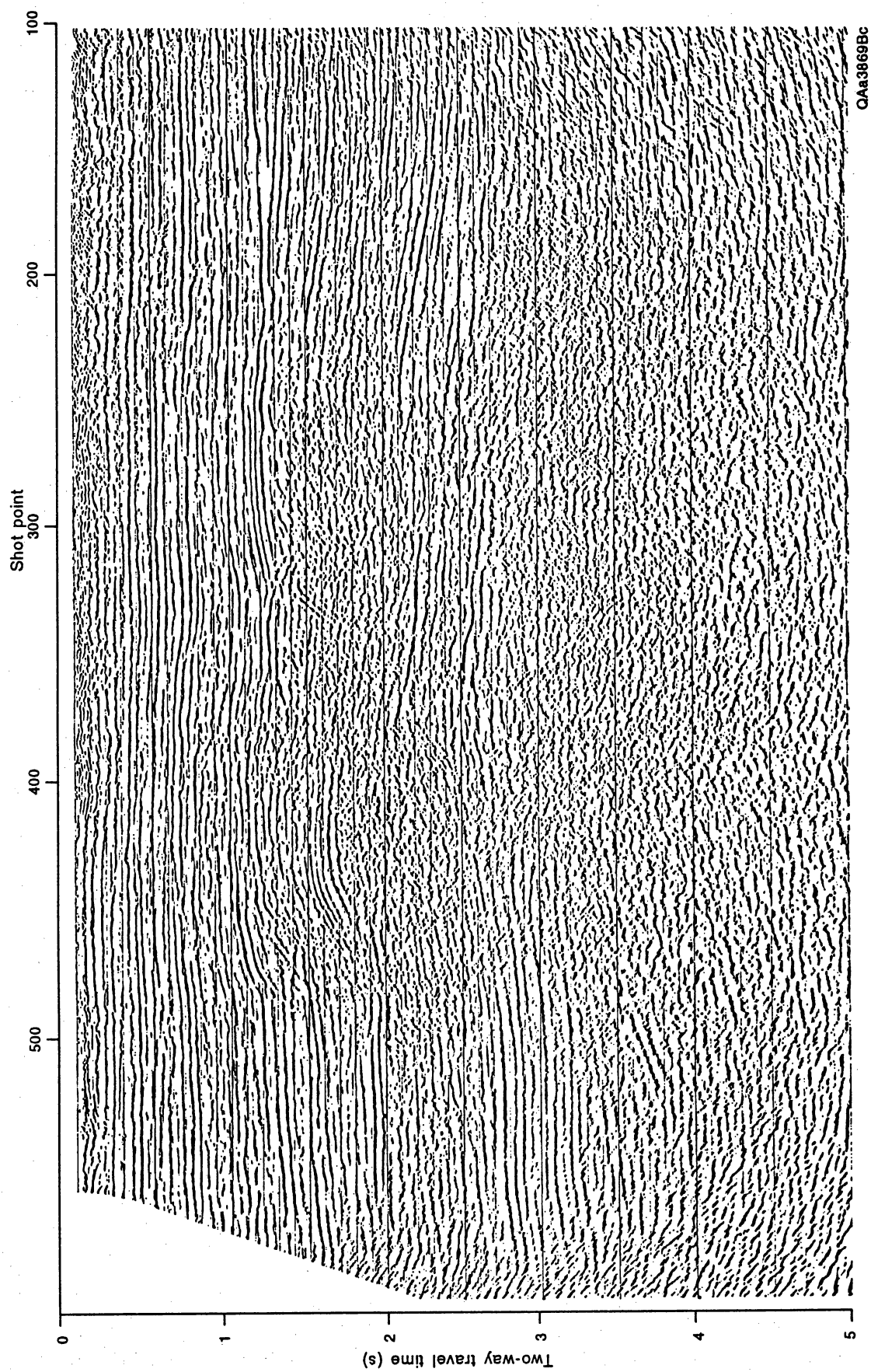


Figure IV 20 (continued). Uninterpreted seismic line CO-90B-30.

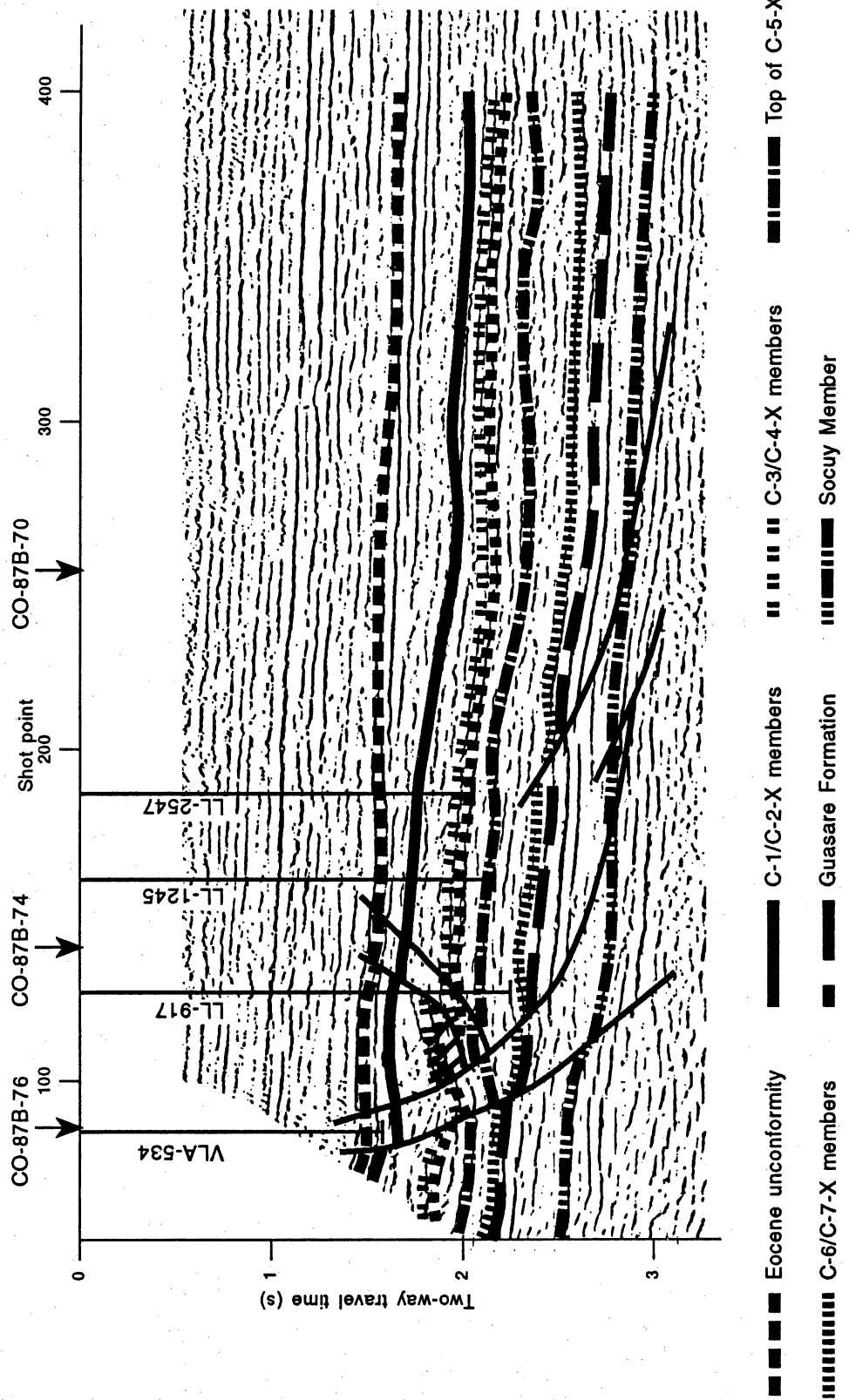
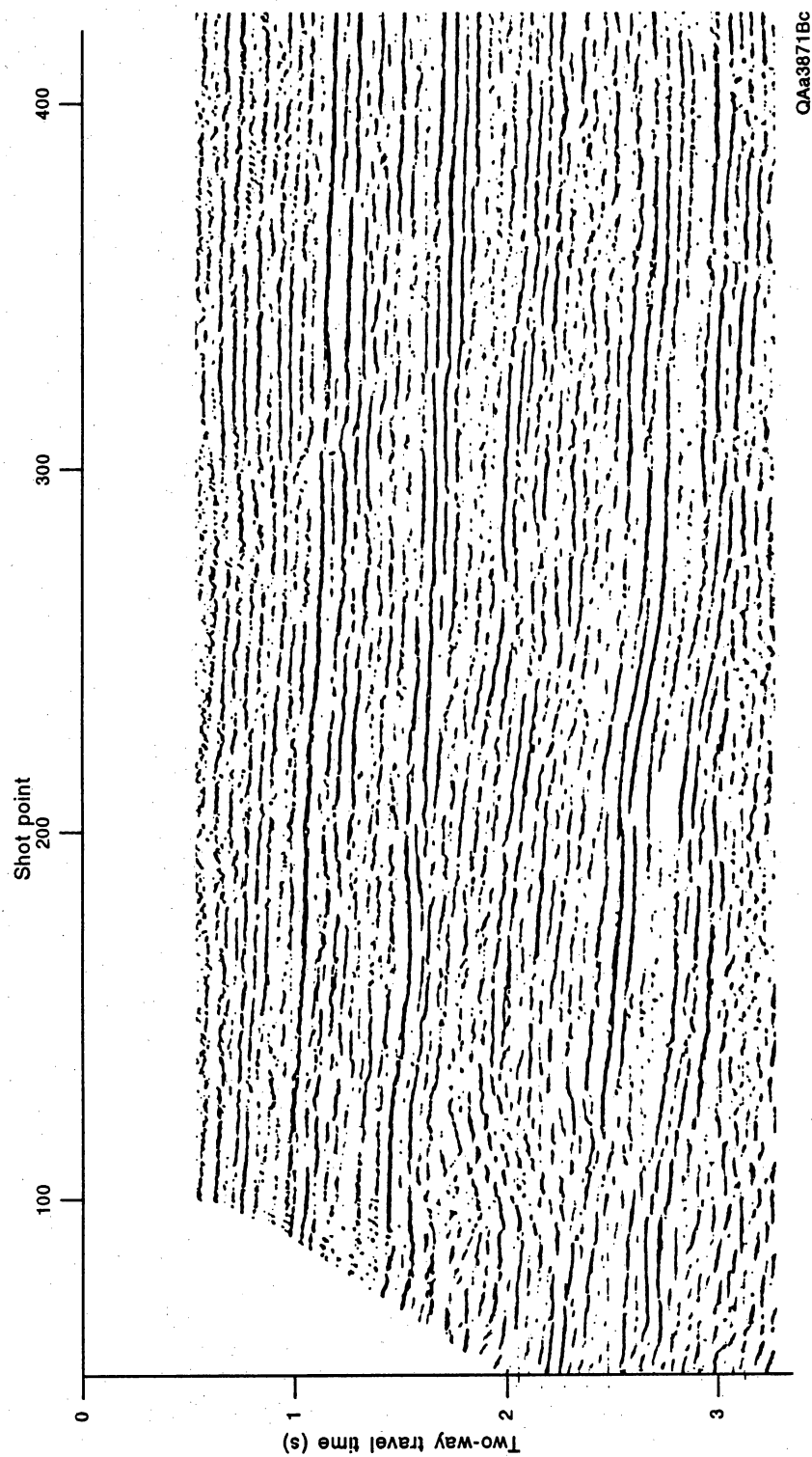


Figure IV 21. Seismic line CO-87B-27.



QAa3871Bc

Figure IV 21 (continued). Uninterpreted seismic line CO-87B-27.

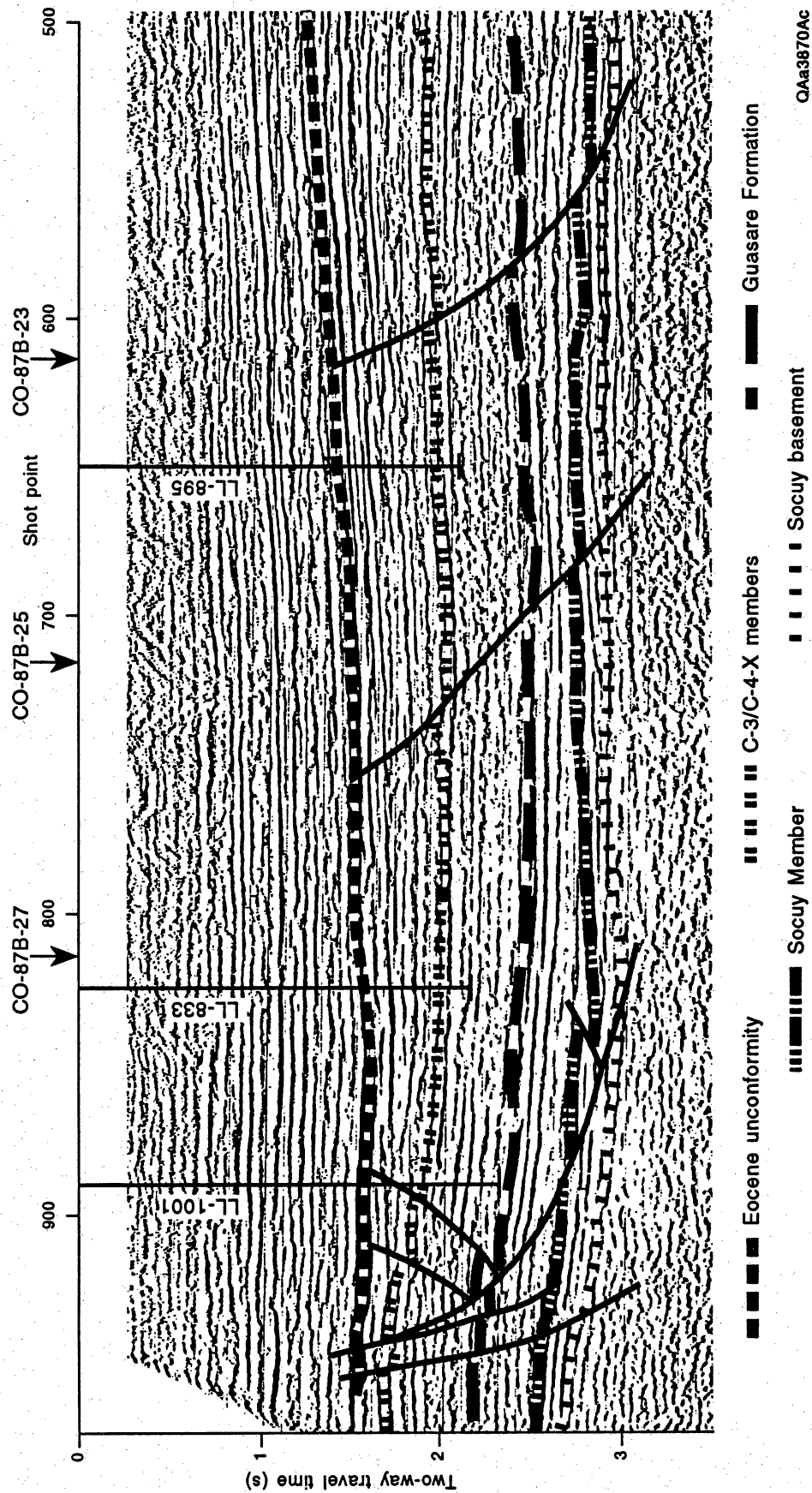


Figure IV 22. Seismic line CO-87B-72.

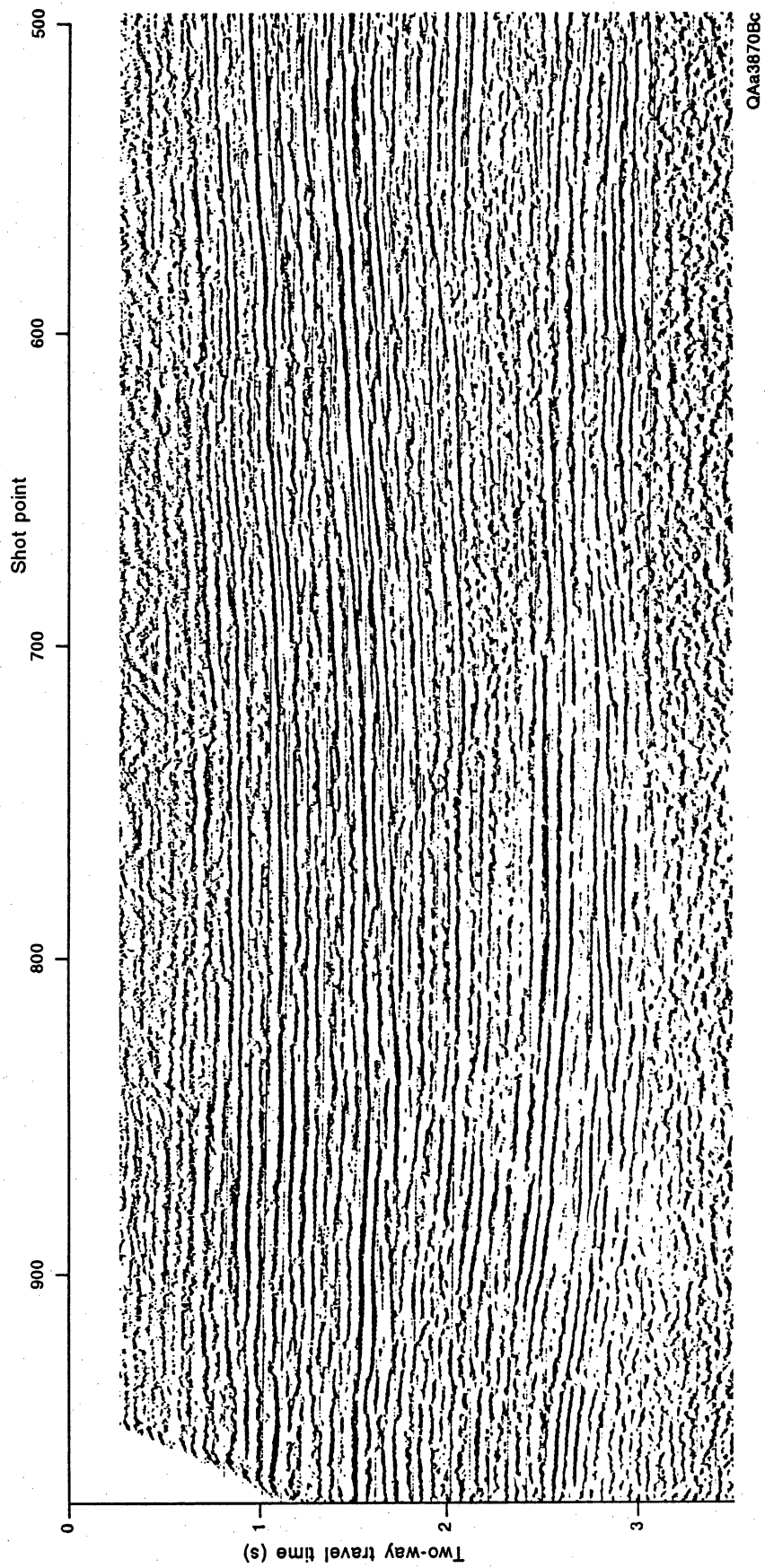


Figure IV 22 (continued). Uninterpreted seismic line CO-87B-72.

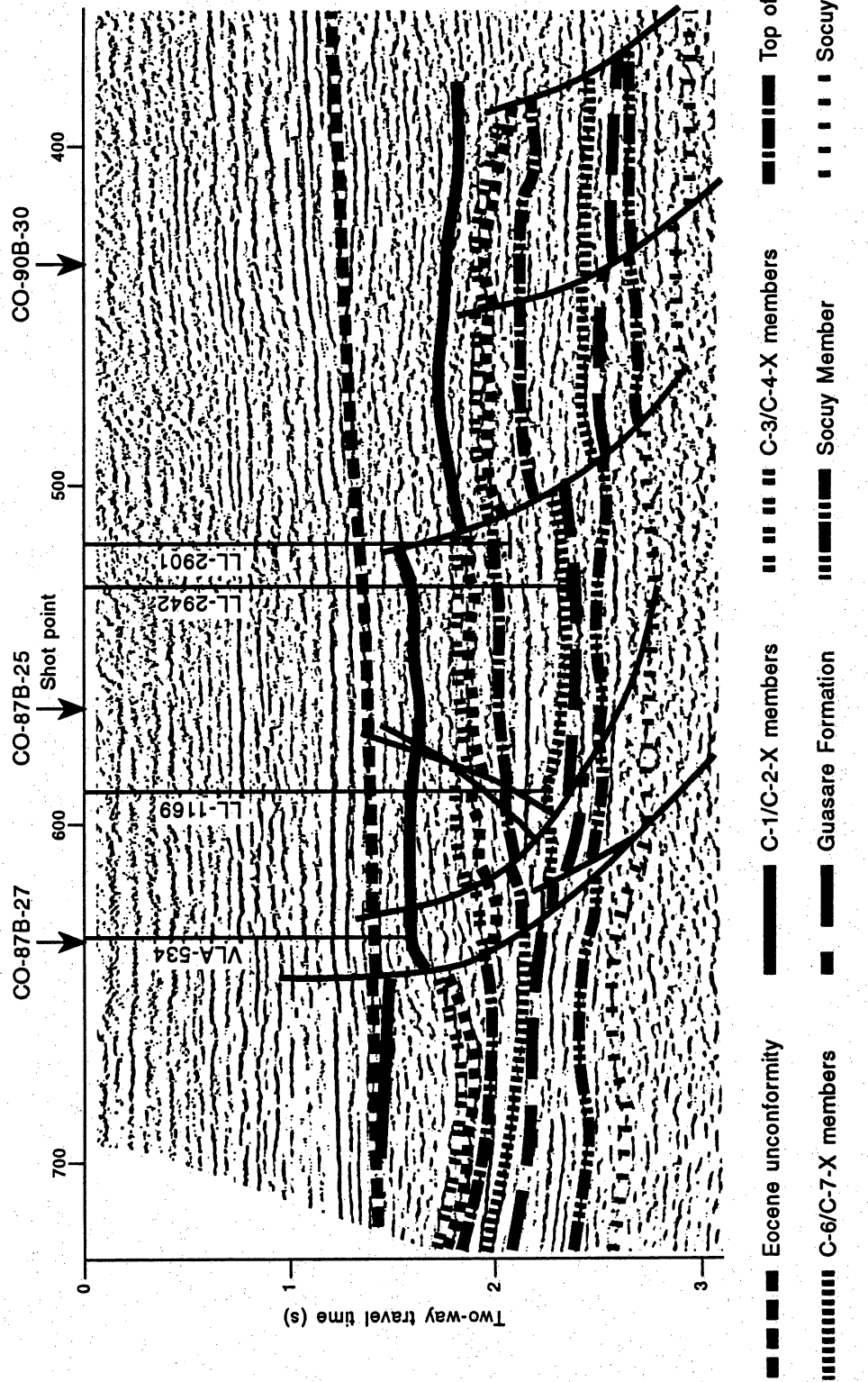


Figure IV 23. Seismic line CO-87B-76.

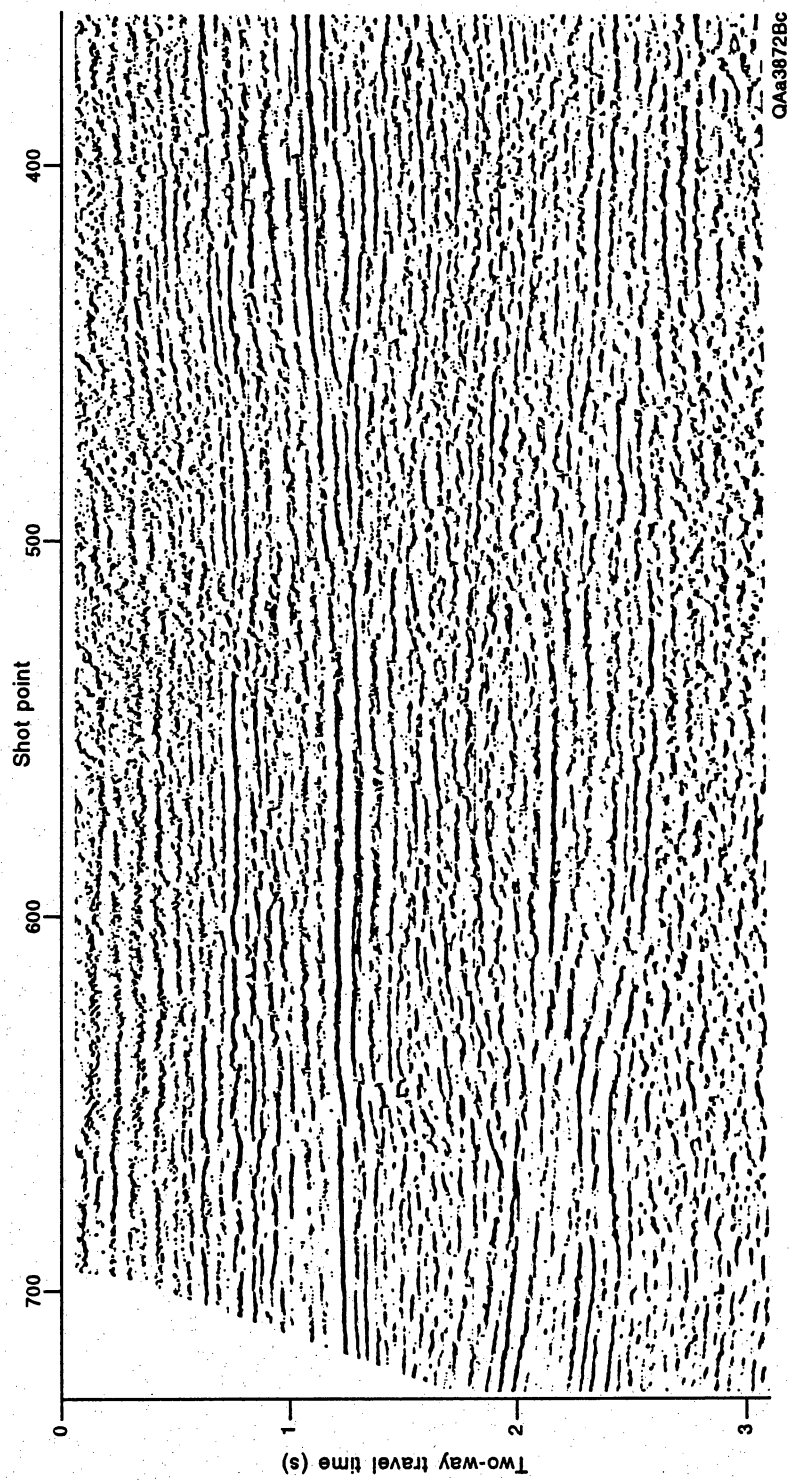


Figure IV 23 (continued). Uninterpreted seismic line CO-87B-76.

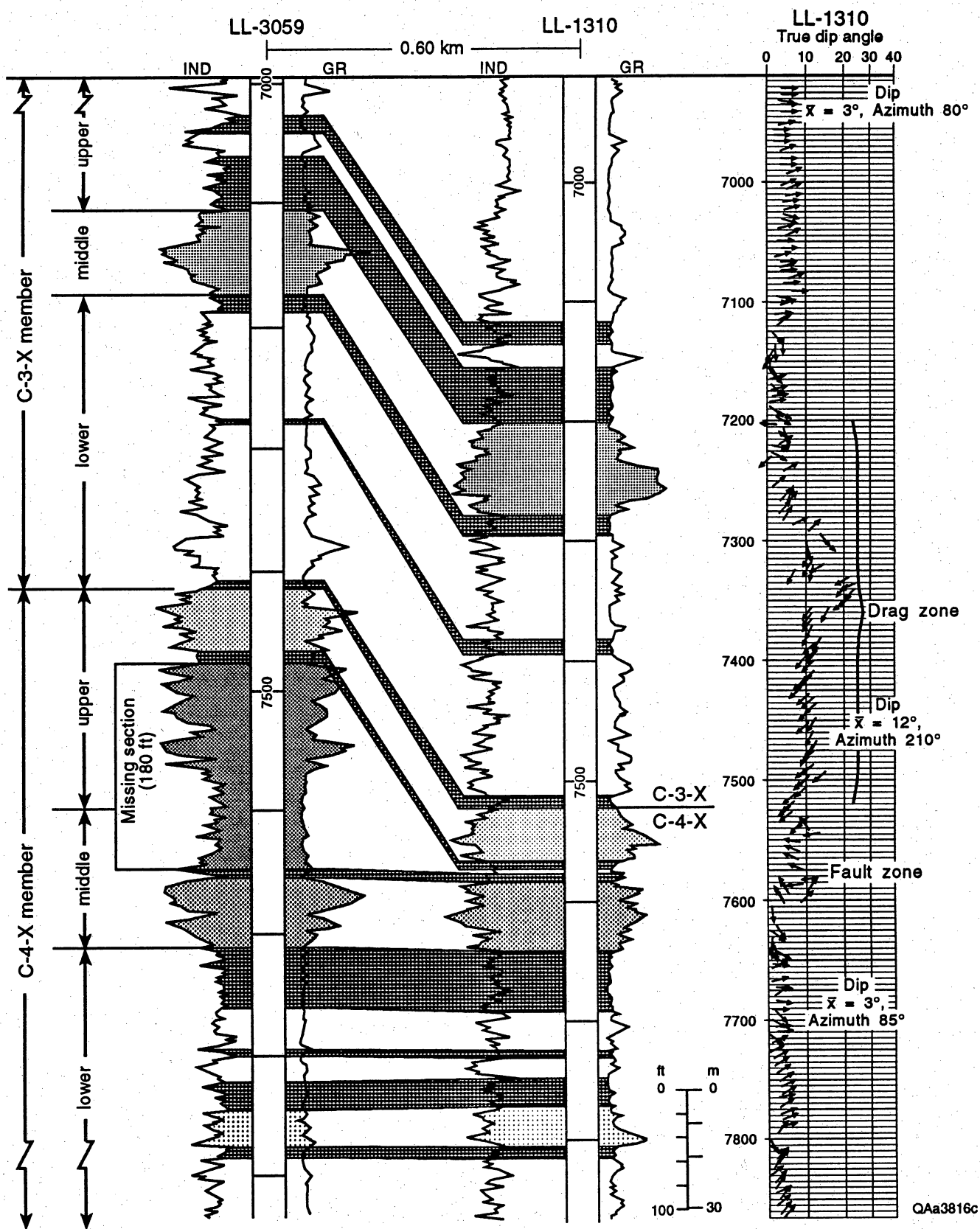


Figure IV 24. Major dip change due to faulting in the LL-1310 well, interpreted from dipmeter log.

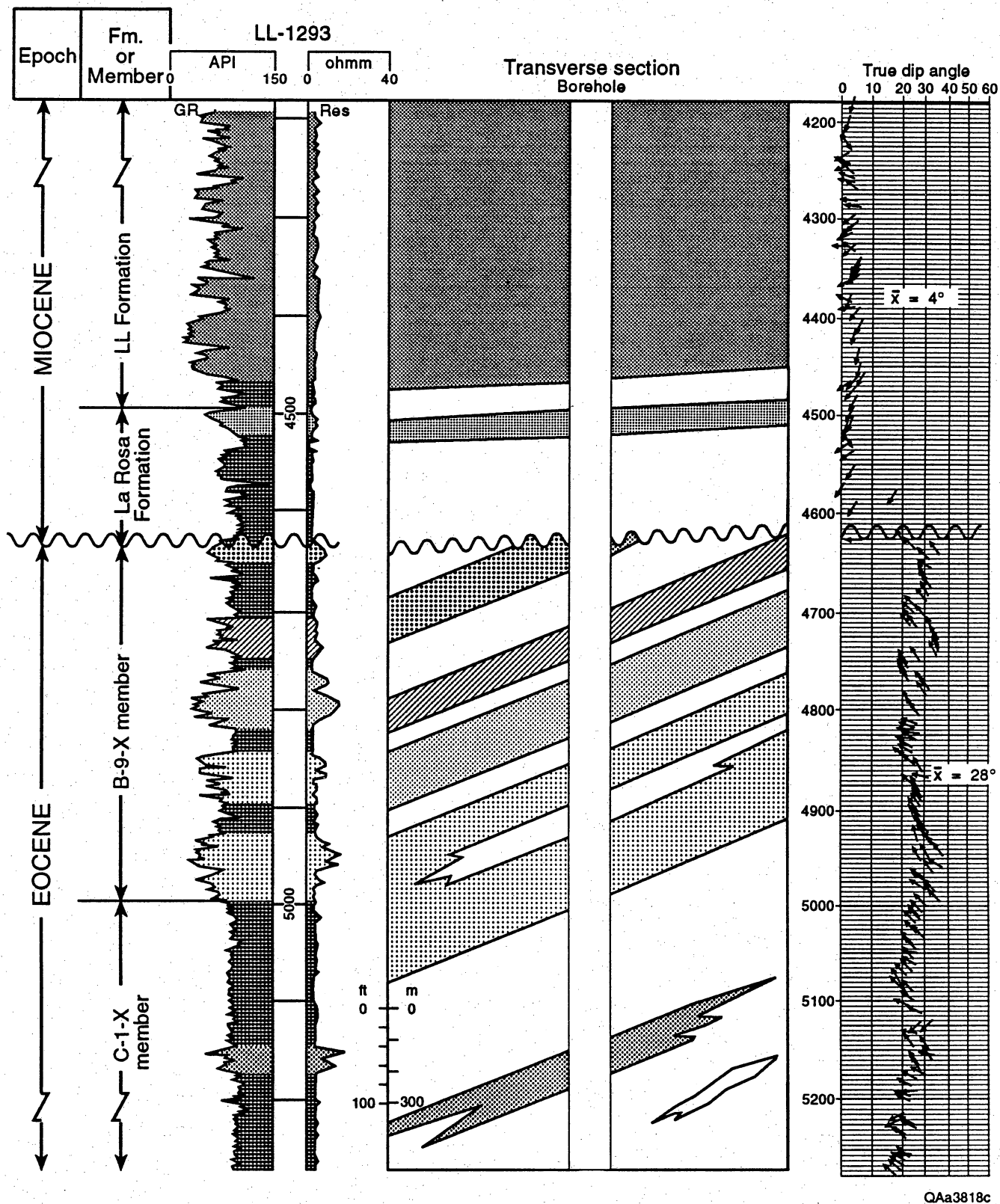


Figure IV 25. The LL-1293 well with dipmeter showing an angular unconformity.

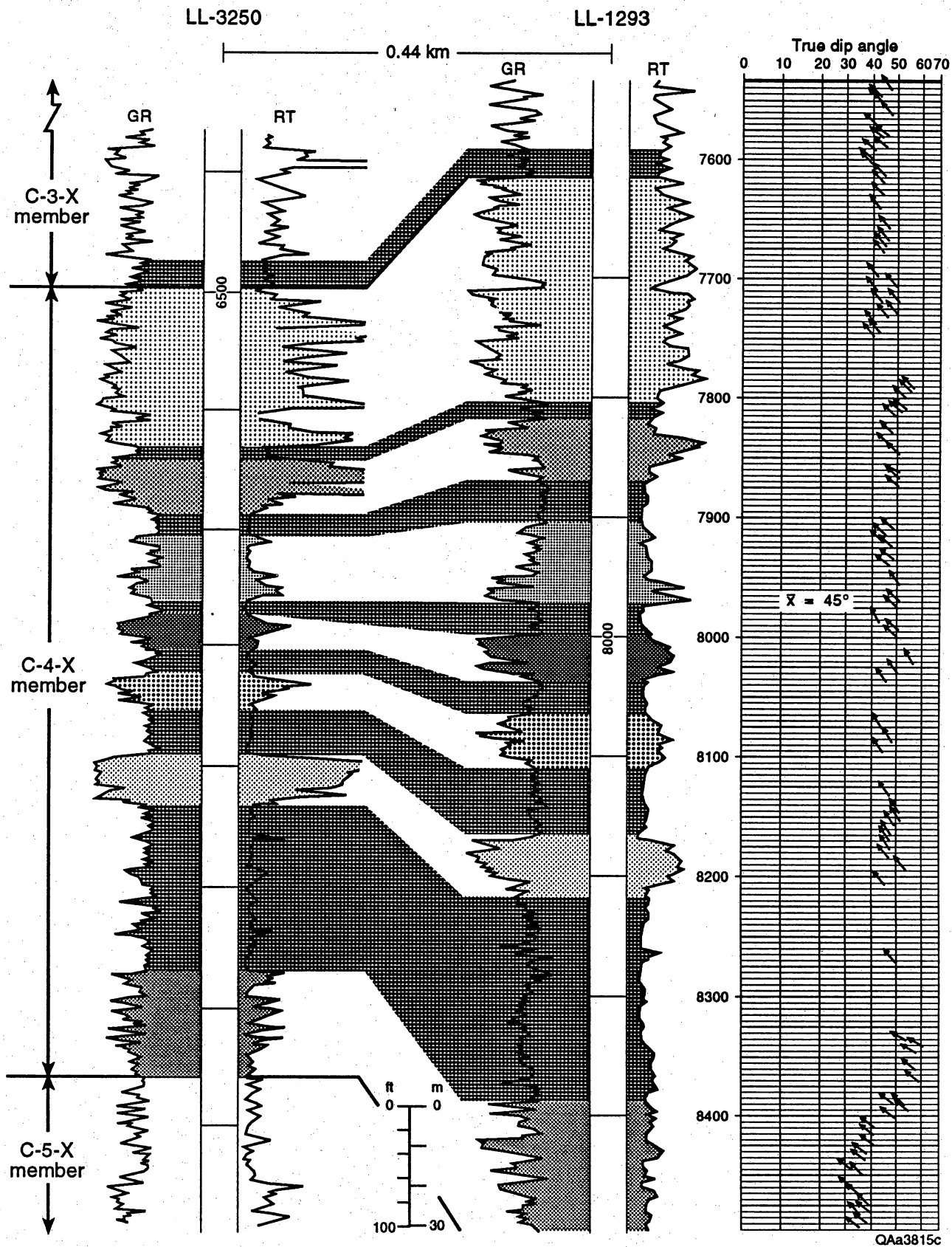
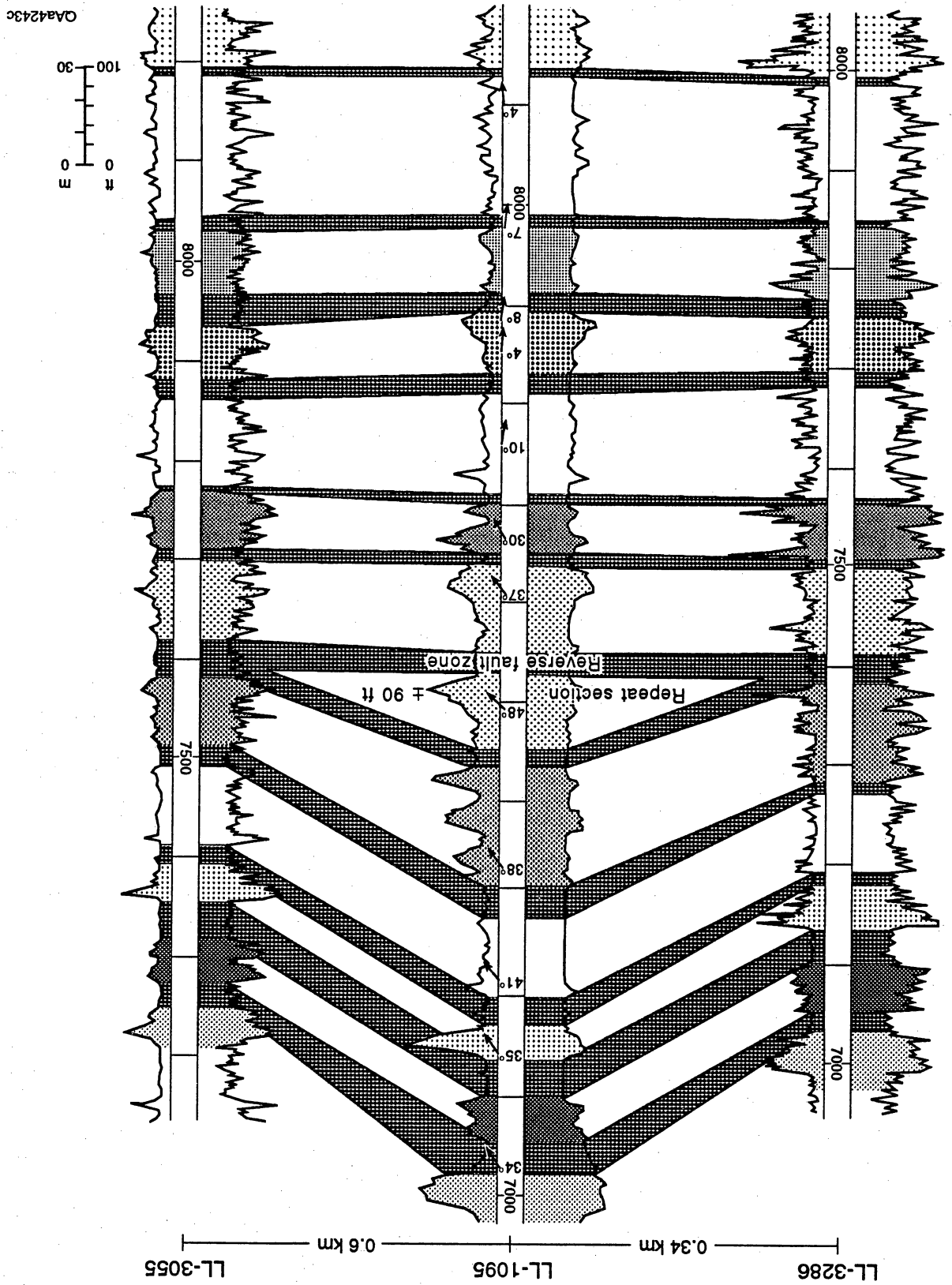


Figure IV 26. Stratigraphic correlation between the LL-1293 (high-dip zone) and LL-3250 wells.

Figure IV 28. Dipmeter response in reverse fault that intersects LL-1095 well.



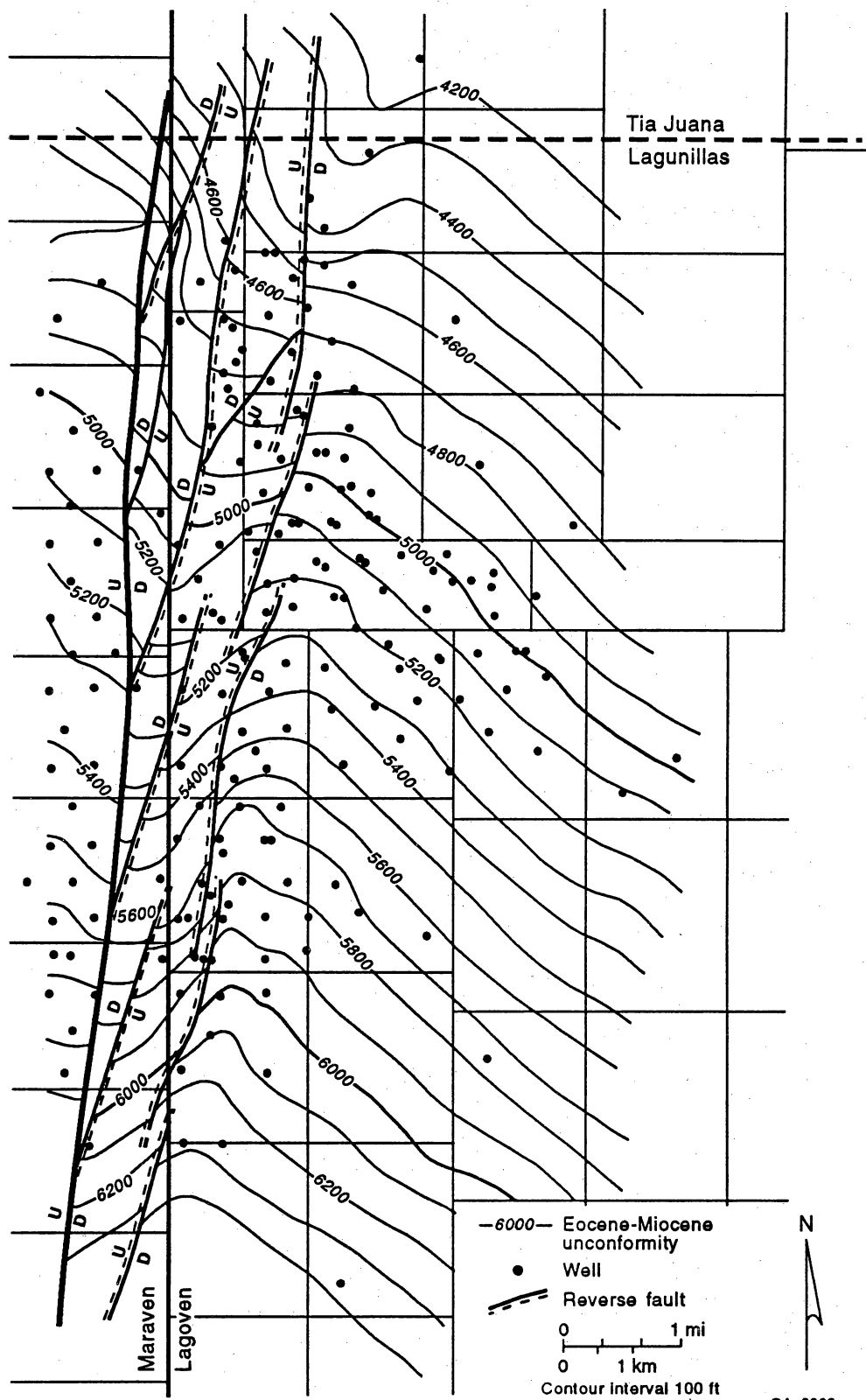


Figure IV 29. Eocene-Miocene unconformity.

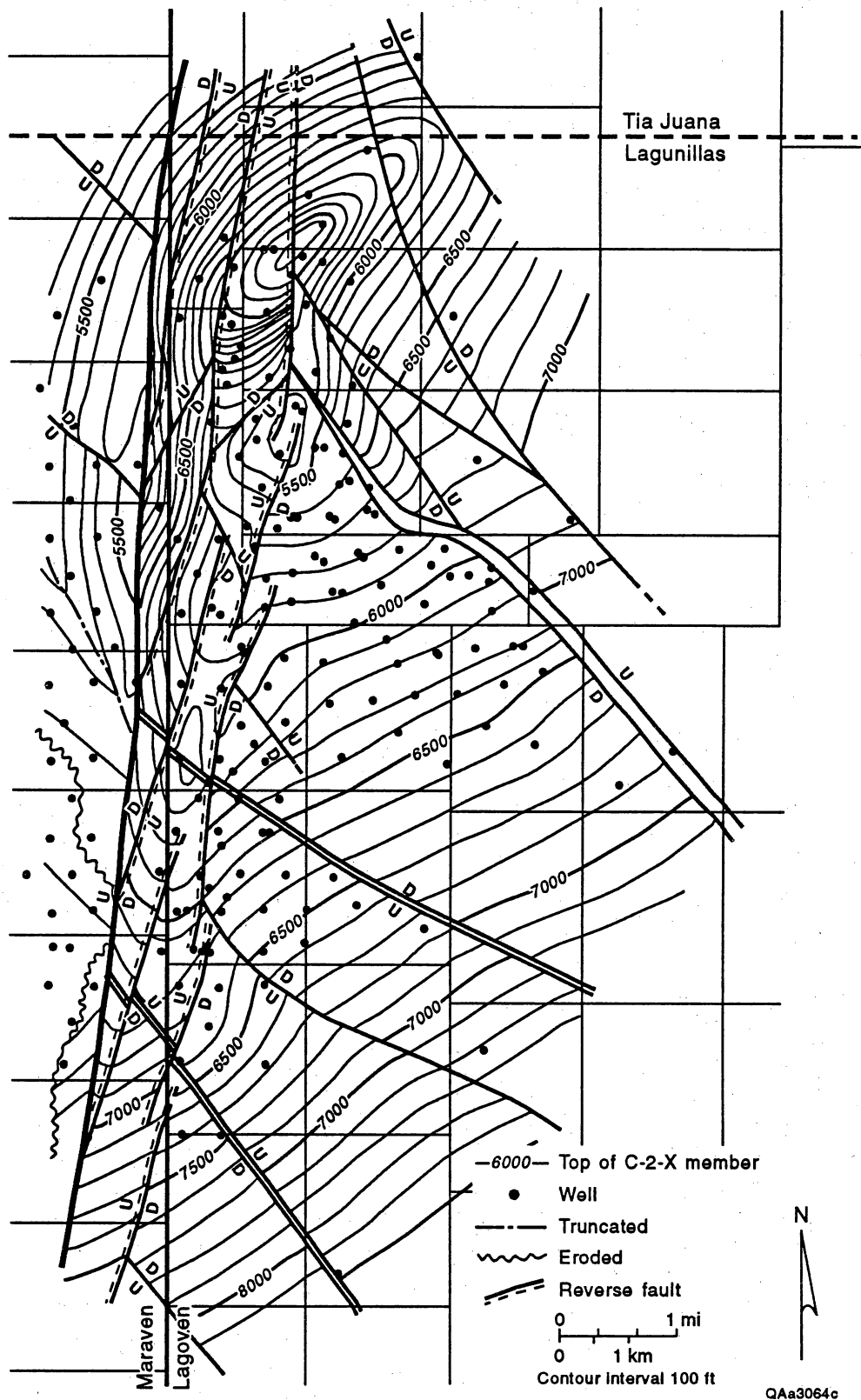


Figure IV 31. Structural top of C-2-X Member.

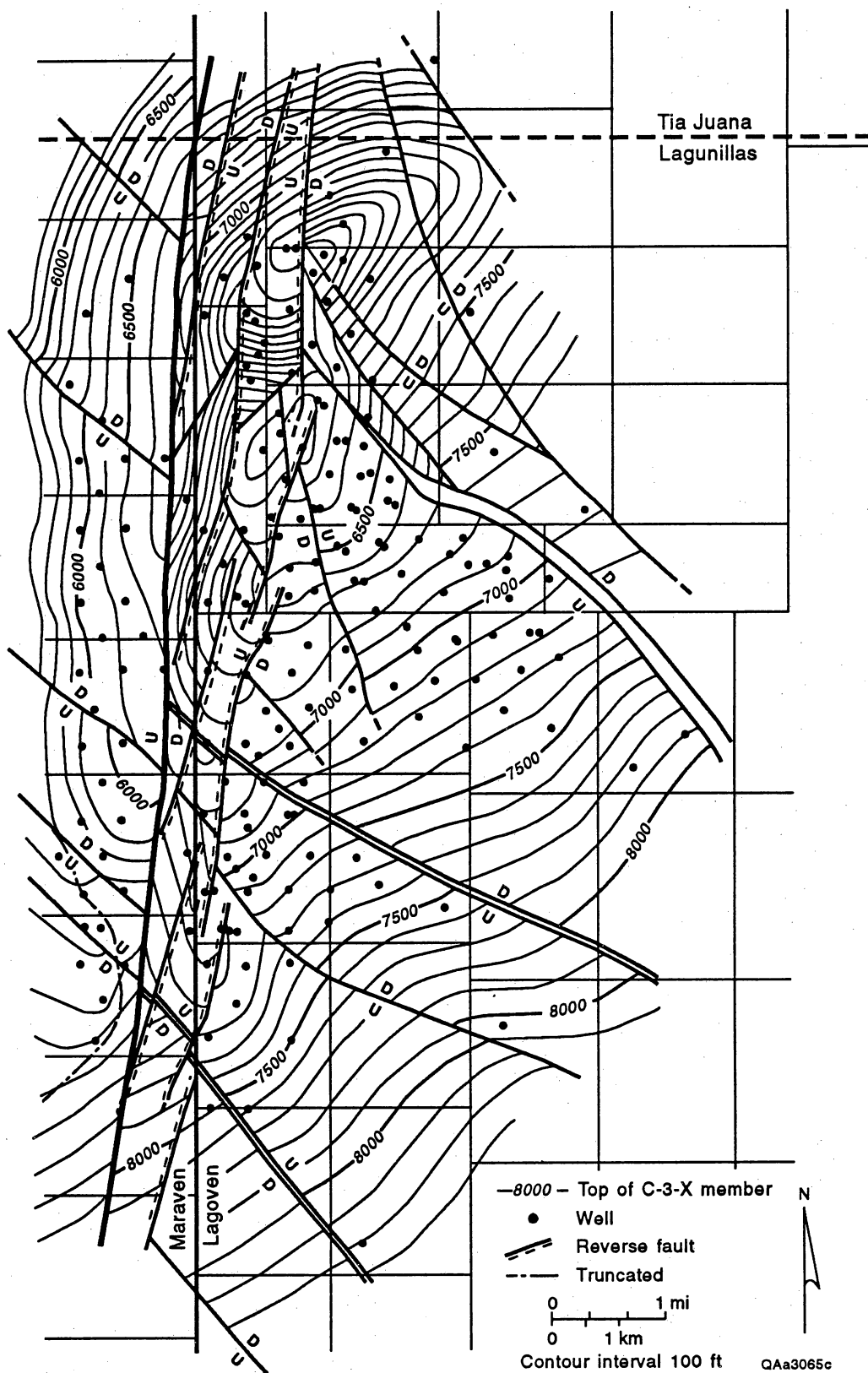


Figure IV 32. Structural top of C-3-X Member.

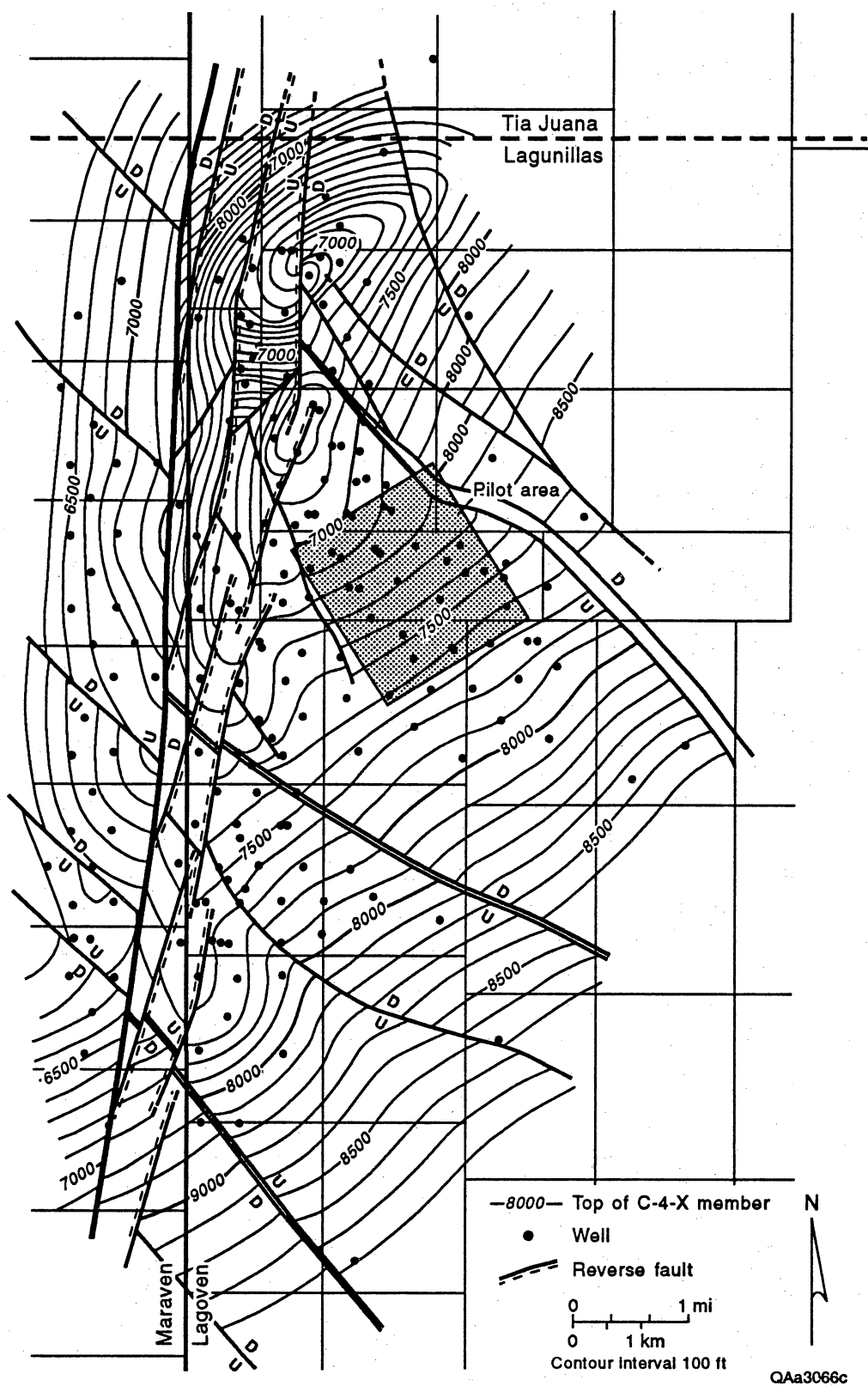


Figure IV 33. Structural top of C-4-X Member, with location of waterflood pilot area in the Upper C-4-X Submember.

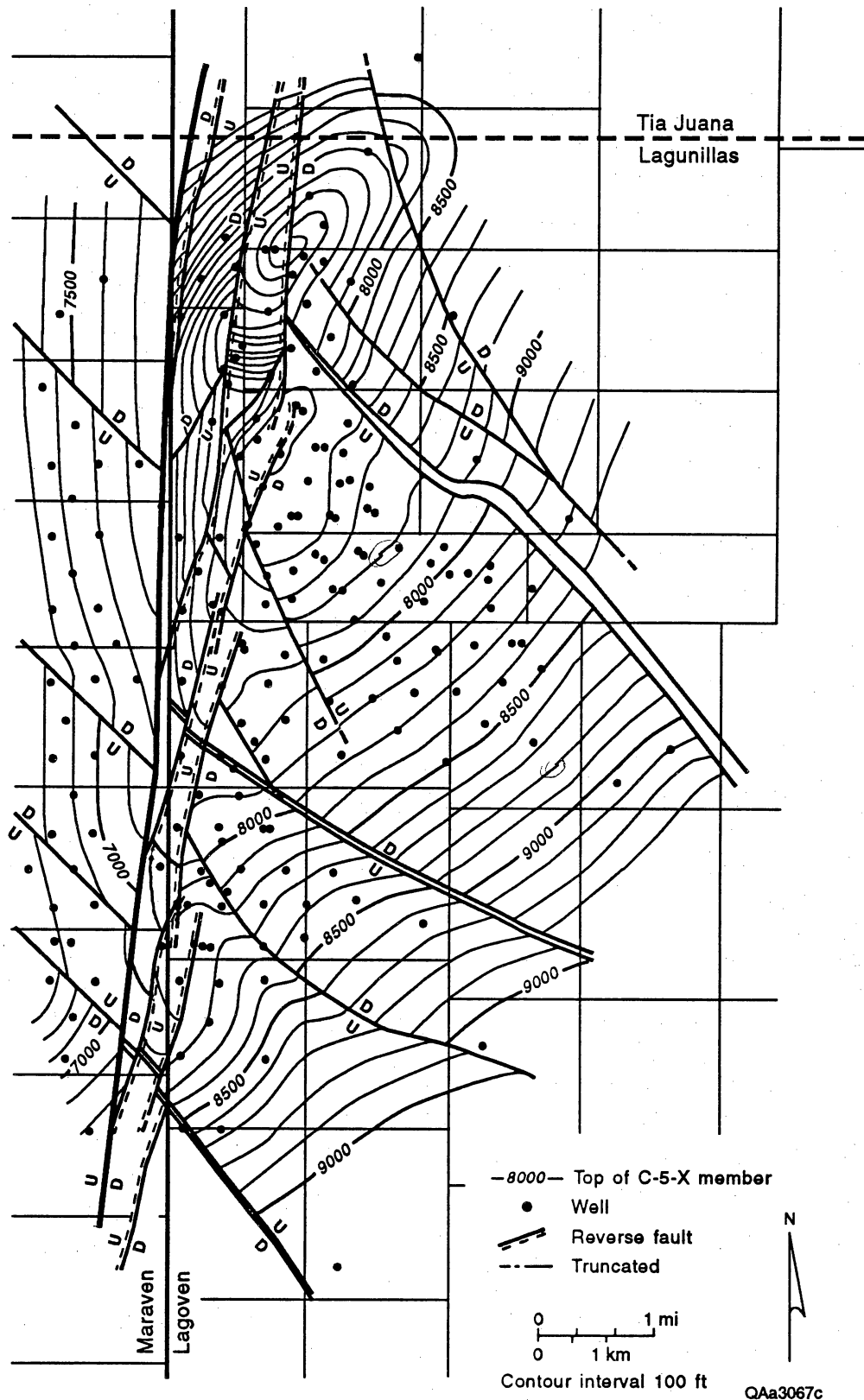


Figure IV 34. Structural top of C-5-X Member.

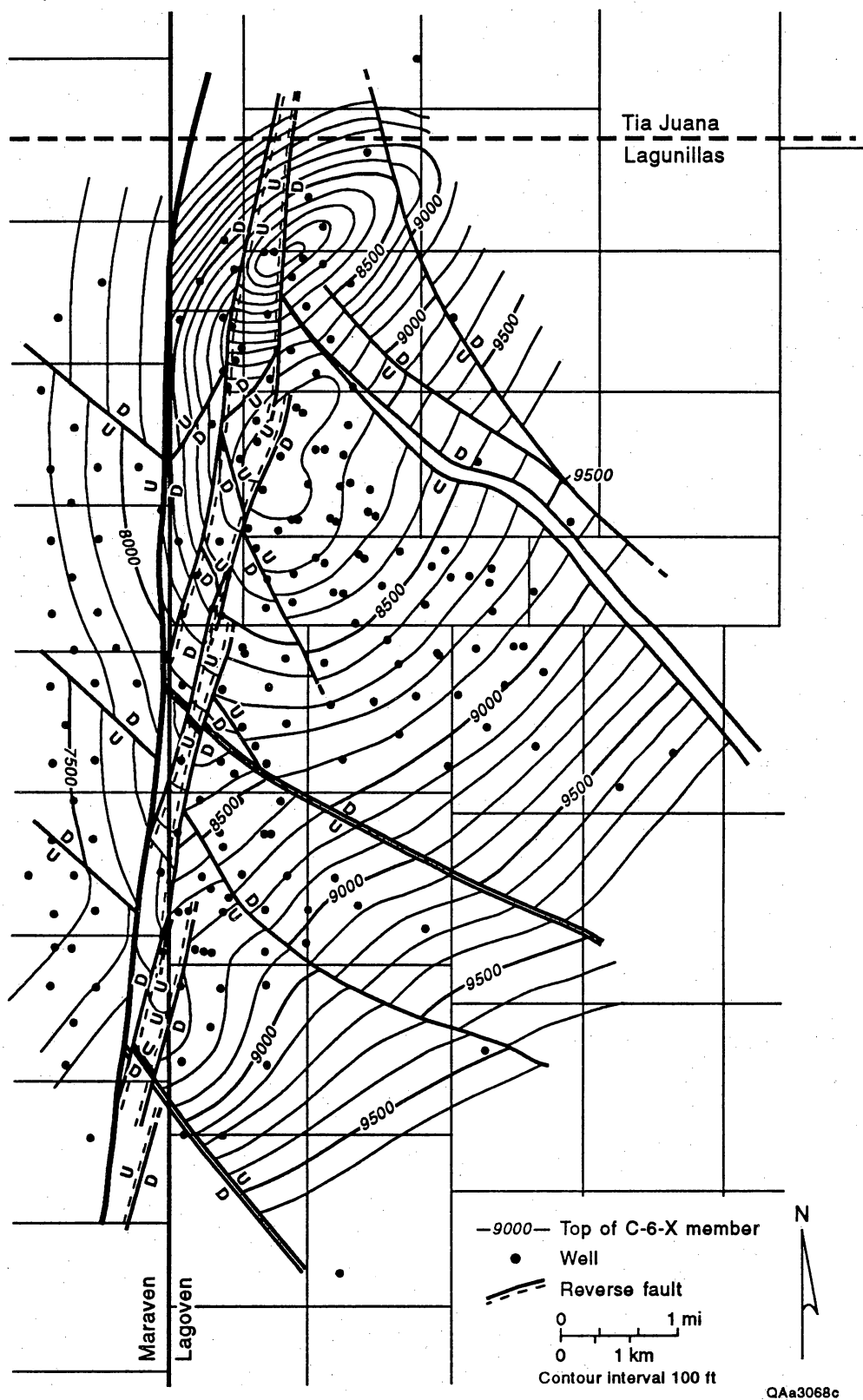


Figure IV 35. Structural top of C-6-X Member.

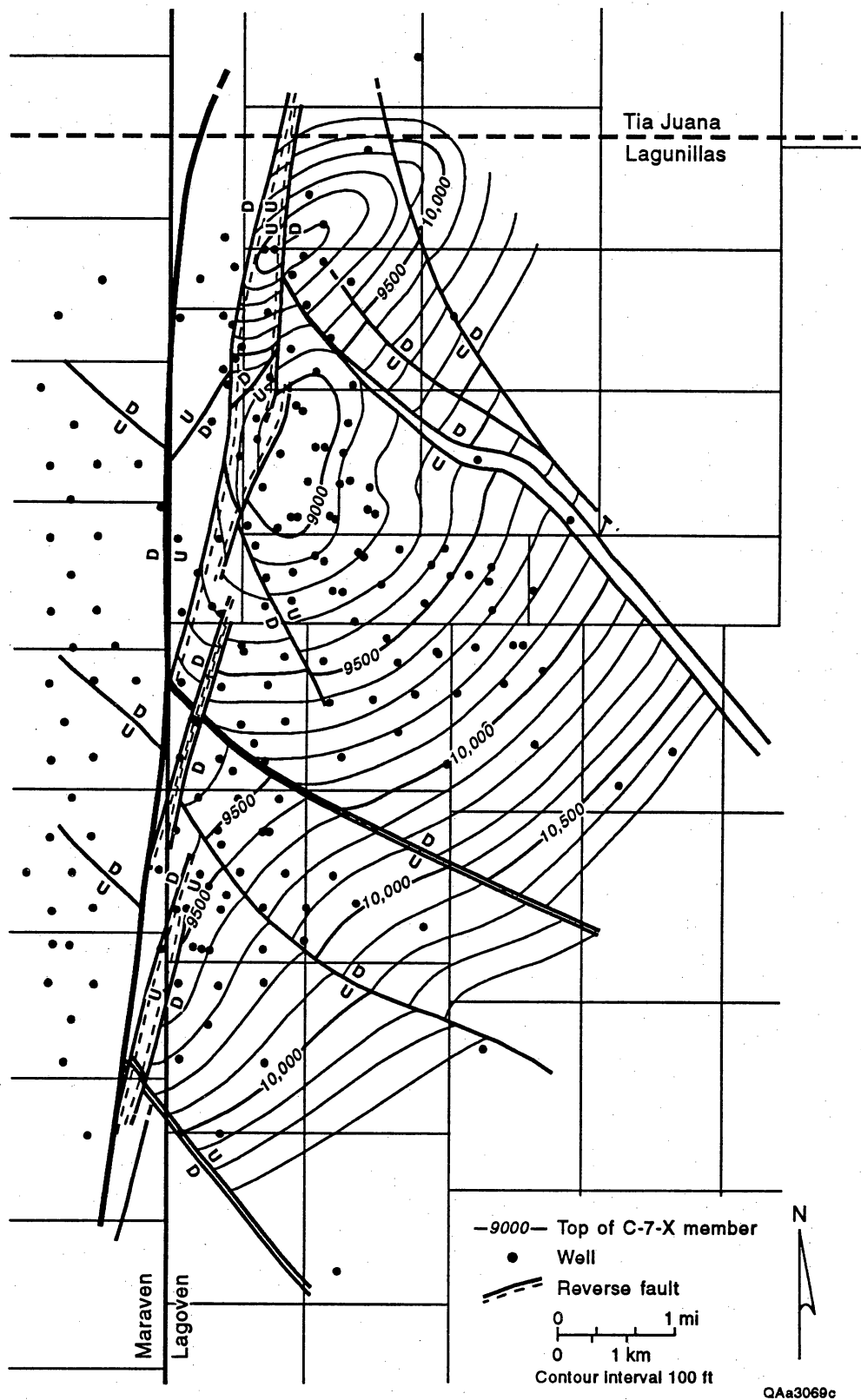


Figure IV 36. Structural top of C-7-X Member.

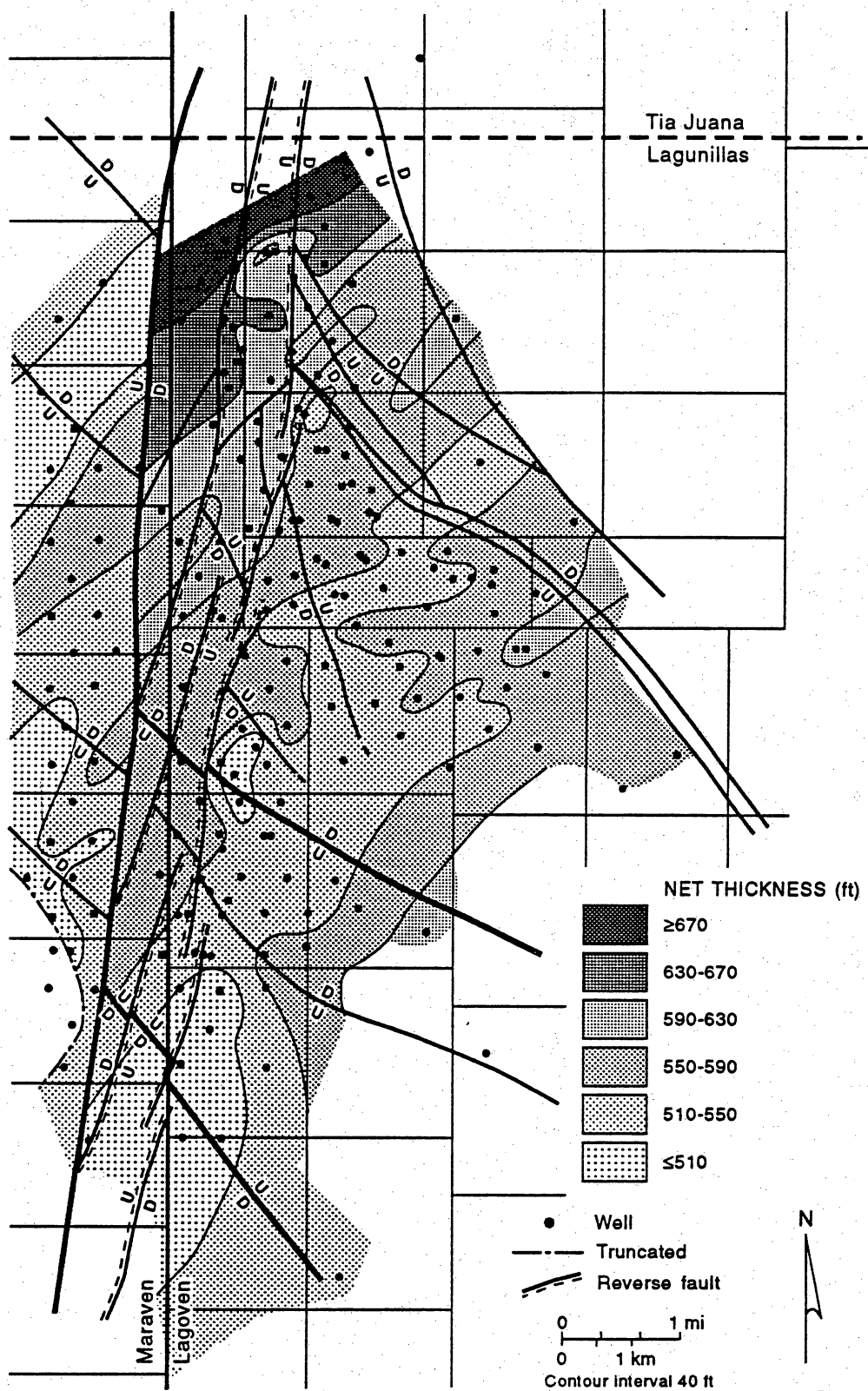


Figure IV 37. Net-thickness map of C-3-X Member.

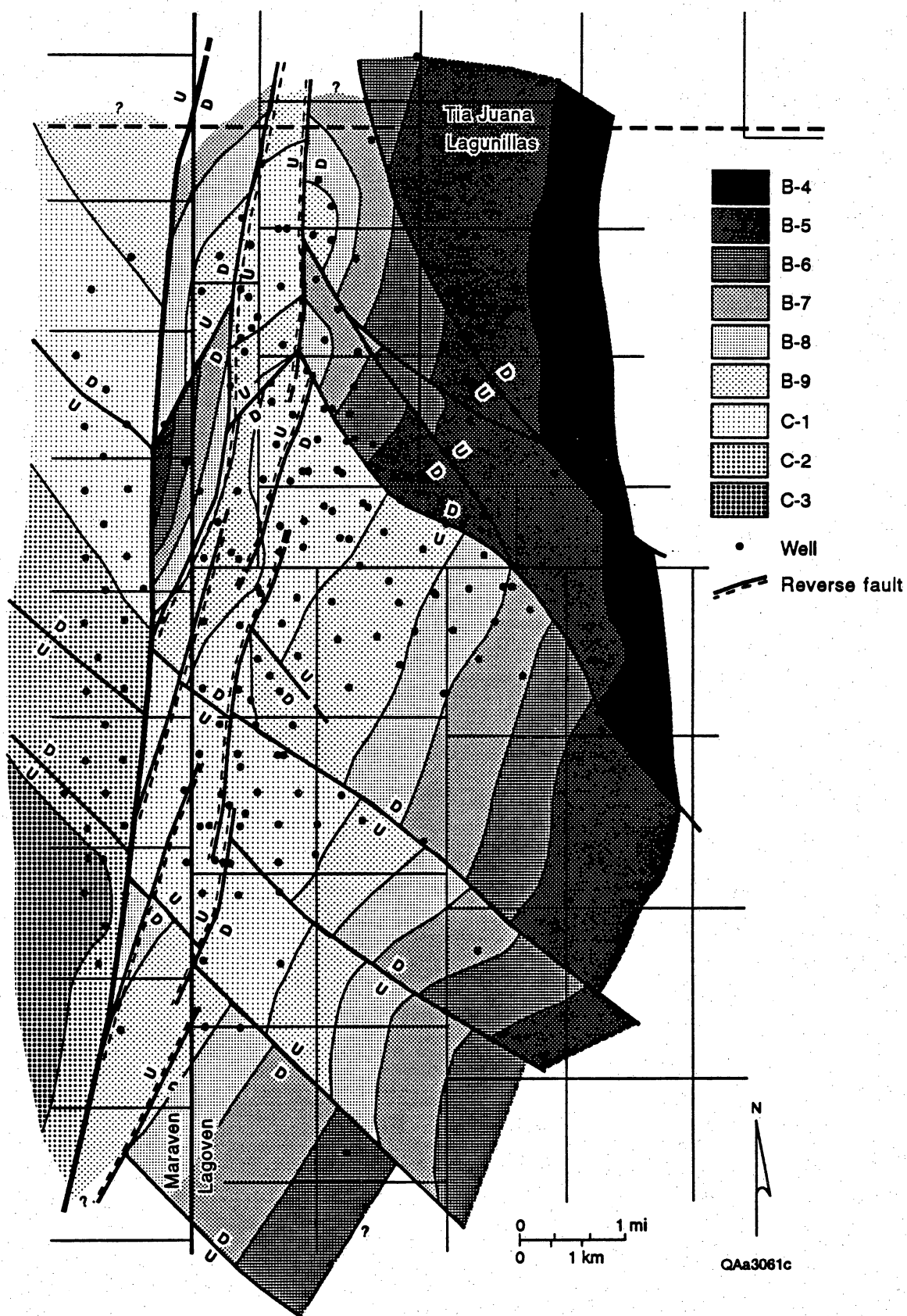
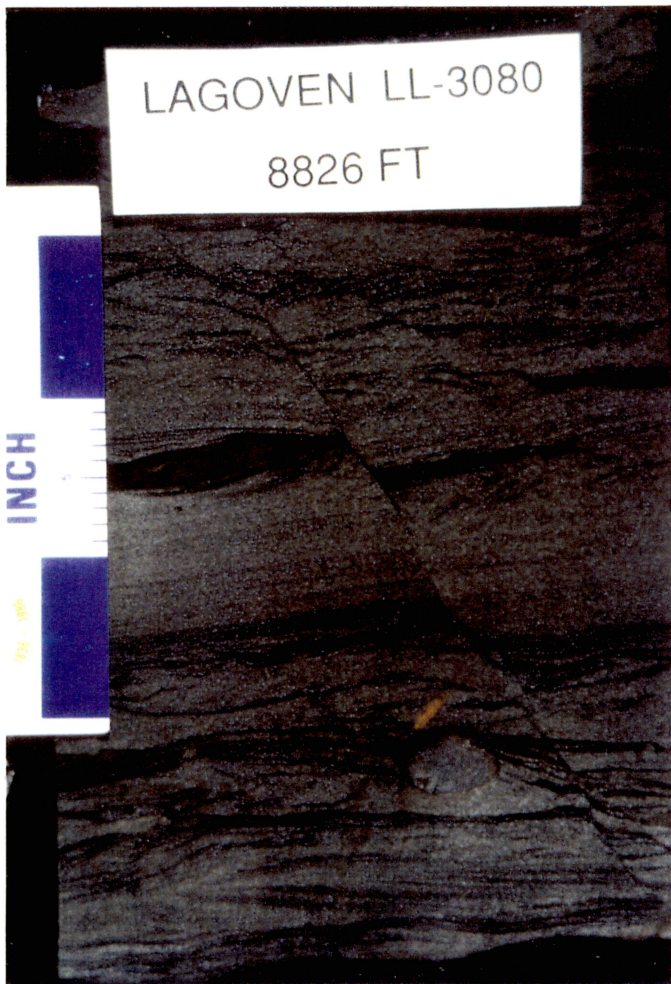


Figure IV 38. Subcrop map of stratigraphic interval below the Eocene-Miocene unconformity.

(a)



(b)

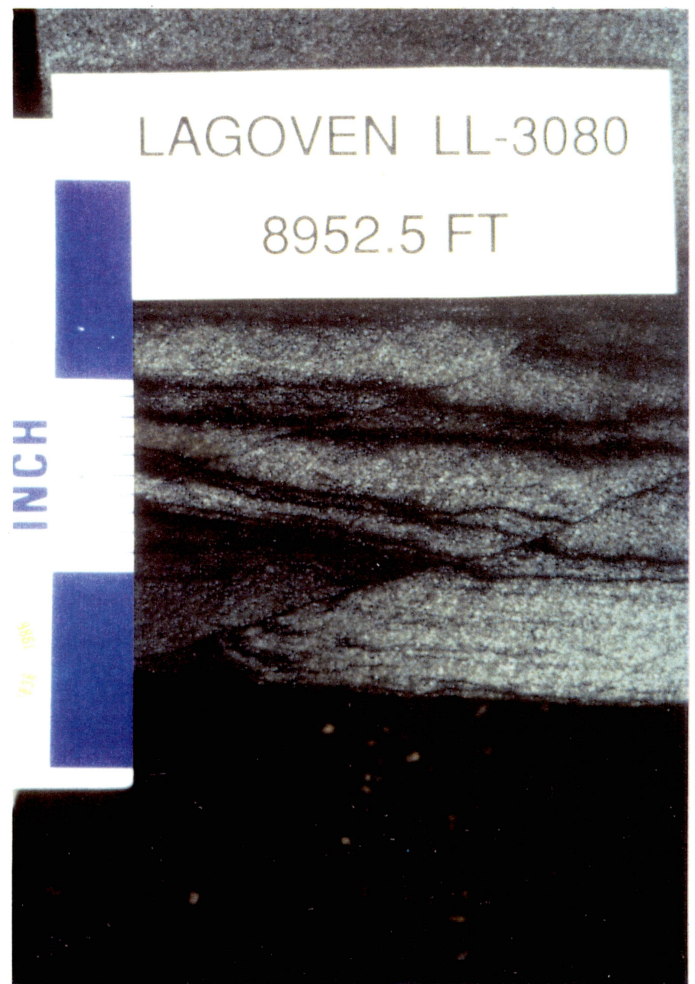
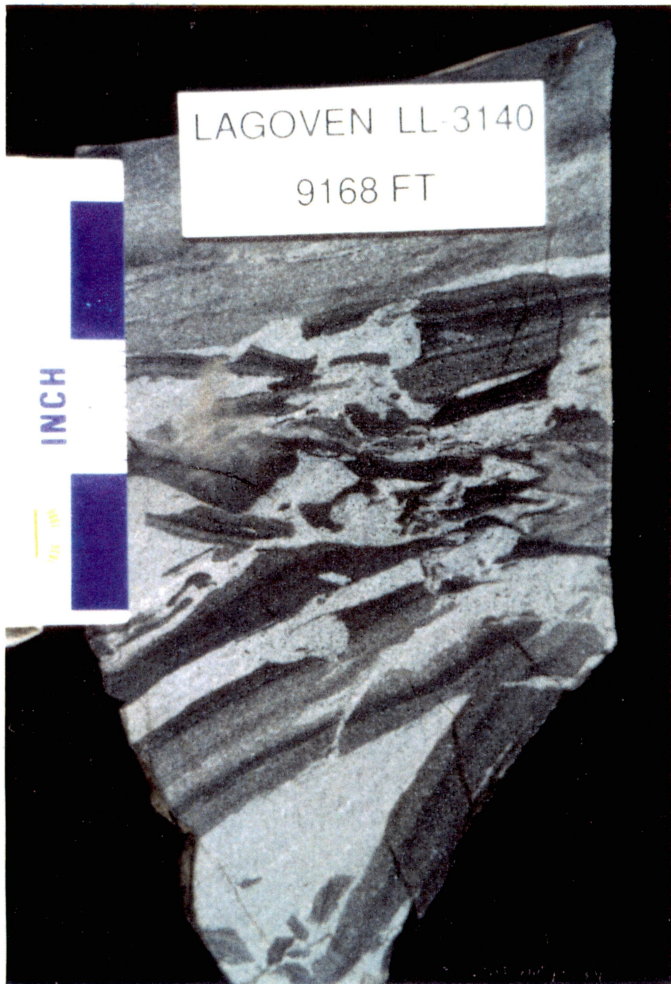


Figure IV 39. Core photograph of (a) normal microfault, and (b) reverse microfault in core of the LL-3080 well. Continued as parts (c) and (d) on next page.

(c)



(d)

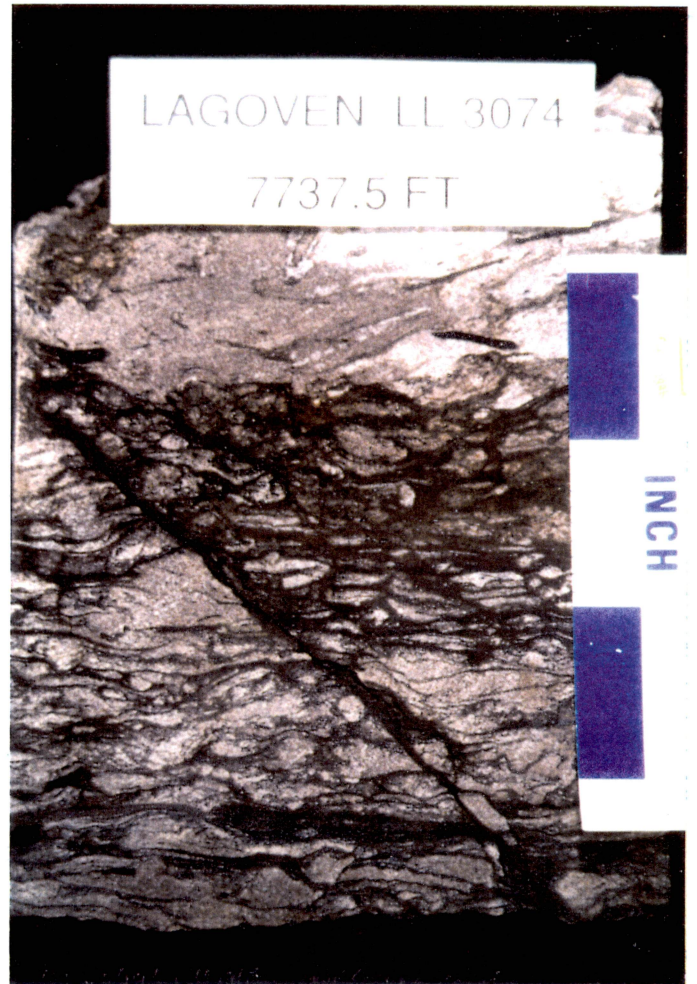
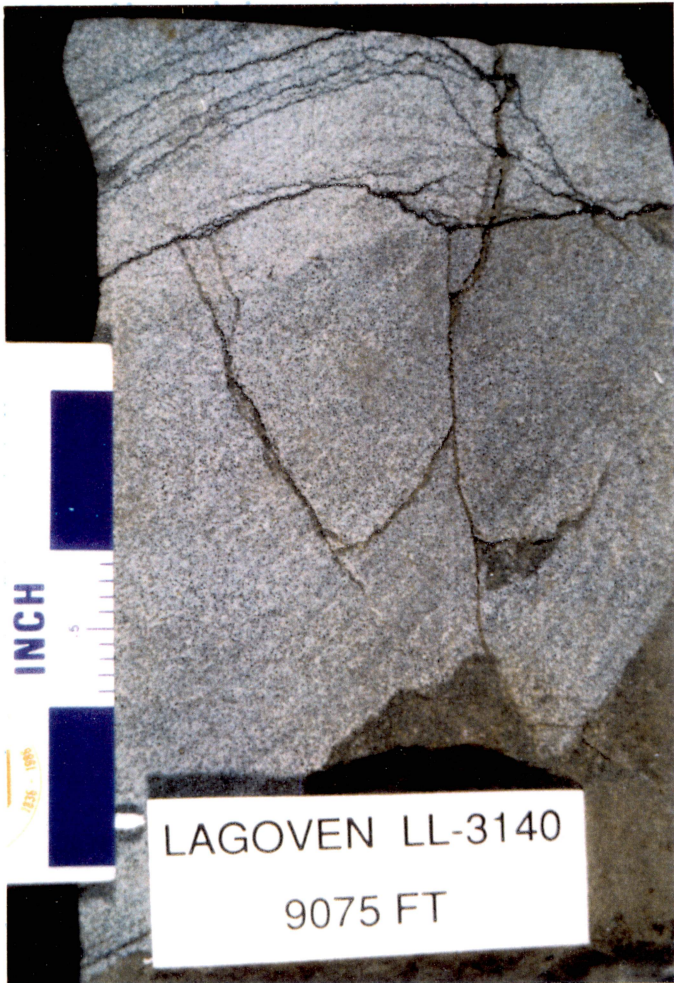


Figure IV 39 (continued). Core photograph of (c) fault breccia in the LL-3140 well, and (d) microfault in the LL-3074 well.

(a)



(b)



Figure IV 40. Core photographs of (a) and (b) fractures in core of the LL-3140 well. Continued as parts (c) and (d) on next page.

(c)



(d)



Figure IV 40 (continued). Core photograph of (c) multiple combination of fractures with microfault in the LL-2425 well and (d) fractures in core of the LL-3074 well.

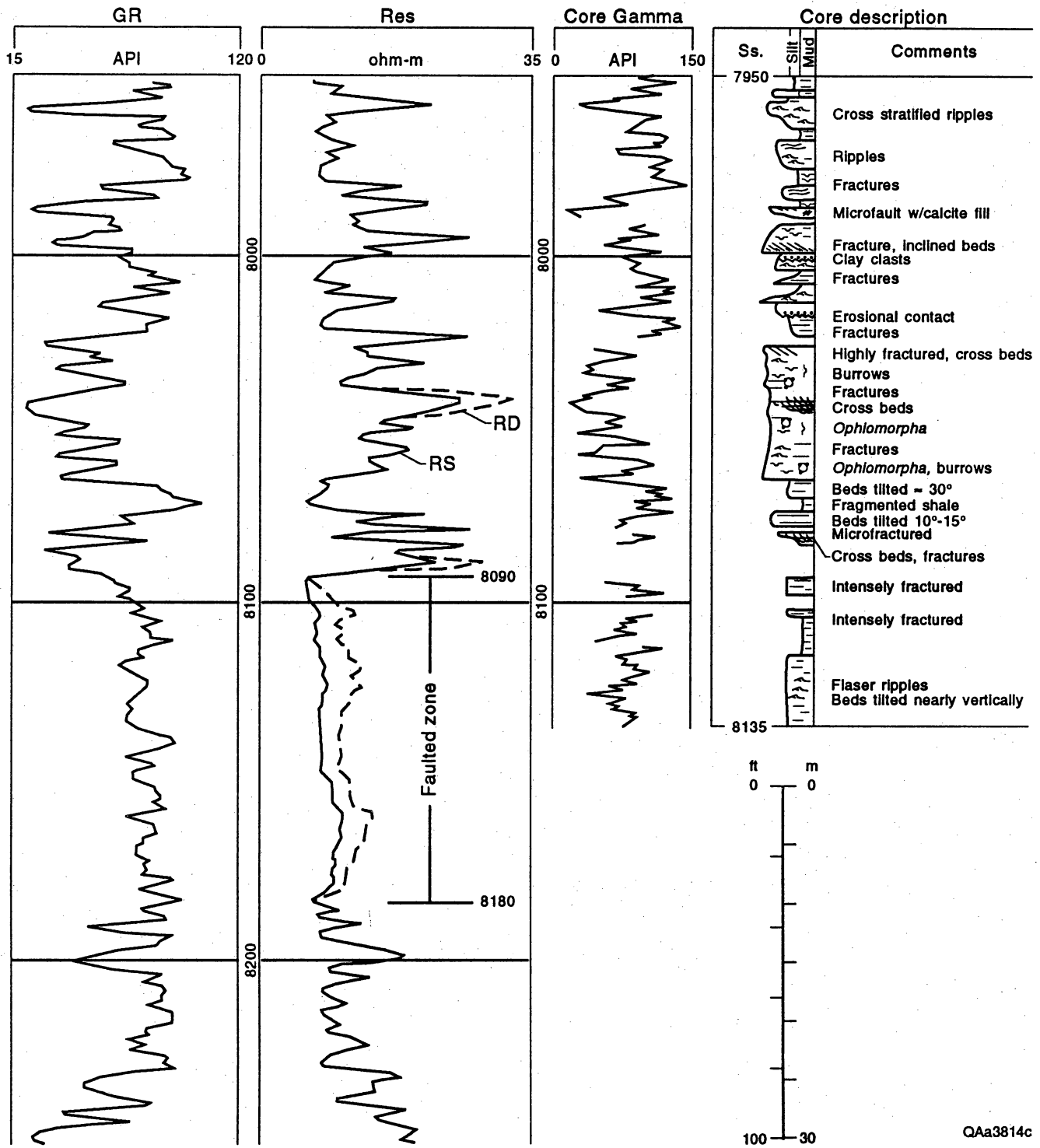


Figure IV 41. Core description and log response in the LL-3282 well, located in a faulted zone.

(a)

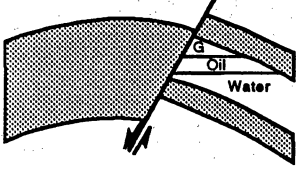
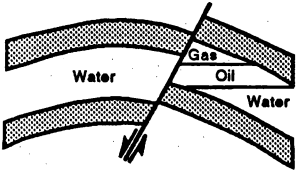
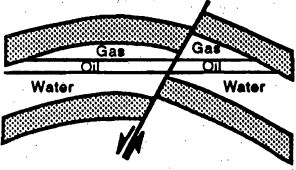
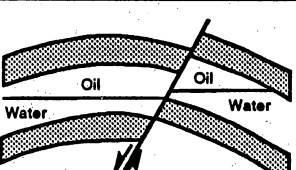


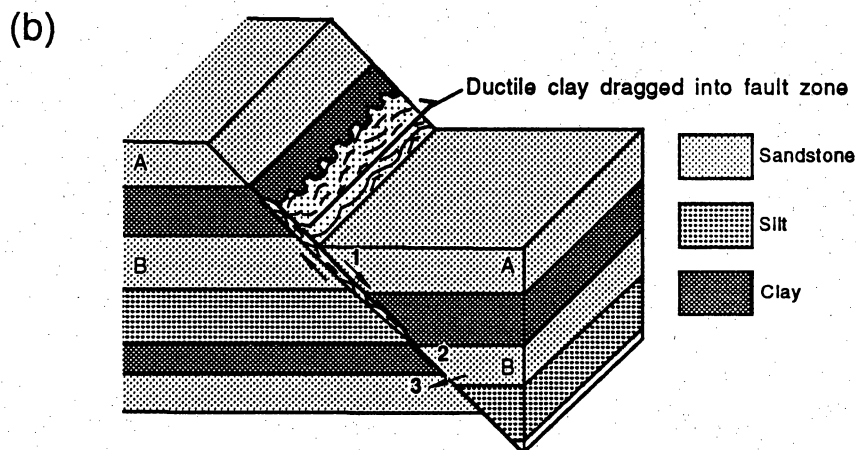
(b)



Figure IV 42. Core photograph of (a) nearly vertically tilted beds associated with reverse fault and (b) intensely fractured zone in core of LL-3282 well.

(a)

Hypothetical situation	Analysis of fault seal	
	Vertical migration	Lateral migration
 <p>Sand opposite shale at the fault. Hydrocarbons juxtaposed with shale.</p>	Sealing	<p>Sealing</p> <p>Reservoir boundary material may be the shale formation or fault zone material.</p>
 <p>Sand opposite sand at the fault. Hydrocarbons juxtaposed with water.</p>	Sealing	<p>Sealing</p> <p>Seal may be due to a difference in displacement pressures of the sands or to fault zone material with a displacement pressure greater than that of the sands.</p>
 <p>Sand opposite sand at the fault. Common hydrocarbon content and contacts.</p>	Sealing	<p>Nonsealing</p> <p>Possibility is remote that fault is sealing and the reservoirs of different capacity have been filled to exactly the same level by migrating hydrocarbons.</p>
 <p>Sand opposite sand at the fault. Different water levels.</p>	Sealing	<p>Unknown</p> <p>Nonsealing if water level difference is due to differences in capillary properties of the juxtaposed sands. Sealing if water level difference is not due to differences in capillary properties of the juxtaposed sands.</p>



QAa4235c

Figure IV 43. Hypothetical fault-lithology-accumulation relation from Smith (1980) and (b) clay smear and lithology juxtaposition. From Bouvier (1989).

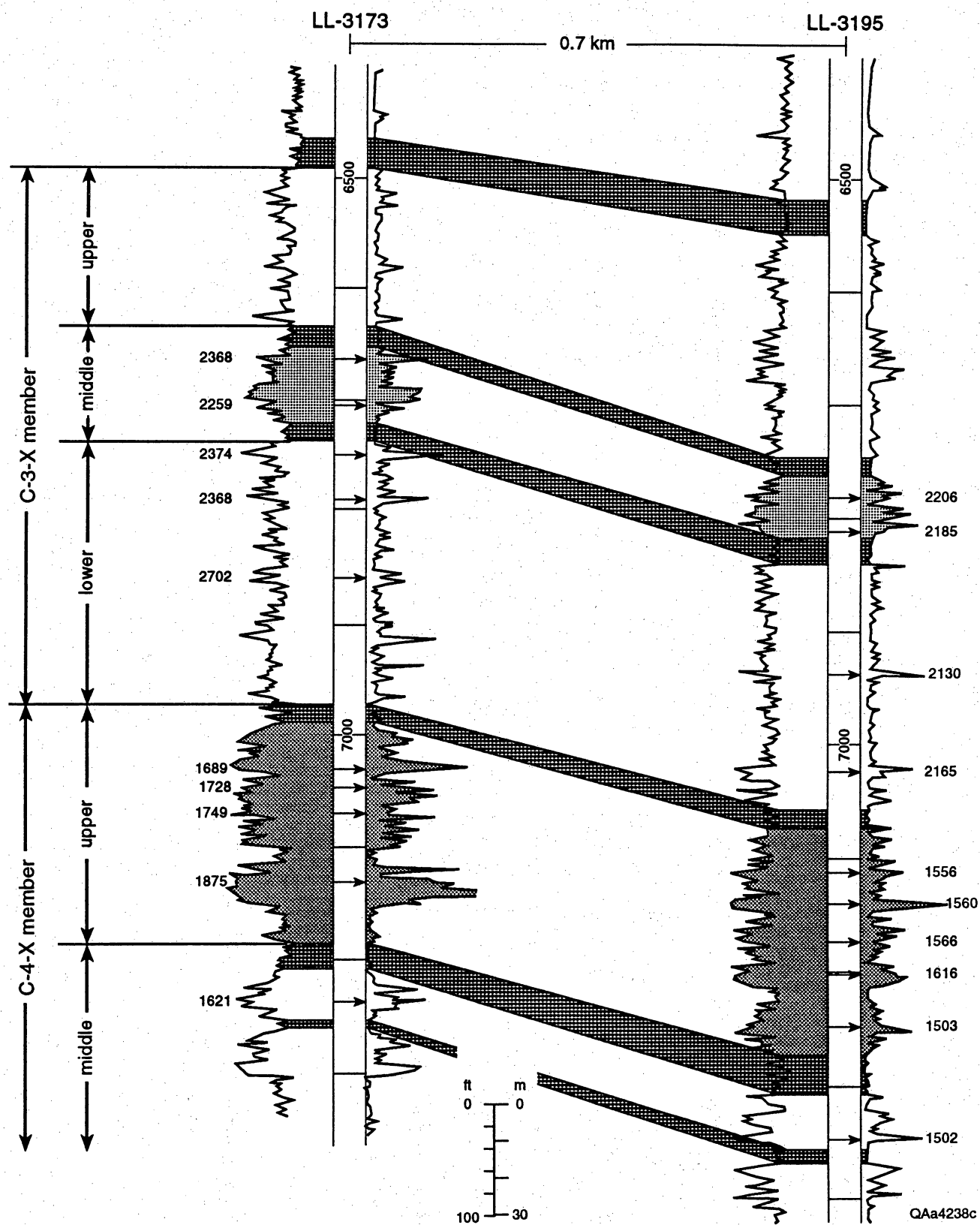
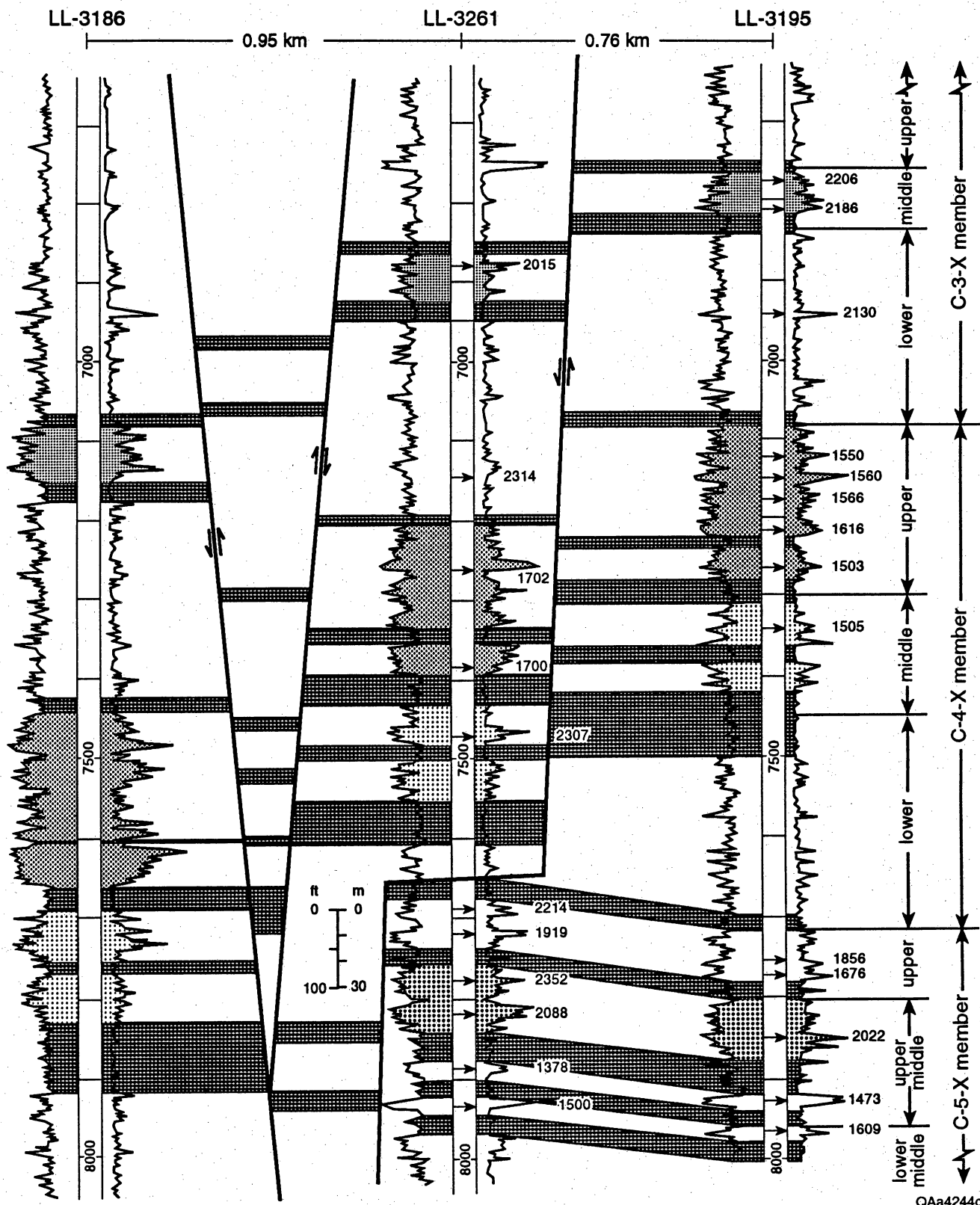


Figure IV 44. RFT data in the LL-3173 and LL-3195 wells.



QAa4244c

Figure IV 45. RFT data in the LL-3195 and LL-3261 wells.

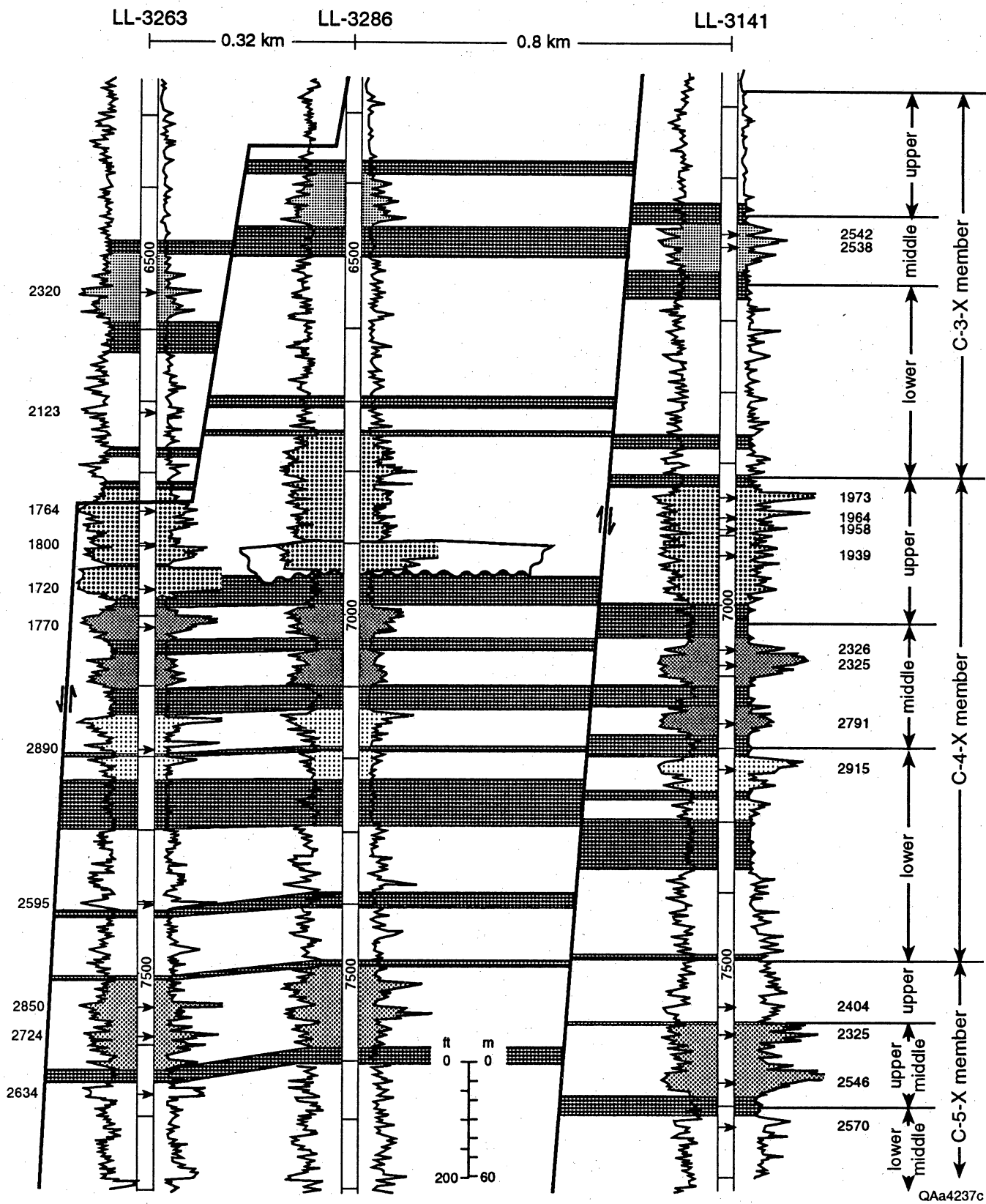


Figure IV 46. RFT data in the LL-3263 and LL-3141 wells.

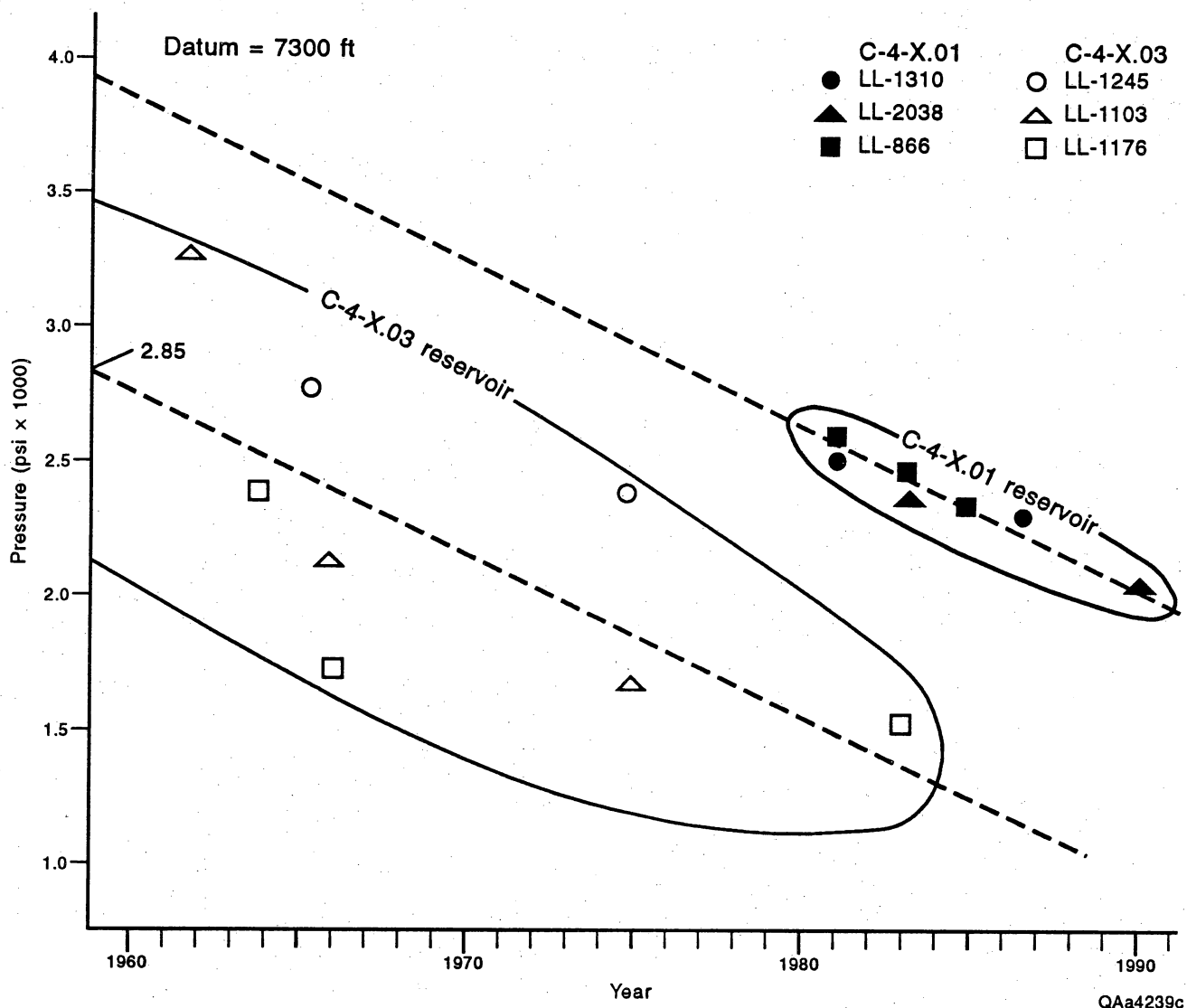


Figure IV 47. Historical trends in pressure between C-4-X.01 (downthrown block) and C-4-X.03 (upthrown block) reservoirs.

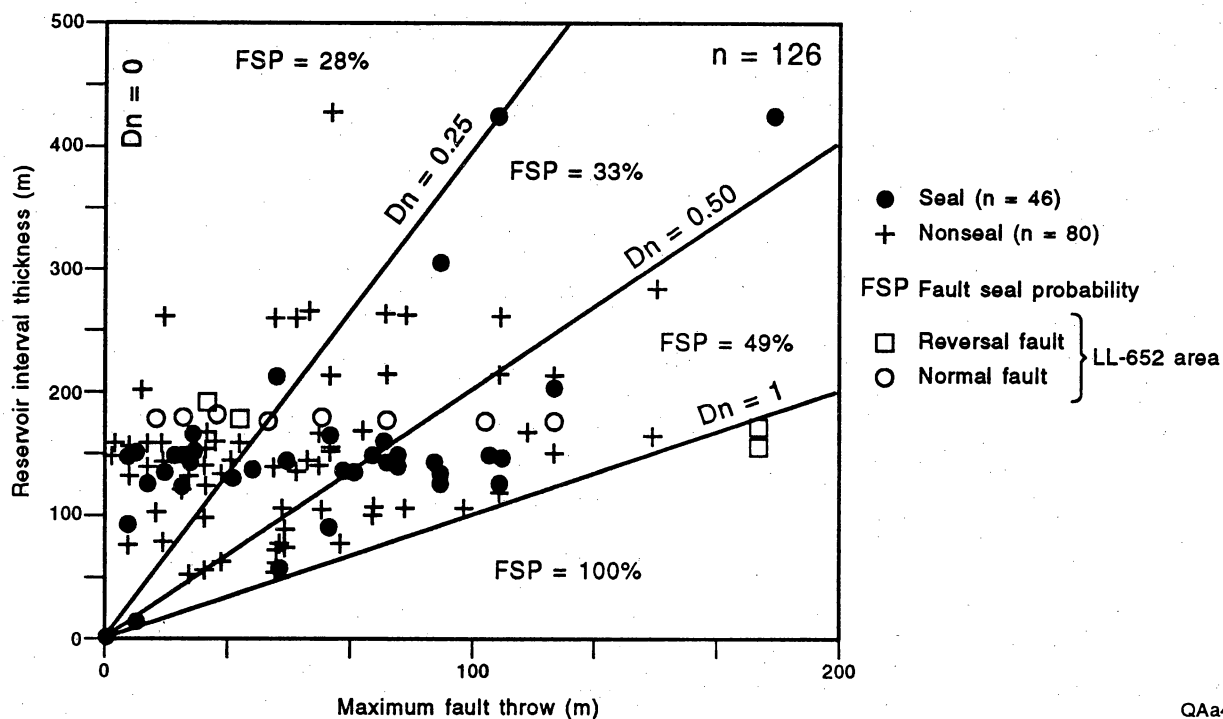
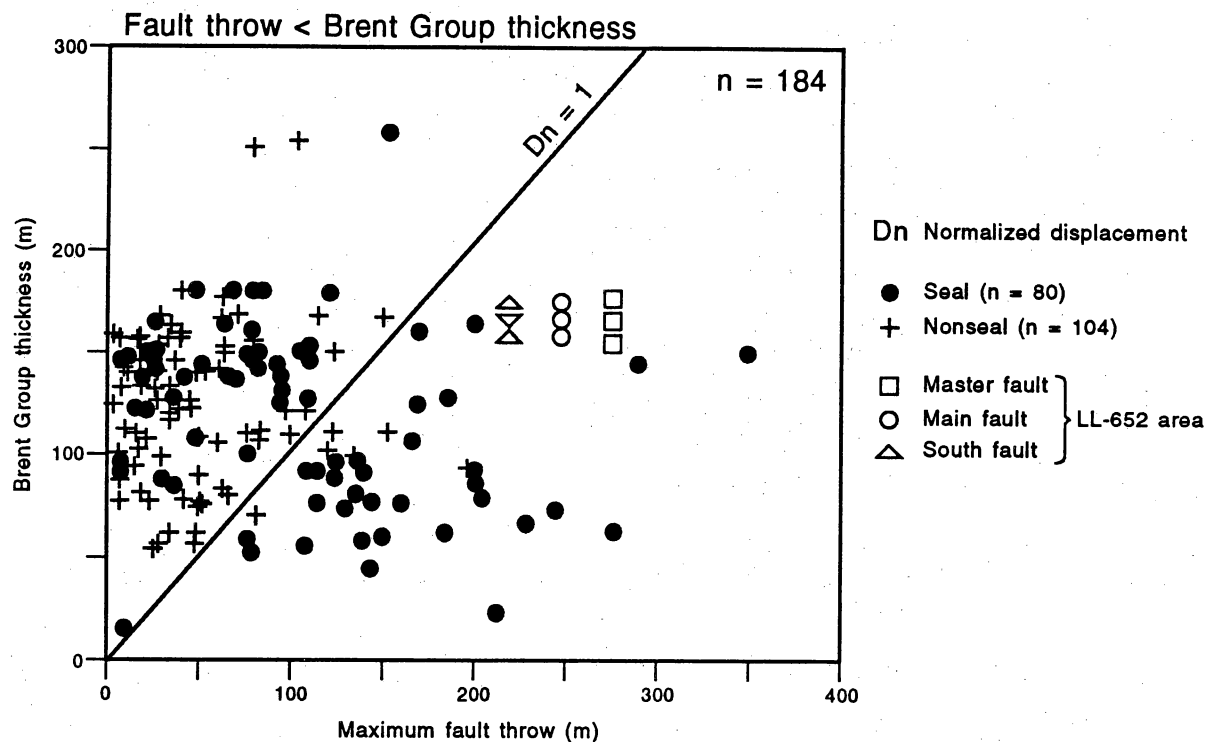


Figure IV 48. Brent Group thickness North Sea) versus fault throw (a) Extra-reservoir and intrareservoir faults, (b) Intrareservoir faults derived from "a" graphic.

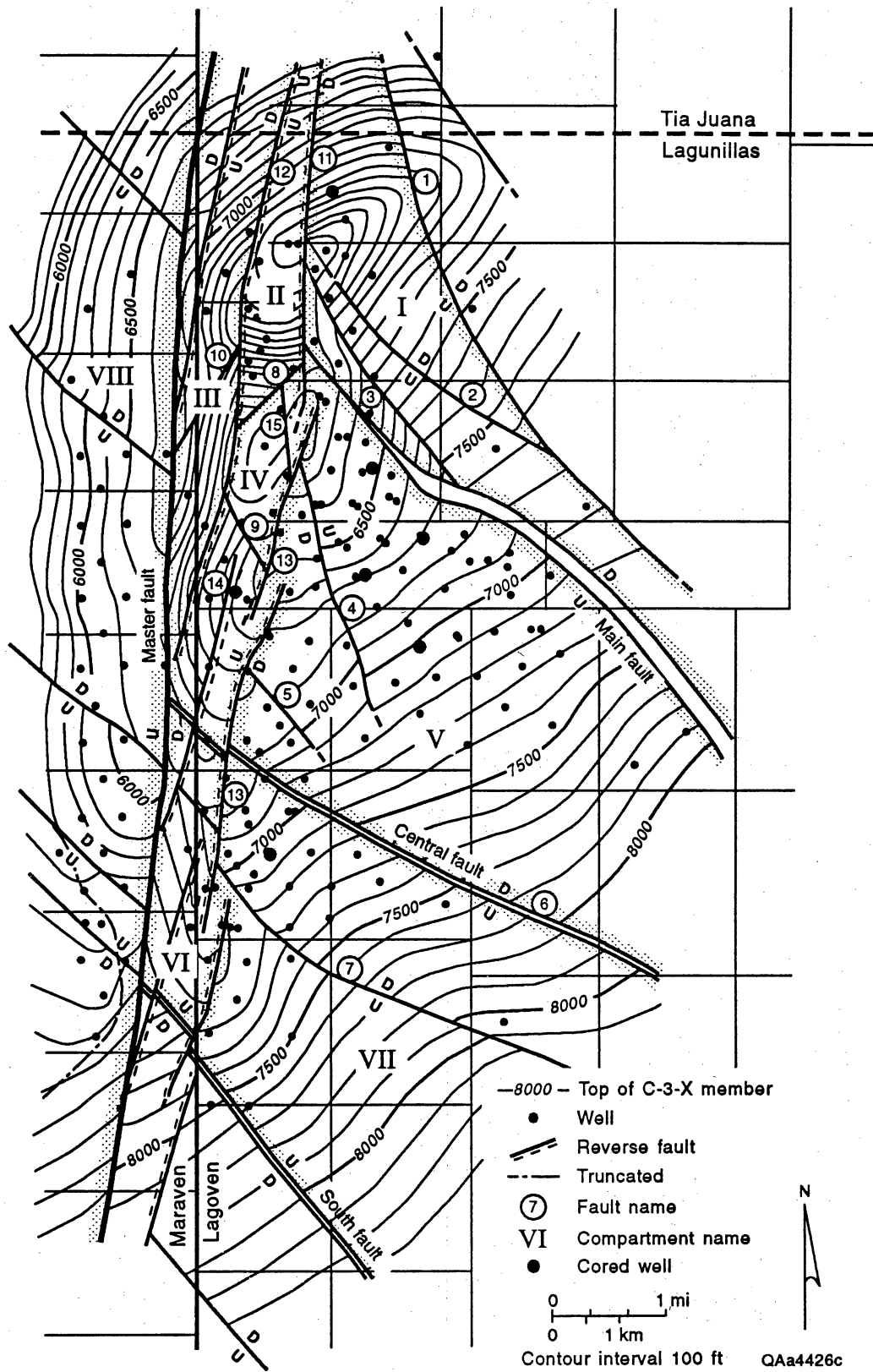


Figure IV 49. Fault compartment geometries.

Table IV 1. Fault characteristics in the LL-652 area.

Fault Name	Style	Dip	Strike	Throw (ft)	Cutting Wells
Master Fault	Normal	70° E	N5° E	900	VLA-613, VLA-13
Main Fault	Normal	58° NE	N45° W	800	LL-601, LL-1060, LL-2191, LL-1339, LL-2039, LL-2969, LL-2896, LL-3075, LL-2901, LL-3249, LL-1126, LL-3140, LL-2997, LL-1312, LL-3238, LL-3055, LL-3274, LL-1166, LL-2729, LL-851
South Fault	Normal	70° SW	N35° W	700	LL-1679
1	Normal	75° NE	N22° W	150	-
2	Normal	75° NE	N50° W	100	-
3	Normal	75° SW	N40° W	100	LL-1066, LL-1209, LL-1166
4	Normal	58° SW	N22° W	100	LL-1129, LL-2187, LL-2938, L-2940, LL-1172, LL-3261, LL-1061, LL-3173
5	Normal	60° SW	N40° W	50	LL-2280, LL-2038, LL-1218
Central Fault 6	Normal	62° NE	N60° W	250	LL-1748, LL-1176, LL-3059, LL-3155, LL-1310
7	Normal	65° NE	N45° W	50	LL-1022, LL-3149, LL-1307, LL-1196
8	Normal	80° NW	N45° E	500	-
9	Normal	65° SW	N25° W	200	LL-1803
10	Normal	80° SE	N30° E	550	-
11 (NE-R)	Reverse	78° W	N-S	500	LL-851, LL-827
12 (NW-R)	Reverse	75° E	N15° E	550	LL-3250, LL-LL-3204, LL-1089, LL-857
13 (CE-R)	Reverse	70° NW	N12° E	80	LL-1095, LL-1169, LL-3301, L-1782, LL-3282, LL-1218, LL-904, LL-1061
14 (CW-R)	Reverse	70° SE	N11° E	100	LL-997
15	Normal	55° SW	N10° W	100	LL-3144, LL-3286, LL-3263, L-3056
16 (SE-R)	Reverse	70° NW	N35° E	100	LL-1303, LL-1005, LL-1196, LL-946, LL-1023, LL-3284, LL-1001

Table IV 2. Tectonic features observed in cores, LL-652 area.

Well	Cored Interval (ft)	Member	Microfault Depth (ft)	Microfault Type	Fractures (ft or %)	Other Tectonic Features
LL-846	78	C-3/C4	-	-	-	-
LL-2425	206	C-3/C4	1) 7429 2) 7377	N N		Combination of fractures and microfaults
LL-2850	428	C-3/C4	7727	N	7612-15 (3), 7251-52 (1) 7276-85 (9)	
LL-3074	376	C-3/C4	1) 7738 2) 7577 3) 7582	N (1 cm offset) N (low angle) N	7651-52(1), 7675-76 (1) 7681-83 (2), 7691-92 (1) 7695-97 (2), 7246-48 (2)	
LL-3075	568	C-5	1) 8334 2) 7919 3) 7942	N N N	8004-05 (1), 8040-41 (1) 8038-39 (1), 8186-87 (1) 8391-92 (1), 8446-47(1)	7919 ft severely distorted SS- possibly microfaulted
LL-3080	646	C-6	1) 8726 2) 8739 3) 8826 4) 8922 5) 8953 6) 9006 7) 9013 8) 9099	N N N N R N N N	8817-19 (2), 8877-78 (1) 8723-24 (1), 9157-59 (2) 9173-74 (1), 9188-89 (1) 9196-97 (1), 9198-99 (1) 9201-03 (2), 9207-08 (1)	
LL-3140	308	C-6/C-7	9181	N	8885-8896 (30%) 8993-8910 (50%) 8917-19 (2), 8935-36 (1) 9076-85 (9), 9090-92 (2) 9118-21 (3), 9125-31 (6) 9143-45 (2), 9150-54 (4) 9156-62 (6), 9180-81 (1) 9193-98 (5), 9202-03 (1)	9036/9168 ft, fault breccia 8993 ft and 9083 ft, tectonically disrupted bed
LL-3282	662	C-4/ C-5/C-6	1) 7988	N	7292'-93 (1), 7309-10 (1) 7352'-53 (1), 7373-74 (1) 7397-98 (1), 7935-36 (1) 7943'-73 (20%) 7974'-78 (4), 7983-86 (3) 7987-90 (3), 7998-99 (1) 7997-8024 (20%) 8027'-34 (7), 8041-47 (6) 8049'-53 (4), 8056-58 (2) 8074'-82 (8), 8093-98 (5) 8102'-34 (32), 8717-23 (6) 8727'-28 (1), 8742-46 (4) 8757'-59 (2), 8778-79 (1) 8677'-78 (1), 8683-85 (2) 8703'-05 (2)	8095'-70' Beds tilted about 30° 8074'-78' Everything tilted 10° to 15° 8102'-8115' intensely fractured in small pieces 8115-34' Beds tilted nearly vertically (fault effect)

N= Normal
R=Reverse

Table IV 3. Summary of RFT data, LL-652 area.

Well	Member	Depth (ft)	Formation Pressure (psi)	DATUM (ft)	Gradient (psi/ft)	DATUM Pressure (PSI)
LL-3141 (03/91)	C-3-X	6473	2310	7300	0.28	2542
	C-3-X	6488	2311	7300	0.28	2538
	C-4-X	6847	1847	7300	0.28	1973
	C-4-X	6871	1844	7300	0.28	1964
	C-4-X	6892	1834	7300	0.28	1958
	C-4-X	6918	1832	7300	0.28	1939
	C-4-X	7060	2259	7300	0.28	2326
	C-4-X	7078	2263	7300	0.28	2325
	C-4-X	7161	2791	7300	0.28	2830
	C-5-X	7539	2302	7900	0.273	2400
	C-5-X	7562	2312	7900	0.273	2404
	C-5-X	7587	2262	7900	0.273	2347
	C-5-X	7600	2247	7900	0.273	2329
	C-5-X	7661	2481	7900	0.273	2546
	C-5-X	7720	2521	7900	0.273	2570
	C-5-X	7827	2920	7900	0.273	2940
LL-3173 (07/91)	C-3-X	6661	2189	7300	0.28	2368
	C-3-X	6706	2104	7300	0.28	2259
	C-3-X	6747	2219	7300	0.28	2374
	C-3-X	6787	2224	7300	0.28	2368
	C-3-X	6852	2577	7300	0.28	2702
	C-3-X	6859	2580	7300	0.28	2703
	C-4-X	7026	1611	7300	0.28	1689
	C-4-X	7052	1659	7300	0.28	1728
	C-4-X	7070	1685	7300	0.28	1749
	C-4-X	7116	1814	7300	0.28	1866
	C-4-X	7136	1829	7300	0.28	1875
	C-4-X	7234	1603	7300	0.28	1621
LL-3186 (07/91)	C-3-X	7098	2258	7300	0.28	2315
	C-3-X	7132	2272	7300	0.28	2319
	C-3-X	7267	2869	7300	0.28	2878
	C-3-X	7357	2406	7300	0.28	2390
	C-3-X	7402	2566	7300	0.28	2537
	C-4-X	7464	2043	7300	0.28	1997
	C-4-X	7482	2016	7300	0.28	1965
	C-4-X	7522	2005	7300	0.28	1943
	C-4-X	7556	2050	7300	0.28	1978
	C-4-X	7593	2270	7300	0.28	2182
	C-4-X	7614	2277	7300	0.28	2189
	C-4-X	7640	2291	7300	0.28	2196
	C-4-X	7726	2040	7300	0.28	1921
	C-5-X	8082	2892	7900	0.273	2842
	C-5-X	8064	2980	7900	0.273	2935

Table IV 3 (continued).

LL-3195 (08/91)	C-3-X	6782	2061	7300	0.28	2206
	C-3-X	6810	2048	7300	0.28	2185
	C-3-X	6943	2030	7300	0.28	2130
	C-3-X	7027	2089	7300	0.28	2165
	C-3-X	7047	2104	7300	0.28	2175
	C-4-X	7121	1506	7300	0.28	1556
	C-4-X	7148	1517	7300	0.28	1560
	C-4-X	7177	1532	7300	0.28	1566
	C-4-X	7216	1592	7300	0.28	1616
	C-4-X	7262	1492	7300	0.28	1503
	C-4-X	7336	1519	7300	0.28	1509
	C-4-X	7358	1518	7300	0.28	1502
	C-5-X	7760	1820	7900	0.273	1858
	C-5-X	7773	1641	7900	0.273	1676
	C-5-X	7851	2009	7900	0.273	2022
	C-5-X	7924	1480	7900	0.273	1473
	C-5-X	7968	1628	7900	0.273	1609
LL-3261 (05/92)	C-3-X	6757	2483	7300	0.28	2635
	C-3-X	6881	1898	7300	0.28	2015
	C-3-X	7136	2268	7300	0.28	2314
	C-4-X	7256	1690	7300	0.28	1702
	C-4-X	7360	1705	7300	0.28	1688
	C-4-X	7380	1722	7300	0.28	1700
	C-4-X	7470	2355	7300	0.28	2307
	C-5-X	7694	2158	7900	0.273	2214
	C-5-X	7716	1865	7900	0.273	1915
	C-5-X	7778	2319	7900	0.273	2352
	C-5-X	7813	2064	7900	0.273	2088
	C-5-X	7886	1371	7900	0.273	1378
	C-5-X	7930	1508	7900	0.273	1500
LL-3260 (05/92)	C-3-X	7229	2286	7300	0.28	2306
	C-3-X	7245	2245	7300	0.28	22 60
	C-3-X	7288	1948	7300	0.28	1951
	C-3-X	7519	3027	7300	0.28	2949
	C-3-X	7650	1684	7300	0.28	1586
	C-3-X	7681	2100	7300	0.28	1993
	C-4-X	7748	1805	7300	0.28	1680
	C-4-X	7795	1998	7300	0.28	1859
	C-4-X	7920	1901	7300	0.28	1727
	C-4-X	7920	1902	7300	0.28	1728
	C-5-X	8464	3778	7900	0.273	3624
	C-5-X	8598	3855	7900	0.273	3664
	C-5-X	8663	3851	7900	0.273	3643
	C-5-X	8709	4039	7900	0.273	3818
	C-5-X	8790	3819	7900	0.273	3576
	C-5-X	8830	3839	7900	0.273	3585
	C-5-X	8860	3418	7900	0.273	3156
	C-5-X	8880	3673	7900	0.273	3406

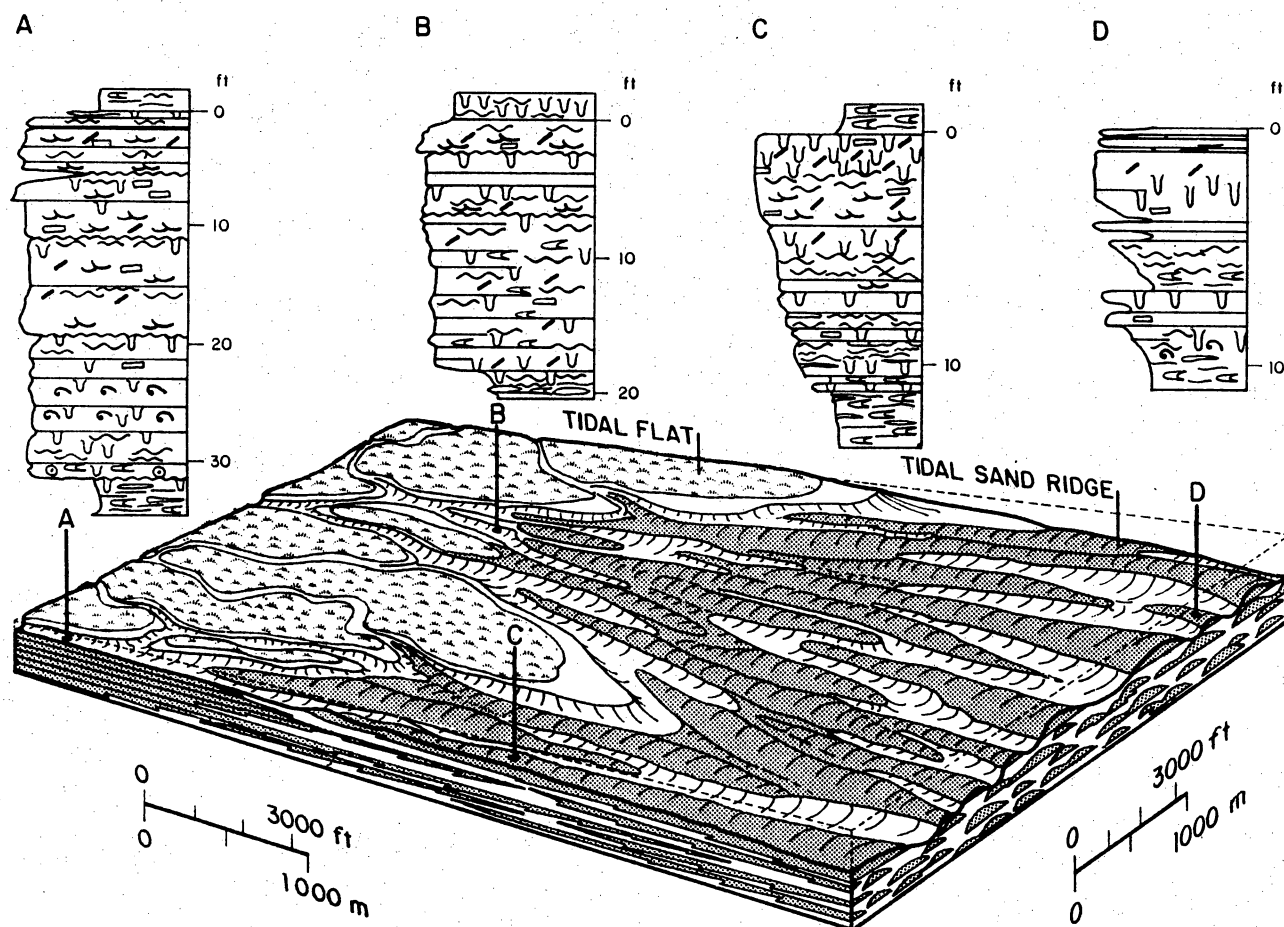
Table IV 3 (continued).

LL-3263 (05/92)	C-3-X	6544	2113	7300	0.28	2325
	C-3-X	6574	2114	7300	0.28	2317
	C-3-X	6710	1964	7300	0.28	2129
	C-3-X	6788	1665	7300	0.28	1808
	C-3-X	6853	1639	7300	0.28	1764
	C-4-X	6904	1652	7300	0.28	1753
	C-4-X	6914	1699	7300	0.28	1807
	C-4-X	6935	1628	7300	0.28	1730
	C-4-X	6960	1629	7300	0.28	1724
	C-4-X	7003	1687	7300	0.28	1770
	C-4-X	7148	2803	7300	0.28	2846
	C-4-X	7182	2857	7300	0.28	2890
	C-4-X	7400	2623	7300	0.28	2595
	C-5-X	7543	2752	7900	0.273	2850
	C-5-X	7583	2637	7900	0.273	2724
	C-5-X	7665	2570	7900	0.273	2634
	C-5-X	7779	3763	7900	0.273	3796

Table IV 4. Fault names in the LL-652 area.

Fault Name	Fault ft	Throw m	FSP(*) (%)	Comments
Master fault	900	274	90	Extrareservoir fault
Main fault	800	244	90	Extrareservoir fault
South fault	700	213	90	Extrareservoir fault
1	150	46	(-) 33	
2	100	30	(+) 28	
3	100	30	(+) 28	
4	100	30	(+) 28	Sealing toward the north, but communication is expected in the south
5	50	15	(-) 28	
Central fault 6	250	76	(+) 33	Sealing by pressure analysis (historican tendency)
7	50	15	(-) 28	
8	500	152	49	
9	200	61	33	
10	550	167	49	
NE-Reverse 11	500	152	90	
NW-Reverse 12	550	167	90	
CE-Reverse 13	80	24	(+) 28	Sealing by pressure (RFT) analysis
CW-Reverse 14	100	30	28	
15	100	30	28	
SE-Reverse 16	100	30	28	

* Fault Seal Probability



QAa3257

Figure V 1. Tide-dominated deltaic depositional model of Eocene reservoirs in the LL-652 area. From Maguregui (1991).

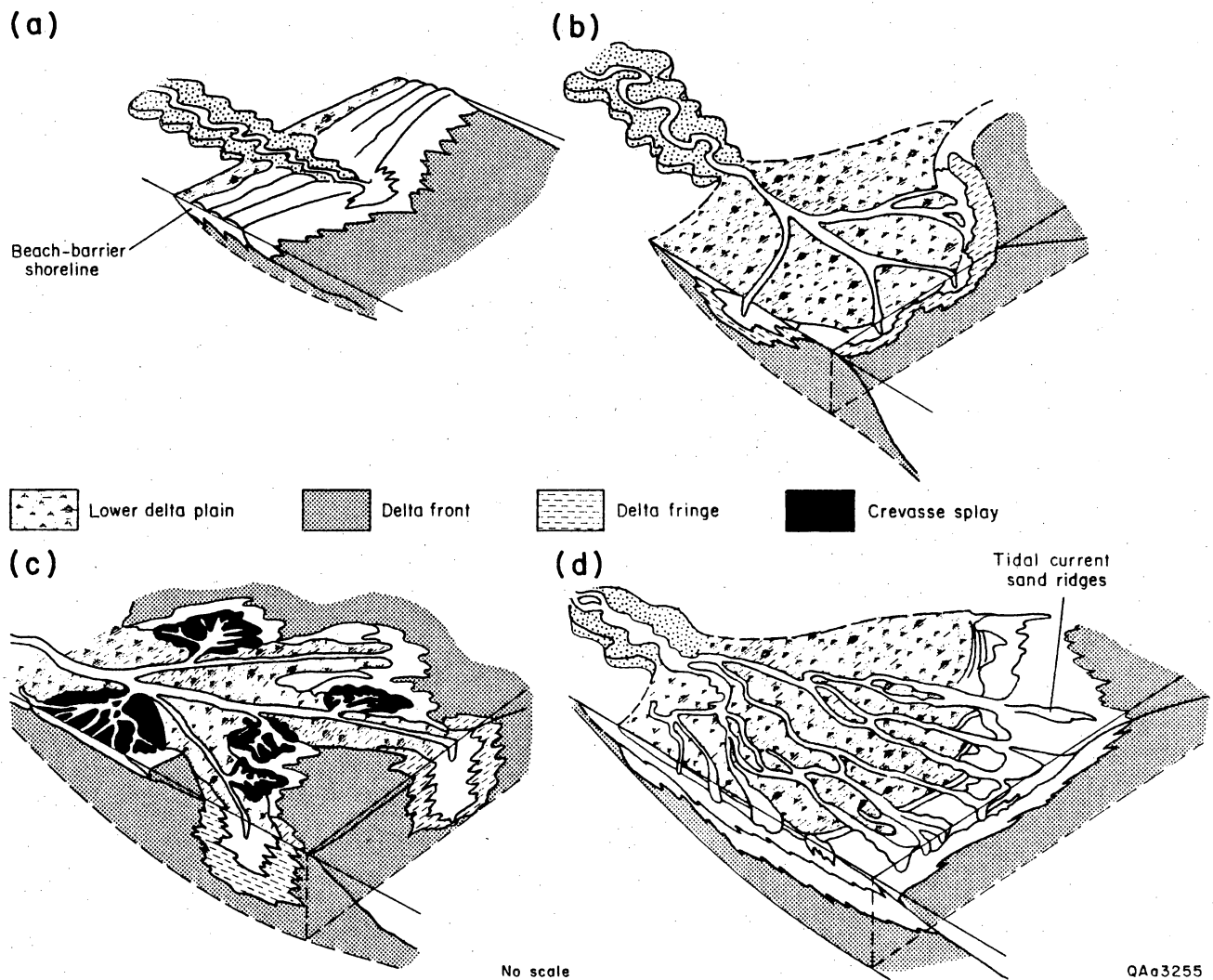
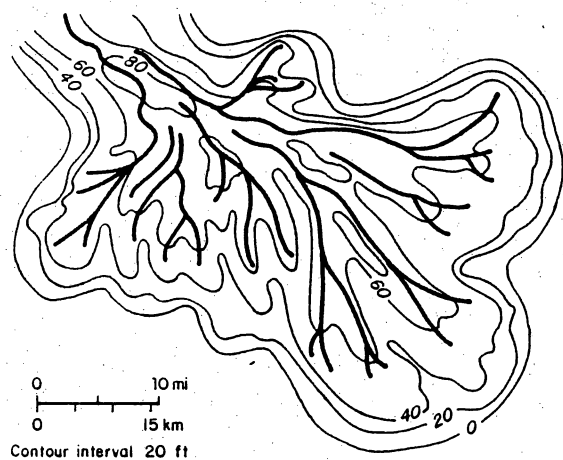
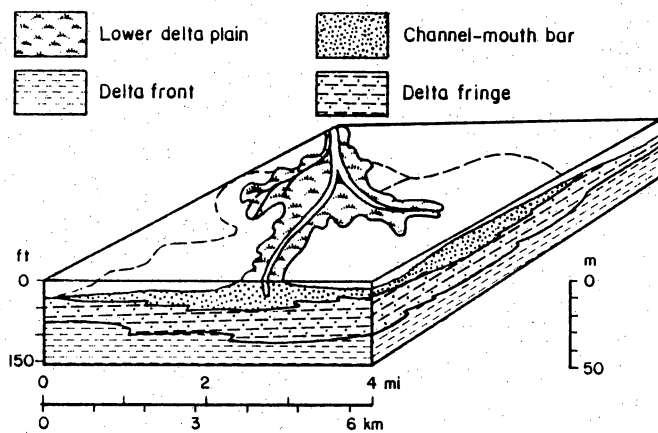
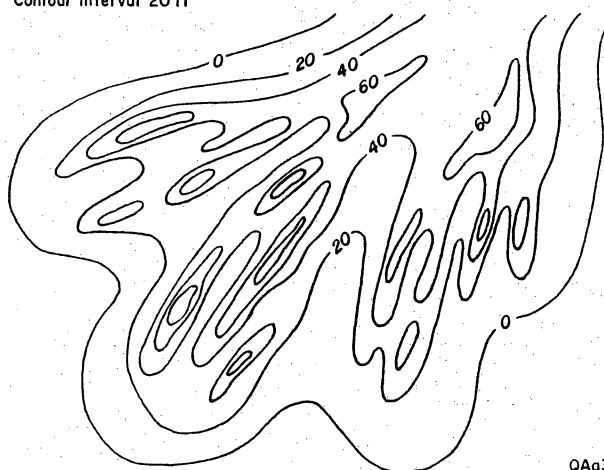
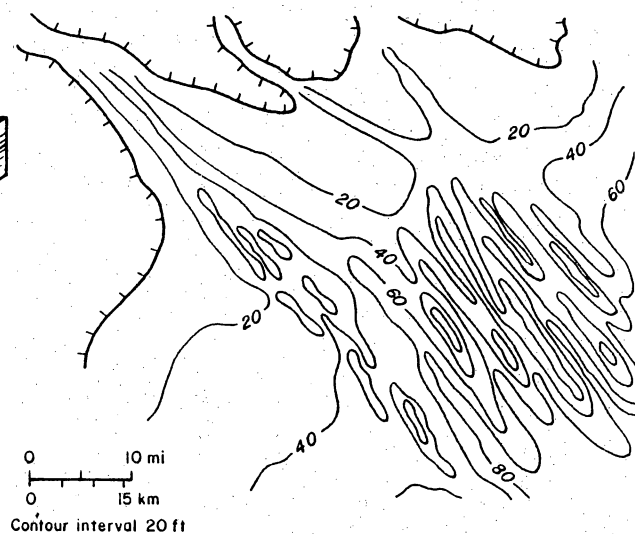


Figure V 2. Spectrum of major delta morphologies. Modified from Fisher and others (1969).

(a)



(b)



QAa3258

Figure V 3. Comparison of net-sandstone thickness patterns in (a) fluvial-dominated deltas and (b) tide-dominated deltas. Modified from Coleman and Prior (1982).

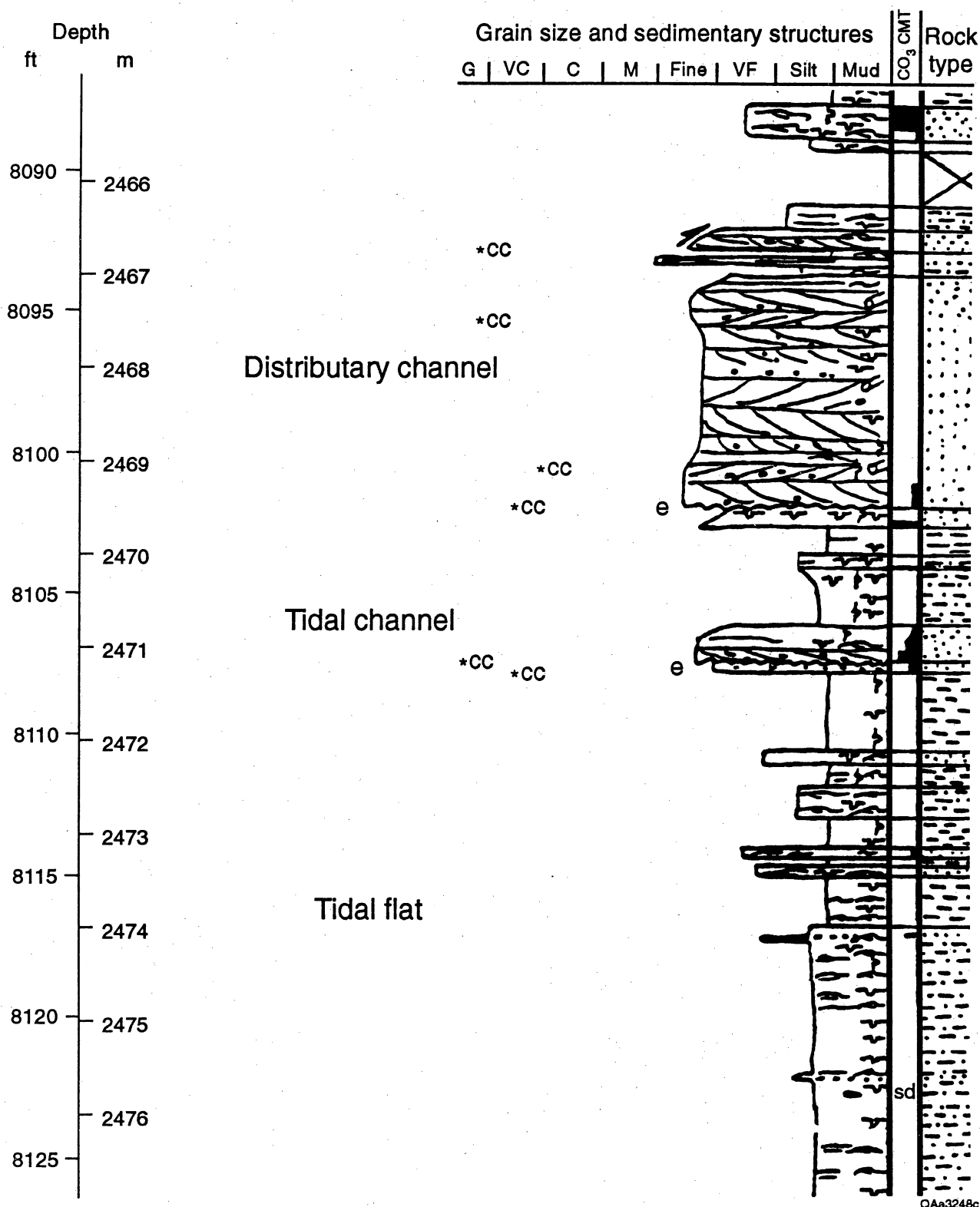


Figure V 4. Core description of distributary-channel and related facies in the Middle C-5-X Submember in the LL-3075 well. Photograph of distributary-channel facies (8,099.5 ft) is shown in figure V 5.

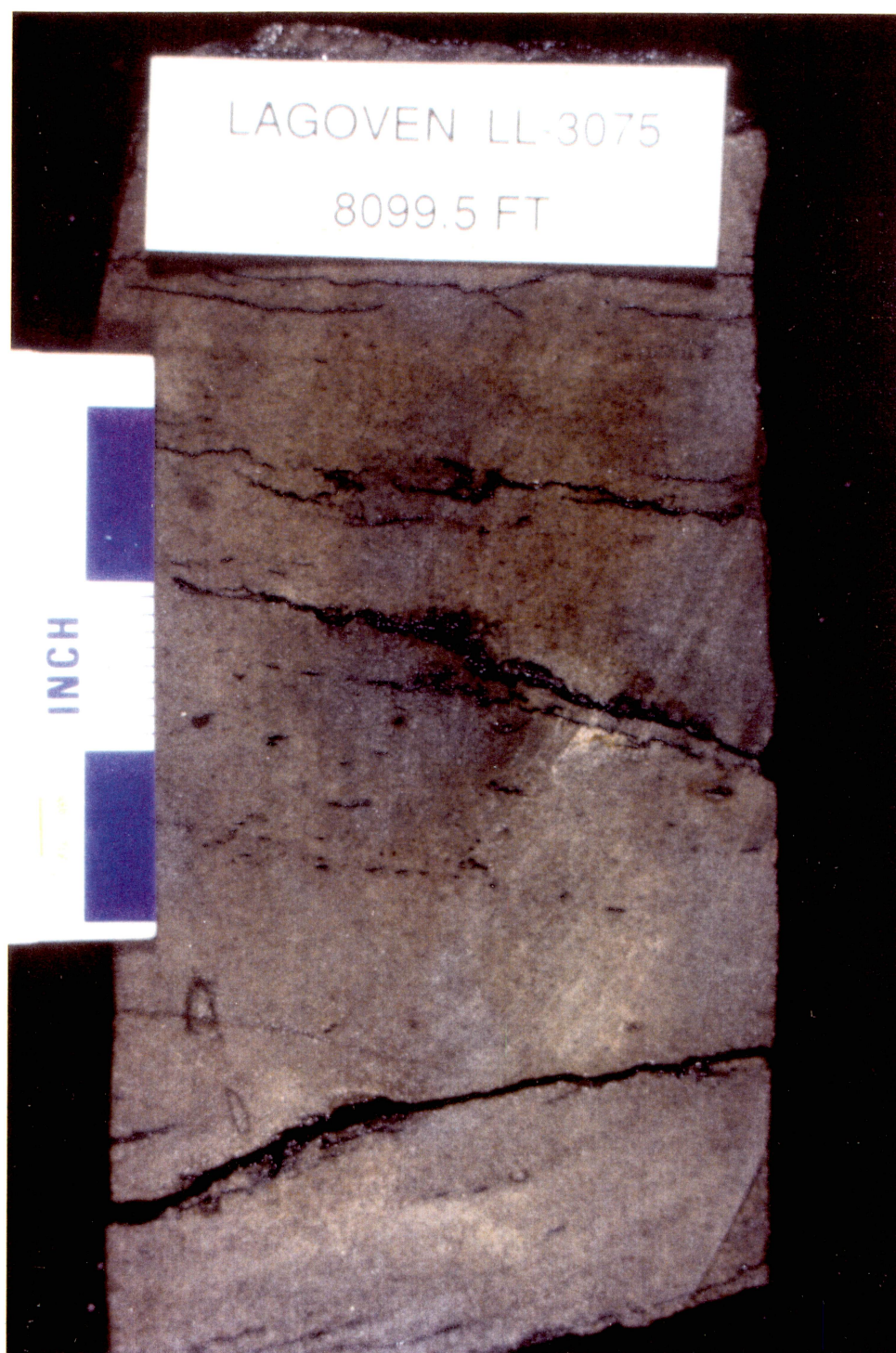


Figure V 5. Core photograph of crossbedded distributary-channel facies in the Middle C-5-X Submember in the LL-3075 well. Core description is shown in figure V 4.

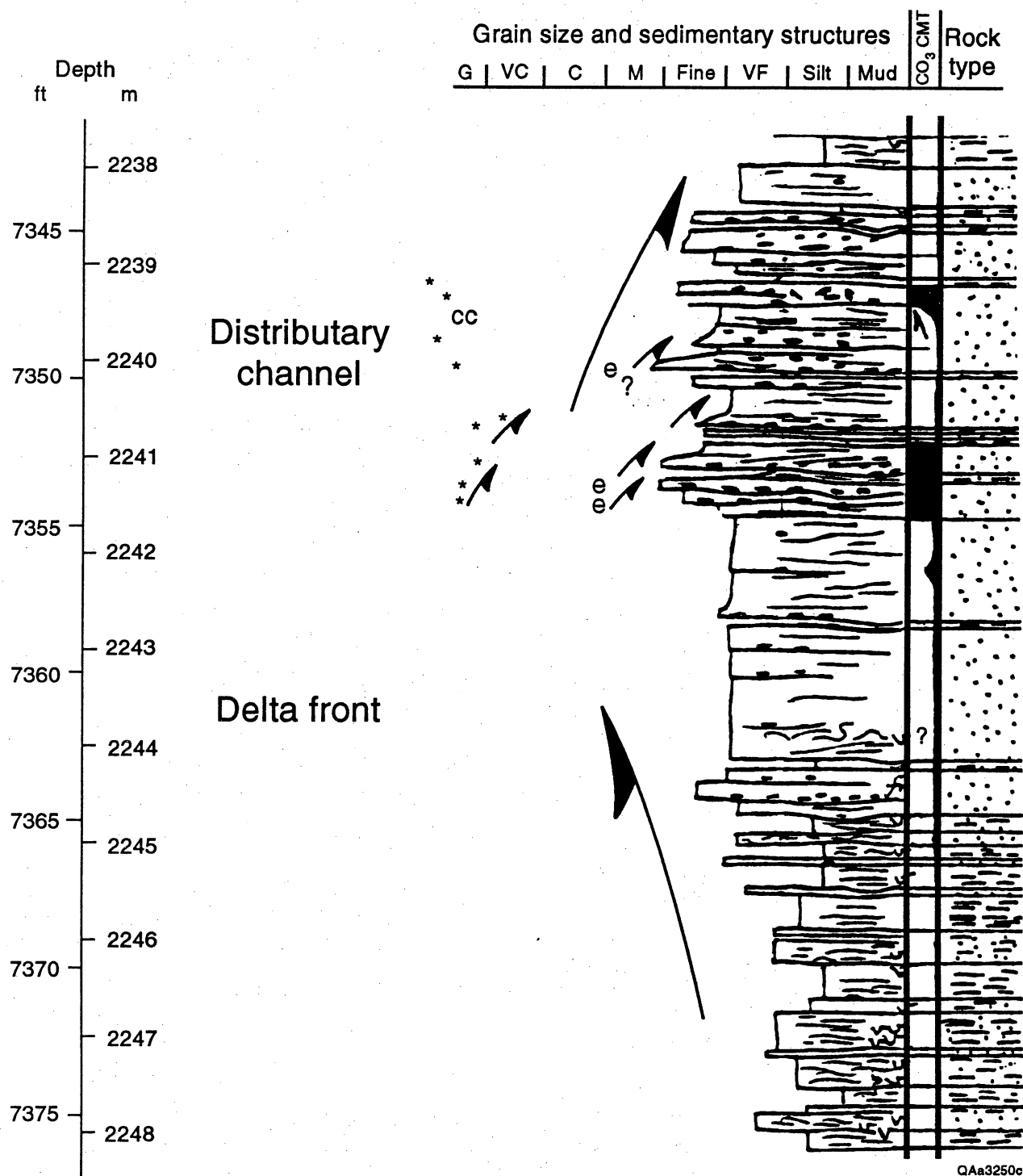


Figure V 6. Core description of distributary-channel facies, overlying delta-front facies in the Middle C-3-X Submember in the LL-3074 well. Photographs of delta-front (7,375 ft) and distributary-channel (7,354 ft) facies are shown in figures V 7a and V 7b, respectively.

(a)



(b)



Figure V 7. (a). Core photograph of burrowed, interbedded mudstone and sandstones in delta-front facies and (b) clay-clast-rich distributary-channel facies in the Middle C-3-X Submember in the LL-3074 well. Core description is shown in figure V 6.

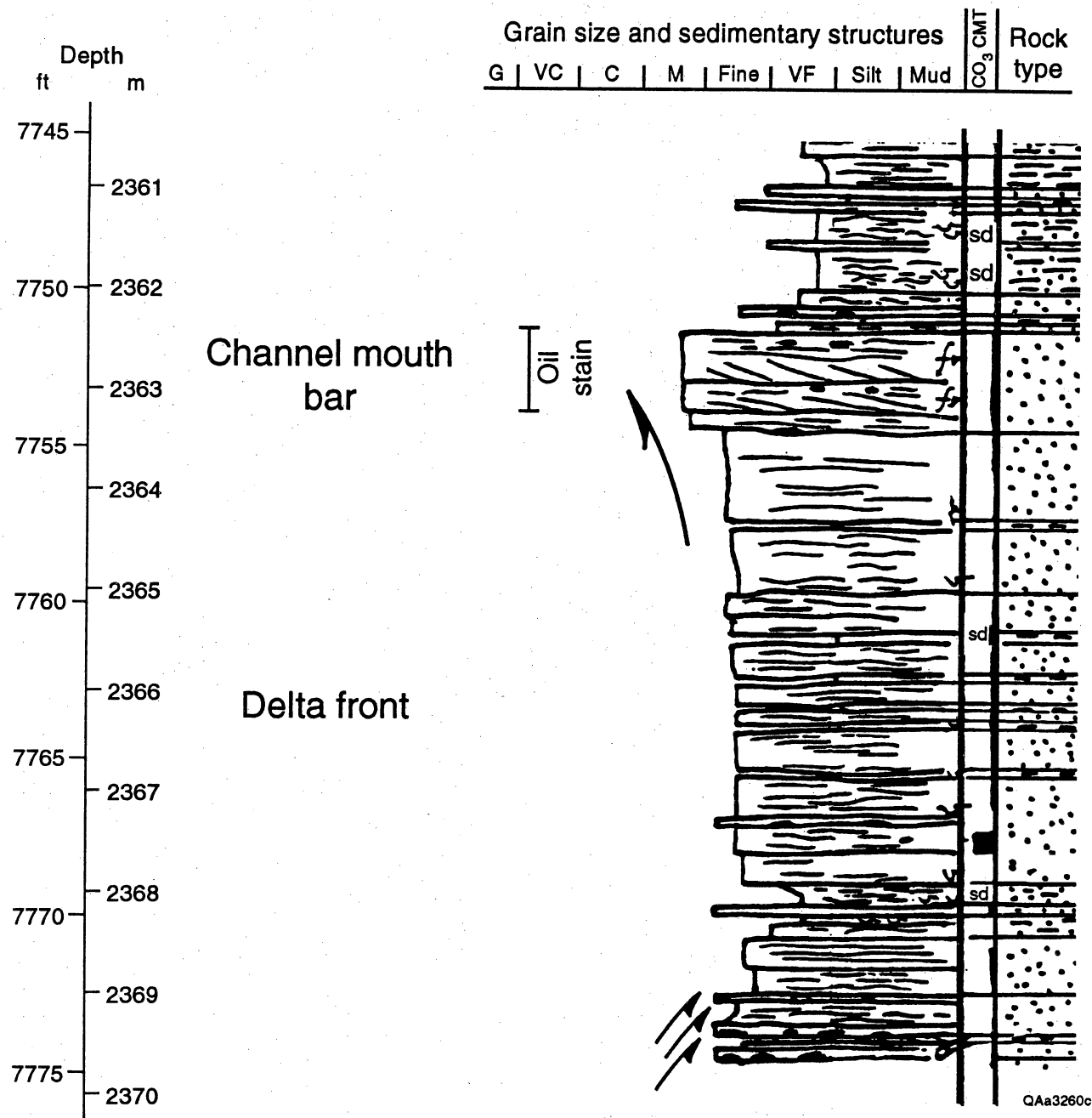


Figure V 8. Core description of channel-mouth bar and delta-front facies in the Upper C-4-X Submember in the LL-3074 well. Photograph of channel-mouth bar crest (7,752 ft) is shown in figure V 9.

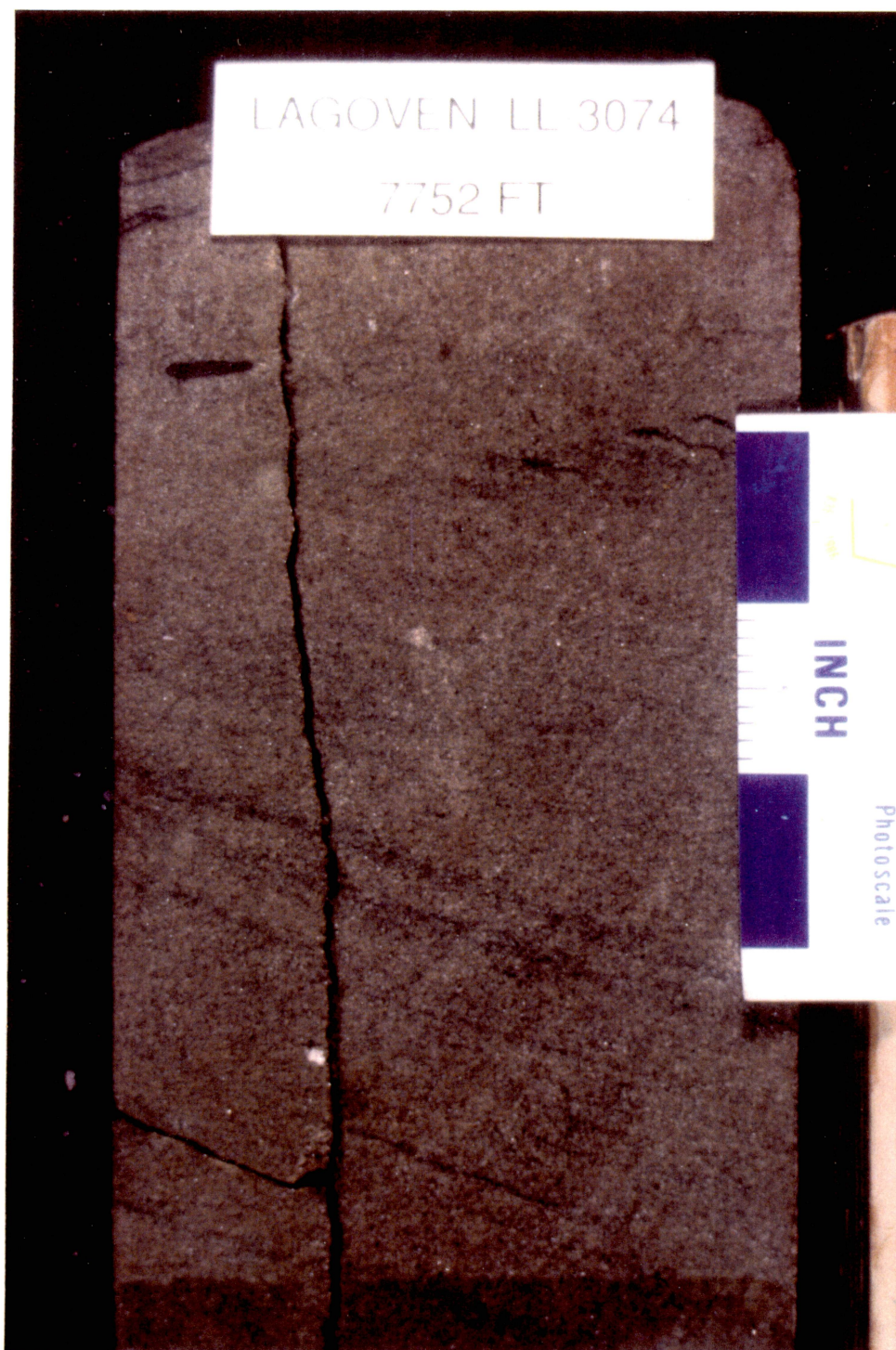


Figure V 9. Core photograph of crossbedded, oil-stained channel-mouth bar crest in the Upper C-4-X Submember in the LL-3074 well. Core description is shown in figure V 8.

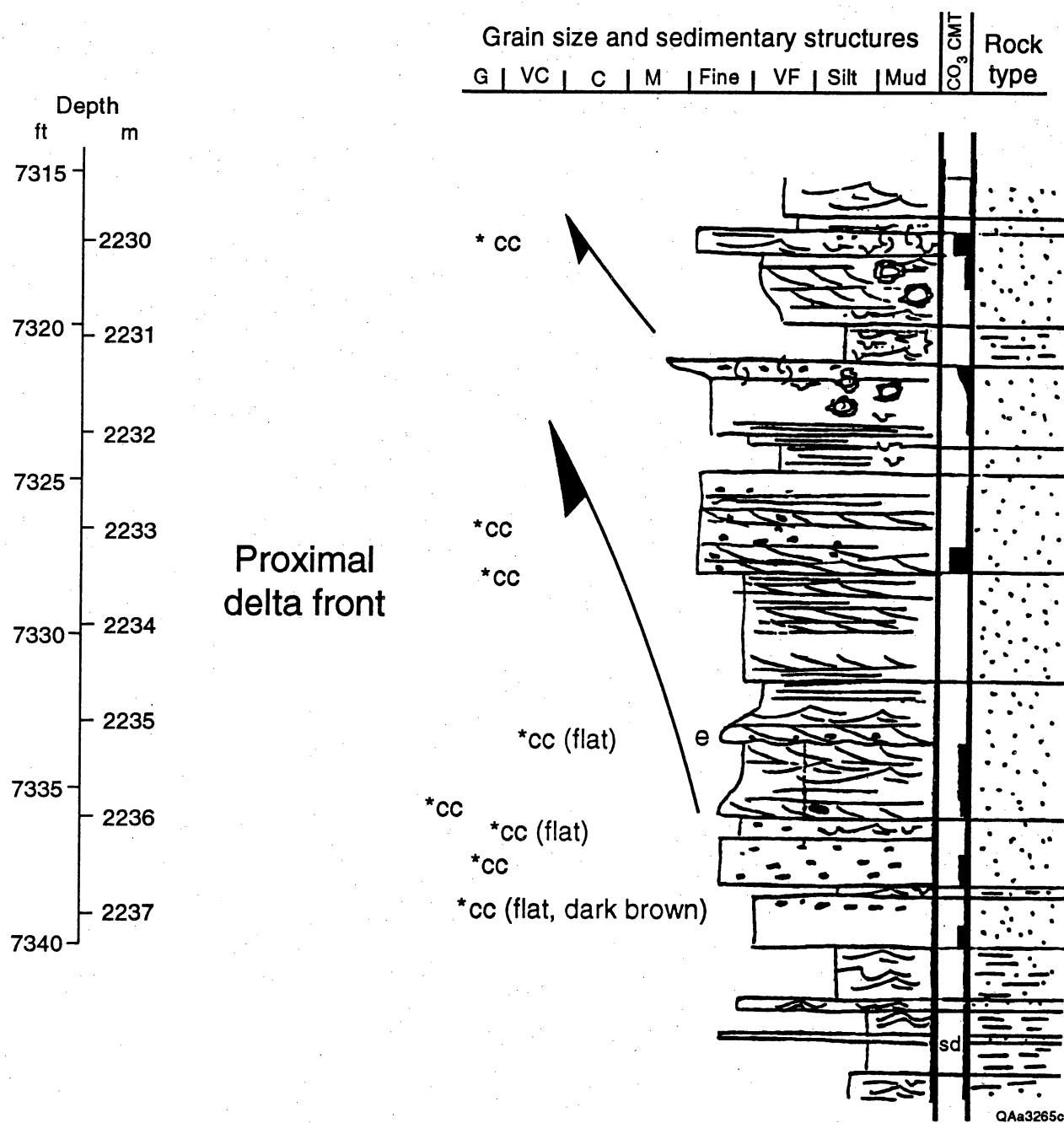


Figure V 10. Core description of proximal delta-front (tidal sand-ridge) facies in the Upper C-4-X Submember in the LL-3282 well. Photograph of upper part of proximal delta-front (7,326 ft) is shown in figure V 11.

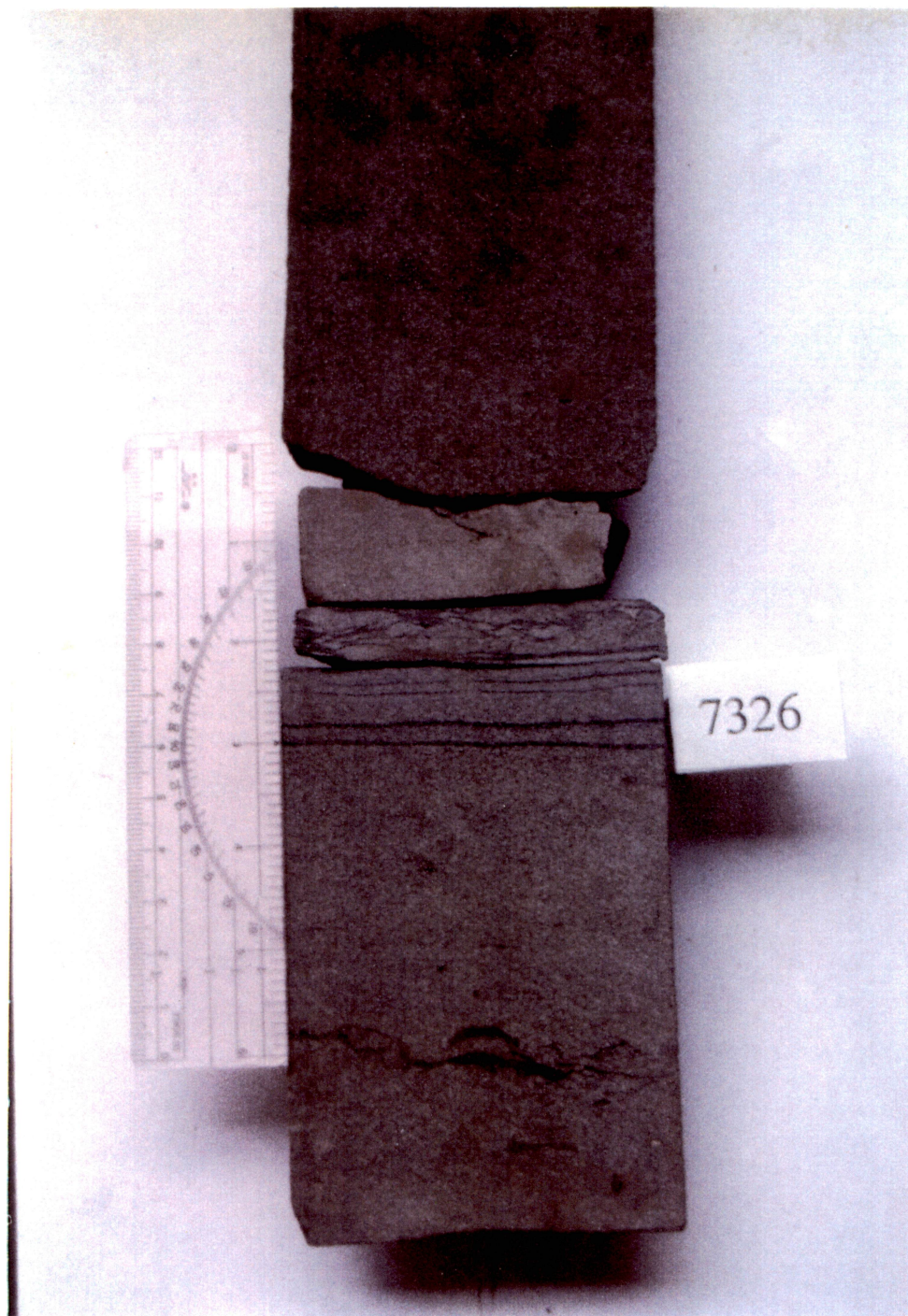


Figure V 11. Core photograph of sandstone-rich, mostly plane-bedded and burrowed proximal delta-front (tidal sand-ridge) facies in the Upper C-4-X Submember in the LL-3282 well. Core description is shown in figure V 10.

(a)



(b)

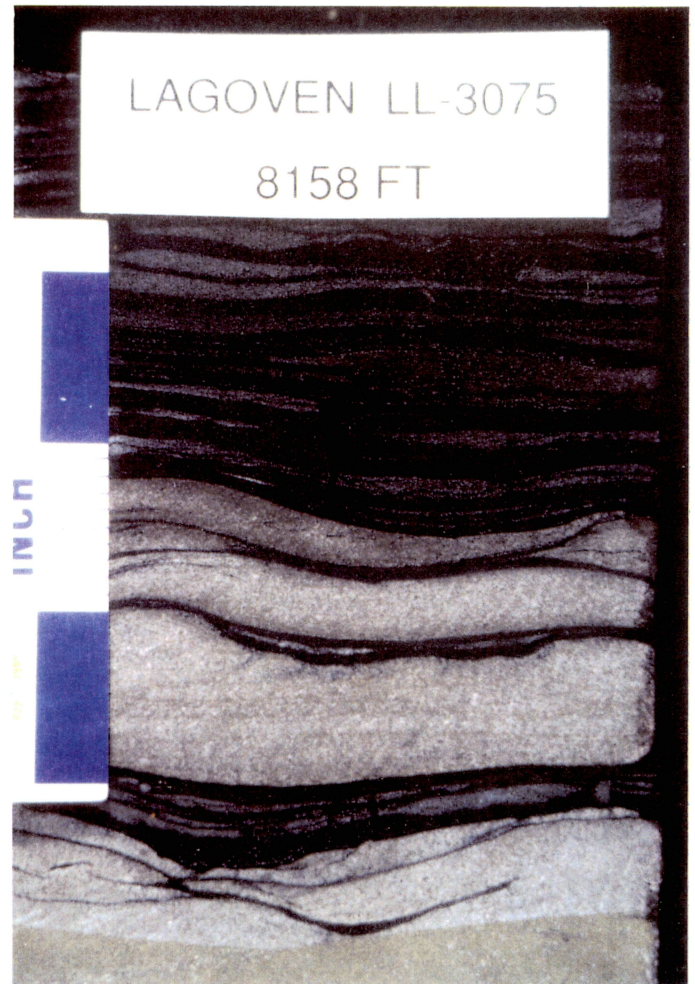


Figure V 13. Core photographs of the medial delta-front (tidal sand-ridge) facies in the Middle C-5-X Submember in the LL-3075 well. (a). Ripple-cross-stratified and laminated sandstones in the upper one-third of tidal sand-ridge and (b) symmetrical ripples at the crest of tidal sand-ridge, overlain by laminated, interridge siltstone. Core description is shown in figure V 12.

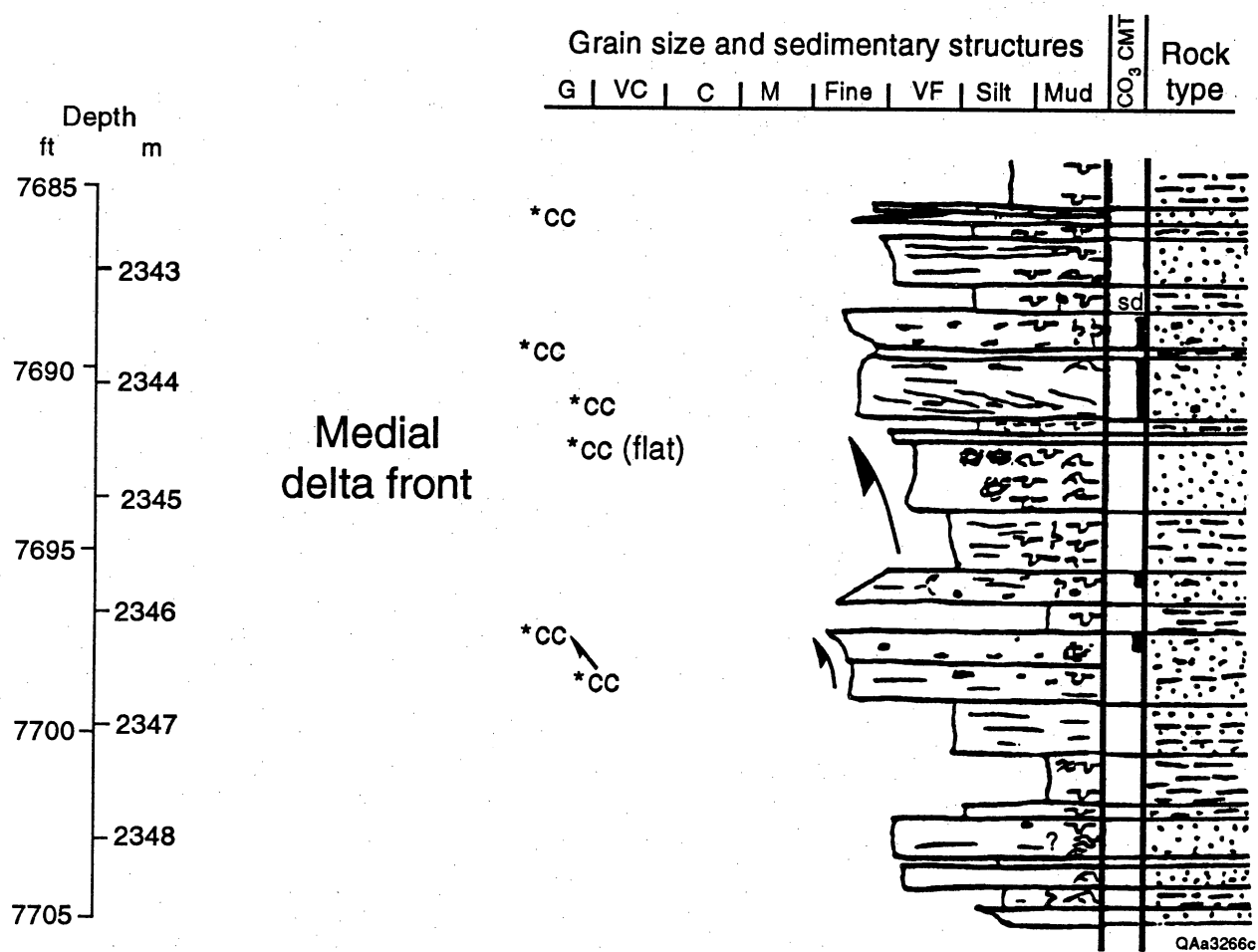


Figure V 14. Core description of medial delta-front facies in the Upper C-4-X Submember in the LL-2850 well. Photographs of burrowed siltstones and sandstones (7,694.5 and 7,692 ft respectively), are shown in figure V 15.

(a)



(b)



Figure V 15. Core photographs of medial delta-front facies in the Upper C-4-X Submember in the LL-2850 well. (a). Middle part of tidal sand-ridge deposit with Planolites burrows. (b). Upper part of tidal sand-ridge deposit with Ophiomorpha burrows. Core description is shown in figure V 14.

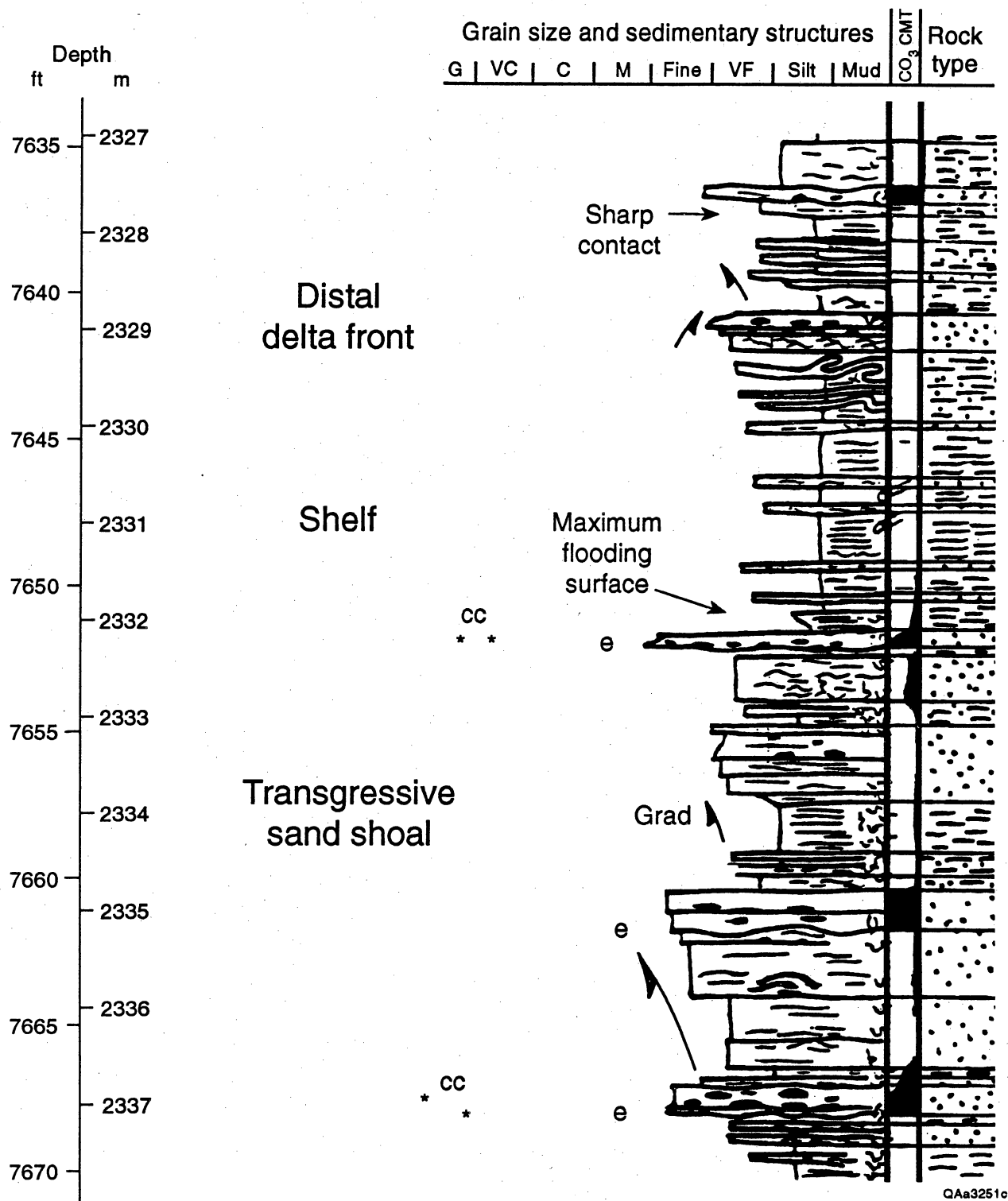


Figure V 16. Core description of distal delta-front facies in the Lower C-3-X Submember, overlying shelf and transgressive sand-shoal facies in the Upper C-4-X Submember in the LL-3074 well. Maximum flooding surface at 7,681 ft corresponds to boundary between C-3-X and C-4-X Members. Photograph of distal delta-front slump deposit (7,642 ft) is shown in figure V 17.

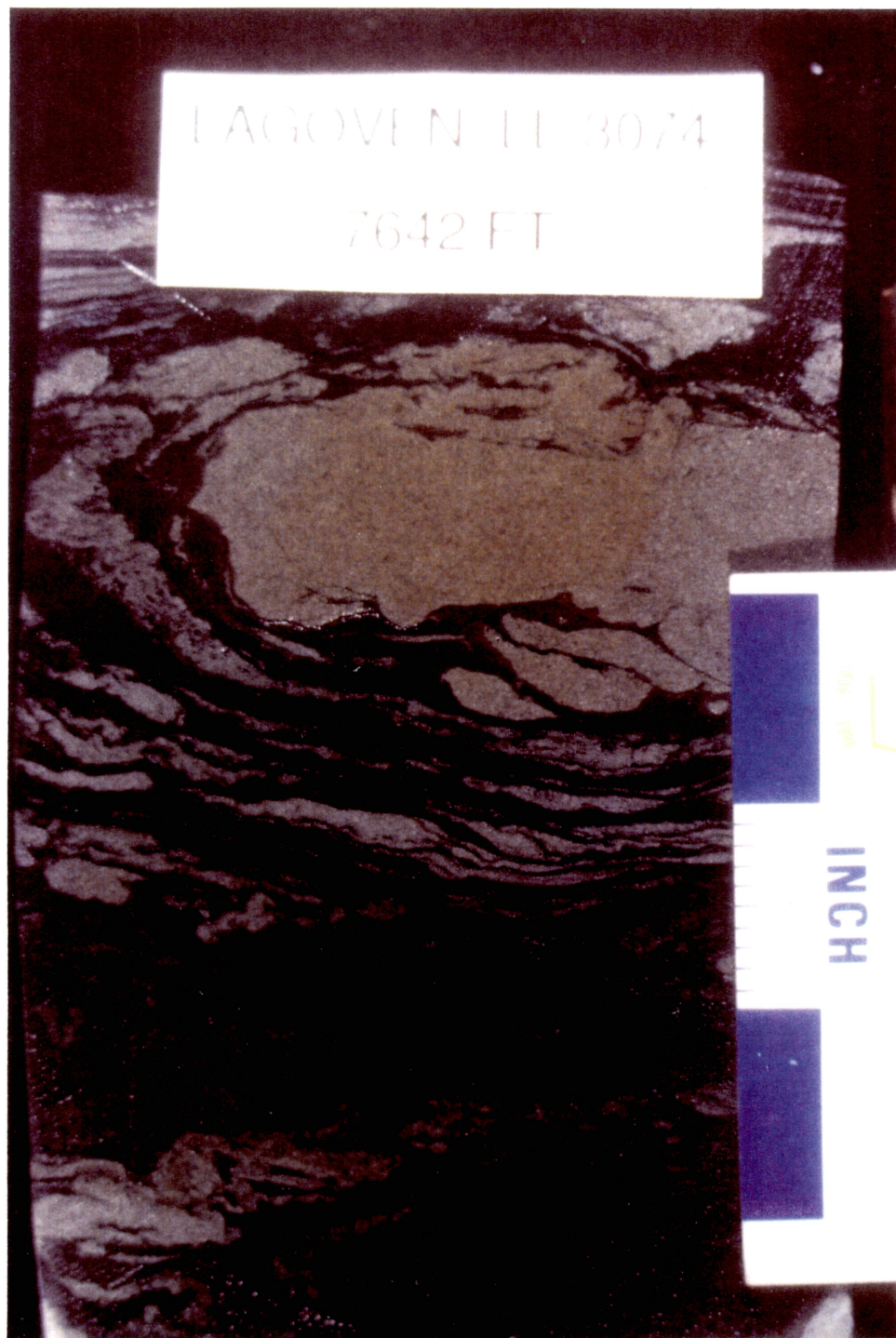


Figure V 17. Core photograph of slump deposits in distal delta-front facies in the Lower C-3-X Submember in the LL-3074 well. Core description is shown in figure V 16.

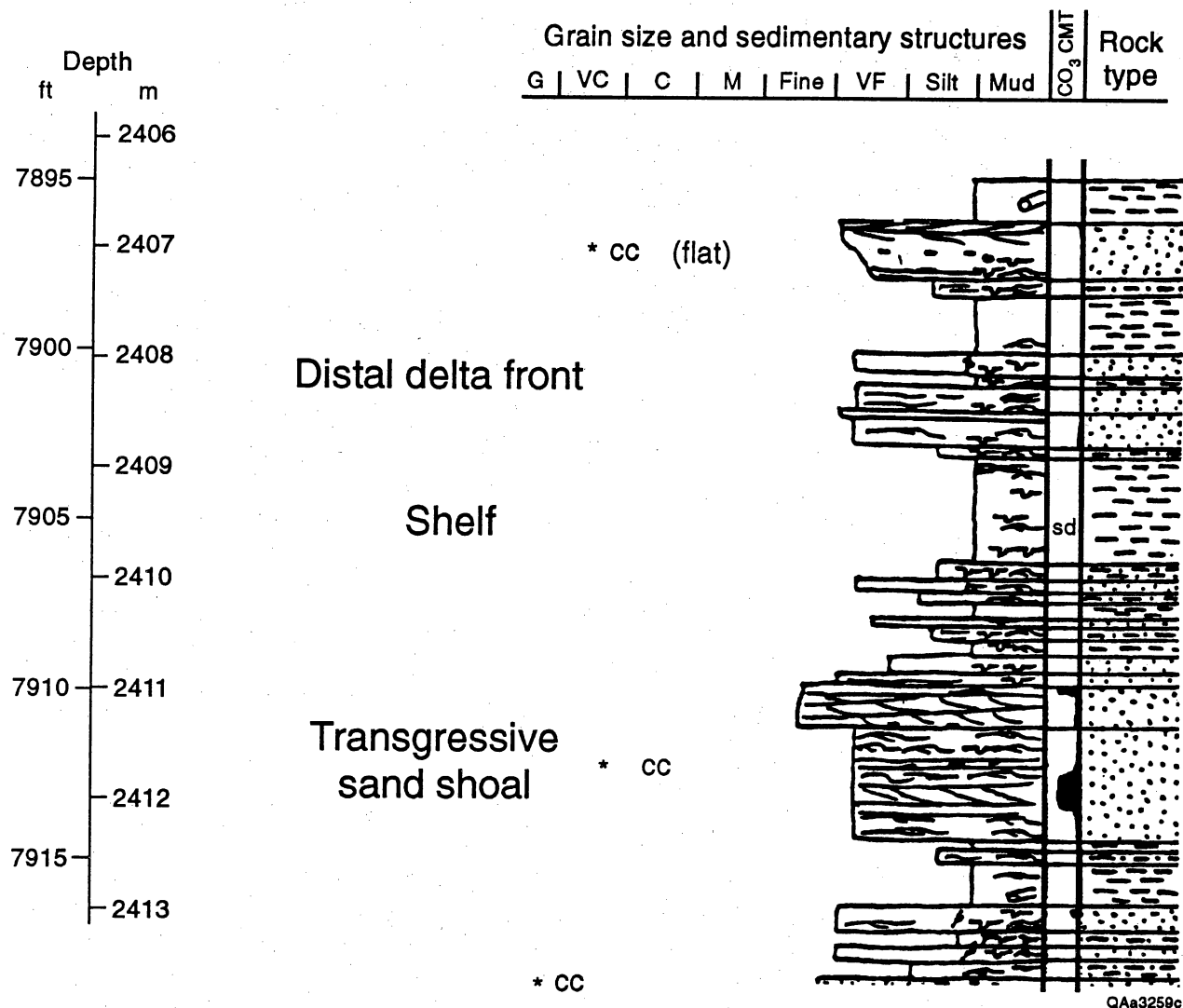


Figure V 18. Core description of distal delta-front facies in the Lower C-4-X Submember, overlying shelf and transgressive sand-shoal facies in the Upper C-5-X Submember in the LL-3075 well. Photograph of shale-draped, asymmetrical current ripples (7,901.5 ft) is shown in figure V 19.

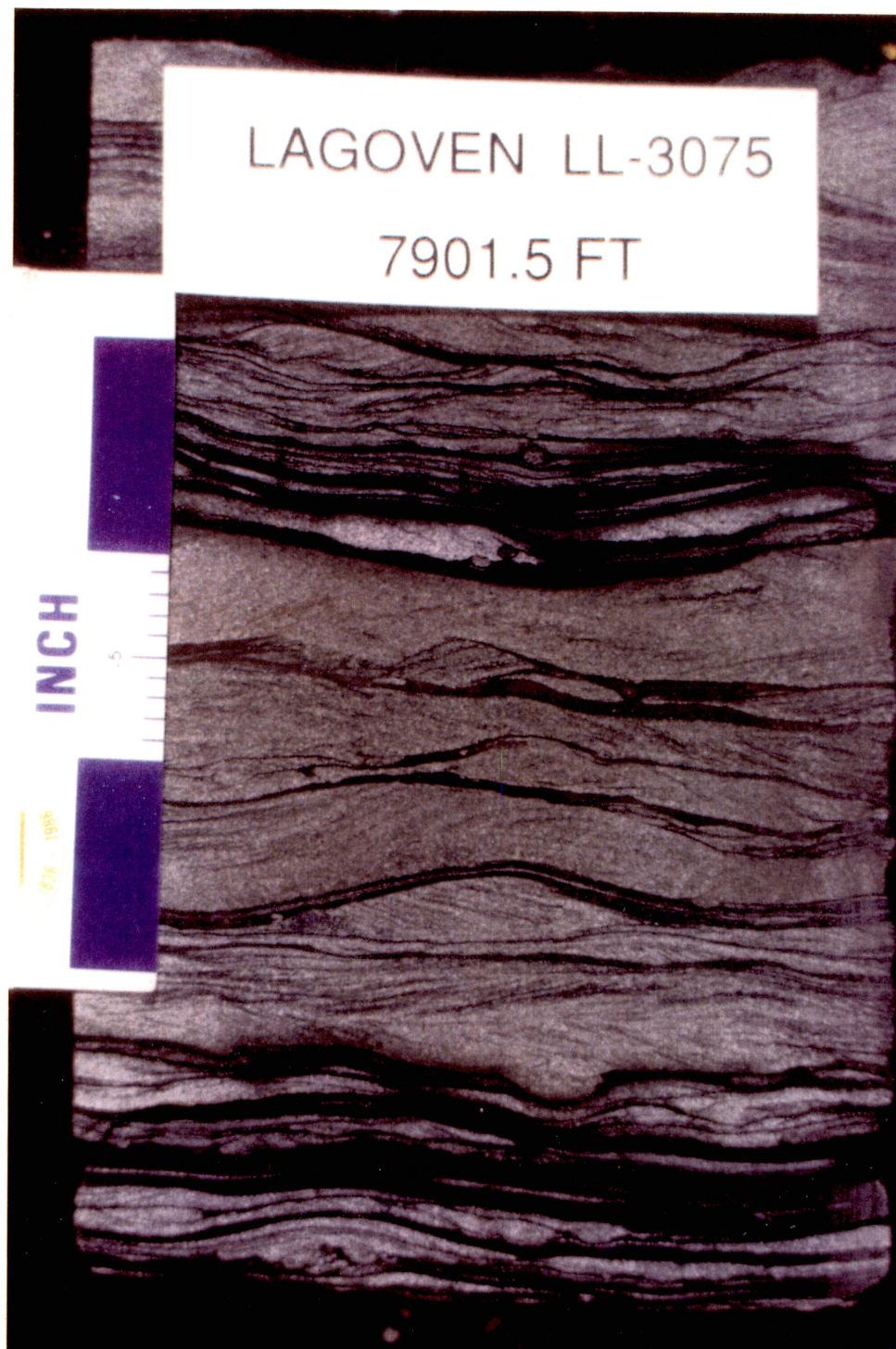


Figure V 19. Core photograph of asymmetrical, bi-directional ripples in distal delta-front facies in the Lower C-4-X Submember in the LL-3075 well. Core description is shown in figure V 18.

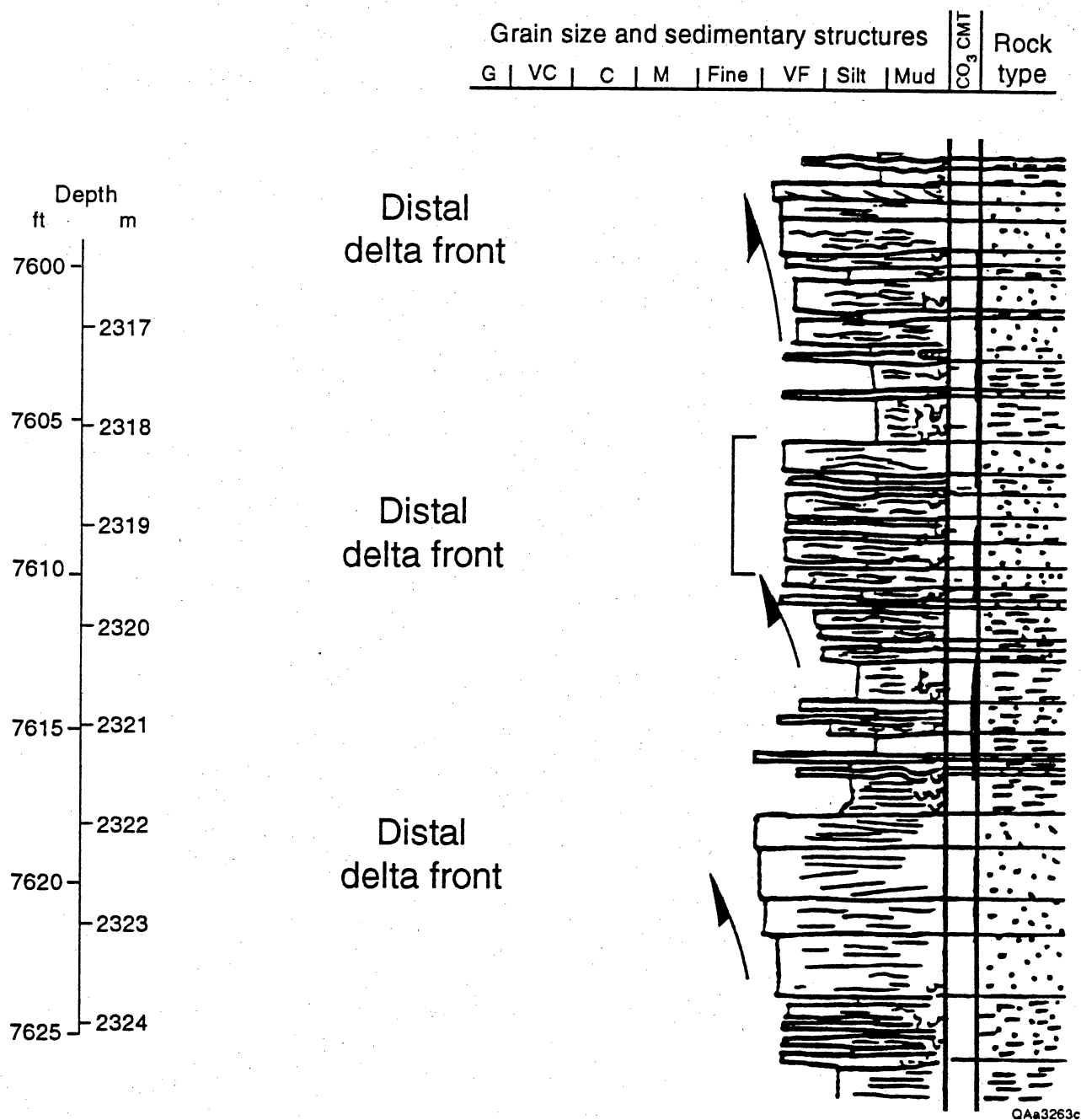


Figure V 20. Core description of multiple distal delta-front deposits in the Lower C-3-X Submember in the LL-3074 well. Individual deposits are upward-coarsening and 6 to 9 ft (1.8 to 2.7 m) thick and interbedded with mudstone.

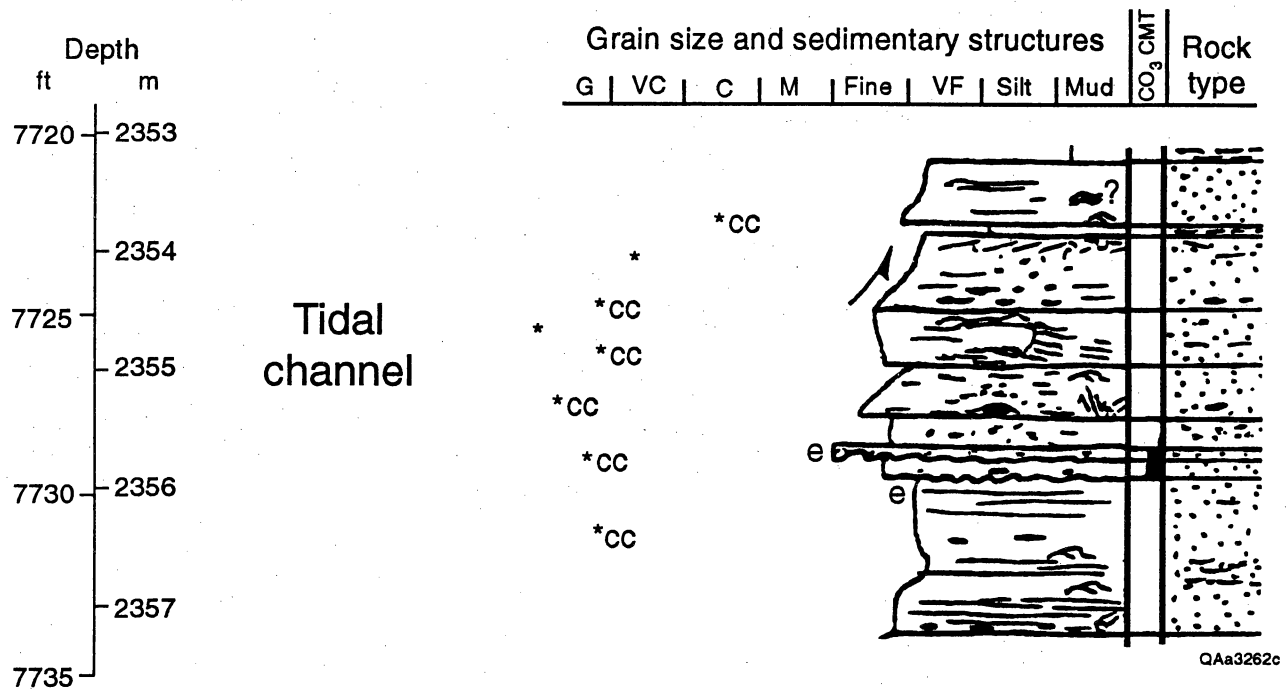


Figure V 21. Core description of tidal-channel facies in the Upper C-4-X Submember in the LL-2850 well. Photograph of channel-margin, bank-collapse deposits (7,726 ft) is shown in figure V 22.

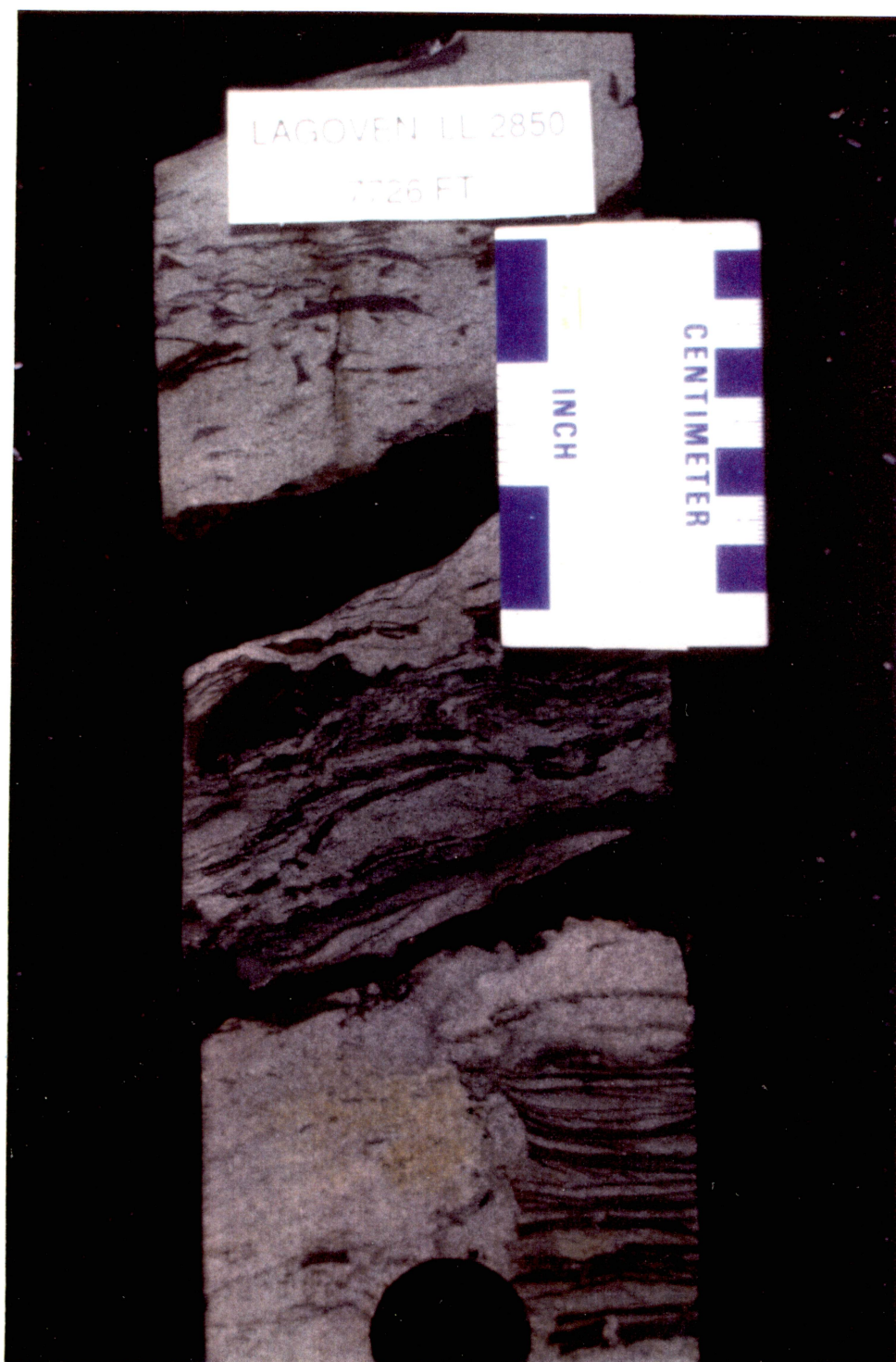


Figure V 22. Core photograph of clay clasts and channel-bank collapse material in a tidal-channel deposit in the Upper C-4-X Submember in the LL-2850 well. Core description is shown in figure V 21.

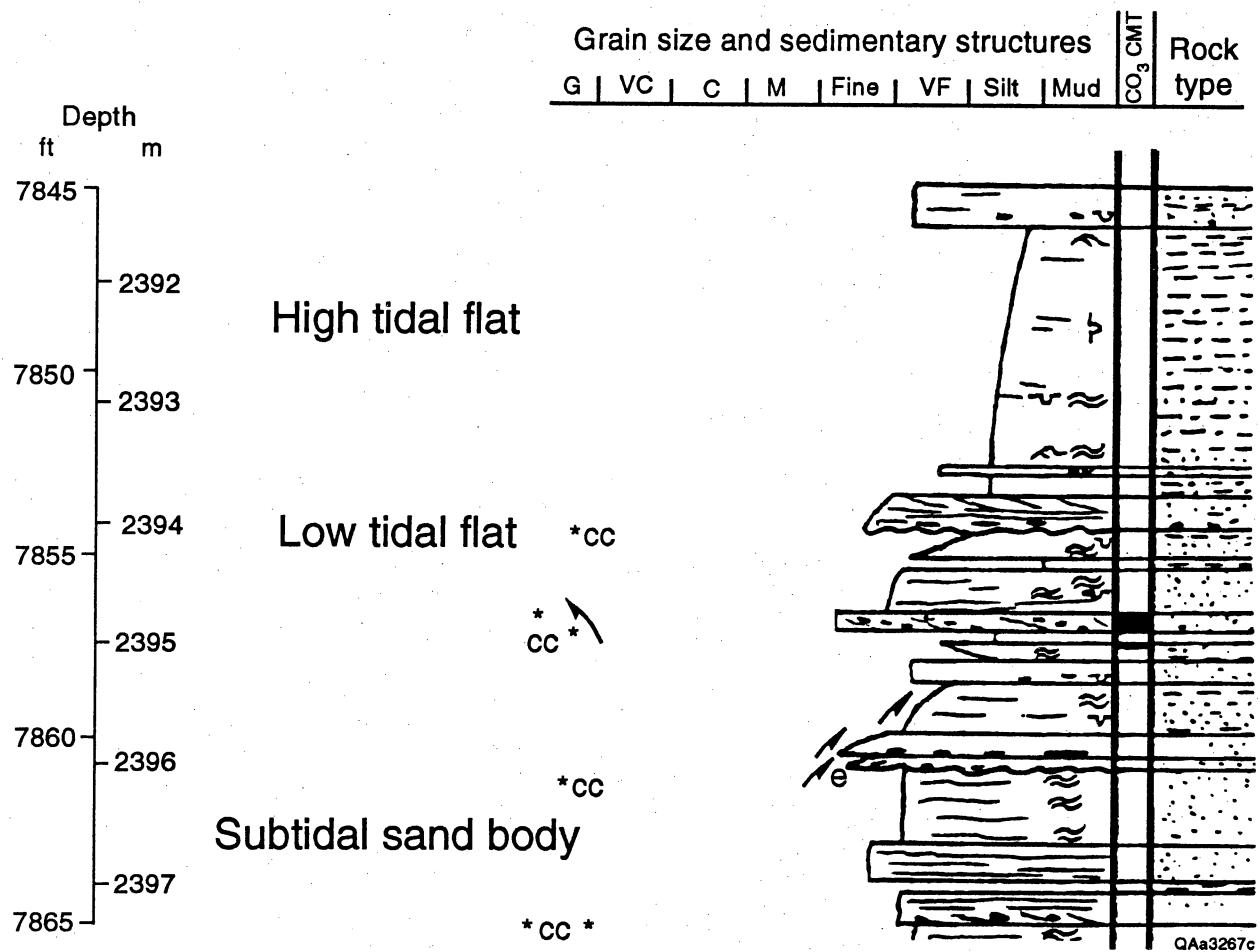


Figure V 23. Core description of progradational tidal-flat facies in the Middle C-4-X Submember in the LL-2850 well. Photograph of mud-draped ripple beds (7,852 ft) is shown in figure V 24.



Figure V 24. Core photograph of asymmetrical flaser ripples in tidal-flat facies in the Middle C-4-X Submember in the LL-2850 well. Core description is shown in figure V 23.



Figure V 25. Core photograph of erosional surface overlain by shells and clay clasts in transgressive sand-shoal facies in the Upper C-4-X Submember in the LL-3074 well. Core description is shown in figure V 16.

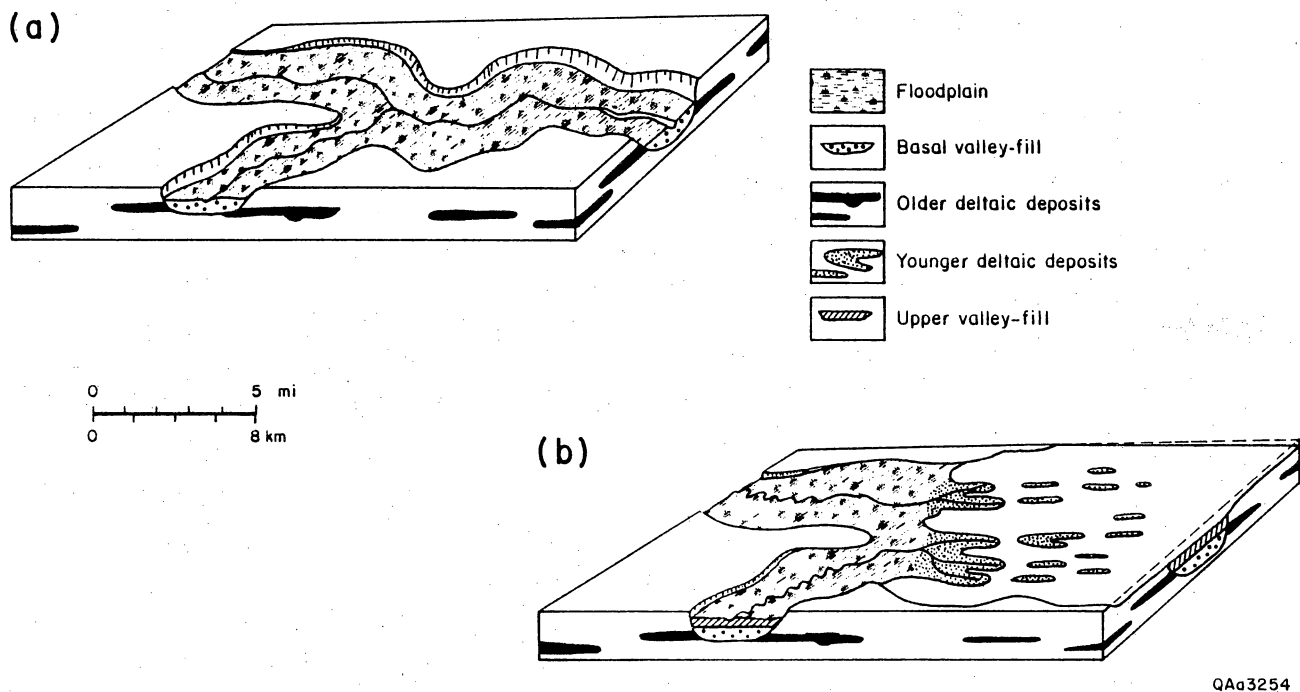
(a)



(b)



Figure V 27. Core photographs of (a) stylolitic limestone in transgressive sand-shoal facies and (b) lensoid beds and starved ripples in mudstone in shelf facies at the top of the Middle C-3-X Submember in the LL-3074 well. Core description is shown in figure V 26.



QAa3254

Figure V 28. Schematic block diagram of (a) low-stand, entrenched paleovalley system with subsequent rise in sea level resulting in deposition of a high-stand, tidally influenced deltaic system in an embayment. Unconformity corresponds to base of C-6-X Member in the LL-652 area.

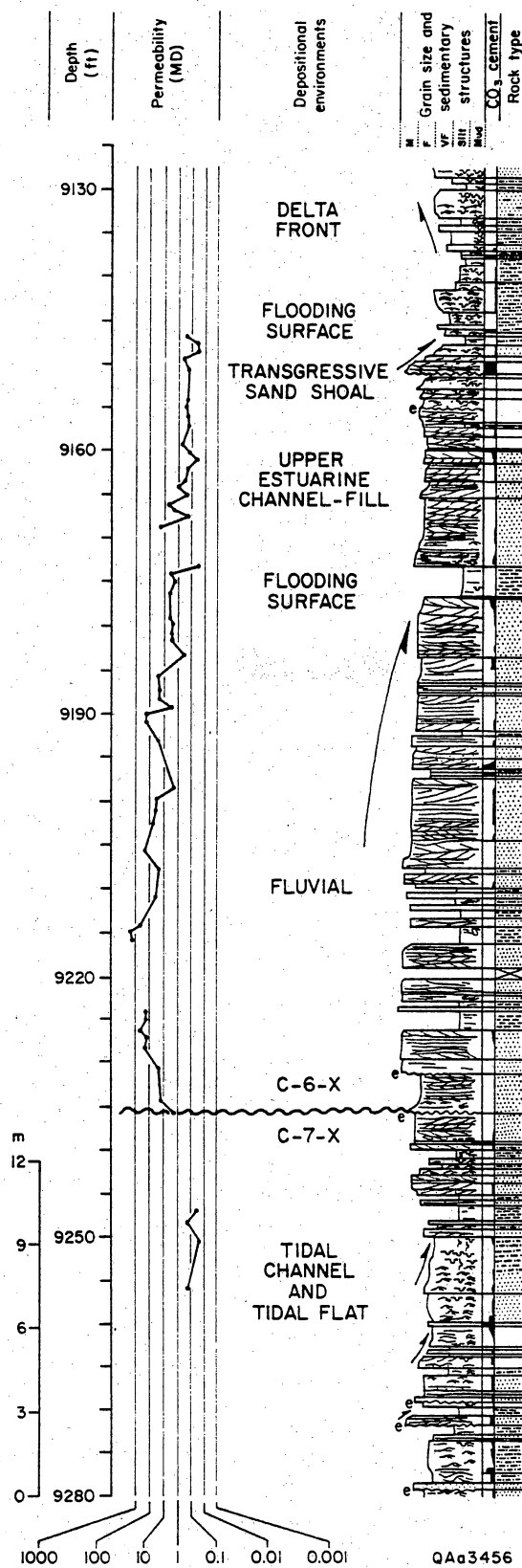


Figure V 30. Core description of fluvial-estuarine channel, upper estuarine channel-fill, and transgressive sand-shoal facies in the Lower Lower C-6-X Submember in the LL-3080 well. Permeability decreases upward in the sequence.

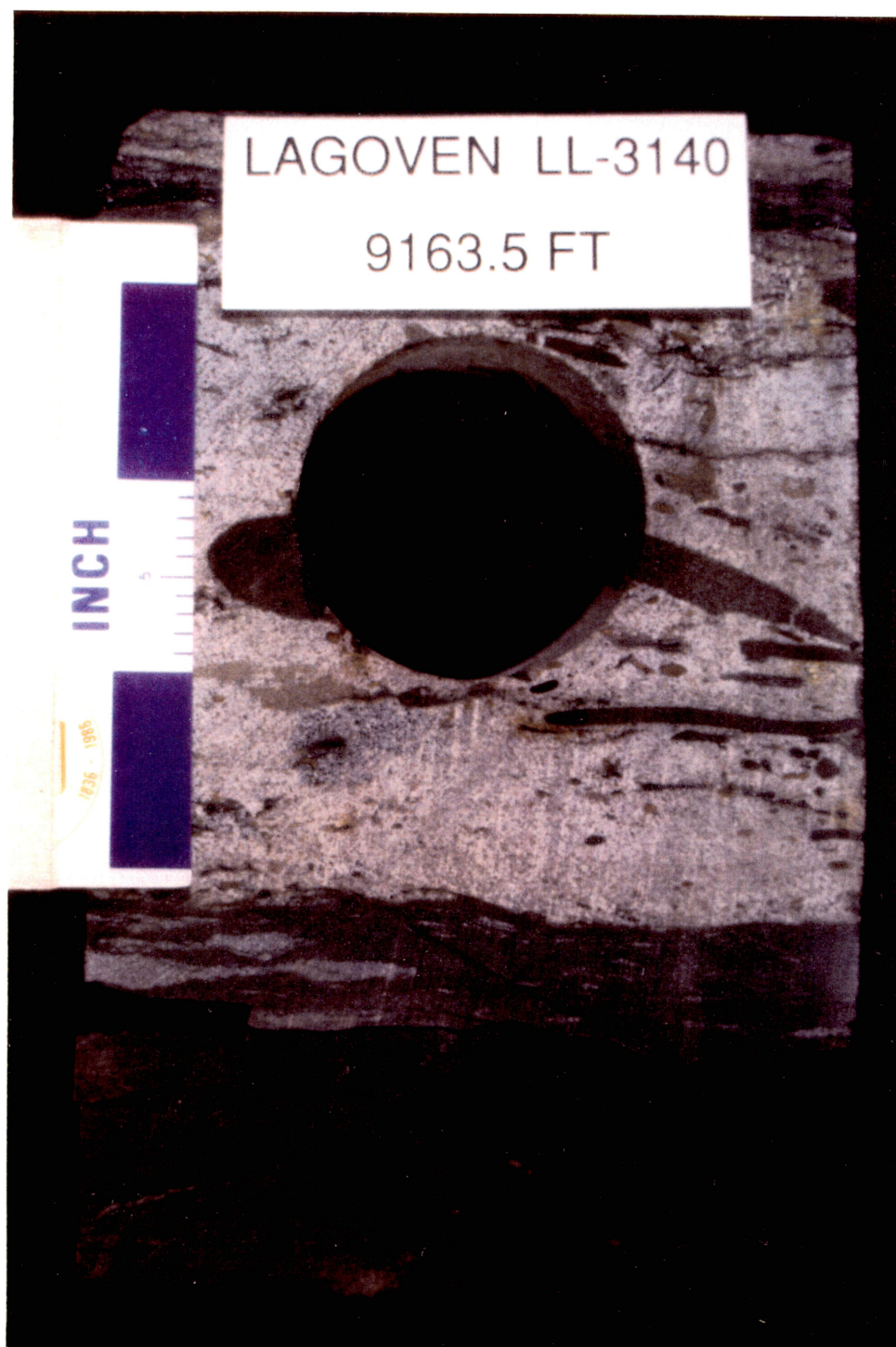


Figure V 31. Core photograph of basal part of fluvial-estuarine channel facies (C-6-X Member) that truncates muddy delta-front facies (C-7-X Member) in the LL-3140 well. Core description is shown in figure V 35.

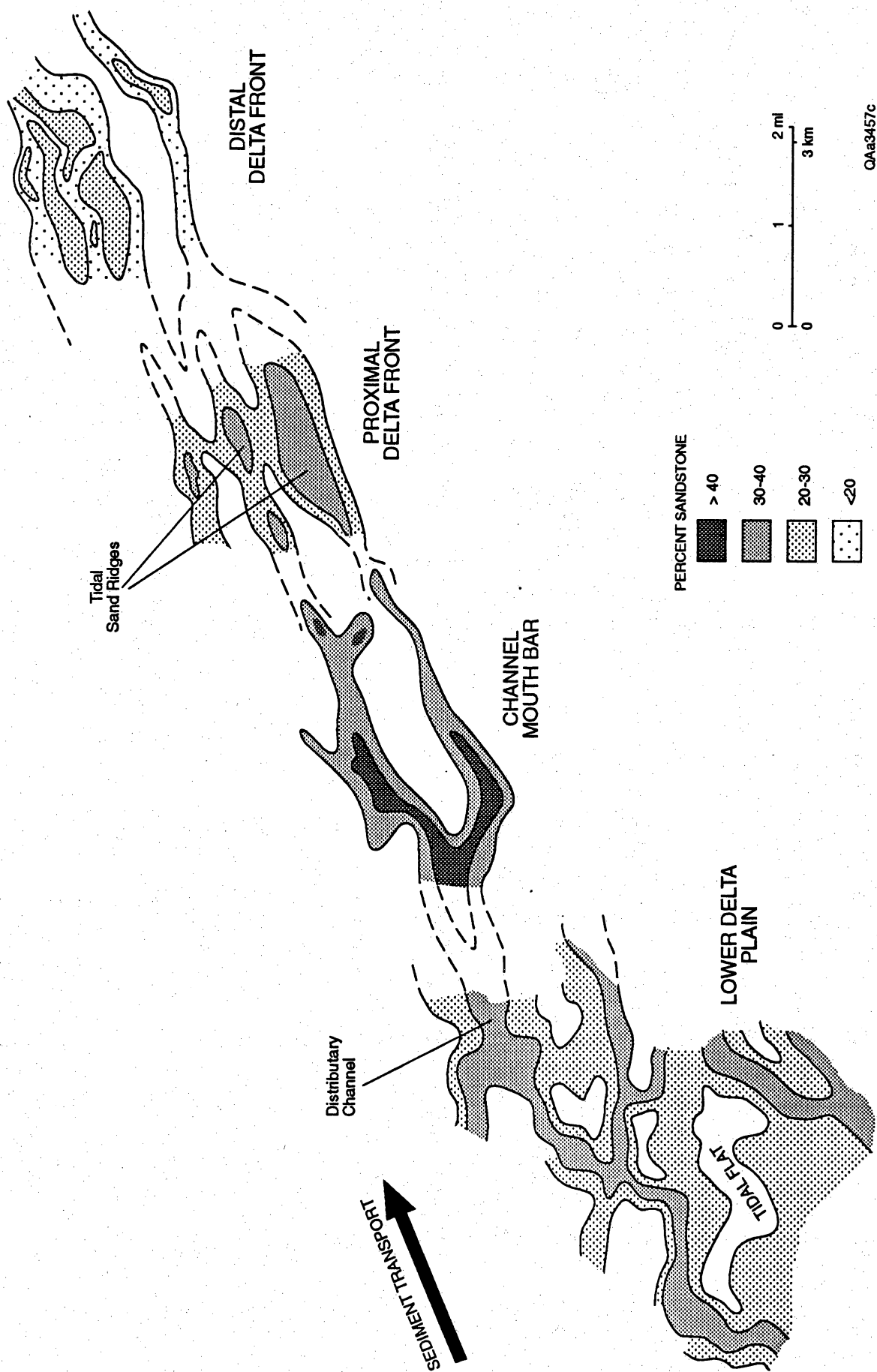


Figure V 32. Relative percent-sandstone values in the tide-dominated deltaic facies tract in the C Members in the LL-652 area. The sandiest part of the deltaic system is the channel-mouth bar and proximal delta-front. Percent-sandstone patterns are from maps of representative C Submembers: lower delta plain (Middle C-4-X Submember), channel-mouth bar (#4 Unit in Upper C-4-X Submember), proximal delta-front (Lower Middle C-5-X Submember), and distal delta-front (Lower C-3-X Submember).

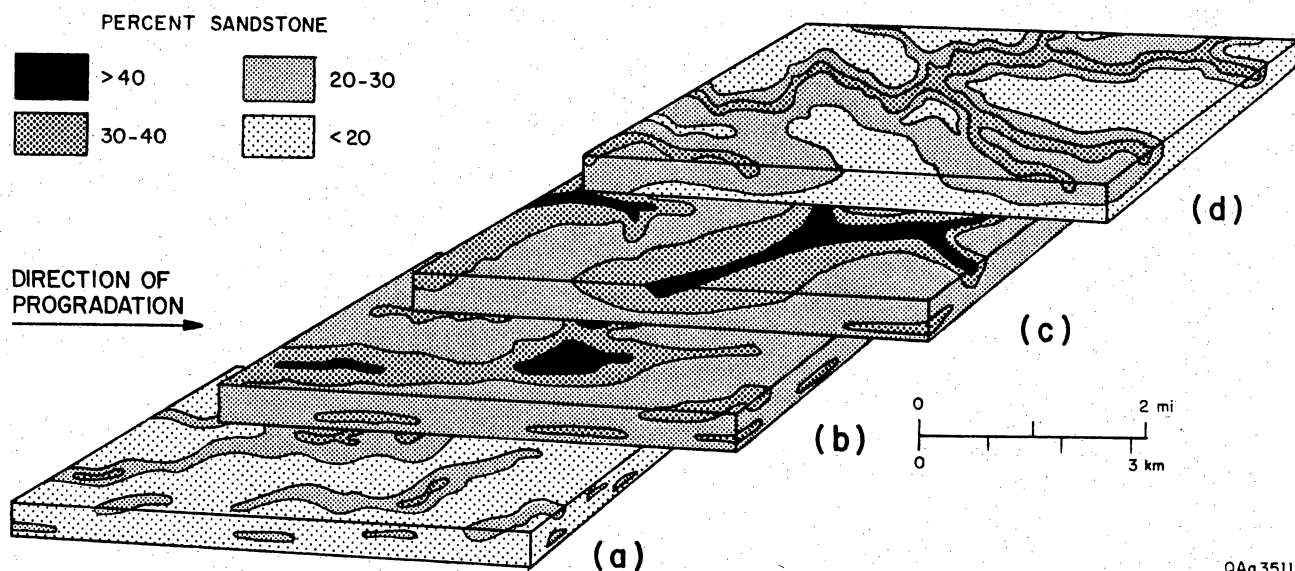


Figure V 33. Typical percent-sandstone patterns in offlapping, progradational sequences in the tide-dominated deltaic facies tract in the C Members in the LL-652 area, showing superposition and basinward progradation of (a) distal delta-front, (b) proximal delta-front, (c) distributary-channel and channel-mouth bar, overlain by (d) lower delta-plain facies. The sandiest part of the facies tract is the distributary-channel and channel-mouth bar.

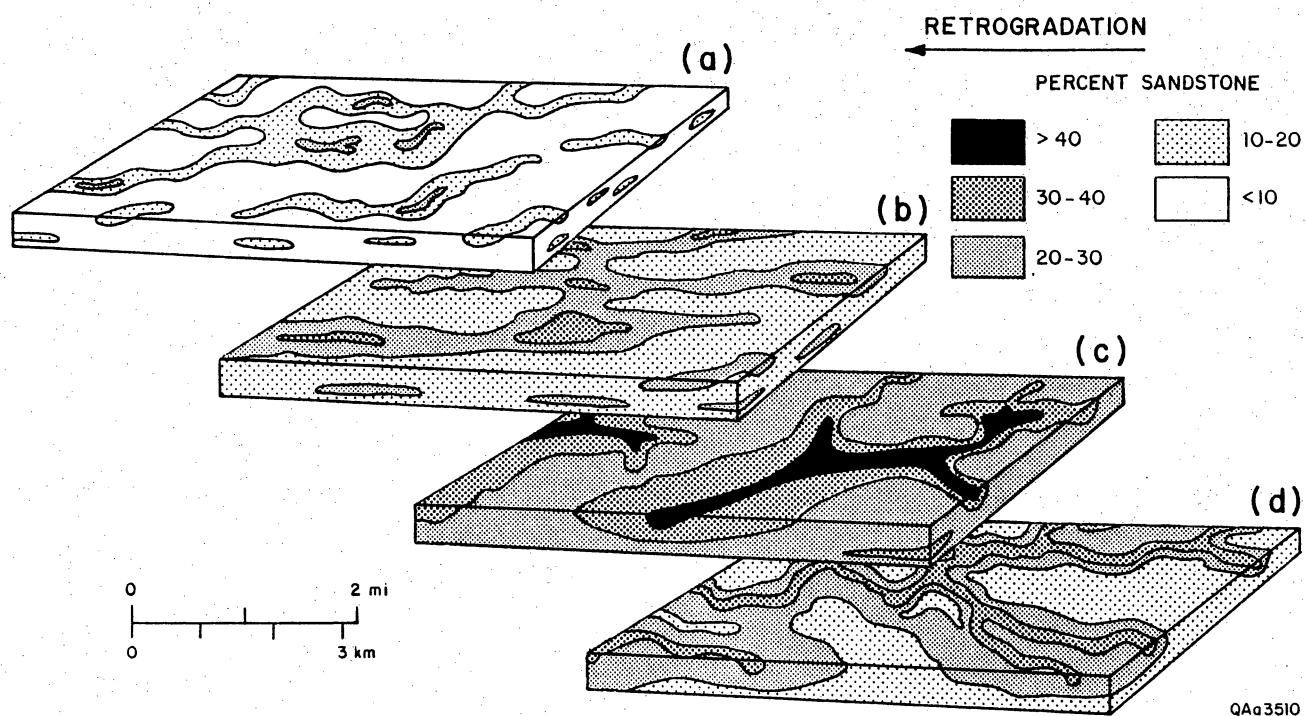


Figure V 34. Typical percent-sandstone patterns in retrogradational sequences in the tide-dominated deltaic facies tract in the C Members in the LL-652 area. The sandiest part of the facies tract is the distributary-channel and channel-mouth bar, whereas both the proximal and distal delta-front are sandstone-poor.

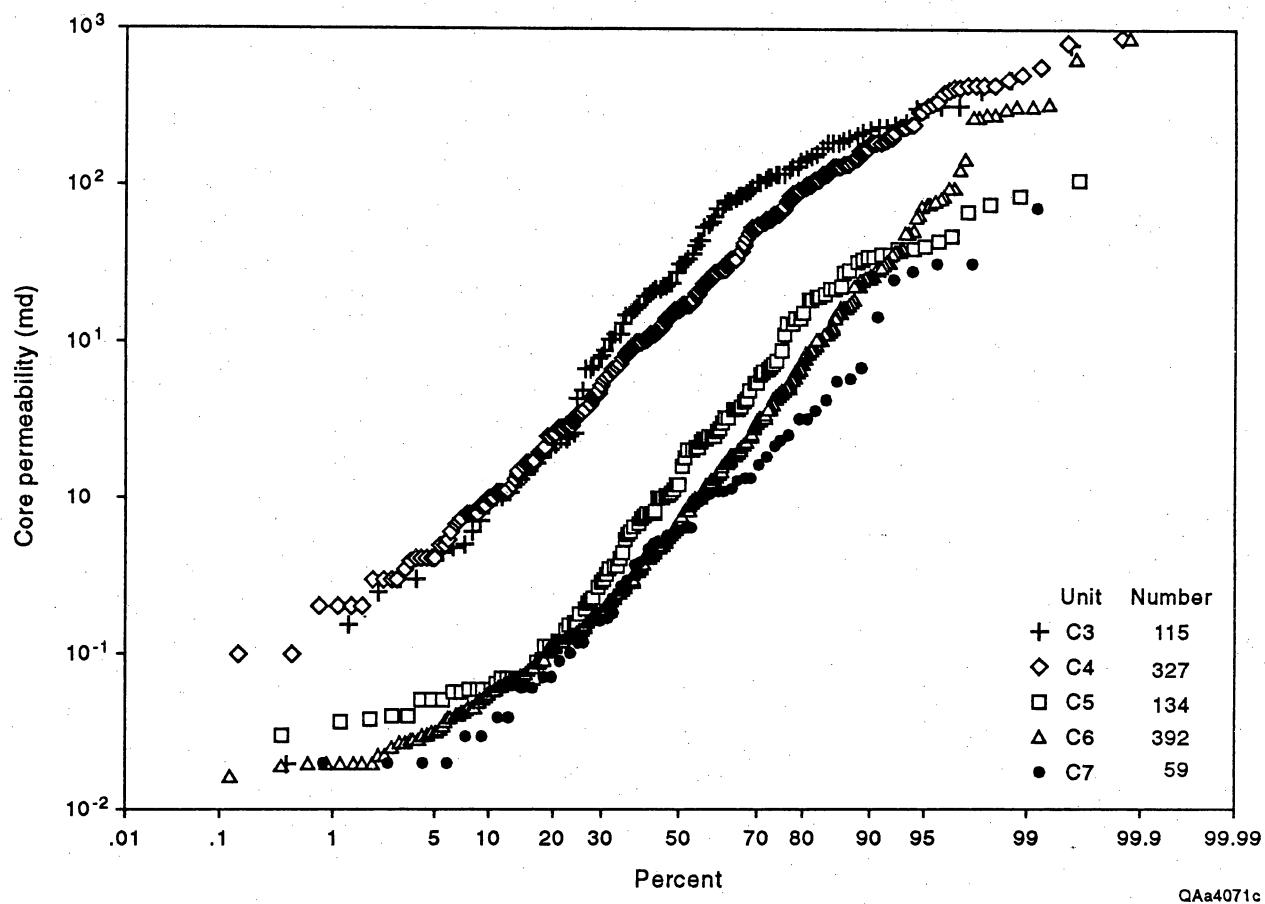


Figure V 35. Cumulative frequency plot of whole-core permeability in the C-3-X to C-7-X Members in the LL-652 area.

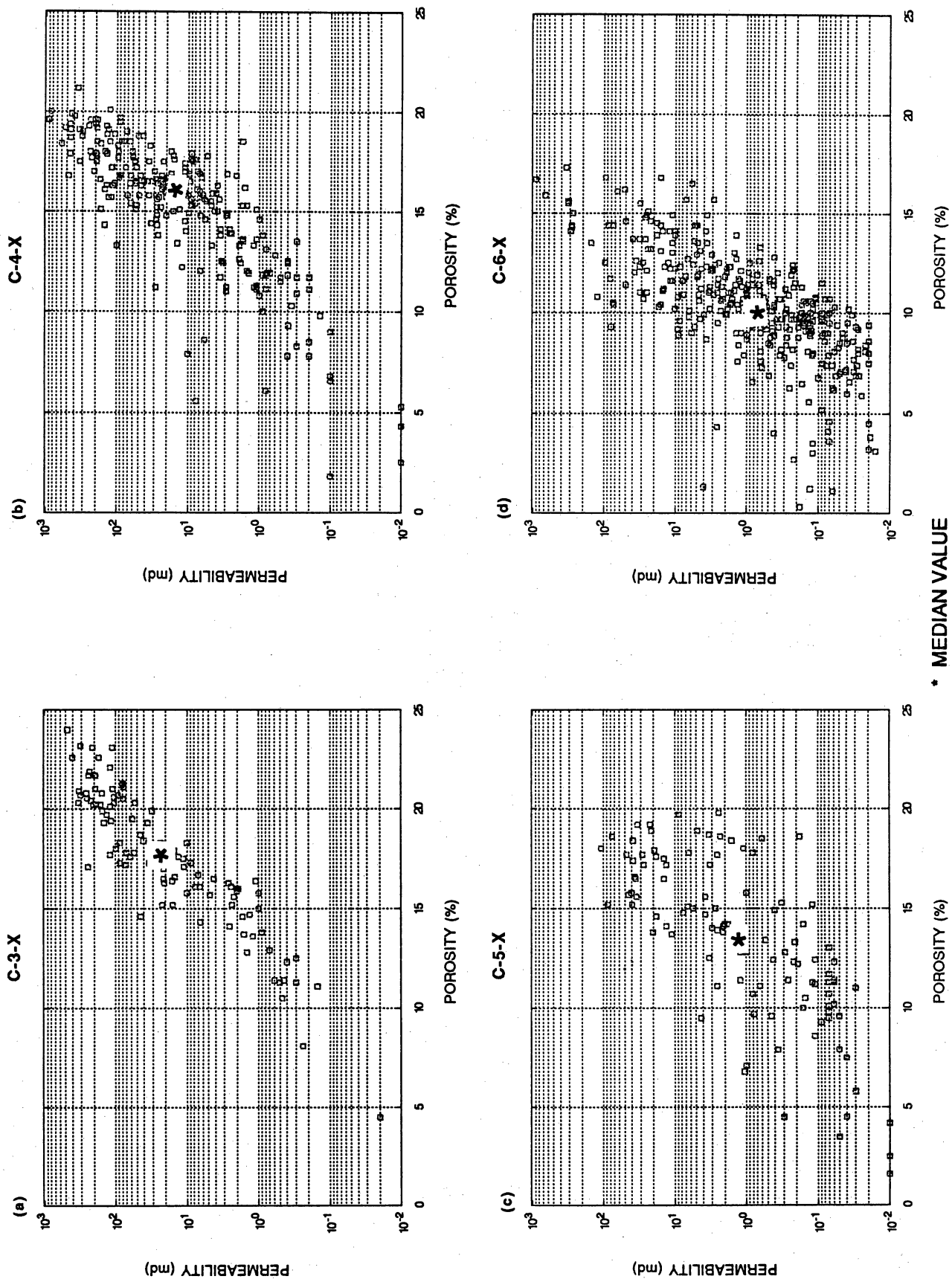


Figure V 36. Permeability-porosity crossplots of the C-3-X to C-7-X Members in the LL-652 area, showing range and median values.

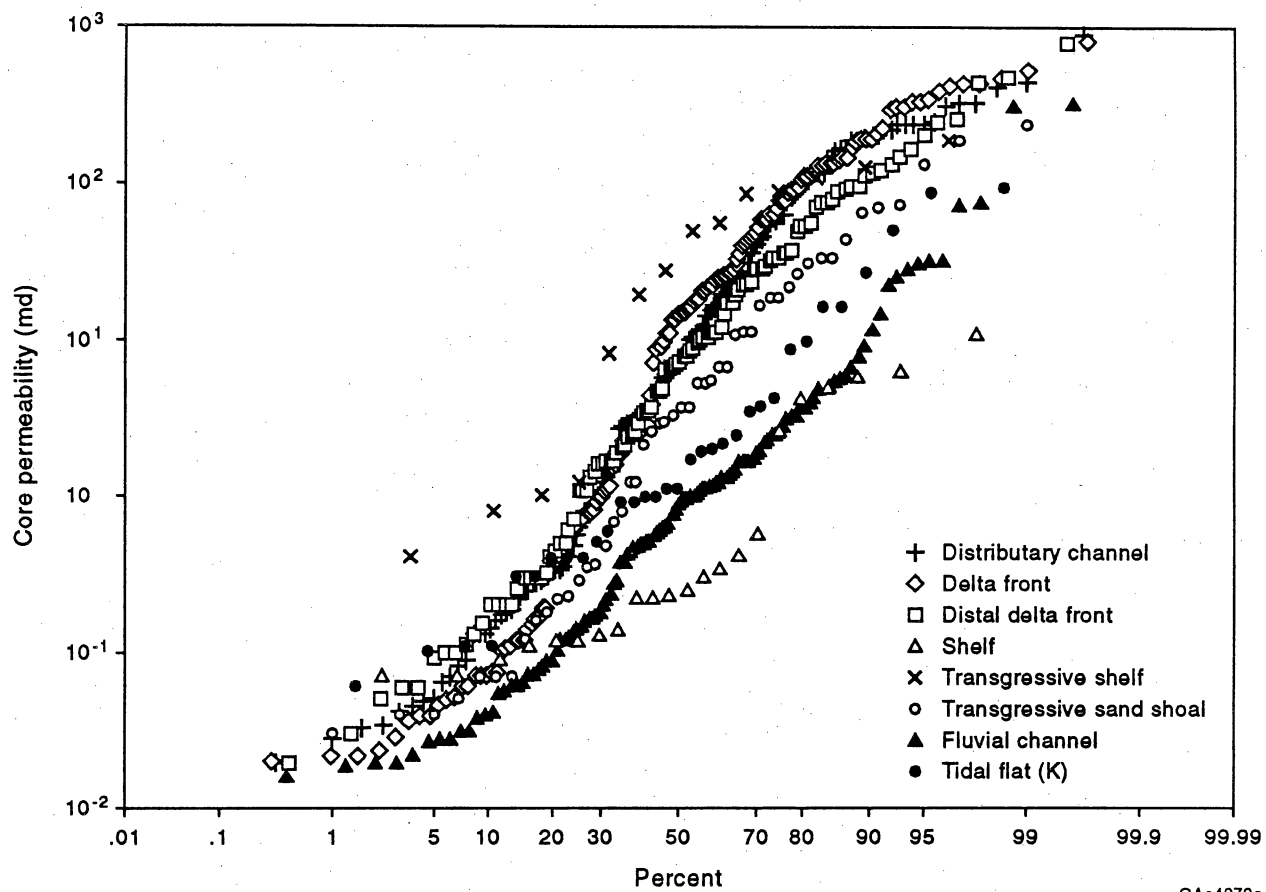
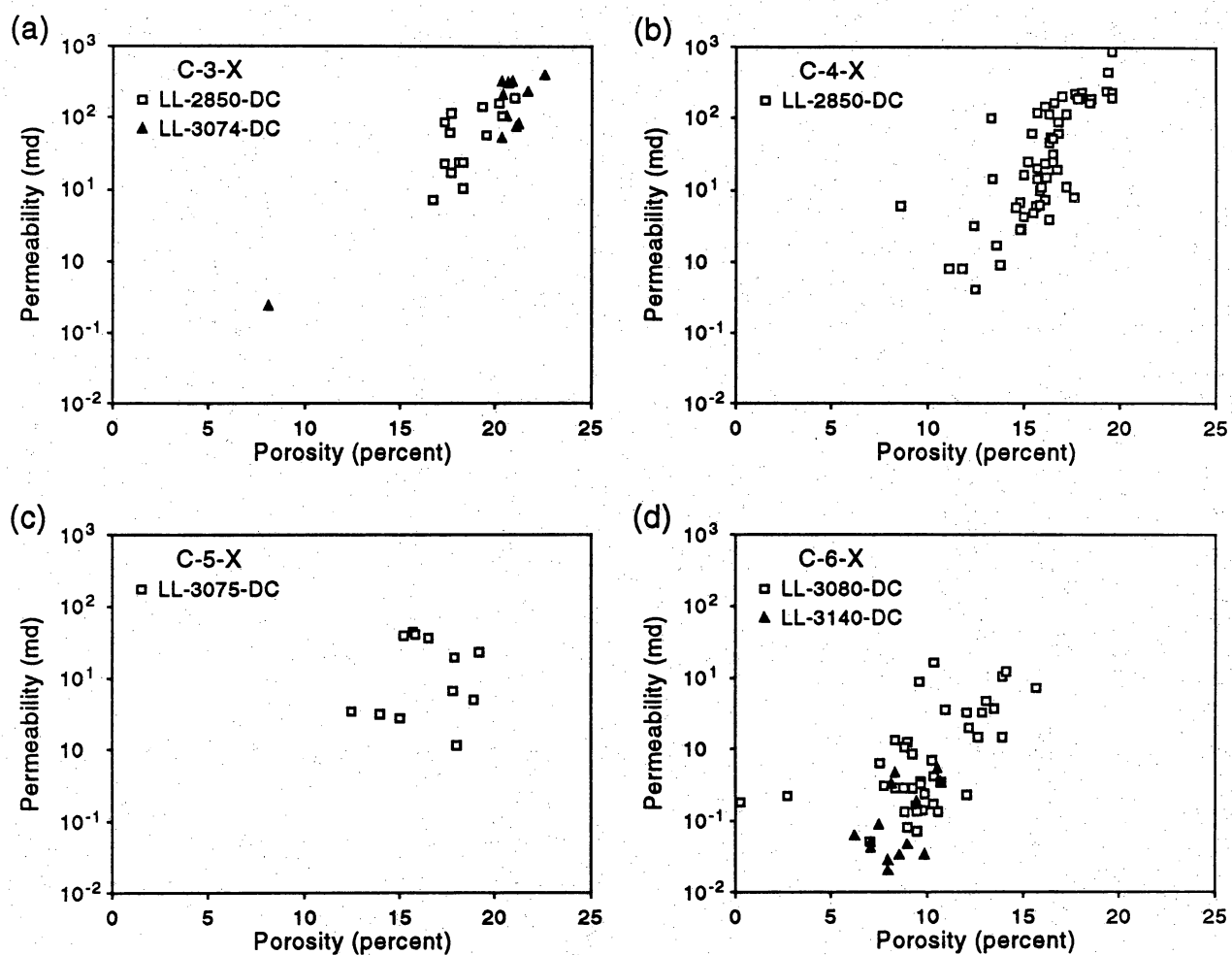


Figure V 37. Cumulative frequency plot of facies permeability in the C-3-X to C-7-X Members in the LL-652 area.



QAa4058c

Figure V 38. Permeability-porosity crossplots of distributary-channel facies per member. Data from whole-core analysis.

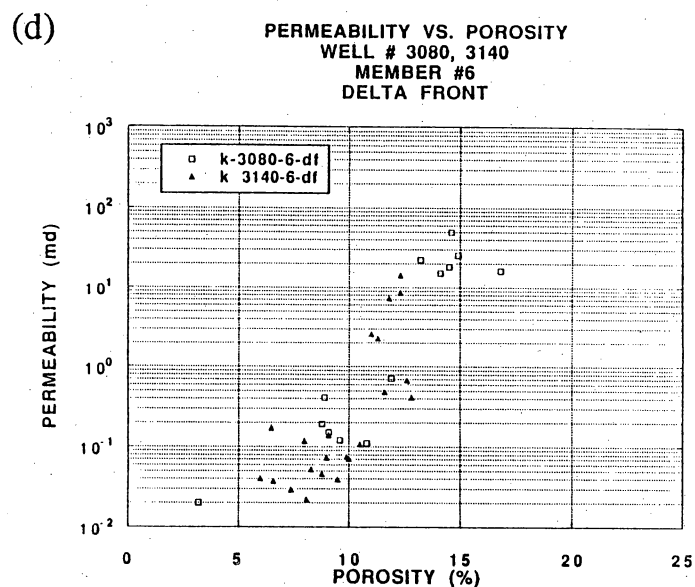
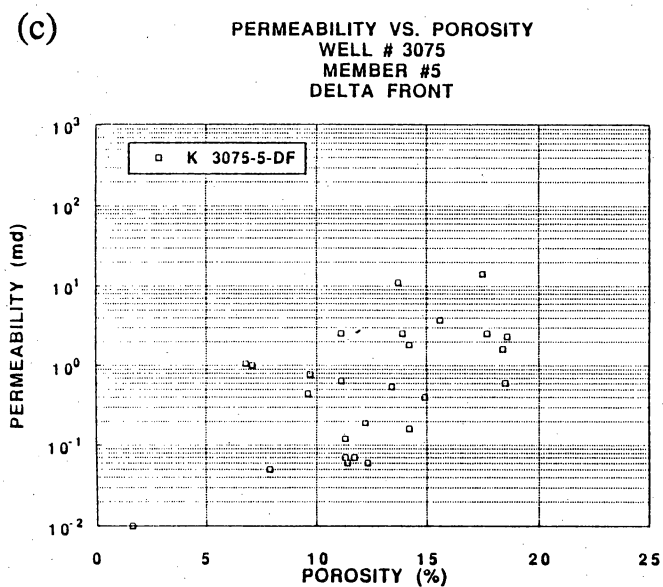
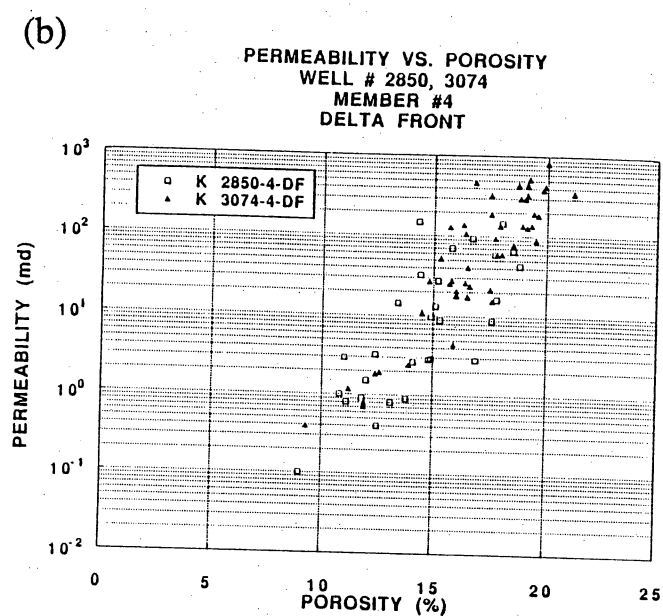
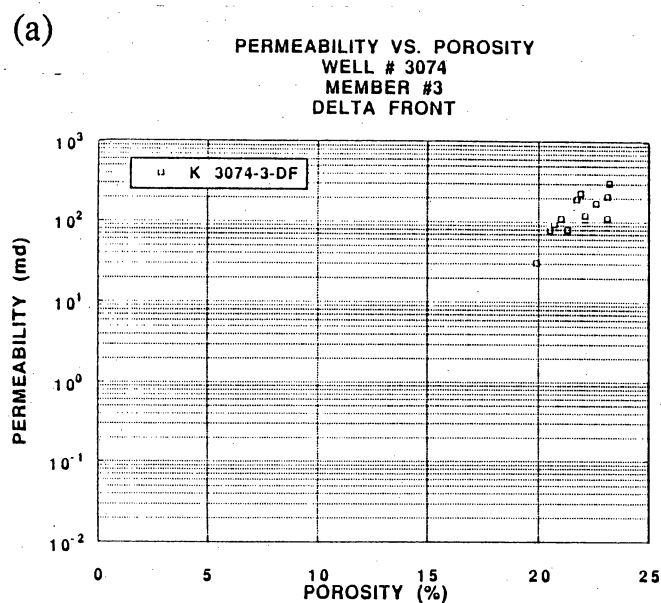
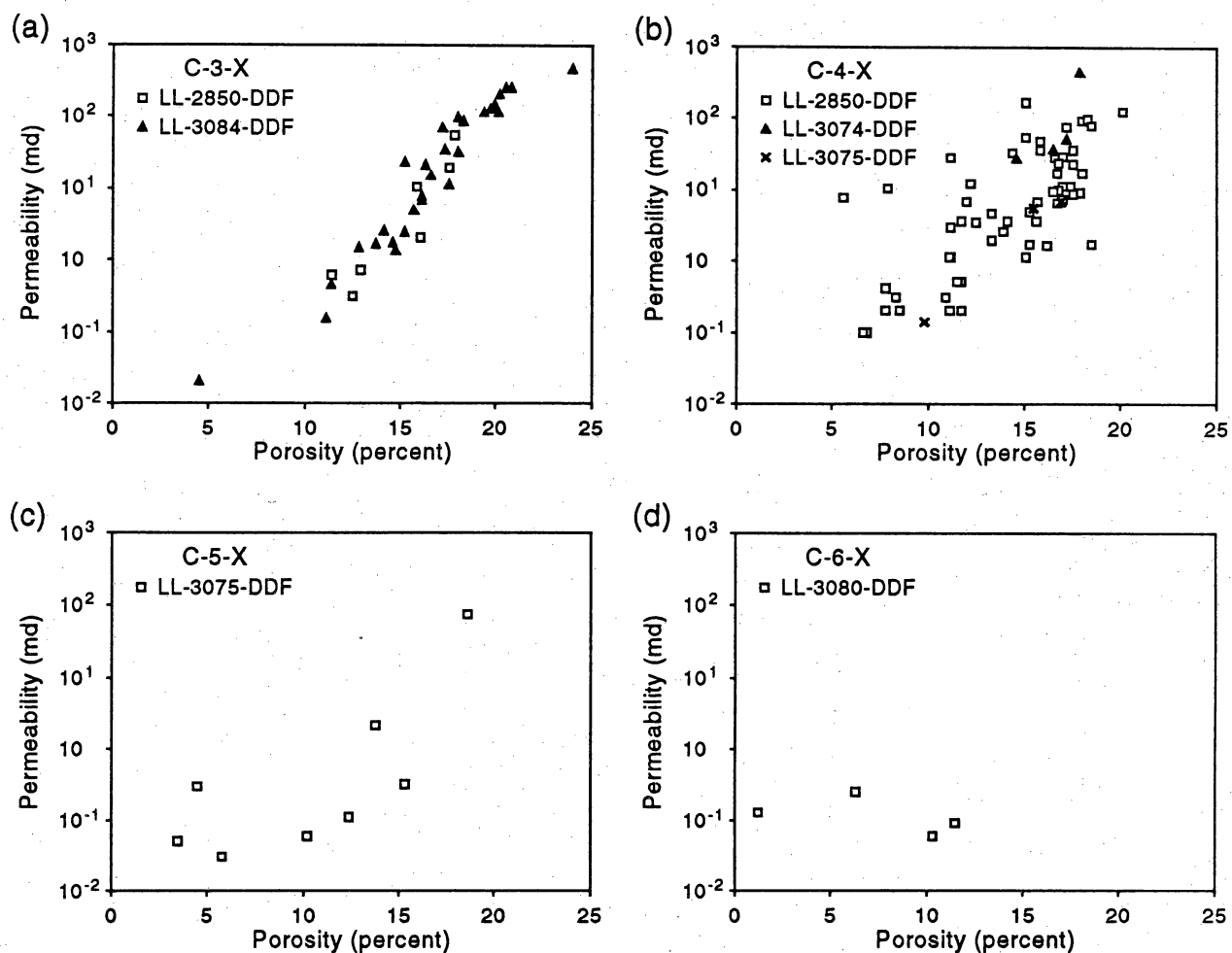
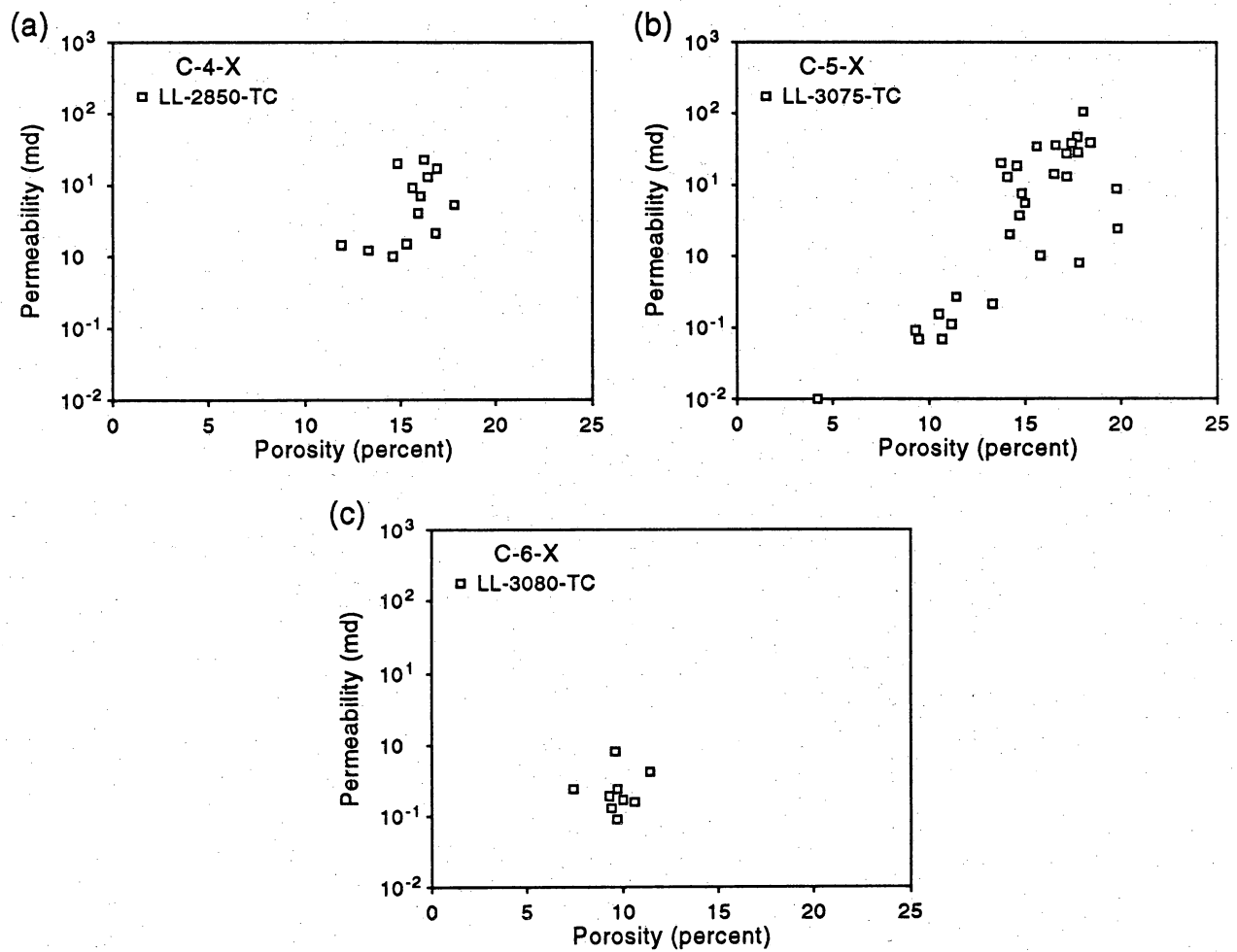


Figure V 39. Permeability-porosity crossplots of delta-front facies per member. Data from whole-core analysis.



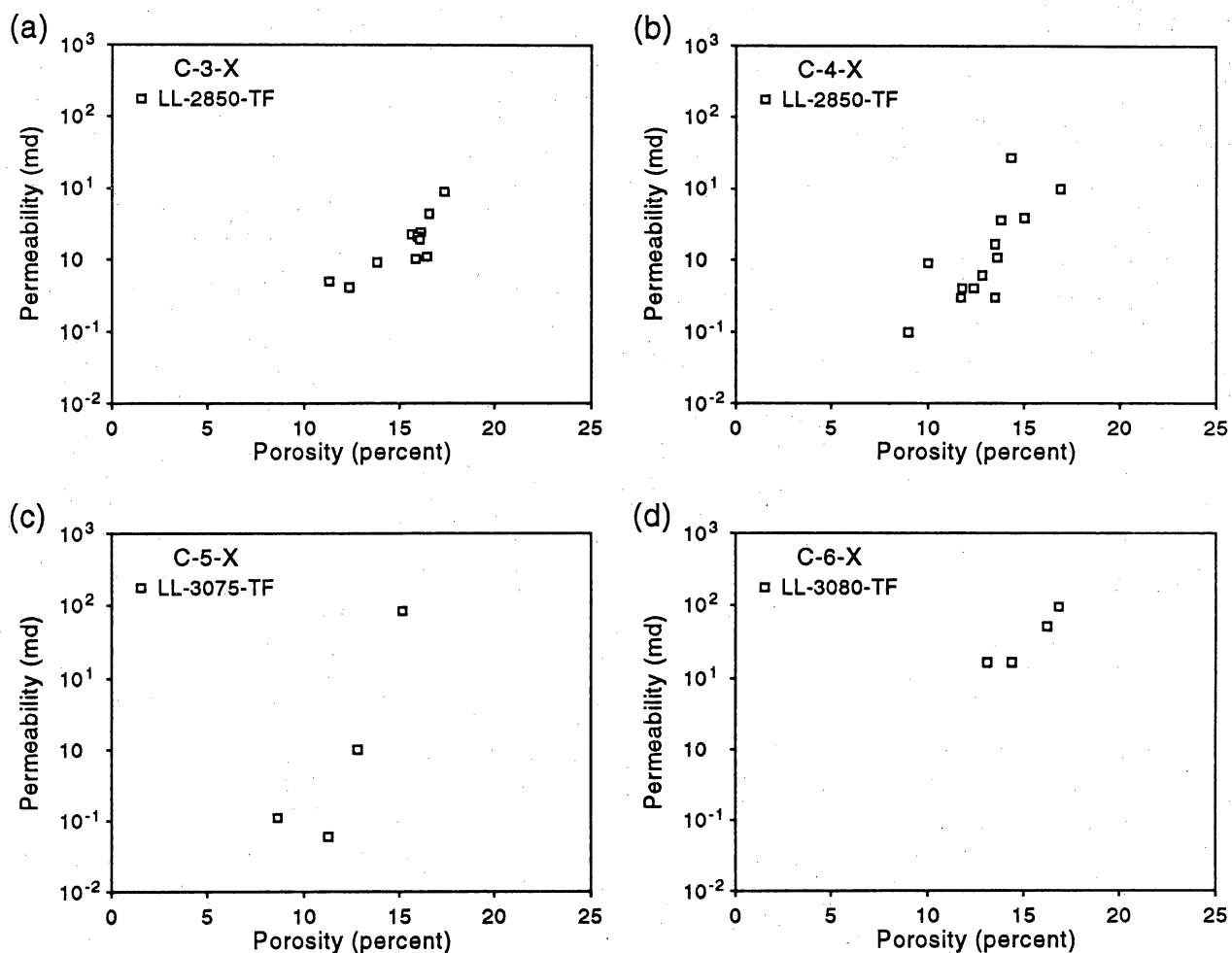
QAa4062c

Figure V 40. Permeability-porosity crossplots of distal delta-front facies per member. Data from whole-core analysis.



QAa4066c

Figure V 41. Permeability-porosity crossplots of tidal-channel facies per member. Data from whole-core analysis.



QAa4063c

Figure V 42. Permeability-porosity crossplots of tidal-flat facies per member. Data from whole-core analysis.

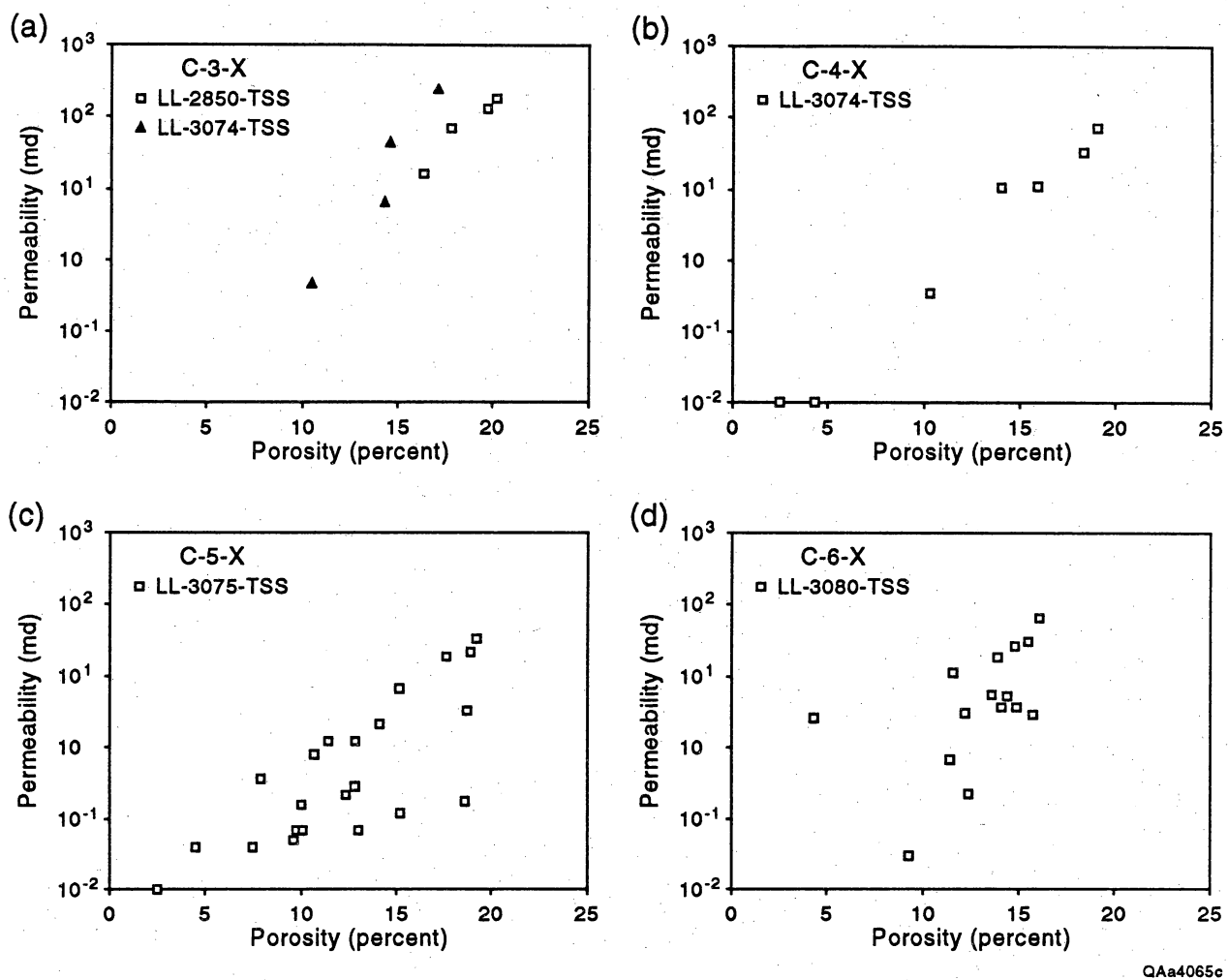


Figure V 43. Permeability-porosity crossplots of transgressive sand-shoal facies per member. Data from whole-core analysis.

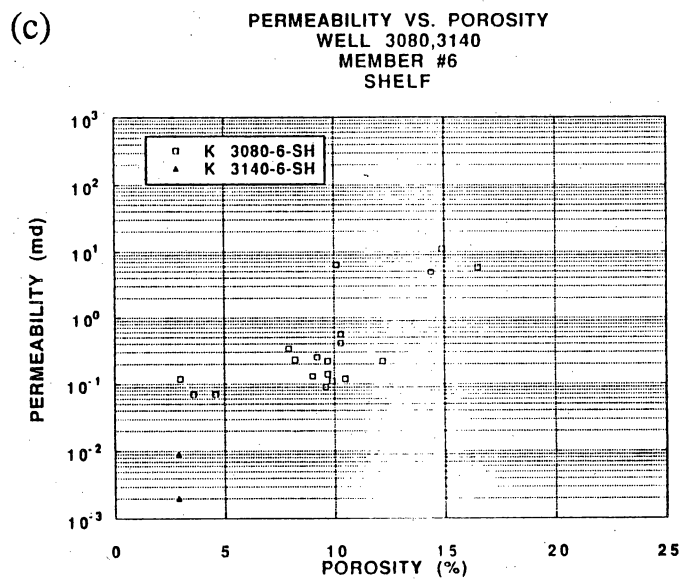
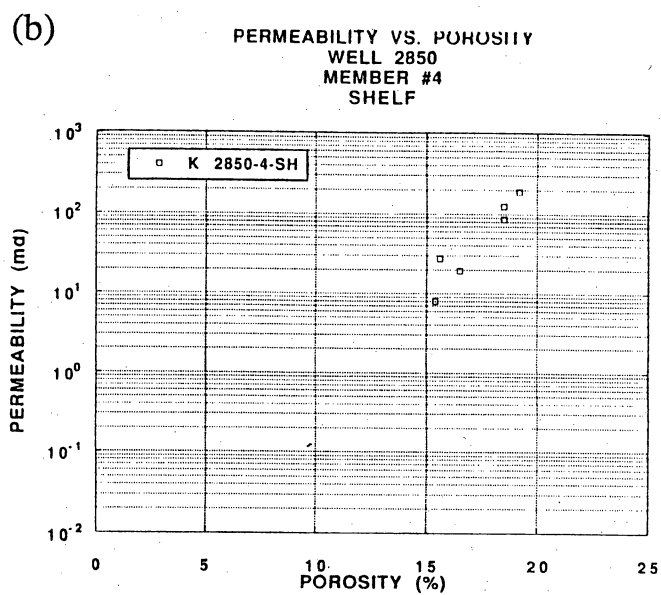
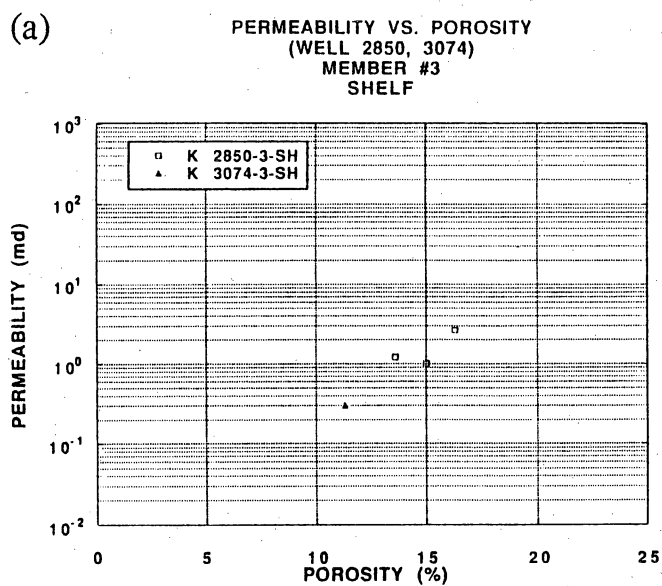
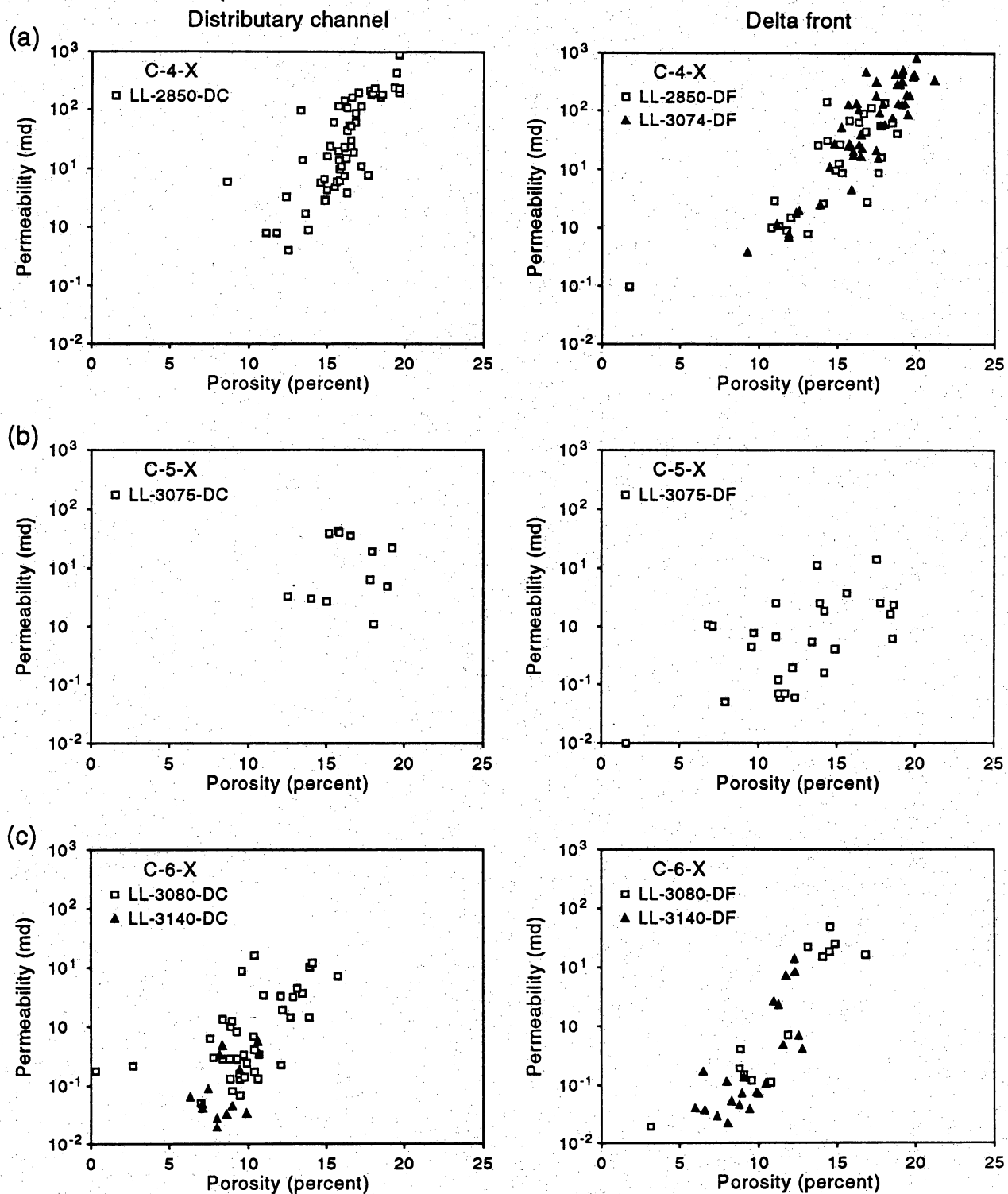


Figure V 44. Permeability-porosity crossplots of shelf facies per member. Data from whole-core analysis.



QAa4067c

Figure V 45. Permeability-porosity crossplots of distributary-channel versus delta-front facies in the C-4-X, C-5-X, and C-6-X Members.

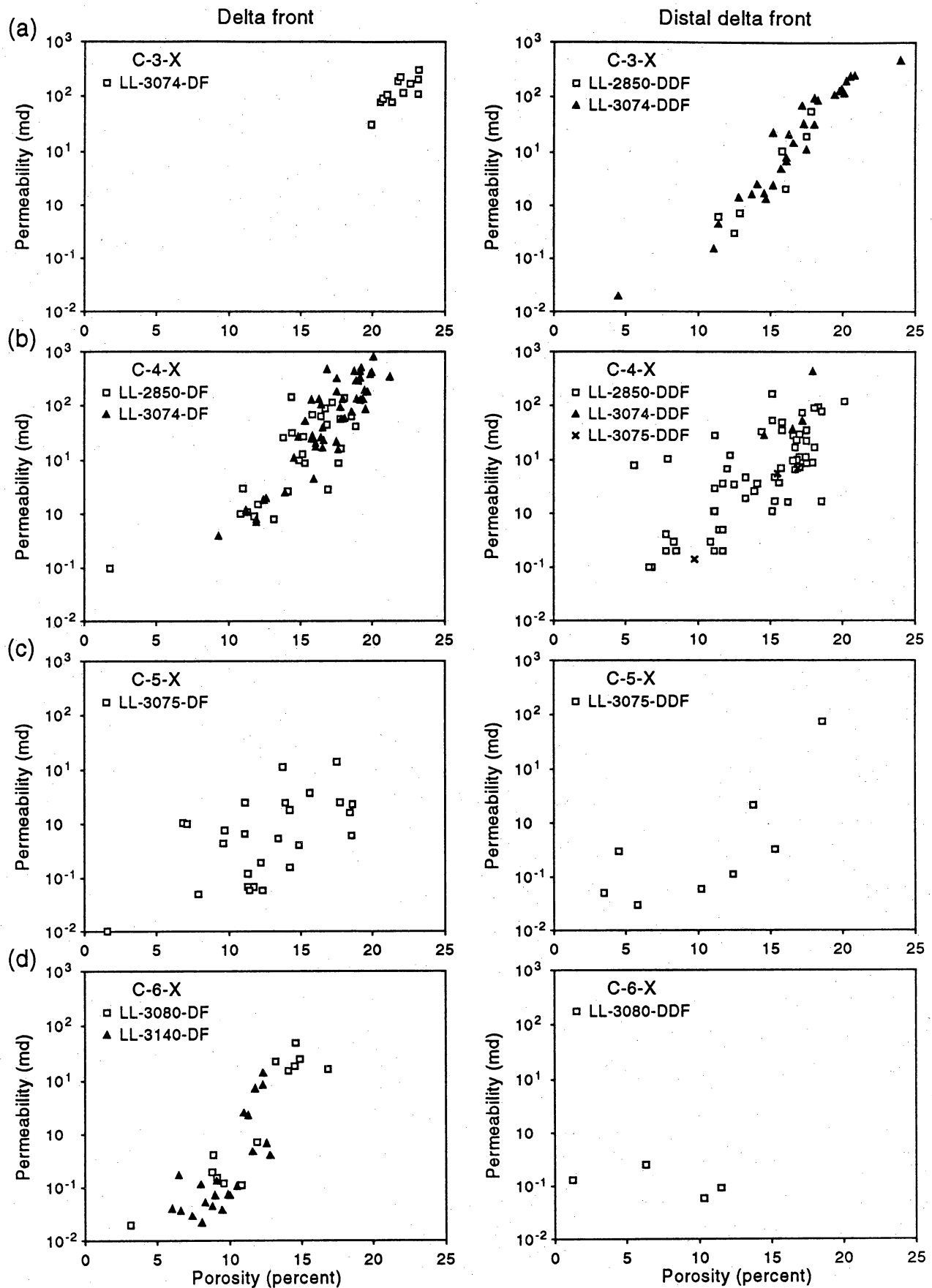


Figure V 46. Permeability-porosity crossplots of delta-front versus distal delta-front facies in the C-3-X to C-6-X Members.

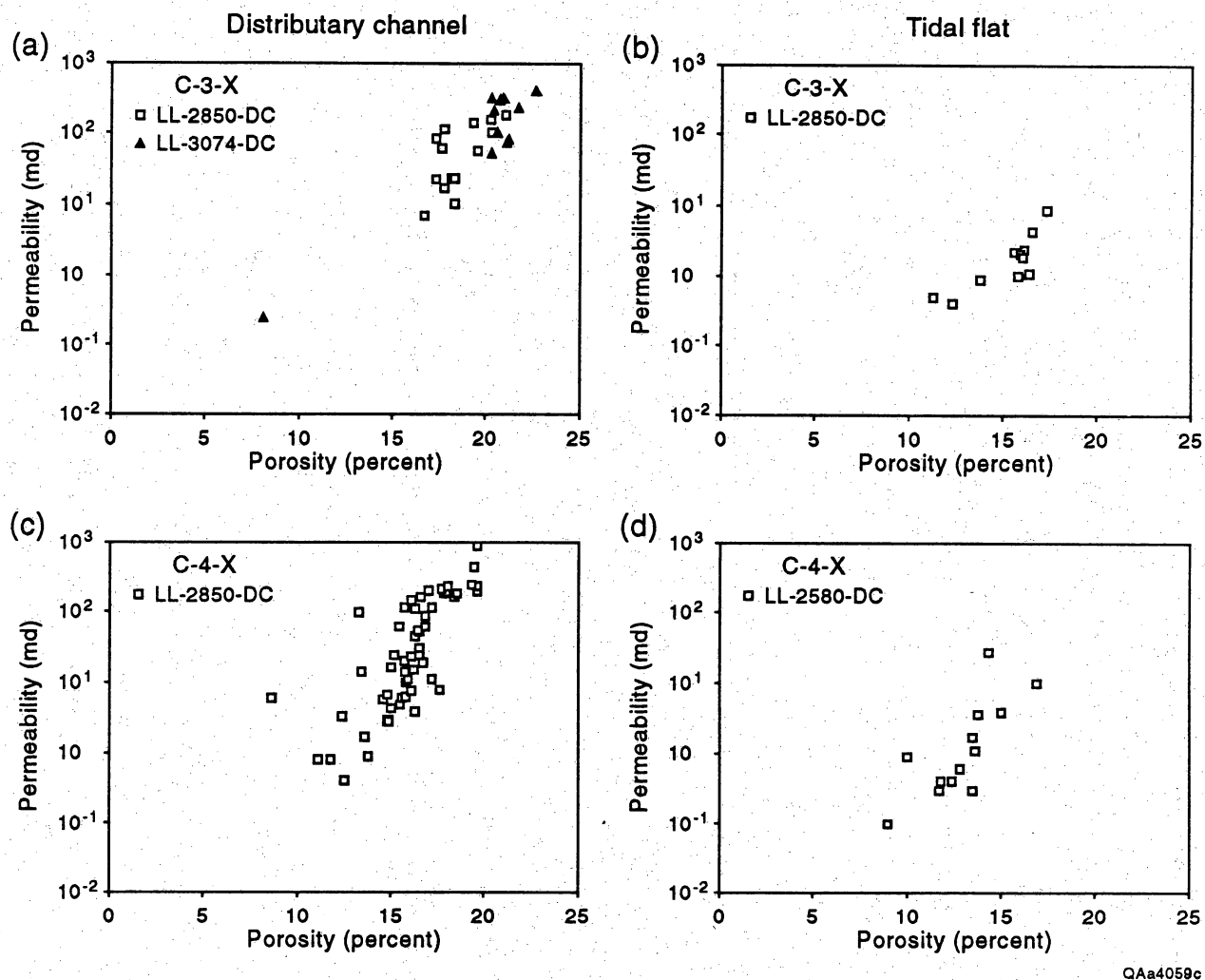


Figure V 47. Permeability-porosity crossplots of distributary-channel versus tidal-flat facies in the C-3-X and C-4-X Members.

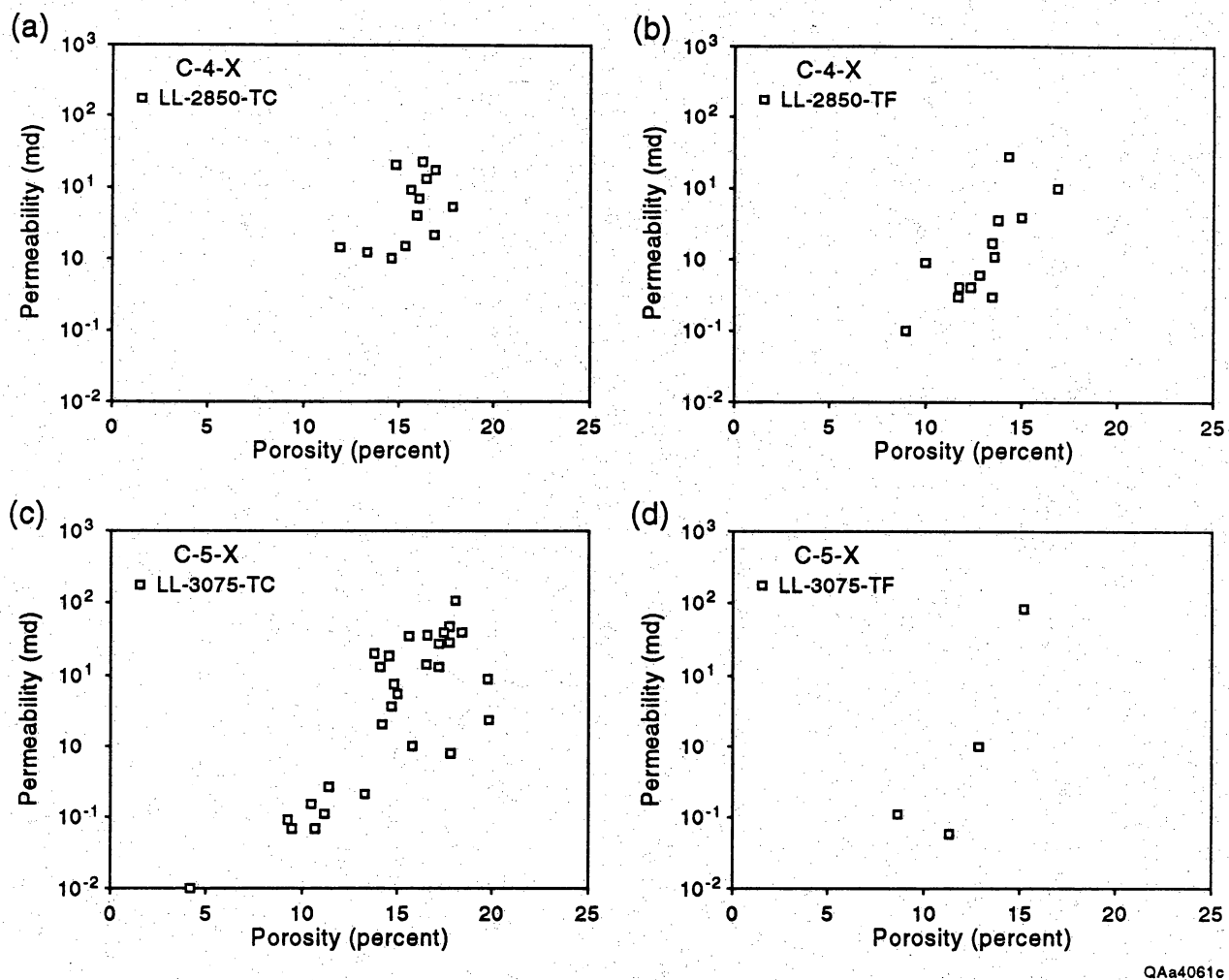


Figure V 48. Permeability-porosity crossplots of tidal-channel (TC) versus tidal-flat (TF) facies in the C-4-X and C-5-X Members.

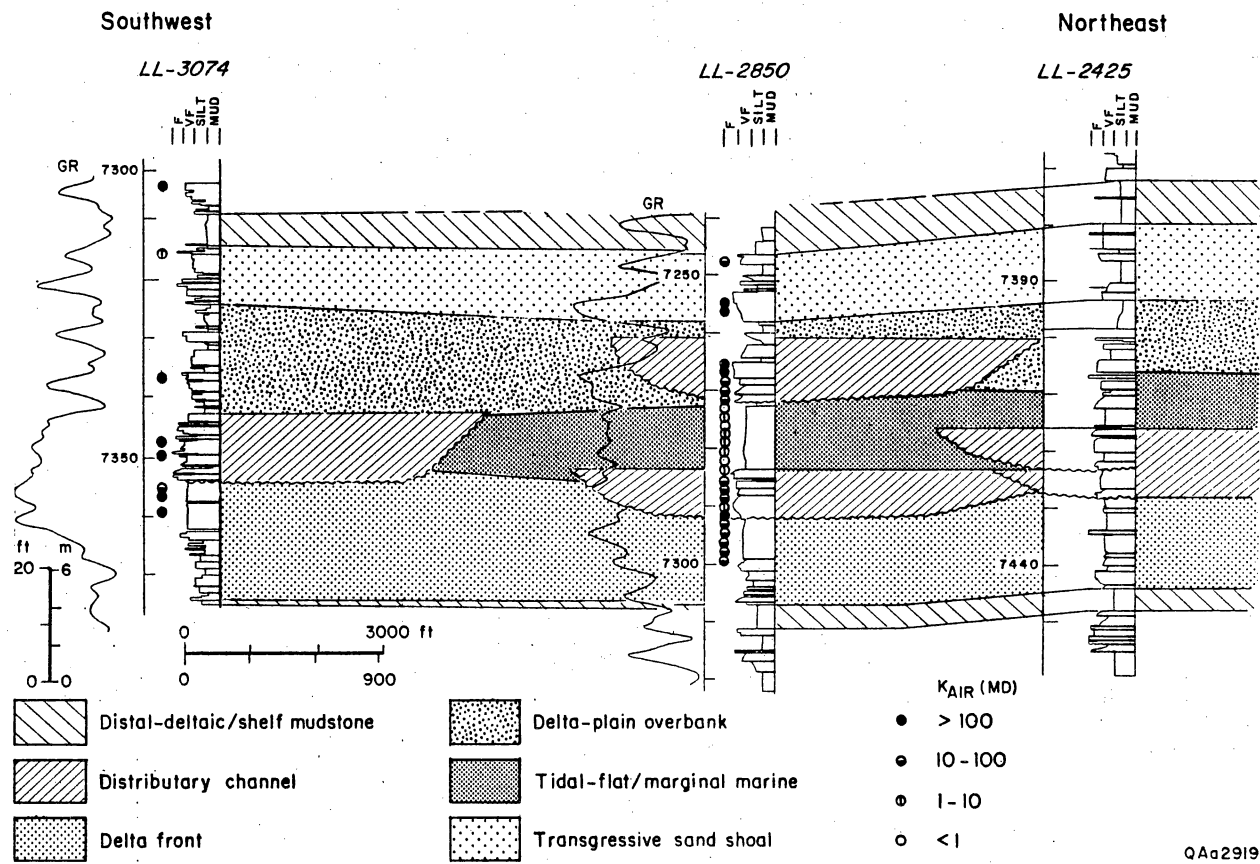
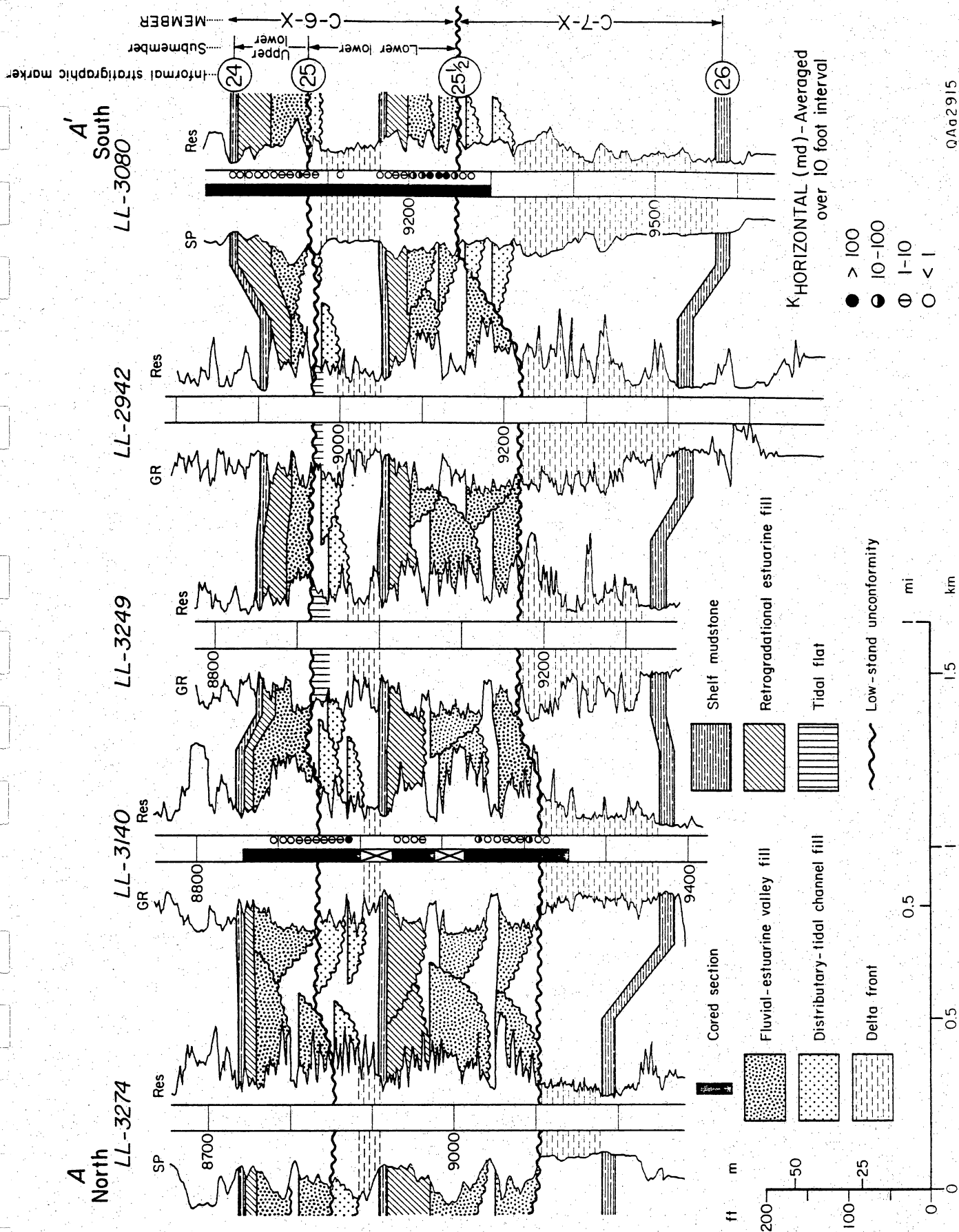


Figure V 49. Stratigraphic dip section from cores in the Middle C-3-X Submember, showing distributary-channel deposits that truncate delta-front deposits and high permeability contrast between tidal-flat and distributary-channel deposits. Cored wells are located in figures VI 26 and VI 27.



QA02915

Figure V 50. Stratigraphic strike section A-A', showing incised-valley, fluvial-estuarine deposits in the Lower C-6-X Submember that truncate deltaic deposits of the C-7-X Member and high permeability contrast across the unconformity at the base of the C-6-X Member in the LL-3080 well. Cross section is located in figures VI 2, VI 3, and VI 4.

Southwest

Northeast

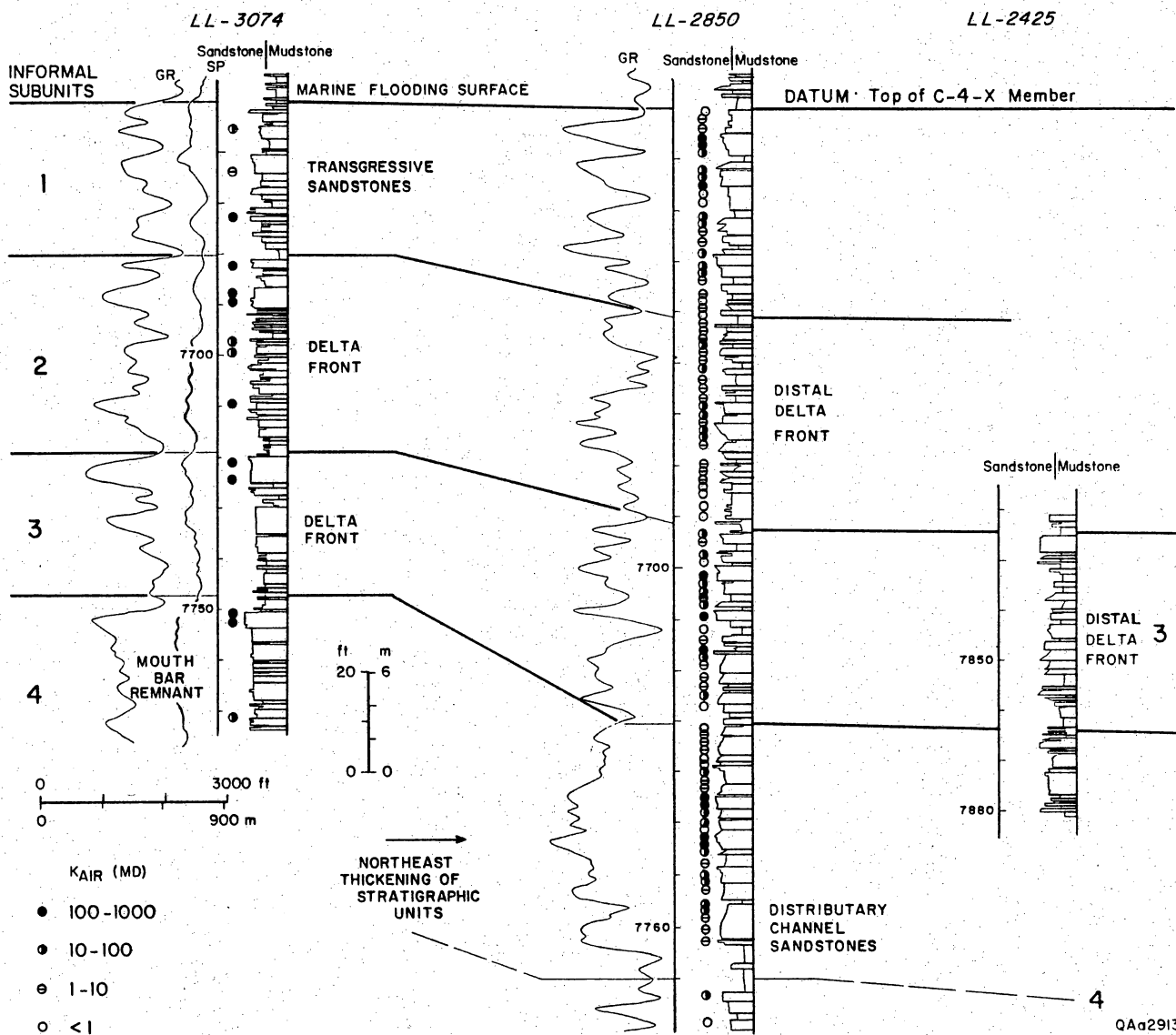


Figure V 51. Stratigraphic dip section from cores in the Upper C-4-X Submember, showing permeability variation and basinward thickening of subunits 1-4 in the transition from delta-front to distal delta-front facies. Cored wells are located in figure VI 22.

Table V 1. Criteria for tide-dominated deltaic model of reservoirs in the C Members in the LL-652 area.
The most diagnostic map criterion is dip-parallel geometry of delta-front sandstones.

SOURCE	CRITERION
MAPS	<ul style="list-style-type: none"> • NORTHEAST-TRENDING AND -BIFURCATING SANDBODIES (UPWARD-FINING LOG RESPONSE) PINCHING OUT INTO MUDDY DEPOSITS (UPWARD-COARSENING LOG RESPONSE) • <u>DIP-PARALLEL DELTA-FRONT SANDSTONE GEOMETRY</u>
CORES	<ul style="list-style-type: none"> • NUMEROUS REPETITIVE, CLAY-DRAPED REACTIVATION SURFACES AND ABUNDANT CLAY CLASTS • BI-DIRECTIONAL RIPPLES PRESENT BUT UNCOMMON

Table V 2. Diagnostic features and characteristics of distributary-channel facies, C Members, LL-652 area.

Diagnostic Features

- Erosional base
- Upward-fining
- Basal crossbeds and clay clasts
- Dip-elongate sand geometry
- Commonly contains marine burrows

Grain-Size Trend	Log Response	Basal Contact	Stratification	Sorting	Visual Porosity
Upward-fining and blocky	Upward-fining and blocky	Erosional	Top: Plane beds, asymmetrical ripples Base: Tabular crossbeds	Variable	Variable but generally good

Thickness (ft)	Width (ft)	Sandbody Geometry
5 to 20 individual Up to 45 composite	1,000 to 4,000	dip-elongate and bifurcating ribbons

Table V 3. Diagnostic features and characteristics of channel-mouth bar facies, C Members, LL-652 area.

Diagnostic Features

- Wavy and cross bedding at top of upward-coarsening sequence

Grain-Size Trend	Log Response	Basal Contact	Stratification	Sorting	Visual Porosity
Blocky, at top of upward-coarsening trend	Upward-coarsening	Gradational with underlying delta front	Wavy beds Small crossbeds	Good to excellent	Good to excellent

Thickness (ft)	Width (ft)	Sandbody Geometry
5 to 10 at top of 20- to 40-ft sequences	2,000 ?	Lobate to dip-linear pods

Table V 4. Diagnostic features and characteristics of delta-front (tidal sand-ridge) facies, C Members, LL-652 area.

Diagnostic Features

- Upward-coarsening
- Stratification mostly ripples and planar laminations
- Clay clasts and shell debris common at top
- Dip-elongate and parallel sand geometry

Grain-Size Trend	Log Response	Basal Contact	Stratification	Sorting	Visual Porosity
Upward-coarsening	Upward-coarsening	Gradational with sandy mudstone	Top: Small crossbeds and inclined laminations Base: Plane beds and ripples	Top: Good Base: Fair	Top: Good Base: Fair

Thickness (ft)	Width (ft)	Sandbody Geometry
5 to 18 individual Up to 40 composite	500 to 3,000	dip-elongate and parallel ribbons

Table V 5. Diagnostic features and characteristics of distal delta-front facies, C Members, LL-652 area.

Diagnostic Features

- Upward-coarsening above marine shale
- Planar and ripple bedding
- May include load structures and slumps

Grain-Size Trend	Log Response	Basal Contact	Stratification	Sorting	Visual Porosity
Upward-coarsening	Upward-coarsening or spiky	Gradational with marine shale	Plane beds and ripples	Fair to poor	Poor

Thickness (ft)	Width (ft)	Sandbody Geometry
5 to 11 individual 20 to 40 composite	500 to 3,000	dip-elongate and parallel ribbons

Table V 6. Diagnostic features and characteristics of tidal-channel facies, C Members, LL-652 area.

Diagnostic Features

- Erosional base
- Small unit thickness

Grain-Size Trend	Log Response	Basal Contact	Stratification	Sorting	Visual Porosity
Upward-fining or blocky	Spiky (thin-bed response)	Erosional	Top: Asymmetrical ripples Base: Crossbeds	Variable moderate	Good to fair

Thickness (ft)	Width (ft)	Sandbody Geometry
5 to 10 individual 10 to 25 composite	1,000 to 2,500	sinuous dip- elongate ribbons

Table V 7. Diagnostic features and characteristics of tidal-flat facies, C Members, LL-652 area.

Diagnostic Features

- Interbedded sandstone and shale
- Flaser ripples
- Variable grain-size trends

Grain-Size Trend	Log Response	Basal Contact	Stratification	Sorting	Visual Porosity
None to slightly upward-fining	Baseline or serrate	Non-Erosional	Plane beds, asymmetrical and symmetrical ripples in sandstone interbedded with mudstone	Fair to poor	Poor

Thickness (ft)	Width (ft)	Sandbody Geometry
10 to 30	1,000 to 5,000	sheet

Table V 8. Diagnostic features and characteristics of transgressive sand-shoal facies, C Members, LL-652 area.

Diagnostic Features

- Thin and calcareous
- Internal erosion surfaces
- Overlain by shelf facies

Grain-Size Trend	Log Response	Basal Contact	Stratification	Sorting	Visual Porosity
Upward-coarsening	Spiky (thin-bed response)	Gradational, but may contain internal erosion surfaces	Top: Inclined laminations, small crossbeds, symmetrical ripples Base: Plane beds and ripples	Variable	Variable, due to calcareous zones

Thickness (ft)	Width (ft)	Sandbody Geometry
2 to 10 individual 15 to 30 composite	many thousands of feet, but irregular	irregular sheet

Table V 9. Diagnostic features and characteristics of shelf facies, C Members, LL-652 area.

Diagnostic Features

- Fine grain size
- Marine burrows
- High degree of lateral continuity

Grain-Size Trend	Log Response	Basal Contact	Stratification	Sorting	Visual Porosity
None	Baseline	May overlie calcareous and erosional zones	Planar laminations and starved ripples	Poor	None

Thickness (ft)	Width (ft)	Sandbody Geometry
Variable; Transgressive shales 2 to 10	> 10,000	sheet

Table V 10. Diagnostic features and characteristics of fluvial-estuarine channel facies, C Members, LL-652 area.

Diagnostic Features

- Thick succession of multiple, massively crossbedded sandstones
- Erosional base; commonly truncates marine shale
- Few or no marine burrows in basal section; marine burrows in upper section

Grain-Size Trend	Log Response	Basal Contact	Stratification	Sorting	Visual Porosity
Upward-fining	Upward-fining or blocky	Erosional	Top: Small crossbeds, plane beds, and ripples Base: Large crossbeds with clay clasts	Fair to poor	Good; decreases upward

Thickness (ft)	Width (ft)	Sandbody Geometry
20 to 40 individual 60 to 100 composite	2,000 to 6,000	dip-elongate belts

Table V 11. Summary of three-dimensional facies geometry and heterogeneity in the C Members in the LL-652 area.

A. Volumetrically Significant Facies

Facies	Individual Thickness (ft)	Width (ft)	Sandbody Shape	Sandbody Trend	Internal Heterogeneities	Common Bounding Facies
(1) Delta Front	5-20	500-3,000	Dip-elongate ribbon	dip	Minor shale interbeds in lower half	(l) distal delta front (v) shelf (l, v) distributary channel
(2) Distal Delta Front	5-10	500-3,000	Dip-elongate ribbon	dip	Multiple shale interbeds	(l) delta front (v) shelf
(3) Distributary Channel	5-20	1,000-4,000	Bifurcating ribbon	dip	Shale interbeds in upper half; clay clasts in lower half	(l) tidal flat (l, v) delta front

B. Volumetrically Less Significant Facies

(4) Tidal Channel	5-10	1,000-2,500	Sinuuous ribbon	dip	Similar to Distributary channel	(l,v) Tidal Flat
(5) Channel-Mouth Bar	5-10	2,000?	Lobate pod	dip?	Few	(l,v) distributary channel (l,v) delta front
(6) Fluvial-Estuarine Channel	20-40	2,000-6,000	Dip-elongate belt	dip	Clay clasts at base	(l,v) any, particularly delta front

C. Other Facies

(7) Transgressive Sand Shoal	2-10	?	Irregular sheet	?	Calcite-cemented zones, clay clasts	(v) shelf (v) delta front
(8) Shelf	2-10	> 10,000	Sheet	?	Mudstone-dominated	(v) transgressive sand shoal (v) delta front (v) distal delta front
(9) Tidal Flat	10-20	1,000-5,000	Sheet	strike	Mudstone-dominated	(l) distributary channel (l, v) tidal channel

(l) Lateral
(v) Vertical

Table V 12. Variations in net-sandstone thickness patterns and net-sandstone distribution in facies in different types of stratigraphic sequences in the C Members in the LL-652 area.

Cycle	Examples	Type of Net-Sandstone Patterns	% Sandstone	Net Sandstone (ft)	Thickness of Interval	Dominant Facies
Extreme Offlap (Base-Level Fall)	Upper Lower C-6-X	Linear belts of locally thick Sandstone	locally >60	locally >70	~150	Fluvial valley fill and delta front
	Lower Lower C-6-X	Linear belts of locally thick sandstone w/ erosional base	locally >60	locally >100	150-200	Fluvial valley fill
Offlap	Upper C-4-X	Elongate belts of variable width	Belts of 50-70	Belts of >100	100-150	Distributary channel and delta front
	#4 Sandstone in Upper C-4-X	Narrow, bifurcating, dip-elongate belts pinching out downdip	Belts of 60-80	Belts of 30-40	50-80	Distributary channel >delta front
	15-16 interval in Middle C-4-X	Narrow, sinuous and reticulated belts	~30*	Belts of 20-30	80-100	Tidal channel/tidal flat
	Middle C-5-X	E- and ne-trending and bifurcating dip-elongate system	wide (>2 mi) belts of 40-50	wide belts of 80-100	200-250	Distributary channel and delta front
Progradation During Retrogradation	Upper C-3-X	Narrow, downdip-bifurcating dip-elongate system	Belts of 20	Belts of 30-40	~200	Proximal delta front
	Middle C-3-X	Sinuous, interconnected dip-elongate belts of variable width	1-2 mi. wide belts of >50	Belts of 40-50	100	Distributary channel truncating delta front
	Lower 21-22 interval in Lower Upper C-6-X	Dip-elongate, bifurcating belts, 1 mile wide	~30*	Belts of >40	~100	Proximal delta front
Retrogradation	Lower C-3-X	Narrow, parallel belts of sandstone, downdip of depocenter	~20	Belts of >50	300	Delta front
	Lower C-4-X	Dip-elongate belts	Belts of 15-25	60-80	250	Delta front
	Lower C-5-X	Dip-elongate, east-trending belts, 1-2 mi wide	Narrow belts of >30	70	250	Delta front
	Upper 21-22 interval in C-6-X	1-2 mi-wide belts, dip-elongate and subparallel	~30*	Belts of >30	100	Delta front

* calculated from net Sandstone thickness

Table V 13. Statistical summary of whole-core porosity and permeability in the C-3-X to C-7-X Members in the LL-652 area.

STATISTIC SUMMARY OF POROSITY

UNIT	C3	C4	C5	C6	C7
Minimum	4.5	1.8	1.6	0.30000001	2.09999999
Maximum	25.4	155.89999	19.799999	17.9	12.7
Sum	2027.4	5209.4	1768.5	4164.7	571.5
Points	116	329	136	412	64
Mean	17.477586	15.834043	13.003677	10.108495	8.9296875
Median	17.6	16.1	13.5	10.2	9.3499999
RMS	17.816415	17.902733	13.639193	10.522183	9.2577754
Std Deviation	3.4731288	8.366822	4.1300598	2.924966	2.4620729
Variance	12.062624	70.00371	17.057394	8.5554264	6.0618031
Std Error	0.32247192	0.46127783	0.35414971	0.14410273	0.30775912
Skewness	-0.65341832	14.227036	-0.61921384	-0.49572763	-0.78173056
Kurtosis	1.0076929	237.31314	-0.034621651	1.0614017	0.042629948

STATISTIC SUMMARY OF PERMEABILITY

Unit	C3	C4	C5	C6	C7
Minimum	0.019999	0.10000	0.0010000	0.0019999	0.019999
Maximum	784.00	1572.9	105.93	1392.0	71.900
Points	115.00	323.00	134.00	392.00	59.000
Mean	20.183	14.724	1.2841	0.88964	0.60700
Median	30.400	15.999	1.1588	0.64498	0.61000
RMS	40.799	28.088	10.411	11.673	8.3949
Std Deviation	8.8748	7.2113	10.363	11.677	8.0525
Variance	7.9250	5.4474	10.745	13.777	6.6177
Std Error	1.2258	1.1162	1.2238	1.1322	1.3120
Skewness	0.20820	0.62612	0.79511	3.0831	1.6358
Kurtosis	0.52228	0.25029	0.18677	0.71966	0.26177

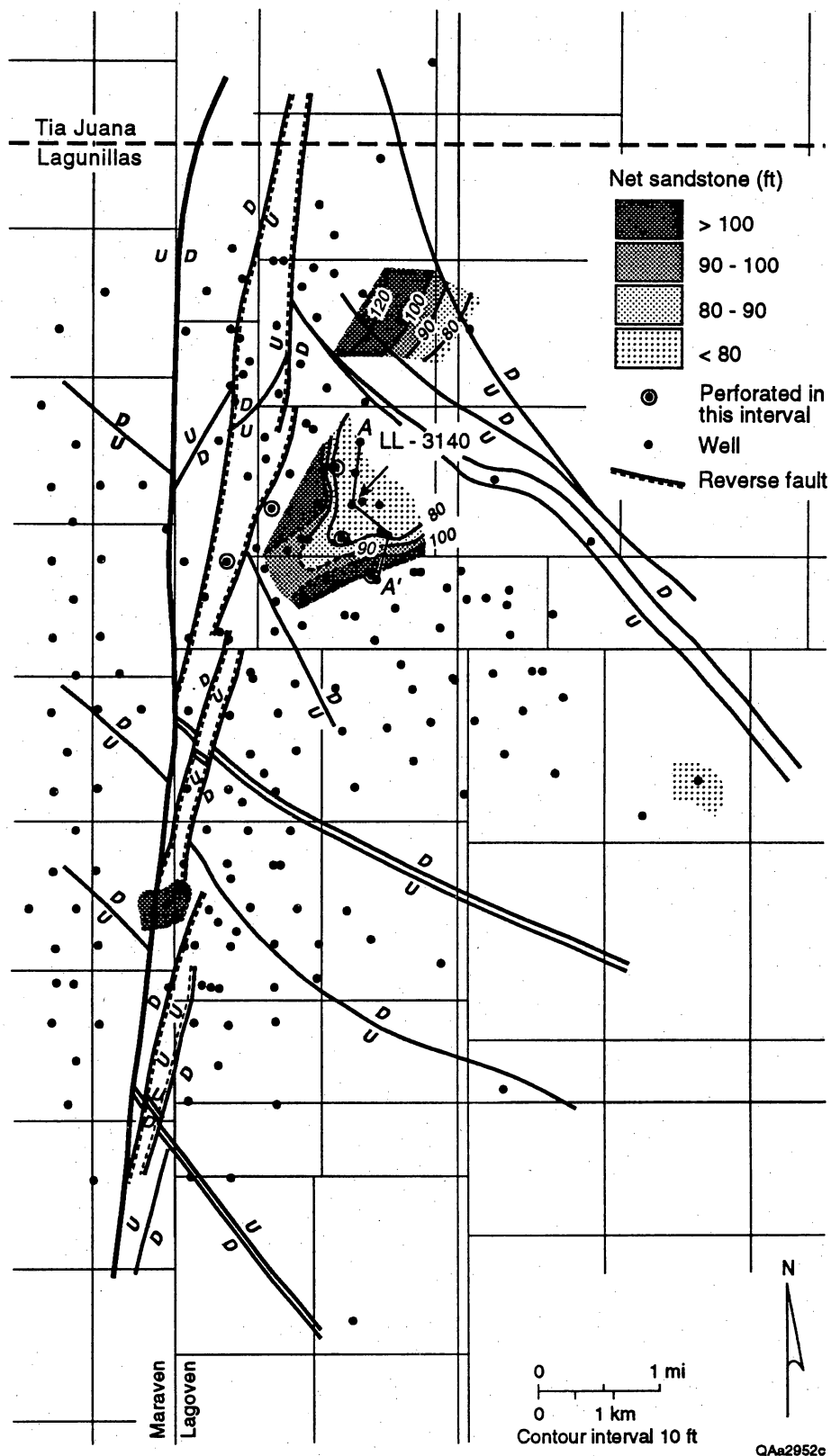


Figure VI 1. Net-sandstone thickness of the C-7-X Member in the LL-652 area.

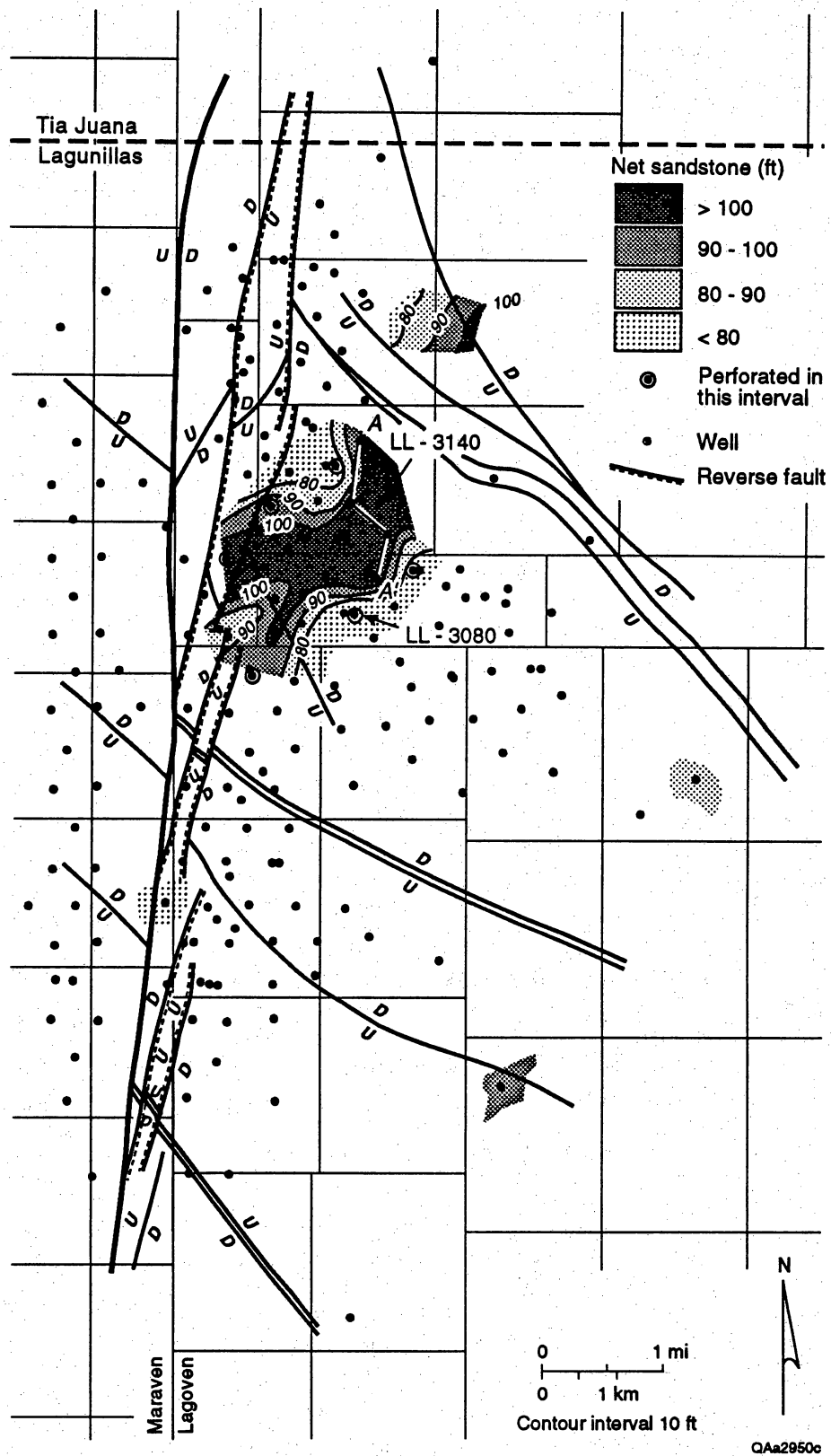


Figure VI 2. Net-sandstone thickness of the Lower Lower C-6-X Submember in the LL-652 area. Cross section A-A' is shown in figure V 50.

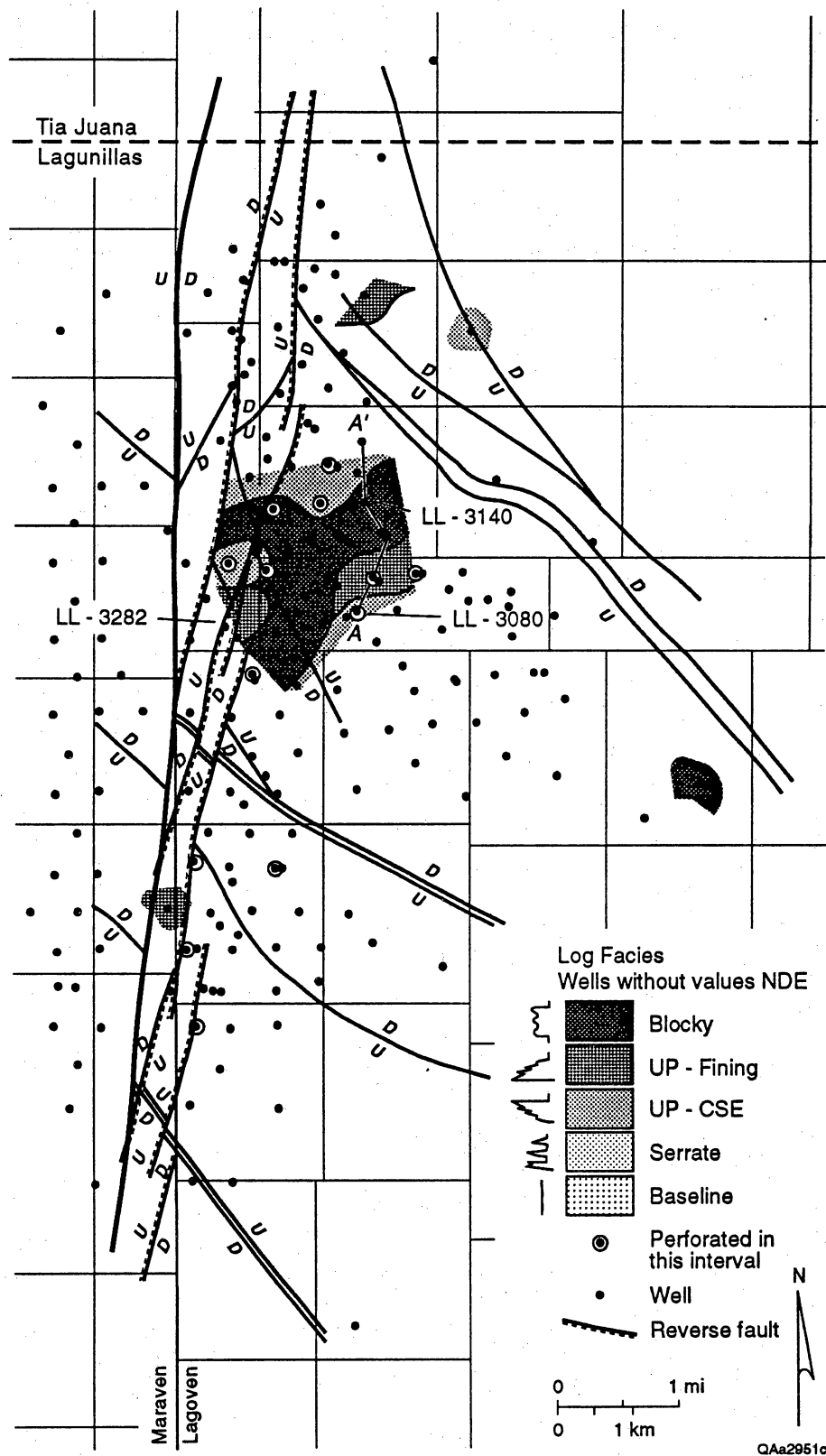


Figure VI 3. Log-facies of the Lower Lower C-6-X Submember in the LL-652 area. Cross section A-A' is shown in figure V 50.

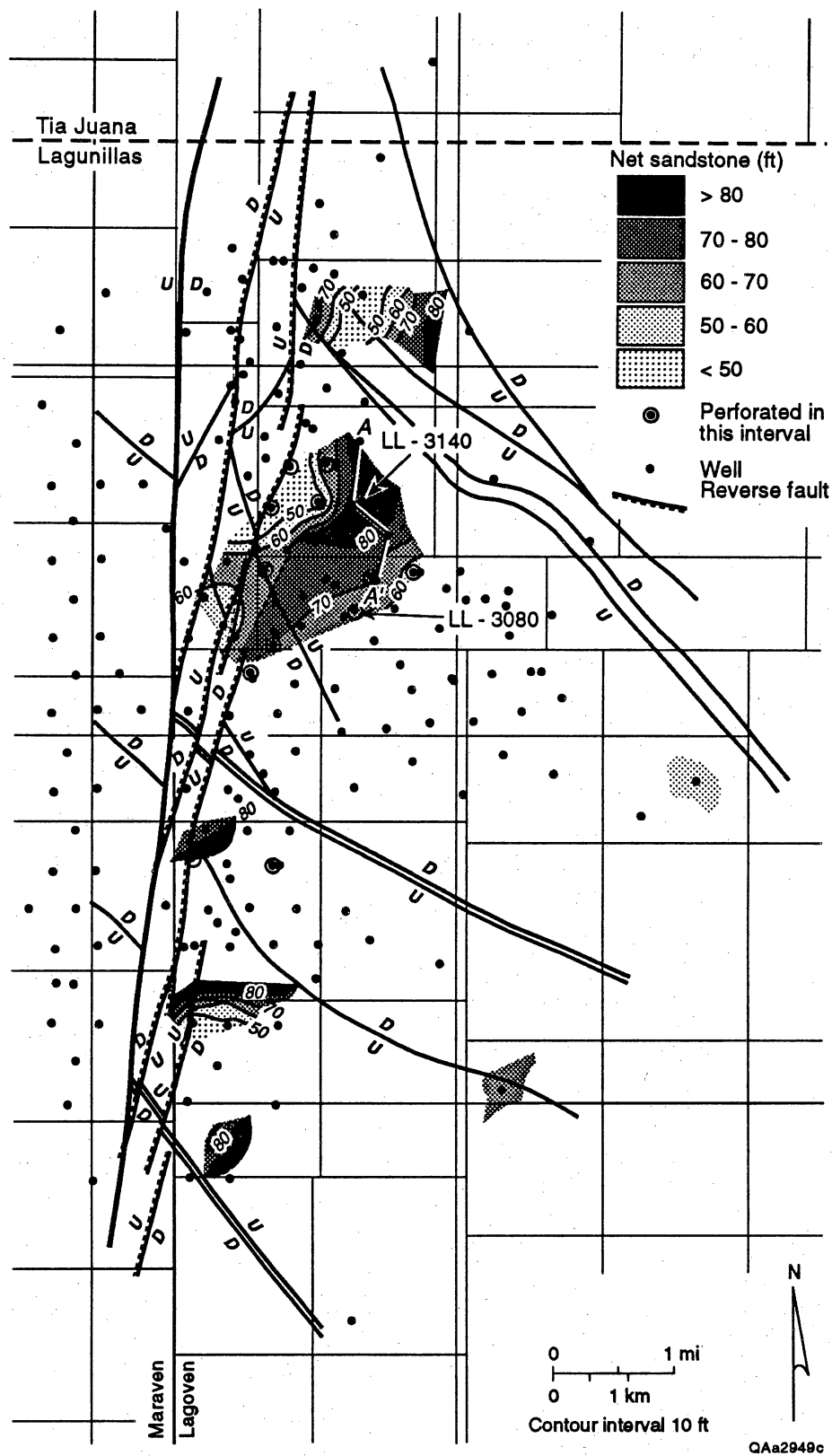


Figure VI 4. Net-sandstone thickness of the Upper Lower C-6-X Submember in the LL-652 area. Cross section A-A' is shown in figure V 50.

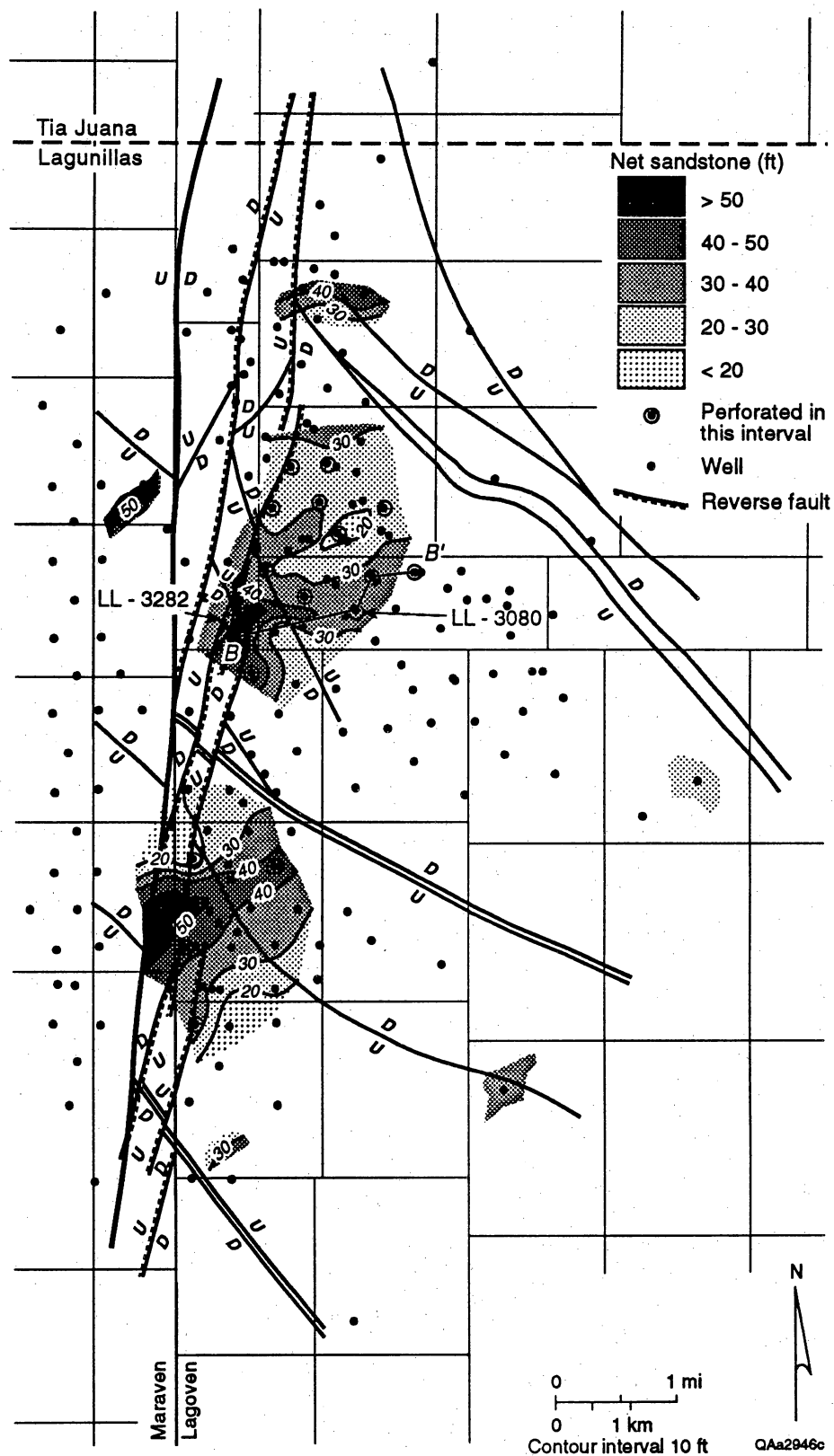


Figure VI 5. Net-sandstone thickness of the Lower 21-22 Interval in the Lower Upper C-6-X Submember in the LL-652 area. Cross section B-B' is located in figure VI 7.

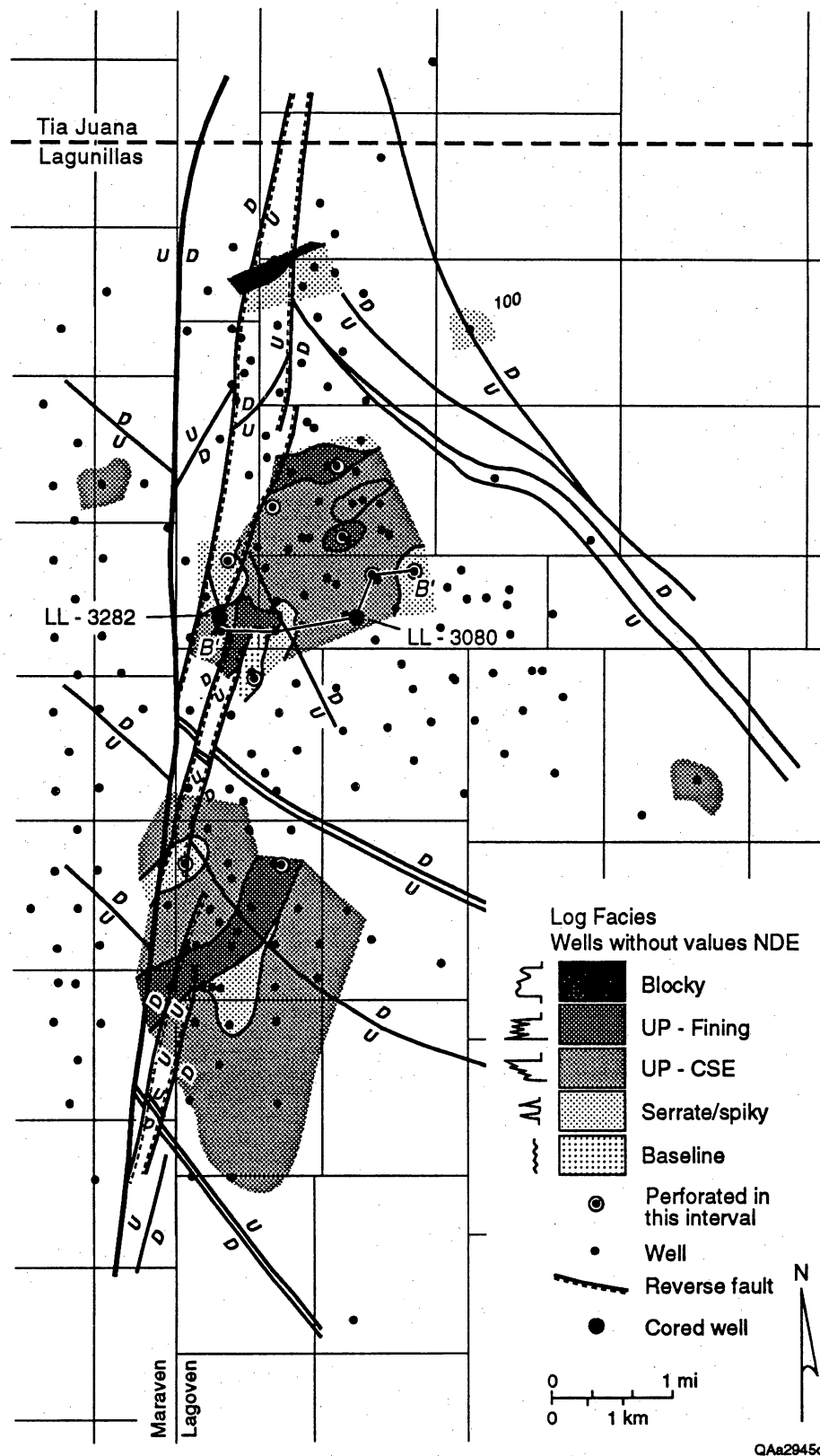


Figure VI 6. Log-facies of the Lower 21-22 Interval in the Lower Upper C-6-X Submember in the LL-652 area. Cross section B-B' is located in figure VI 7.

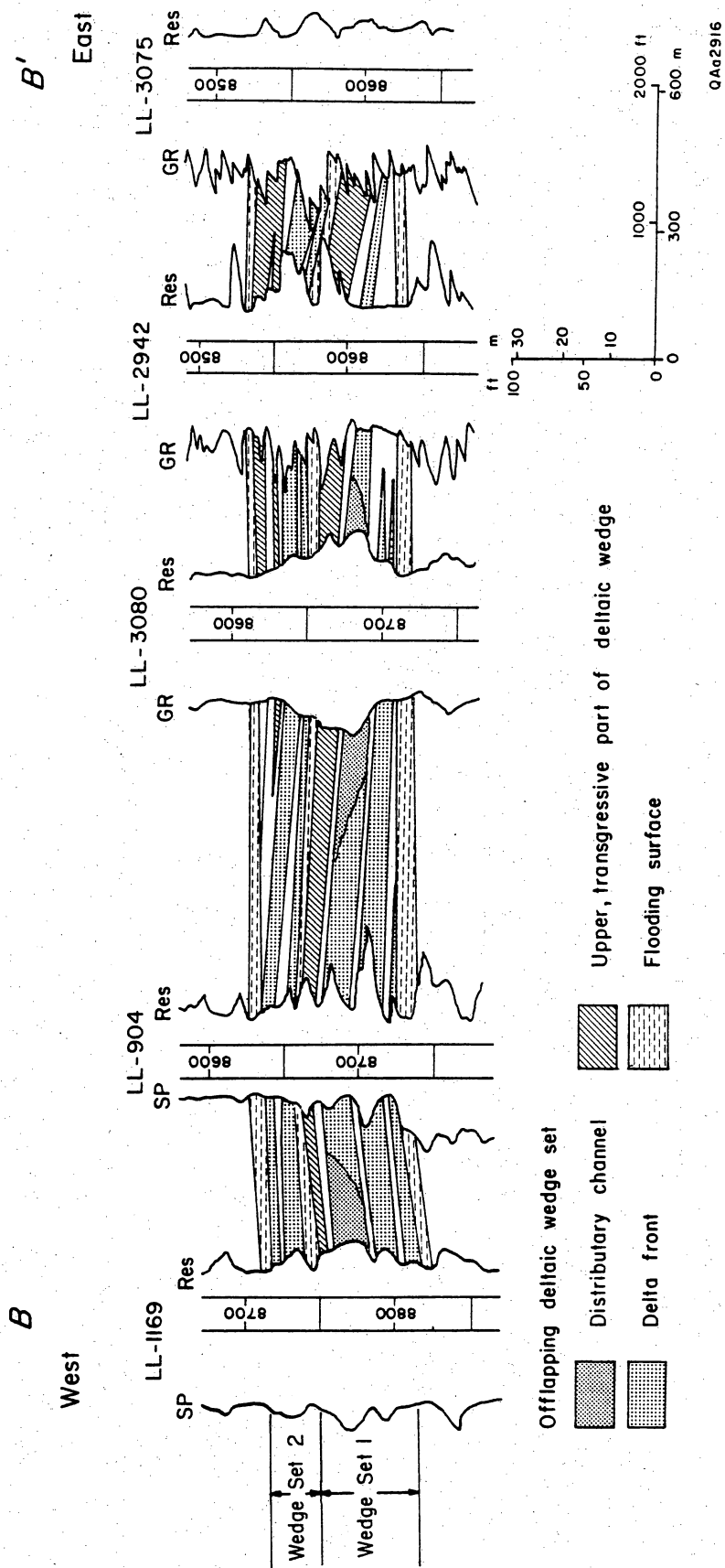


Figure VI 7. Stratigraphic dip section B-B' in the Lower 21-22 Interval in the Lower Upper C-6-X Submember, showing eastward-thinning, progradational deltaic wedges overlain by westward-thinning transgressive sandstones deposited during phases of deltaic abandonment. Individual depositional cycles (parasequences) are 40 to 80 ft (12 to 24 m) thick. Cross section is located in figures VI 5 and VI 6.

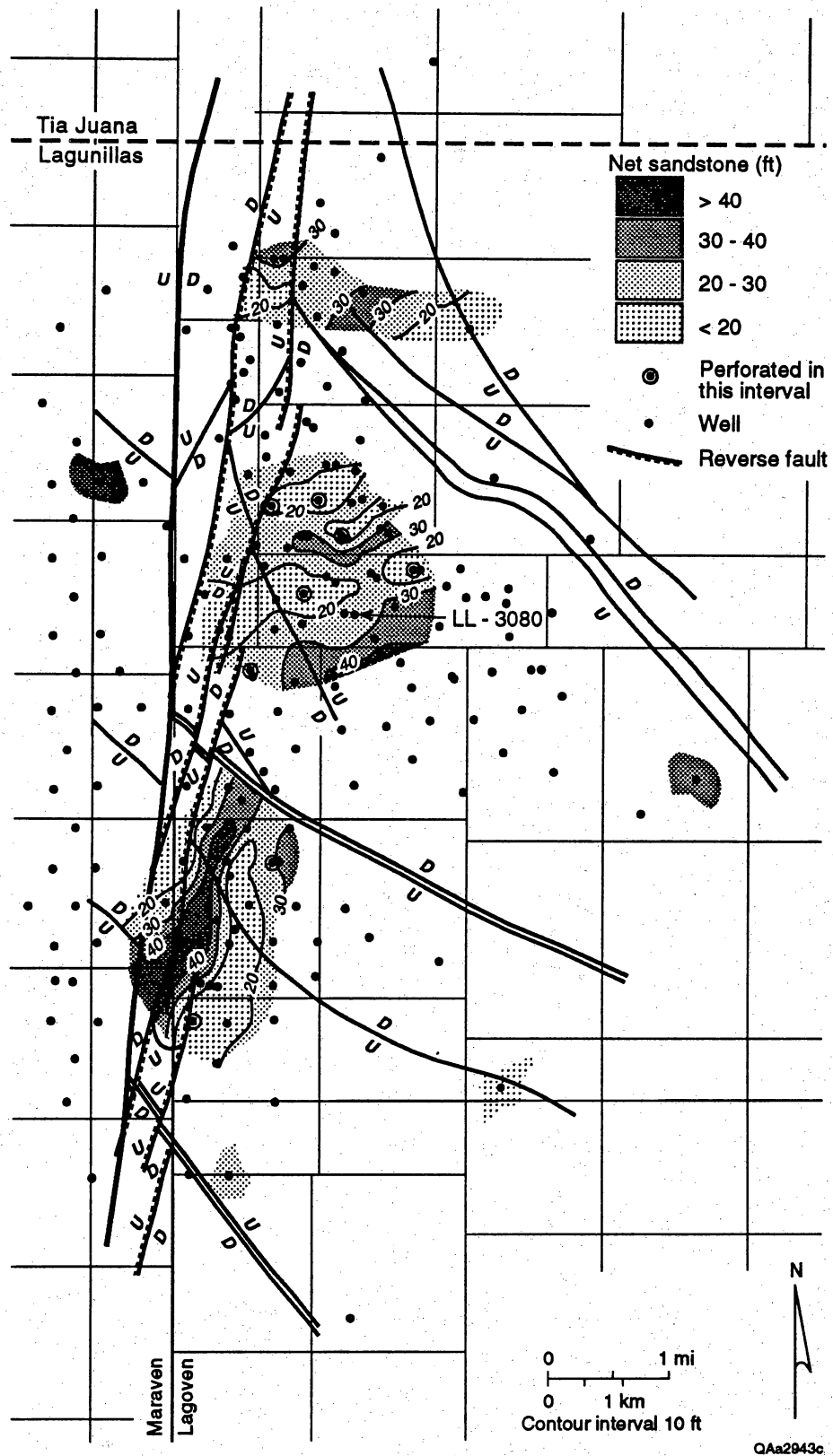


Figure VI 8. Net-sandstone thickness of the Upper 21-22 Interval in the Lower Upper C-6-X Submember in the LL-652 area.

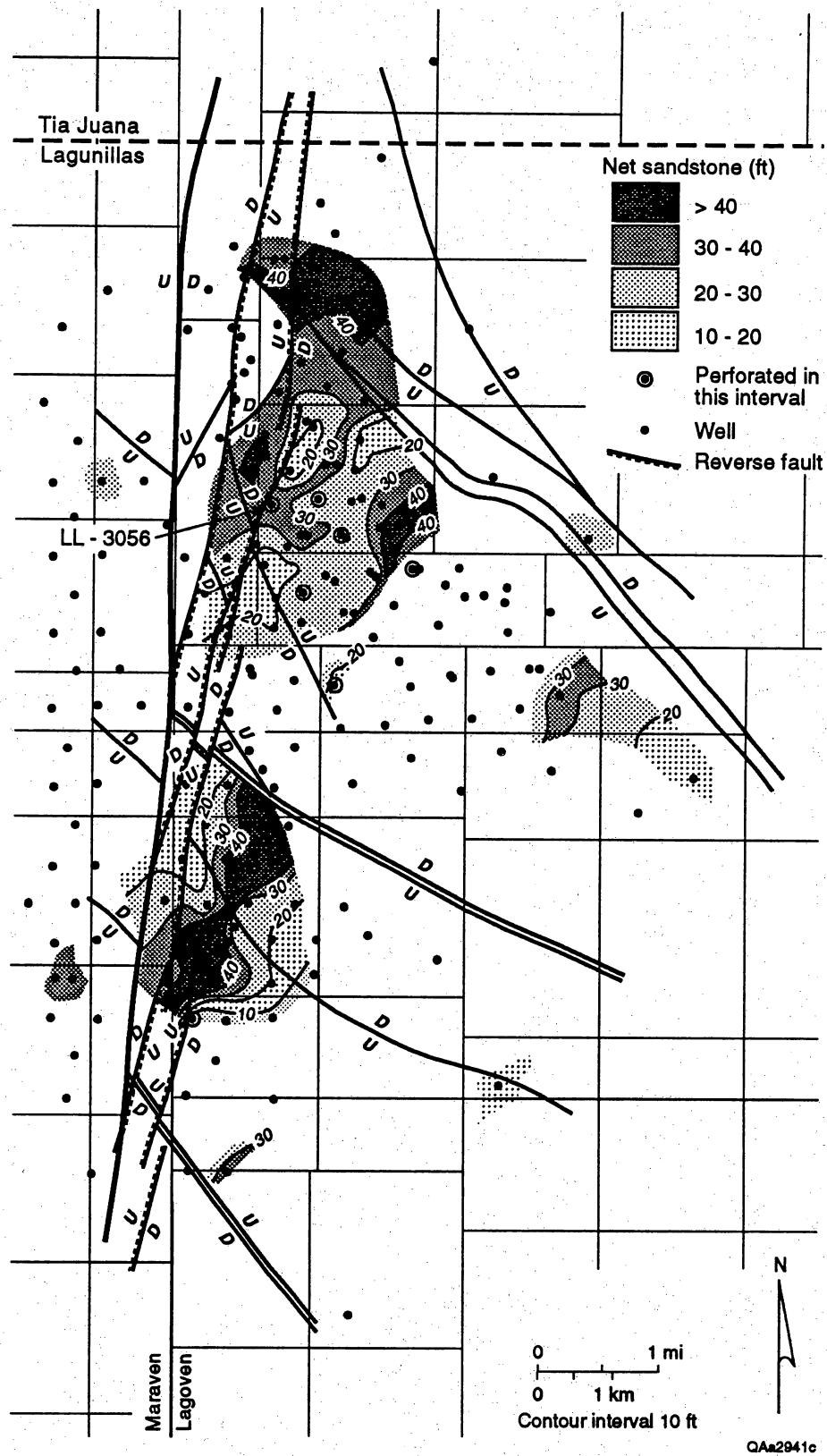


Figure VI 9. Net-sandstone thickness of the Upper Upper C-6-X Submember in the LL-652 area.

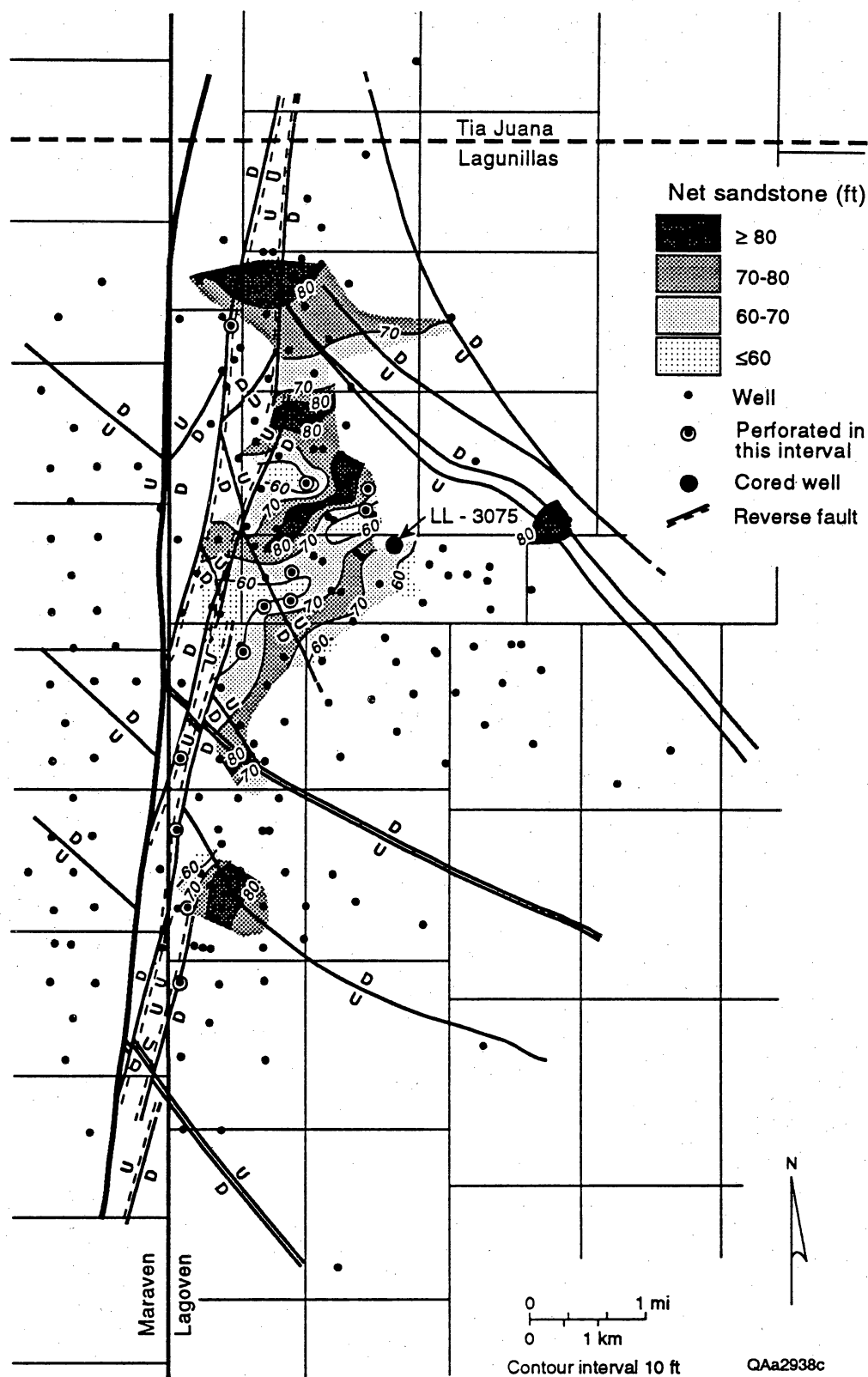


Figure VI 10. Net-sandstone thickness of the Lower C-5-X Submember in the LL-652 area.

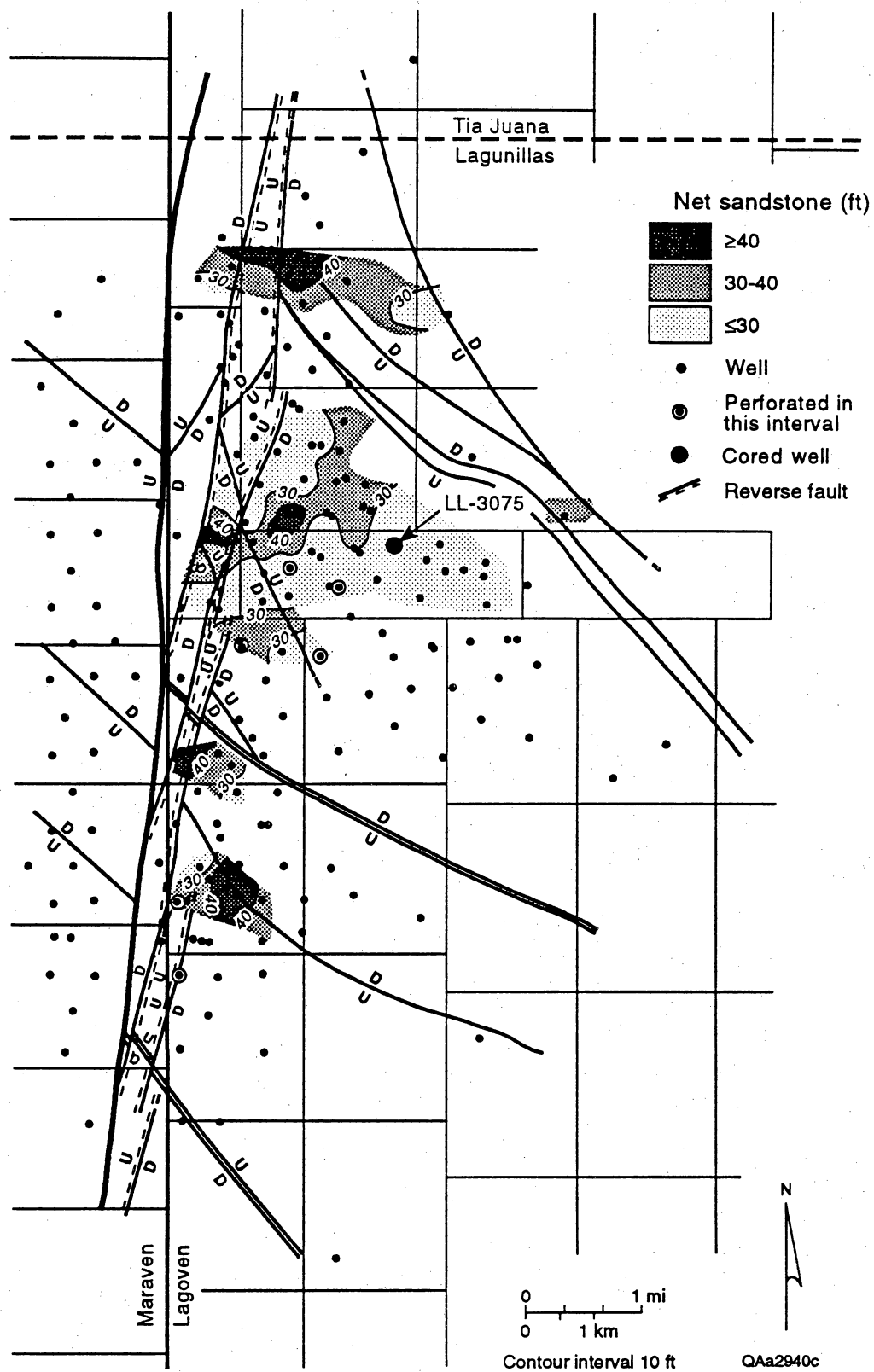


Figure VI 11. Net-sandstone thickness of the Lower Lower C-5-X Submember in the LL-652 area.

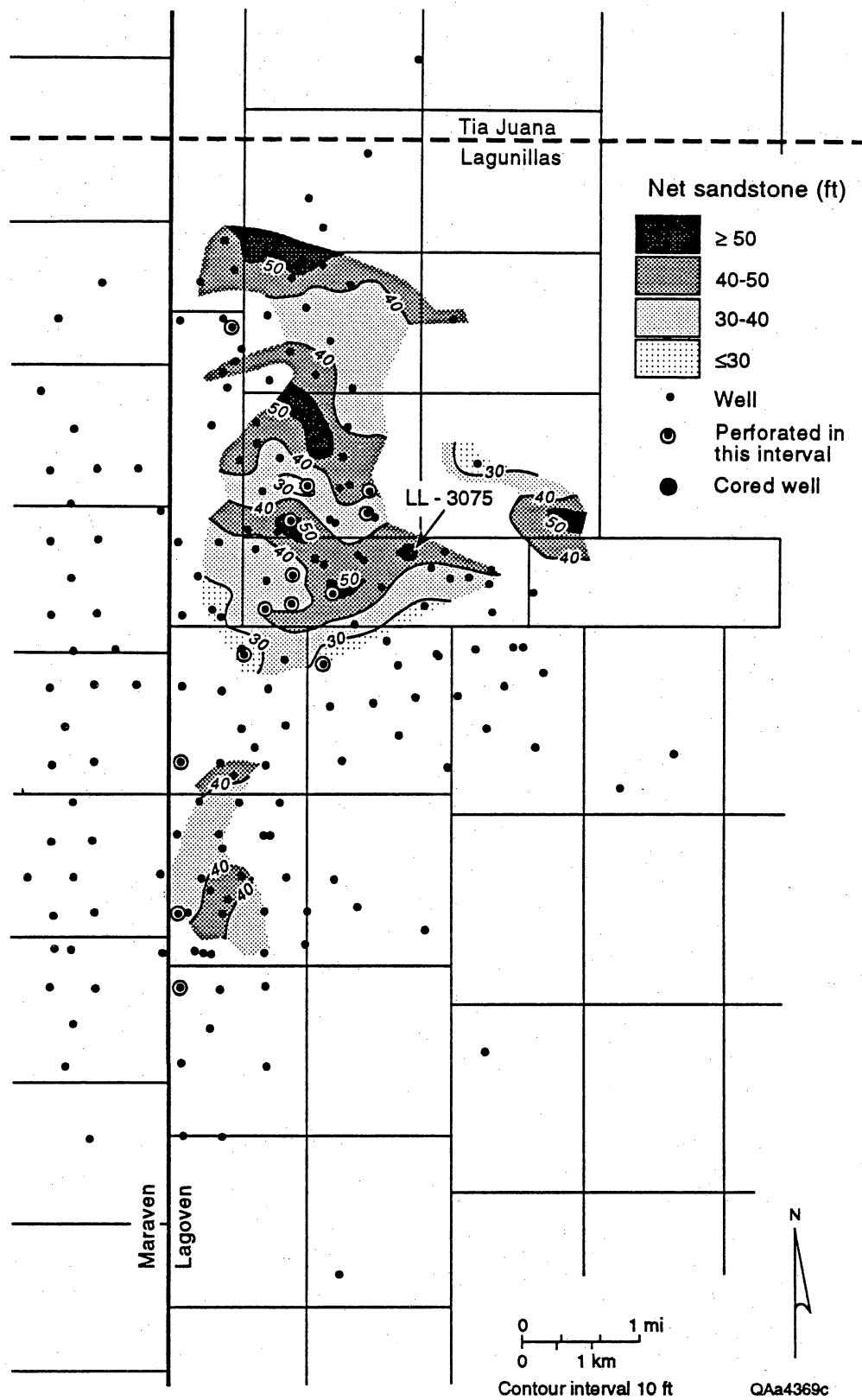


Figure VI 12. Net-sandstone thickness of the Upper Lower C-5-X Submember in the LL-652 area.

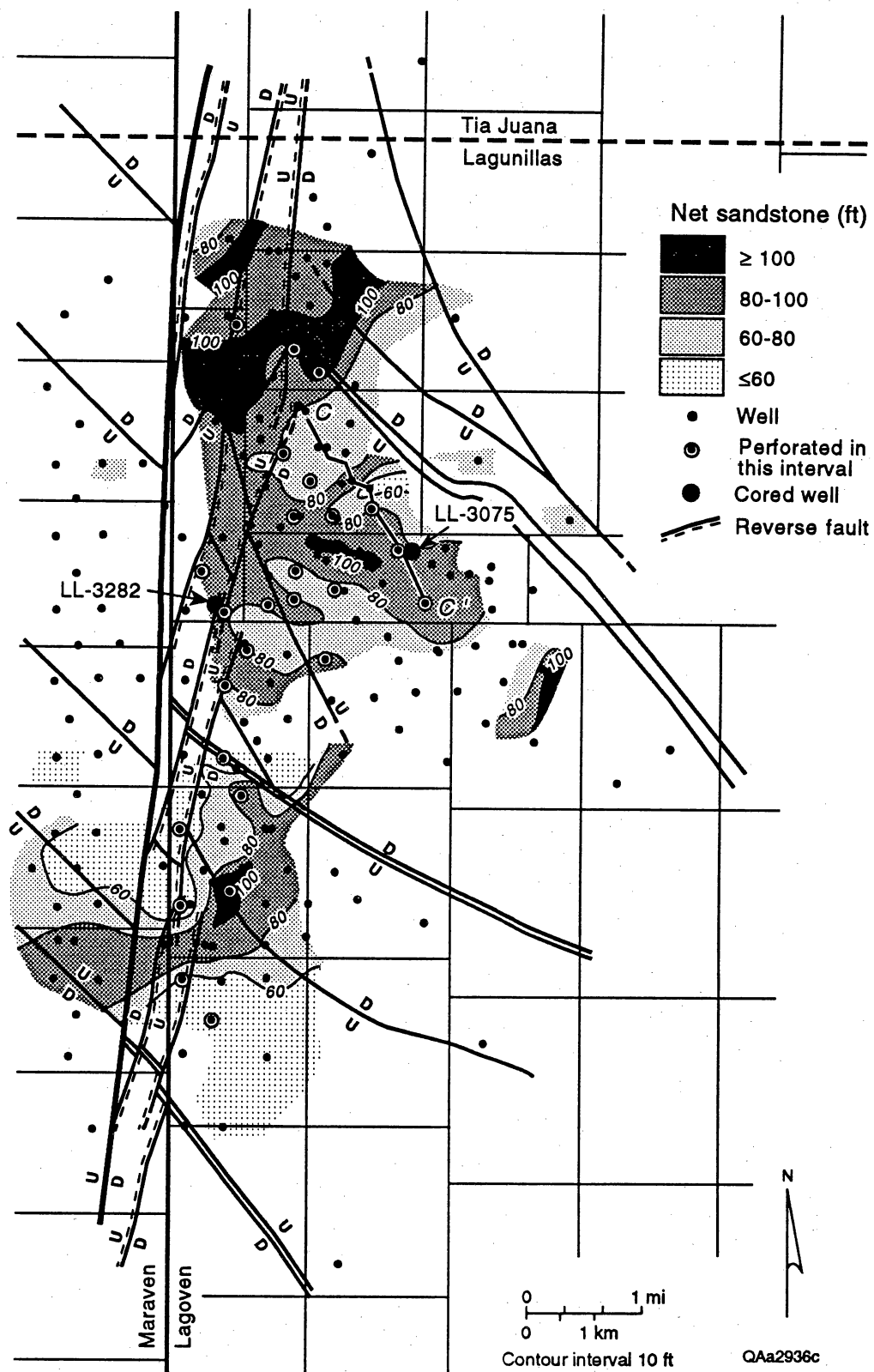


Figure VI 13. Net-sandstone thickness of the Middle C-5-X Submember in the LL-652 area. Cross section C-C' is shown in figure VI 14.

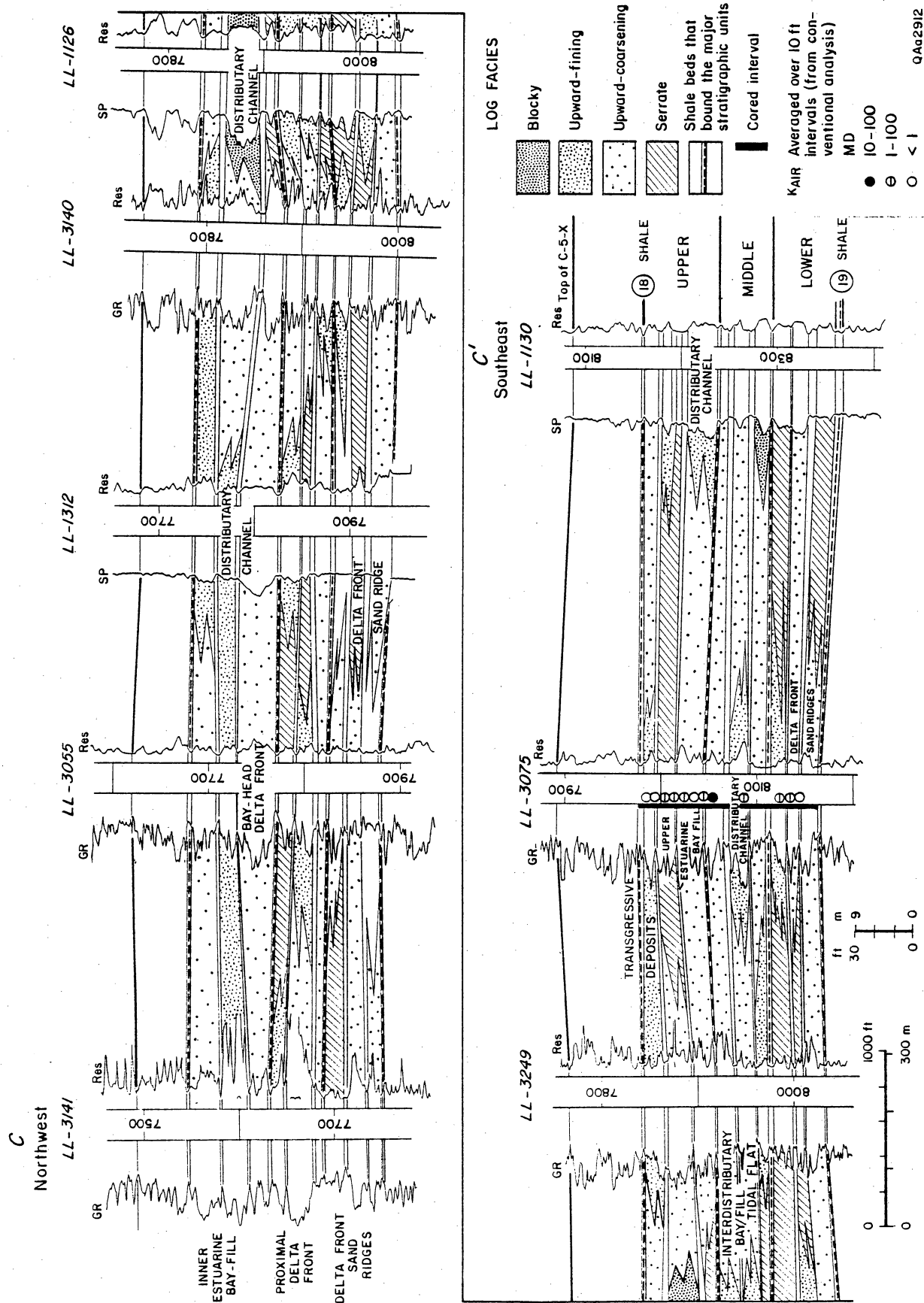


Figure VI 14. Stratigraphic strike section C-C' in the Middle C-5-X Submember, an offlapping deltaic sequence with tidal sand-ridge deposits overlain by proximal delta-front and lower delta plain deposits. Section is located in figures VI 13, VI 15, VI 16, and VI 17.

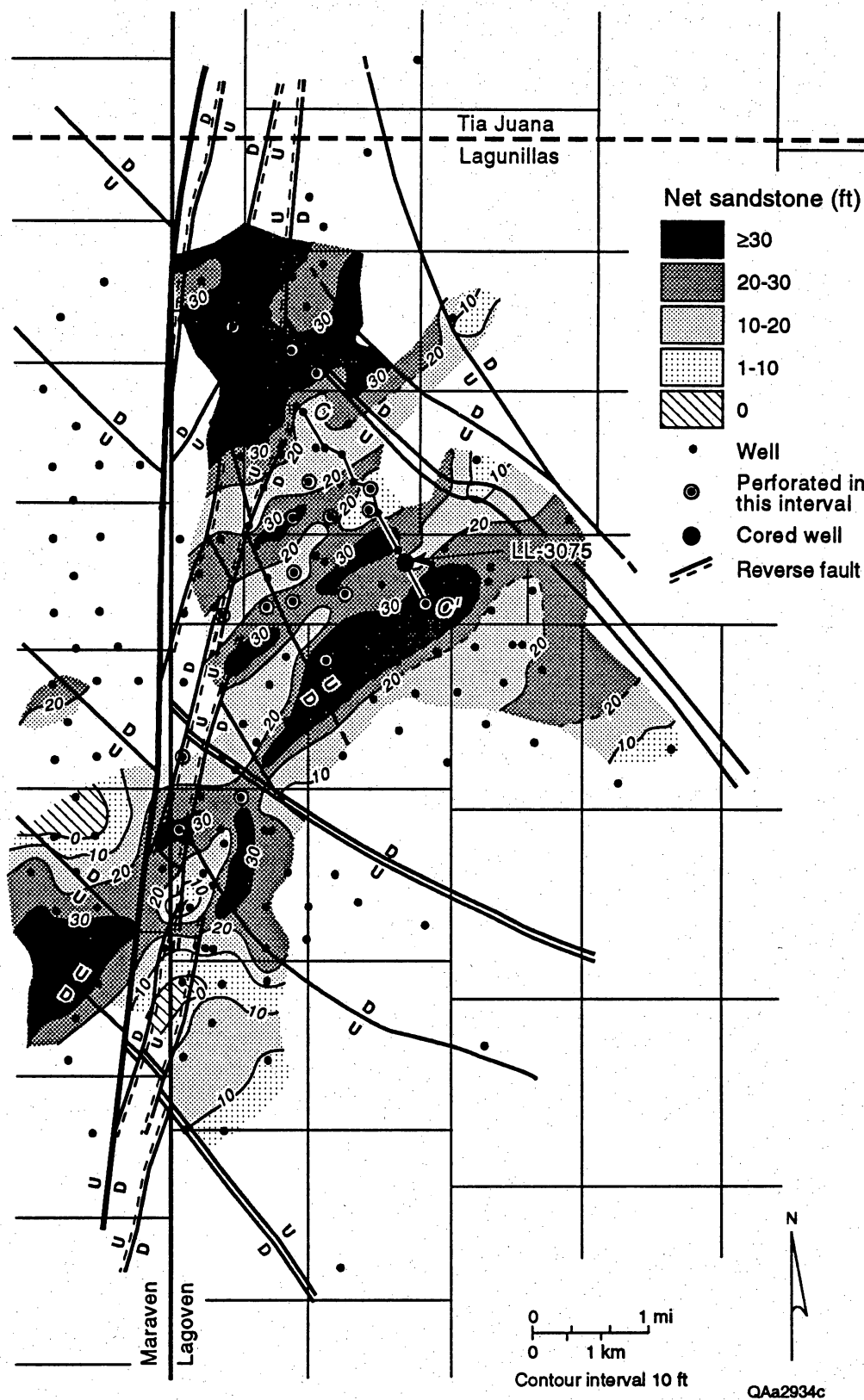


Figure VI 15. Net-sandstone thickness of the Lower Middle C-5-X Submember in the LL-652 area. Cross section C-C' is shown in figure VI 14.

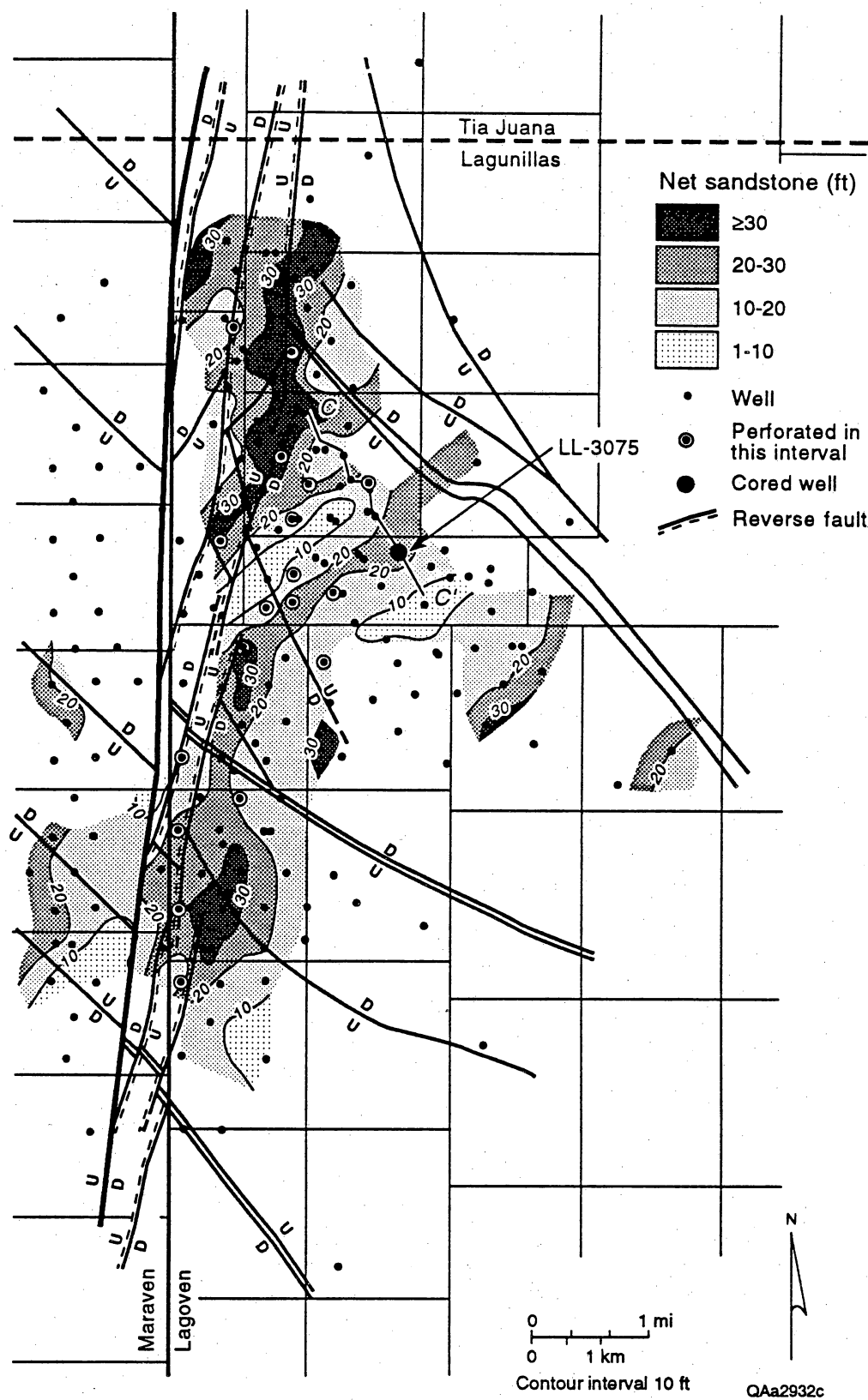


Figure VI 16. Net-sandstone thickness of the Middle Middle C-5-X Submember in the LL-652 area. Cross section C-C' is shown in figure VI 14.

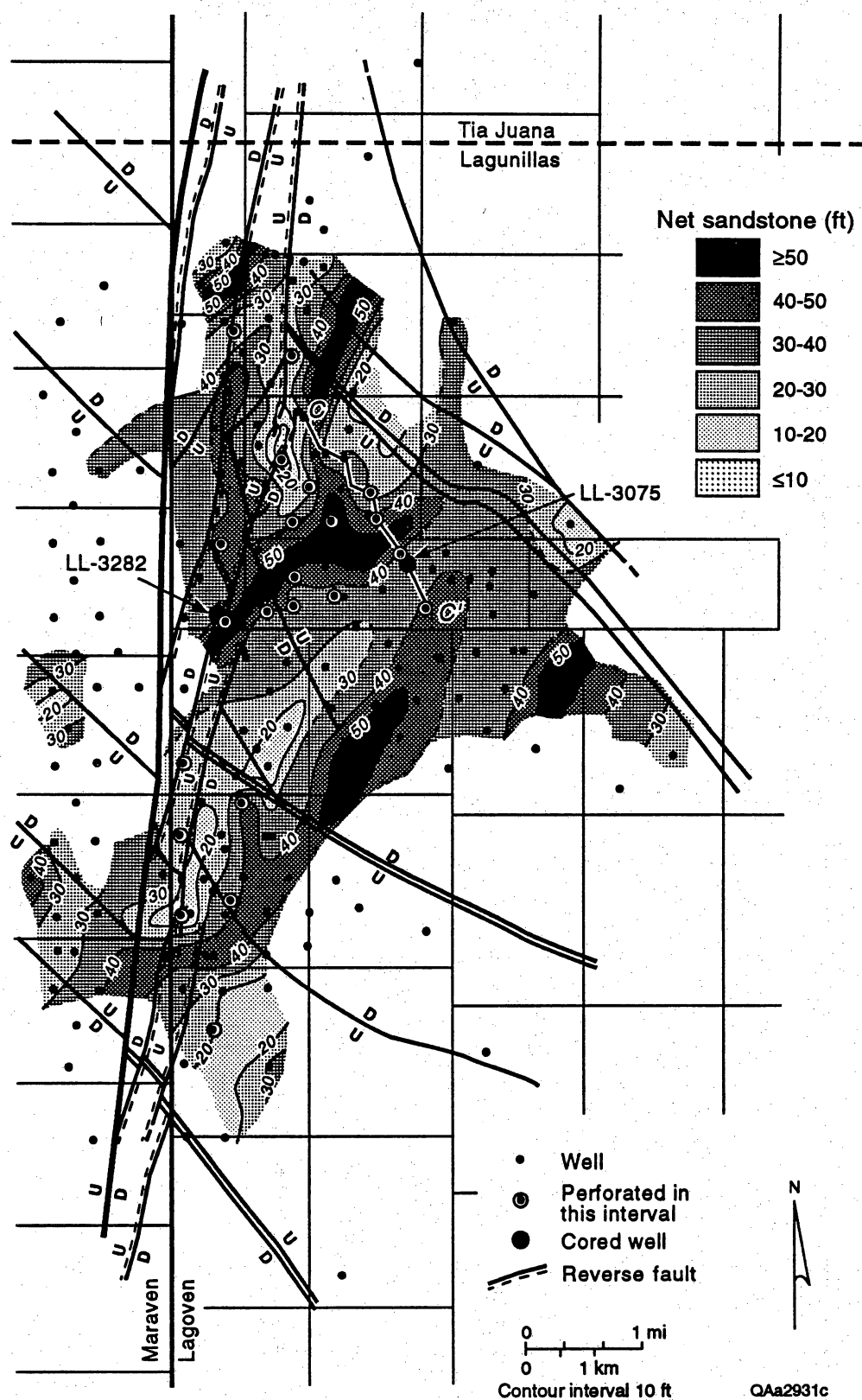


Figure VI 17. Net-sandstone thickness of the Upper Middle C-5-X Submember in the LL-652 area. Cross section C-C' is shown in figure VI 14.

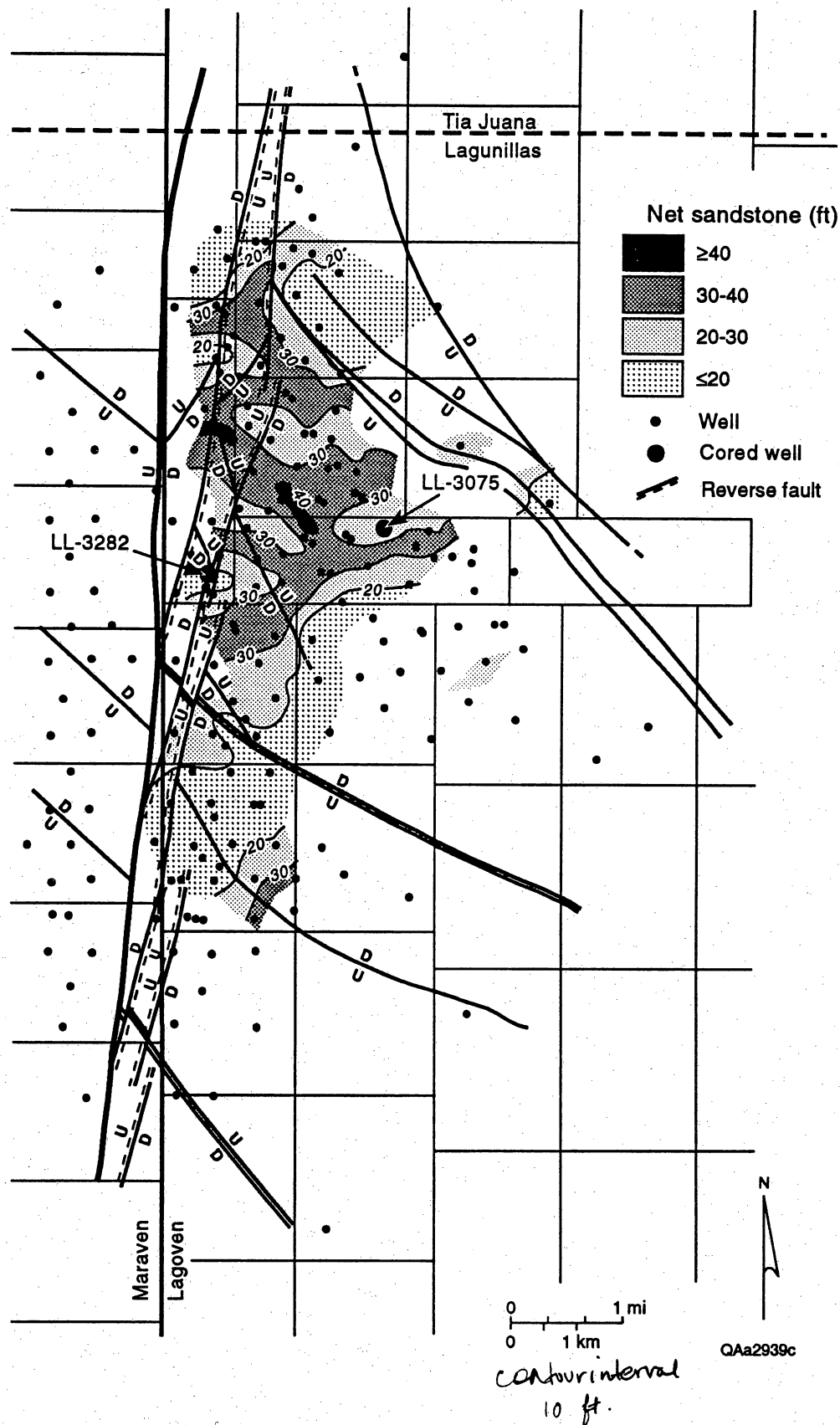


Figure VI 18. Net-sandstone thickness of the Upper C-5-X Submember in the LL-652 area.

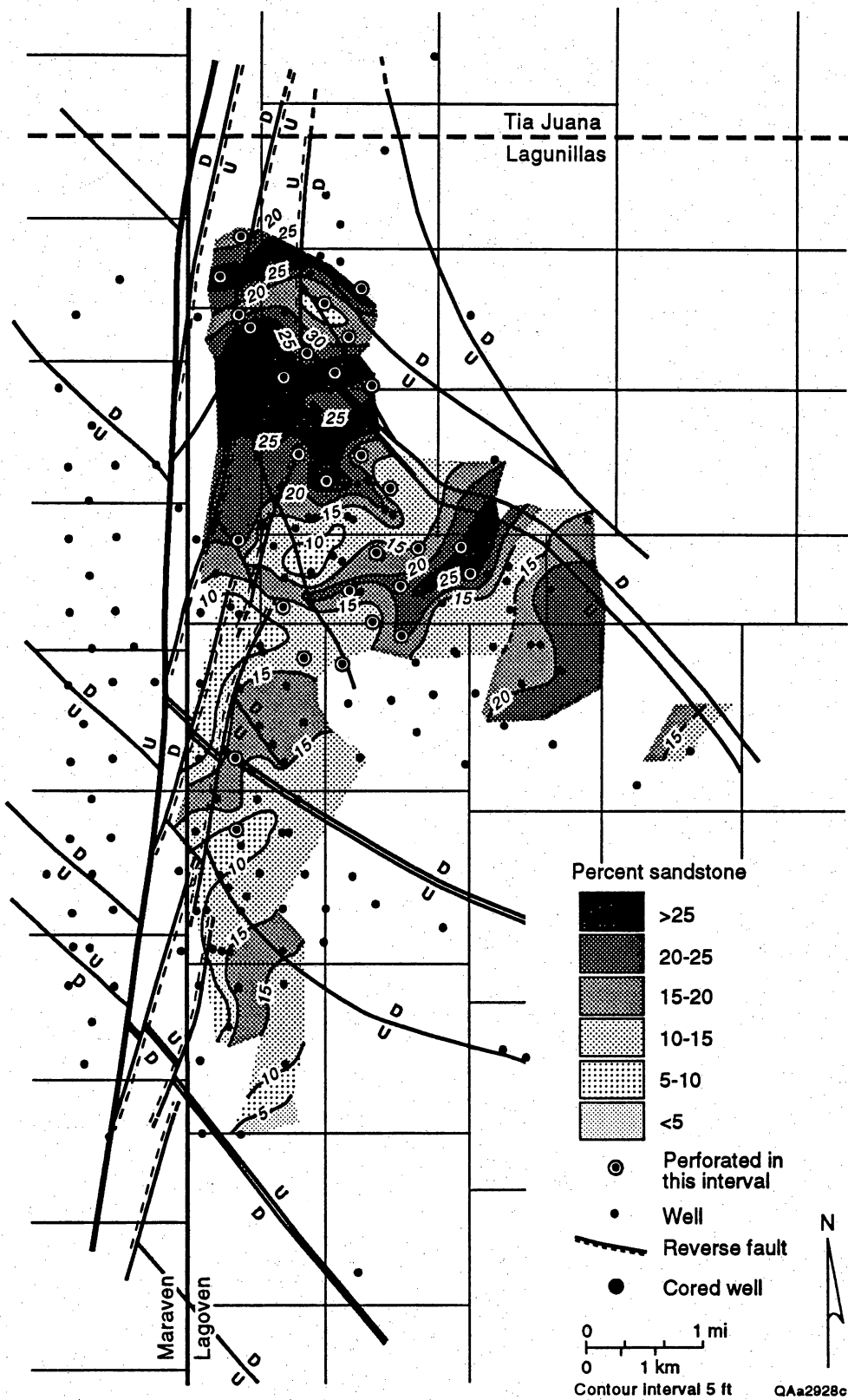


Figure VI 19. Percent sandstone of the Lower C-4-X Submember in the LL-652 area.

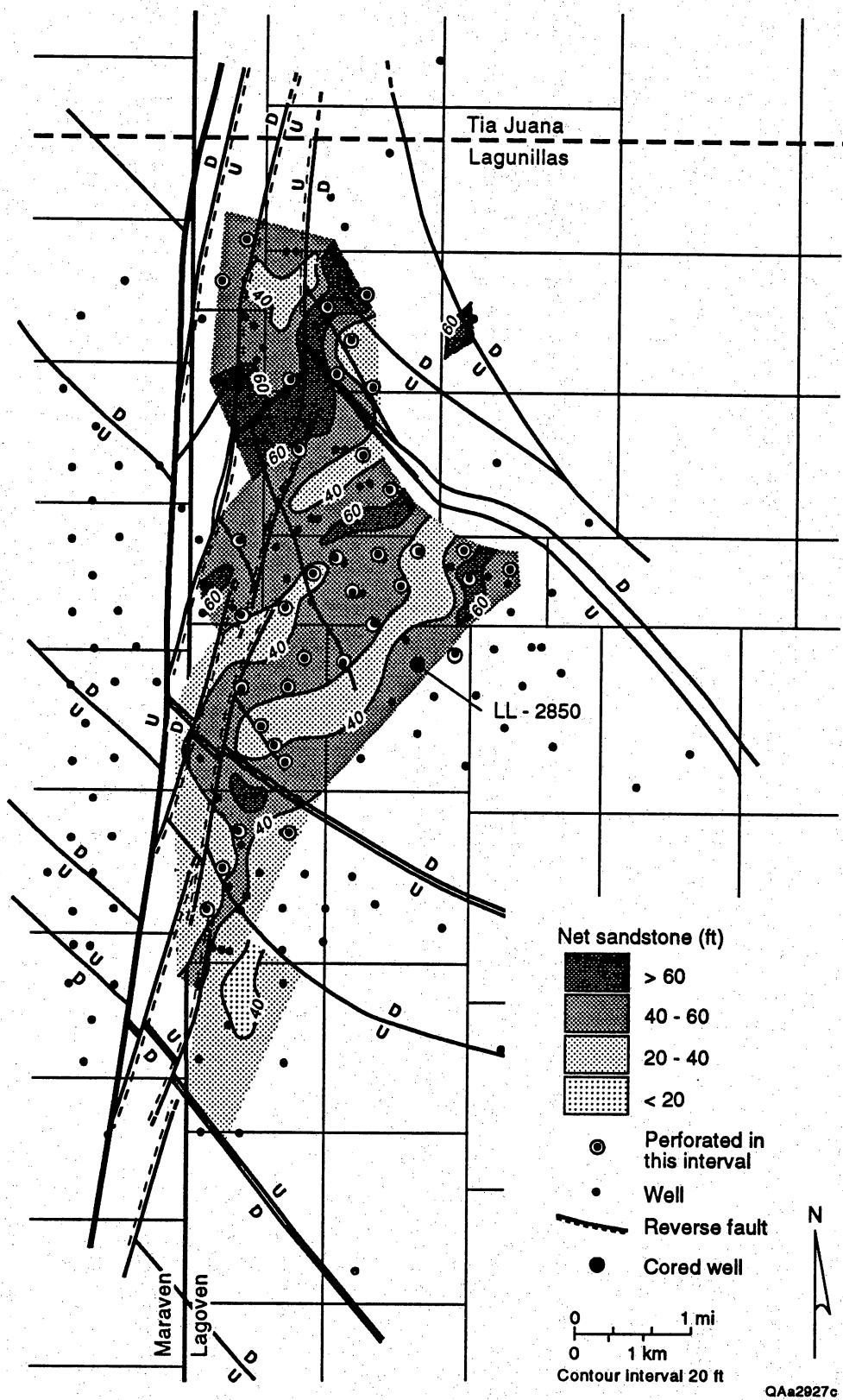


Figure VI 20. Net-sandstone thickness of the Middle C-4-X Submember in the LL-652 area.

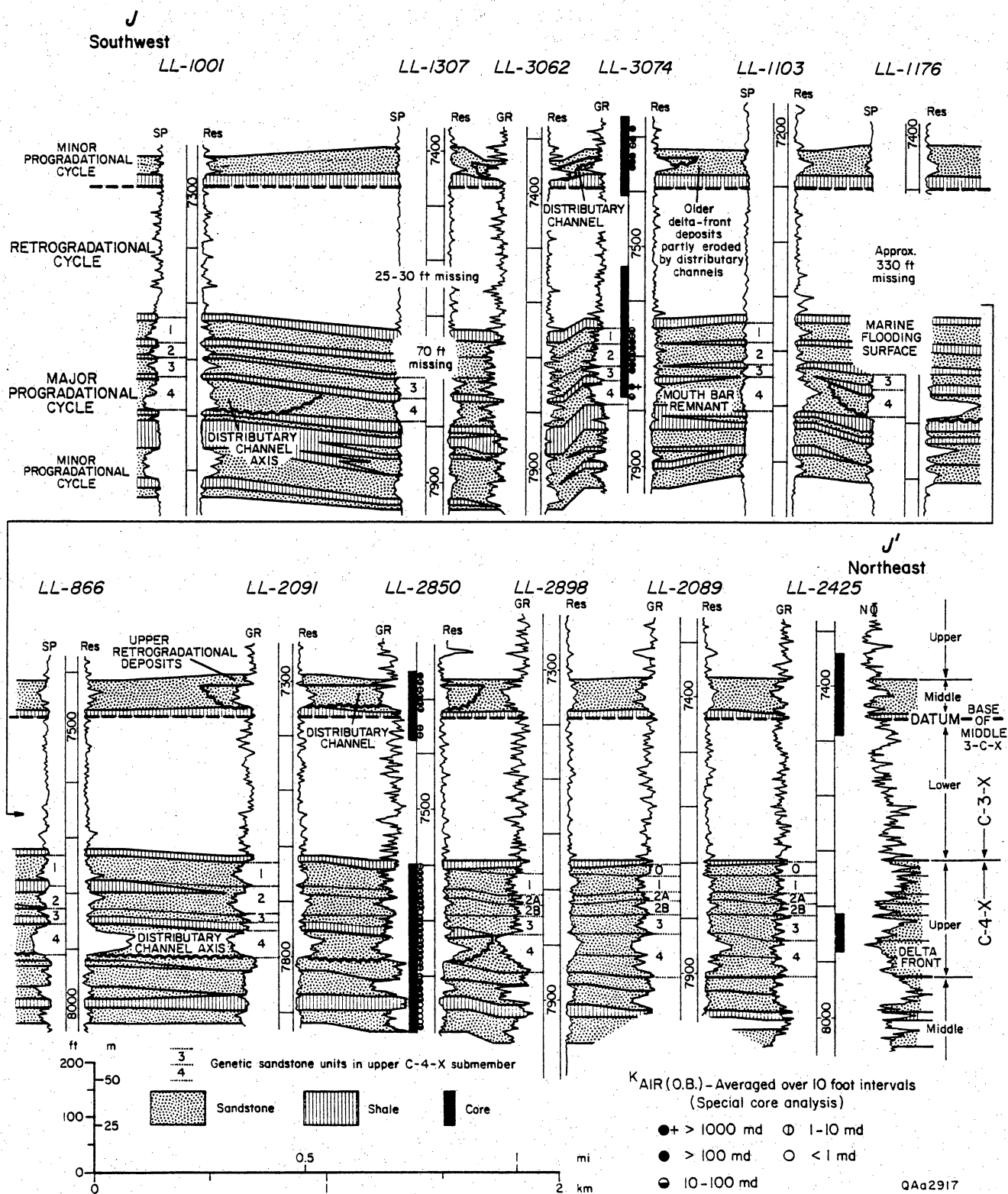


Figure VI 21. Stratigraphic dip section J-J' in the Middle C-4-X to Middle C-3-X Submembers, showing major depositional cycles and lateral variability in facies and sandbody thickness. Sandstone depositional cycles are bounded by thin (less than 10-ft [3-m]) shale beds, too thin to be depicted at this scale. Cross section is located in figure VI 22.

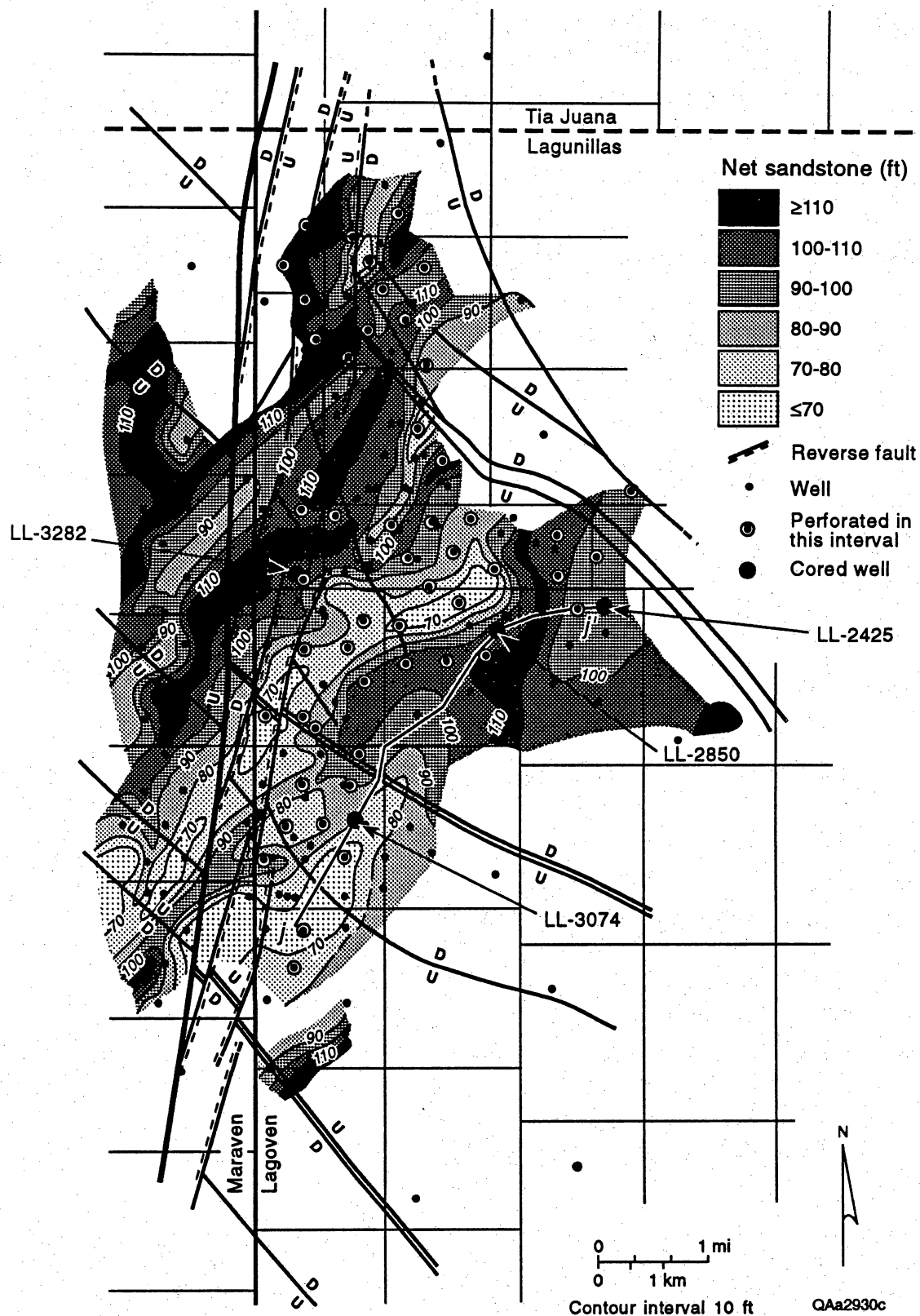


Figure VI 22. Net-sandstone thickness of the Upper C-4-X Submember in the LL-652 area. Cross section J-J' is shown in figure VI 21.

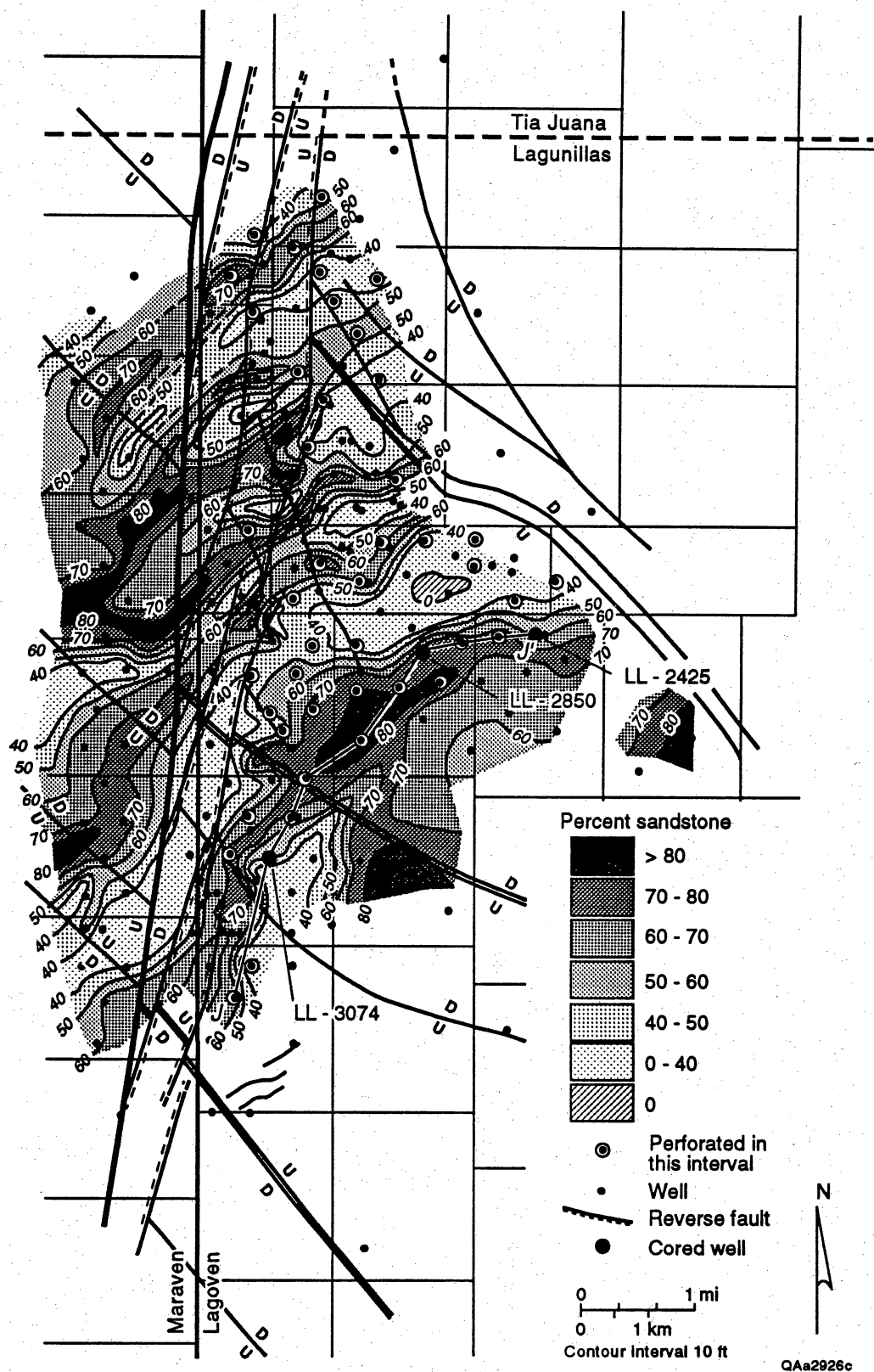


Figure VI 23. Percent sandstone of the #4 Sandstone Unit in the Upper C-4-X Submember in the LL-652 area. Cross section J-J' is shown in figure VI 21.

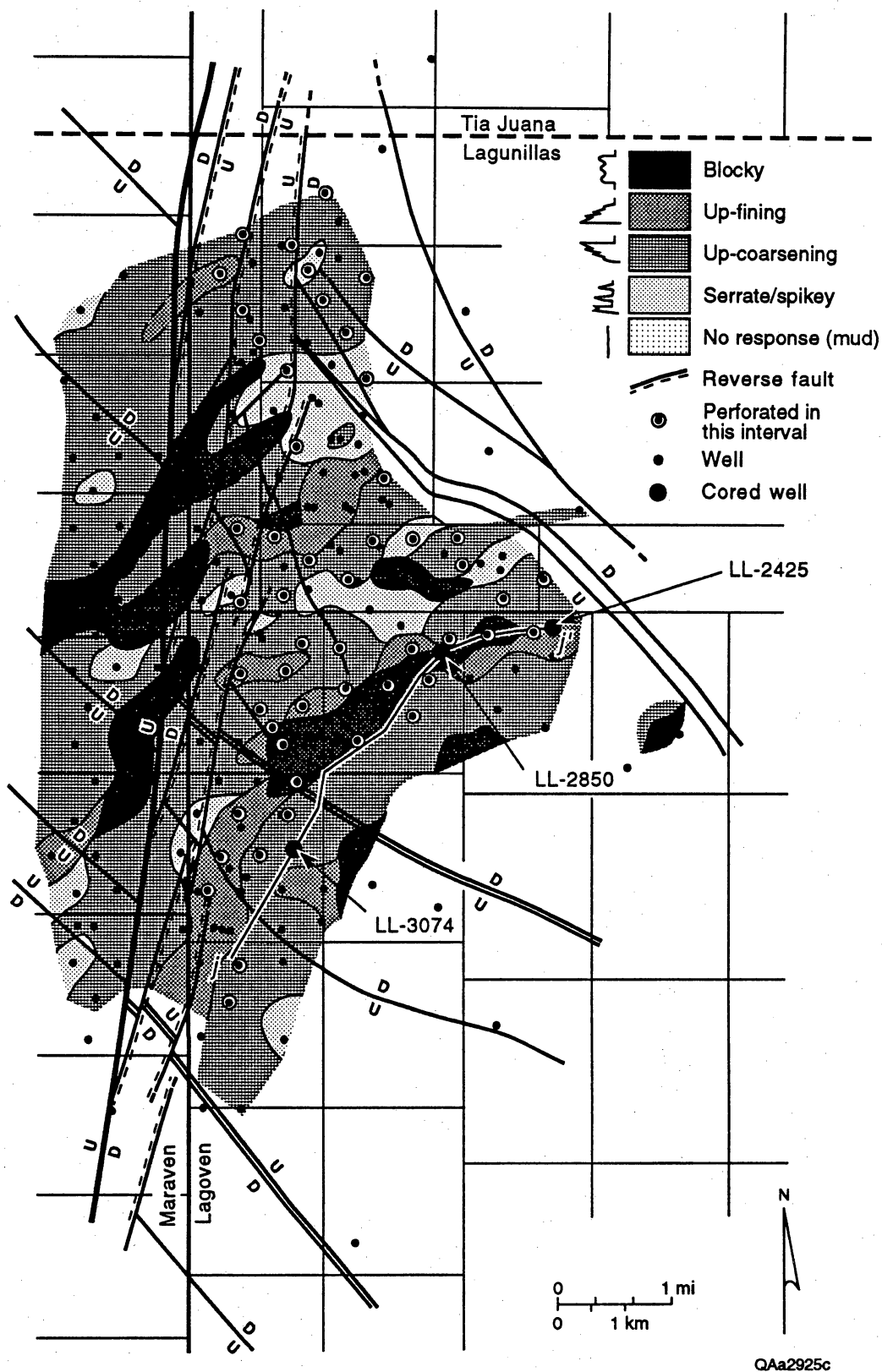


Figure VI 24. Log-facies of the #4 Sandstone Unit in the Upper C-4-X Submember in the Ll-652 area.

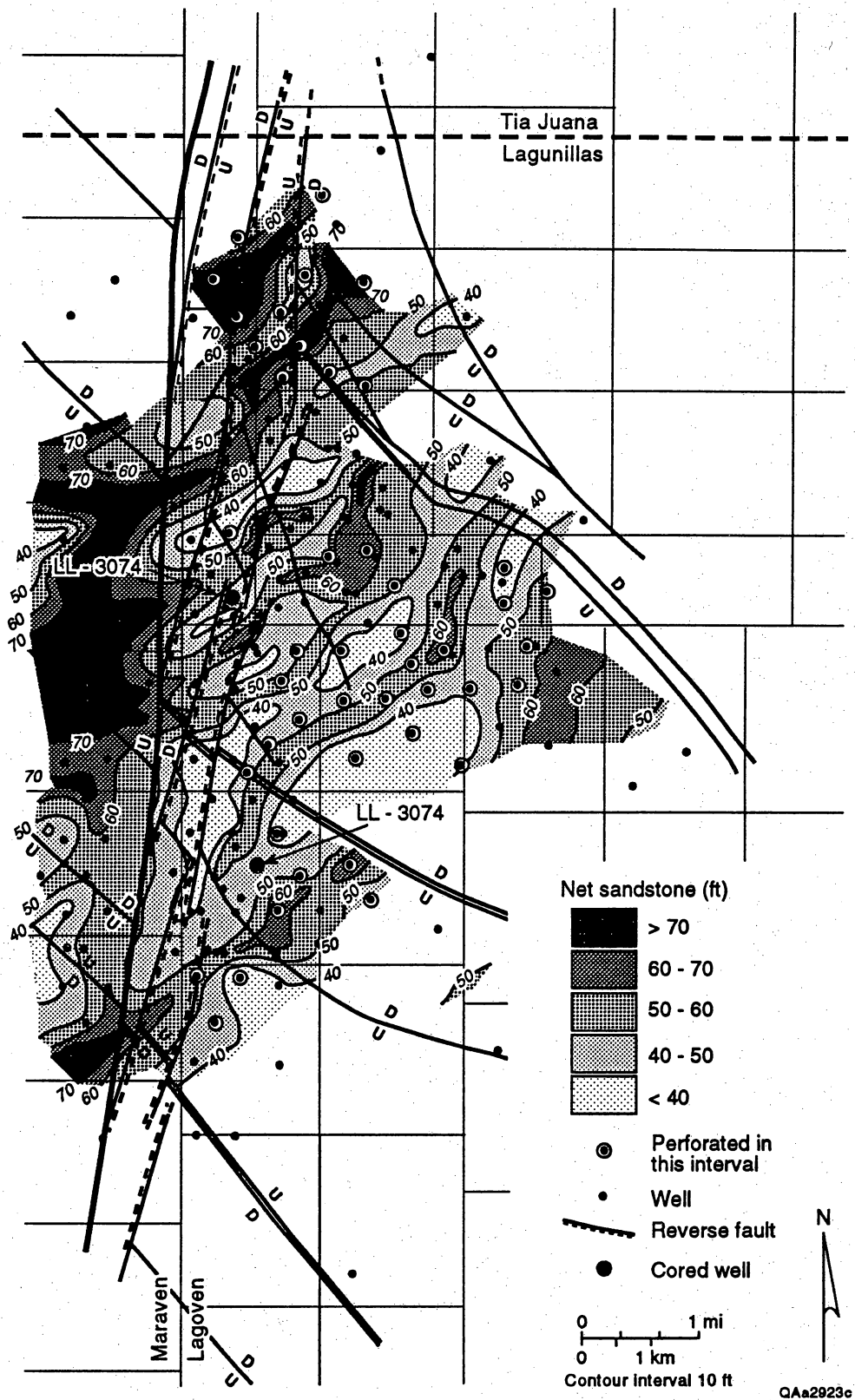


Figure VI 25. Net-sandstone thickness of the Lower C-3-X Submember in the LL-652 area.

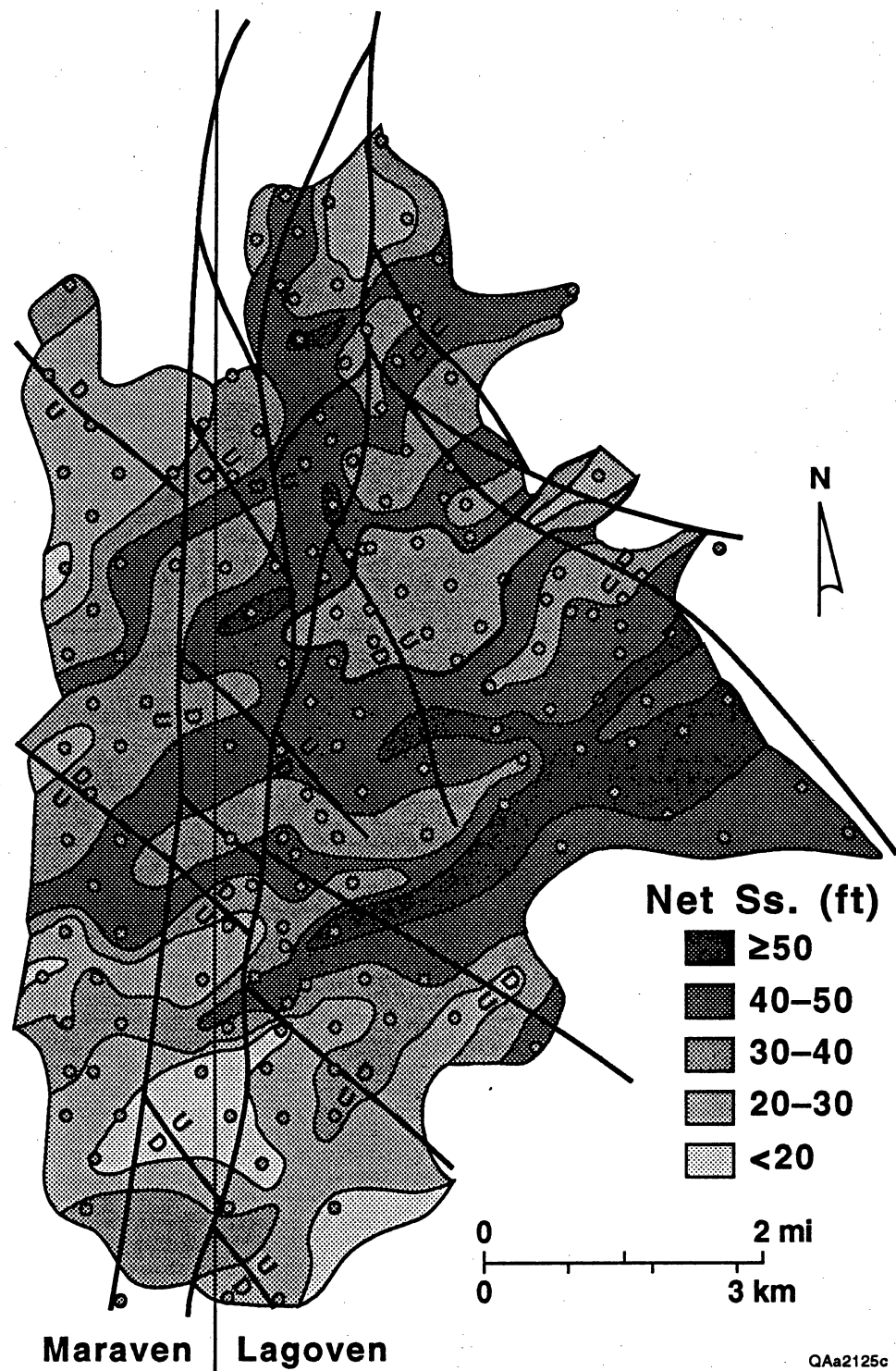


Figure VI 26. Net-sandstone thickness of the Middle C-3-X Submember in the LL-652 area.

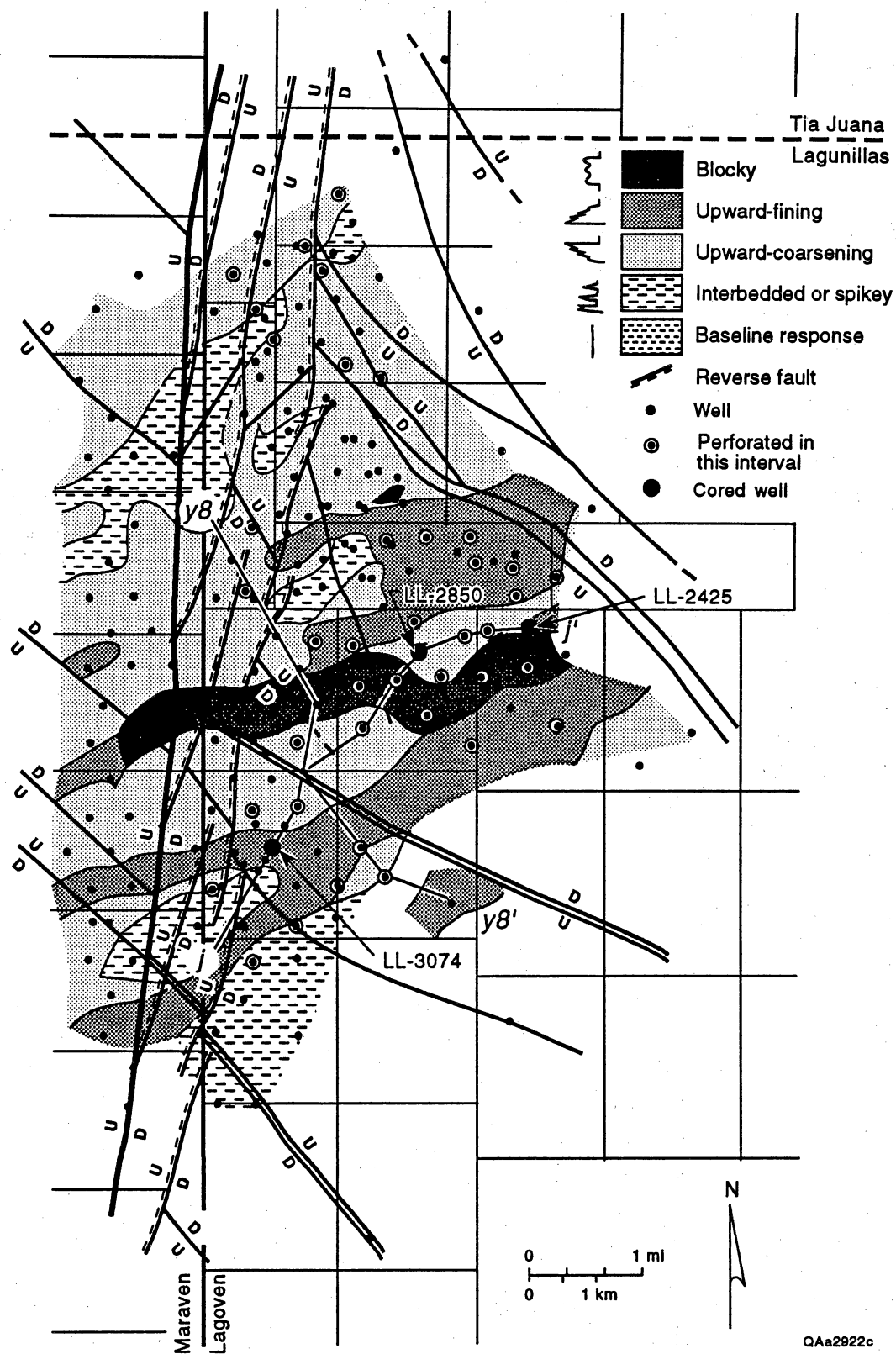


Figure VI 27. Log facies of the Middle C-3-X Submember. Cross sections J-J' and Y8-Y8' are shown in figures VI 21 and VI 28, respectively.

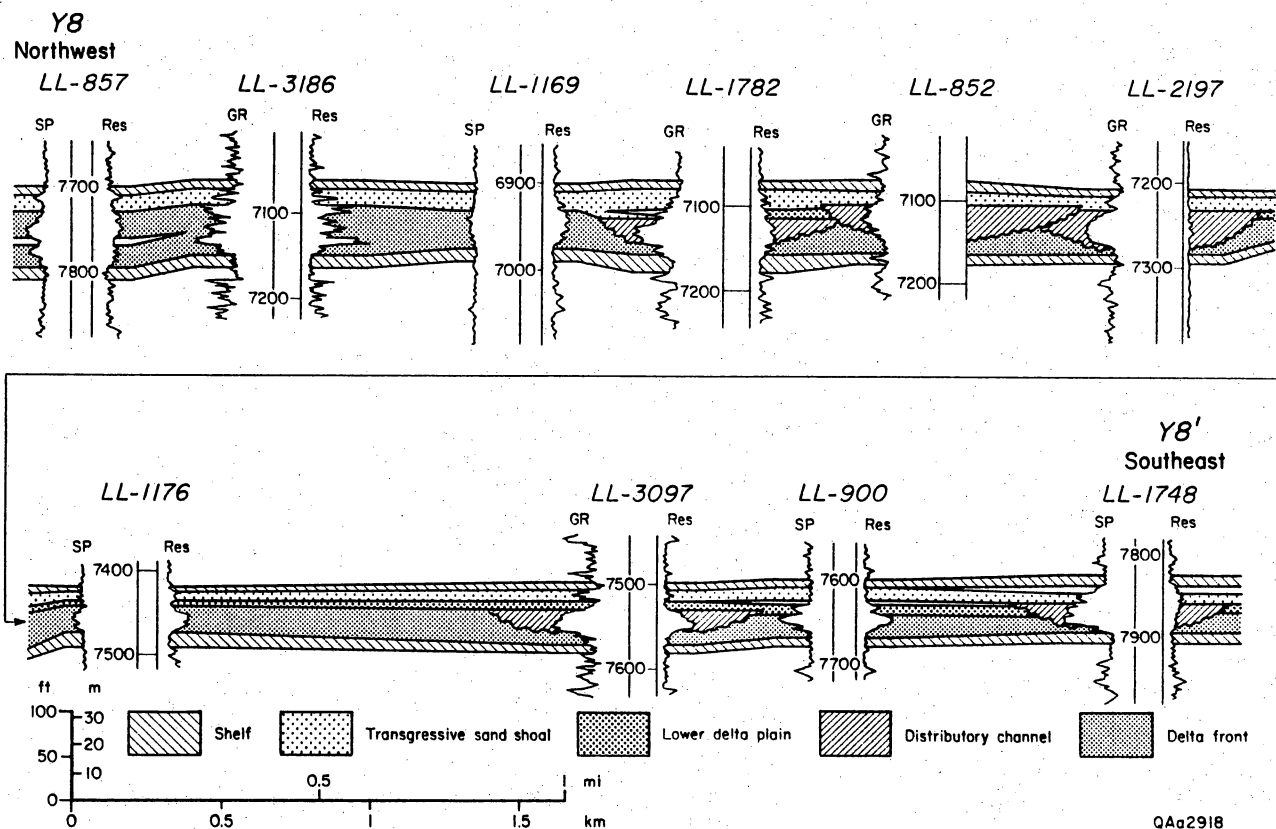
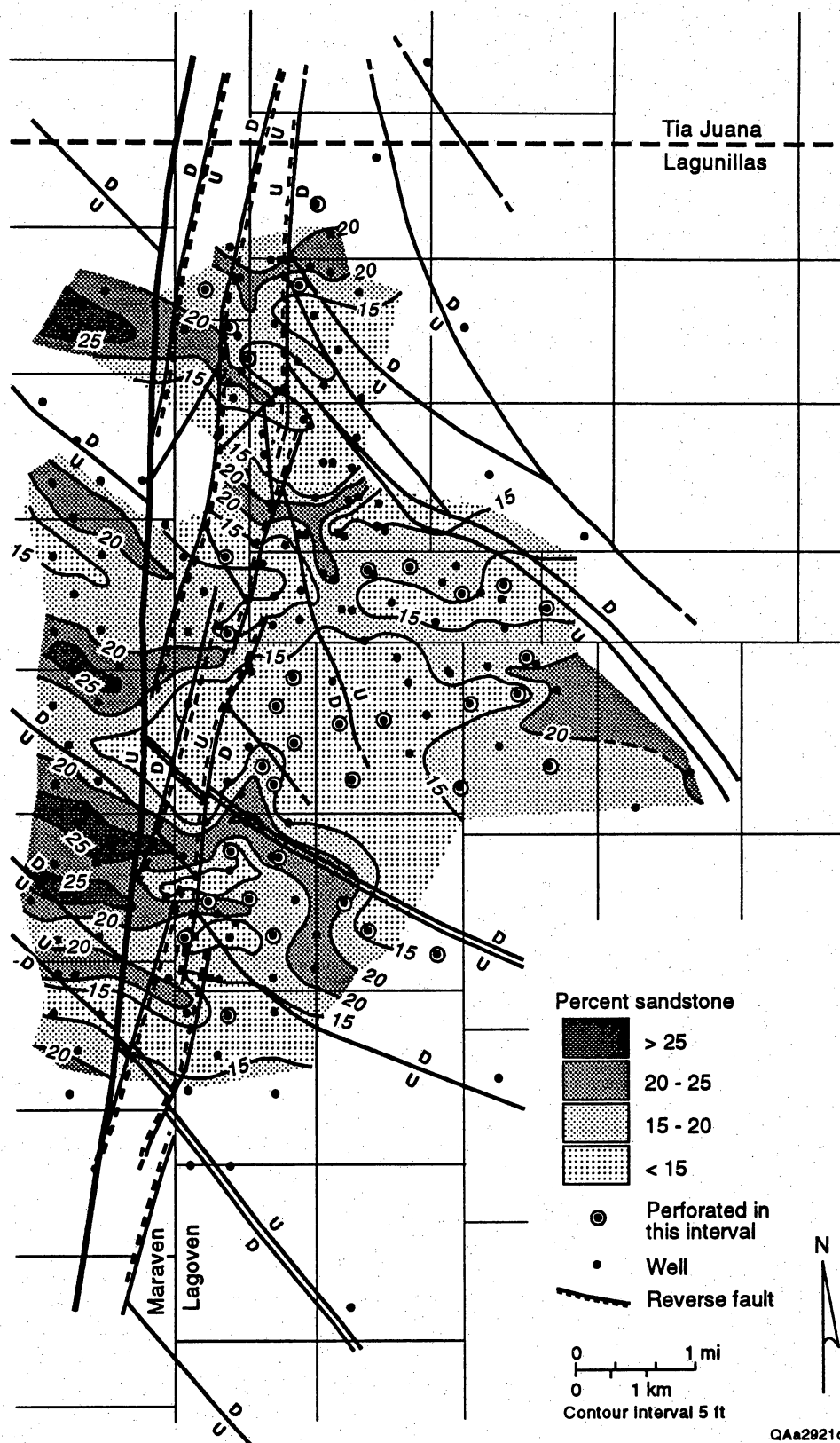


Figure VI 28. Stratigraphic cross section Y8-Y8' in the Middle C-3-X Submember, showing sandbody architecture and facies heterogeneity resulting from multiple, lenticular distributary-channel sandstones locally truncating muddy delta-front sandstones. The top reservoir seal is partly provided by a sheetlike, calcareous transgressive sand-shoal deposit. Cross section is located in figures VI 26 and VI 27.



QAa2921c

Figure VI 29. Percent sandstone of the Upper C-3-X Submember. In contrast to other C-3-X submembers, percent sandstone in the Upper C-3-X Submember is southeast-trending and exhibits bifurcating trends.

Table V1 1. Depositional systems and reservoir characteristics of the C-7-X Member in the LL-652 area.

Sand-Body Geometry	Sheetlike (?) sandstones more than 100' thick and locally truncated by overlying C-6-X submember in northern part of the map area where net-sandstone thickness is as low as 45'.
Depositional Facies	Delta-front deposits locally truncated by incised-valley fluvial deposits of overlying C-6-X member.
Cored Wells	LL-3080 (upper 25' only), LL-3140 (upper 40' only).
Perforated Wells, Estimated or Apportioned Production	Central area: LL-1803, 2942, 3056 wells.
General Area(s) of Greatest Potential for Secondary Oil Recovery	Along erosional contact with overlying C-6-X member where permeability barriers may exist.

Table VI 2. Depositional systems and reservoir characteristics of the Lower Lower C-6-X Submember in the LL-652 area.

Sand-Body Geometry	Northeast-trending belts of sandstone, 90-130' thick and 2,000-6,000' wide, bounded by broad (?) areas of less than 80' of net sandstone. The thicker sandstones have upward-fining and blocky log responses.
Depositional Facies	Incised valley fluvial deposits that truncate older delta-front and distributary-channel deposits in the underlying C-7-X member. These fluvial deposits are overlain by transgressive estuarine-fill deposits.
Cored Wells	LL-3080 and LL-3140 (entire interval).
Perforated Wells, Estimated or Apportioned Production	Central area: LL-1782, 1803, 2942, 3055, 3056, 3075, 3080 wells.
General Area(s) of Greatest Potential for Secondary Oil Recovery	See comments for upper lower C-6-X submember.

Table VI 3. Depositional systems and reservoir characteristics of the Upper Lower C-6-X Submember in the LL-652 area.

Sand-Body Geometry	Northeast-trending sandstones, more than 70' thick with upward-fining and blocky log responses, bounded laterally by upward-coarsening sandstones less than 50' thick.
Depositional	Incised-valley fluvial deposits that truncate deltaic deposits. The sequence is capped by transgressive estuarine-fill deposits.
Cored Wells	LL-3080 (entire interval), LL-3140 (all but 40' in lower half).
Perforated Wells, Estimated or Apportioned Production	Central area: good density of perforated wells; southwestern area: poor density.
General Area(s) of Greatest Potential for Secondary Oil Recovery	Possible permeability boundaries at contacts of fluvial sandstones and underlying deltaic deposits. Other permeability contrasts possible lateral to and overlying these fluvial sandstones.

Table VI 4. Depositional systems and reservoir characteristics of the Lower 21-22 Interval in the Lower Upper C-6-X Submember in the LL-652 area.

Sand-Body Geometry	Northeast-trending, dip-elongate and upward-fining sandstones 40-58' thick and approximately 2,000' wide, bounded laterally by areas of generally less than 30' of sandstone and merging northeastward with areas of less than 40' of net sandstone.
Depositional Facies	Distributary channel deposits, overlying delta-front deposits in a offlapping progradational parasequence.
Cored Wells	LL-3080 (lower 70%), LL-3282 (lower 90%).
Perforated Wells, Estimated or Apportioned Production	Southwest: LL-946, 992, 1001, 1005 wells; Central: Multiple perforated wells.
General Area(s) of Greatest Potential for Secondary Oil Recovery	Channel-mouth-bar sandstones pinching out into sandstone-poor delta-front deposits and narrow, isolated distributary-channel deposits.

Table VI 5. Depositional systems and reservoir characteristics of the Upper 21-22 Interval in the Lower Upper C-6-X Submember in the LL-652 area.

Sand-Body Geometry	Northeast-trending, dip-elongate sandstones, 30-45' thick and 1,500-2,500' wide, bounded by sandstone-poor areas with minimum of 10-15' of net sandstone.
Depositional Facies	Distal delta-front and shelf deposits.
Cored Wells	None
Perforated Wells, Estimated or Apportioned Production	Southwest: LL-946, LL-992, LL-1001 wells. Central: LL-1172, LL-1782 wells.
General Area(s) of Greatest Potential for Secondary Oil Recovery	Isolated distal delta-front tidal ridge deposits.

Table VI 6. Depositional systems and reservoir characteristics of the Upper Upper C-6-X Submember in the LL-652 area.

Sand-Body Geometry	Northeast-trending, dip-elongate sandstones, 40-50' thick and 500-3,500' wide, bounded laterally by sandstone -- poor areas 10-30' thick.
Depositional Facies	Upward-coarsening delta-front (tidal-ridge) sandstones in central part of map area and upward-fining distributary-channel sandstones in the southwest part of map area.
Cored Wells	None
Perforated Wells, Estimated or Apportioned Production	Central area: fair level of development (LL-847, 1129, 1172, 1276, 3056, 3075 wells); southwestern area: poor level (LL-946, 1001 wells).
General Area(s) of Greatest Potential for Secondary Oil Recovery	Narrow distributary-channel and tidal ridge sandstones.

Table VI 7. Depositional systems and reservoir characteristics of the Lower C-5-X Submember in the LL-652 area.

Sand-Body Geometry	Narrow (1,500-3,000' wide), dip-parallel and semi-continuous belts of more than 70' (30%) sandstone.
Depositional Facies	System of upward-coarsening tidal sand ridges (distal delta-front) consisting of interbedded sandstone and mudstone.
Cored Wells	LL-3075 (entire interval).
Perforated Wells, Estimated or Apportioned Production	North-central area: moderate level of development (LL-904, LL-1111, LL-1126, LL-1172, LL-1276, LL-1782, LL-2938, and LL-2940 wells); southwestern and northern areas: poor levels of development.
General Area(s) of Greatest Potential for Secondary Oil Recovery	Tidal ridge sandstones that are isolated by faults or muddy interridge areas.

Table VI 8. Depositional systems and reservoir characteristics of the Lower Lower C-5-X Submember in the LL-652 area.

Sand-Body Geometry	Dip-elongate (?), discontinuous belts of sandstone, 40-55' thick and 1,000-2,000' wide, thinning laterally into 20-30' of muddy sandstone.
Depositional Facies	Distal delta-front and shelf deposits.
Cored Wells	LL-3075 (entire interval).
Perforated Wells, Estimated or Apportioned Production	Central area: LL-1111, 1129, 1172, 1782 wells; southwestern area: LL-946, 1001 wells.
General Area(s) of Greatest Potential for Secondary Oil Recovery	Relatively thicker (individual sandstones 5-10' thick) sandstones encased in marine mudstone.

Table VI 9. Depositional systems and reservoir characteristics of the Upper Lower C-5-X Submember in the LL-652 area.

Sand-Body Geometry	East-trending, dip-parallel sandstones, 40-60' thick and 2,000-5,000' wide. These sandstones have upward-coarsening and/or serrate log responses.
Depositional Facies	Distal delta-front.
Cored Wells	LL-3075 (entire interval).
Perforated Wells, Estimated or Apportioned Production	Moderate density of perforated wells only in central area.
General Area(s) of Greatest Potential for Secondary Oil Recovery	Areas where tidal ridge sandstones are isolated by faults or muddy interridge areas.

Table VI 10. Depositional systems and reservoir characteristics of the Middle C-5-X Submember in the LL-652 area.

Sand-Body Geometry	East- and northeast-trending sandstones, 80-110' thick and 2,000-8,000' wide. In northern part of field, net-sandstone thickness generally decreases eastward from 90-100' to 60-80'.
Depositional Facies	Composite unit of 3 offlapping depositional cycles, consisting of an aggregate of distributary-channel, delta-front and transgressive sandstones.
Cored Wells	LL-3075 (entire interval), LL-3282 (upper 30%).
Perforated Wells, Estimated or Apportioned Production	Good density of perforated wells throughout, except for southwestern and extreme northern areas.
General Area(s) of Greatest Potential for Secondary Oil Recovery	See maps of individual depositional cycles (upper, middle, and lower).

Table VI 11. Depositional systems and reservoir characteristics of the Lower Middle C-5-X Submember in the LL-652 area.

Sand-Body Geometry	Dip-parallel, mainly upward-coarsening sandstones, 30-45' thick and 1,000 to 6,000' wide, separated by broad areas of 15-30' of muddy sandstone.
Depositional Facies	Delta-front (tidal ridge) sandstones bounded by muddy interridge deposits. Possible distributary channel system in southwest corner of map area in Maraven concession.
Cored Wells	LL-3075 (entire interval).
Perforated Wells, Estimated or Apportioned Production	Main concentration of perforated wells in central area; all other areas have poor density of perforated wells.
General Area(s) of Greatest Potential for Secondary Oil Recovery	

Table VI 12. Depositional systems and reservoir characteristics of the Middle Middle C-5-X Submember in the LL-652 area.

Sand-Body Geometry	Narrow (550-3,000 ft wide), northeast-trending bands of more than 20' of mostly upward-fining sandstones bounded laterally by broad areas of 5-15' of muddy sandstone with either upward-coarsening or serrate log responses.
Depositional Facies	Distributary- and tidal-channel deposits bounded by muddy lower delta-plain (tidal-flat) deposits.
Cored Wells	LL-3075 (entire interval).
Perforated Wells, Estimated or Apportioned Production	North-central and central areas: moderate to good density of perforations; southwestern area: fair density.
General Area(s) of Greatest Potential for Secondary Oil Recovery	Distributary- and tidal-channel sandstones isolated in fault compartments or partly encased in tidal-flat mudstone.

Table VI 13. Depositional systems and reservoir characteristics of the Upper Middle C-5-X Submember in the LL-652 area.

Sand-Body Geometry	Digitate, dip-elongate, northeast-trending and -bifurcating sandstones more than 40' thick and 1,550 to 4,000' wide, extending across map area. These sandstones have upward-fining and blocky log responses and are flanked by thinner (10-30') sandstones with upward-coarsening and serrate log responses.
Depositional Facies	Distributary-channel (bayhead delta?) and channel mouth-bar deposits overlain by transgressive delta-front sandstones.
Cored Wells	LL-3075 (entire interval), LL-3282 (upper 80%).
Perforated Wells, Estimated or Apportioned Production	Central area: moderate to good density of perforated wells; southwestern area: fair density; all other areas: poor density.
General Area(s) of Greatest Potential for Secondary Oil Recovery	Narrow distributary-channel sandstones and channel mouth-bar sandstones where they pinch out into delta-front deposits.

Table VI 14. Depositional systems and reservoir characteristics of the Upper C-5-X Submember in the LL-652 area.

Sand-Body Geometry	East-trending, interconnected belts of more than 30' (>30%) sandstone 2,000 to 3,500 ft wide in the northern part of the map area. In the southern part of the map area, sandstones are generally less than 30' thick. Sandstones have a dominantly upward-coarsening or serrate log response.
Depositional Facies	Mainly delta-front and distal delta-front deposits.
Cored Wells	LL-3075 (entire interval), LL-3282 (entire interval).
Perforated Wells, Estimated or Apportioned Production	Central area: good density of perforated wells; southwestern area: fair density; all other areas: poor density.
General Area(s) of Greatest Potential for Secondary Oil Recovery	Areas where delta-front and distal delta-front tidal ridge sandstones pinch out into interridge mudstones.

Table VI 15. Depositional systems and reservoir characteristics of the Lower C-4-X Submember in the LL-652 area.

Sand-Body Geometry	Northeast-trending, dip-elongate sinuous belts of sandstone, more than 40' thick (>15% sandstone) in the central and southwest part of the map area, merging into wide (>2 mi) area in the northern part of the map area where there is more than 60' (>20%) of sandstone. Almost all sandstones have upward-coarsening and serrate log responses.
Depositional Facies	Delta-front and distal delta-front tidal ridge sandstones.
Cored Wells	None
Perforated Wells, Estimated or Apportioned Production	Good completion density throughout, except for southwestern area.
General Area(s) of Greatest Potential for Secondary Oil Recovery	Areas where tidal ridge sandstones are encased in interridge mudstones.

Table VI 16. Depositional systems and reservoir characteristics of the Middle C-4-X Submember in the LL-652 area.

Sand-Body Geometry	North-northeast-trending belts of sandstone, more than 40' thick and 2,000 to 7,500' wide. These sandstones are locally as much as 60' thick.
Depositional Facies	Composite interval of 2 depositional parasequences, consisting mostly of distributary-channel, tidal-channel, and delta-front sandstones.
Cored Wells	LL-2850 (upper 90% of interval).
Perforated Wells, Estimated or Apportioned Production	High density of perforated wells throughout the field, except west-northwest area (A-188 concession).
General Area(s) of Greatest Potential for Secondary Oil Recovery	Thick distributary- and tidal-channel sandstones and overbank deposits partly encased in muddy tidal-flat deposits.

Table VI 17. Depositional systems and reservoir characteristics of the Upper C-4-X Submember in the LL-652 area.

Sand-Body Geometry	Northeast-trending, dip-elongate sandstones, 90-140' thick (>50% sandstone) and 1,050-5,000' wide, distributed throughout the map area. These sandstones are bounded laterally by sandstone poor areas with a minimum of 40' of sandstone.
Depositional Facies	System of dip-elongate, mainly upward-coarsening delta-front sandstones. Proximal delta-front sandstones are located in the western and southwestern part of the map area and merge northeastward into distal delta-front sandstones. However, the lower part of this sub-member (#4 sandstone) consists mostly of distributary-channel sandstones.
Cored Wells	LL-2425 (60' from middle), LL-2850 (entire), LL-3074 (all except lower 30'), LL-3282 (all except 35').
Perforated Wells, Estimated or Apportioned Production	Multiple perforated wells in east-central area; fewer perforated wells in south and north-central areas.
General Area(s) of Greatest Potential for Secondary Oil Recovery	Thick delta-front and distributary-channel sandstones isolated by faults or areas on the margin of these sandstones where they form stratigraphic traps by pinching out laterally into interridge or interdistributary mudstones.

Table VI 18. Depositional systems and reservoir characteristics of the #4 Sandstone Unit in the Upper C-4-X Submember in the LL-652 area.

Sand-Body Geometry	Northeast-trending and -bifurcating system of upward-fining sandstones more than 30' thick (70%) sandstone pinching out into and merging with and muddy areas of less than 20' (40%) sandstone in the northern part of the map area. In the southern part of the map area, the sandstones are continuous.
Depositional Facies	System of distributary-channel sandstones pinching out into channel-mouth bar and delta-front deposits in the northern part of the map area. Interdistributary areas consist of sandstone-poor tidal-flat deposits.
Cored Wells	LL-2425 (top 16' only), LL-2850 (entire), LL-3074 (all except lower 30'), LL-3282 (top 6' only).
Perforated Wells, Estimated or Apportioned Production	Densely perforated area in south-central and southeastern areas; moderate to fair perforation density elsewhere.
General Area(s) of Greatest Potential for Secondary Oil	Areas where distributary-channel and channel-mouth bar deposits pinch-out northeastward into muddy delta-front deposits (northern part of map area) and laterally into muddy tidal-flat deposits (other areas).

Table VI 19. Depositional systems and reservoir characteristics of the Lower C-3-X Submember in the LL-652 area.

Sand-Body Geometry	Two lobes of more than 70' of sandstone in Maraven concession (main one in west-central part of map and minor one in southwestern part of map), connected to narrow (500-2,000 ft wide), continuous lands of sandstone more than 50' thick. Log response of sandstone in lobes is variable, whereas log response in bands is upward-coarsening and serrate.
Depositional Facies	Depocenters consisting of distributary-channel complexes in Maraven concession located updip (westward and southwestward) of dip-elongate, narrow tidal sand ridge deposits that occur throughout the Lagoven concession.
Cored Wells	LL-2850 (lower 7' only), LL-3074 (lower 110'), LL-03282 (lower 10' only).
Perforated Wells, Estimated or Apportioned Production	Southeastern and southern areas: high density of perforated wells; northern area: good density; all other areas: poor density.
General Area(s) of Greatest Potential for Secondary Oil Recovery	Where narrow tidal sand ridges pinch out laterally into muddy interridge areas; also in channel-mouth-bar sandstones along boundary between Maraven and Lagoven concessions in area between LL-917 and LL-933.

Table VI 20. Depositional systems and reservoir development of the Middle C-3-X Submember in the LL-652 area.

Sand-Body Geometry	Northeast-trending, dip-elongate and upward-fining sandstones 40-60' thick and 1,500-3,500' wide, transecting a system of northeast-trending, upward-coarsening sandstones, 30-50' thick and 1,500-5,000' wide. Net-sandstone thickness, generally, increases northeastward.
Depositional Facies	A system of northeast-trending distributary-channel sandstones in the southern part of the field area that truncates a dip-elongate system of upward-coarsening delta-front sandstones.
Cored Wells	LL-2425 (entire interval), LL-2850 (entire interval), LL-3074 (entire interval).
Perforated Wells, Estimated or Apportioned Production	Southern, South-central, and eastern areas: high density of perforated wells; Northern area: moderate density; North-central area: virtually none.
General Area(s) of Greatest Potential for Secondary Oil Recovery	Where distributary-channel sandstones pinch out laterally into delta-plain (tidal-for flat) mudstones in the southern part of the field, or where lenticular tidal-ridge sandstones are partly isolated in muddier interridge sandy mudstones.

Table VI 21. Depositional systems and reservoir characteristics of the Upper C-3-X Submember in the LL-652 area.

Sand-Body Geometry	Multiple, east-trending, dip-elongate, bifurcating lenticular sandstones more than 40' thick (>20% sandstone) and 700 to 1,600 ft wide.
Depositional Facies	Distributary channel deposits in the Maraven concession merging eastward with delta-front and interdistributary bay deposits in the Lagoven concession.
Cored Wells	LL-2425 (lower 35 ft only), LL-3074 (lower 70 ft only).
Perforated Wells, Estimated or Apportioned Production	Southern and south-central areas: good density of perforated wells; northern area: moderate density; north-central and extreme western areas: poor density.
General Area(s) of Greatest Potential for Secondary Oil Recovery	Where distributary-channel deposits pinch out laterally into interdistributary bay deposits or where channel-mouth-bar deposits pinch out into delta-front deposits.

Plate VII-1a.

Loss of porosity by deformation of ductile biotite (B) and metamorphic rock fragment (M). Sample of C-6-X sandstone from a depth of 9,174 ft in the LL-3140 well. Long dimension of photo = 0.65 mm. Plane-polarized light.

Plate VII-1b.

Typical Missoa sandstone with abundant detrital quartz grains and sedimentary and metamorphic rock fragments. Quartz cement fills much of the intergranular porosity, typical of deeper Missoa C-X sandstones. Sample of C-6-X sandstone from a depth of 9,174 ft in the LL-3140 well. Long dimension of photo = 2.6 mm. Cross-polarized light.

Plate VII-1c.

Shallow Missoa C-3-X sandstone with high primary and secondary porosity and little quartz cement. Sample from a depth of 7,272 ft in the LL-2850 well. Long dimension of photo = 2.6 mm. Plane-polarized light.

Plate VII-1d.

Deep Missoa C-6-X sandstone, in which most intergranular porosity is occluded by quartz cement. Same sample and field of view as in photo (b) but plane-polarized light.

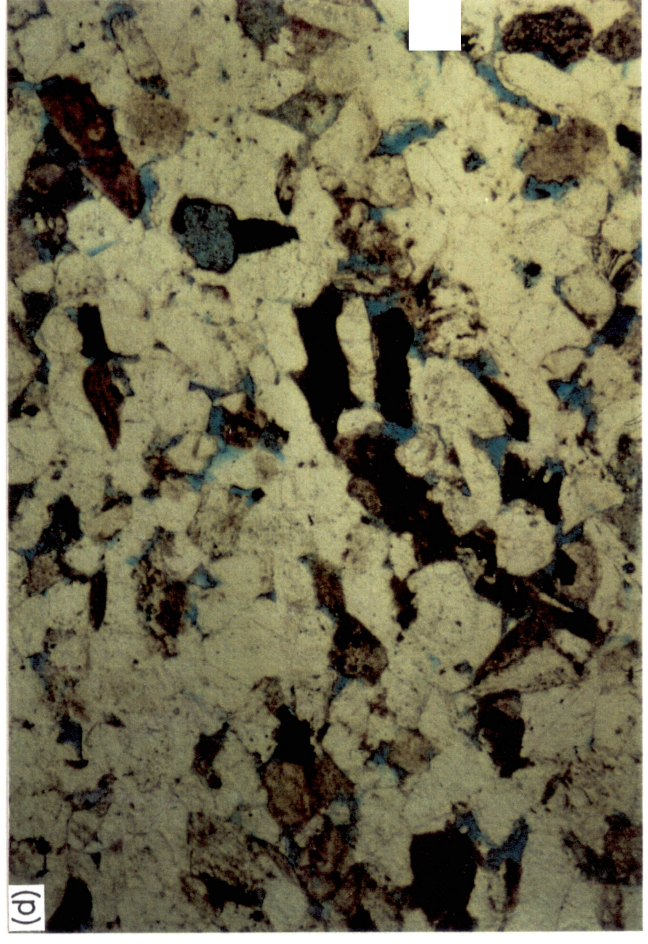
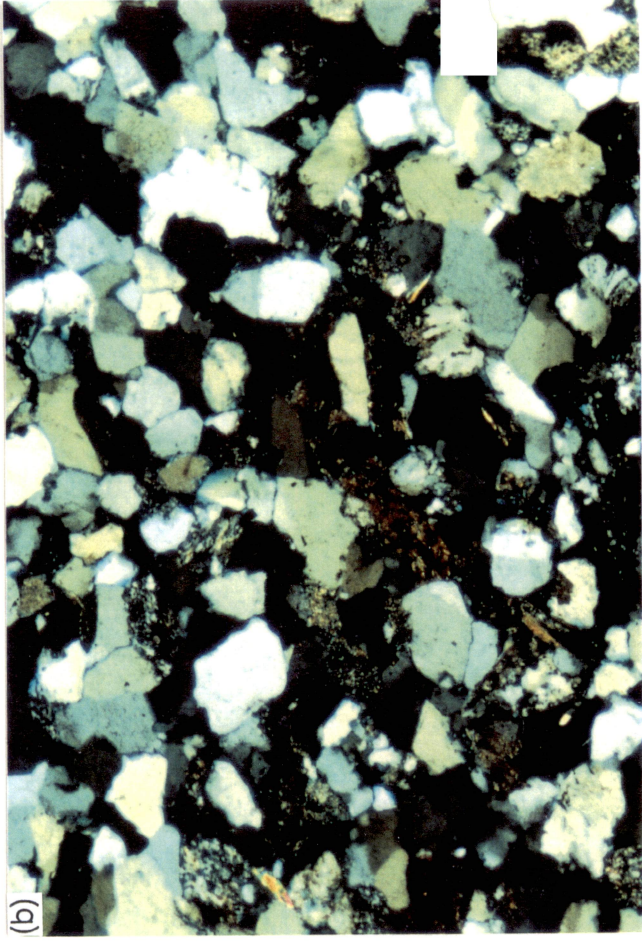
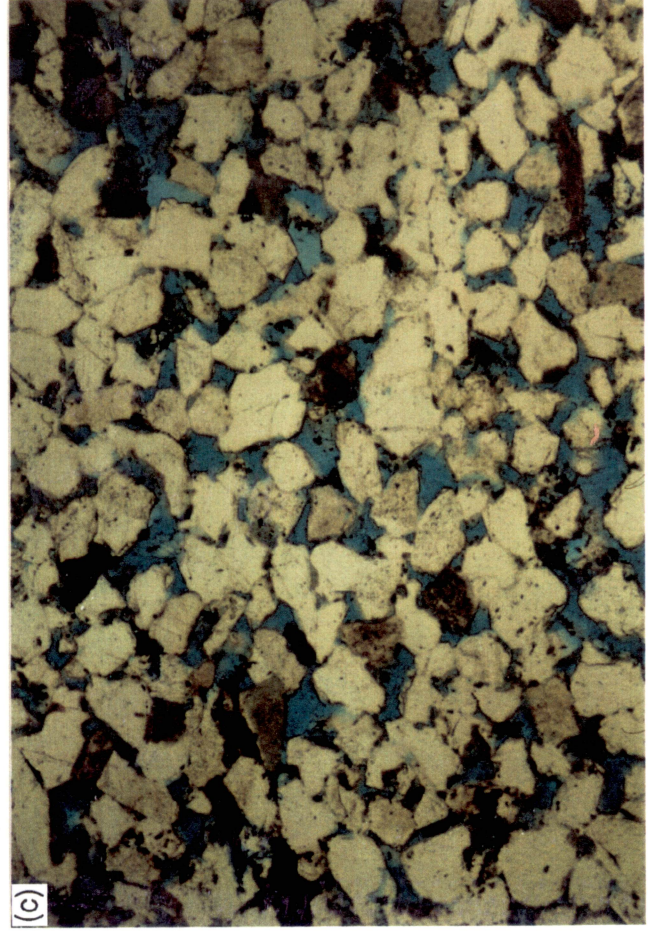
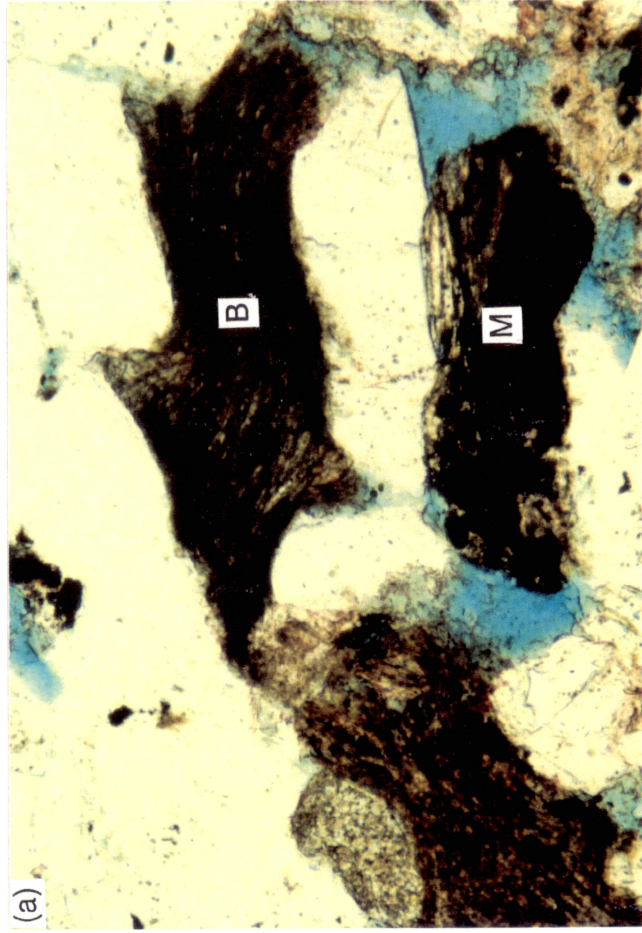


Plate VII-2a.

Typical C-3-X distributary-channel sandstone from a depth of 7,304 ft in the LL-2850 well. Abundant primary porosity and well developed quartz overgrowths are characteristic of sandstones at this depth. SEM photo by J. M. Mendenhall. Scale bar is 100 μm .

Plate VII-2b.

Typical C-6-X fluvial/estuarine channel sandstone from a depth of 9,215 ft in the LL-3140 well. Primary pores (P) remain at this depth, but quartz overgrowths (Q) are well developed and occlude much of the intergranular porosity. SEM photo by J. M. Mendenhall. Scale bar is 100 μm .

Plate VII-2c.

Illite rim (I) developed around what was probably a detrital feldspar grain. The feldspar later dissolved, and kaolinite (K) precipitated in the resulting secondary pore. Sample is from well LL-2425 from a depth of 7,422.5 ft. SEM photo by J. M. Mendenhall. Scale bar is 10 μm .

Plate VII-2d.

Authigenic illite extending into an intergranular pore. Sample is from well LL-2425 from a depth of 7,422.5 ft. SEM photo by J. M. Mendenhall. Scale bar is 10 μm .

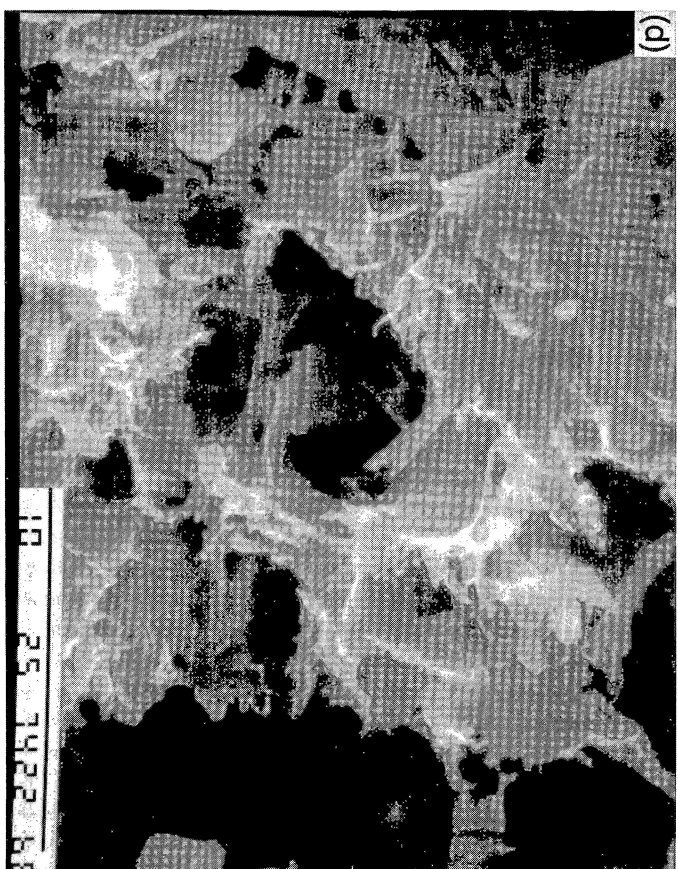
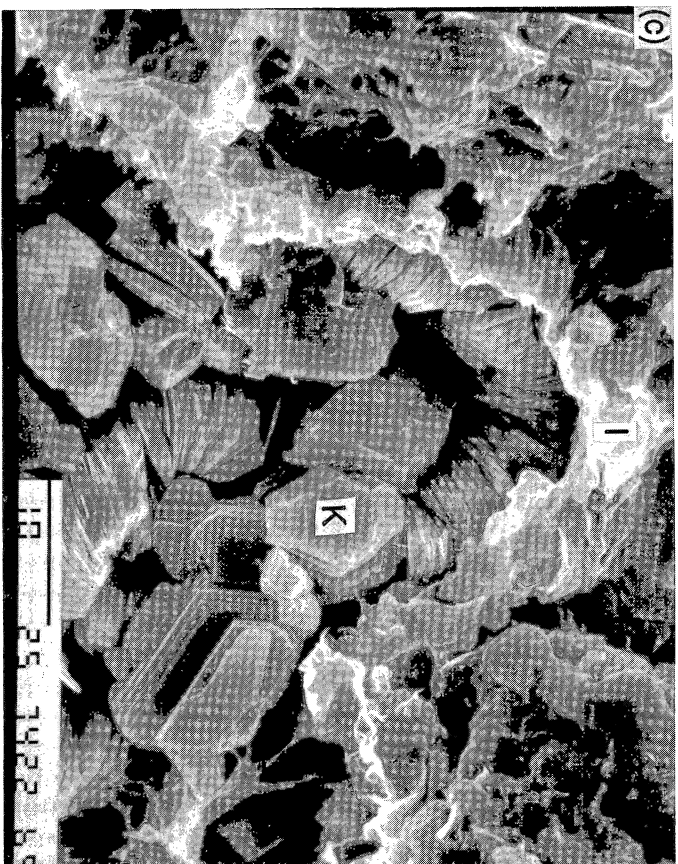
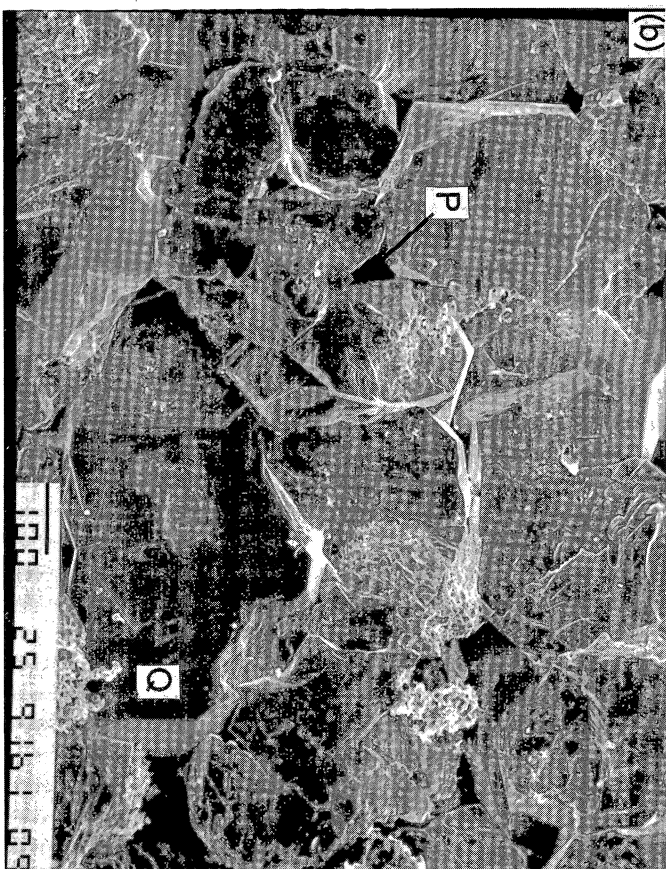
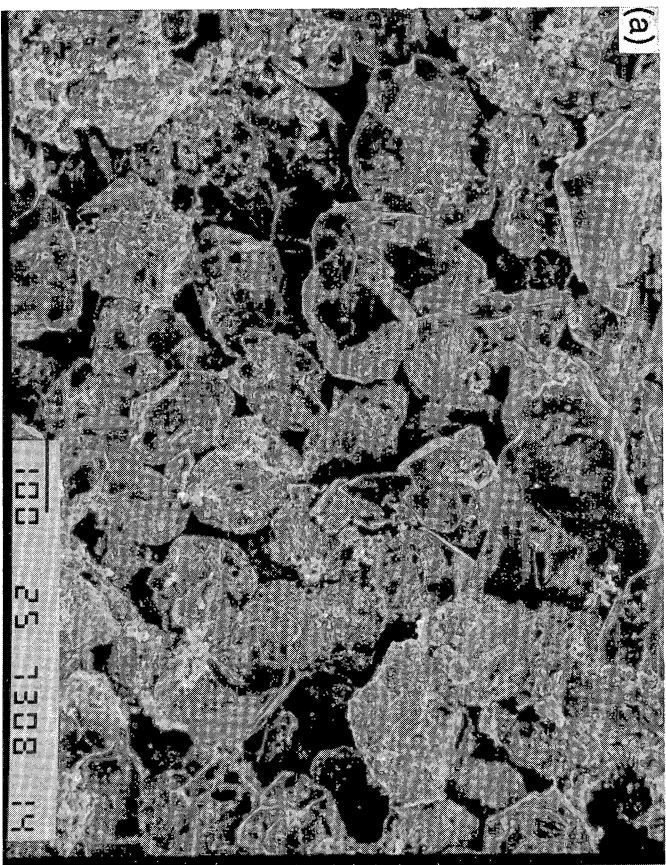


Plate VII-3a.

Rims of siderite (brown) around detrital grains. Precipitation of early siderite rims may have inhibited later precipitation of quartz cement. Sample of C-4-X sandstone from a depth of 7,622 ft in the LL-2850 well. Long dimension of photo = 2.6 mm. Plane-polarized light.

Plate VII-3b.

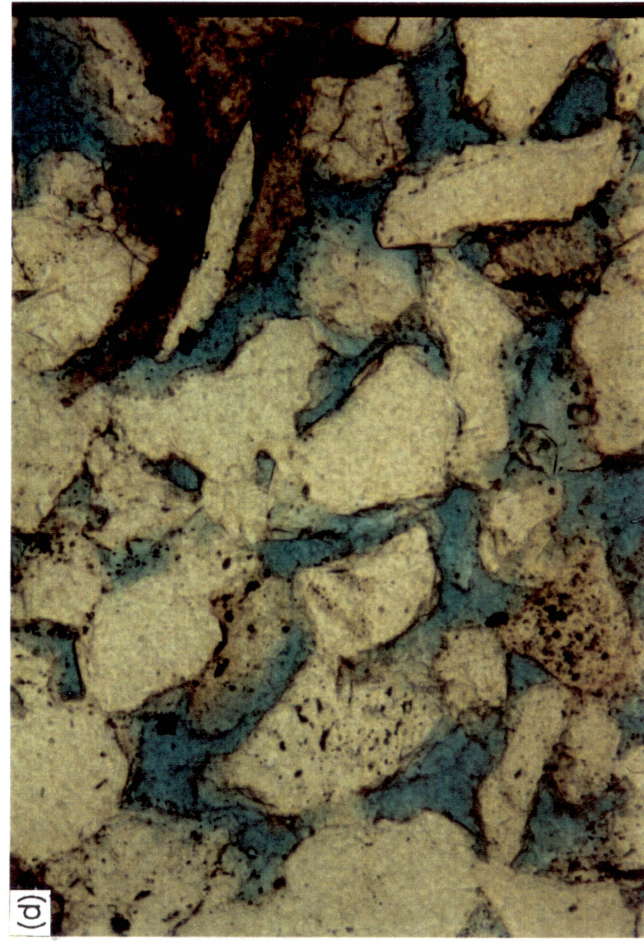
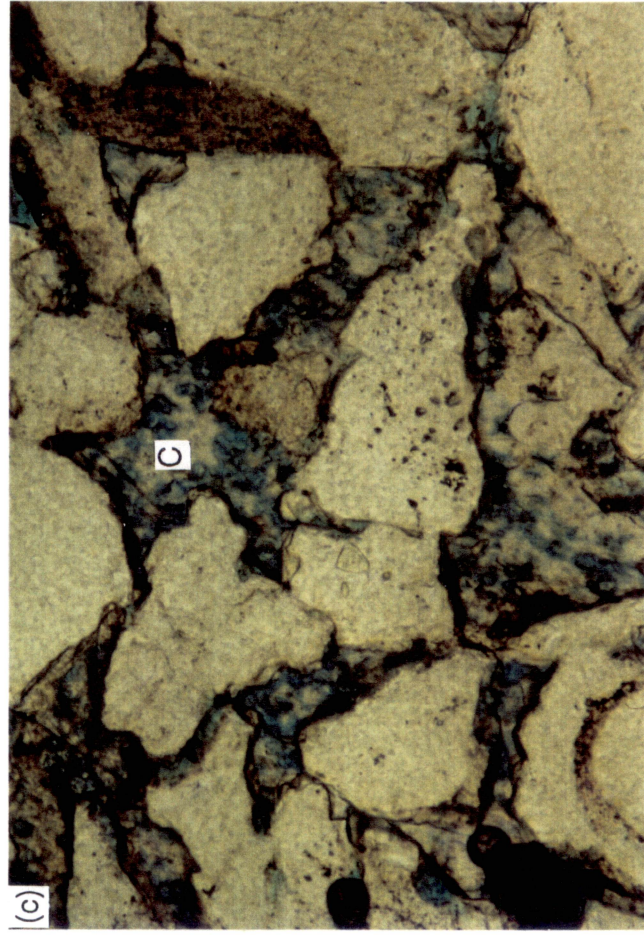
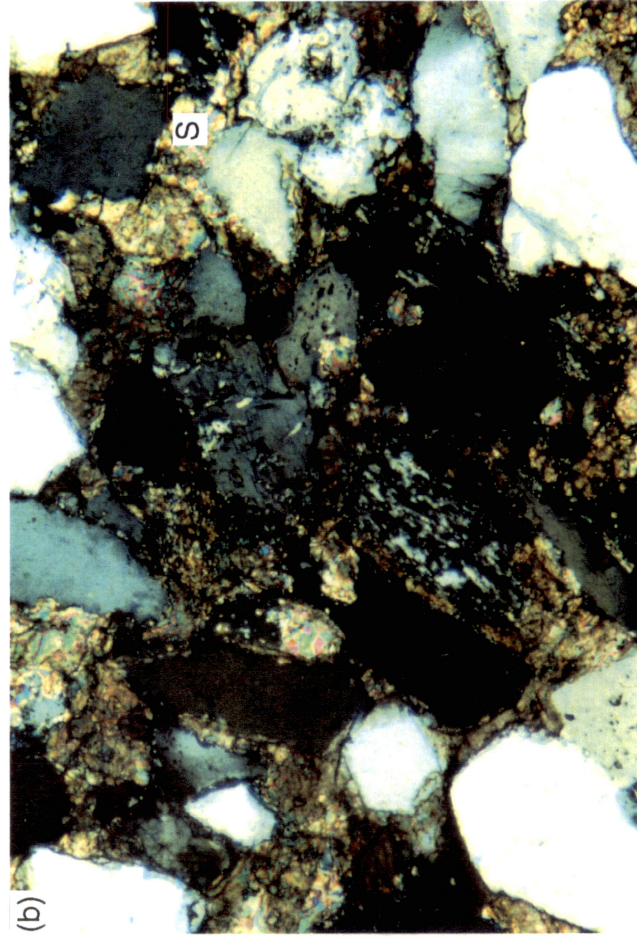
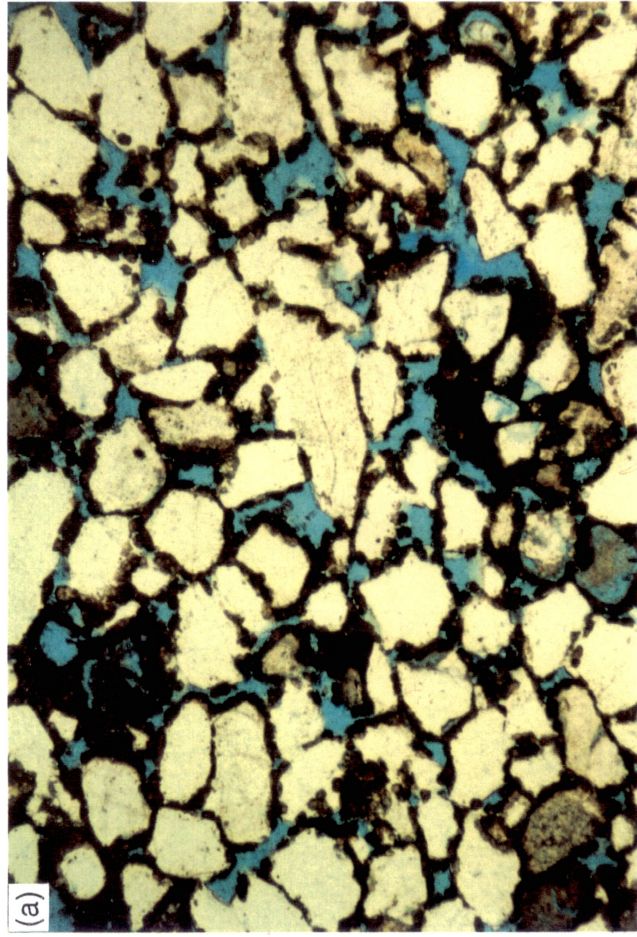
Porosity completely occluded by early siderite cement (S). Sample of C-6-X sandstone from a depth of 8,667 ft in the LL-3080 well. Long dimension of photo = 0.65 mm. Cross-polarized light.

Plate VII-3c.

Iron-bearing calcite cement (C, stained blue) precipitated after quartz overgrowths. The irregular, corroded shape of grains indicates that calcite replaced some detrital framework grains and quartz cement. Sample of C-3-X sandstone from a depth of 7,345 ft in the LL-3074 well. Long dimension of photo = 0.65 mm. Plane-polarized light.

Plate VII-3d.

Enlarged intergranular pores (blue) and irregular margins of grains suggest that calcite cement previously filled this sandstone but has since been dissolved, resulting in high porosity. Sample of C-3-X sandstone from a depth of 7,244 ft in the LL-3074 well. Long dimension of photo = 0.65 mm. Plane-polarized light.



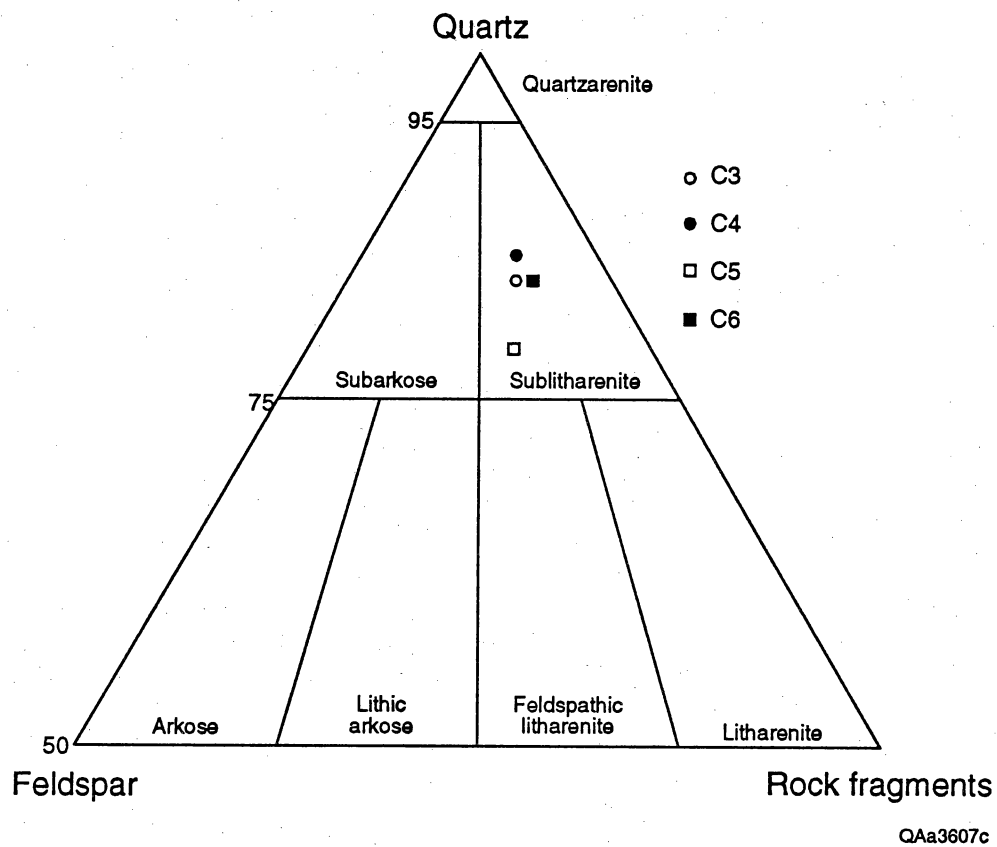


Figure VII 1. Compositional classification of Missoi sandstones by sandstone interval. Note that this diagram shows only the upper half of Folk's (1974) sandstone classification triangle, from 50 to 100 percent quartz.

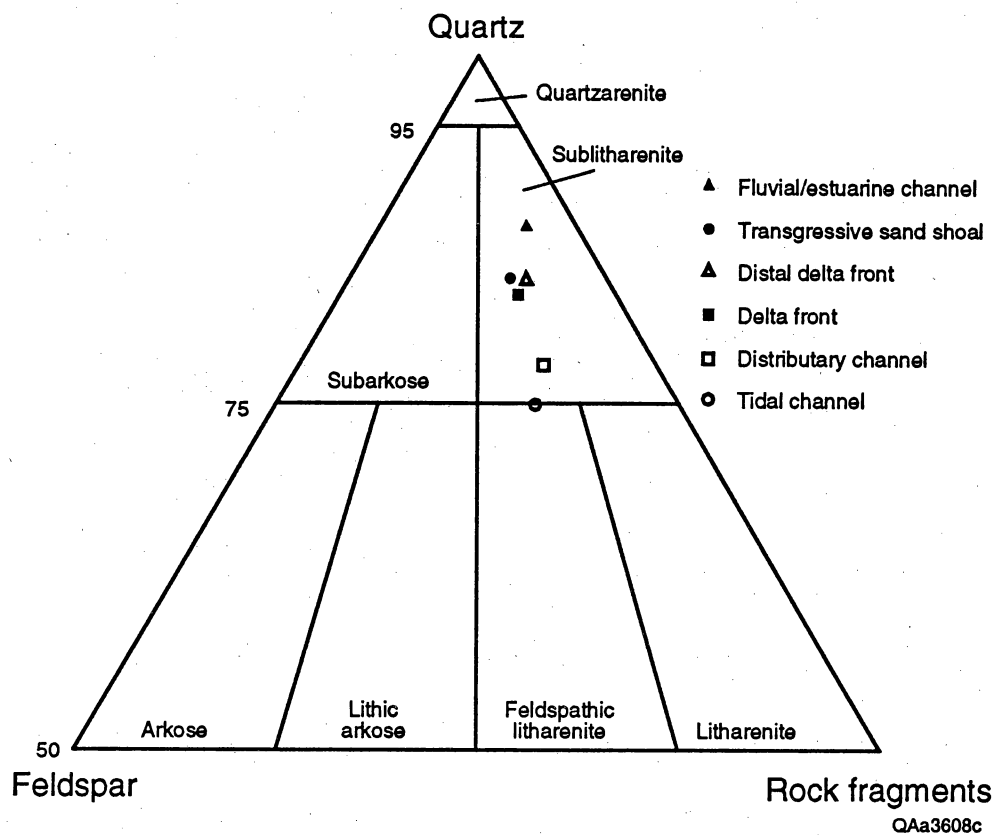
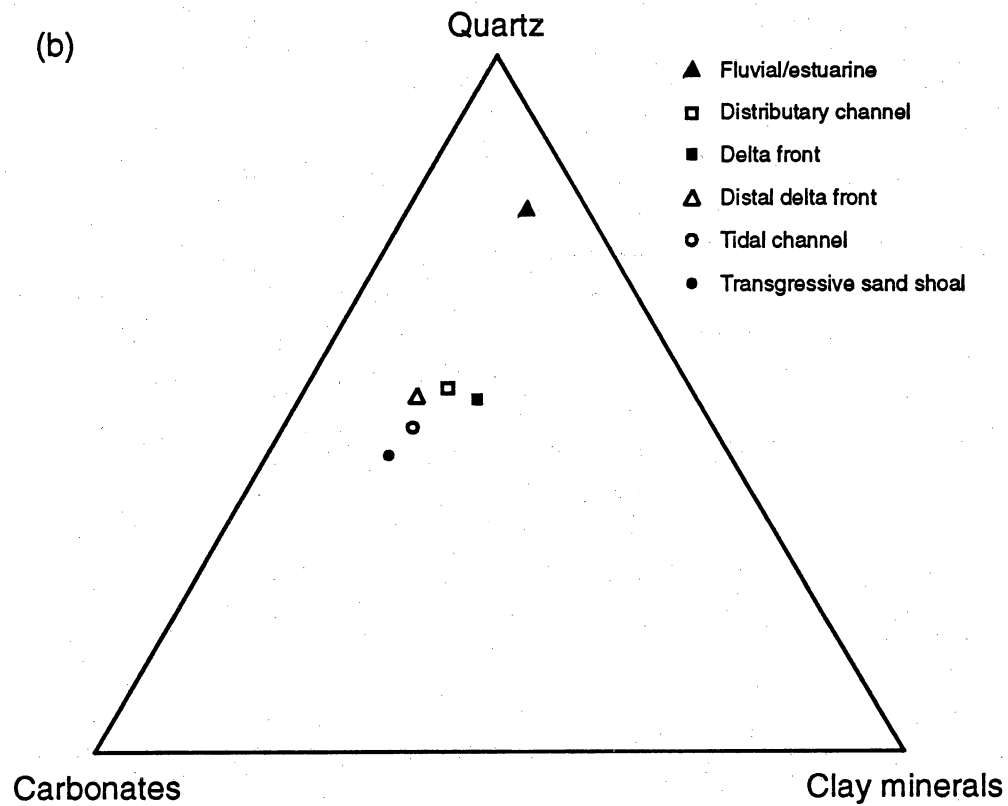
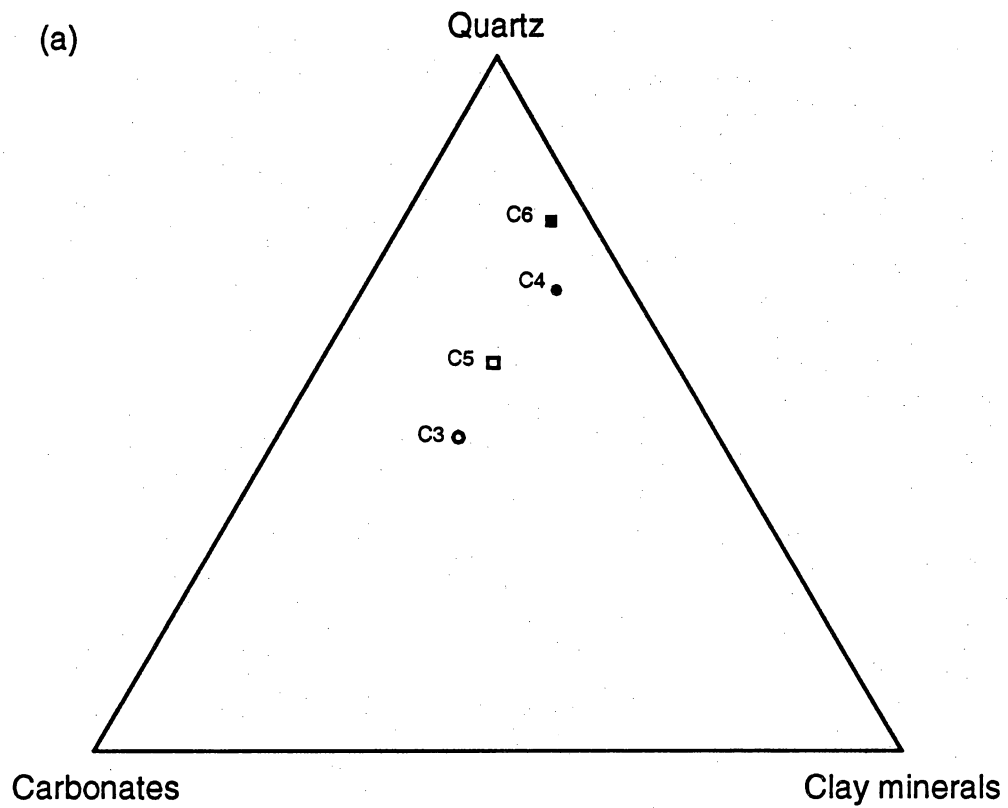


Figure VII 2. Compositional classification of Misoa sandstones by facies. Note that this diagram shows only the upper half of Folk's (1974) sandstone classification triangle, from 50 to 100 percent quartz.



QAa3609c

Figure VII 3. (a) Relative proportions of quartz, carbonate, and clay cements by Missoa sandstone intervals. (b) Relative proportions of cements by facies.

Process	Stage	
	Early	Late
Siderite rims, nodules	—	
Illite rims	—	
Mechanical compaction	— . . .	
Quartz overgrowths	—	— . . .
Calcite cement		—
Dissolution feldspar, calcite		— . .
Authigenic kaolinite		— . .
Ankerite		—
Oil migration		—

QAa3610c

Figure VII 4. Generalized paragenetic sequence for Misoa C-3-X through C-6-X sandstones, Lagunillas field, LL-652 area, Lake Maracaibo.

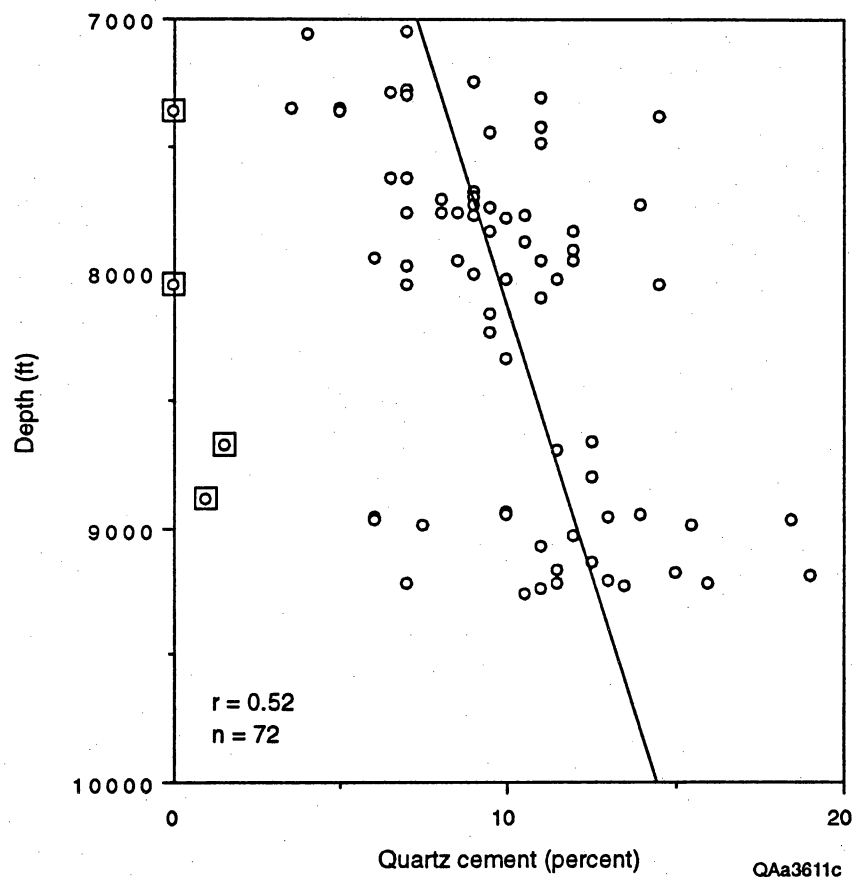
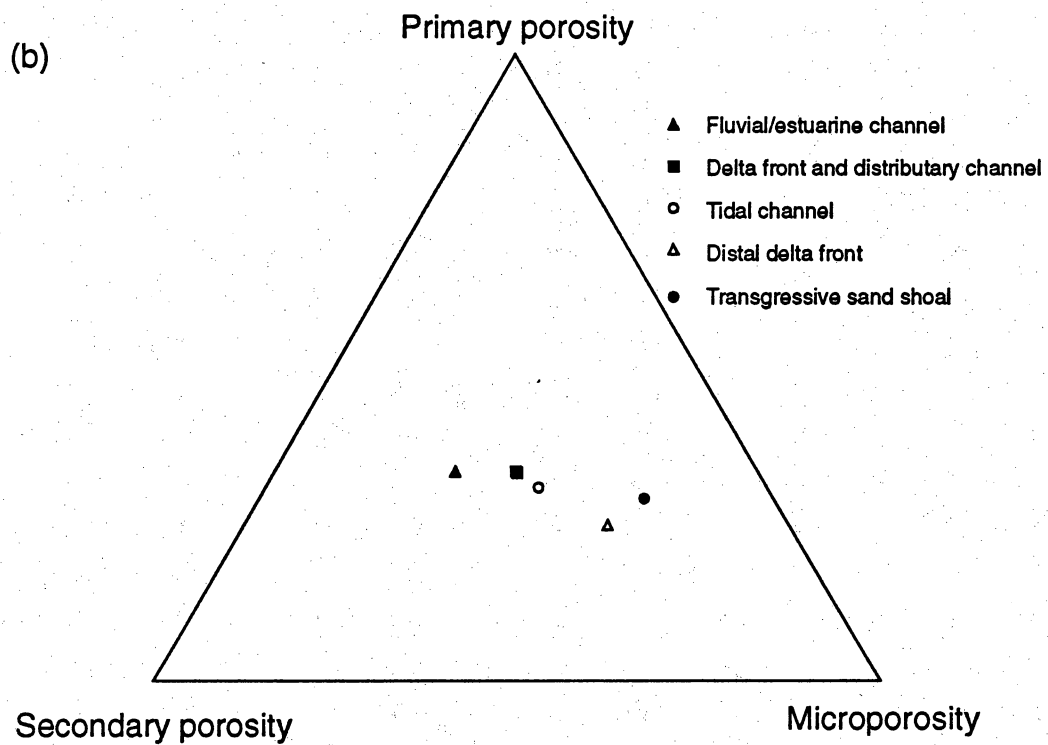
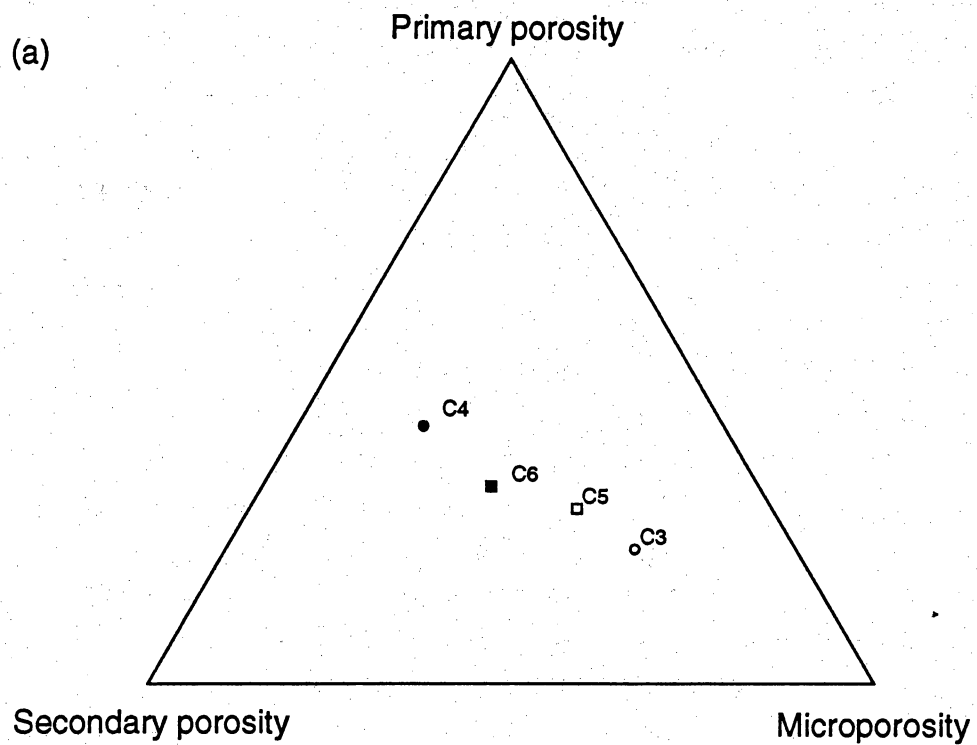


Figure VII 5. Quartz cement volume in Missoa C-3-X through C-6-X sandstones as a function of present burial depth. Quartz cement increases significantly with depth. Linear regression equation relating depth and quartz cement is:

$$\text{quartz cement (percent)} = -9.03 + 2.34 \times \text{depth (ft)} \times 10^{-3}.$$

Four outliers (boxed) were not included in the calculation of the regression equation.



QAa3612c

Figure VII 6. (a) Relative proportions of primary, secondary, and micropores by Misosa sandstone intervals.
 (b) Relative proportions of pore types by facies.

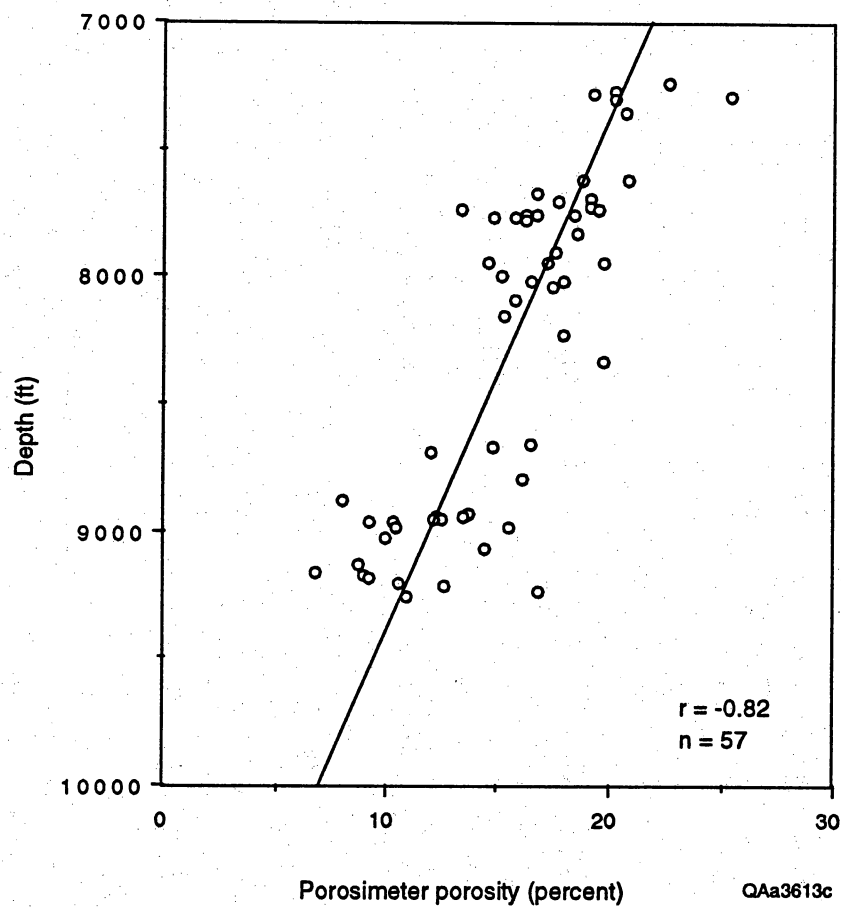


Figure VII 7. Porosimeter-measured porosity as a function of present burial depth of Misso C-3-X through C-6-X sandstones. Porosity decreases significantly with depth. Linear regression equation relating depth and porosity is:

$$\text{porosity (percent)} = 56.62 - 4.97 \times \text{depth (ft)} \times 10^{-3}.$$

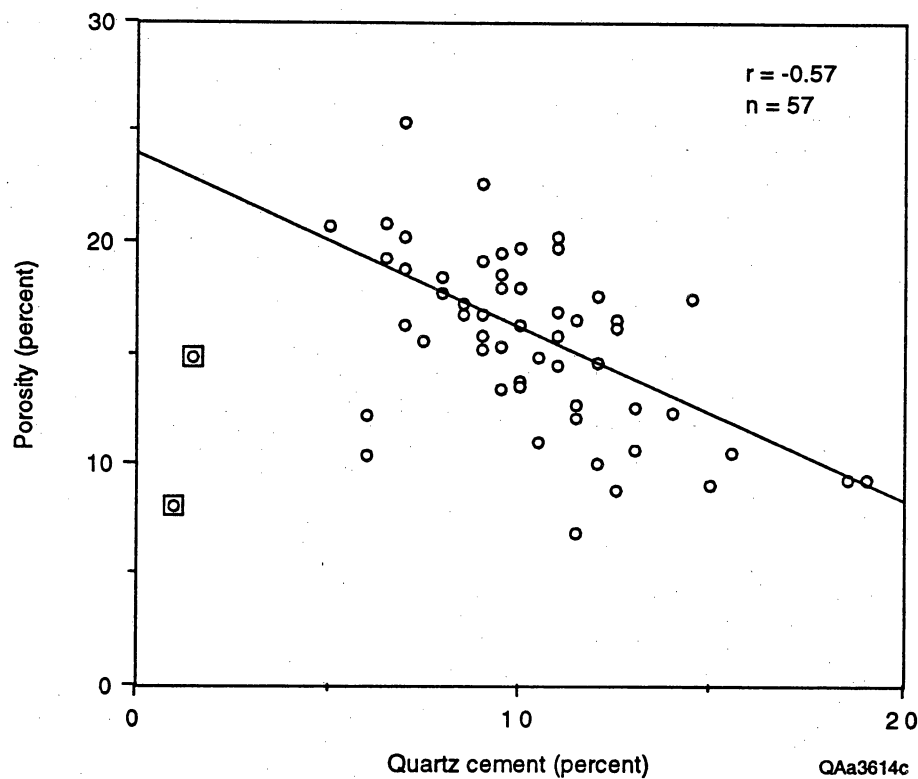


Figure VII 8. Porosimeter-porosity as a function of quartz cement volume in Misso C-3-X through C-6-X sandstones. Porosity decreases significantly with increasing quartz cement. Linear regression equation relating porosity and quartz cement is:

$$\text{porosity (percent)} = 23.7 - 0.78 \times \text{quartz cement (percent)}.$$

Two outliers (boxed) were not included in the calculation of the regression equation.

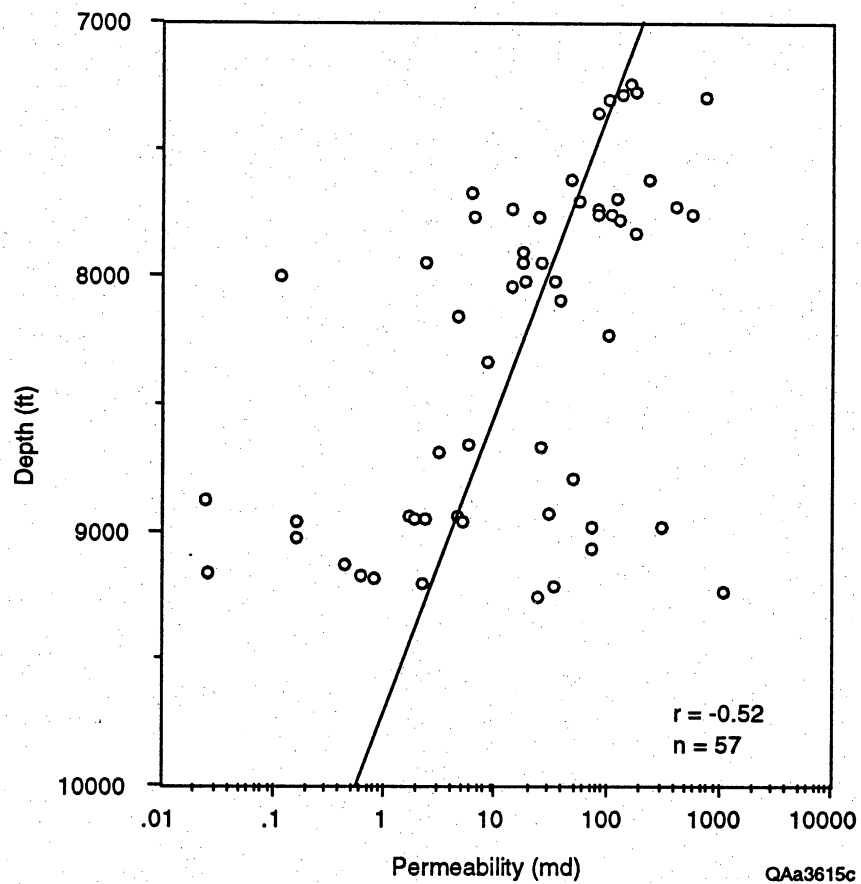


Figure VII 9. Semi-log plot of permeability versus depth for 57 Misso C-X sandstones. Linear regression equation relating depth and permeability is:
 $\log \text{ permeability} = 8.21 - 8.44 \times \text{depth (ft)} \times 10^{-4}$.

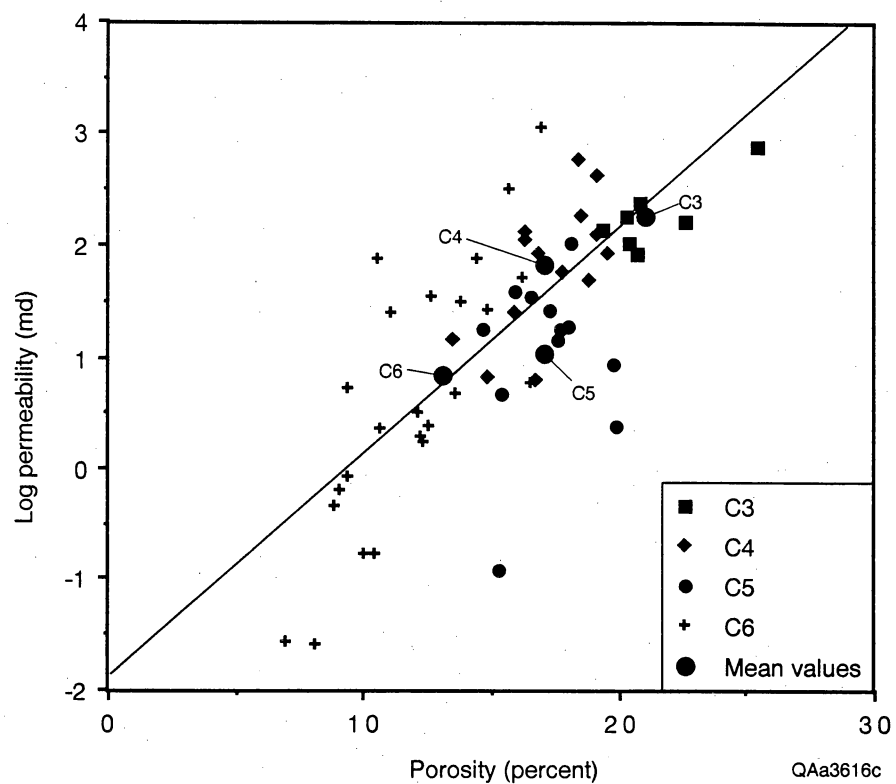


Figure VII 10. Plot of log permeability versus porosity for 57 Misosa C-X sandstones. Mean values for each sandstone interval are shown. Linear regression equation relating porosity and log permeability is:
 $\text{Log permeability} = -1.87 + 0.20 \times \text{porosity (percent)}.$

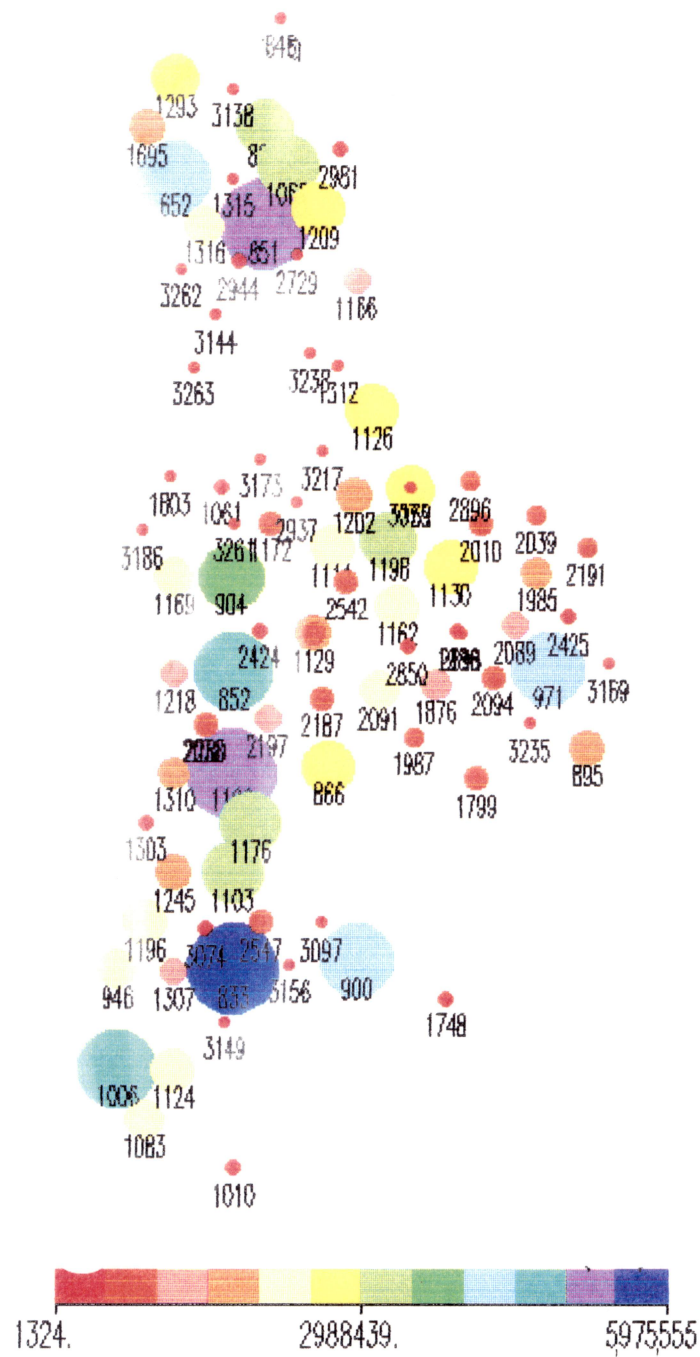


Figure VIII 1. Cumulative production by well in the C-3-X/C-4-X Members.

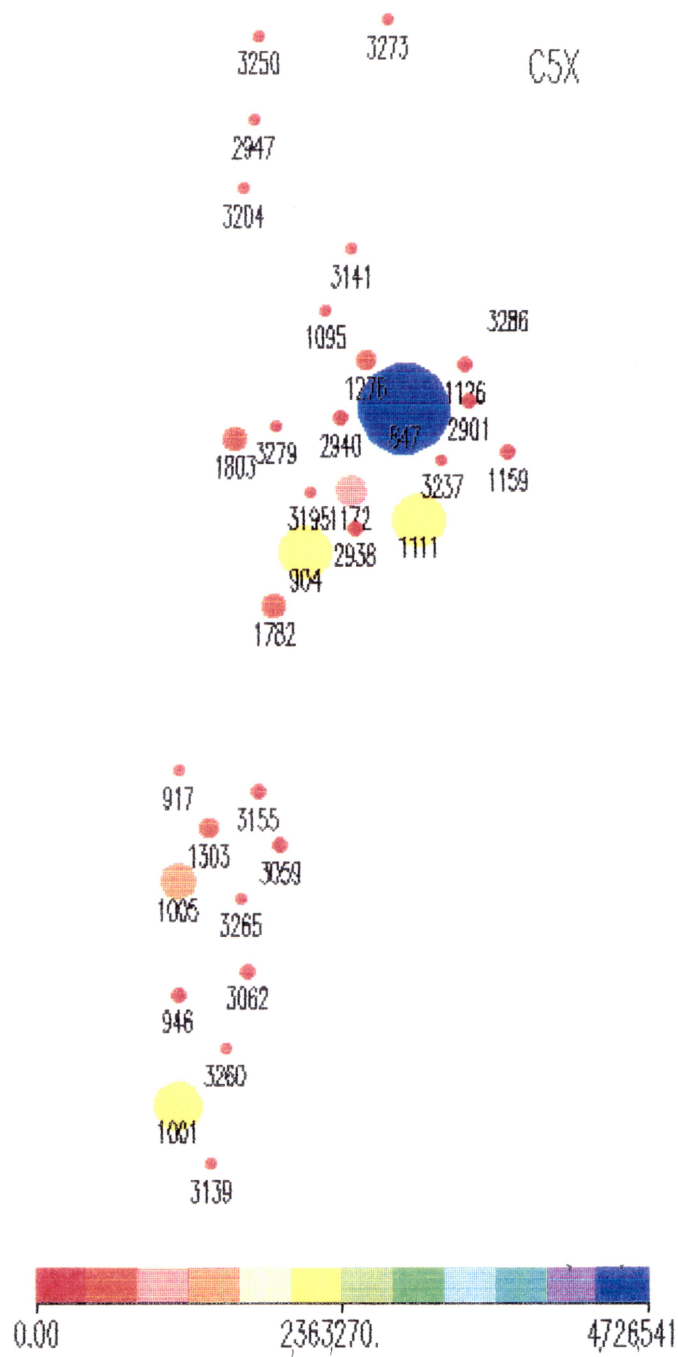


Figure VIII 2. Cumulative production by well in the C-5-X Member.

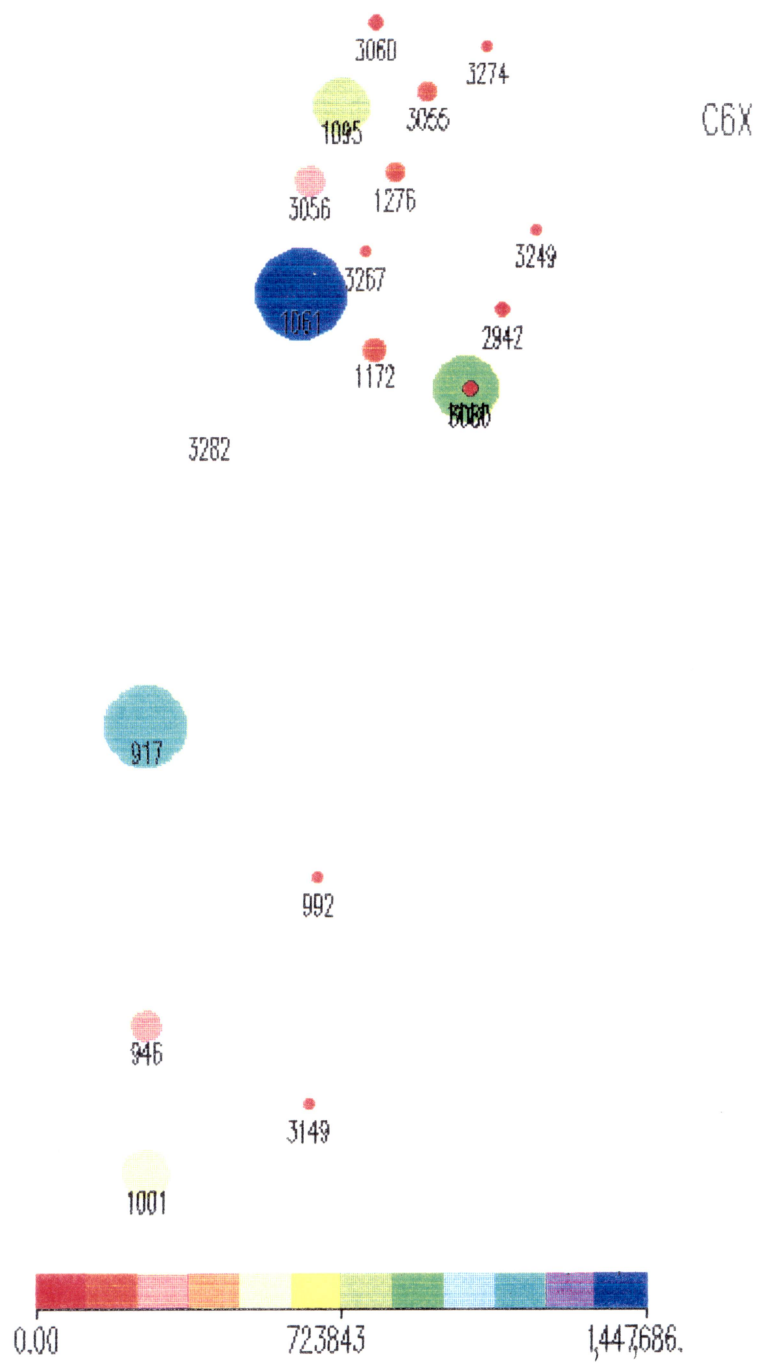


Figure VIII 3. Cumulative production by well in the C-6-X Member.

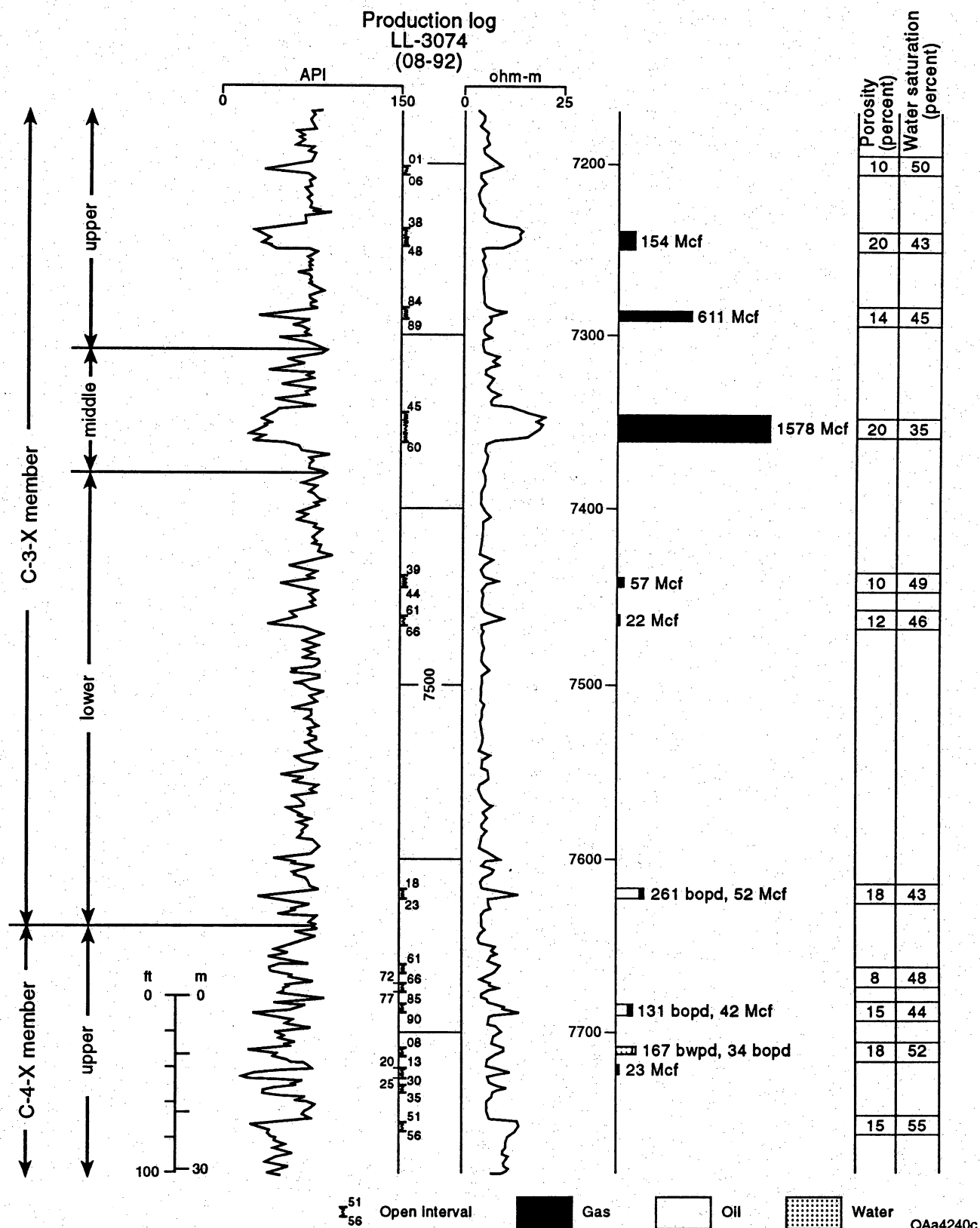


Figure VIII 4. Production log of the LL-3074 well.

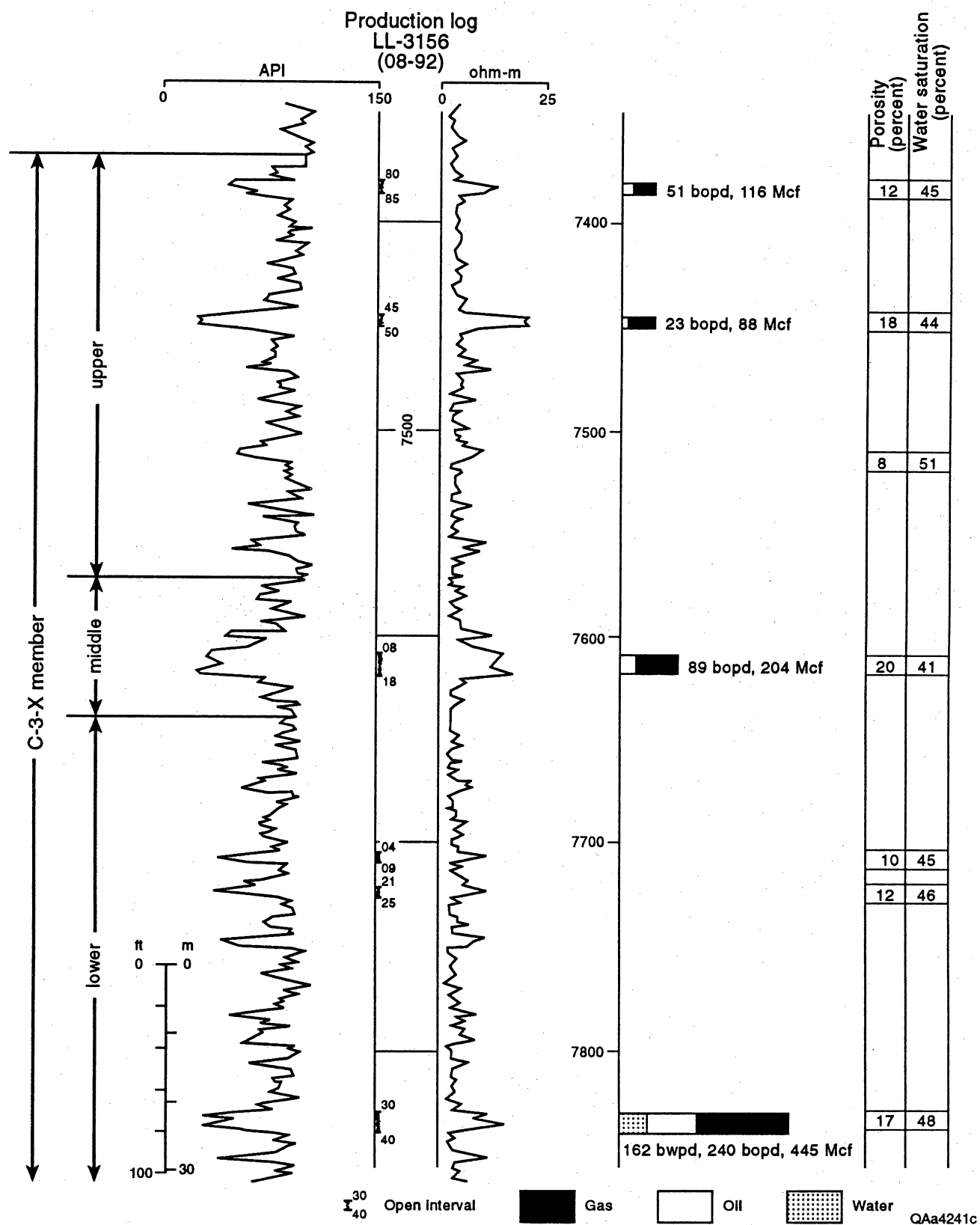


Figure VIII 5. Production log of the LL-3156 well.

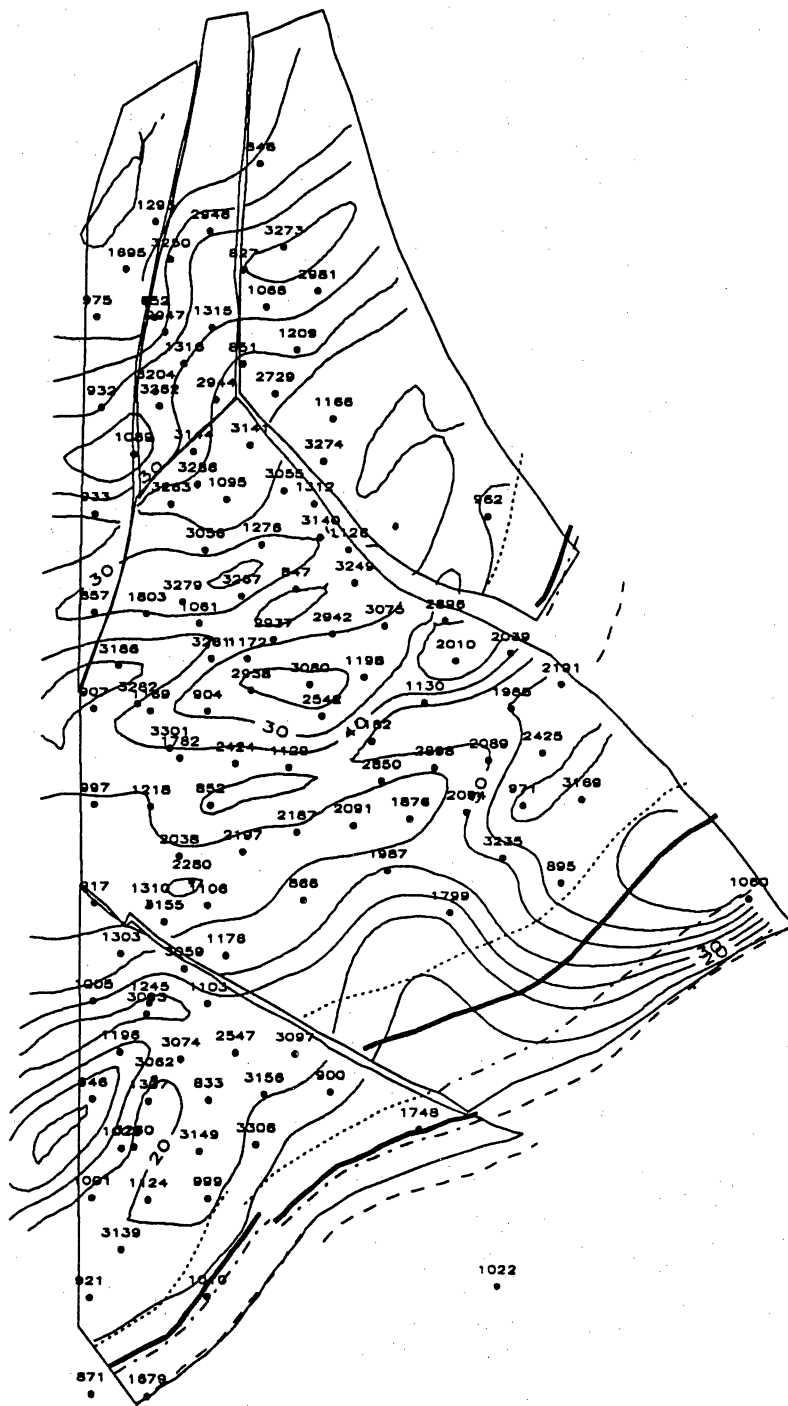


Figure VIII 6. Original and current oil-water contacts in the Middle C-3-X Submembers

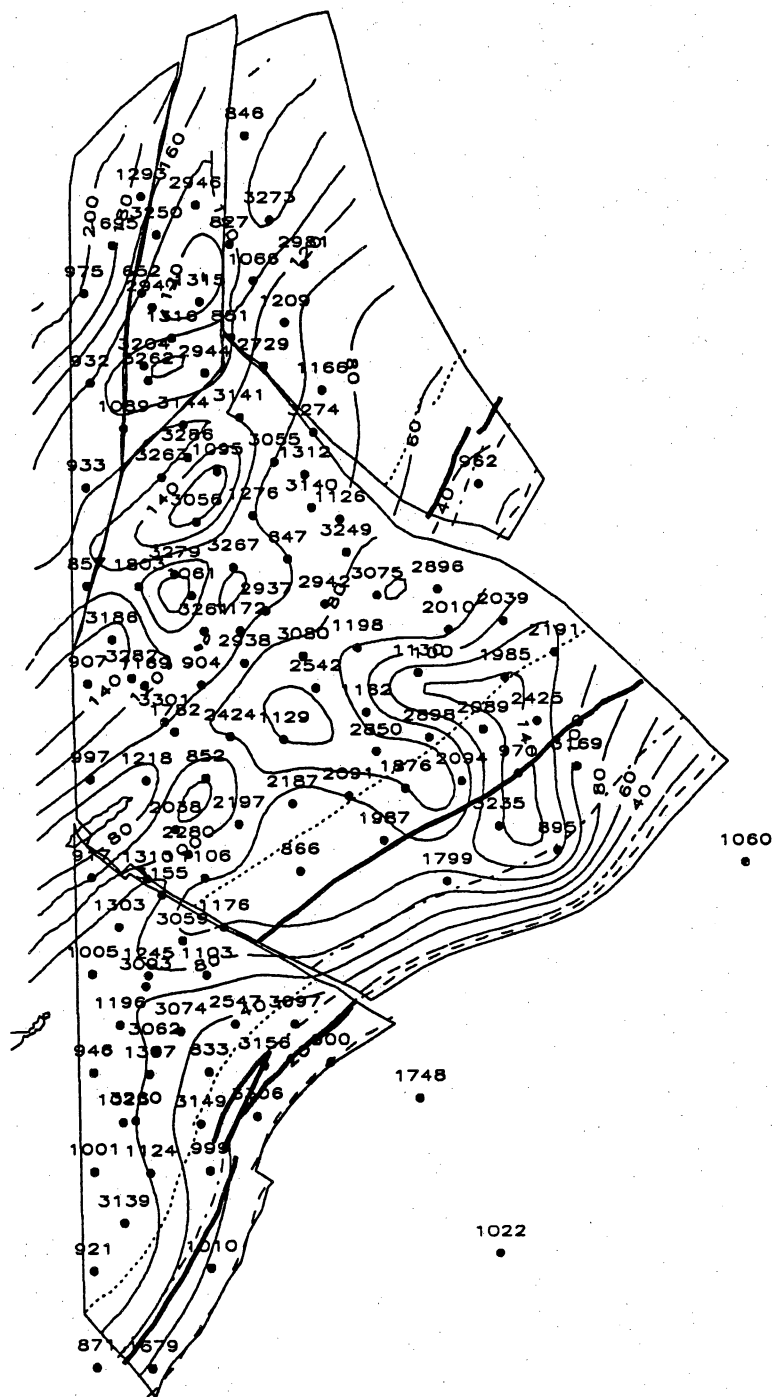


Figure VIII 7. Original and current oil-water contacts in the Upper C-4-X Submember.

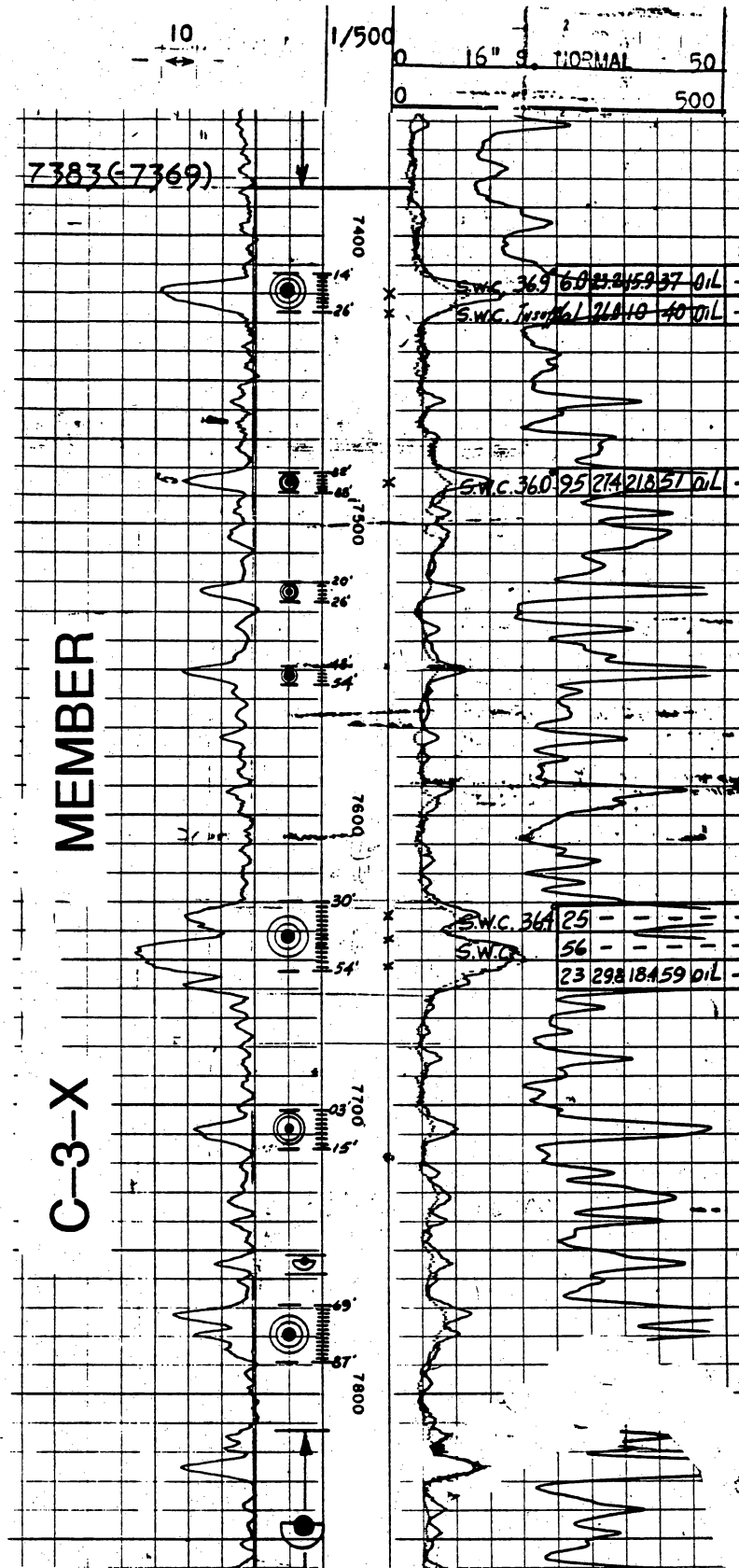


Figure VIII 9. Open intervals in low-resistivity sandstones in the LL-900 well.

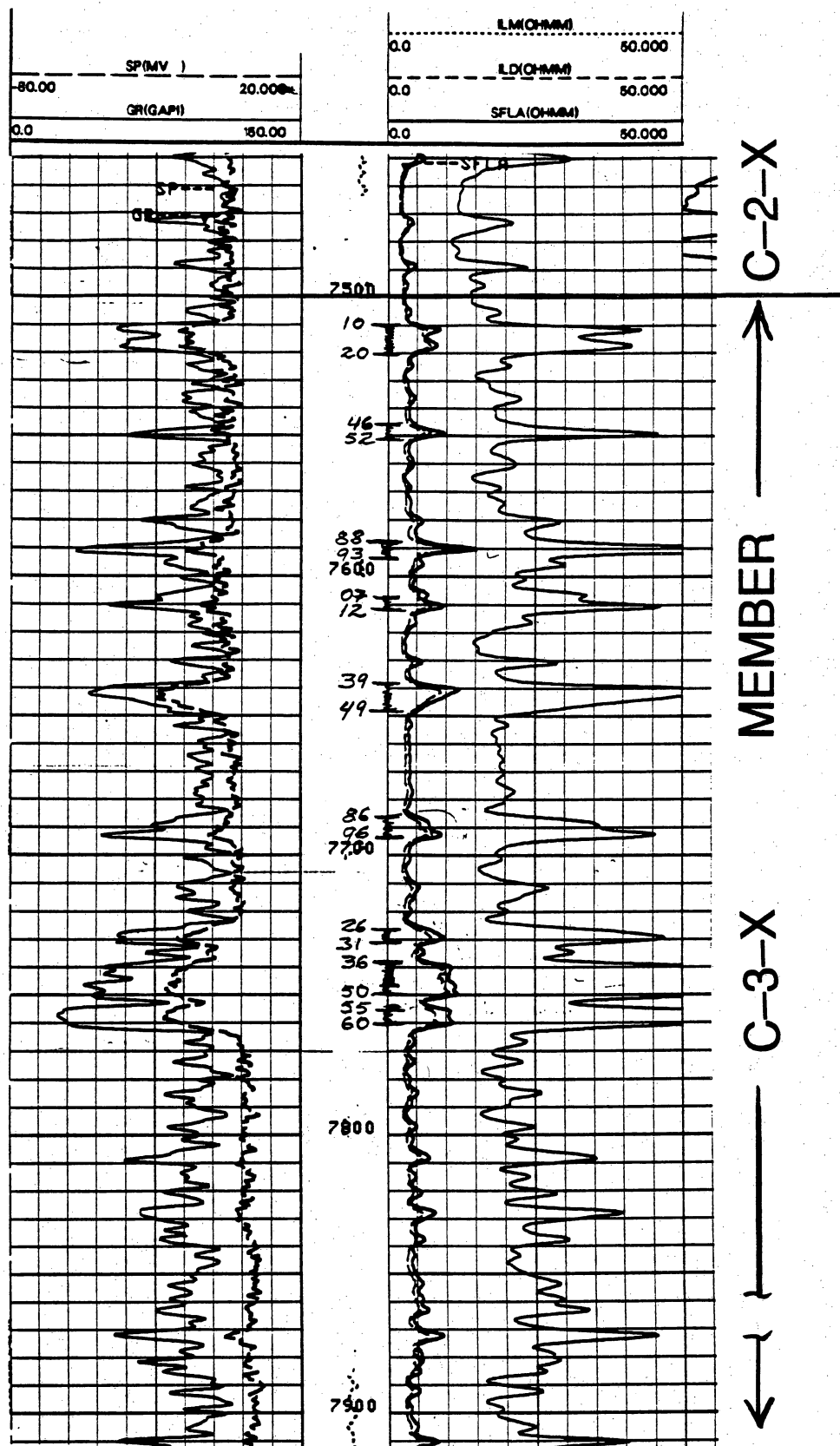


Figure VIII 10. Open intervals in low-resistivity sandstones in the LL-3306 well.

Table VIII 1. Cumulative production (MMbbl) of C Members in the LL-652 area.

Compart- ments	Member C-2-X	Member C-2-X	Member C-2-X	Members C-3-X/ C-4-X	Members C-3-X/ C-4-X	Members C-3-X/ C-4-X	Member C-5-X	Member C-5-X	Member C-5-X	Member C-6-X	Member C-6-X	Member C-6-X	Total	Total	Total	Total
	Oil	Water	Wells	Oil	Water	Wells	Oil	Water	Wells	Oil	Water	Wells	Oil	Water	Well- Member	Average Production
I	-	-	-	17.05	0.23	8	0.04	0.03	1	-	-	-	17.06	0.26	9	1.9
II	-	-	-	5.43	0.31	6	0.17	0.02	3	0.10	0.01	1	5.71	0.34	10	0.6
III	-	-	-	5.07	0.10	2	-	-	-	-	-	-	5.07	0.10	2	2.5
IV	-	-	-	3.77	0.06	5	0.67	0.01	2	0.02	0.01	1	4.46	0.08	8	0.6
V	-	-	-	66.05	1.99	47	14.20	0.28	15	5.50	0.50	14	85.75	2.77	76	1.1
VI	0.83	0.11	2	8.20	2.98	4	3.58	0.04	33	1.87	0.49	2	14.47	3.62	11	1.3
VII	-	-	-	30.24	1.06	18	1.81	0.09	8	0.89	0.02	2	32.94	1.17	28	1.2
LL-652 Area	0.83	0.11	2	135.81	6.73	90	20.47	0.47	32	8.38	1.03	20	165.49	8.34	144	1.2

Table VIII 2. Best production by well and compartment in the LL-652 area.

Compartment	Cumulative Well	Cumulative MMbbl	Current Well	Current Date	Current Reservoir	Current Oil (BOPD)	Current Gas (MCFD)	Current Water (BWPD)	API
I	LL-851	5.3	LL-1066	03/93	C-4-X.01	296	2800	0	36
			LL-1209	01/93	C-4-X.01	219	1092	2	37
			LL-2981	03/93	C-4-X.01	432	1400	0	36
			LL-3273	03/93	C-5-X.02	235	585	2	37
II	LL-652	4.2	LL-1316	02/93	C-4-X.01	238	1092	10	38
III	LL-1293	2.6	LL-1695	03/93	C-4-X.01	201	1960	7	36
IV	LL-1169	2.1	LL-3186	03/93	C-4-X.01	635	516	33	37
V	LL-852	4.5	LL-1111	03/93	C-5-X.02	346	1357	5	36
			LL-1198	01/93	C-4-X.01	217	1960	0	36
	LL-971	4.1	LL-2091	11/92	C-4-X.01	212	1577	7	37
			LL-2197	01/93	C-4-X.01	223	3645	12	36
	LL-1106	5.8	LL-2896	03/93	C-4-X.01	249	1926	3	38
			LL-3056	03/93	C-6-X.01	324	1344	0	40
			LL-3217	02/93	C-4-X.01	215	952	1	38
			LL-3235	03/93	C-4-X.01	220	560	19	36
			LL-3238	03/93	C-4-X.01	480	2632	0	38
			LL-3261	02/93	C-4-X.01	358	3037	0	37
			LL-3267	02/93	C-6-X.01	243	555	1	38
VI	LL-1006	5.3	-	-	-	-	-	-	-
VII	LL-833	5.9	LL-1124	02/93	C-4-X.03	250	1204	7	39
			LL-1245	02/93	C-4-X.03	231	1681	1	39
	LL-900	4.2	LL-3059	11/92	C-5-X.16	511	1011	162	41
			LL-3062	03/93	C-5-X.16	253	1262	5	42
			LL-3155	02/93	C-5-X.16	464	1888	0	42
			LL-3284	02/93	C-4-X.03	250	1800	0	38

Table VIII 3. Kh from pressure tests in wells in the LL-652 area.

Member	Well	Kh (md•ft)	Average (md•ft)
C-3-X/C-4-X	LL-895	428	590
	LL-1162	337	
	LL-1169	533	
	LL-1293	241	
	LL-1803	1789	
	LL-1876	200	
	LL-2010	997	
	LL-2089	196	
	LL-2094	593	
C-5-X	LL-1111	876	490
	LL-1276	296	
	LL-2905	298	
C-6-X	LL-847	154	155
	LL-1001	185	
	LL-1061	170	
	LL-1095	197	
	LL-1111	149	
	LL-1276	76	

Table VIII 4. Oil-water contacts in the LL-652 area.

COMPARTMENT

		COMPARTMENT							
		I (FT)		V (ft)		VII A (North) (ft)		VII B (South) (ft)	
Member	Sub-M	Original	Current	Original	Current	Original	Current	Original	Current
C-3-X	U	7900	7750	8000	7800	7900	7800	7700	7500
	M	8000	7900	8200	7850	7950	7880	7850	7700
	L	8000	7900	8000	7850	7950	7800	7850	7700
C-4-X	U	8200	8080	8120	7800	7980	7950	8080	7950
	M	8150	8100	8200	7850	7950	7850	8000	7900
	L	8200	8150	8100	7950	7950	7900	8000	7900
C-5-X	U	8500	8400	8300	8200	8350	8300	8400	8300
	U•Mid	8500	8400	8300	8150	8350	8300	8400	8300
	L•Mid	8450	8350	8300	8150	8350	8300	8400	8350
	L	8450	8400	8250	8100	8300	8250	8350	8300
C-6-X	U•Up	8900	8850	8850	8750	8900	8900	9000	8950
	L•Up	8900	8850	8850	8750	8900	8900	9000	8450
	M	8850	8800	8850	8750	8900	8900	9050	9000
	U•Low	9200	9150	9100	9050	9200	9200	9200	9150
	L•Low	9200	9200	9100	9050	Prosp. Arbitrary	—	Prosp. Arbitrary	—
C-7-X		—	—	9300	9300	—	—	—	—

Table VIII 5. Cutoff values for low-resistivity sandstones in the C Members, LL-652 area.

Member	Well	Open Interv.	Low-Resist. Interval (ft)	Resistivity (OHM-M)	Production			Comments
					BOPD	GOR	Water %	
C-3-X C-4-X	LL-866	7214-7718 7746-7900	(several) 7746-60 7827-7837	10	281	772	4.4	01/65
				10	186	1323	1.0	05/73
				10				
LL-900	7414-7787	7520-7526 7548-7554 7703-7715 7769-7787	7520-7526 7548-7554 7703-7715 7769-7787	10	923	961	0.3	05/55
				10				
				12	455	1308	4.0	10/88
LL-904	6750-7720	6750-6755 7667-7673 7687-7697	6750-6755 7667-7673 7687-7697	10	940	1640	0.0	01/63
				13	520	1269	0.0	09/85
LL-971	7424-7592	7424-7429 7460-7475	7424-7429 7460-7475	13	1008	658	0.0	04/57
				10				
LL-1106	7087-7516 7615-7800	7087-7092 7414-7419 7615-7640 7790-7800	7087-7092 7414-7419 7615-7640 7790-7800	11	319	1749	5.0	03/78
				12	1509	1074	0.1	04/63
LL-1124	7262-7830	7298-7323(2) 7534-7627(2) 7533-7538	7298-7323(2) 7534-7627(2) 7533-7538	11	1158	1852	1.2	10/72
				11	1151	1033	0.4	09/62
				12				
LL-1126	7154-7703	7358-7458 (4 intervals)	7358-7458 (4 intervals)	11	2534	807	1.0	08/62
LL-1130	7508-7770	(9 intervals)	(9 intervals)	10-13	2189	946	1.6	10/62
LL-1159	7272-7816	7272-82 7224-7396(3)	7272-82 7224-7396(3)	11	1003	1512	0.4	08/63

Still producing 223 BOPD and 0.1% water.

		7537-7559(2) 7727-7816(3)	10	292	8705	0.8	08/82	
C-3-X C-4-X	LL-1162	7504-7910	9 intervals	11-13	1321	1272	0.0	04/63
	LL-1192	7339-7756	6 intervals	11-12	1259	1050	0.4	12/63
	LL-1307	7323-7656	5 intervals	12	1014	1839	0.0	
	LL-1748	7634-7768	7670-7675 7748-7768	8-10	335	1391	5.0	05/73
	LL-1799	7455-7820	7 intervals	8-12	459	915	0.0	06/72
	LL-2039	7656-7861	7825-7830 7856-7861	12	328	1622	0.2	02/77
	LL-2094	7402-7708	4 intervals	10	631	1464	0.0	04/78
	LL-2280	7472-7780	4 intervals	8-10	793	1280	0.3	11/79
	LL-2424	6910-7380	5 intervals	10-12	148	8628	2.6	08/85
	LL-2547	7362-7747	6 of 7 intervals	10-12	739	1138	3.4	12/81
	LL-2850	7281-7591	All intervals (8)	10-12	85	3765	4.2	05/84
	LL-3306	7510-7744	4 of 5 intervals	9-12	224	480	4.0	03/93
			C-3-X/C-4-X AVERAGE 10					
C-5-X	LL-946	8240-8560	8240-8256 8303-8310 8323-8328	10 12				The water production was less than 5%.

LL-1001	8150-8622	8375-8380	12-13	461	1534	2.0	08/62	High rate of oil with only 4% of water. 11/87 (118 BOPD and 1.0% water). 04/91 (176 BOPD and 0.0% water).
LL-1126	7780-8063	8525-8540 8555-8575	12	461	1534	2.0	08/62	
LL-1303	8016-8216	7813-8063 (7 intervals)	12-13	175	3657	1.2	08/80	
LL-2901	7771-8097	8016-8030 8135-8140 4 of 7 intervals	11	201	3761	0.7	02/86	
		C-5-X AVERAGE		12				

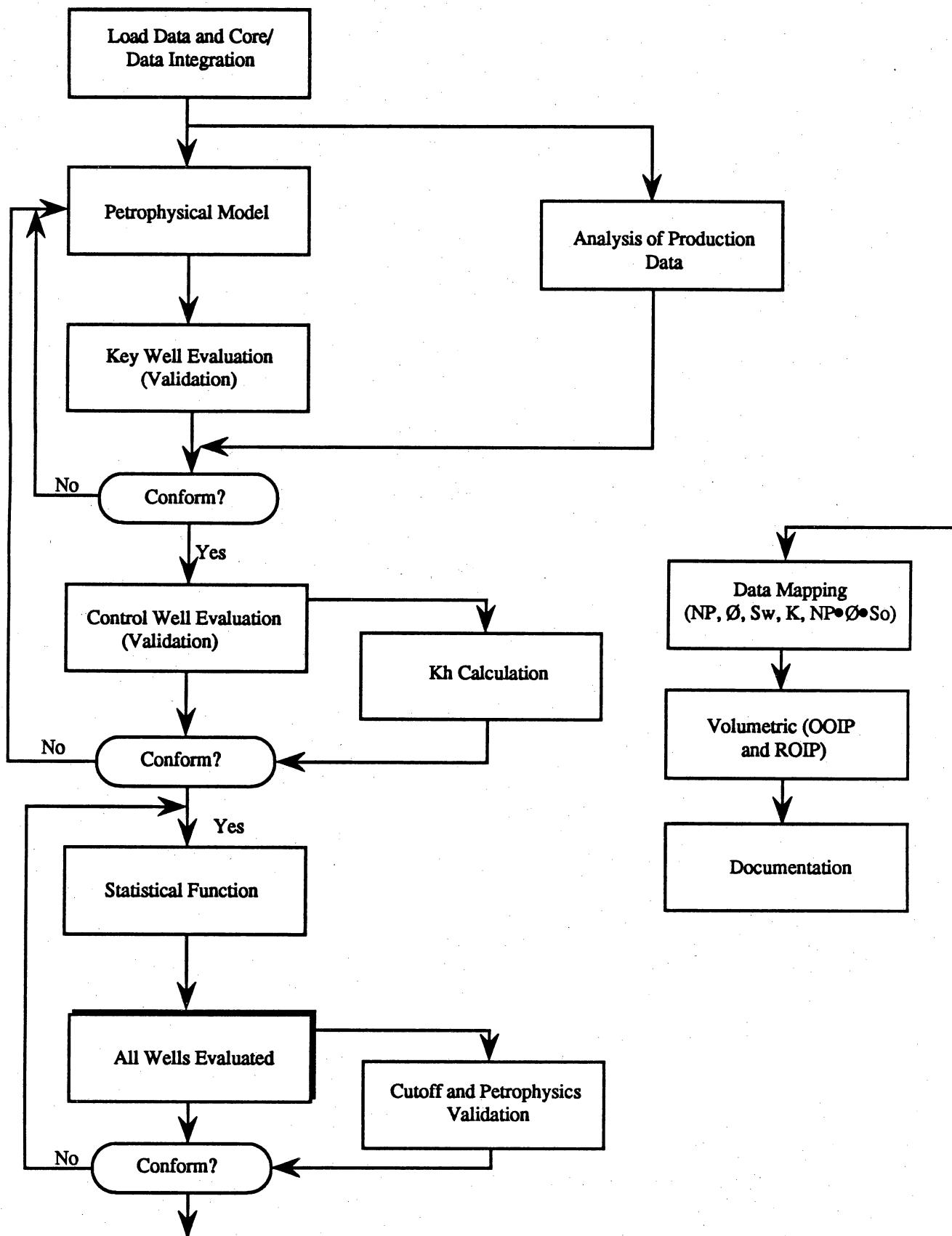


Figure IX 1. Flow chart of procedures for petrophysical characterization and volumetrics calculations.

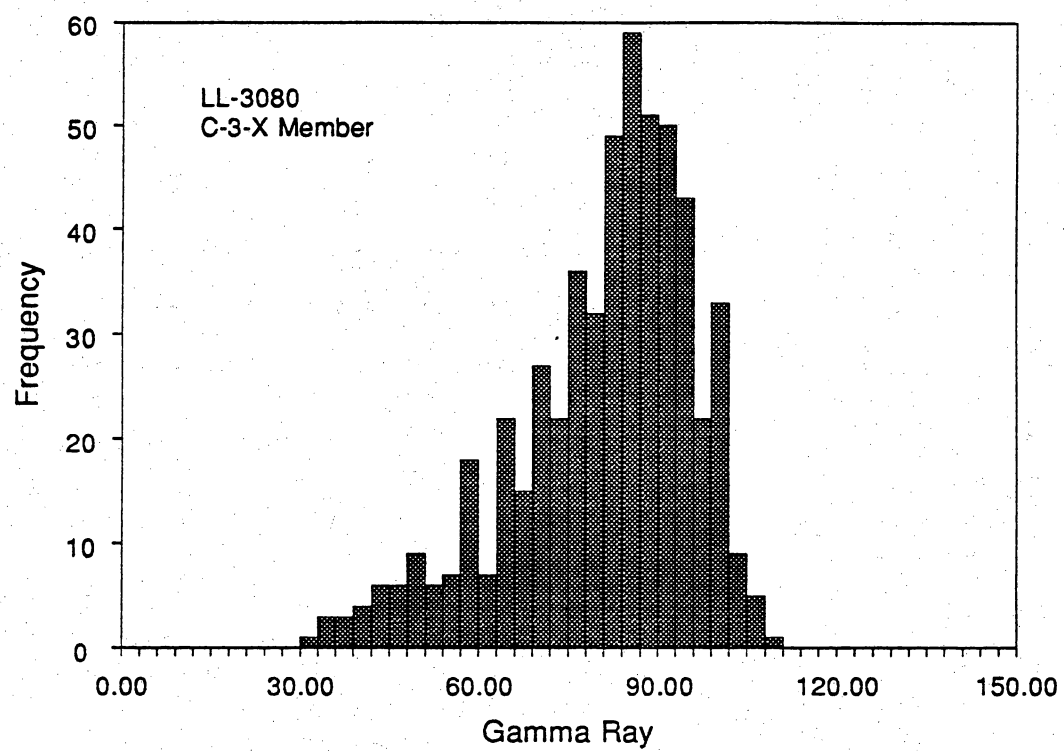
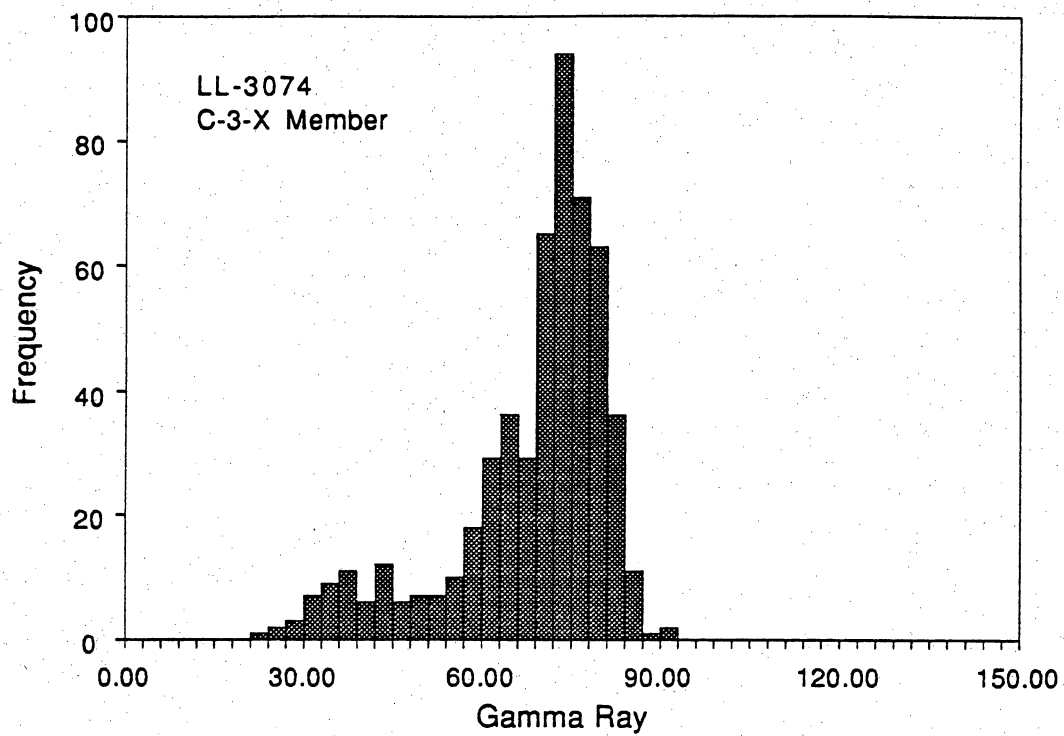


Figure IX 2. Histograms of gamma ray values from Schlumberger logs in the LL-652 area.

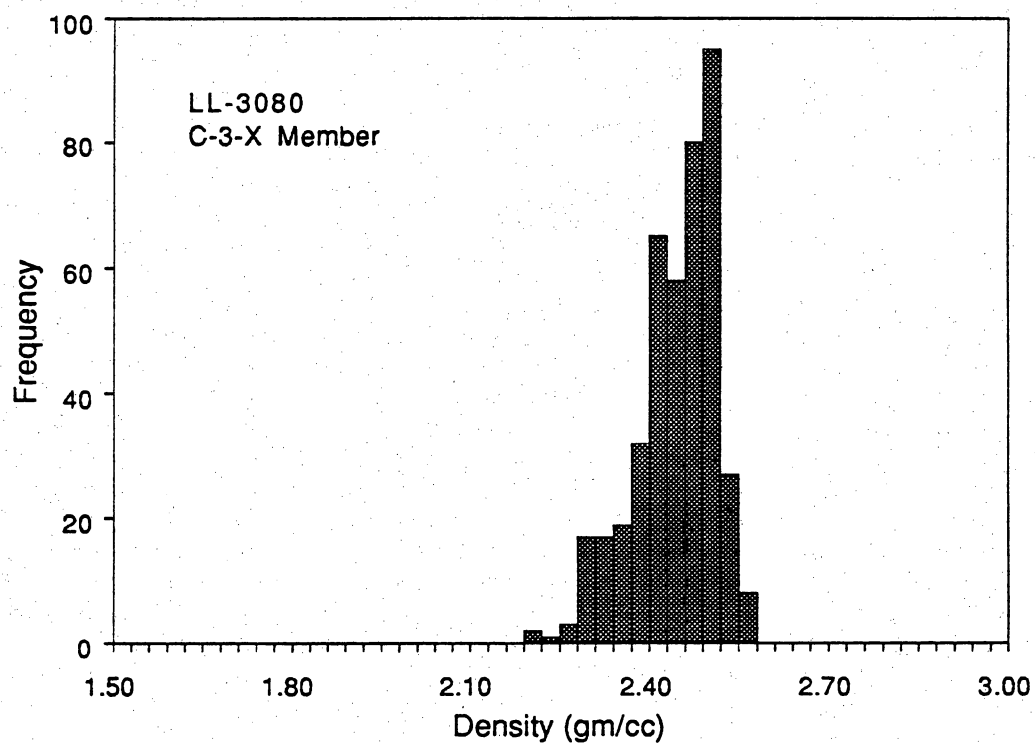
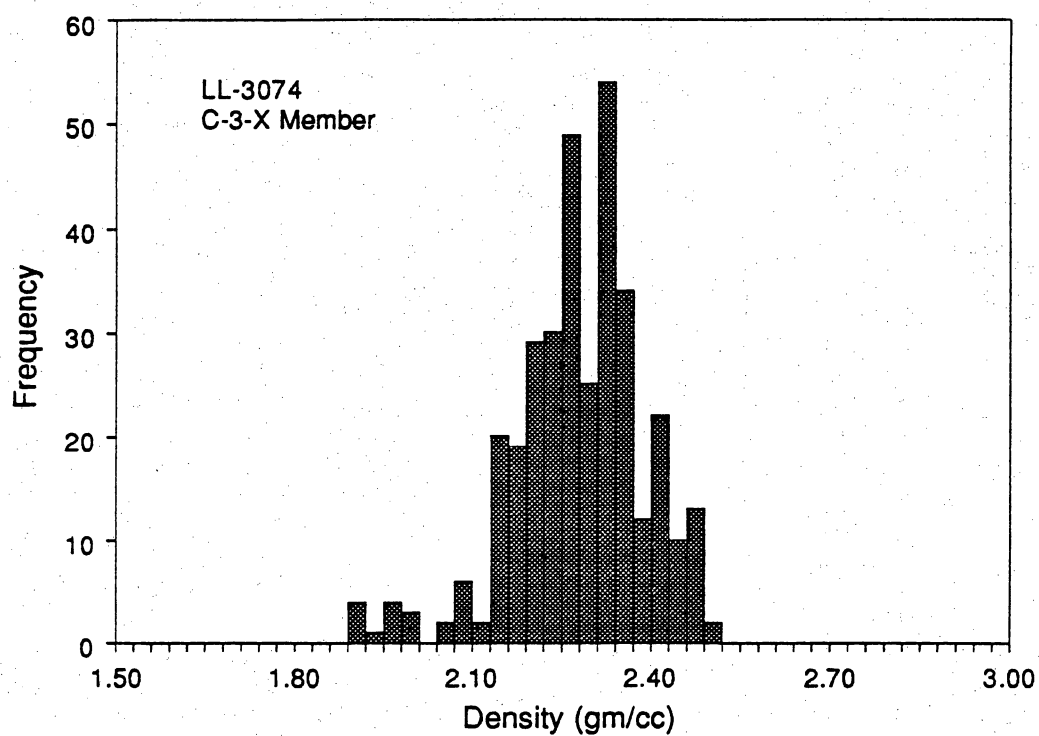


Figure IX 3. Histograms of density-log values in the LL-652 area.

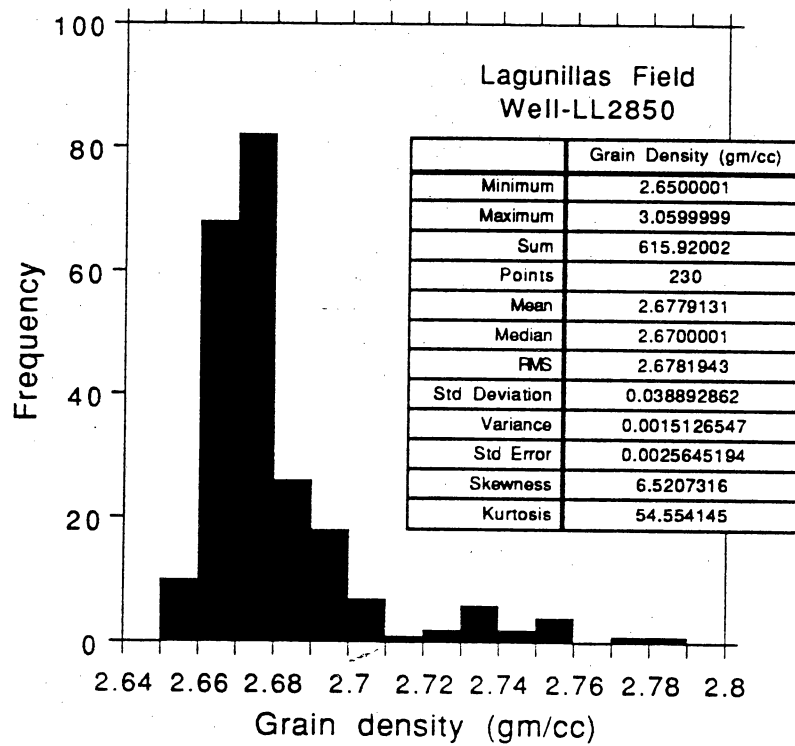


Figure IX 4. Histogram of core grain density with a mean of 2.68 gm/cc and a median of 2.67 gm/cc.

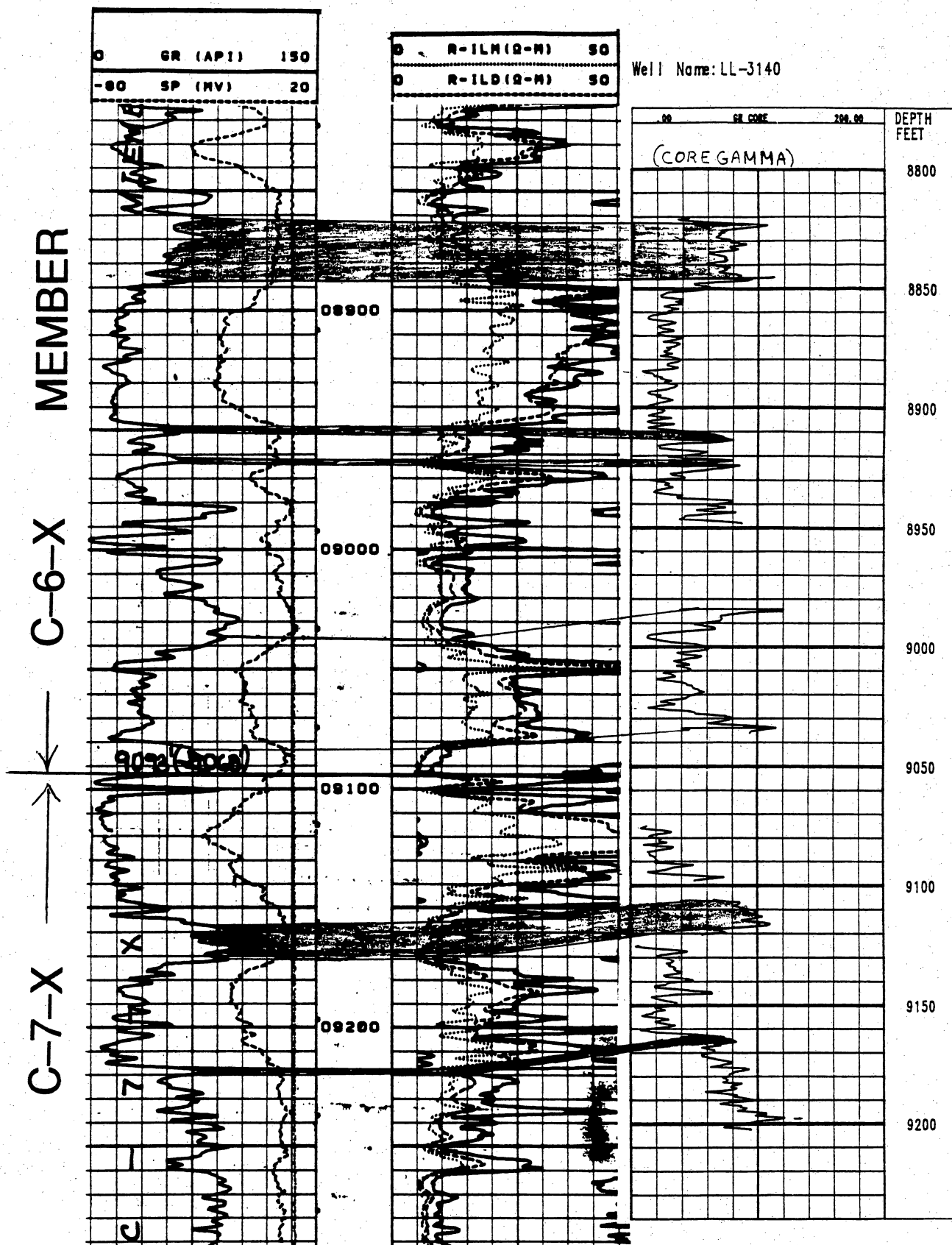


Figure IX 5. Core gamma-ray log versus well gamma-ray log showing a 54-ft (16.5 m) difference.

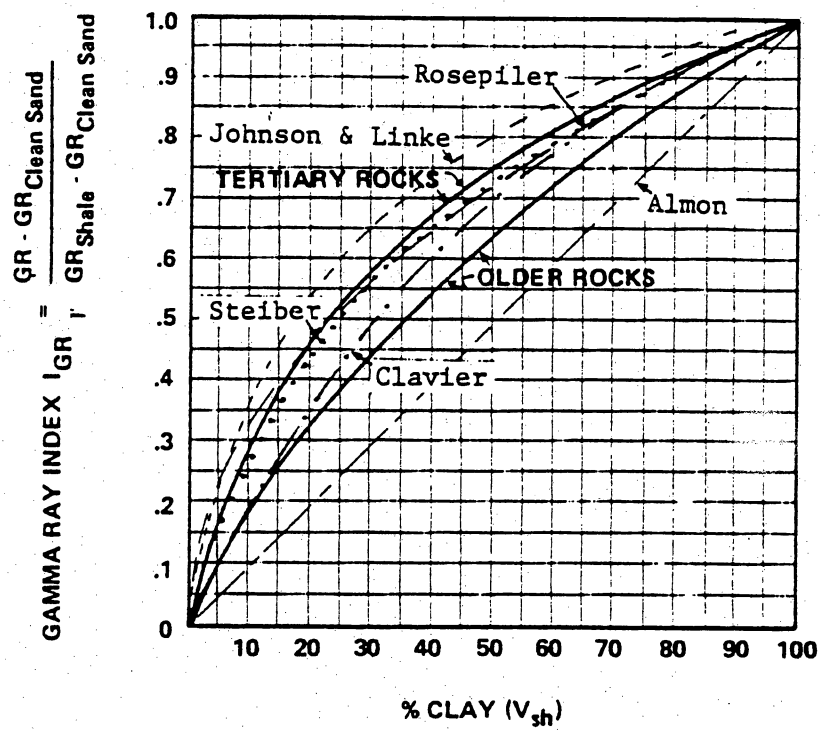


Figure IX 6. Model for calculating V_{sh} from gamma-ray logs. After Hilchie (1989).

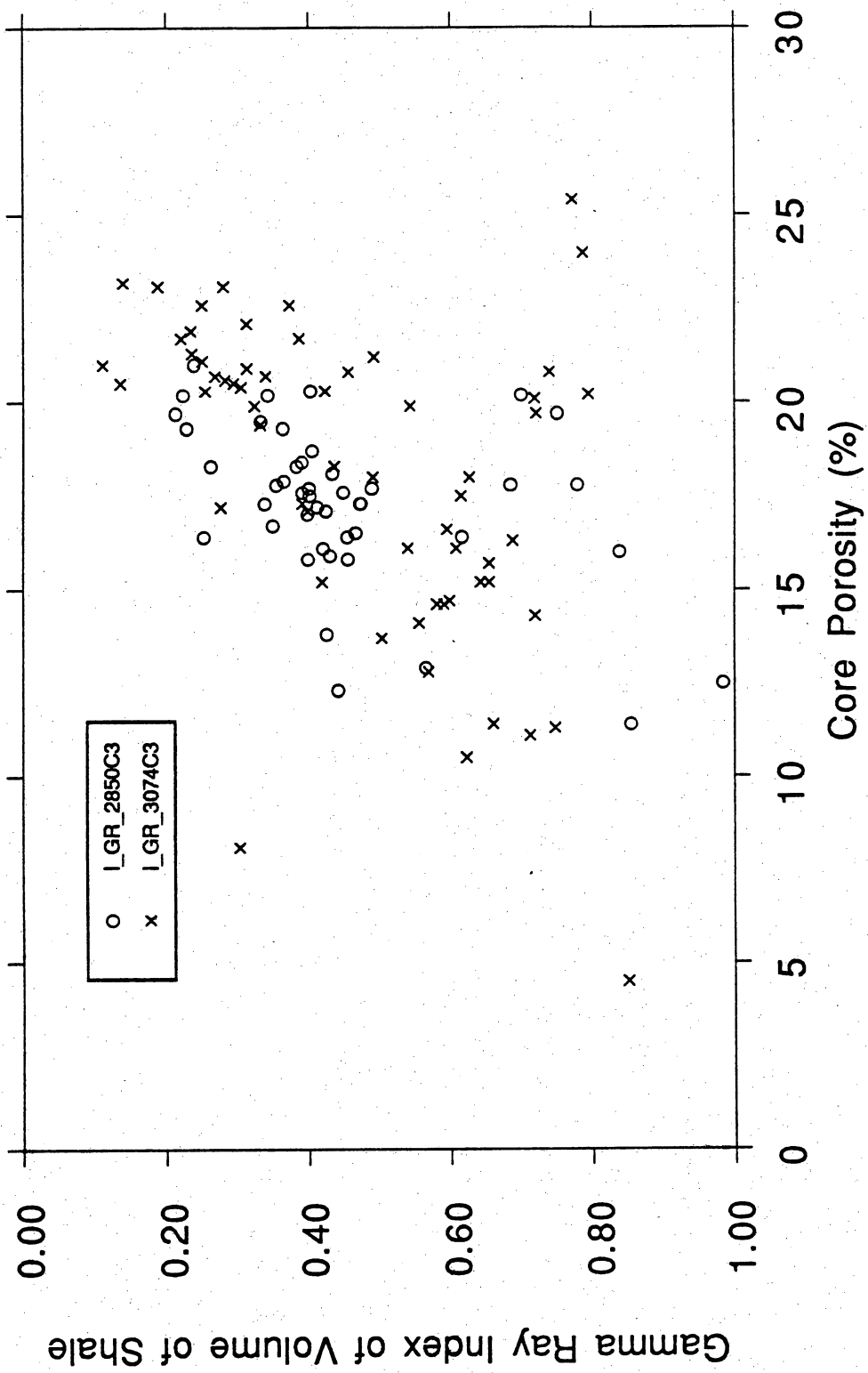


Figure IX 7. Gamma-ray index versus core porosity of the C-3-X Member showing porosity decreasing with increasing V_{sh}.

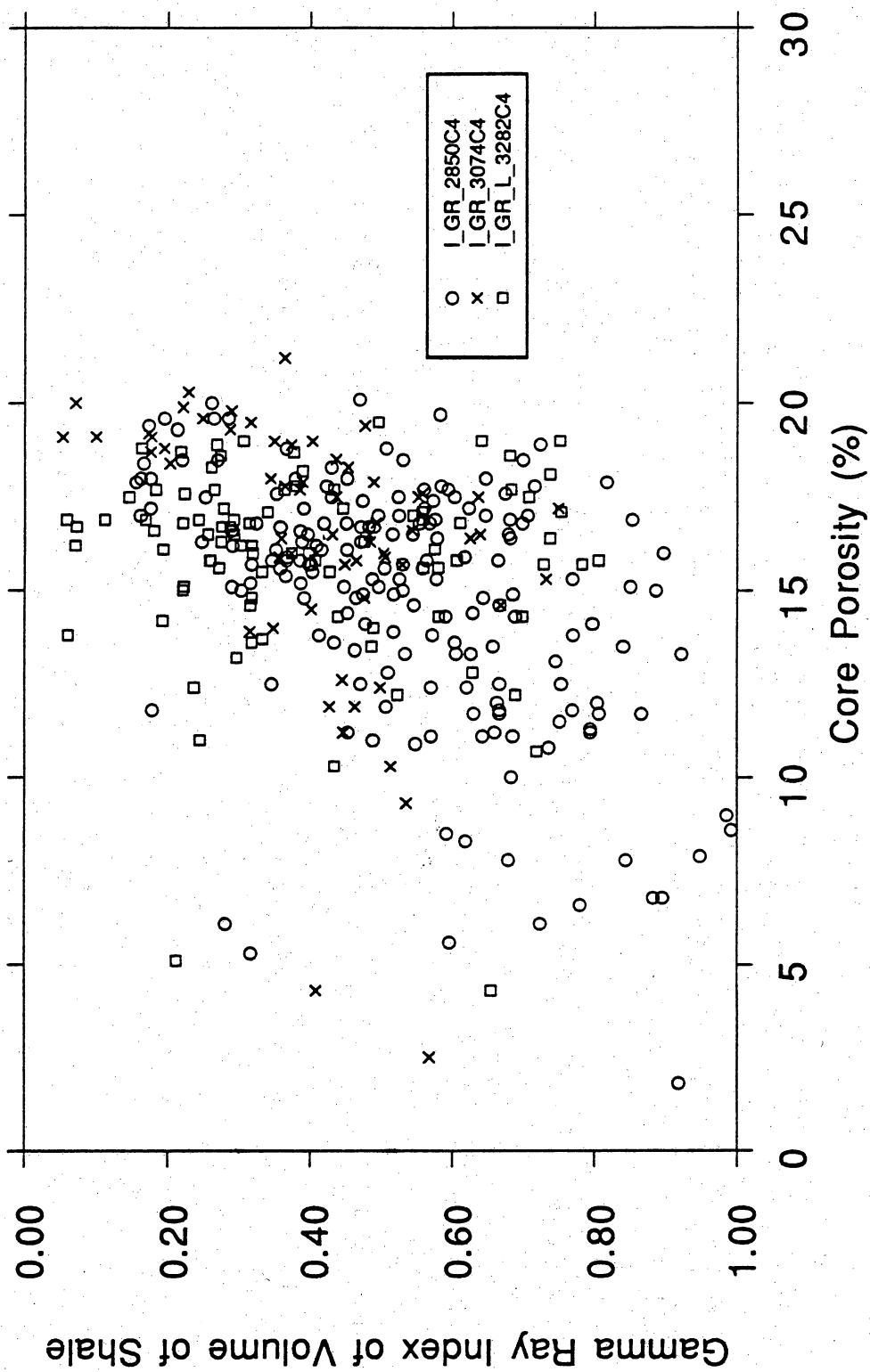


Figure IX 8. Gamma-ray index versus core porosity of the C-4-X Member. Although data points are scattered, there is a trend of porosity decreasing with increasing V_{sh} .

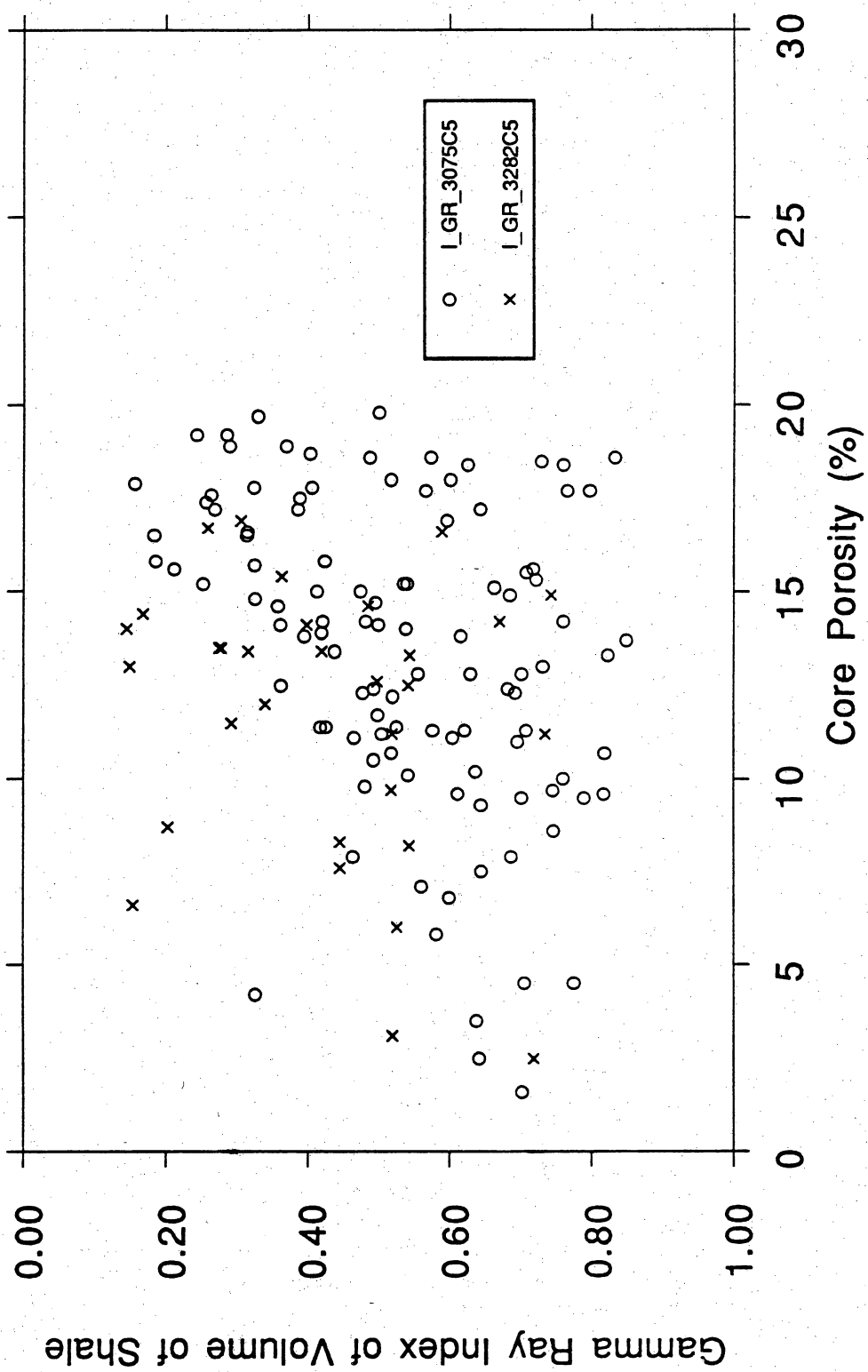


Figure IX 9. Gamma-ray index versus core porosity of the C-5-X Member. There is no apparent trend of porosity decreasing with increasing Vsh.

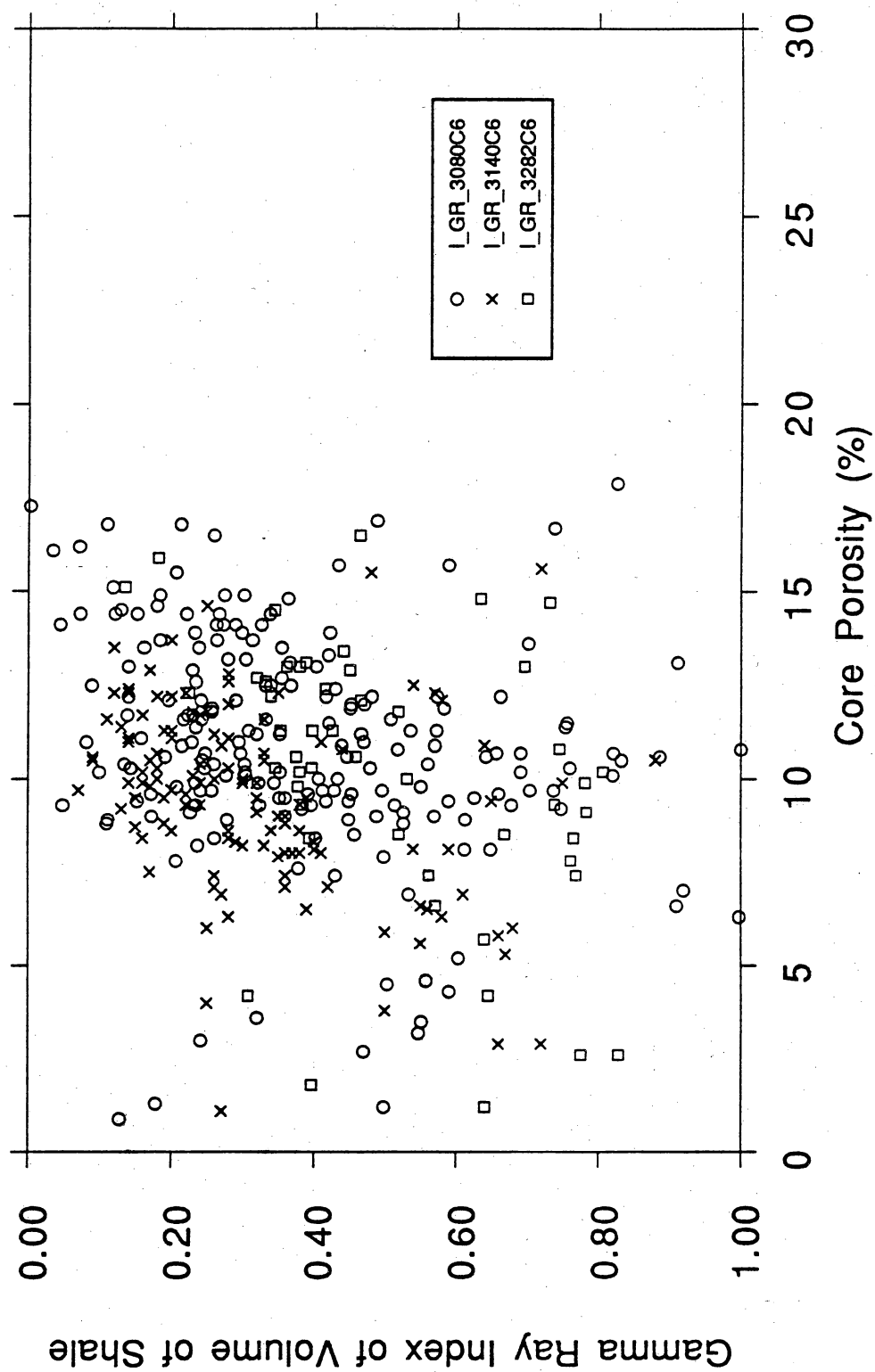


Figure IX 10. Gamma-ray index versus core porosity of the C-6-X Member.

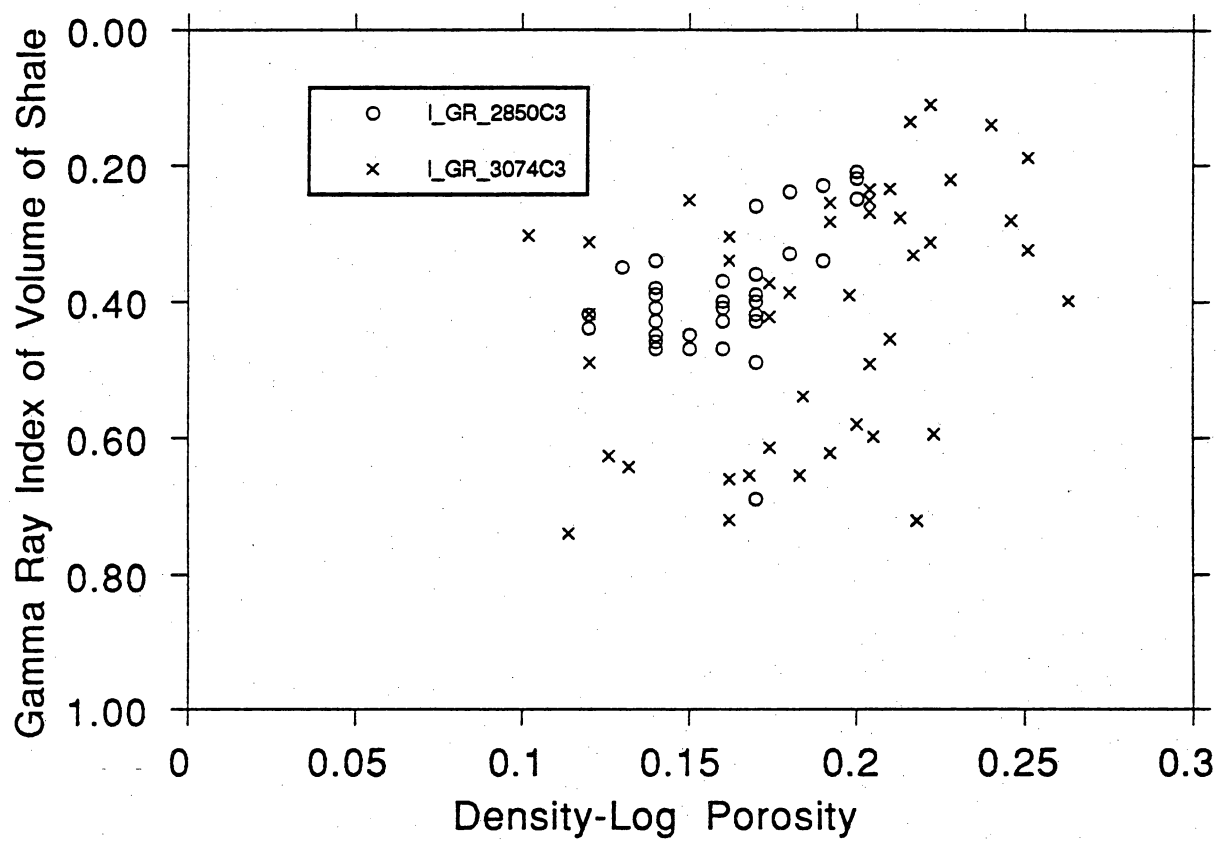
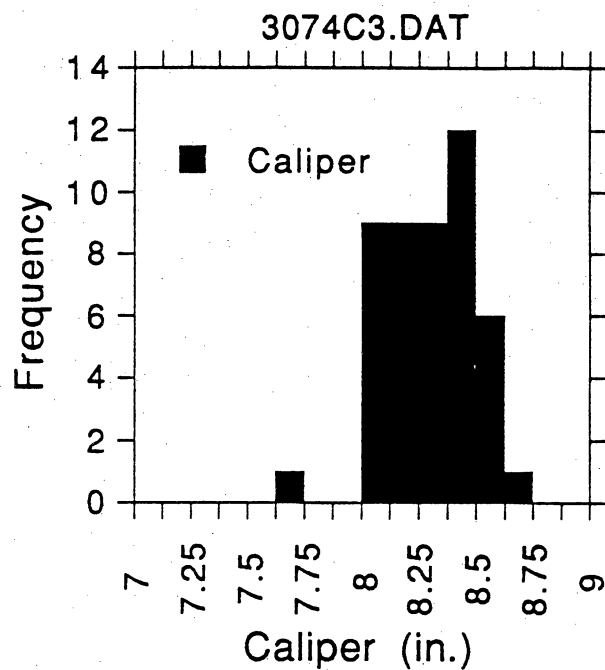
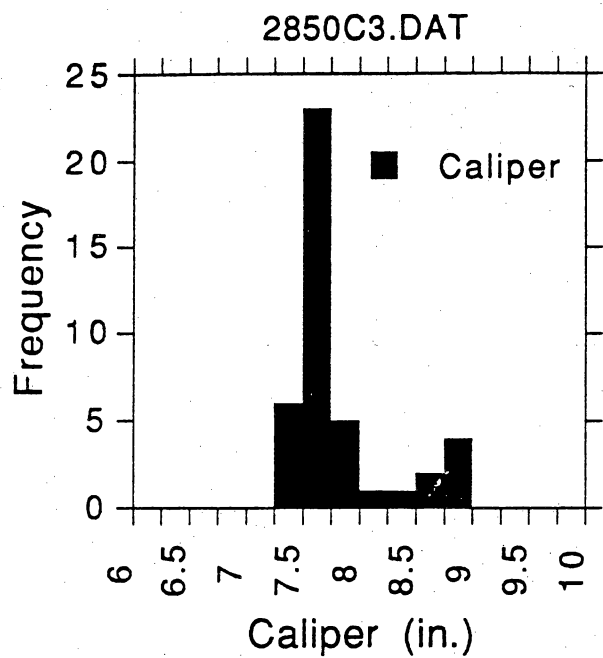


Figure IX 11. Gamma-ray index versus density porosity of the C-3-X Member.

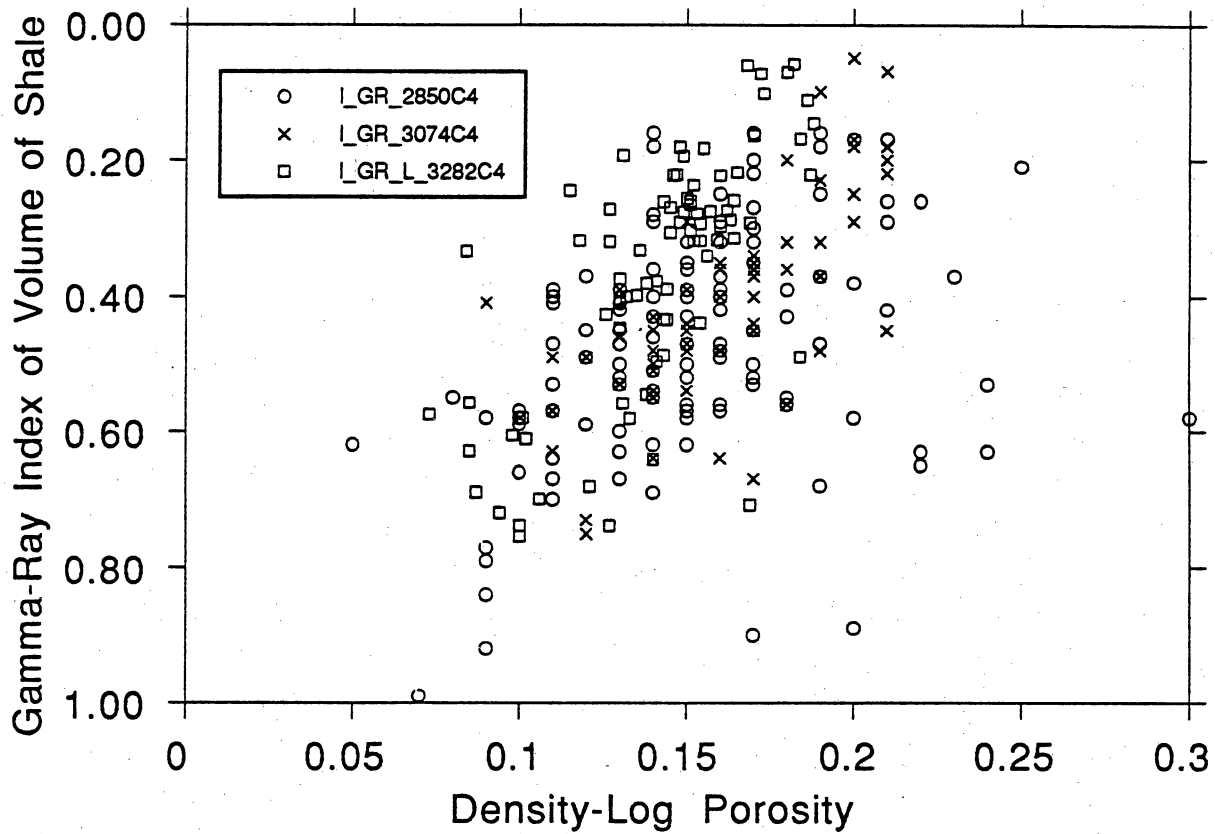
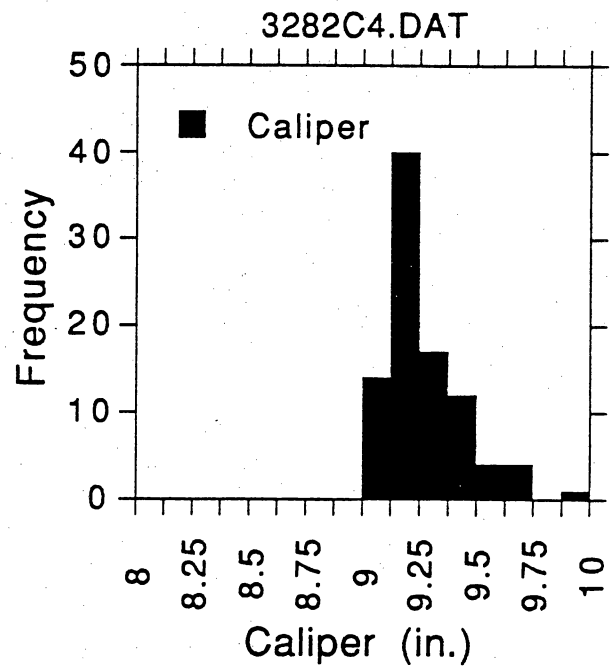
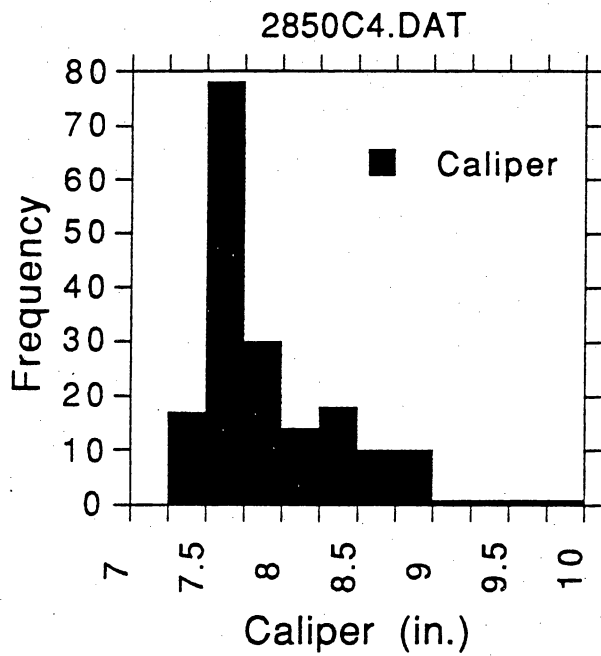


Figure IX 12. Gamma-ray index versus density porosity of the C-4-X Member.

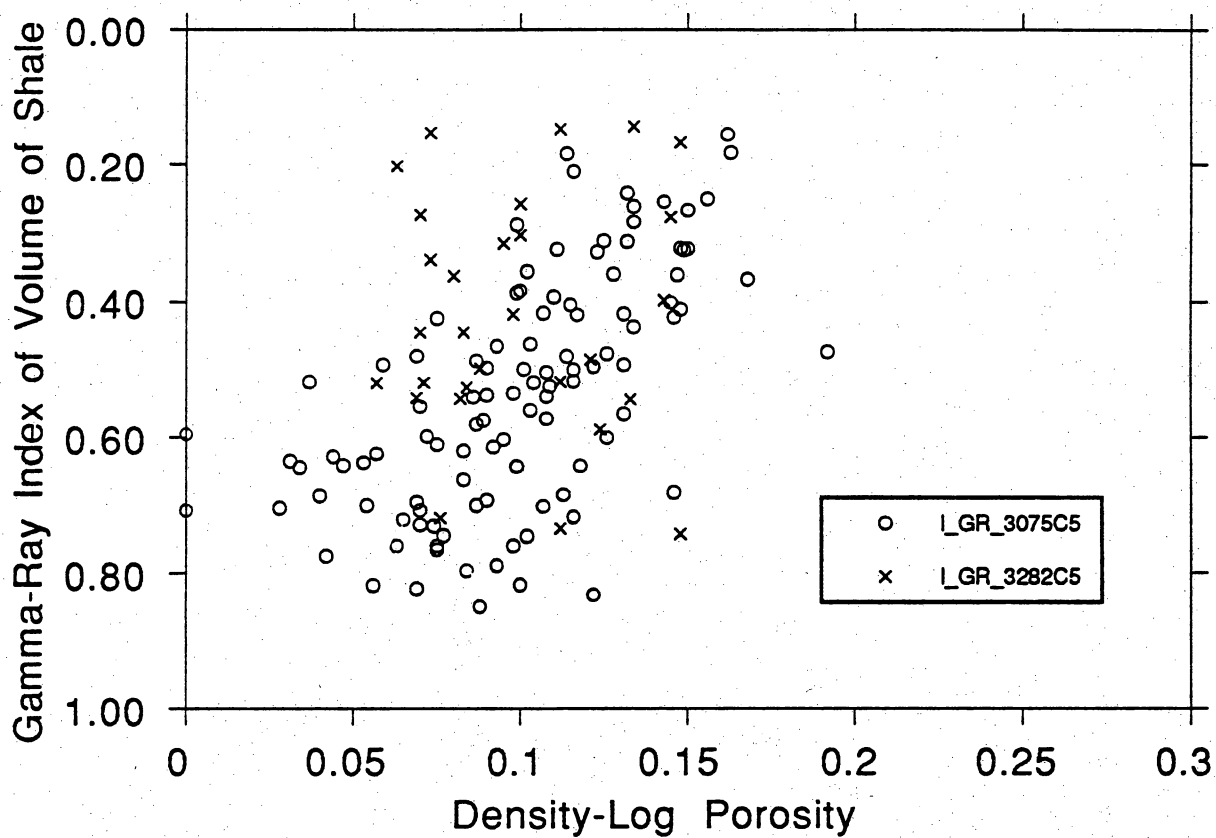
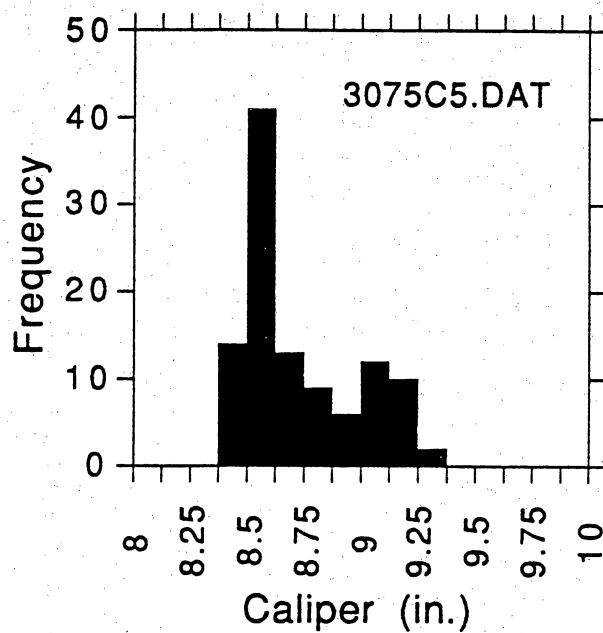
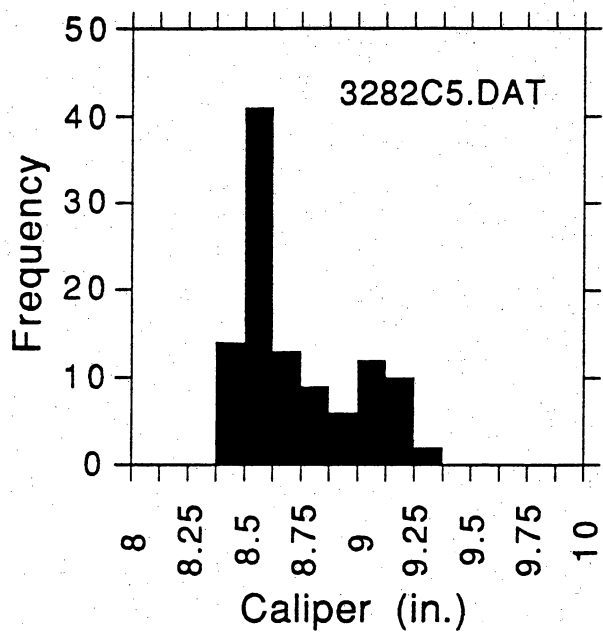


Figure IX 13. Gamma-ray index versus density porosity of the C-5-X Member.

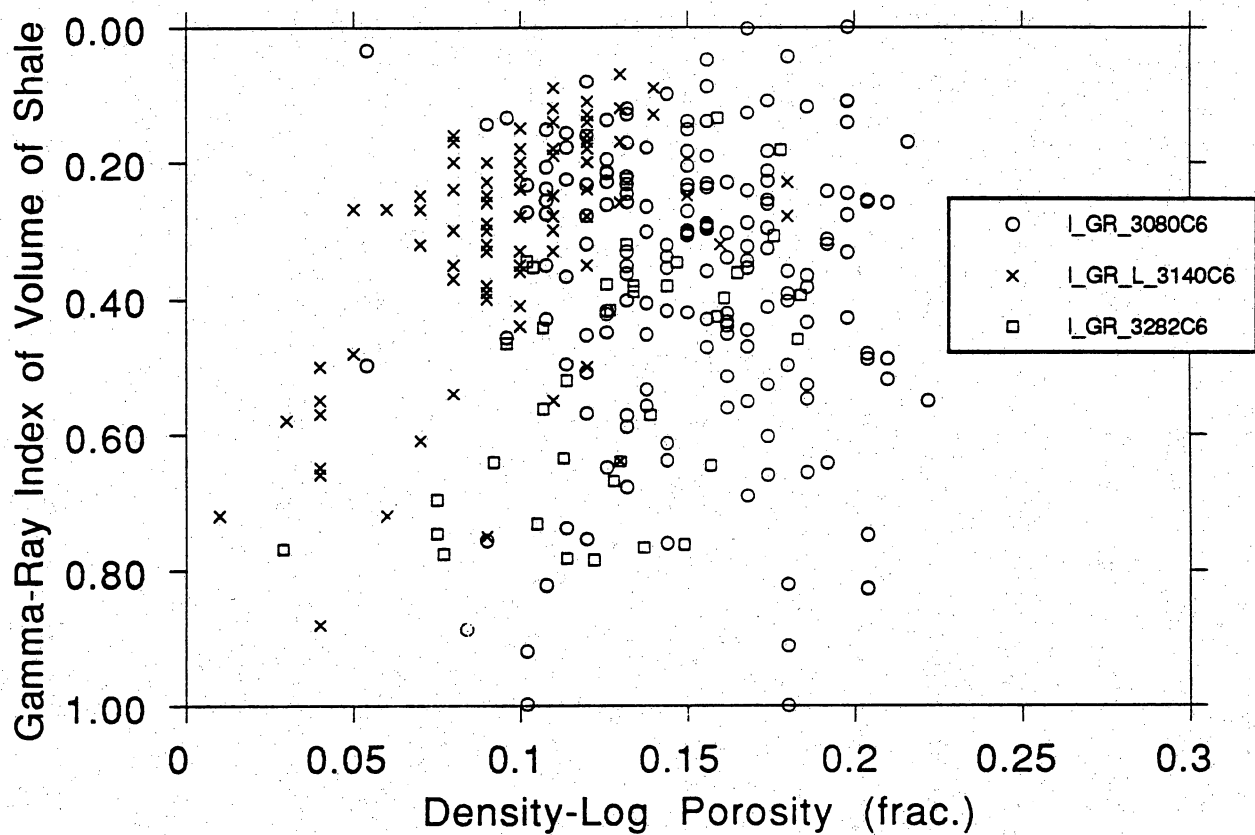
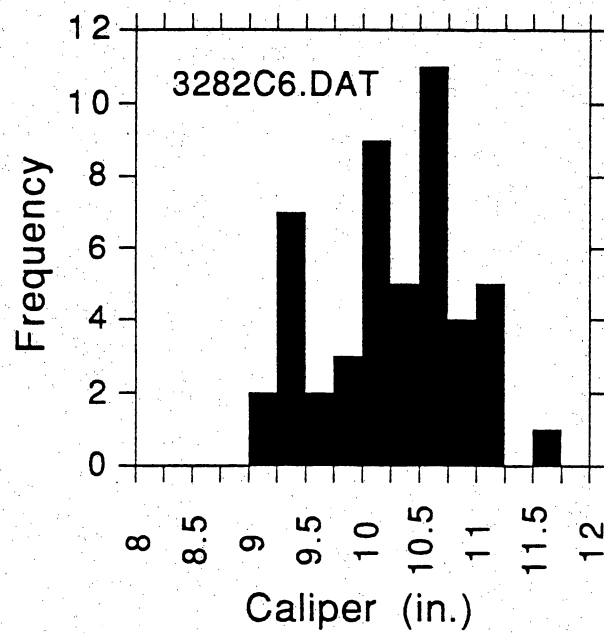
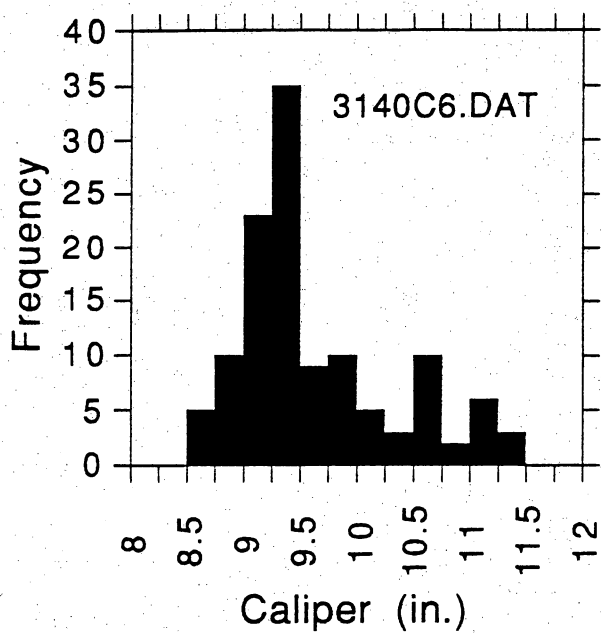


Figure IX 14. Gamma-ray index versus density porosity of the C-6-X Member.

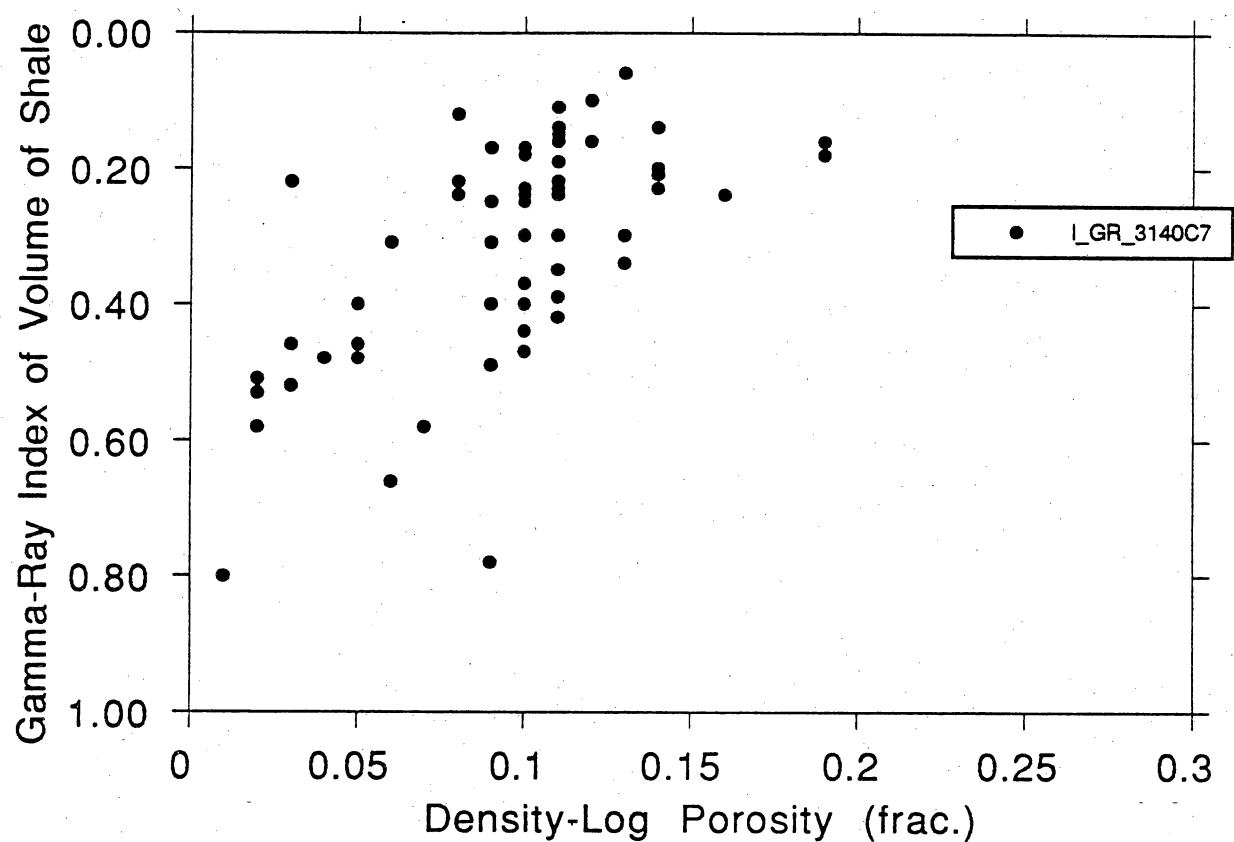
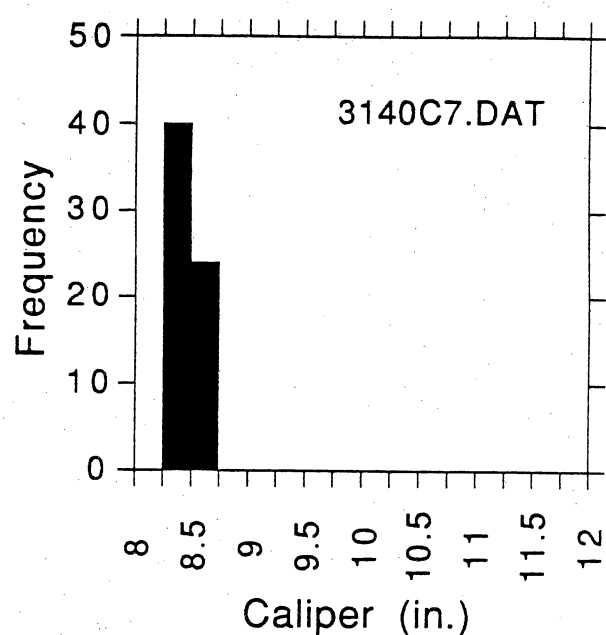
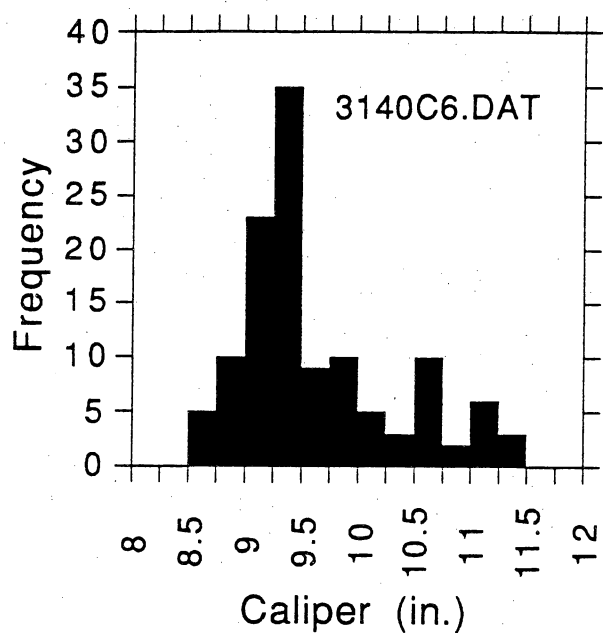


Figure IX 15. Gamma-ray index versus density porosity of the C-7-X Member.

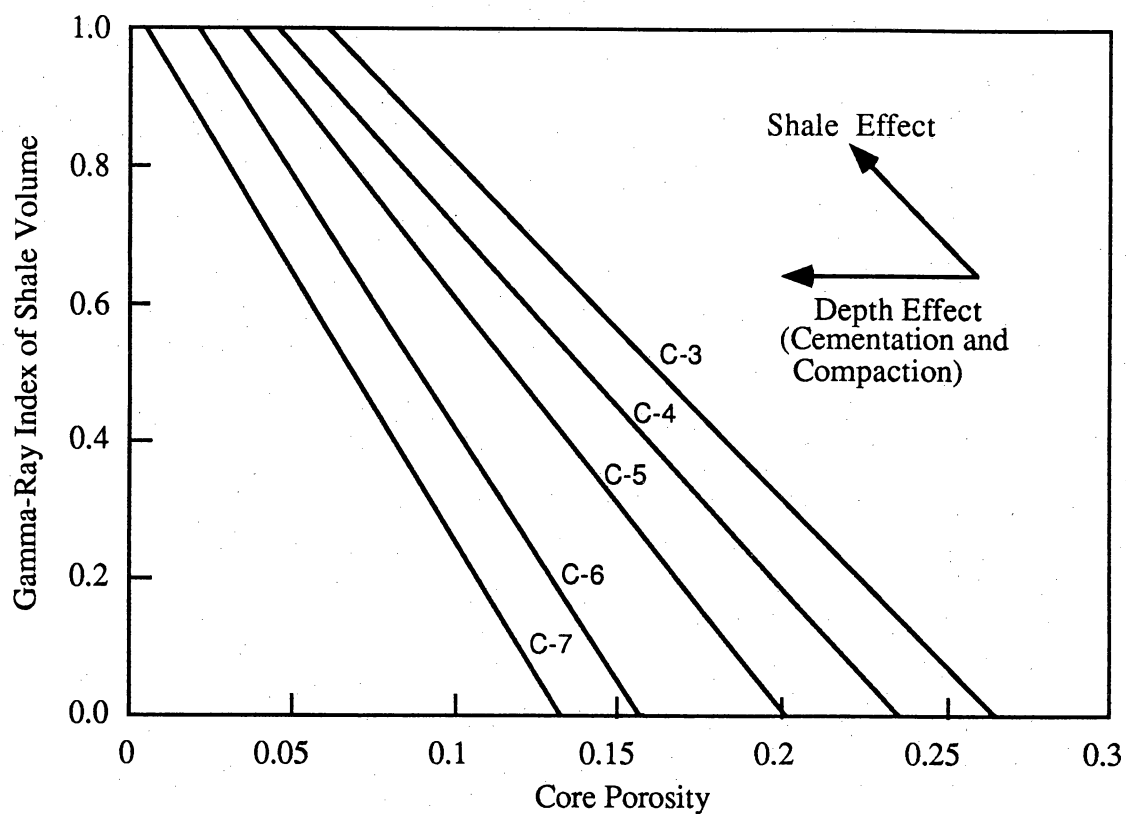


Figure IX 16. Relationships between gamma-ray index of V_{sh} and porosity in the C-3-X to C-7-X Members, determined from key wells. Porosity loss with depth resulted from compaction and cementation. Within members, porosity decreases with increasing V_{sh} .

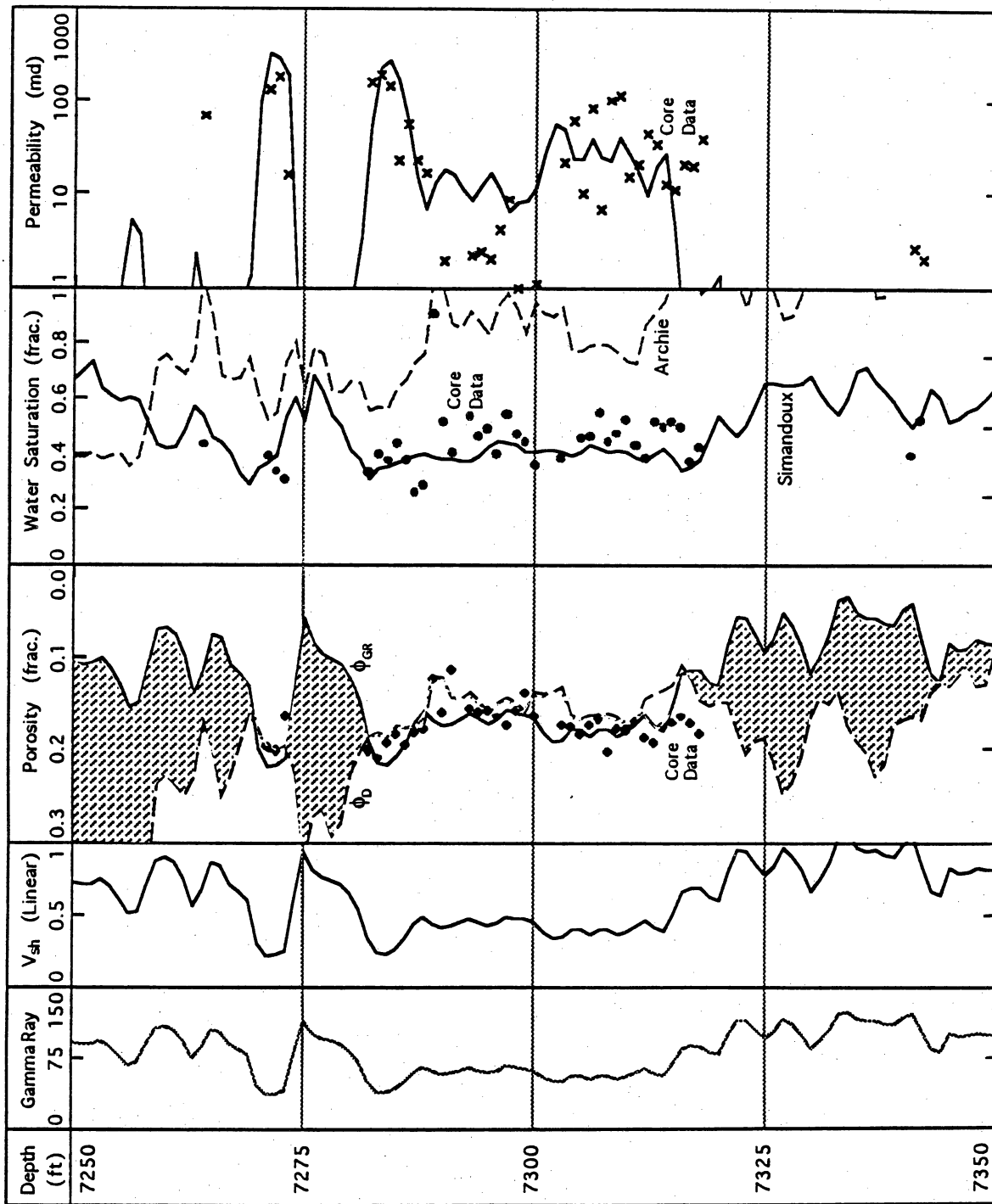


Figure IX 17. Comparison of petrophysical properties between core data and those calculated with porosity values derived from V_{sh} -porosity transforms in the C-3-X Member in the LL-2850 well.

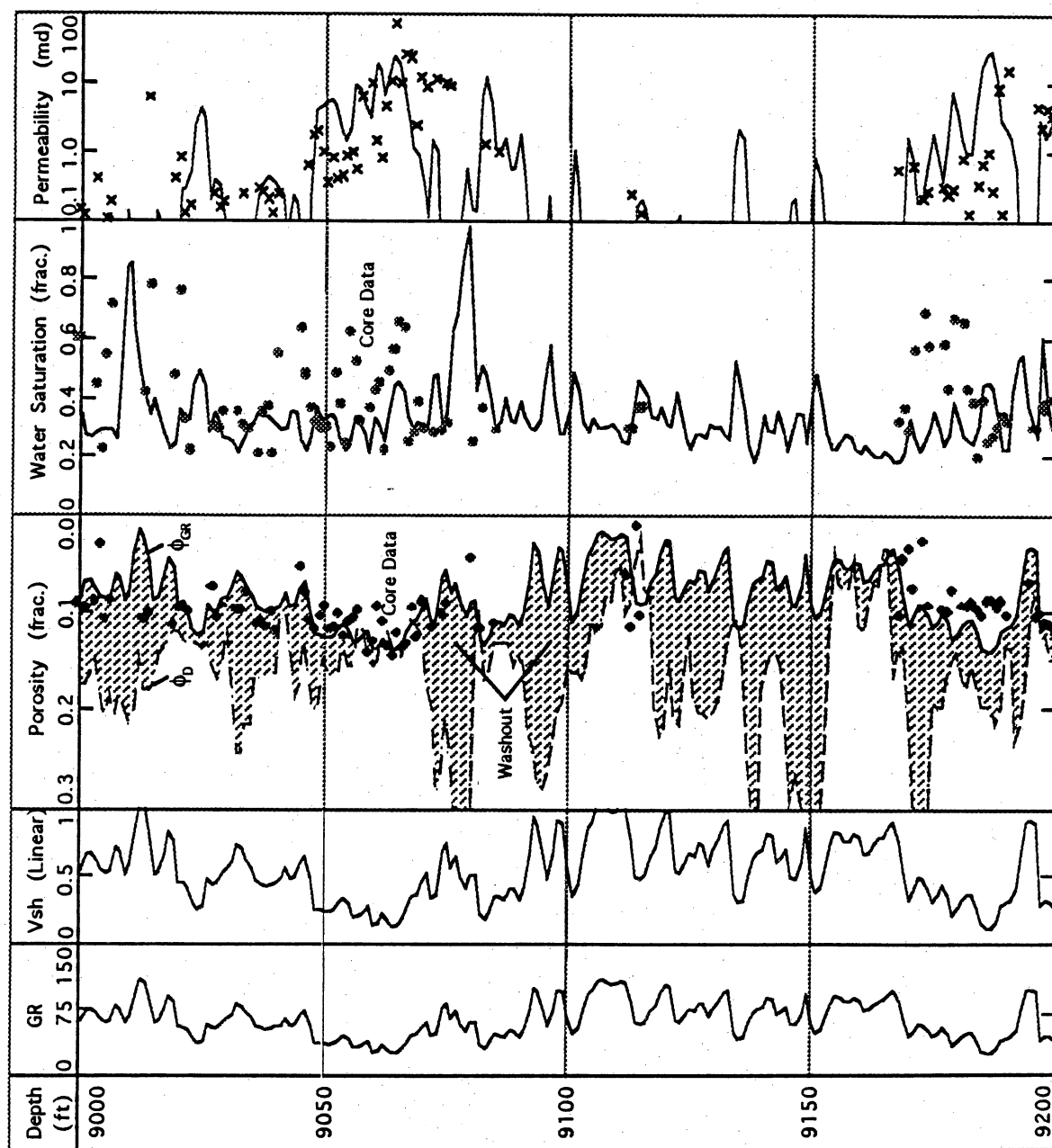


Figure IX 18. Comparison of petrophysical properties between core data and those calculated with porosity values derived from V_{sh} -porosity transforms in the C-6-X Member in the LL-3080 well.

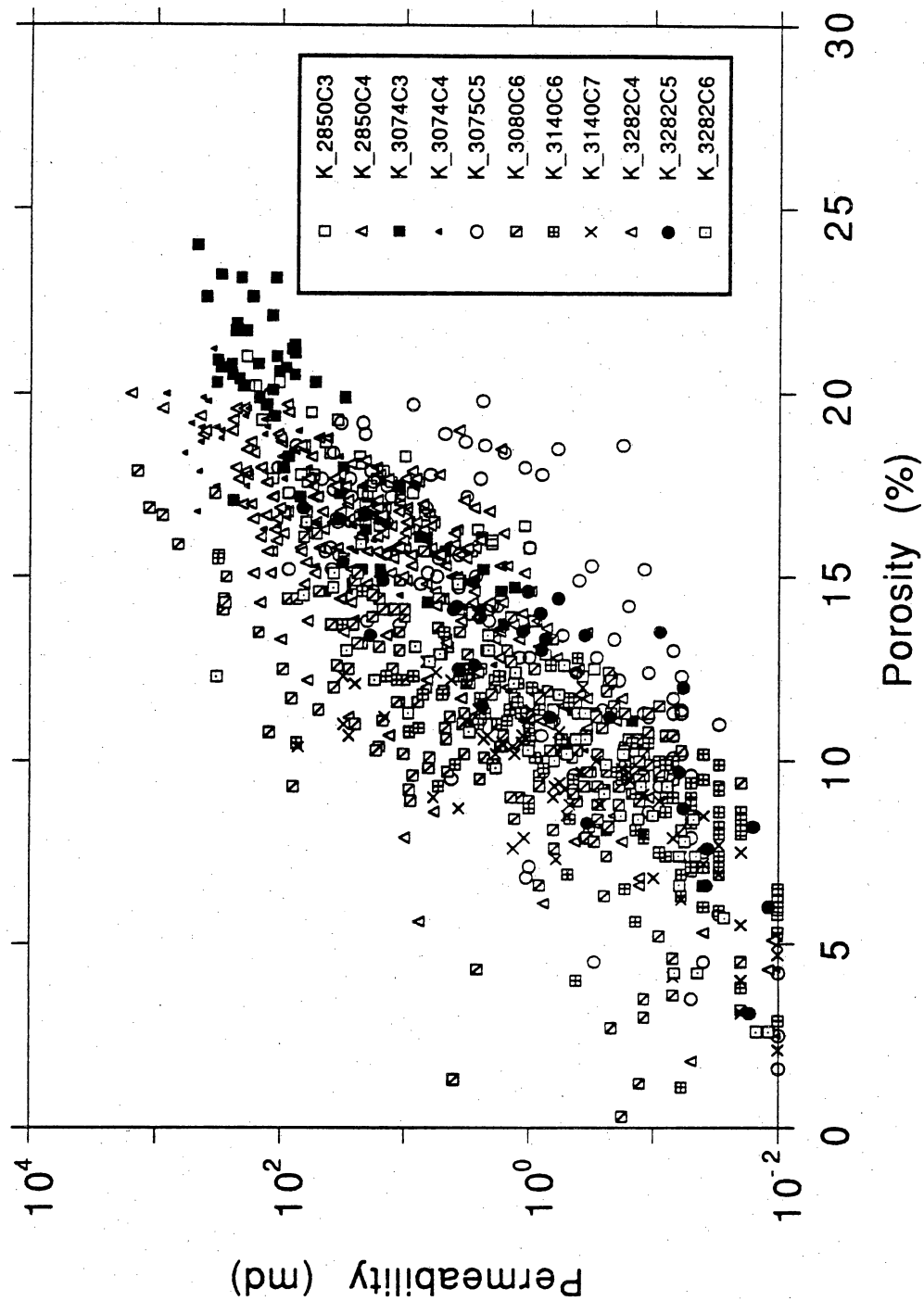


Figure IX 19. Core permeability versus core porosity of the C-3-X to C-6-X Members from key wells.

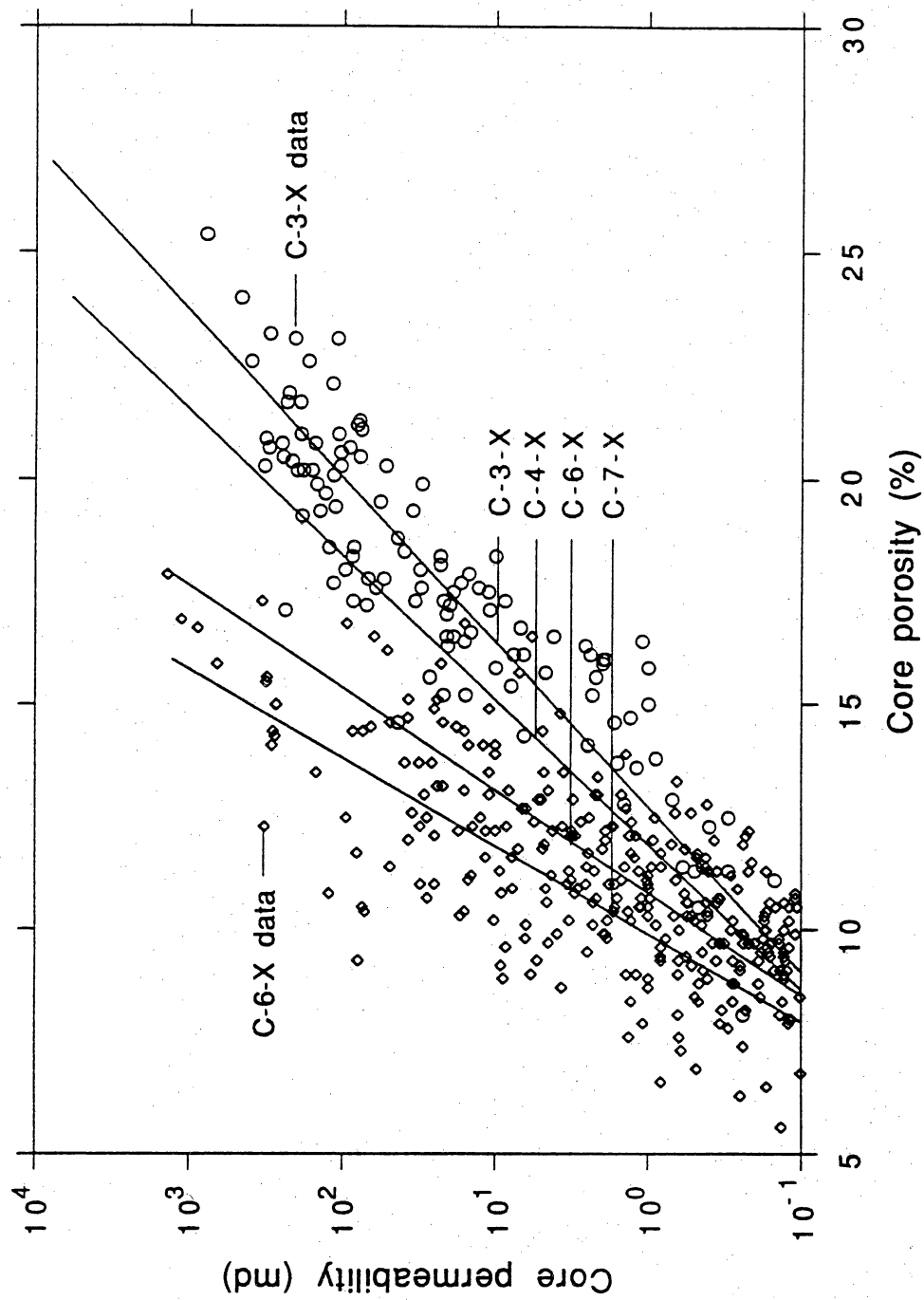


Figure IX 20. Relationships between permeability and porosity for the C-3-X, C-4-X, C-6-X and C-7-X Members and data derived from cores in the C-3-X and C-6-X Members.

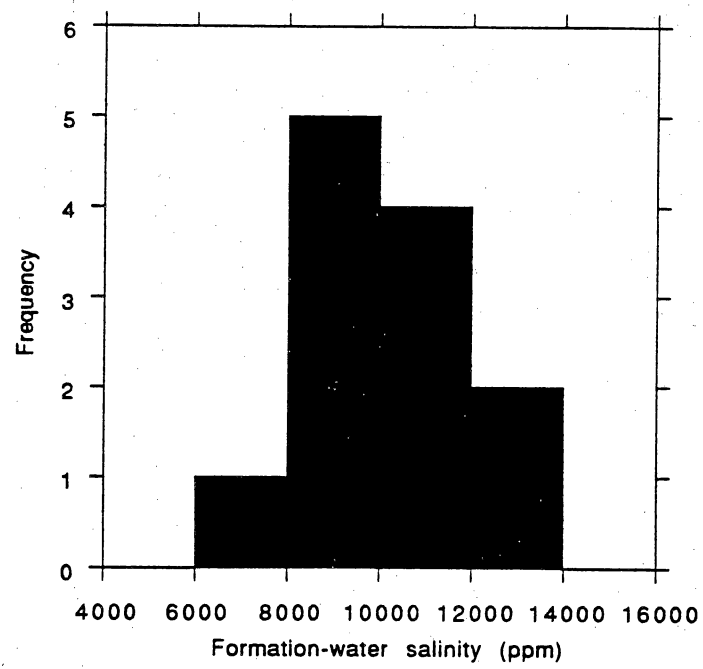


Figure IX 21. Histogram of formation-water salinity.

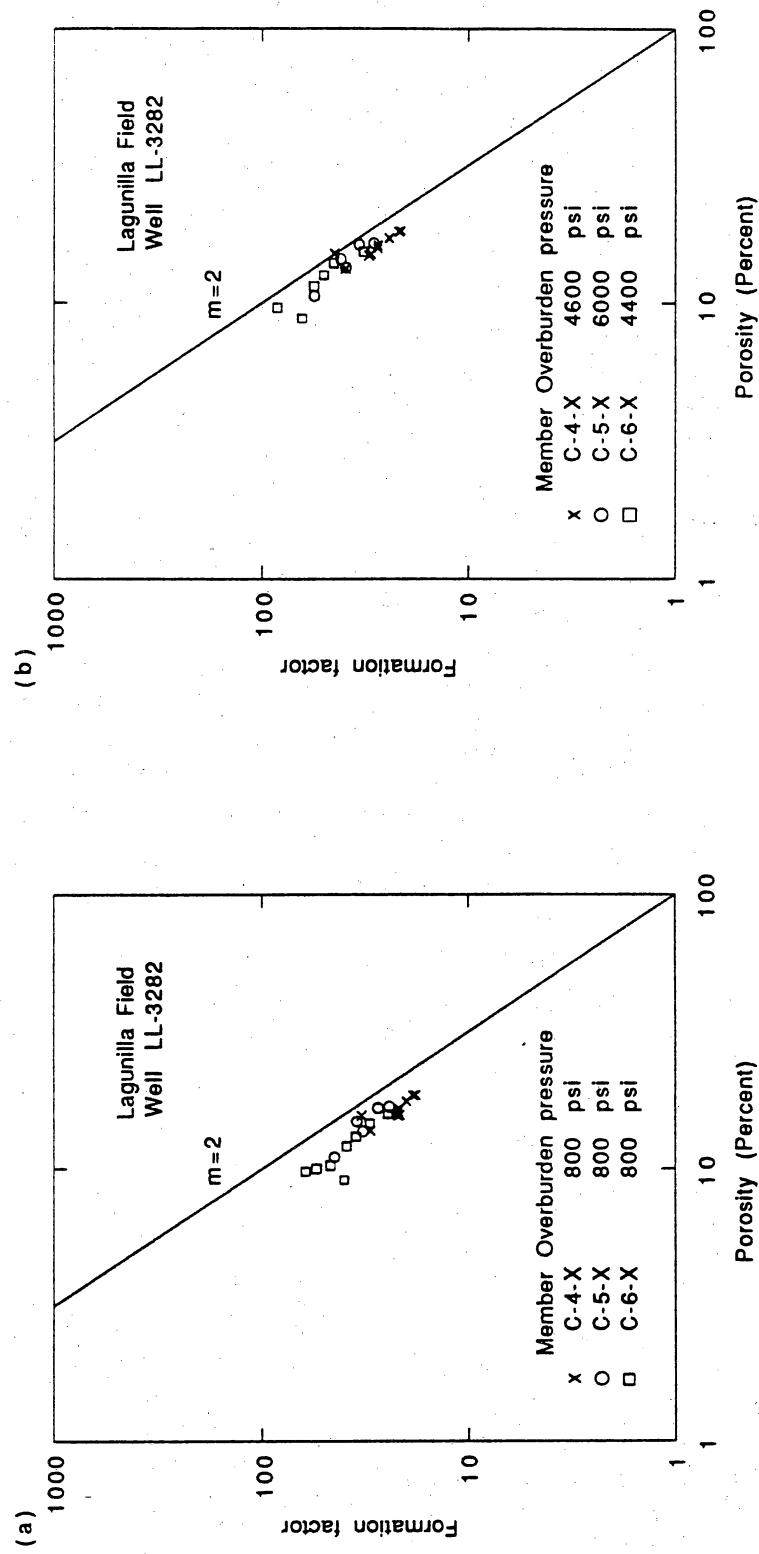


Figure IX 22. Overburden effect on cementation exponent (m).

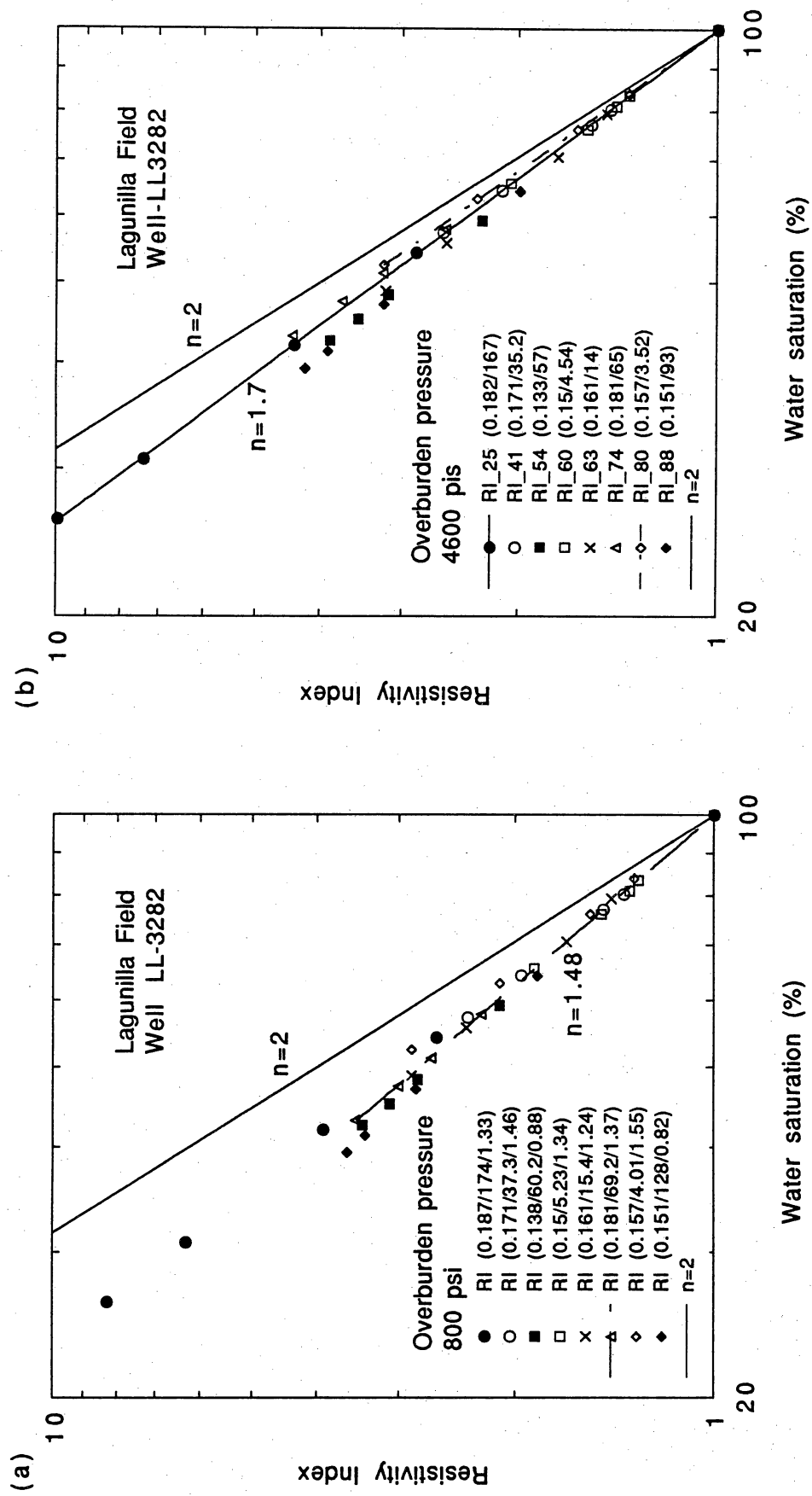


Figure IX 23. Overburden effect on saturation exponent (n).

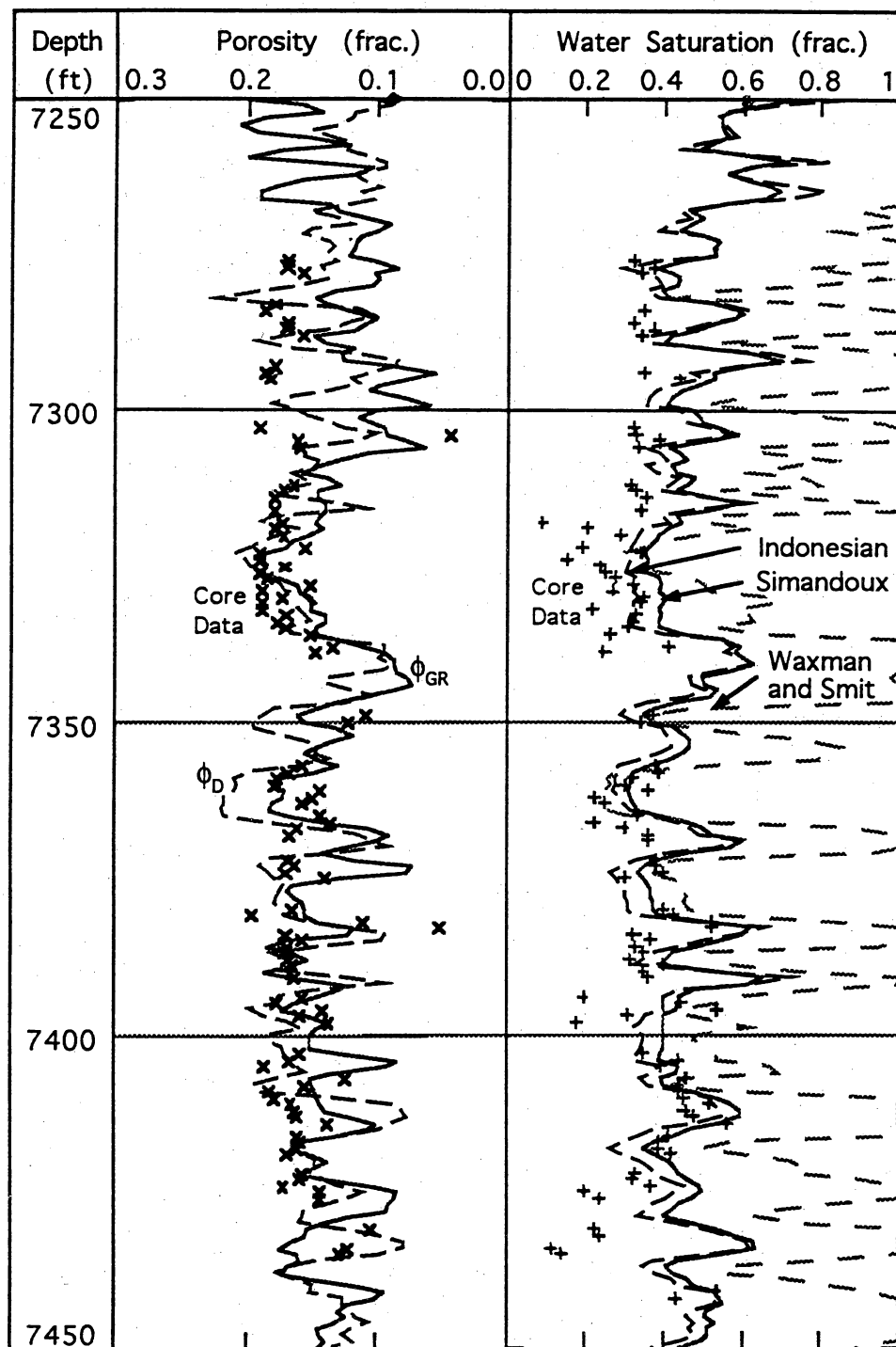


Figure IX 24. Comparison of water-saturation values calculated by Archie, Poupon, Simandoux, and Waxman and Smits models. Data are from the C-3-X Member in the LL-3282 well.

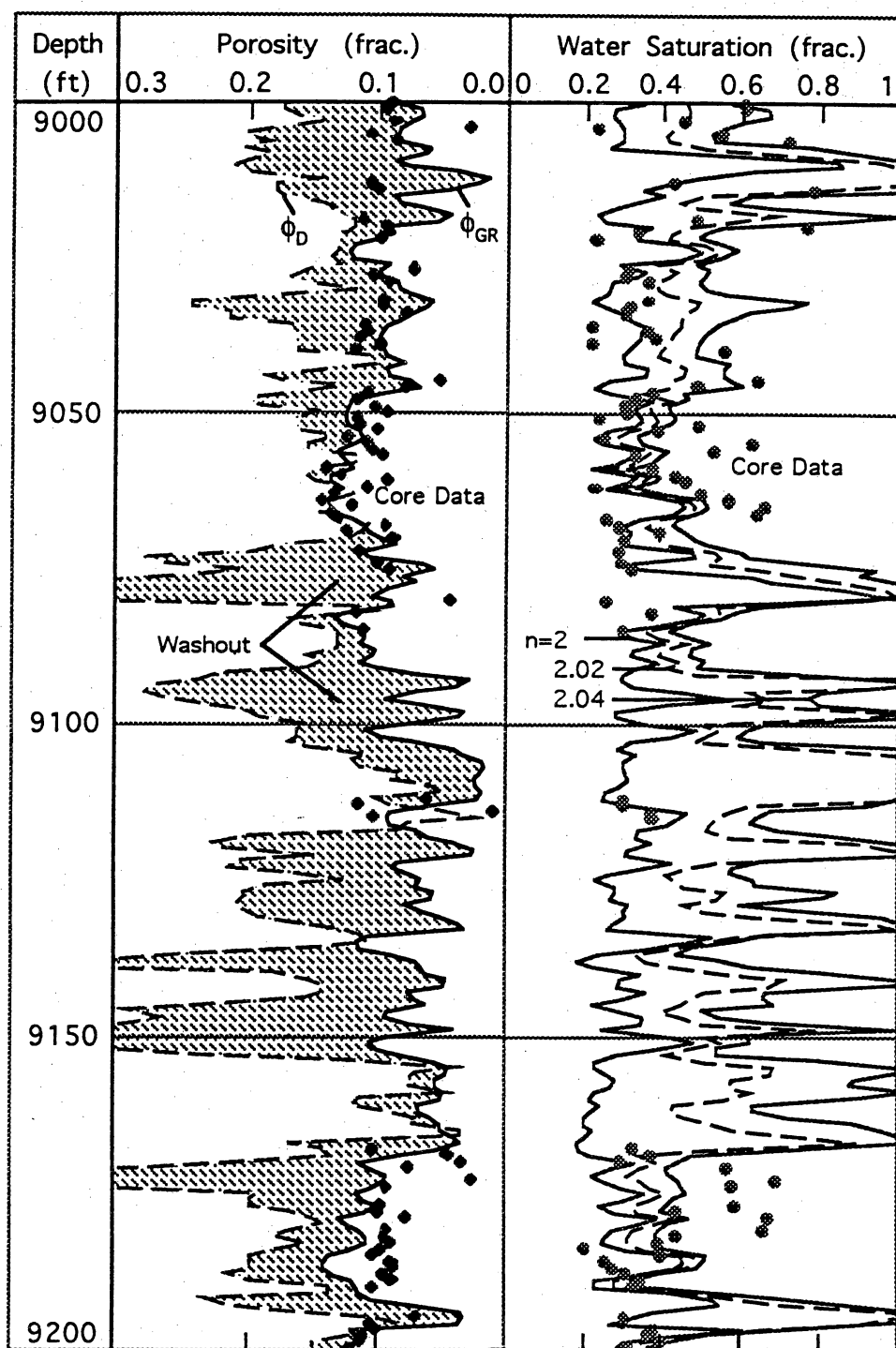


Figure IX 25. Effect of saturation exponent (n) on water-saturation values calculated by Simandoux equation. Data from the C-6-X Member in the LL-3080 well.

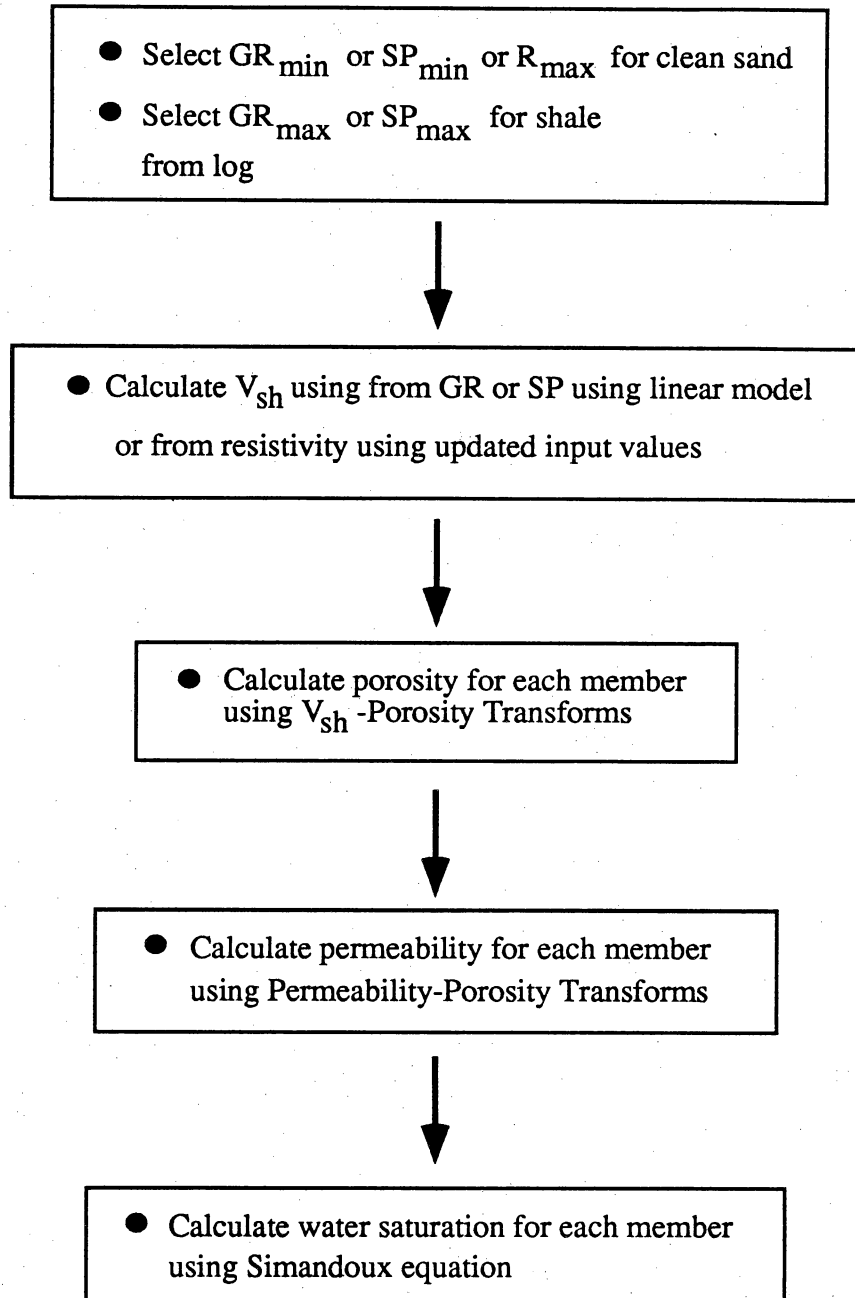


Figure IX 26. Flow chart of procedures used in fieldwide formation evaluation.

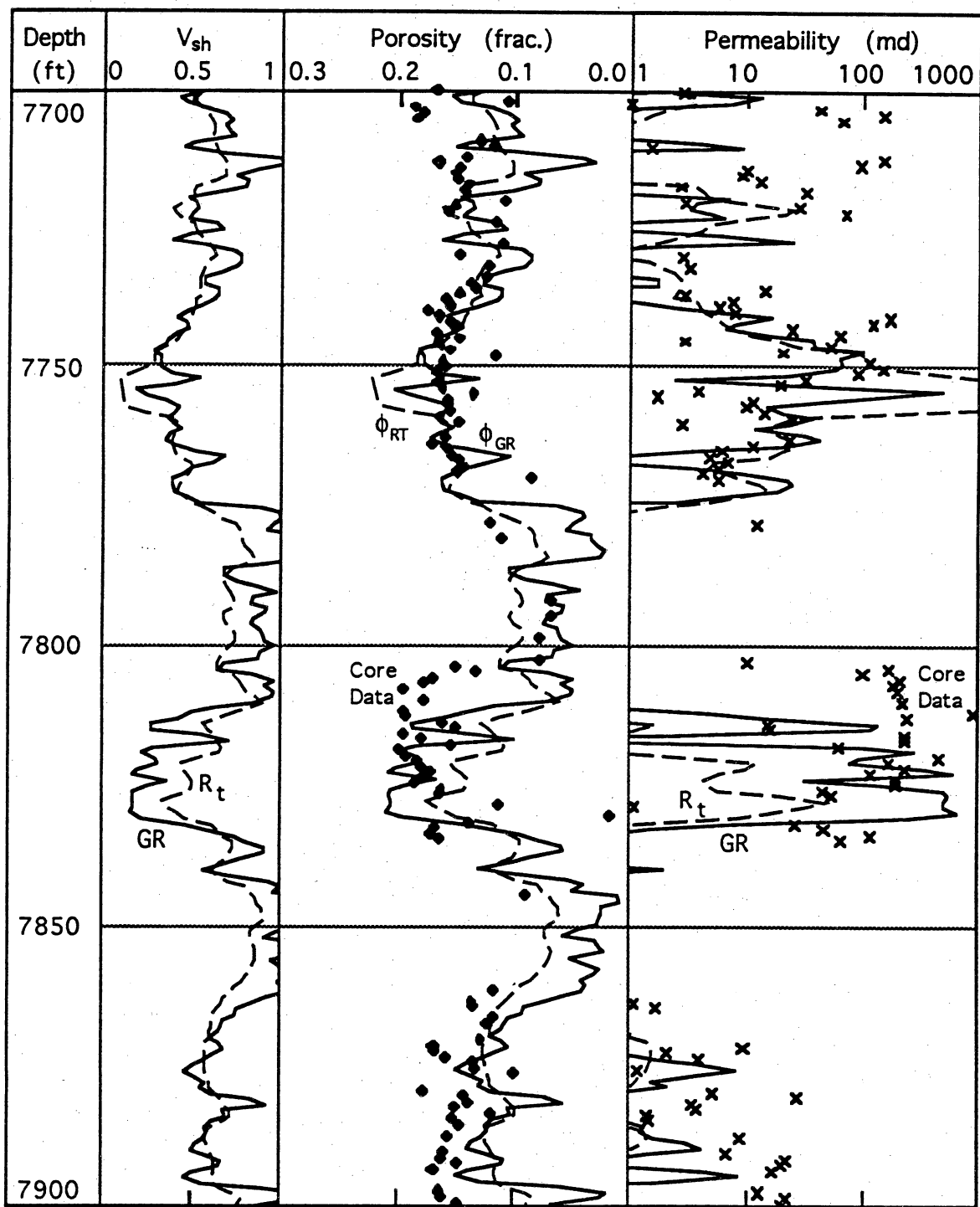


Figure IX 27. Comparison between V_{sh} derived from V_{sh} -porosity transforms and V_{sh} derived from resistivity. Data from the C-4-X Member in the LL-2850 well.

Table IX 1. List of shifts in core depth in key wells.

Cored Well	Member	(1) Core-Depth (ft)	(2) Log-Depth (ft)	(2)-(1) (ft)	(3) Special Analysis (ft) (Core- Gamma/Ø, k)	(2)-(3) (ft)	Comments
LL-2850 (core lab)	C-3	7240-4362	7258-7274	18	7240-7256	18	
			7275-7322	14	7261-7308	14	
			7323-7374	12	7311-7362	12	
	C-4	7590-7898	7602-7620	12	7590-7608	12	
			7621-7776	10	7611-7766	10	
			7771-7846	8	7769-7838	8	
			7851-7910	12	7839-7898	12	
LL-3074 (core lab)	C-3	7240-7376	7240-7376	0	7240-7340	0	
					7341-7366	-2	
					7367-7376	0	
LL-3075 (Impeluz)	C-4	7535-7775	7535-7775	0	7535-7775	0	
	C-5	7882-8452	7869-8439	-13	7871-7980	-2	
					7981-8030	-3	
					8031-8100	-2	
					8101-8230	0	
					8231-8260	-2	
					8261-8320	-1	
					8321-8360	0	
					8361-8440	-1	
LL-3080 (Impeluz)	C-6	8633-9280	8651-9298	18	8650-8670	1	
					8671-8990	0	
					8991-9160	2	
					9161-9295	3	
LL-3140 (core lab)	C-6/C-7	8820-8948	8859-8882	39	8820-8843	39	
			8887-8992	43	8844-8948	43	
			9025-9257	54	8971-9203	54	
LL-3282 (core lab)	C-4	7280-7440	7275-7340	-5	7280-7345	-5	
			7344-7412	-2	7346-7414	-2	
			7412-7436	-4	7416-7440	-4	
	C-5	7920-8134	7918-8053	-2	7920-8055	-2	
			8055-8084	-1	8056-8085	-1	
			8086-8134	0	8086-8134	0	
	C-6	8670-8990	8668-8714	-2	8670-8716	-2	
			8715-8780	-3	8718-8783	-3	
			8782-8844	-2	8784-8846	-2	
			8846-8930	-1	8847-8931	-1	
			8931-8988	-2	8933-8990	-2	

Table IX-2. Petrophysical Parameters

Formation-water salinity (ppm)	11,000
Water resistivity (ohm-m)	0.50
Cementation exponent (m)	2.0
Saturation exponent (n)	2.0

Table IX-3. Cutoff Values for Volume of Shale, Water Saturation and Porosity

Member	Volume of Shale	Water Saturation	Porosity
C-1-X	0.55	0.55	0.08
C-2-X	0.55	0.55	0.08
C-3-X	0.55	0.55	0.08
C-4-X	0.55	0.55	0.08
C-5-X	0.50	0.50	0.08
C-6-X	0.50	0.50	0.08
C-7-X	0.50	0.50	0.08

Table IX 4. Net-sandstone thickness of C submembers from log analysis.

WELL	C1	C2U	C2L	C3U	C3M	C3L	C4U	C4M	C4L	C5U	C5M	C5LM	C5L	C5LU	C5LU	C6M	C6LU	C7
652	31.00																	
827	90.00	6.00	60.00	30.00	19.00	133.00	147.00	61.00	61.00	15.00	61.00	57.00	14.00	23.00	163.00	165.00	65.00	68.00
846	51.00	11.00	3.00	30.00	35.00	35.00	99.00	10.00				22.00	28.00	19.00	4.00	4.00		
847	86.00	10.00	6.00	24.00	21.00	85.00	65.00	35.00	4.00	22.00		33.00	17.00					
851			2.00		37.00	32.00	20.00					68.00						
852	38.00	28.00	16.00	10.00	22.00	21.00	83.00	34.00		4.00		30.00						
866	25.00	58.00	50.00	50.00	68.00	188.00	145.00	43.00				52.00						
800	4.00	5.00	33.00	33.00	30.00	26.00	54.00	2.00				30.00						
917		12.00	5.00	5.00	27.00	5.00	35.00	51.00		18.00		24.00		2.00	45.00	105.00		
946	21.00	113.00	6.00	33.00	16.00	64.00	152.00	12.00				22.00		18.00	71.00			
971	18.00	3.00	18.00	62.00	73.00	169.00						68.00						
975	40.00	66.00	2.00	51.00	33.00	30.00	91.00	57.00	38.00	2.00	64.00	14.00		2.00				
997	18.00	81.00	6.00	75.00	61.00	256.00	172.00	126.00	201.00	8.00	54.00	28.00		19.00	71.00	163.00	65.00	68.00
1010		58.00	12.00	46.00	76.00	4.00	48.00		96.00	40.00	60.00	3.00		6.00	22.00	4.00	15.00	
1022																		
1060																		
1061																		
1089		65.00	1.00	9.00	12.00	76.00	201.00	132.00	82.00			30.00						
1095																		
1106	15.00	42.00	128.00	151.00	23.00	17.00	190.00	50.00				30.00		6.00	22.00	37.00	52.00	28.00
1129	18.00	28.00	45.00	83.00	62.00	185.00	150.00					14.00						
1130	3.00	9.00	3.00	15.00	72.00	348.00	143.00	164.00	241.00			25.00		71.00	89.00	123.00		
1162	3.00	3.00	3.00	17.00	55.00	55.00	78.00	49.00	90.00			28.00						
1172	2.00	34.00	4.00	12.00	30.00	45.00	112.00	41.00	38.00			23.00						
1176	42.00	4.00	38.00	43.00	55.00	55.00	46.00	20.00	22.00	15.00		62.00		20.00	58.00	31.00	65.00	3.00
1198	16.00	25.00	4.00	4.00	21.00	50.00	86.00	40.00	31.00	16.00		67.00		11.00				
1218		1.00	4.00	42.00	16.00	33.00	67.00	134.00	40.00									
1245				9.00	3.00	13.00	78.00	8.00	3.00			30.00	112.00					
1276				33.00	33.00	104.00	48.00		1.00			12.00	34.00	32.00	83.00	123.00	60.00	118.00
1293	3.00	11.00	11.00	11.00	36.00	105.00	164.00	33.00	40.00	3.00		33.00	14.00					
1303		91.00	77.00	146.00	69.00	103.00	115.00	69.00	74.00	19.00		72.00						
1307			2.00	9.00	12.00	60.00	35.00	13.00	2.00			36.00						
1310			1.00	3.00	30.00	9.00			6.00			31.00						
1312		13.00		16.00	33.00	72.00	94.00	32.00	68.00			34.00	23.00	103.00				
1316	50.00	45.00	15.00	28.00	33.00	86.00	184.00	39.00	34.00			12.00	5.00	26.00	34.00	94.00	51.00	92.00
1679	50.00	27.00	19.00	18.00	17.00	18.00	119.00	12.00	8.00			12.00	20.00					
1695	22.00	42.00	4.00	48.00	27.00	161.00	166.00	54.00	68.00	50.00		12.00	5.00					
1748		25.00	2.00	18.00	30.00	28.00												
1782		17.00	9.00	17.00	35.00	14.00	75.00	16.00				17.00	5.00	5.00	39.00	40.00	51.00	
1799					12.00	6.00	72.00	31.00	12.00			62.00						
1803	15.00	4.00	33.00	36.00	46.00	22.00	136.00	25.00				35.00	13.00					
1876	47.00	45.00	7.00	20.00	36.00	96.00	103.00	43.00	47.00			32.00						
1885	1.00	5.00		3.00	36.00	78.00	143.00	76.00				41.00						
1886	13.00	9.00	1.00	13.00	37.00	47.00	66.00	28.00				27.00						
1987	114.00	58.00	21.00	6.00	57.00	113.00	150.00	11.00				27.00						
2010	9.00	7.00	2.00	17.00	23.00	57.00	92.00	31.00	33.00	9.00		36.00						
2038	22.00	44.00	32.00	57.00	19.00	50.00	111.00	42.00	13.00	22.00		33.00	60.00					
2089	5.00	24.00		19.00	40.00	50.00	113.00	31.00				30.00						
2094	5.00	22.00	6.00	10.00	51.00	72.00	115.00	45.00				37.00						
2187			3.00	13.00	38.00	165.00	108.00	50.00	6.00	5.00		51.00						
2191	231.00			178.00	68.00	108.00	108.00	48.00	36.00			24.00						
2197			1.00	11.00	32.00	28.00	83.00	17.00	8.00			23.00						
2280	6.00	13.00		8.00	28.00	30.00	78.00	36.00	9.00			28.00						
2542				4.00	37.00	76.00	73.00					38.00						
2547		3.00		27.00	30.00	30.00	47.00		102.00	94.00		37.00	27.00					
2729	94.00	56.00	20.00	34.00	40.00	109.00	80.00	26.00	46.00			35.00						
2850			11.00	24.00	41.00	46.00	118.00	49.00	32.00			30.00						
2886		52.00	8.00	30.00	36.00	72.00	108.00	28.00	24.00	286.00		38.00	8.00					
2901		46.00		16.00	36.00	39.00	98.00											
2938		9.00		11.00	22.00	39.00	99.00	28.00				68.00	18.00					

Table IX 4. Table continued.

2942	16.00	10.00	28.00	30.00	106.00	102.00	43.00	38.00	30.00	32.00	21.00	35.00	97.00	59.00	110.00	104.00			
2947	69.00	14.00	36.00	24.00	110.00	127.00	38.00	54.00	21.00	52.00	70.00								
2981	141.00	88.00	36.00	43.00	180.00	122.00	94.00	124.00	16.00	44.00				82.00	105.00	116.00			
3055		91.00	23.00	35.00	49.00	173.00	146.00	48.00	66.00	24.00	5.00			20.00	28.00	77.00			
3059	12.00		17.00	28.00	24.00	90.00	36.00	6.00	69.00	7.00	42.00								
3074		68.00	35.00	28.00	31.00	18.00	75.00	9.00	2.00	204.00	49.00								
3075		41.00	6.00	12.00	30.00	42.00	86.00	25.00	55.00	17.00				28.00	43.00	107.00			
3080		27.00	4.00	12.00	25.00	61.00	100.00	27.00	36.00	10.00				20.00	43.00	66.00			
3086		13.00	8.00	24.00	29.00	37.00	70.00	6.00	17.00		165.00			70.00	48.00	36.00			
3138		53.00	6.00	21.00	24.00	122.00	139.00	36.00	23.00		126.00								
3139		59.00	49.00	22.00	17.00	52.00	101.00	20.00	15.00	8.00	48.00								
3140		40.00	4.00	33.00	34.00	88.00	115.00	39.00	41.00	27.00				16.00	54.00	107.00			
3144		22.00	6.00	10.00	41.00	81.00	118.00	63.00	68.00	22.00				4.00	34.00	188.00			
3149		43.00	12.00	25.00	24.00	80.00	55.00	2.00	32.00	5.00				42.00	35.00	6.00			
3155		35.00	13.00	27.00	34.00	109.00	55.00	41.00	35.00	30.00	10.00								
3156		49.00	15.00	34.00	24.00	57.00	78.00	42.00	40.00		15.00								
3169	104.00	23.00	1.00	23.00	60.00	66.00	101.00	42.00	46.00										
3173		24.00	10.00	10.00	32.00	66.00	124.00	42.00	34.00	16.00									
3195		25.00	5.00	22.00	25.00	59.00	95.00	40.00	24.00										
3204	18.00		60.00	31.00	27.00	90.00	159.00	42.00	41.00	86.00									
3235	68.00	58.00	17.00	60.00	62.00	165.00	130.00	118.00	33.00	26.00				14.00	20.00				
3260		66.00	12.00	29.00	14.00	41.00	68.00	18.00	38.00	6.00	52.00			69.00					
3261		17.00	3.00	19.00	22.00	49.00	124.00	47.00	32.00	10.00									
3263		35.00	11.00	17.00	31.00	166.00	90.00	56.00	25.00	16.00	69.00								
3265		46.00	6.00	50.00	32.00	82.00	90.00	74.00	37.00	2.00	48.00								
3267		37.00	13.00	15.00	38.00	79.00	130.00	50.00	22.00	27.00				47.00					
3273	204.00	45.00	12.00	51.00	17.00	144.00	158.00	77.00	43.00	29.00	125.00			24.00	32.00	67.00			
3274	86.00	29.00												69.00	110.00	116.00			
3279		31.00	14.00	31.00	52.00	119.00	136.00	38.00	28.00	12.00									
3282		37.00	37.00	36.00	69.00	126.00	53.00	26.00	31.00		70.00			13.00	29.00	47.00			
3286		28.00	3.00	1.00	36.00	44.00	52.00	54.00	32.00	11.00				18.00					
3306		47.00	8.00	23.00	28.00	31			36.00										
AVERAGE	42.97	39.04	14.21	29.78	35.52	70.78	105.93	43.82	45.35	52.03	35.75	22.47	79.63	27.78	47.73	77.53	79.63	86.31	91.67

Table IX 5. Net-pay thickness of C submembers from log analysis.

WELL	C1	C2U	C2L	C3U	C3M	C3L	C4U	C4M	C4L	C5U	C5UM	C5LM	C5L	C6LU	C6M	C6UL	C6LL	C7
652		31.00		30.00	19.00	133.00	147.00	61.00	61.00	15.00	53.00							
827		40.00		20.00	25.00	58.00	94.00				39.00							
846				3.00	30.00	35.00	99.00	10.00			22.00			4.00				
847		20.00			24.00	15.00	85.00	35.00	4.00			19.00						
851		13.00	4.00			55.00	65.00				5.00	17.00						
852				8.00	37.00	13.00	18.00				66.00							
866				7.00	22.00	15.00	93.00	3.00			30.00							
895	20.00	56.00		46.00	64.00	160.00	135.00	24.00			33.00							
900	4.00	5.00		33.00	30.00	26.00	54.00											
917		12.00		5.00	27.00	5.00	35.00		8.00		30.00							
946		81.00		33.00	18.00		63.00	12.00			22.00							
971	21.00	31.00	18.00	82.00	73.00	189.00	152.00				64.00							
975	18.00	3.00																
997																		
1010		33.00	3.00	26.00	5.00		14.00	16.00	2.00	2.00	64.00							
1022		25.00		20.00	53.00	162.00												
1060				46.00	78.00	221.00	172.00	126.00	96.00		3.00							
1061						4.00	22.00				29.00							
1089		65.00	1.00	9.00	12.00	76.00	201.00	132.00	11.00		30.00							
1095					23.00	17.00	181.00	50.00	82.00		18.00							
1106				1.00	40.00	25.00	117.00				20.00							
1129				12.00	57.00	139.00		42.00	30.00		18.00							
1130	15.00	19.00		15.00	64.00	190.00	140.00	46.00	64.00		20.00							
1162	3.00	9.00	3.00	17.00	55.00	55.00	78.00	43.00	38.00		23.00	52.00						
1172		34.00	3.00	12.00	30.00	45.00	112.00	41.00	22.00		20.00							
1176	2.00	43.00	4.00	39.00	43.00	55.00		44.00	17.00		40.00							
1198	16.00	25.00		4.00	21.00	50.00	86.00	40.00	30.00	16.00	62.00							
1218			4.00	42.00		33.00	67.00	134.00	38.00									
1245				9.00	16.00	13.00	79.00	8.00	3.00		27.00							
1276				3.00	15.00	23.00	16.00				12.00	5.00						
1293	2.00	6.00		9.00	36.00	102.00	145.00	33.00	37.00	2.00	33.00	3.00						
1303		35.00	3.00	43.00	43.00	31.00	64.00	25.00	19.00	15.00								
1307			2.00	9.00	12.00	60.00		13.00			36.00							
1310			1.00	3.00	30.00	9.00	35.00		6.00		21.00							
1312		13.00		16.00	33.00	72.00	94.00	32.00	68.00		28.00	21.00						
1316			8.00	13.00	28.00	66.00	154.00	34.00	34.00									
1679		5.00					12.00	3.00			12.00							
1695	6.00			44.00	27.00	161.00	166.00	54.00	68.00	6.00								
1748	22.00	25.00	2.00	19.00	30.00	28.00					12.00	20.00						
1782		17.00	3.00		35.00	14.00	75.00	16.00			5.00							
1799				14.00	12.00	3.00	13.00				47.00							
1803	15.00	2.00	1.00	36.00	36.00	22.00	134.00	25.00	12.00		25.00	13.00						
1876	3.00	8.00	2.00	7.00	3.00	42.00	78.00	3.00		3.00	32.00							
1965		5.00		3.00	35.00	77.00	137.00	48.00			39.00							
1986		2.00		7.00	37.00	42.00	61.00	28.00			27.00							
1987		42.00	9.00		39.00	50.00	122.00	1.00										
2010	5.00	3.00		15.00	21.00	44.00	80.00	27.00	24.00	5.00	35.00							
2038	22.00	44.00	32.00	57.00			111.00	42.00	13.00	22.00	15.00							
2089				15.00	39.00	34.00	93.00				27.00							
2094		2.00	3.00	8.00	42.00	51.00	76.00	2.00			37.00							
2187				13.00	38.00	48.00	117.00	50.00	6.00		42.00							
2191	2.00			80.00	66.00	160.00	109.00	48.00	9.00		24.00							
2197				8.00	32.00	22.00	81.00	9.00			21.00							
2197				6.00	28.00	17.00	71.00	13.00										
2280																		
2542				11.00	24.00	33.00	47.00	29.00	7.00		28.00							
2542							9.00				38.00							
2729	1.00		6.00	17.00	40.00	109.00			89.00	1.00	28.00	22.00						
2850				5.00	39.00	36.00	72.00	19.00			35.00							
2886				18.00	32.00	92.00	95.00	29.00	37.00		24.00							
2901		38.00		6.00	34.00	37.00	91.00	36.00	17.00		32.00	5.00						
2938		5.00		5.00	22.00	30.00	83.00	13.00	11.00		53.00	16.00						

Table IX 6. Averaged V_{sh} of C submembers from log analysis.

WELL	C1	C2U	C2L	C3U	C3M	C3L	C4U	C4M	C4L	C5U	C5M	C5L	C6U	C6L	C7
652		0.31		0.29	0.28	0.30	0.28	0.28							
827		0.52		0.52	0.37	0.48	0.43	0.49							
846		0.45		0.24	0.24	0.24	0.24	0.24							
847		0.45			0.31	0.48	0.34	0.37	0.46	0.40	0.37		0.19	0.23	
851		0.50	0.50			0.32	0.32								
852				0.46	0.29	0.47	0.42	0.42		0.41	0.41				
866				0.46	0.38	0.41	0.31	0.46			0.45				
895	0.52	0.51		0.45	0.41	0.48	0.46	0.47							
900	0.41	0.46		0.44	0.41	0.45	0.44	0.32	0.36	0.24	0.31		0.37	0.34	0.33
917		0.35		0.32	0.29	0.36	0.35	0.32	0.36		0.31		0.15	0.18	
946		0.35		0.11	0.10	0.26	0.26	0.34							
971	0.48	0.47	0.49		0.37	0.45	0.43								
975	0.39	0.46													
1010		0.53	0.53	0.52	0.50	0.50	0.55	0.53	0.54	0.53	0.42				
1022		0.50		0.51	0.47	0.50	0.30	0.32	0.51		0.40		0.29		
1060				0.34	0.32	0.34	0.39	0.32	0.34		0.33		0.20	0.19	0.18
1061						0.52	0.32		0.26				0.26	0.14	
1089		0.34		0.37	0.37	0.36	0.34	0.32	0.32	0.39	0.33		0.36	0.37	0.35
1095					0.10	0.22	0.26	0.26	0.26	0.46	0.46		0.40	0.29	0.29
1106					0.42	0.50	0.33		0.47	0.47	0.10				
1129		0.53		0.52	0.35	0.45	0.41	0.41	0.47	0.46	0.46				
1130	0.50	0.52		0.54	0.42	0.49	0.47	0.44	0.51	0.46	0.46				
1162	0.46	0.50	0.47	0.46	0.39	0.44	0.44	0.43	0.45	0.42	0.42	0.32	0.45	0.42	
1172		0.45	0.48	0.43	0.42	0.45	0.40	0.39	0.47	0.52	0.42	0.44			
1176	0.53	0.53	0.52	0.48	0.43	0.47	0.44	0.46	0.45	0.46	0.37				
1198	0.46	0.44		0.50	0.47	0.46	0.44	0.37	0.46	0.46	0.42	0.44			
1218			0.46	0.30		0.44	0.38	0.37	0.46						
1245				0.43	0.40	0.32	0.38	0.44	0.49		0.45	0.36	0.39	0.44	0.42
1276				0.52	0.40	0.46	0.44	0.44	0.49		0.37	0.42			0.43
1293	0.34	0.48		0.42	0.33	0.40	0.34	0.37	0.34	0.34	0.43	0.45			
1303		0.41	0.46	0.42	0.35	0.45	0.40	0.45	0.49	0.50	0.35	0.43			
1307			0.48	0.42	0.37	0.37	0.28	0.45	0.25	0.36	0.33				
1310				0.31	0.21	0.31	0.43	0.50	0.45	0.43	0.43	0.31			
1312		0.47		0.46	0.43	0.45	0.31	0.33	0.36		0.36	0.43	0.31		

Table IX 6. Table continued.

2947	0.47	0.47	0.29	0.26	0.33	0.25	0.31	0.25	0.47	0.26	0.21	0.38	0.40	0.33	0.36	0.37	
2981	0.50		0.48	0.45	0.44	0.39	0.43	0.45	0.40	0.44		0.44	0.33	0.28	0.21	0.28	
3055	0.40		0.48	0.43	0.48	0.45	0.43	0.43	0.26			0.29	0.39	0.28	0.33	0.38	
3059			0.47	0.37	0.39	0.38	0.28	0.48	0.52								
3074			0.43	0.36	0.43	0.45	0.48										
3075	0.44		0.51	0.43	0.49	0.47	0.49	0.48				0.39	0.43	0.41	0.33	0.40	
3080	0.39			0.46	0.49	0.45	0.48	0.48				0.38	0.39	0.35	0.33	0.39	
3097		0.53	0.44	0.37	0.47	0.49			0.36	0.48	0.19						
3138			0.42	0.35	0.38	0.32	0.35	0.30	0.37		0.19						
3139	0.50	0.48	0.42	0.36	0.42	0.39	0.49	0.41		0.45		0.42	0.42	0.33	0.31	0.38	
3140	0.40		0.47	0.43	0.47	0.45	0.46	0.48	0.40	0.44							
3144	0.46	0.43	0.50	0.38	0.44	0.39	0.33	0.39	0.37	0.44		0.40	0.40	0.24	0.29		
3149	0.50	0.48	0.40	0.34	0.43	0.48	0.44	0.46	0.35	0.45		0.40	0.40	0.24	0.29		
3155	0.51	0.48	0.46	0.31	0.39	0.48	0.38	0.43	0.21	0.35		0.27	0.34	0.38			
3156	0.54	0.53	0.45	0.42	0.47	0.52		0.43	0.38		0.14	0.36					
3169	0.49		0.39	0.35	0.43	0.44	0.42	0.43	0.42								
3173	0.35	0.47	0.38	0.31	0.35	0.31	0.35	0.53	0.31								
3195	0.42	0.43	0.40	0.38	0.42	0.40	0.42	0.44	0.42	0.32							
3204		0.50	0.43	0.40	0.42	0.34	0.37	0.35	0.38	0.24							
3235			0.52	0.47	0.52	0.48			0.38								
3260	0.53	0.46	0.38	0.33	0.39	0.41	0.51	0.40	0.39	0.31	0.29	0.33					
3261	0.45	0.51	0.32	0.40	0.40	0.36	0.40	0.43	0.31	0.30	0.23						
3263	0.35	0.36	0.42	0.32	0.31		0.31	0.33	0.38	0.26	0.27						
3265			0.47	0.45	0.39	0.42	0.48		0.29			0.41					
3267	0.39	0.45	0.42	0.39	0.41	0.35	0.40	0.41	0.40	0.25		0.32	0.34	0.27	0.23	0.16	
3273	0.51		0.39	0.37	0.35	0.33	0.43	0.43	0.45	0.43	0.33					0.28	
3274	0.52																
3279	0.53			0.45	0.49	0.45	0.46		0.37								
3282			0.43	0.38	0.42	0.37	0.38	0.37	0.32		0.33	0.36	0.32	0.29	0.27	0.36	
3286	0.37	0.50		0.36	0.45	0.34	0.36	0.40	0.45	0.45		0.37				0.44	
3306		0.50	0.49	0.46	0.51				0.36								
AVERAGE	0.46	0.46	0.48	0.42	0.37	0.42	0.40	0.42	0.46	0.37	0.38	0.28	0.35	0.34	0.32	0.28	0.34

Table IX 7. Average porosity of C submembers from log analysis.

WELL	C1	C2U	C2L	C3U	C3M	C3L	C4U	C4M	C4L	C5U	C5UM	C5LM	C5L	C6U	C6LU	C6M	C6LL	C7
652		0.16		0.17	0.17	0.16	0.16	0.16			0.20							
827		0.18		0.18	0.19	0.15	0.16				0.19							
846				0.15	0.17	0.16	0.15	0.14			0.17							
847		0.19			0.18	0.16	0.17	0.16	0.14		0.20	0.14		0.08	0.08			
851		0.24				0.18	0.18			0.15	0.21	0.15						
852			0.17		0.18	0.15	0.14				0.20							
866				0.16	0.17	0.16	0.18	0.14		0.17	0.18							
895	0.16	0.16		0.18	0.18	0.17	0.16	0.16			0.18							
900	0.17	0.15		0.16	0.20	0.15	0.14	0.16	0.14									
917		0.15		0.16	0.18	0.15	0.14											
946		0.20		0.16	0.15		0.14	0.14						0.09	0.10	0.11		
971	0.16	0.16		0.16	0.19	0.17					0.17			0.10	0.12			
975	0.19	0.15					0.16				0.20							
1010		0.19	0.19	0.20	0.21		0.17	0.18	0.18	0.15	0.20							
1061					0.15	0.15	0.16	0.15	0.15		0.19			0.09	0.10			
1089		0.16		0.15	0.15	0.16	0.14	0.15	0.15		0.16			0.09	0.10	0.11	0.11	0.08
1095					0.20	0.17	0.19	0.15	0.15		0.19							
1106						0.16	0.16	0.16	0.15	0.15	0.18	0.14		0.10	0.11			
1129		0.15		0.15	0.16	0.16	0.16	0.17	0.15		0.16	0.14						
1130	0.16	0.16		0.15	0.19	0.16	0.16	0.17	0.15									
1162	0.16	0.16		0.16	0.18	0.16	0.15	0.17	0.15									
1172		0.15		0.17	0.17	0.16	0.16	0.16	0.14									
1176	0.15	0.15		0.16	0.18	0.17	0.17	0.17	0.14		0.20	0.14	0.11	0.10	0.11			
1198	0.17	0.18		0.15	0.16	0.16	0.16	0.15	0.16	0.17	0.21							
1218			0.15	0.20		0.16	0.16	0.17	0.14									
1245				0.17	0.18	0.21	0.17	0.15	0.14				0.12					
1276				0.19	0.18	0.18	0.18	0.16	0.16		0.15	0.16	0.12	0.11	0.11	0.11	0.12	0.10
1293	0.16	0.16		0.16	0.18	0.16	0.16	0.16	0.16	0.16	0.18	0.13						
1303		0.18		0.17	0.19	0.17	0.16	0.16	0.15	0.16	0.16							
1307			0.15	0.17	0.18	0.18	0.15	0.14	0.13		0.18							
1310				0.15	0.20	0.15	0.15	0.14	0.16		0.20							
1312		0.17		0.17	0.17	0.18	0.17	0.14	0.15		0.17	0.15	0.12					
1316			0.19	0.17	0.16	0.18	0.18	0.16	0.15									
1679		0.17		0.17	0.19	0.17	0.17	0.14	0.14		0.19	0.14	0.11			0.10	0.11	0.11
1695	0.16			0.17	0.16	0.15	0.15		0.17	0.16								
1748	0.15	0.16	0.16	0.18	0.16	0.15	0.15	0.15										
1782		0.16	0.15		0.17	0.16	0.16	0.15										
1799				0.17	0.16	0.16	0.16	0.15			0.20	0.12	0.11	0.10	0.11	0.10	0.11	
1803	0.14	0.18		0.17	0.17	0.17	0.16	0.15	0.15		0.19	0.13						
1876	0.17	0.16	0.16	0.16	0.19	0.16	0.17	0.19	0.15	0.17	0.19			0.10	0.10	0.11	0.11	0.09
1985		0.15		0.17	0.17	0.16	0.16	0.17		0.17	0.18							
1986		0.15		0.16	0.17	0.17	0.16	0.18			0.19							
1987	0.18	0.18	0.18		0.19	0.19	0.18	0.18										
2010	0.15	0.17		0.17	0.17	0.17	0.16	0.15	0.16	0.15	0.17							
2038	0.15	0.15	0.16	0.17	0.17	0.17	0.17	0.15	0.15	0.15			0.11					
2069				0.19	0.19	0.17	0.17	0.15	0.15		0.17							
2094		0.16	0.15	0.16	0.17	0.17	0.17	0.16	0.16	0.15	0.20							
2187				0.16	0.20	0.17	0.17	0.16	0.16		0.17							
2191	0.20			0.19	0.20	0.18	0.17	0.16	0.15		0.20							
2197				0.16	0.19	0.18	0.17	0.14	0.15		0.17							
2280				0.17	0.17	0.18	0.16	0.16	0.15		0.17							
2542					0.17	0.17	0.16	0.15	0.15		0.21							
2547				0.18	0.18	0.17	0.14		0.15		0.20							
2729			0.18	0.17	0.18	0.18	0.16	0.18	0.16		0.17	0.13						
2850				0.18	0.18	0.17	0.16	0.17	0.16		0.17							
2896				0.18	0.18	0.18	0.19	0.17	0.16		0.19							
2901		0.19		0.17	0.17	0.16	0.18	0.17	0.17	0.14	0.18	0.14						
2938		0.17		0.17	0.17	0.17	0.16	0.15	0.15	0.21	0.15							
2942		0.18	0.17	0.19	0.18	0.17	0.18	0.17	0.17	0.17	0.16	0.16	0.11	0.11	0.11	0.11	0.12	0.10
2947		0.16	0.17	0.17	0.19	0.17	0.17	0.16	0.16		0.16							
2981			0.17	0.18	0.17	0.19	0.17	0.18	0.17		0.18	0.15	0.11	0.11	0.11	0.12	0.12	

Table IX 7. Table continued.

3055	0.20	0.19	0.20	0.18	0.19	0.16	0.17	0.15	0.18	0.19	0.13	0.10	0.11	0.11	0.12	0.09
3059	0.17	0.18	0.21	0.20	0.18	0.15	0.16	0.15	0.20	0.19	0.13	0.11				
3074	0.18	0.20	0.20	0.19	0.17	0.16	0.15	0.15	0.18	0.13		0.11	0.10	0.10	0.11	0.09
3075	0.18	0.20	0.20	0.19	0.17	0.16	0.15	0.15	0.18	0.13		0.11	0.10	0.10	0.11	0.09
3080													0.11	0.11	0.11	0.10
3087	0.18	0.20	0.20	0.20	0.17	0.16	0.15	0.17	0.18	0.12						
3138	0.17	0.17	0.17	0.18	0.18	0.16	0.15	0.15	0.16	0.14	0.13	0.13				
3139	0.17	0.17	0.17	0.18	0.18	0.16	0.15	0.15	0.16	0.14	0.13	0.13				
3140	0.18	0.18	0.18	0.17	0.18	0.16	0.15	0.15	0.16	0.14	0.13	0.13	0.10	0.11	0.12	0.10
3144	0.16	0.17	0.18	0.19	0.17	0.18	0.18	0.17	0.18	0.13			0.10	0.10	0.11	0.13
3149	0.15	0.16	0.17	0.18	0.17	0.18	0.18	0.15	0.18	0.13			0.10	0.10	0.11	0.13
3155	0.17	0.17	0.17	0.17	0.17	0.17	0.17	0.17	0.20	0.14			0.11	0.11	0.10	
3156	0.16	0.15	0.18	0.20	0.18	0.15	0.17	0.17	0.17	0.17			0.11	0.11	0.10	
3169	0.16	0.17	0.17	0.20	0.17	0.16	0.17	0.15	0.17	0.17			0.10	0.10		
3173	0.17	0.18	0.16	0.18	0.18	0.16	0.18	0.16	0.17	0.19	0.10	0.10				
3195	0.16	0.17	0.17	0.18	0.18	0.18	0.18	0.16	0.17	0.19	0.15					
3204	0.16	0.16	0.19	0.17	0.18	0.17	0.17	0.16	0.14	0.15						
3235																
3260	0.15	0.17	0.18	0.19	0.18	0.17	0.17	0.15	0.17	0.15	0.15	0.10				
3261	0.16	0.15	0.19	0.17	0.17	0.16	0.16	0.15	0.16	0.15	0.11	0.10				
3263	0.17	0.18	0.16	0.19	0.18	0.16	0.16	0.16	0.16	0.15	0.11	0.11				
3265																
3267	0.17	0.17	0.17	0.17	0.18	0.18	0.18	0.16	0.18	0.15	0.11	0.11				
3273	0.18	0.17	0.17	0.16	0.18	0.16	0.17	0.17	0.16	0.17	0.14	0.11	0.12	0.10	0.11	0.12
3274	0.17	0.13		0.16	0.18	0.17	0.17	0.17	0.17	0.17	0.14	0.11	0.12	0.10	0.11	0.12
3279	0.18			0.18	0.18	0.16	0.16	0.15	0.18	0.18	0.11	0.10	0.10	0.10	0.11	0.10
3282				0.18	0.18	0.17	0.17	0.15	0.19	0.13		0.11	0.10	0.10	0.11	0.12
3286	0.17	0.19		0.18	0.17	0.16	0.16	0.16	0.18	0.13		0.11	0.10	0.10	0.11	0.12
3306	0.16	0.16	0.18	0.18	0.18	0.16	0.16	0.16	0.18	0.15		0.10	0.10	0.10	0.11	0.11
1060	0.17	0.19		0.20	0.19	0.17	0.16	0.16		0.17		0.10	0.10	0.10	0.11	0.09
1022	0.19	0.19		0.20	0.19	0.16	0.16	0.17	0.17	0.17		0.10	0.10	0.10	0.11	0.09
AVERAGE	0.16	0.17	0.16	0.17	0.18	0.17	0.16	0.16	0.16	0.15	0.16	0.14	0.11	0.10	0.11	0.10

Table IX 8. Average permeability of C submembers from log analysis.

WELL	C1	C2U	C2L	C3U	C3M	C3L	C4U	C4M	C4L	C5U	C5LM	C5L	C6U	C6M	C6LL	C7
652		6.93		16.82	25.70	10.56	44.10	114.19	43.85	2.08	94.19					
827		39.83		33.78	176.64	5.95	117.55				57.80					
846				5.50	54.72	8.61	17.57	4.70			72.67					
847		496.49			54.72	7.46	86.32	58.01	3.57		195.03	3.64				
851		1909.63	28.40			68.20	88.78			5.15	459.16	6.76	0.20	0.17		
852				17.51	63.73	4.73	5.30			24.05	226.18					
866				10.24	19.20	10.28	144.92	31.23			73.99					
895	6.70	7.98		82.84	298.98	15.96	38.39									
900	24.05	4.24		7.64	106.31	4.97	5.54									
917		5.06		10.33	82.98	3.72	6.98									
946		328.92		7.19	4.52		8.62									
971	13.26	11.76	5.63	9.33	233.36	22.11	23.44		3.41		54.21		0.16	1.44	1.82	
975	191.28	4.10									54.72		0.61	5.12		
1010		61.36	46.55	155.70	459.16	64.34	47.77	122.81	58.79	3.70	259.47		1.12			
1022		58.20		53.16	94.19	7.57	36.91	17.62	81.08		10.63		0.68	0.57	2.34	3.84
1060				5.96	15.02	3.88	152.78		7.61		269.52			0.21	0.79	0.46
1061		6.59		3.33	3.31	3.92	8.77	22.44	8.48		7.59					
1089					7.23	6.10	23.54	15.98	15.22		117.05		0.19	0.74	0.51	3.34
1095					173.36	23.34	94.45				98.50		0.39	1.10		1.64
1106					9.97	13.35		26.10	12.48		121.81	1.80				0.18
1129	4.46			4.58	259.47	13.02	22.74	93.61	9.48		7.23	3.05				
1130	10.37	6.26		4.04	49.49	14.59	21.30	22.97	12.94		2.60	2.14	1.16	2.98		
1162	7.97	4.29	6.44	8.37	25.53	14.12	86.35	99.46	6.69		173.36	5.74				
1172	12.20	5.17		16.12	129.88	17.21		213.14	4.77		578.09					
1176	3.70	3.90	4.58	18.12	13.13	15.50	91.37	37.40	23.58	16.70						
1198	16.70	45.12		5.79	8.88	58.59	109.18	5.85			67.07					
1218			5.69	320.78	94.02	400.14	129.33	9.35	4.07		5.23		2.83	2.36	2.49	10.92
1245				11.86	70.26	115.11	211.43				3.31	12.69			8.04	2.45
1276				43.75	98.01	56.25	45.15	45.15	66.91	7.94	108.14	1.36				
1293	7.94	7.00		9.22	53.88	98.01	56.25	35.26	11.85	10.37	9.97					
1303		33.25	10.14	48.03	26.51	28.69	86.93	6.57	2.70		53.88					
1307		3.56	3.56	23.51	162.03	97.21					284.25					
1310				4.47	144.98	4.82	33.47		27.06		32.07	5.75				
1312		17.55		25.37	108.14	46.65	224.27	8.60	48.75				8.23			
1316			95.82	44.56	9.75	118.47	187.69	30.49	7.36		162.03	1.86		1.17	1.86	1.39
1679		24.59					5.21	4.06		99.99	6.61	2.84				
1695	9.58			31.31	274.51	45.04	154.42	52.53		9.58						
1748	5.15	8.86	7.34	132.31	7.59	7.21	12.65	15.61					0.67	3.81	0.34	0.92
1782		8.56	2.99		21.79	5.08	78.17				213.04			0.35	3.81	3.44
1799				27.55	6.61	6.40					176.64	0.96				
1803	2.08	27.28		35.00	173.35	28.91	72.79	11.99	13.14	28.52			1.13	0.74	2.45	2.86
1876	28.52	7.28	7.25	9.80	23.29	18.22	173.11	131.79			91.20					0.89
1965		4.02		18.23	39.13	21.82	69.94	88.72			57.79					
1986		4.28		11.10	57.80	100.93	161.19	177.98			274.51					
1987	28.82	29.84	28.99	16.96	19.09	17.13	53.52	16.94	52.60	4.13	23.29					
2010	4.13	10.84		105.23			133.51	22.89	7.68	5.01	70.26	10.92				
2038	5.01	6.11	11.45	86.05	19.94	27.51	109.88				69.48					
2099		7.69	4.44	7.33	156.24	65.64	75.06	16.80			39.13					
2094				35.67	169.22	27.73	120.70	48.39	23.95		156.24					
2187				293.52	296.18	47.81	108.42	71.08	9.59		296.43					
2191	112.31			7.47	81.20	16.14	22.16	5.05			19.09					
2197				25.79	215.22	38.25	120.32	27.00	6.92		215.22					
2280				26.29	20.41	29.52		11.39			169.22					
2542				42.81	216.69	19.86	4.51				26.29	2.41				
2547				24.92	81.29	248.65			36.11		21.79					
2729			39.81	44.25	57.79	24.12	38.19	220.42			216.69					
2850				70.86	78.69	79.12	155.22	114.72	42.55		216.69					
2896				23.36	70.71	99.96	252.19	114.21	163.60		78.69	2.89				
2901	162.84										311.37	4.81				
2938	17.57			15.04	72.67	20.32	25.68	12.11			25.58	21.64	1.93	2.22	2.47	2.14
2942	154.39		16.21	118.73	67.07	33.12	295.78	209.73	88.08						6.72	3.89

Table IX 8. Table continued.

2947	11.03	16.74	29.52	103.74	75.30	118.88	84.52	65.95	13.13	6.67	3.32								
2981		21.19	60.74	27.23	247.21	183.31	166.81	137.50	94.02	11.01									
3055	319.18		78.30	152.48	59.62	341.66	36.79	126.58	103.74										
3059			26.01	90.83	14.74	73.44	52.35	18.10	28.82	0.95									
3074			209.06	284.25	54.16	46.72	18.42		268.51	152.48									
3075	50.33		277.56	69.48	17.25	71.57	11.80	30.84		1.42									
3080	46.92			98.50	84.34	136.53	14.85	61.15	73.09	0.71									
3097		31.84	539.43	195.03	19.54	38.84			369.51	3.84									
3138			23.05	43.10	68.70	221.20	89.75	67.75	9.59	23.95									
3139	30.98	41.22	43.78	369.51	107.00	127.06	153.97	11.05	5.89	2.45									
3140	72.13		88.81	32.07	92.72	131.78	33.53	55.78	26.22	0.23									
3144	11.26	11.45	8.03	124.79	54.75	255.69	119.65	133.89	81.29	1.54									
3149	4.86	3.57	76.96	296.43	54.03	99.56	0.10	12.75	43.10	2.10									
3155	18.81	10.50	32.67	143.88	193.23		94.77	181.53	144.98	2.80									
3156	7.44	4.11	187.77	214.13	55.49	14.73			19.84										
3169	29.54	9.42	26.38	269.52	27.60	45.88	52.84	27.25	173.35	0.70									
3173	70.96	50.65	9.64	38.49	49.29	140.38	79.12		143.88										
3195	10.61	15.86	31.78	192.13	76.29	189.78	123.22	27.73	214.13	9.16									
3204		9.00	129.12	26.22	134.28	136.10	39.56	5.89	124.79	4.48									
3235			50.72	213.04	78.96	29.64			9.75										
3280	5.44	56.18	133.25	117.05	84.32	88.47	72.12	32.63	29.39	7.12									
3281	10.89	6.40	181.35	35.12	28.82	152.01	85.18	12.92	38.49	43.69									
3283	37.62	48.10	18.58	177.46	163.75		56.28	116.13	192.13	4.35									
3285			41.44	159.78	197.19	205.64	220.54		63.73										
3287	27.00	17.44	27.27	20.39	52.83	187.32	102.20	99.98	35.12	6.76									
3273	48.11		32.23	9.59	62.29	114.06	154.78	119.23	27.23	6.30									
3274	18.64									5.53									
3279	32.19			73.99	76.49	211.77	55.88		90.83										
3282			32.09	73.09	78.75	113.86	202.51	26.33	177.46										
3286	38.77	63.87		74.08	24.44	141.20	31.42	125.55	159.78	0.78									
3306		8.74	63.29	121.81	103.45				74.08										
AVERAGE	28.17	77.72	21.35	59.68	110.72	56.65	67.44	45.17	19.72	121.87	6.12	5.36	1.59	1.80	1.85	5.36	6.24	2.25	

Table IX 9. Table continued.

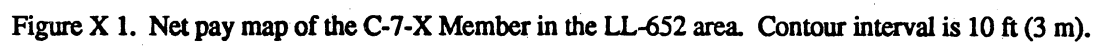
2981	84.78	1154.03	816.86	30901.81	19614.03	13177.58	10312.60	1504.25	165.19	103.44	145.27	313.43	465.19	158.53					
3055		391.51	5946.75	2742.30	31774.63	1103.75	4303.73	2282.27		2.03	19.45	115.58	222.19	285.09					
3059	11490.53	312.17	2361.64	309.51	6389.21	1622.87	90.48	11546.01	3.81	91.56									
3074		2508.76	5969.18	216.63	2196.03	73.68		5946.75											
3075	1711.34	1942.91	1876.01	396.78	4437.25	176.94	647.68	2721.97	9.54	28.43	10.49	84.98	602.85	32.10					
3080	1173.02		1773.00	1686.83	8874.43	103.93	611.53	2631.35	2.14	96.57	111.89	228.00	666.35	129.14					
3097		8630.81	5070.80	254.05	932.13			6281.70		633.06									
3138		368.85	1034.41	7694.05	30304.71	3231.00	1558.22	143.84	2969.52										
3139	929.48	412.19	6281.70	5243.16	12324.46	2001.64	1115.56	35.34	117.53										
3140	2813.03		1421.02	897.90	11596.32	636.98		576.82	0.46	4.02	100.70	485.34	732.72	1382.09					
3144	146.34	22.91	40.15	4866.77	26335.54	6819.84	8033.41	3251.71	23.17										
3149	38.87	10.72	1616.13	7114.42	4106.40	0.19	344.31	1034.41	31.53	1.02	21.24	705.57	2969.52						
3155	169.31	62.98	686.04	4891.92	20095.36	3601.10	5362.72	4349.37	27.95	69.87	84.63	2.73							
3158	14.89	8.22	4881.95	4282.51	1997.61	206.23		777.66											
3169	160.06		474.91	15622.31	1545.43	4037.55	871.92	6240.49	11.80	39.84									
3173	1419.24	151.96	77.10	1039.18	2760.24	17126.21	3164.69	4891.92											
3195	63.45	508.70	4034.74	3585.44	15561.88	4312.54	554.59	4282.51	146.63										
3204	212.18	35.99	1807.65	576.82	9936.51	20143.24	253.29	4866.77	385.30										
3235			557.97	10013.05	1895.07	148.20		272.97											
3260	43.55	393.27	3597.71	1521.59	3288.65	5661.87	793.33	717.68	1058.06	68.58									
3261	130.67	12.80	2901.68	772.71	1296.73	18697.13		1039.18	393.22	223.95									
3263	1278.99	384.79	222.98	5501.31	27019.23		3151.56	8477.52	4034.74	69.63	162.65								
3265			621.61	2875.97	3352.28	12338.45	4851.82	2357.92		65.01									
3267	863.92	156.95	299.99	1058.06	3698.34	23415.28	4190.14	2399.47	175.87	208.42	43.20	85.45	223.95	700.80					
3273	481.13		1353.64					772.71						782.27					
3274	149.08	2109.13	143.84	8844.99	18022.05	7739.02	9776.43	816.86	62.95	602.85									
3279	96.57		2441.69	4742.28	20753.78	670.53		2361.64											
3282		802.16	2631.35	4961.50	14232.14	9922.75	631.94	5501.31	228.00	2.20	25.16	63.73	162.65	504.64					
3286	1046.88	191.62	2518.89	659.84	16802.90	1539.41	5649.61	2875.97	2.35	81.12									
3306		17.47	1012.60	2436.29	1034.54			2518.69											
Average	332.88	1841.25	707.60	1440.14	3646.77	3740	9612.56	2619.95	1782.60	142.42	4026.08	102.50	463.17	36.61	67.39	176.16	493.26	472.65	146.37

Table IX 10. Values of k_h of C submembers from log analysis.

WELL	C1	C2L	C3U	C3M	C3L	C4U	C4M	C4L	C5U	C5LM	C5L	C6LU	C6M	C6UL	C6LL	C7	
652	4.85		5.00	3.20	21.30	23.06	9.72	9.80	2.06	10.46							
827	7.30		3.57	4.81	8.96	14.80				7.30							
846			0.46	4.94	5.51	14.69	1.39			3.82							
847	3.89			4.30	2.36	13.98	5.68	0.54		5.18	2.72						
851	3.09	0.68			9.85	11.37			3.35	1.05	2.62	0.37	0.36				
852			1.35		1.97	2.54			0.70	13.11							
866			1.14	3.68	2.41	16.30	0.41			5.48							
895	3.13	8.93	8.25	12.83	26.67	22.11	3.84			5.92							
900	0.70	0.75	5.13	5.48	3.95	7.63				4.94							
917	1.83		0.81	4.96	0.74	4.95	7.97	1.08		4.30							
946	16.49		5.15	2.72		9.09	1.72			3.68							
971	3.34	4.95	971							12.83							
975	3.43	0.45								12.22							
1010		6.31	5.10	1.05		2.42	2.94	0.35	0.30								
1022		4.77	3.76	10.46	30.61			8.07									
1060			7.13	12.91	34.68	29.88	20.66	15.03		0.50							
1061					0.59	3.58				4.29							
1089			1.32	1.76	11.30	28.89	20.22	1.63		11.61							
1095		10.15		3.61	2.63	28.07	7.62	12.37		4.70							
1106				7.82	4.31	22.59				2.43							
1129		0.60	1.81	9.15	22.01		6.64	4.50		3.39							
1130	2.43	2.97	2.23	12.22	30.77	22.10	7.75	9.31		3.67							
1162	0.48	1.35	0.47	2.69	9.80	11.86	6.63	5.66		7.41							
1172		5.51	0.46	2.01	5.09	7.19	18.10	6.73		3.61							
1176	0.30	6.39	0.61	7.82	9.06		7.39	2.37		1.18							
1198	2.69	4.37		3.43	8.17	13.73	6.18	4.68		1.64							
1218			8.52		5.20	10.86	22.07	5.35	2.69	7.82							
1245			0.61	2.80	2.66	13.11	1.19	0.41		13.05							
1276			0.56	2.73	4.28	2.82				4.88							
1293	0.32	0.94	1.44	6.34	18.15	22.92	5.33	5.97	0.32	0.78							
1303		6.13	7.48	8.06	5.40	10.31	4.06	2.81	2.43	0.39							
1307			0.30	2.22	10.94		1.86	0.27		9.15							
1310			0.45	5.89	1.36			6.34		6.34							
1312		2.17	2.71	5.96	12.37	15.93	4.60	9.96		4.27							
1316		1.50	2.23	4.48	12.02	27.24	5.42	4.98		3.08	10.82						
1676		0.87															
1695	0.97		7.47	5.06	28.09	28.18	8.68	11.23	0.97	2.22	7.30	8.04	7.30	3.61			
1748	3.35	3.90	3.45	4.70	4.30					1.87							
1782		2.72		5.91	2.13	11.20	2.41			0.82	5.66	0.49	4.11	3.86	10.22		
1799			2.44	1.87	0.47	2.12				1.85							
1803	2.06	0.35	6.12	3.72	3.72	21.80	3.72	1.76		9.26							
1876	0.52	1.25	1.13	6.87	7.70	13.37	0.56		0.52	4.81							
1985		0.75	0.50	6.02	12.65	22.52	8.02			6.16							
1986		0.30	1.14	6.40	7.08	9.71	5.03			5.06							
1987	4.42	7.52	1.60	7.30	9.32	21.84											
2010	0.75	0.50	2.51	3.52	7.37	12.75	3.97	3.87	0.75	6.02							
2038	3.34	6.78	9.89			18.97	6.37	1.99	3.34	2.73							
2089			2.78	6.57	5.78	15.84				5.03							
2094		0.32	1.25	8.25	8.70	12.74	0.32			6.40							
2187			2.13	7.49	8.34	19.95	7.85	0.93		8.25							
2191	0.40		15.31	13.11	28.18	18.37	7.84	1.33		4.73							
2197			1.26	6.16	3.63	12.46	1.26			3.52							
2280			1.04	5.77	2.98	11.58	2.09										
2542			4.77	5.49	7.41	4.33		1.01		5.77							
2547			1.99	4.62	1.99	1.23				7.49							
2729		1.09	2.89	7.39	20.48			13.99		4.77	2.90						
2850			0.91	7.00	6.08	11.22	3.33			5.91							
2896			3.25	5.88	16.50	17.73	4.80	5.79		4.62							
2901		7.20	0.99	6.38	6.74	16.22	5.93			5.88	0.71						
2938		0.85	0.83	3.82	5.11	13.16	2.04	1.62		11.02	2.34						
2942		0.73	3.40	4.88	8.65	14.87	5.92	2.35		5.09	3.86						
												0.98	1.93	8.05	5.67	12.00	8.98

Table IX 10. Table continued.

2947	2.91	1.17	5.89	4.13	17.76	20.86	5.90	6.83	3.43	7.08	7.48								
2981		0.68	3.43	5.19	23.23	18.42	13.92	12.89	2.80	2.30									
3055	7.14		0.96	7.60	8.22	17.52	4.80	5.77	4.13										
3059			2.00	4.78	3.45	14.84	5.14	0.77	4.42	8.06	0.51								
3074			2.48	4.27	0.73	7.29	0.62			7.60									
3075	6.07		1.38	5.03	3.81	9.99	2.21	3.24		9.90	0.80								
3080	4.58		3.38	3.38	3.57	10.90	1.07	1.66		6.61	0.37								
3097		0.36		5.18	2.16	3.87			3.13			17.62							
3138			3.15	4.22	19.95	24.23	5.88	3.87	2.40			16.12							
3139	5.05	1.66	2.70	3.13	8.57	16.70	2.36	1.75		0.84									
3140	6.97		2.82	4.86	9.66	14.77	3.06	3.14	3.65	0.22									
3144	2.12	0.33	0.79	7.30	8.39	18.49	9.96	10.30	7.39	1.96									
3149	1.21	0.44	3.84	4.73	13.38	7.87	0.28	4.13	4.22	2.01									
3155	1.49	0.95	3.62	6.42	17.91		6.39	4.62	5.89	1.39									
3156		0.32	0.30	4.73	4.02	6.31	2.14		6.57										
3169	1.16		2.99	11.81	9.45	14.14	5.80	4.90	1.16		1.54								
3173	3.42	0.54	1.29	4.80	9.79	21.38	6.45		6.42										
3195	3.23	0.67	2.73	3.82	8.40	14.64	5.92	3.09	4.02	2.43									
3204		0.64	2.68	3.85	13.50	25.33	6.17	6.17	7.30	12.48									
3235			1.98	9.26	4.45	0.80			4.48										
3260	1.22	1.22	4.06	2.43	6.97	10.90	1.87	3.39	6.27	0.90	5.64								
3261	1.94	0.31	3.07	3.71	7.50	20.78	7.06	0.74	4.80	1.51	7.56								
3263	5.76	1.42	1.97	5.72	29.42		9.17	11.76	3.92	2.34	4.77								
3265			2.75	3.41	3.29	10.79	3.83		6.60										
3267	5.48	1.51	1.92	6.27	12.36	22.49	6.72	3.88	3.71	3.82									
3273	1.83		7.30	2.40	25.05	25.98	8.53	14.19	5.19	1.44	11.96								
3274	1.33	98.95																	
3279	0.53			5.92	11.16	17.23	1.95		4.78										
3282			4.19	6.51	11.09	20.89	8.33	3.61	5.72										
3286	4.83	0.57		5.99	4.59	20.34	7.75	7.37	3.41	0.38									
3306		0.32	2.86	3.67	1.84				5.99										
AVERAGE	1.88	3.65	3.62	5.77	10.17	14.87	5.63	4.93	1.50	5.78	2.49	8.11	2.01	3.52	7.40	8.11	8.96	5.16	



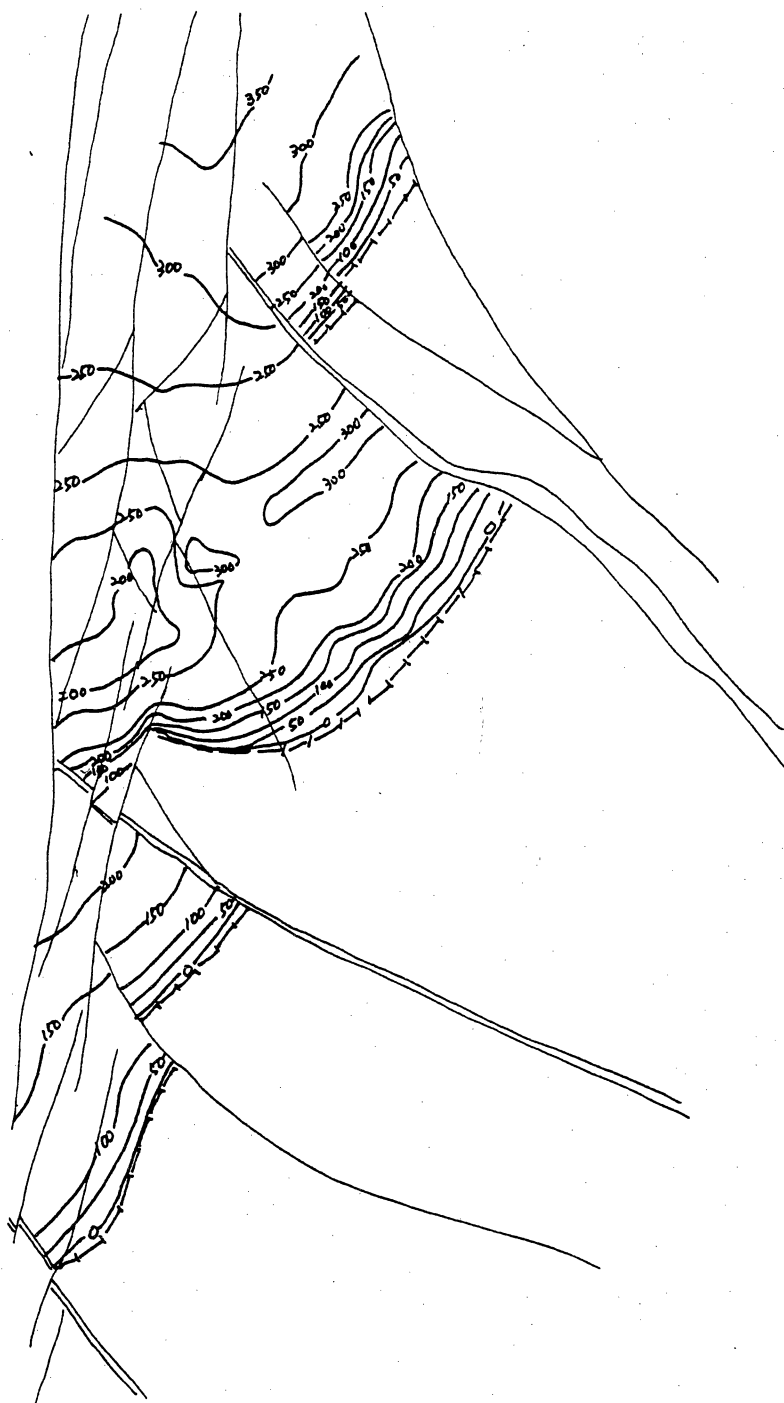


Figure X 2. Net pay map of the C-6-X Member in the LL-652 area. Contour interval is 10 ft (3 m).

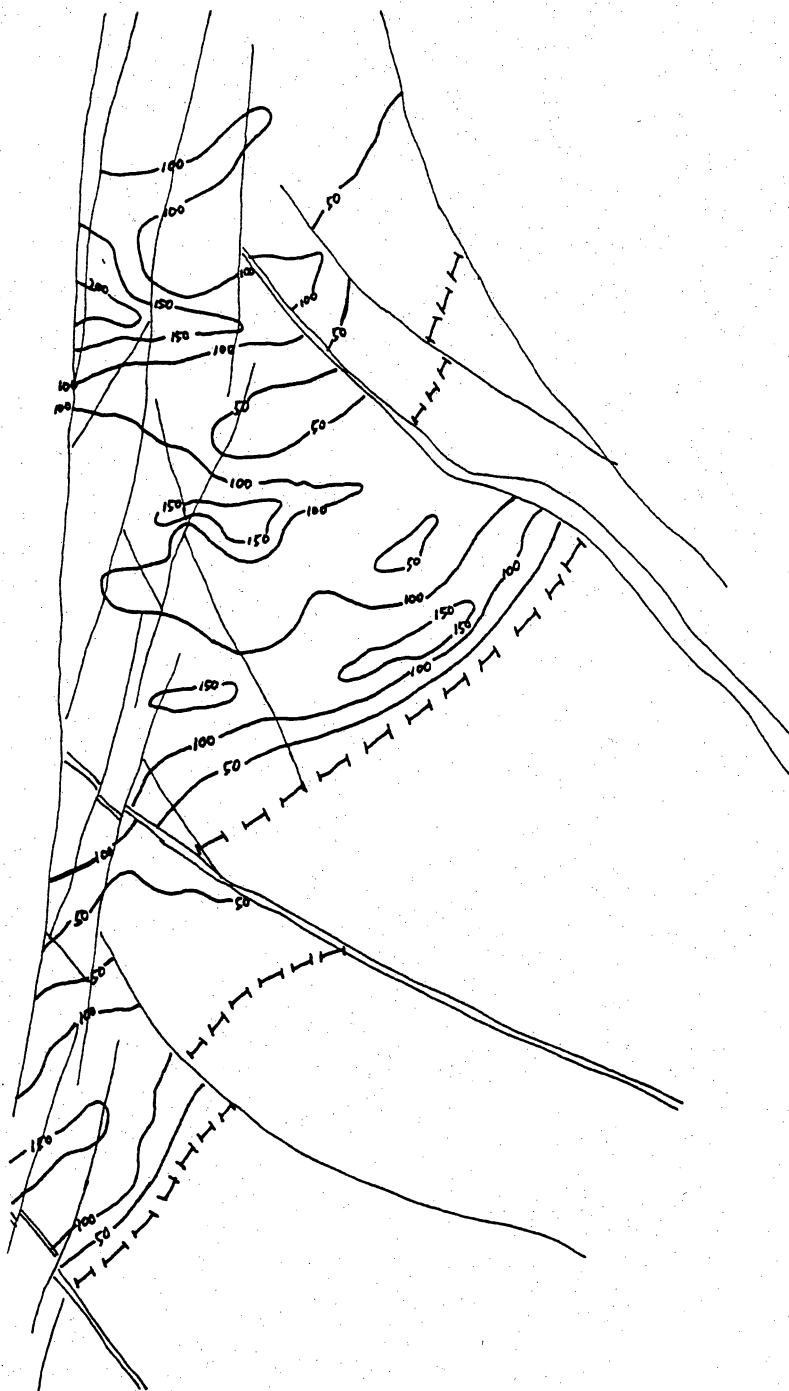


Figure X 3. Net pay map of the C-5-X Member in the LL-652 area. Contour interval is 10 ft (3 m).

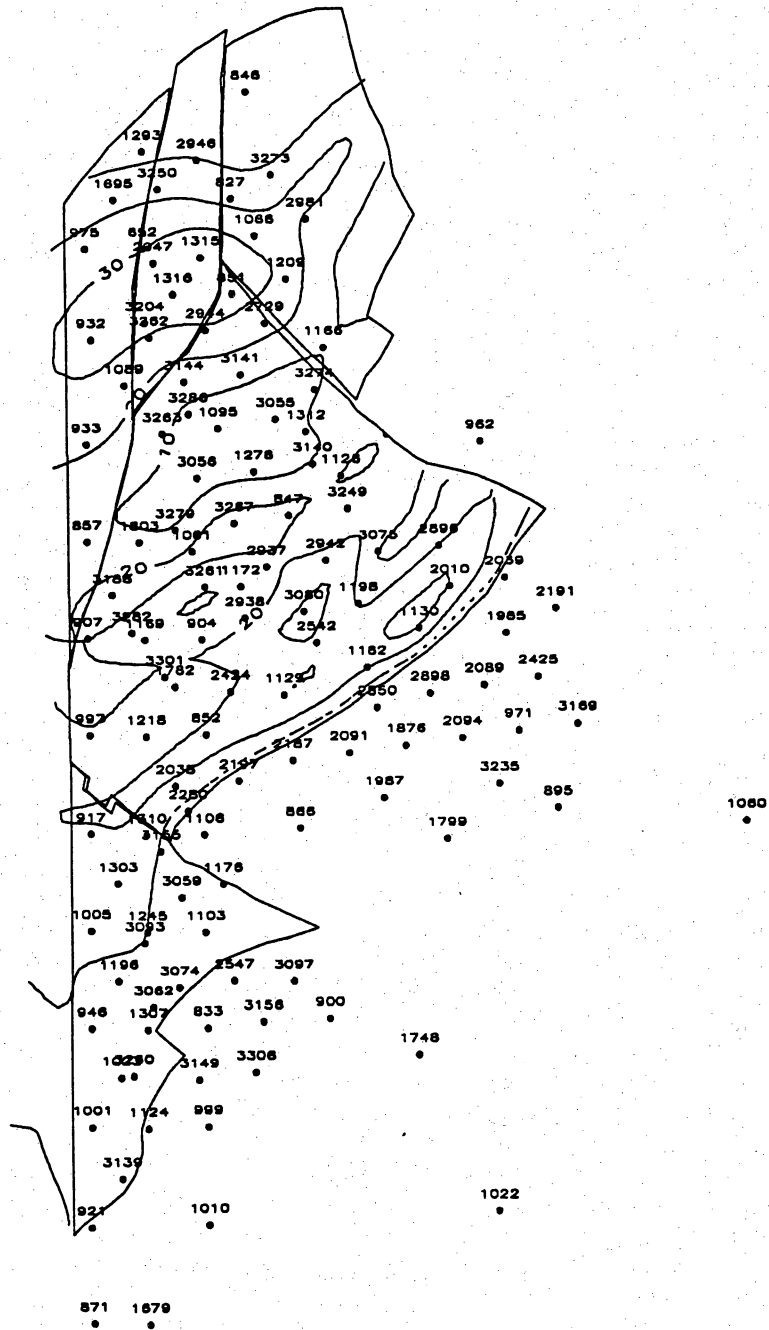


Figure X 4. Net pay map of the Lower Middle C-5-X Submember in the LL-652 area. Contour interval is 10 ft (3 m).

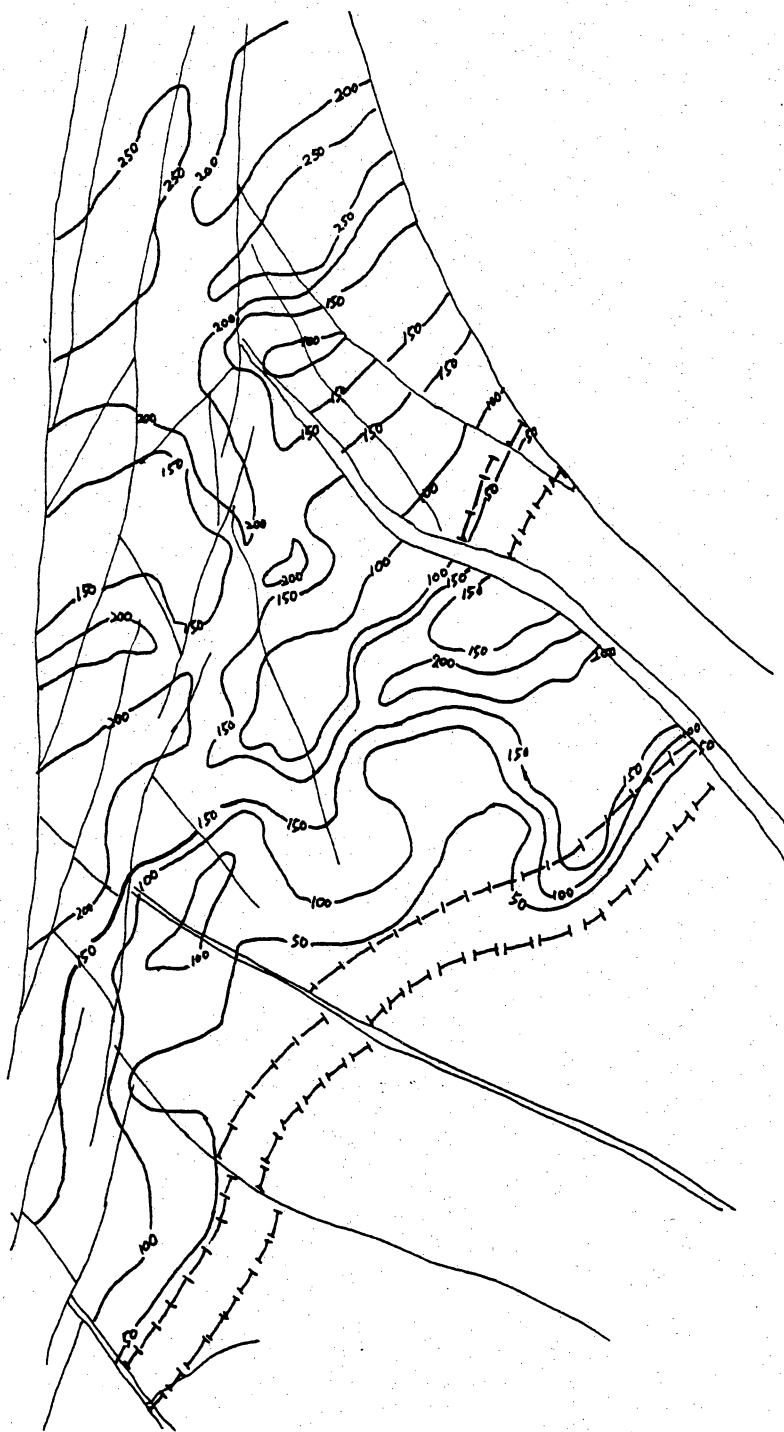


Figure X 5. Net pay map of the C-4-X Member in the LL-652 area. Contour interval is 10 ft (3 m).

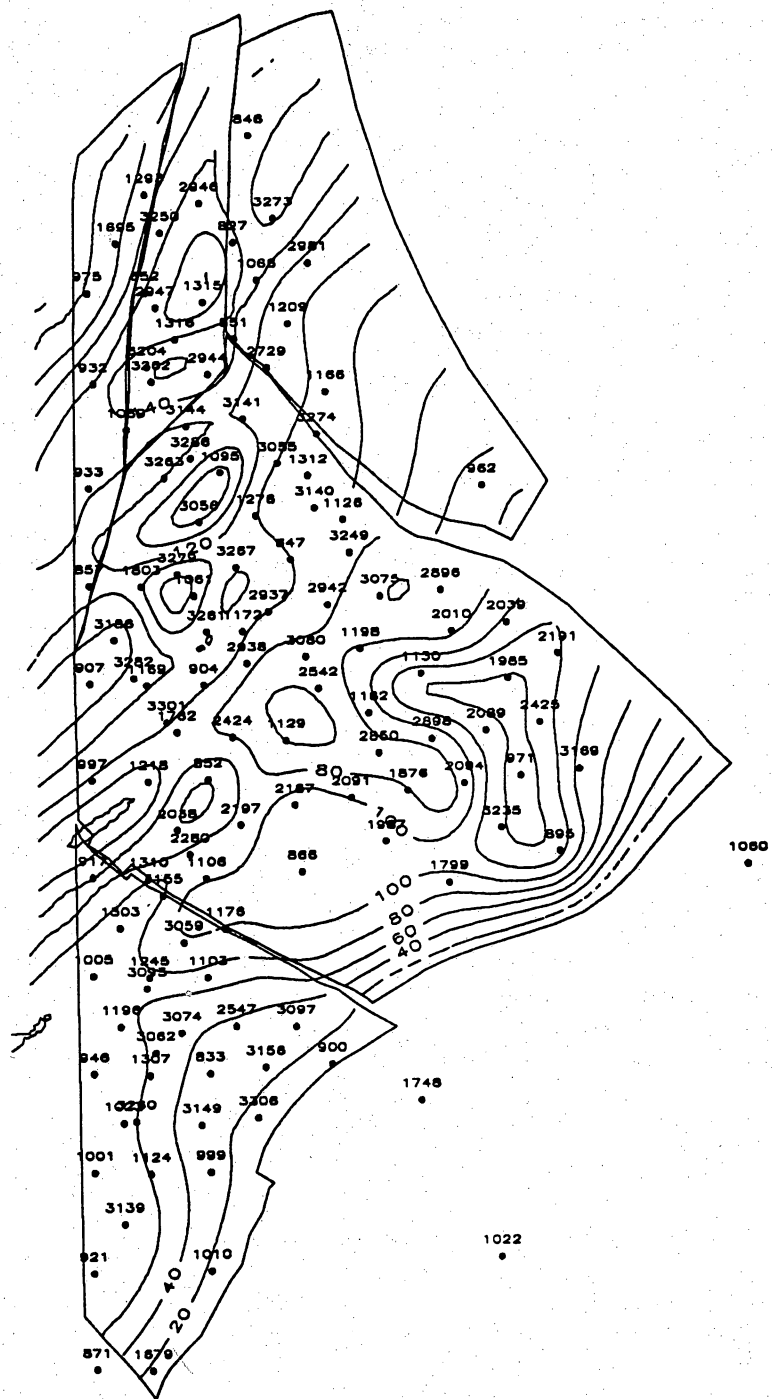


Figure X 6. Net pay map of the Upper C-4-X Submember in the LL-652 area. Contour interval is 20 ft (6 m).

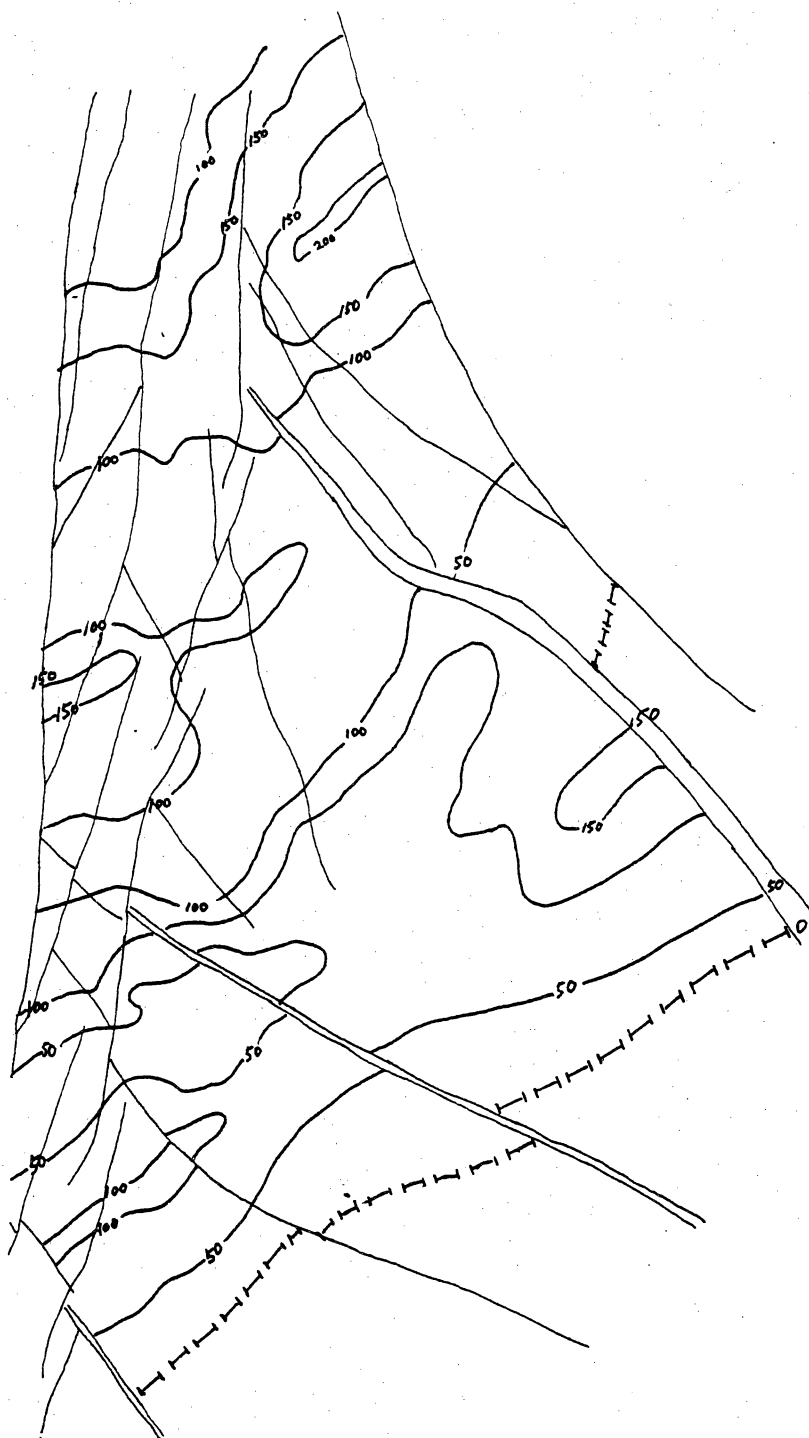


Figure X 7. Net pay map of the C-3-X Member in the LL-652 area. Contour interval is 50 ft (15.2 m).

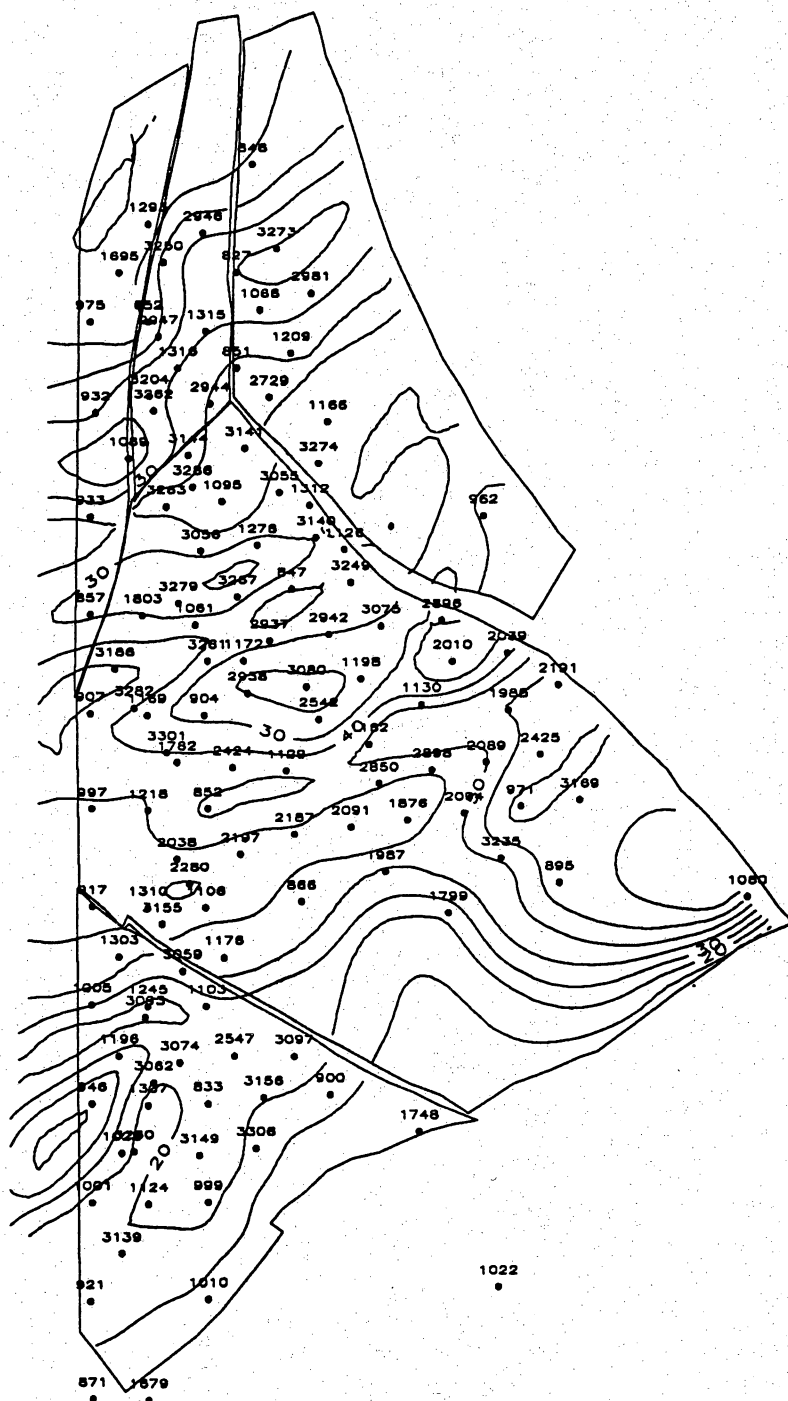


Figure X 8. Net pay (map of the Middle C-3-X Submember in the LL-652 area. Contour interval is 10 ft (3 m).

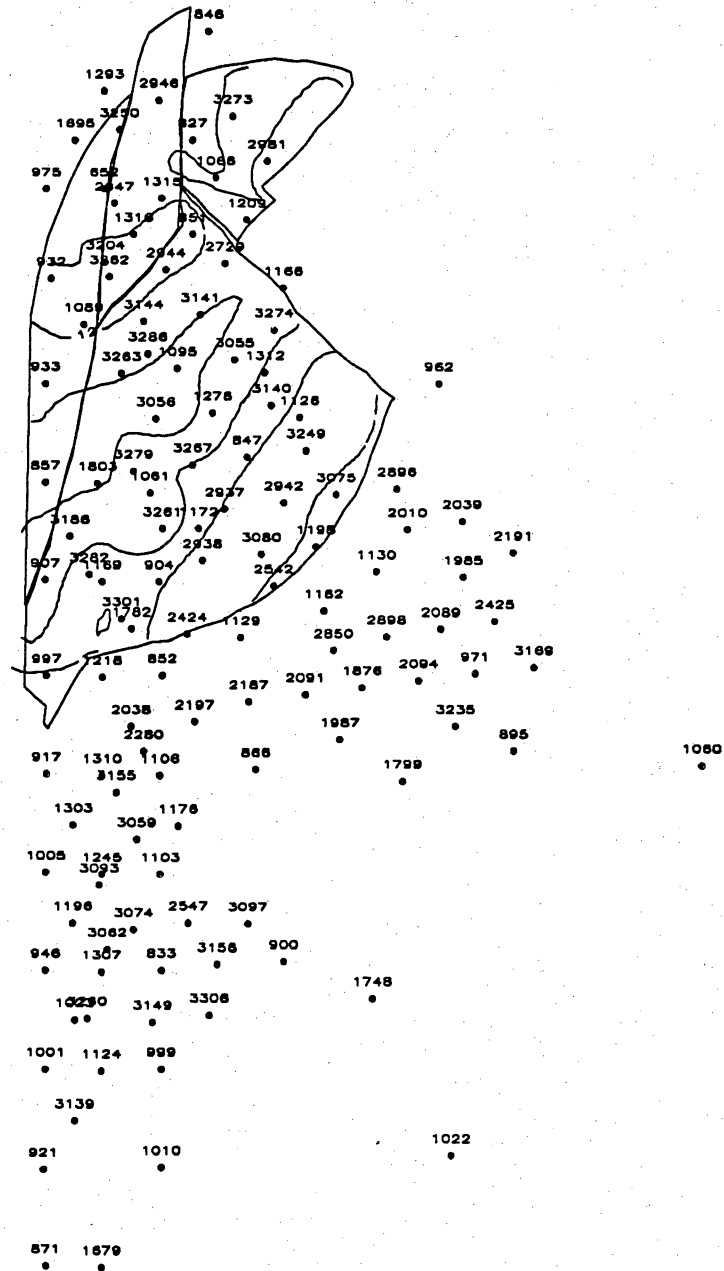


Figure X 9. Porosity map of the Lower Lower C-6-X Submember in the LL-652 area. Contour interval is 1 percent.

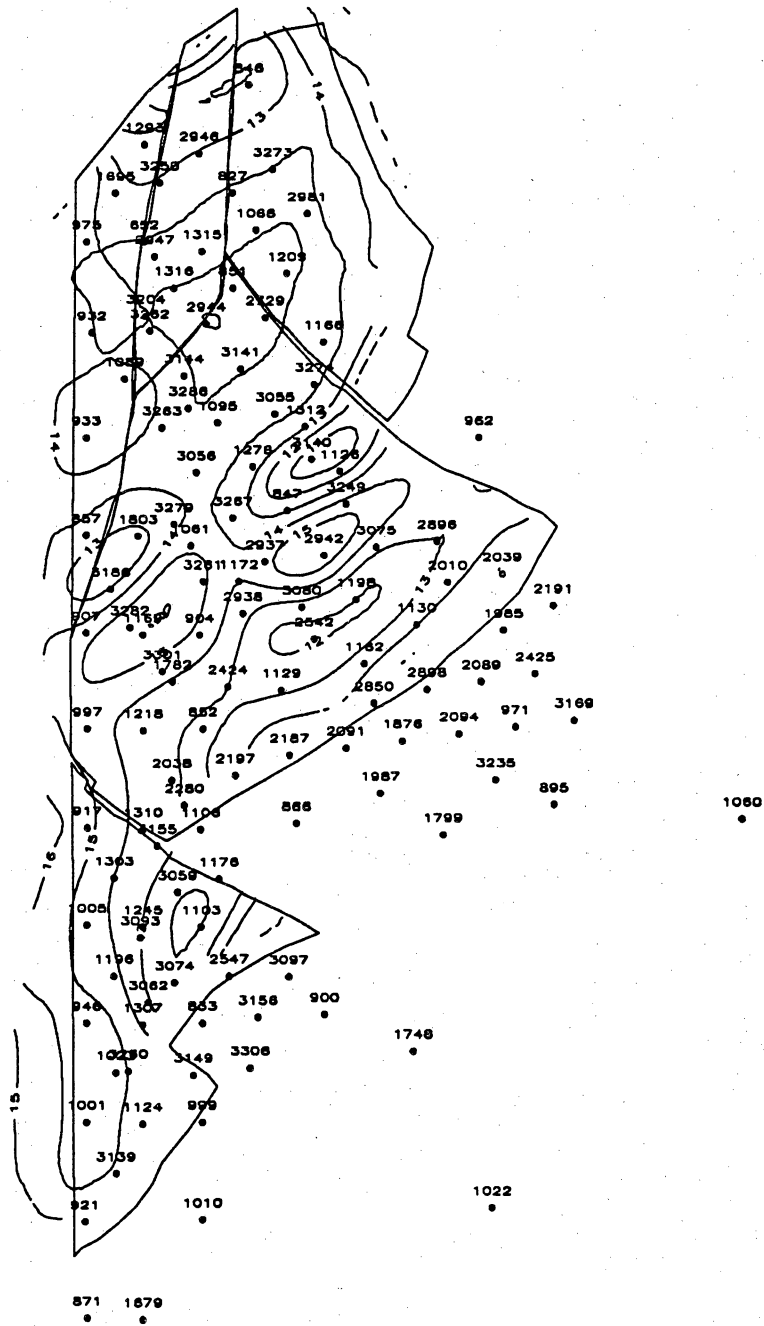


Figure X 10. Porosity map of the Lower Middle C-5-X Submember in the LL-652 area. Contour interval is 1 percent.

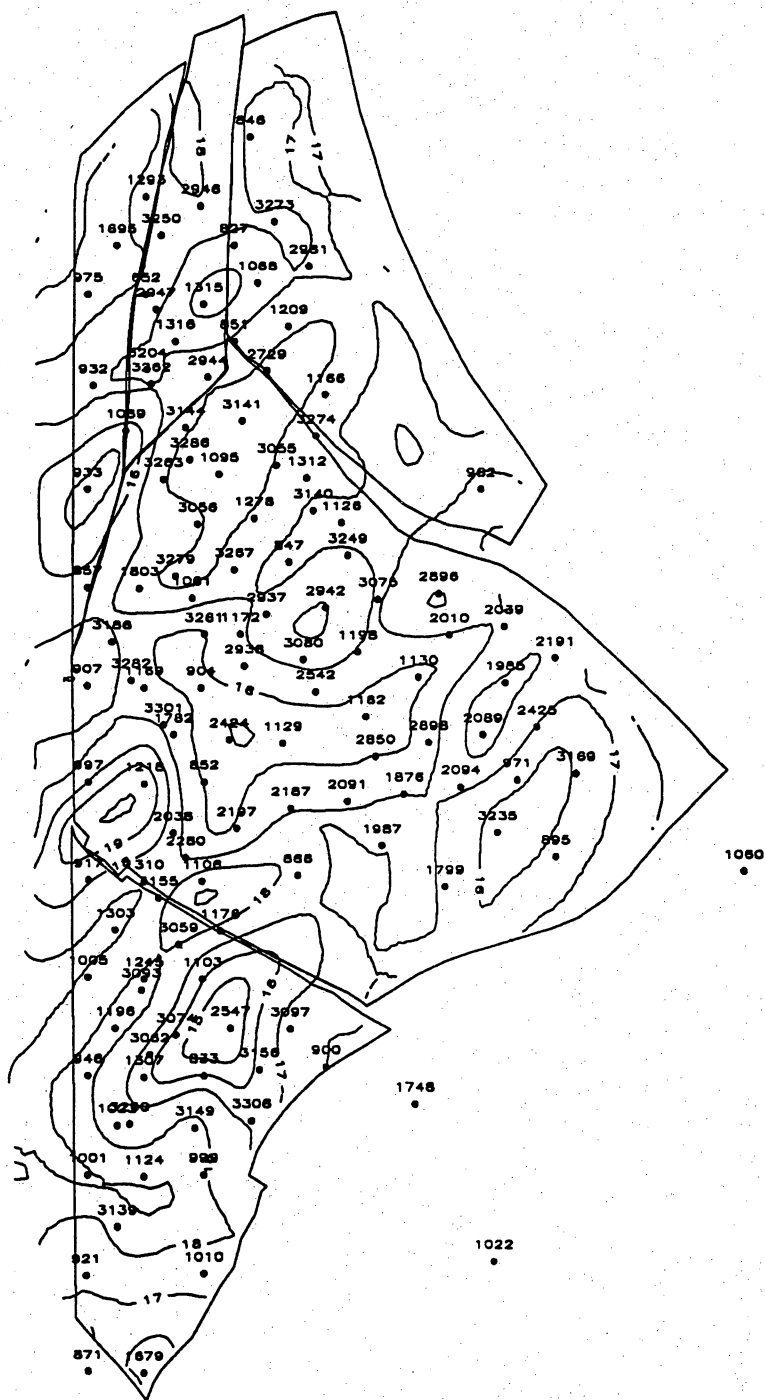


Figure X 11. Porosity map of the Upper C-4-X Member in the LL-652 area. Contour interval is 1 percent.

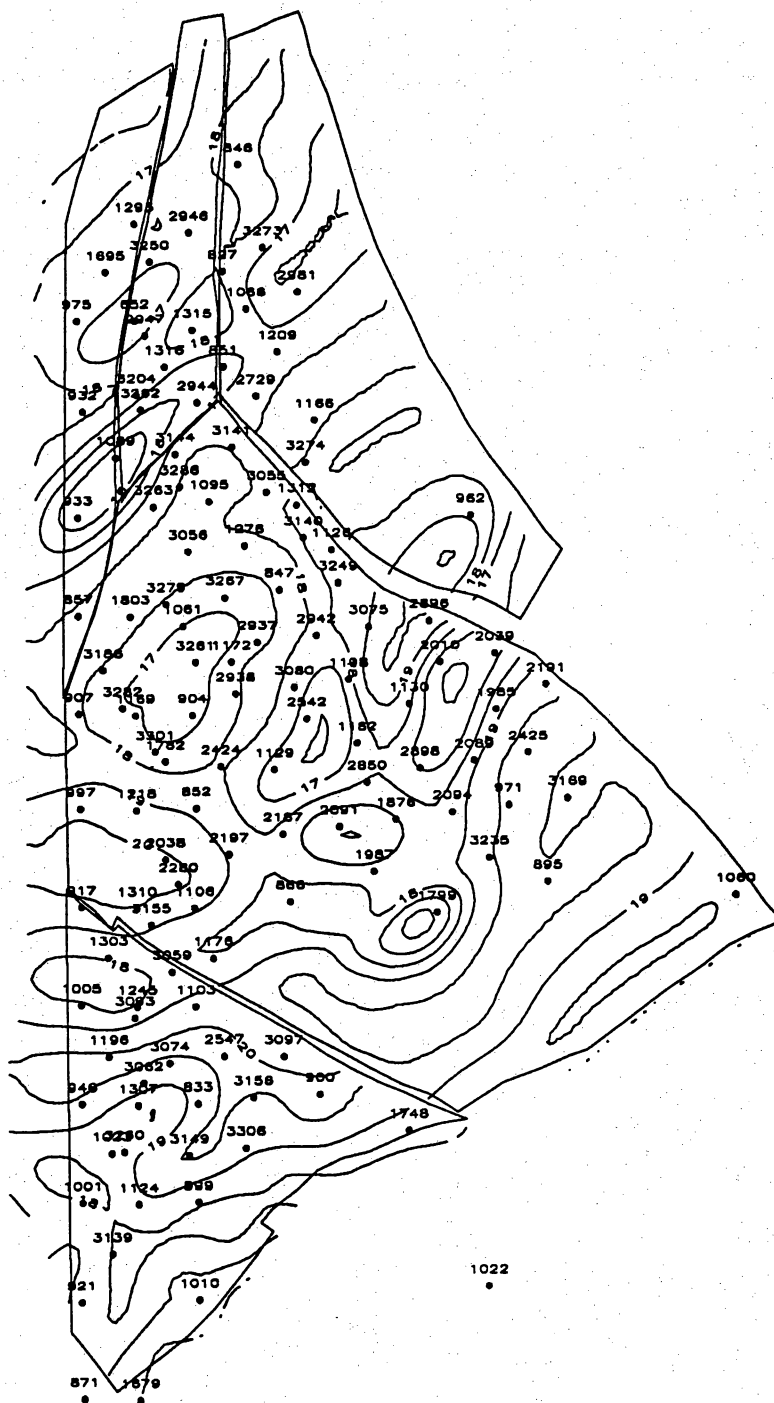


Figure X 12. Porosity map of the Middle C-3-X Submember in the LL-652 area. Contour interval is 1 percent.



Figure X 13. Permeability map of the C-7-X Member in the LL-652 area. Contour interval is 2 md.

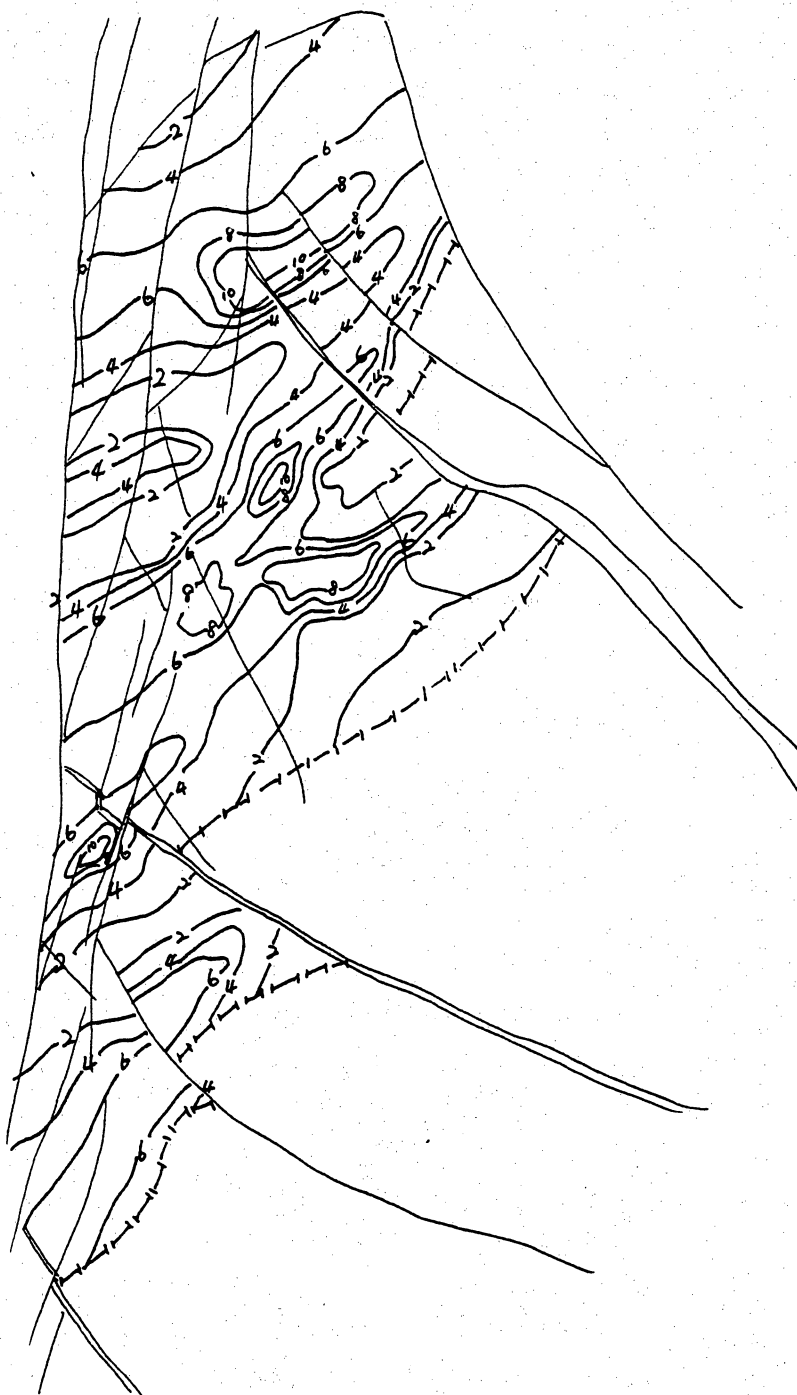


Figure X 14. Permeability map of the Lower Middle C-5-X Submember in the LL-652 area. Contour interval is 2 md.

Figure X 15. Permeability map of the Upper C-4-X Submember in the LL-652 area. Contour interval is 50 md.



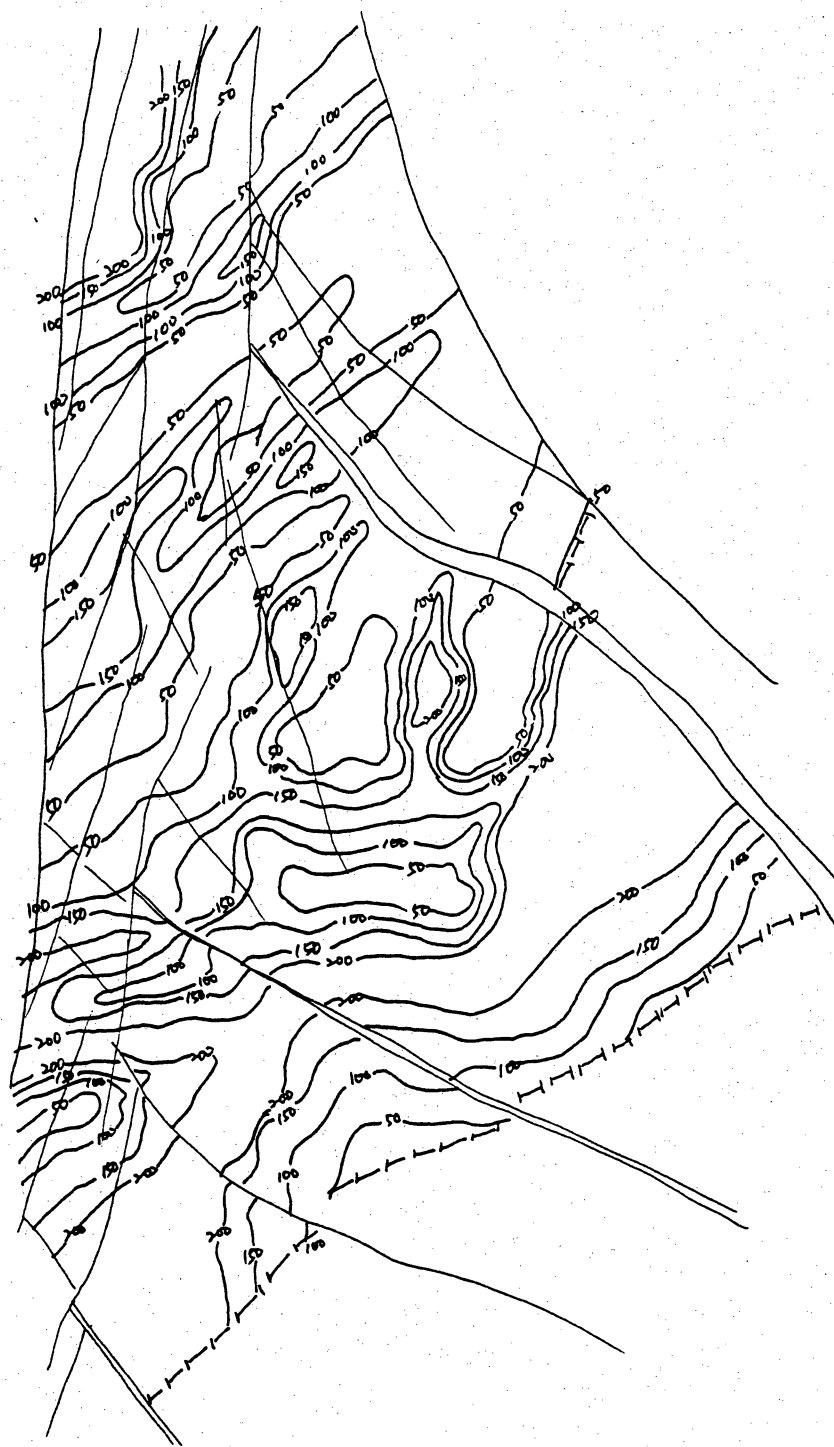


Figure X 16. Permeability map of the Middle C-3-X Submember in the LL-652 area. Contour interval is 50 md.



Figure X 17. Permeability map of the Upper C-2-X Submember in the LL-652 area. Contour interval is 20 md.

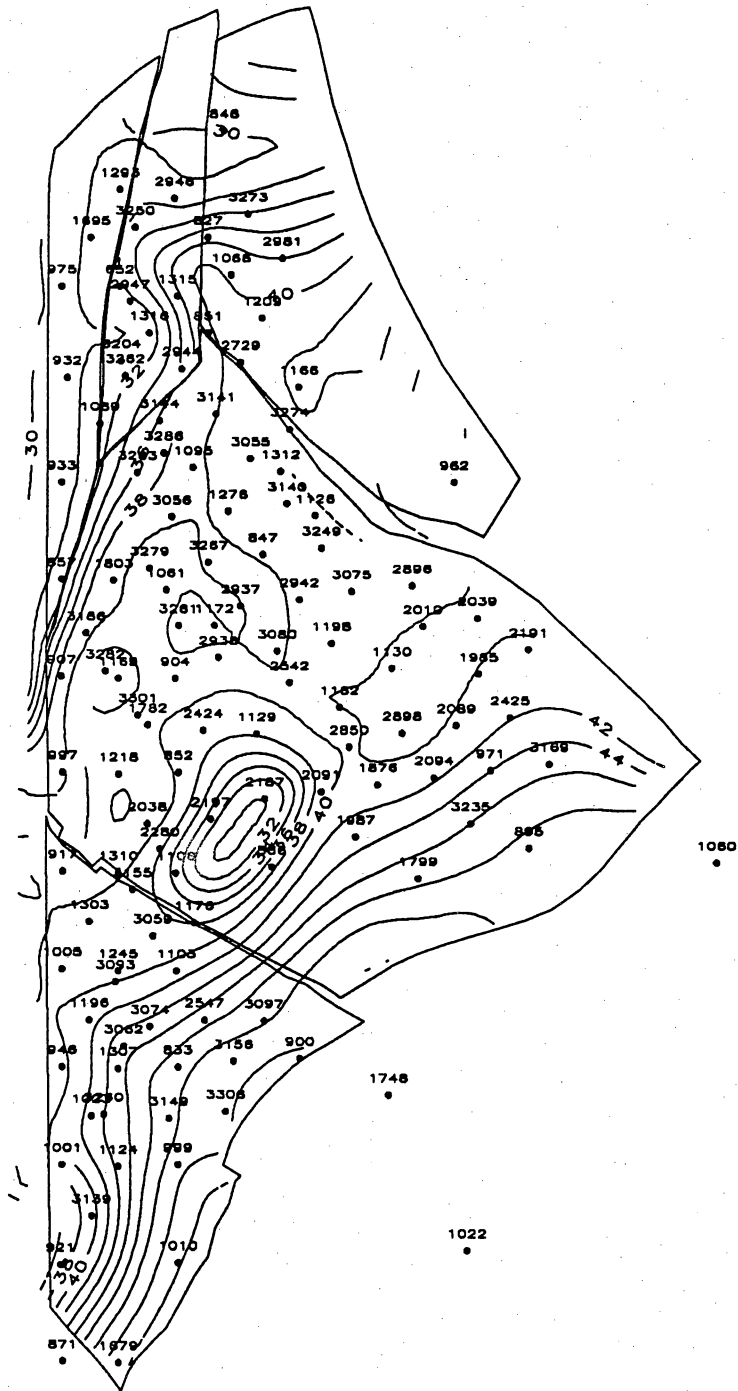


Figure X 18. Water saturation map of the Upper C-4-X Submember in the LL-652 area. Contour interval is 2 percent.

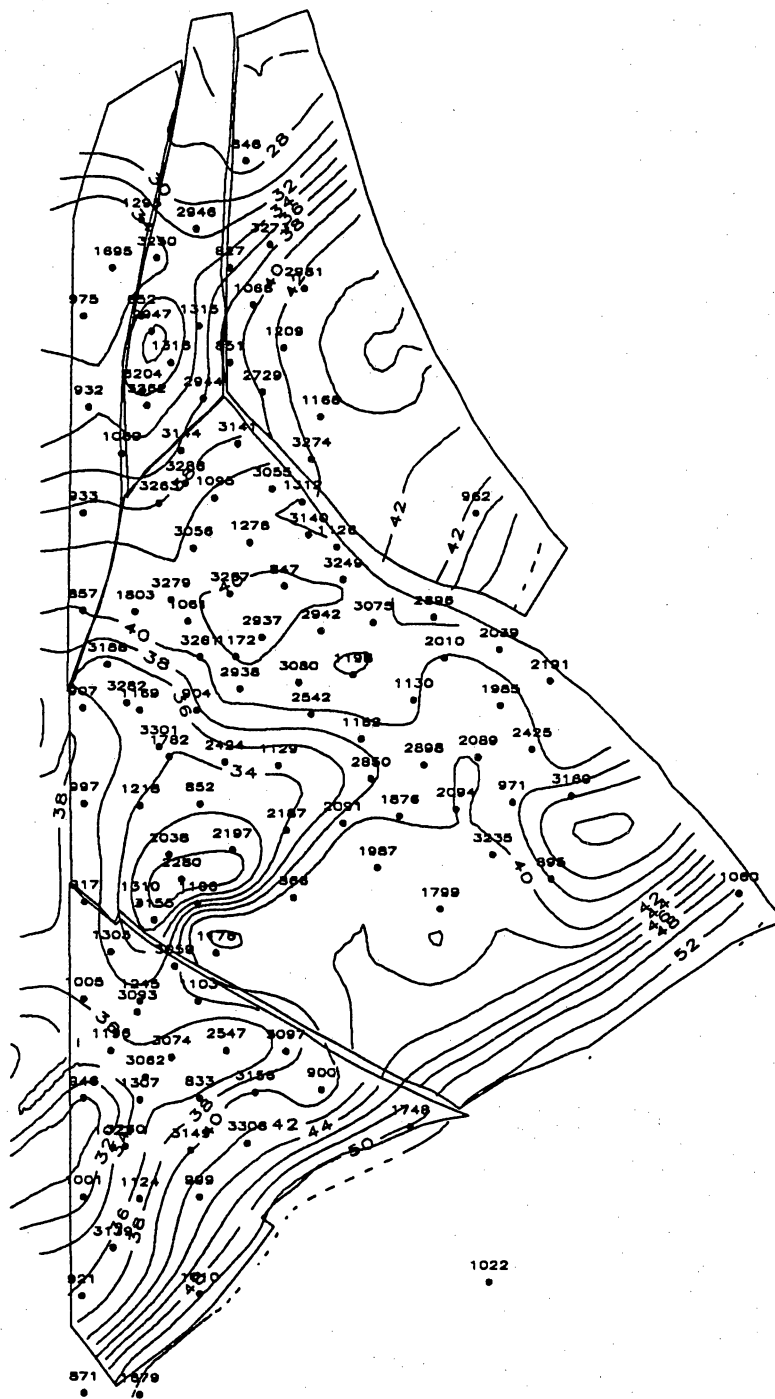


Figure X 19. Water saturation map of the Middle C-3-X Submember in the LL-652 area. Contour interval is 2 percent.

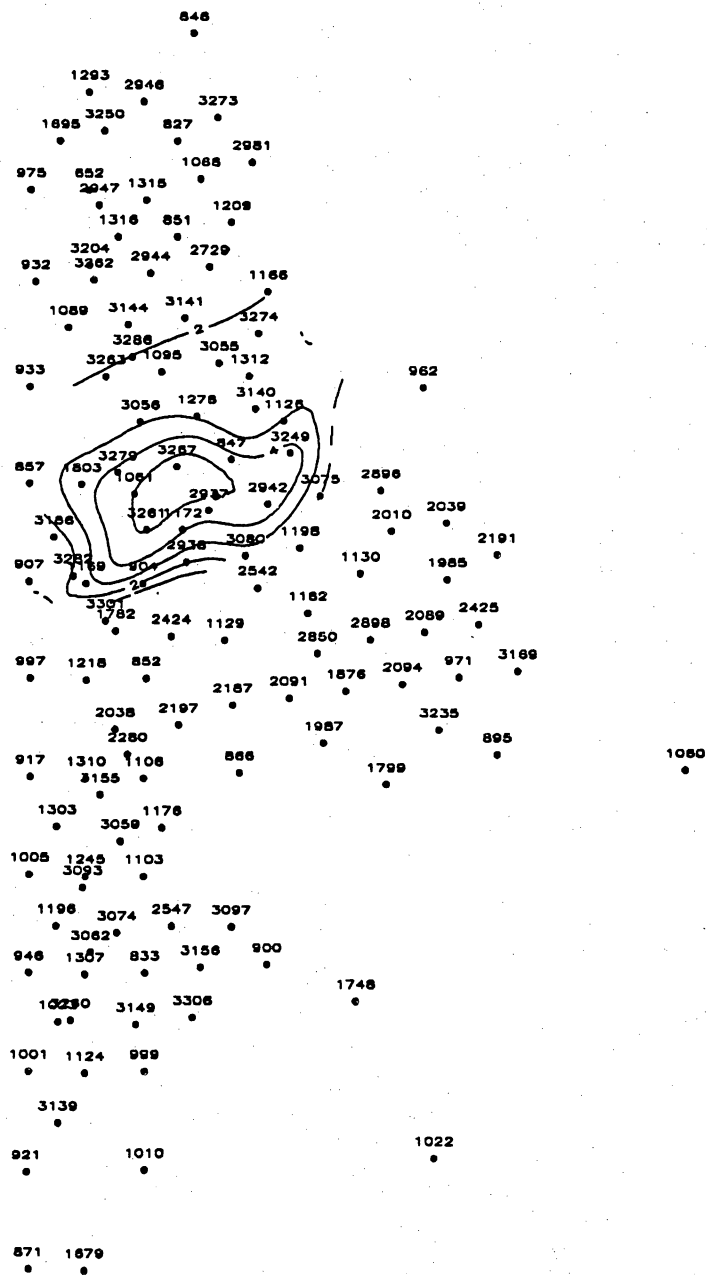


Figure X 20. $S_0\theta h$ map of the C-7-X Member in the LL-652 area. Contour interval is 1 ft (0.3 m).

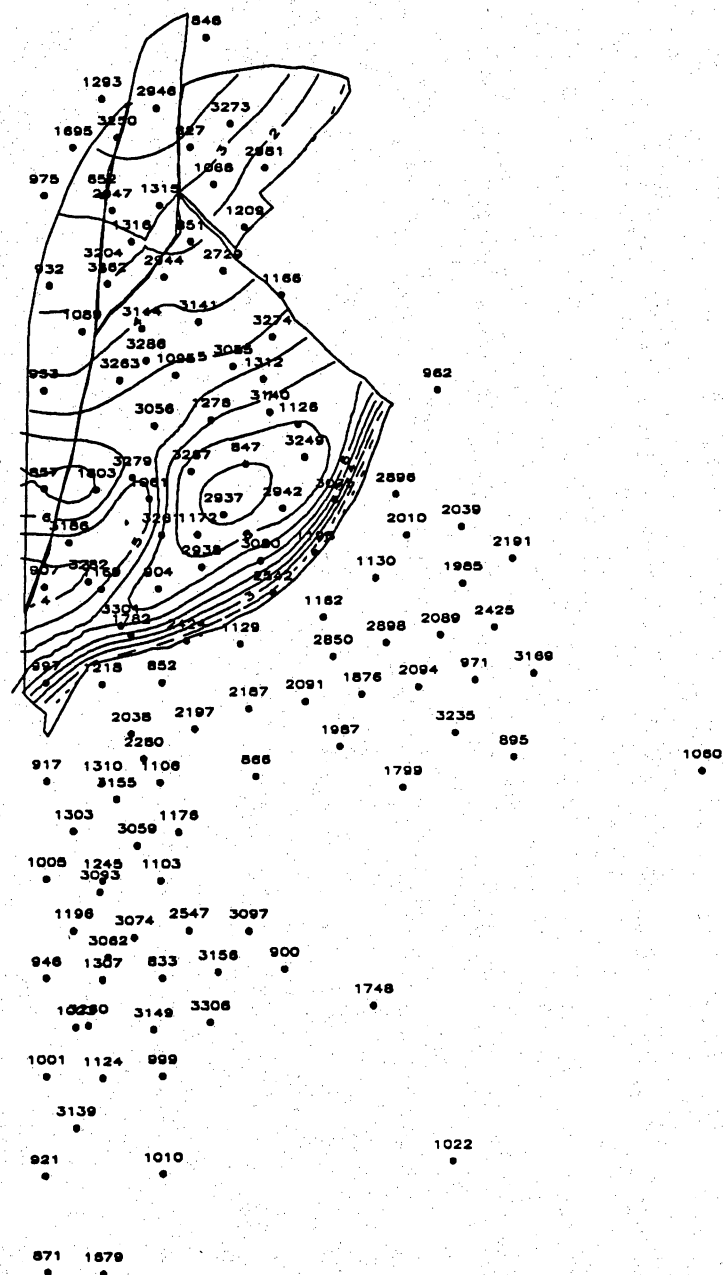


Figure X 21. $S_0\theta h$ map of the Lower Lower C-6-X Submember in the LL-652 area. Contour interval is 1 ft (0.3 m).



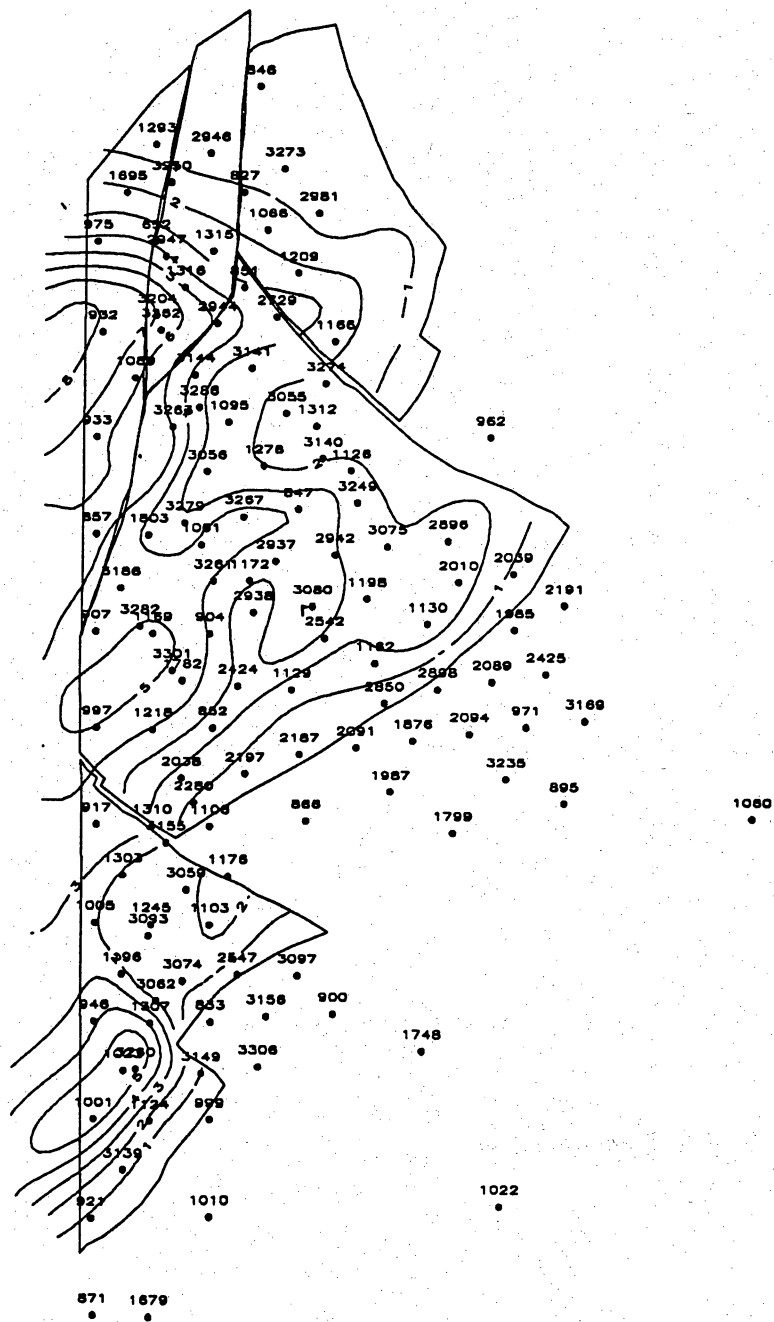


Figure X 23. $S_0\phi_h$ map of the combined Middle and Upper C-5-X Submembers in the LL-652 area. Contour interval is 1 ft (0.3 m).

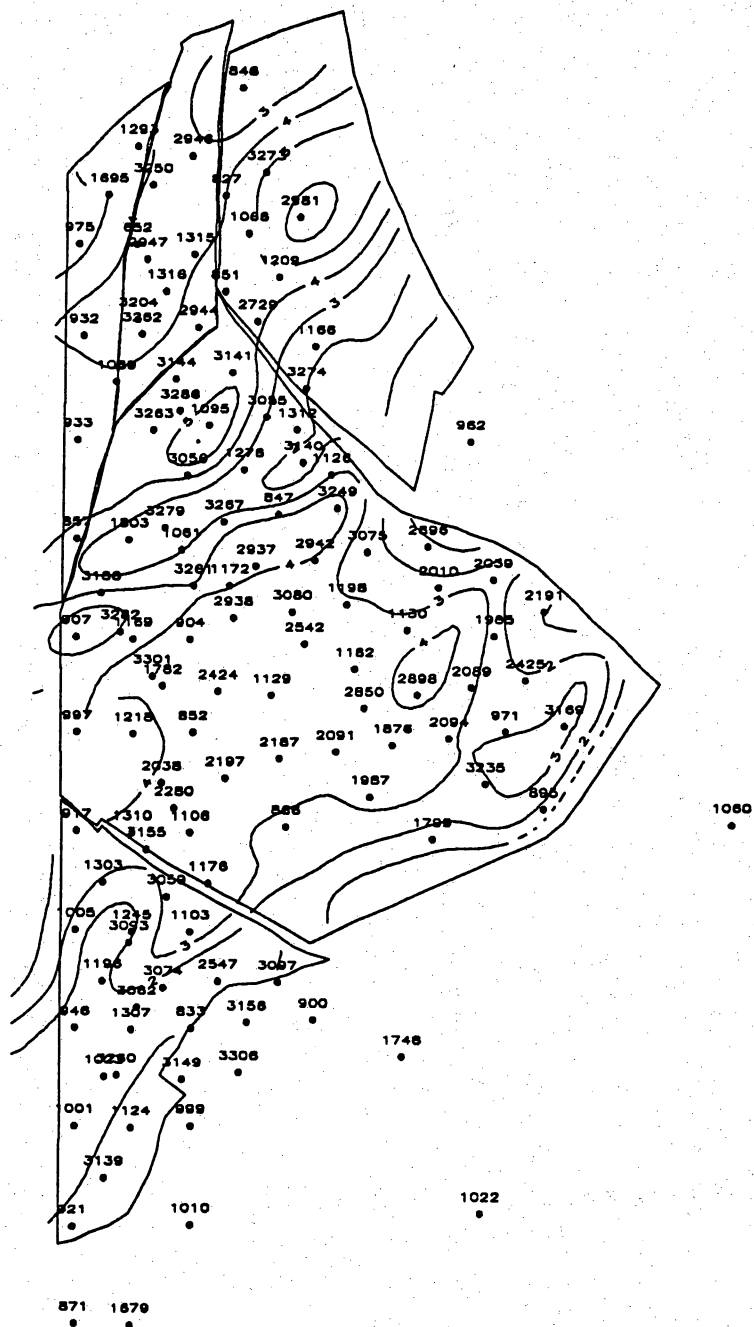


Figure X 25. $S_o\phi_h$ map of the Middle C-4-X Submember in the LL-652 area Contour interval is 1 ft (0.3 m).

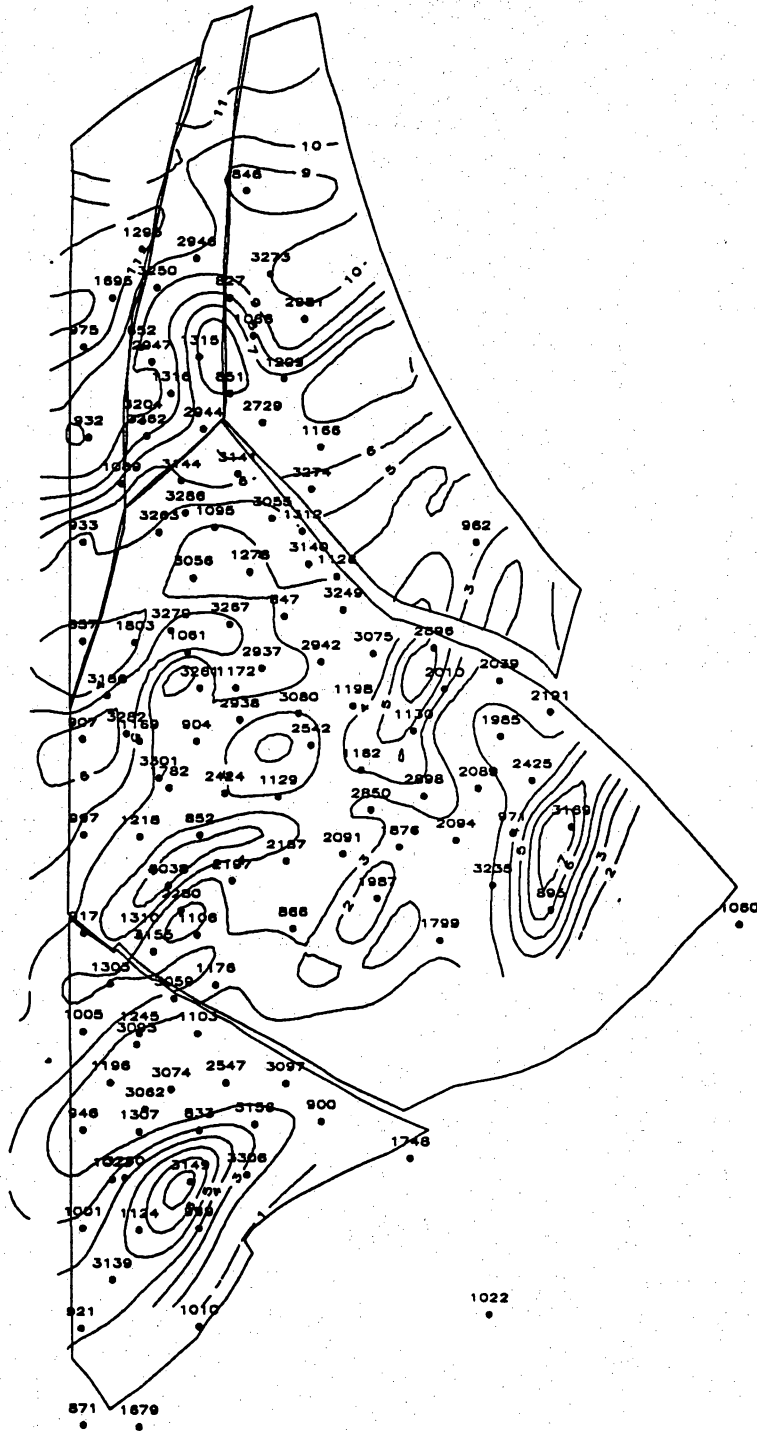


Figure X 26. S₀Øh map of the Lower C-3-X Submember in the LL-652 area. Contour interval is 1 ft (0.3 m).

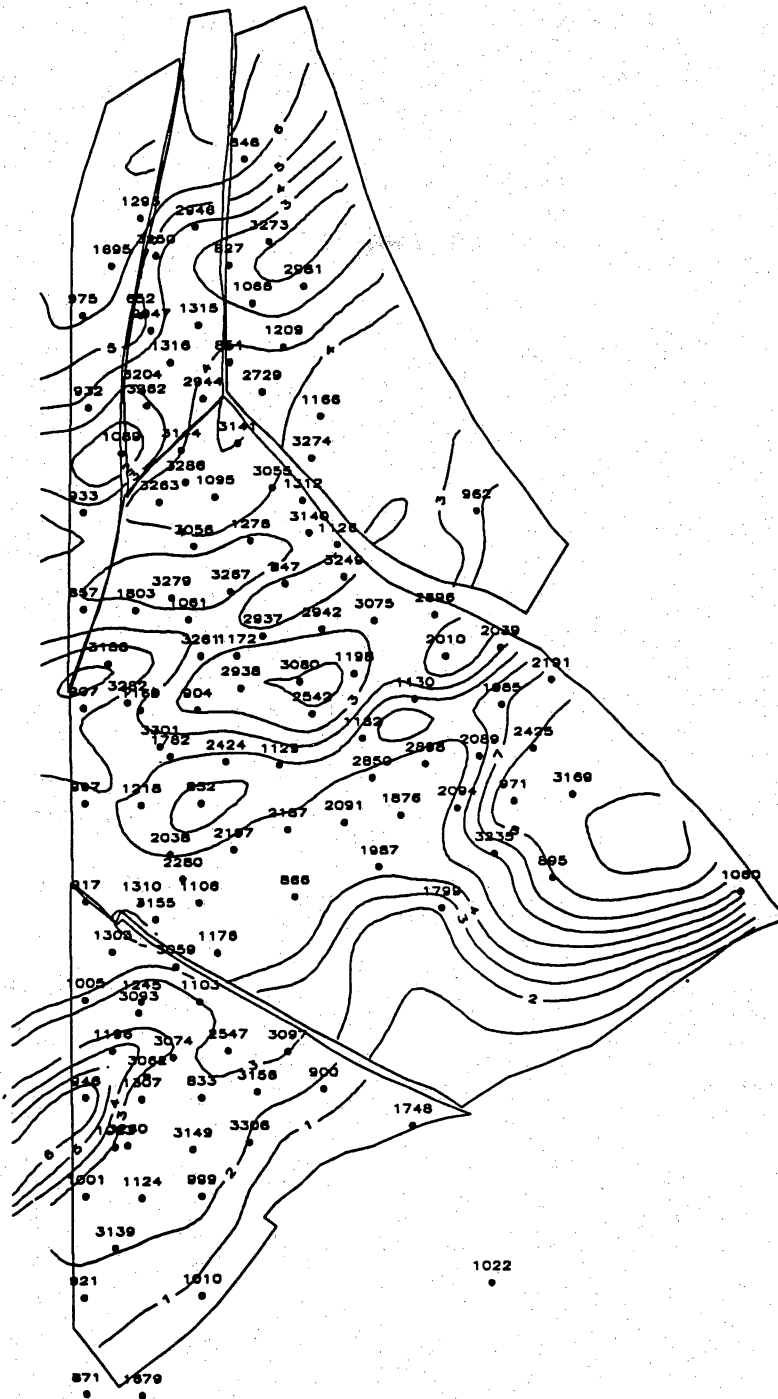


Figure X 27. $S_0\theta h$ map of the Middle C-3-X Submember in the LL-652 area. Contour interval is 1 ft (0.3 m).

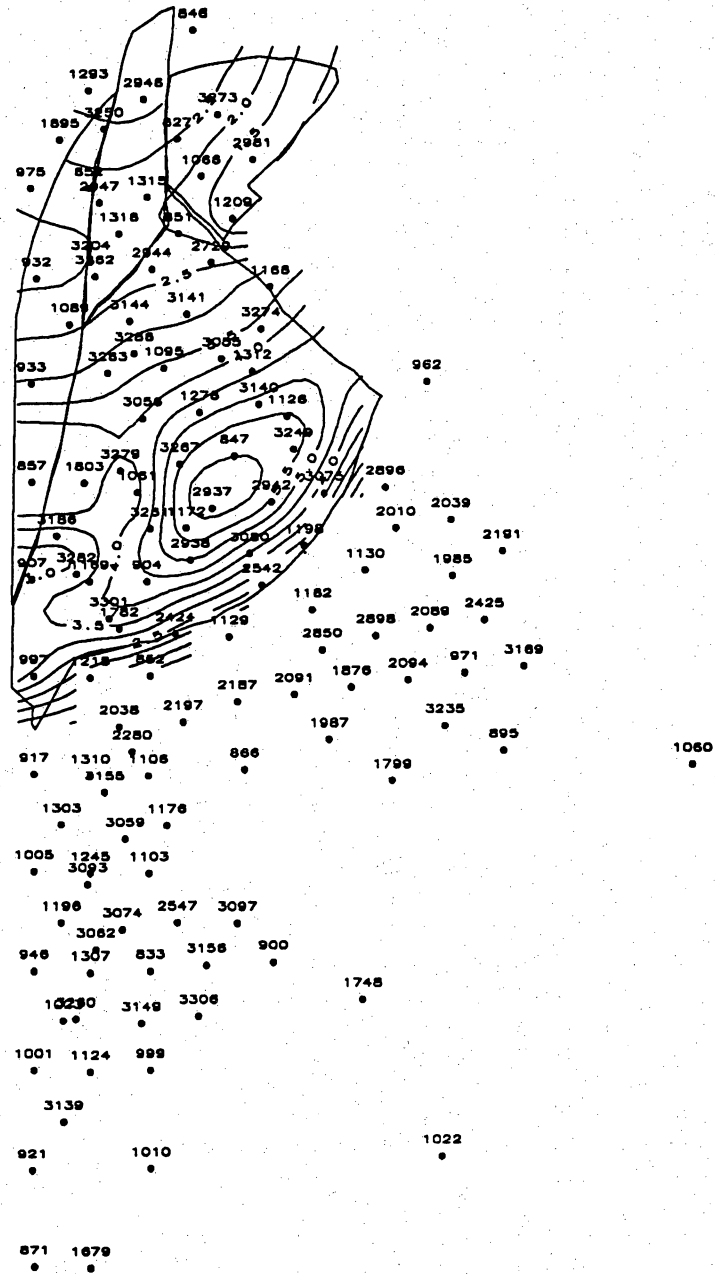
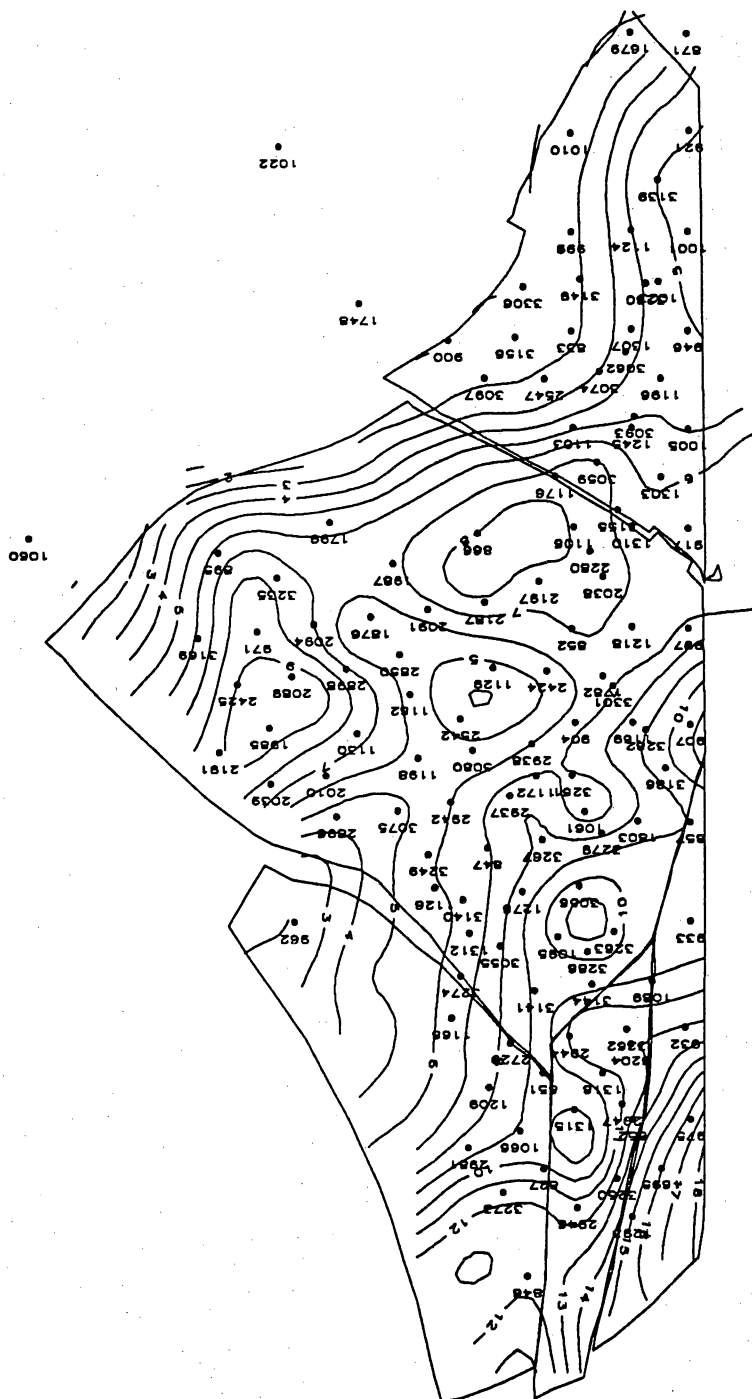


Figure X 28. OOIP map of the Lower Lower C-6-X Submember in the LL-652 area. Contour interval is 0.5 MMbbl.

Figure X 31. ODP map of the Upper C-4-X Submember in the LL-652 area. Contour interval is 1 MMbbl.



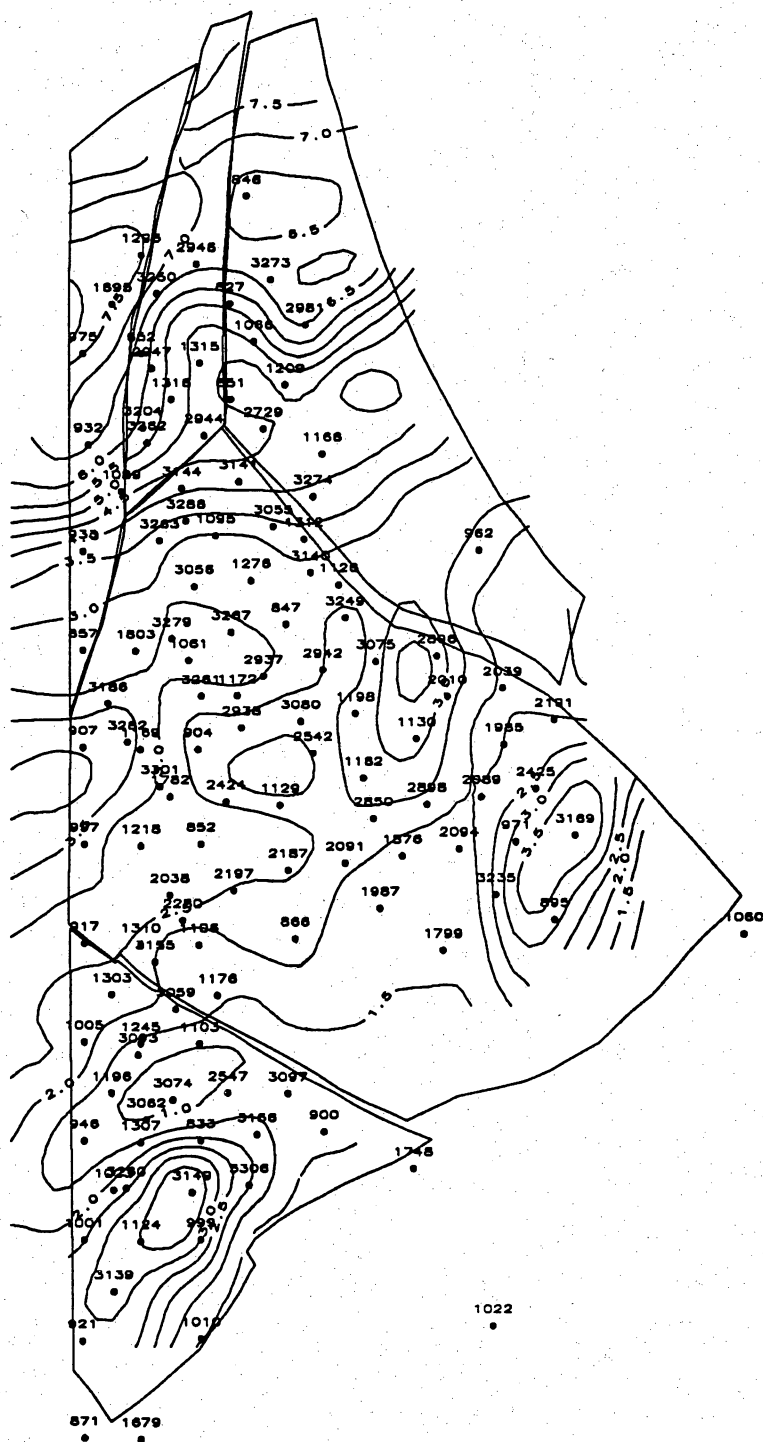
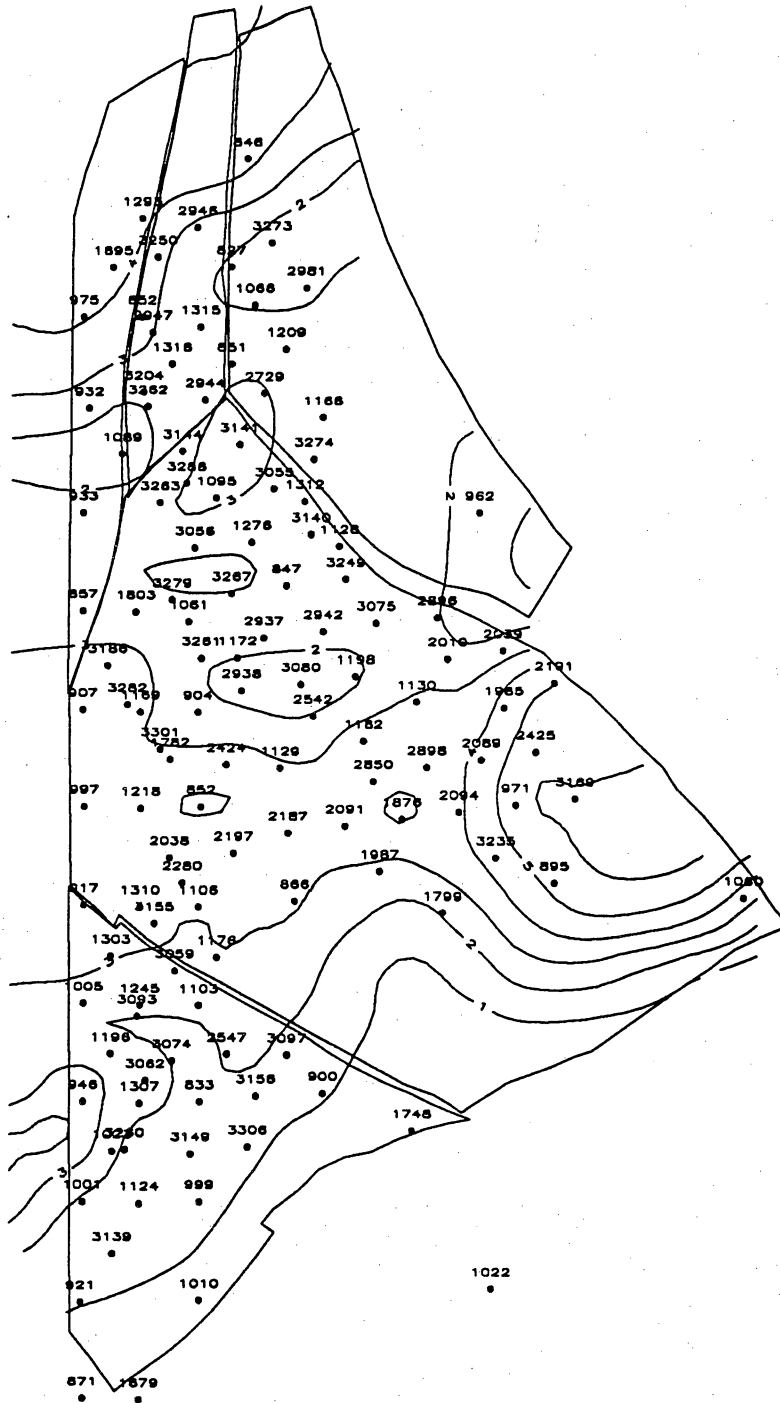


Figure X 32. OOIP map of the Lower C-3-X Submember in the LL-652 area. Contour interval is 0.5 MMbbl.



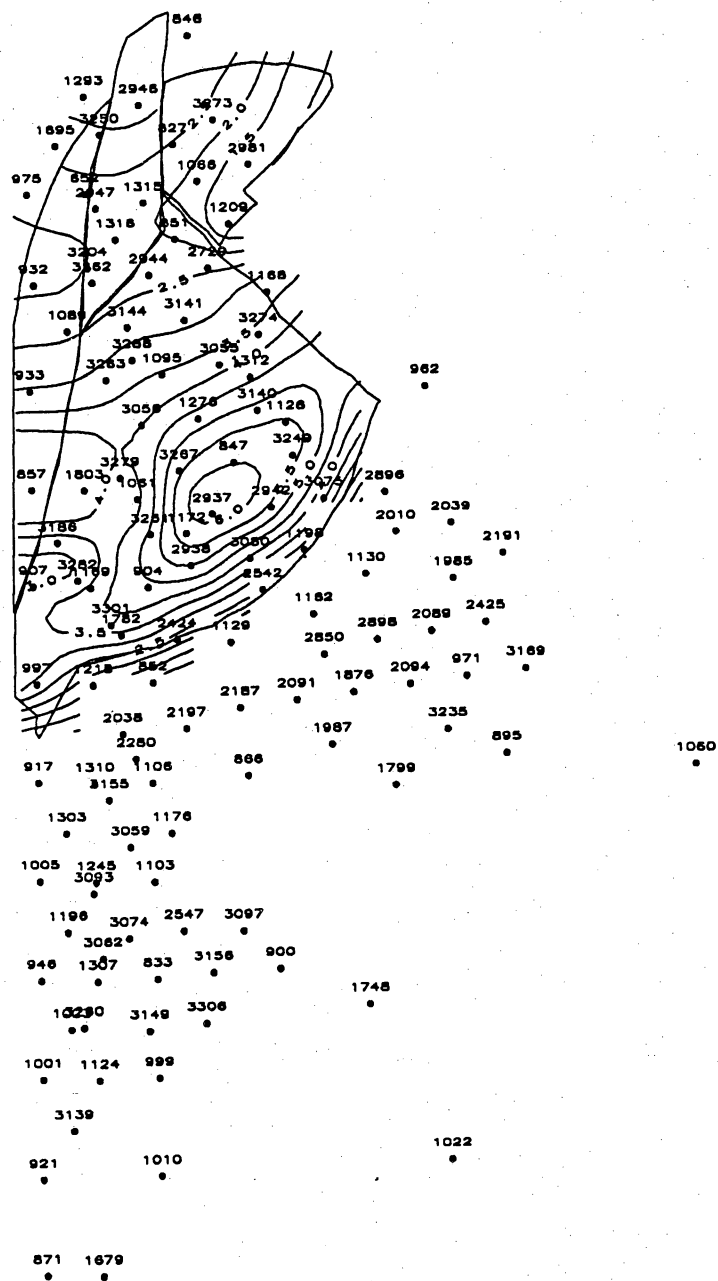


Figure X 34. Remaining oil map of the Lower Lower C-6-X Submember in the LL-652 area. Contour interval is 0.5 MMbbl.

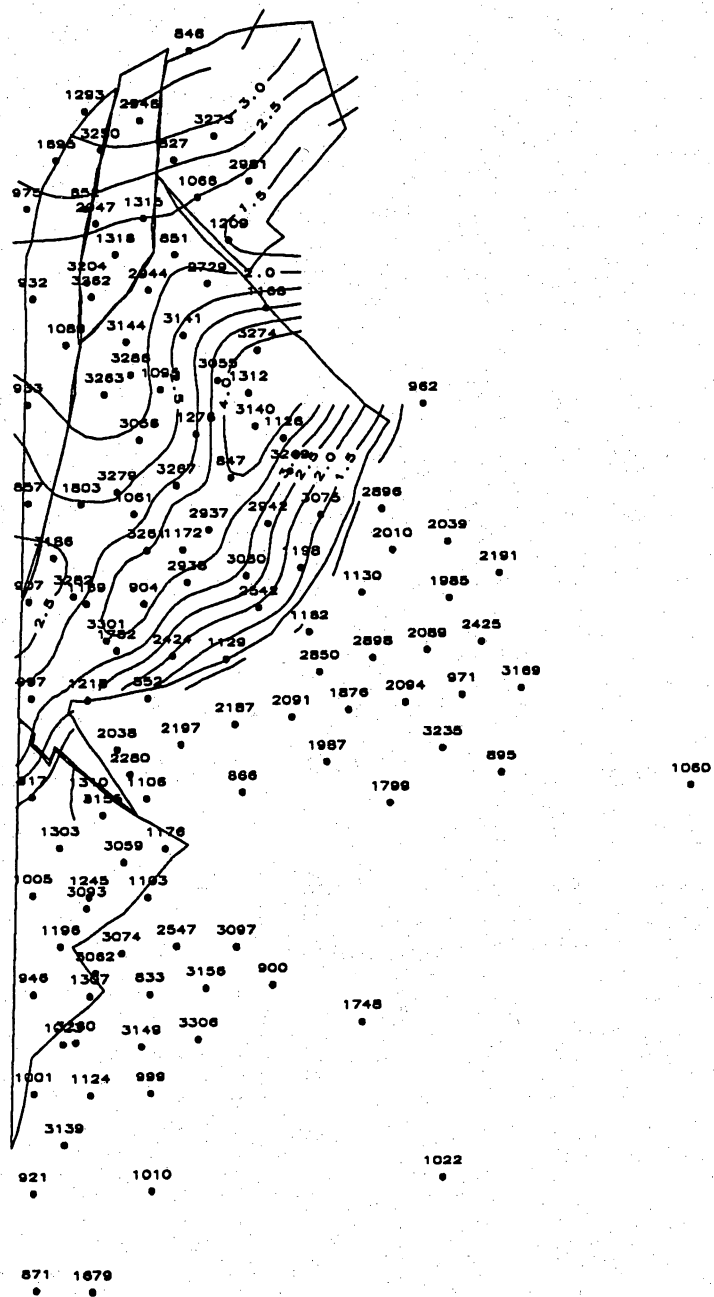


Figure X 35. Remaining oil map of the Upper Lower C-6-X Submember in the LL-652 area. Contour interval is 0.5 MMbbl.

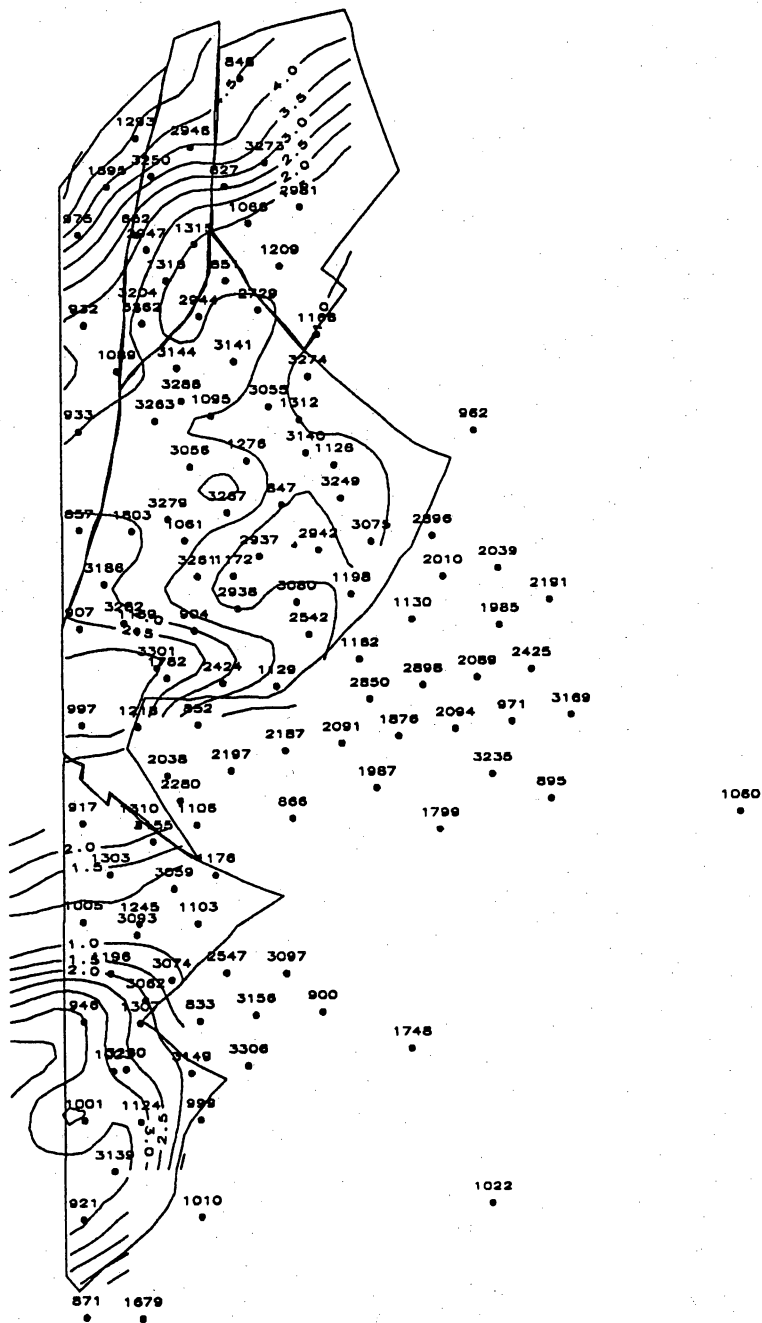


Figure X 36. Remaining oil map of the Lower C-5-X Submember in the LL-652 area. Contour interval is 0.5 MMbbl.

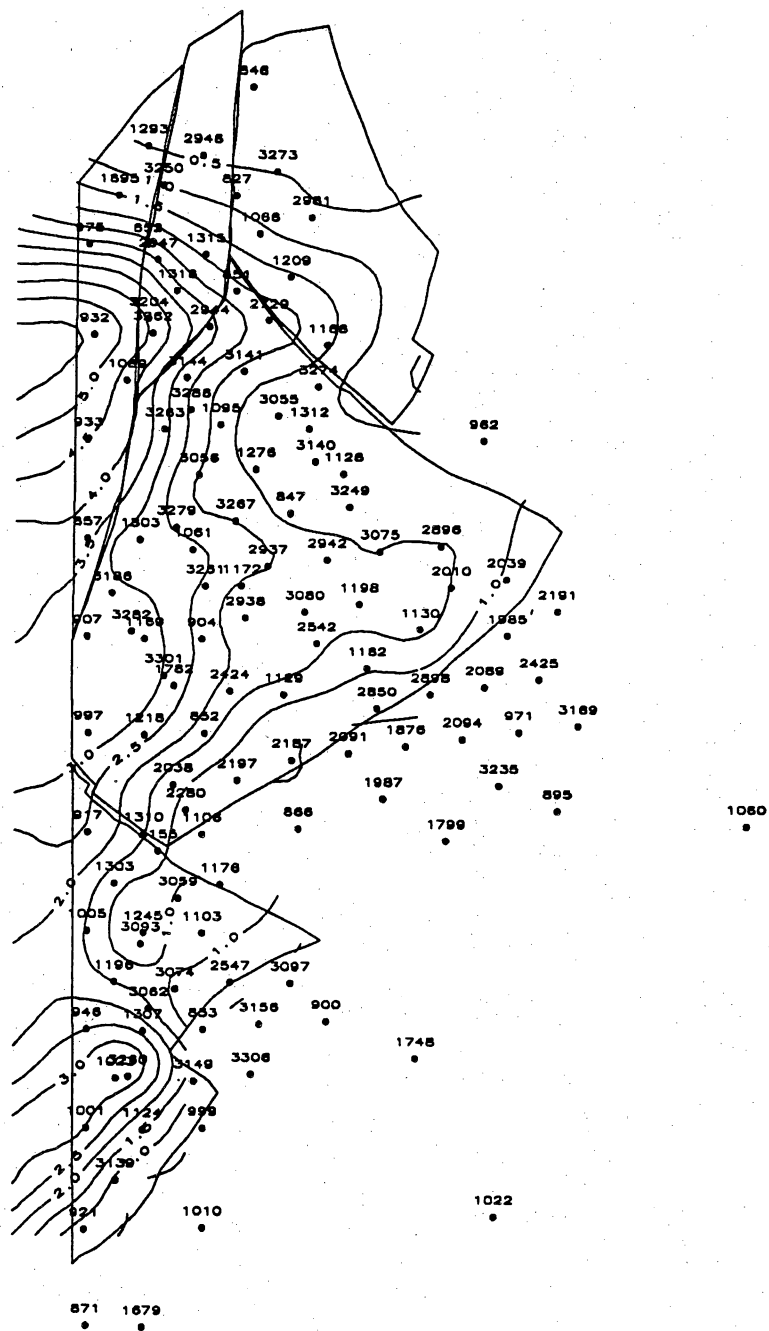


Figure X 37. Remaining oil map of the combined Middle and Upper Middle C-5-X Submembers in the LL-652 area. Contour interval is 0.5 MMbbl.

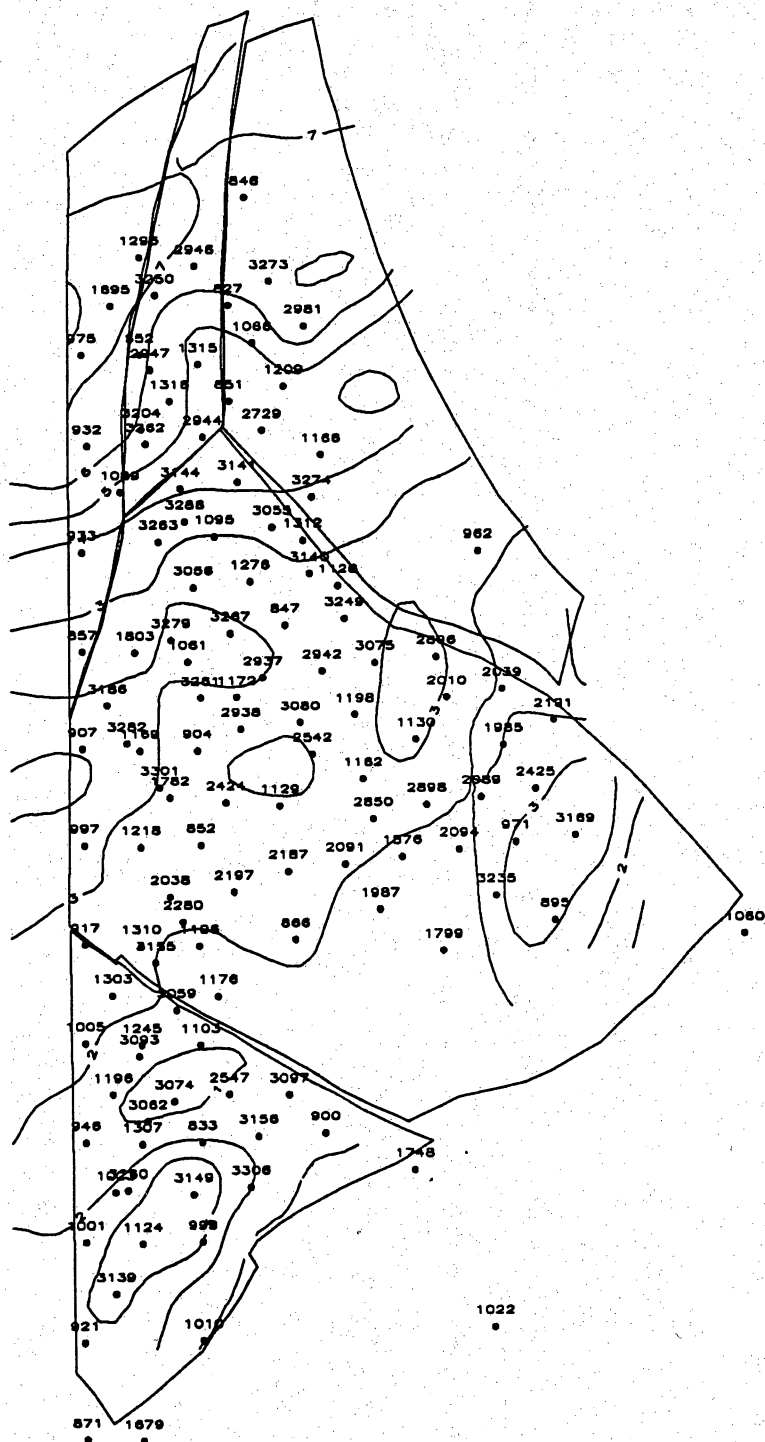


Figure X 39. Remaining oil map of the Lower C-3-X Submember in the LL-652 area. Contour interval is 1 MMbbl.

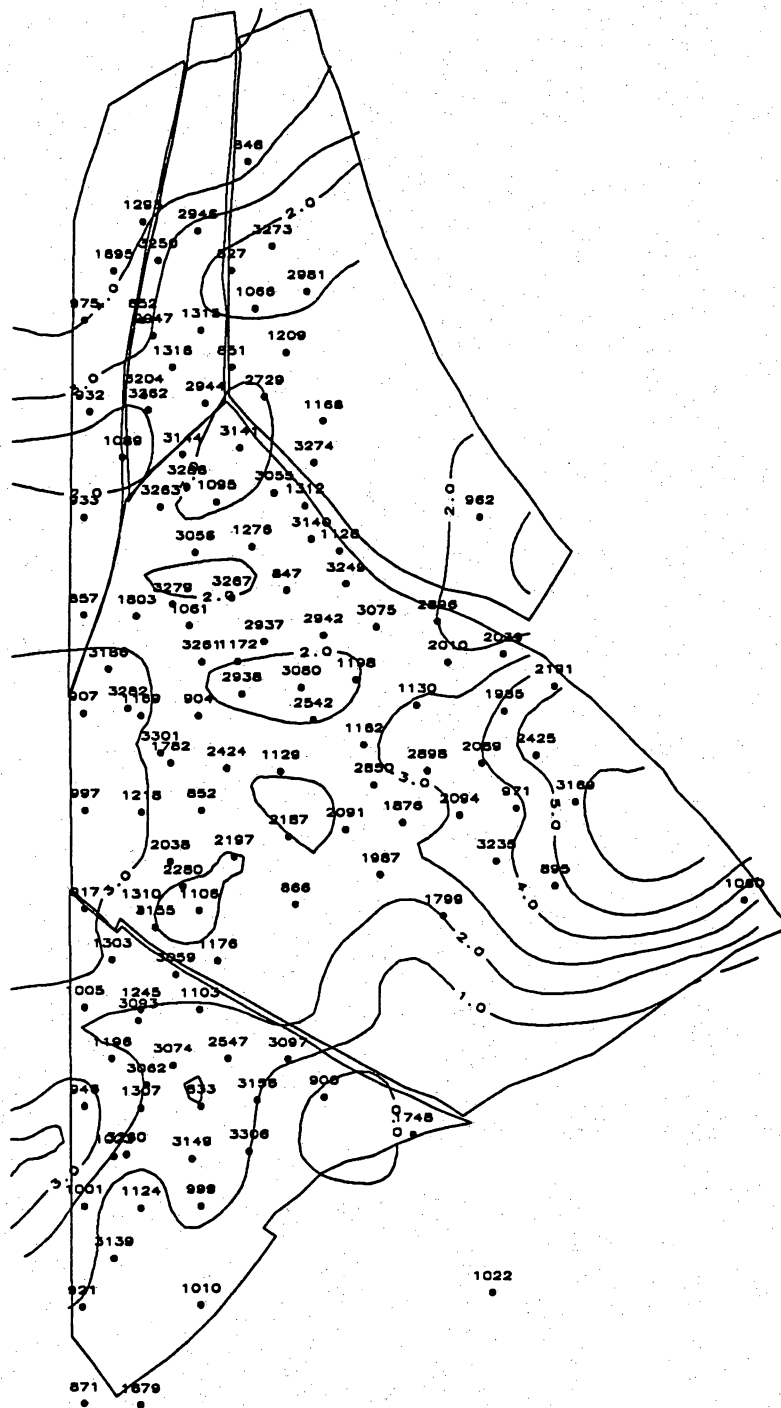


Figure X 40. Remaining oil map of the Middle C-3-X Submember in the LL-652 area. Contour interval is 1 MMbbl.

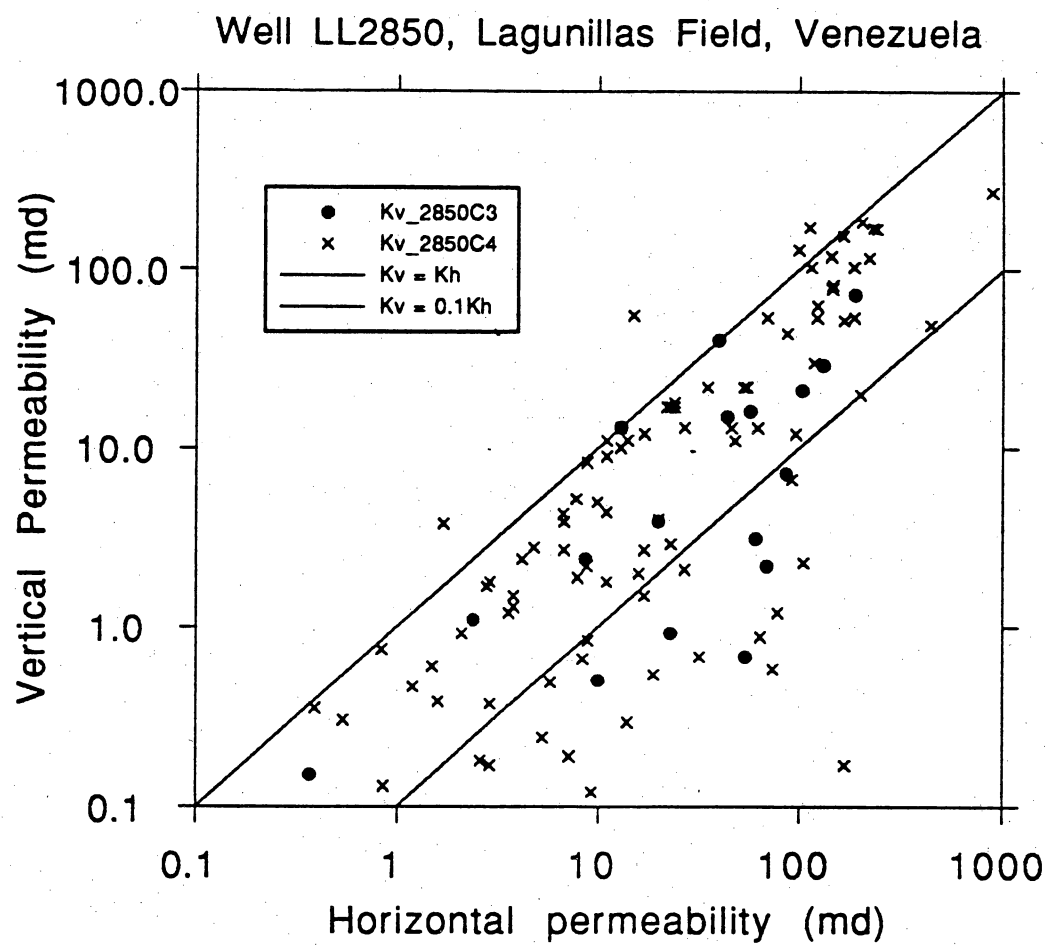


Figure X 41. Horizontal versus vertical permeability in the LL-2850 well.

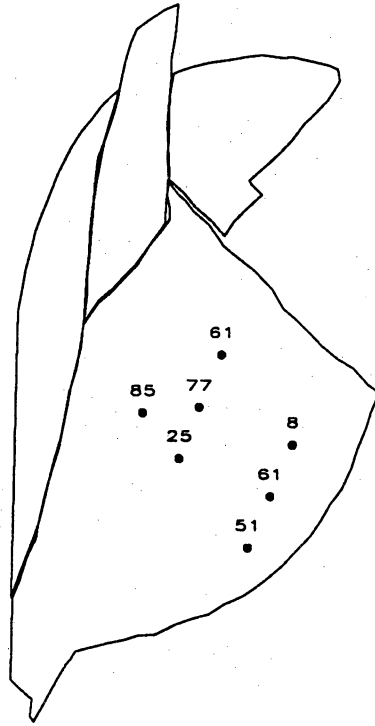


Figure X 42. Cumulative production map of the Upper Lower C-6-X Submember in the LL-652 area. Values are in Mbbl.

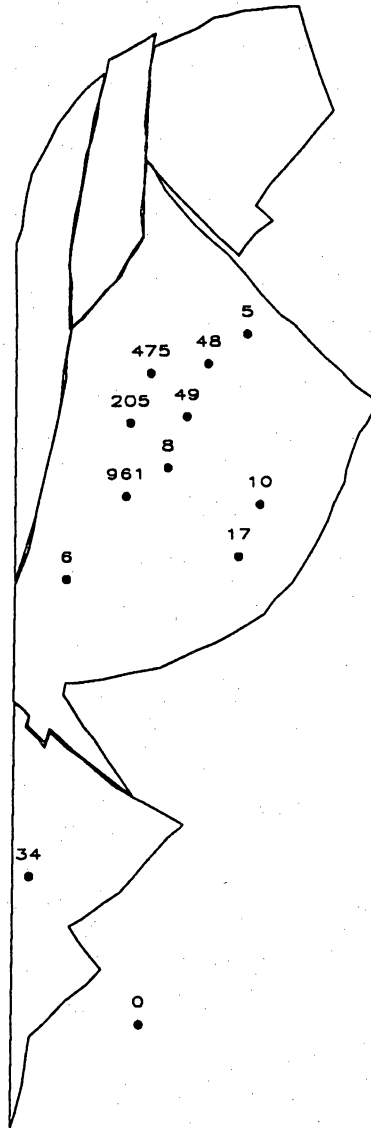


Figure X 43. Cumulative production map of the Lower Upper C-6-X Submember in the LL-652 area. Values are in Mbbl.

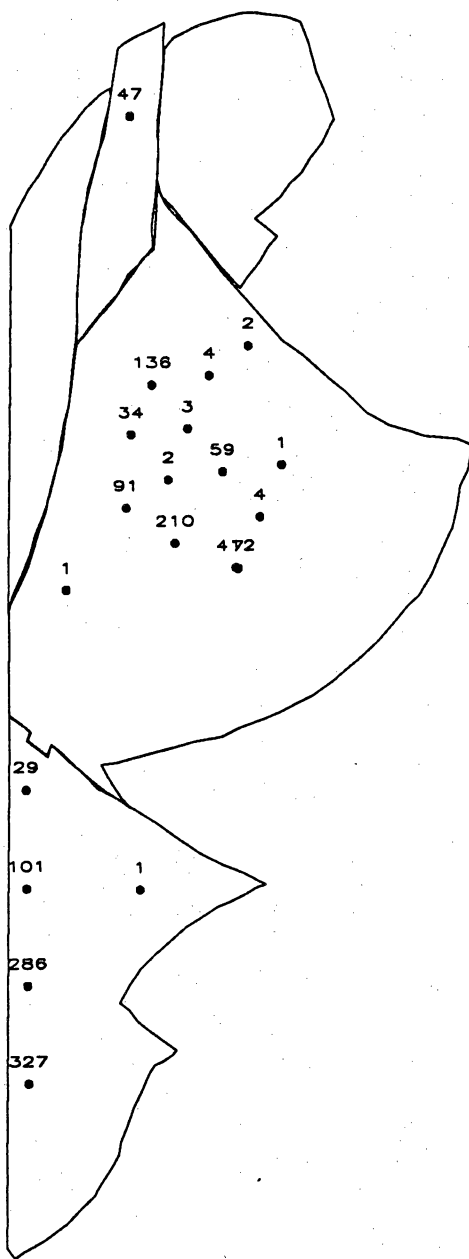


Figure X 44. Cumulative production map of the Lower C-5-X Submember in the LL-652 area. Values are in Mbbl.

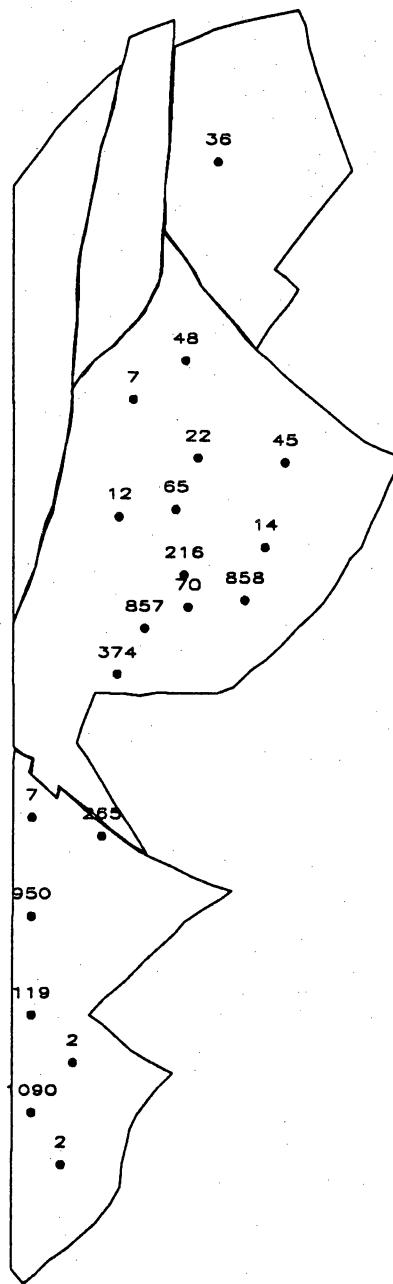


Figure X 45. Cumulative production map of the combined Middle and Upper Middle C-5-X Submember in the LL-652 area. Values are in Mbbl.

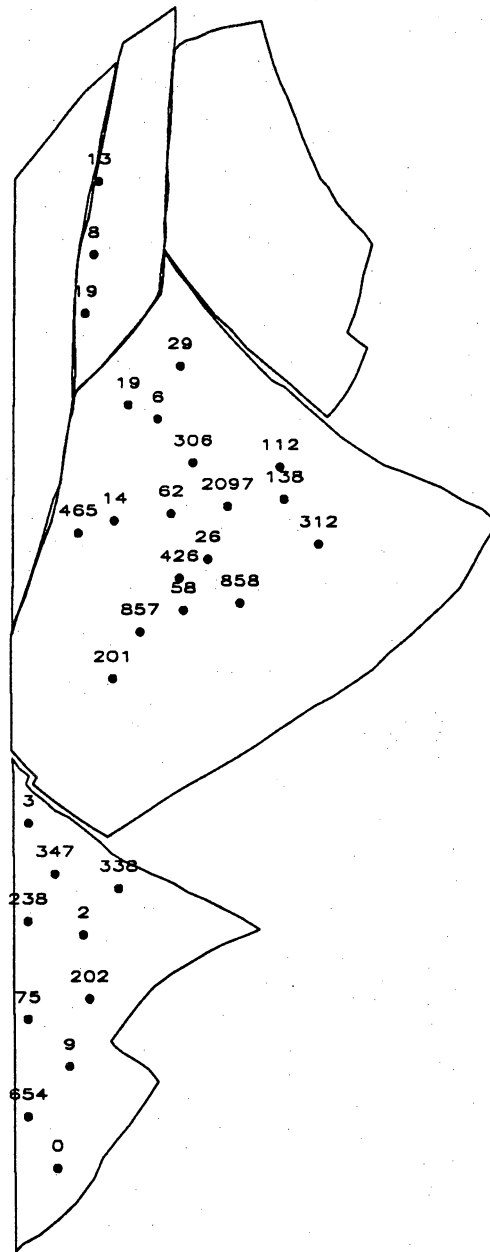


Figure X 46. Cumulative production map of the Middle C-4-X Submember in the LL-652 area. Values are in Mbbl.

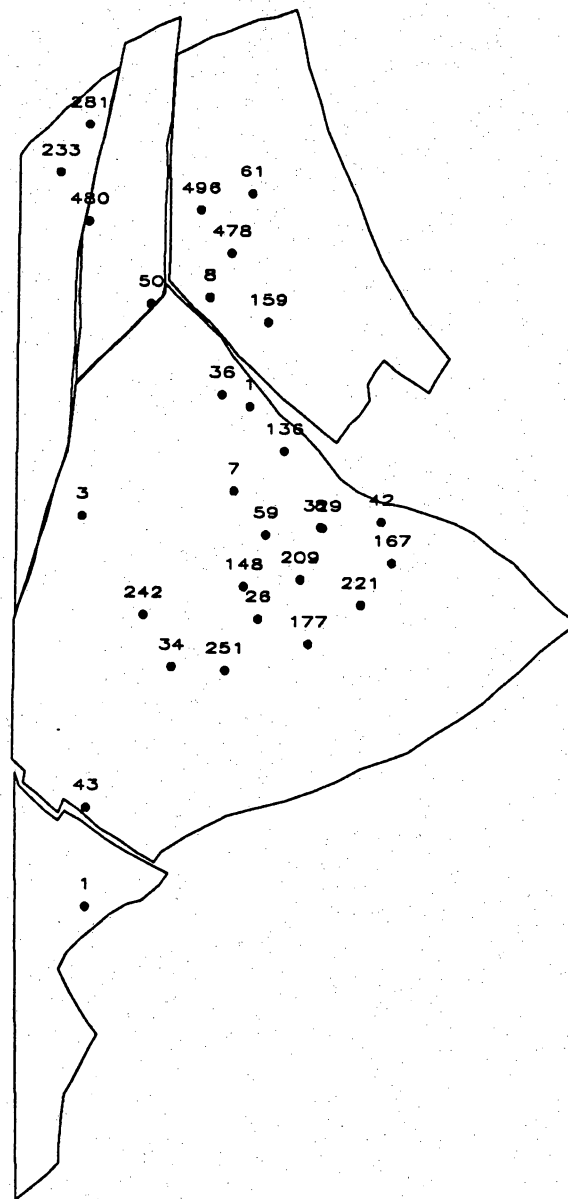


Figure X 47. Cumulative production map of the Upper C-4-X Submember in the LL-652 area. Values are in Mbbl.

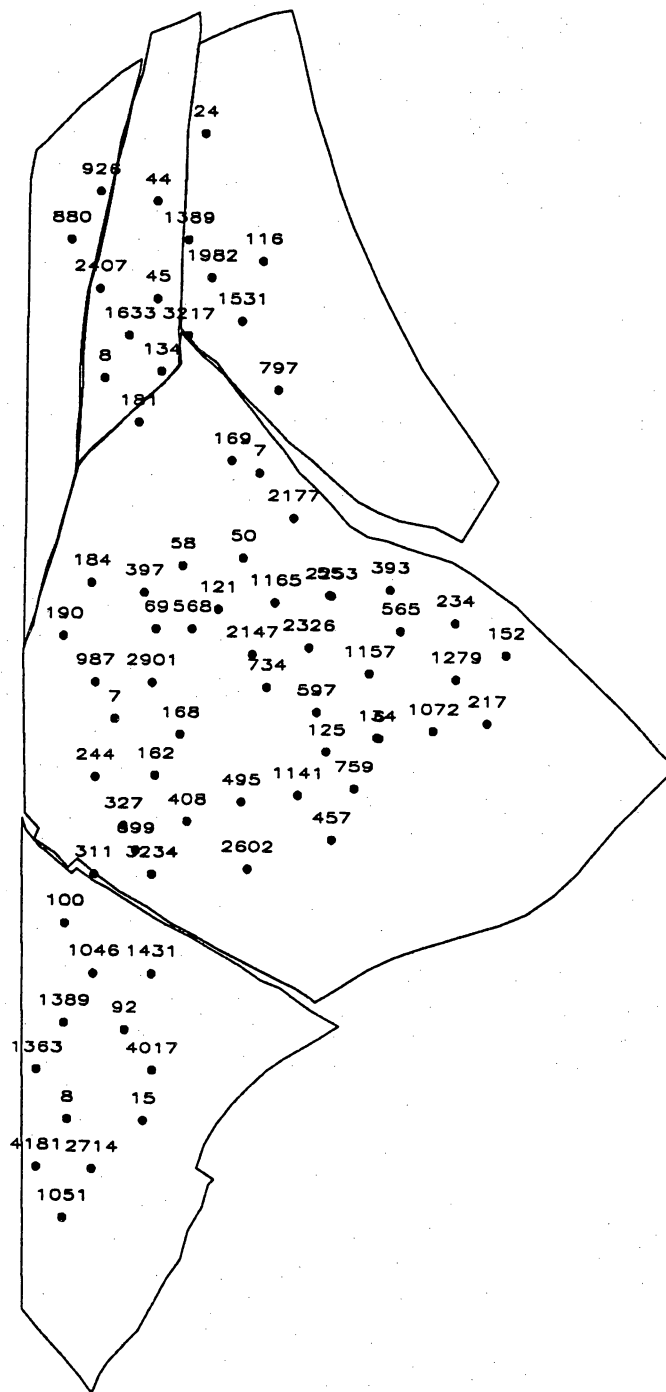


Figure X 48. Cumulative production map of the Lower C-3-X Submember in the LL-652 area. Values are in Mbbl.

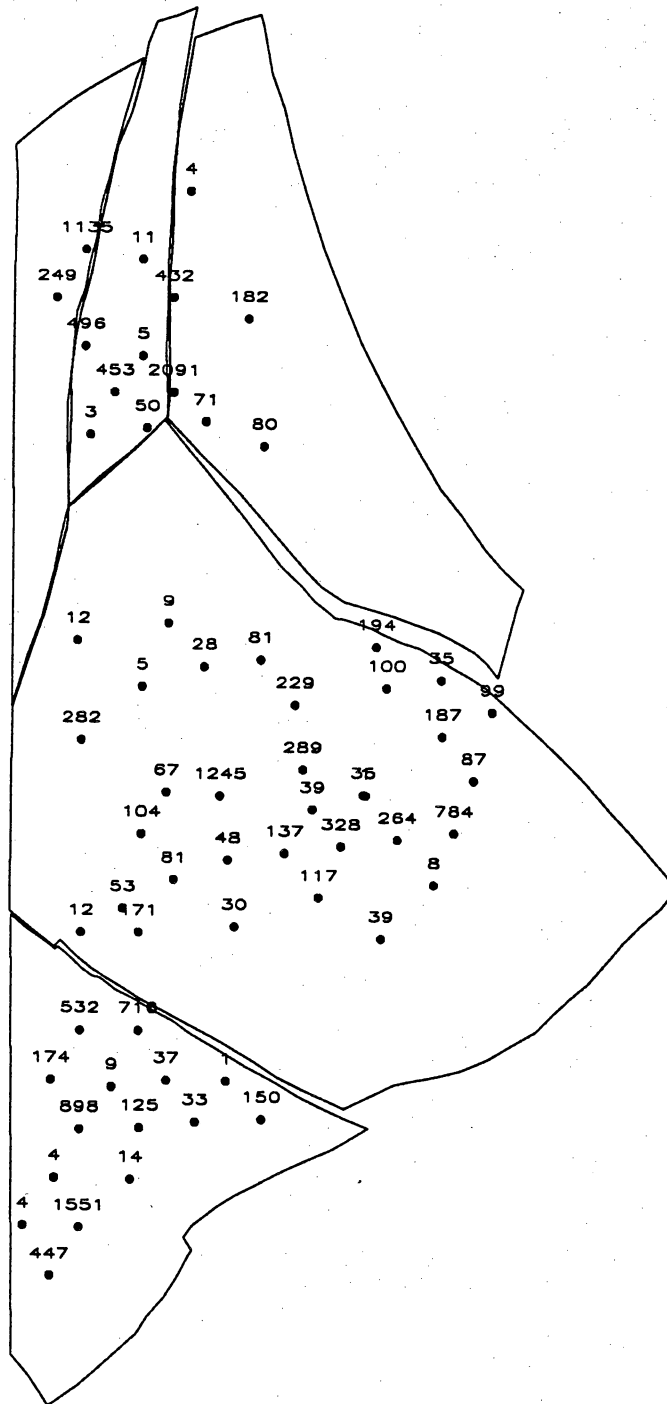


Figure X 49. Cumulative production map of the Middle C-3-X Submember in the LL-652 area. Values are in Mbbl.

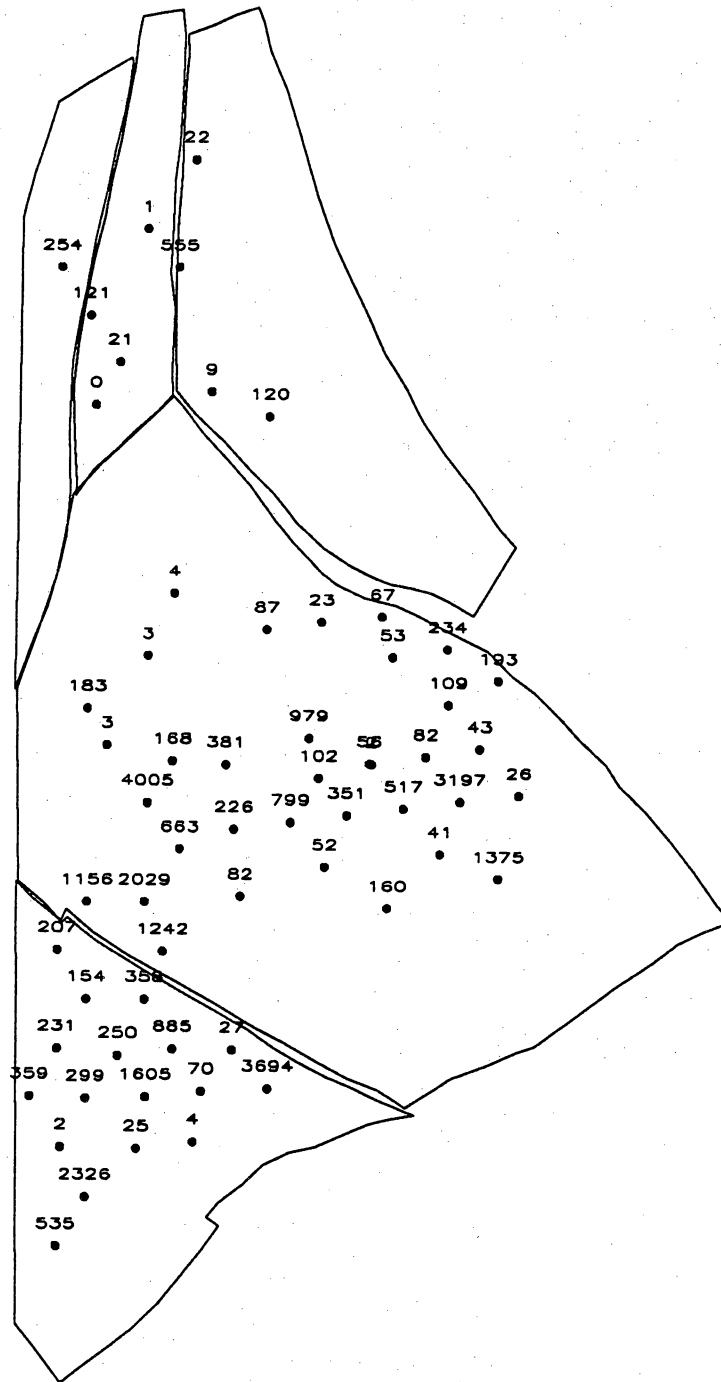


Figure X 50. Cumulative production map of the Middle C-3-X Submember in the LL-652 area. Values are in Mbbl.

Table X 1. Comparison of previous and current estimates of OOP in the C Members in the LL-652 area.

Member	Official (Lagoven)	BEG/ Lagoven Study	Incremental	Percent Change
C-1-X	18.8	22.5	3.7	+20
C-2-X	15.9	20.9	5.0	+31
C-3-X-C-4-X	624.8	1,555.8	931.0	+150
C-5-X	220.8	296.1	75.3	+34
C-6-X	571.3	394.5	-176.8	-31
C-7-X	-	28.4	28.4	100
<u>TOTAL</u>	<u>1,451.6</u>	<u>2,318.2</u>	<u>866.6</u>	<u>+60</u>

Table X 2. Comparison of previous and current estimates of OOIP, EUR, CP, and reserves in the C Members in the LL-652 area.

	Official (Lagoven)	BEG/ Lagoven Study	Incremental	Percent Change
OOIP	1,451.6	2,318.2	866.6	+60
EUR	293	468	175.0	+60
CP	165.5	265.5	-	-
Reserves	127.5	302.5	175.0	+137

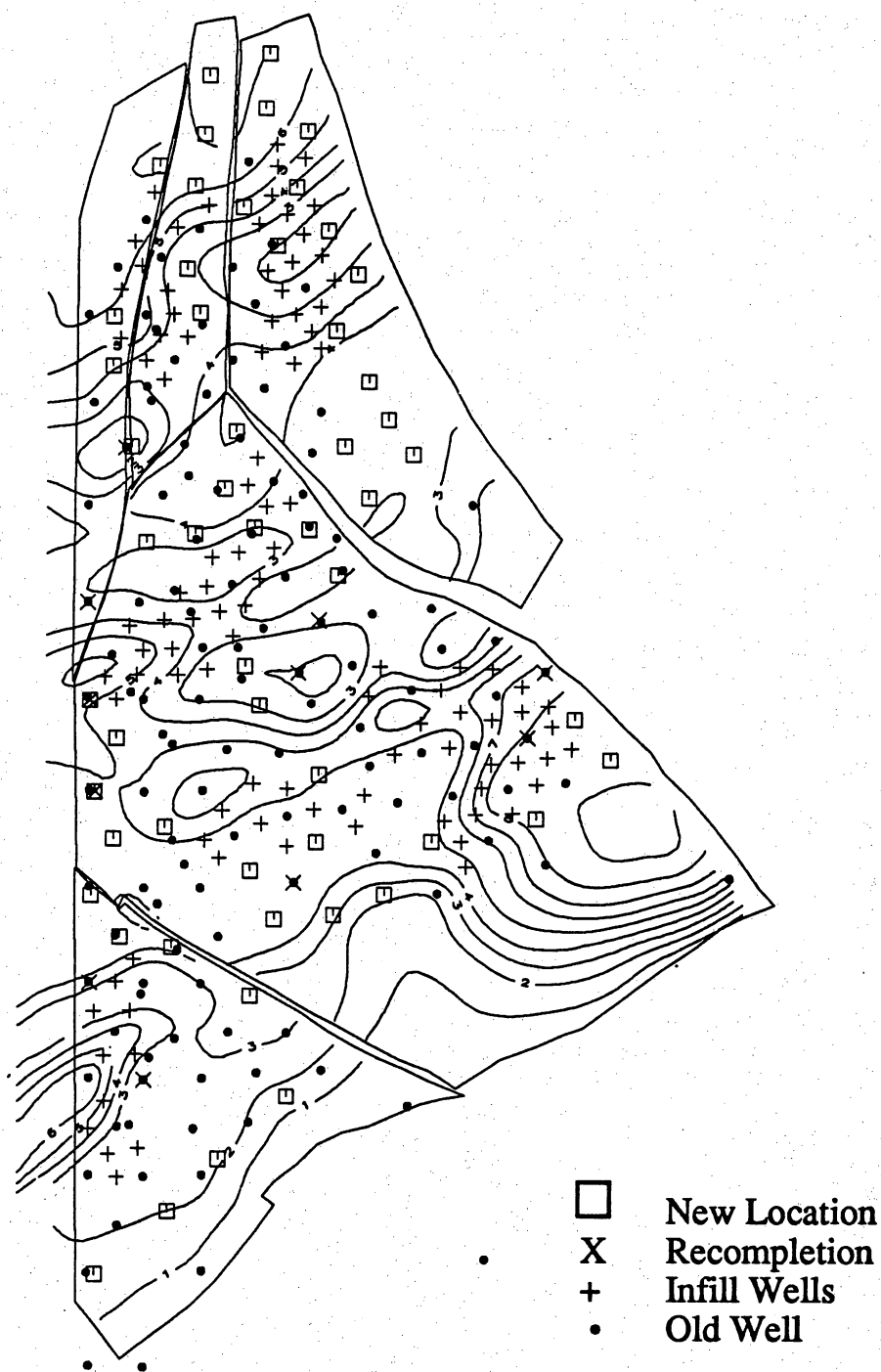


Figure XI 2. Porous hydrocarbon volume in the Middle C-3-X Submember, showing new locations, recompletions, redrilled wells, deepened wells, and infill wells for the C-3-X and C-4-X Members.

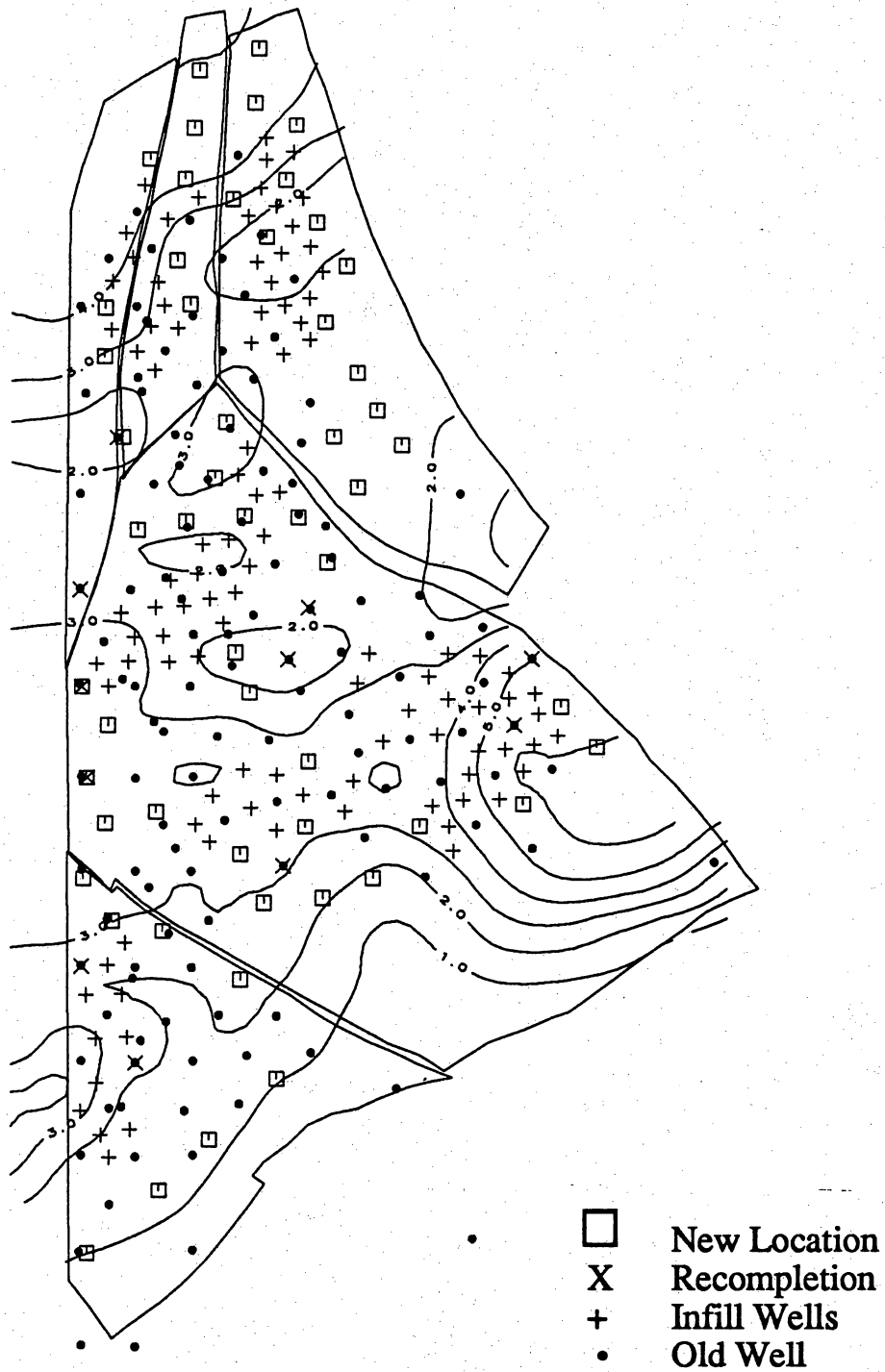


Figure XI 3. Remaining oil in the Middle C-3-X Submember showing new locations, recompletions, redrilled wells, deepened wells, and infill wells for the C-3-X and C-4-X Members.

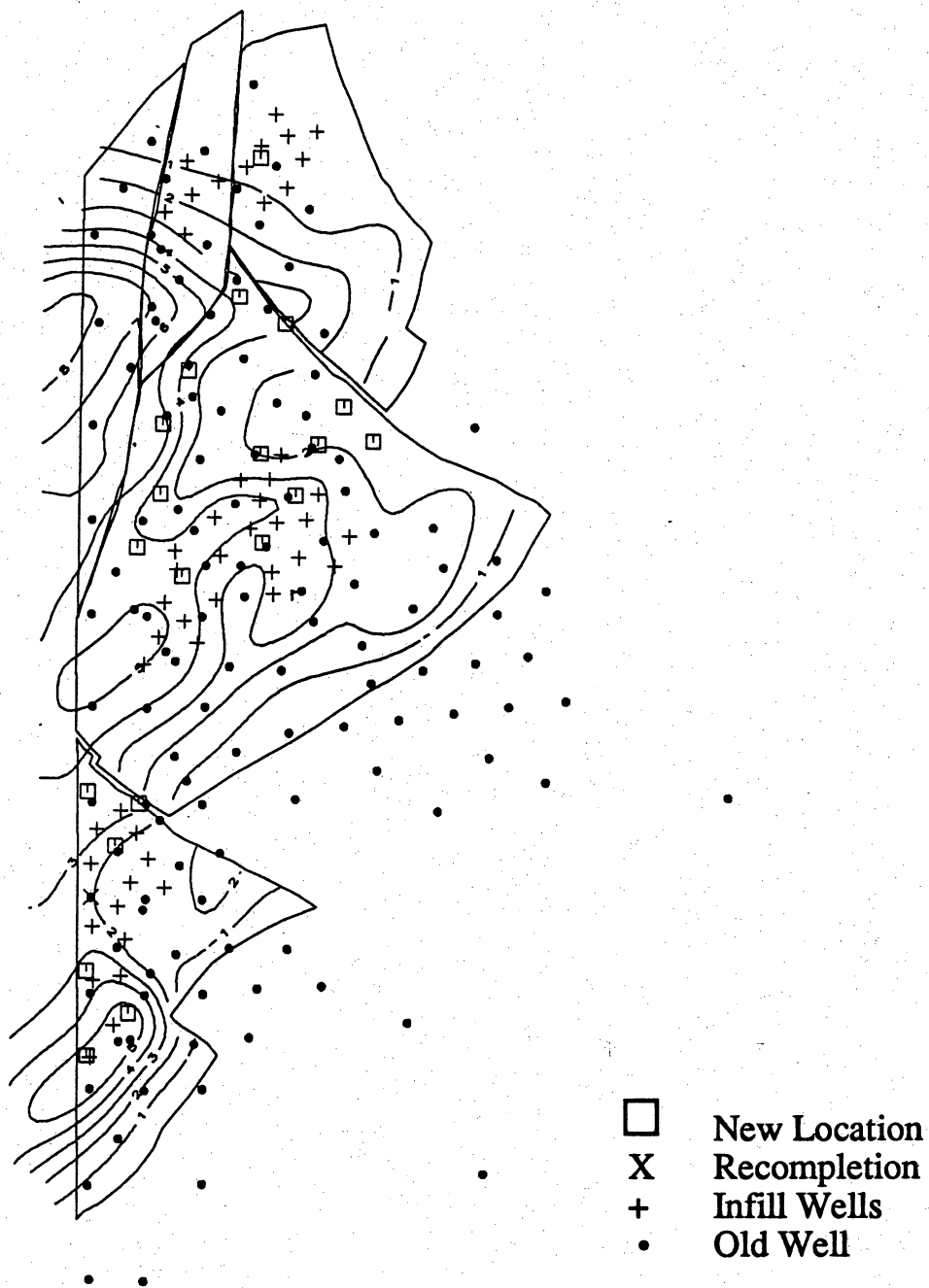


Figure XI 4. Porous hydrocarbon volume in the combined Middle and Upper Middle C-5-X Submember with new locations and infill wells for the C-5-X Member.

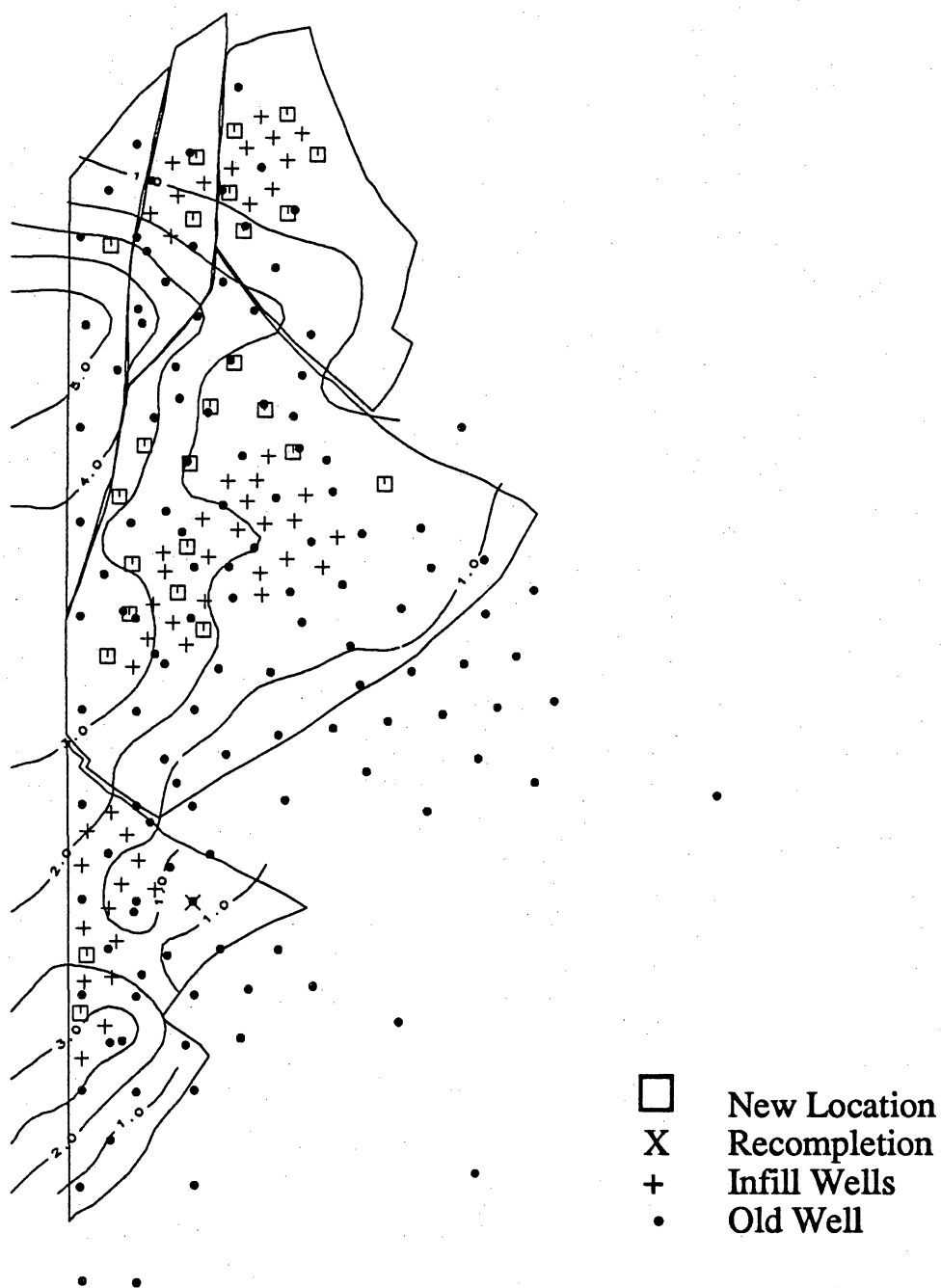


Figure XI 5. Remaining oil in the combined Middle and Upper C-5-X Submembers with new locations and infill wells for the C-5-X Member.

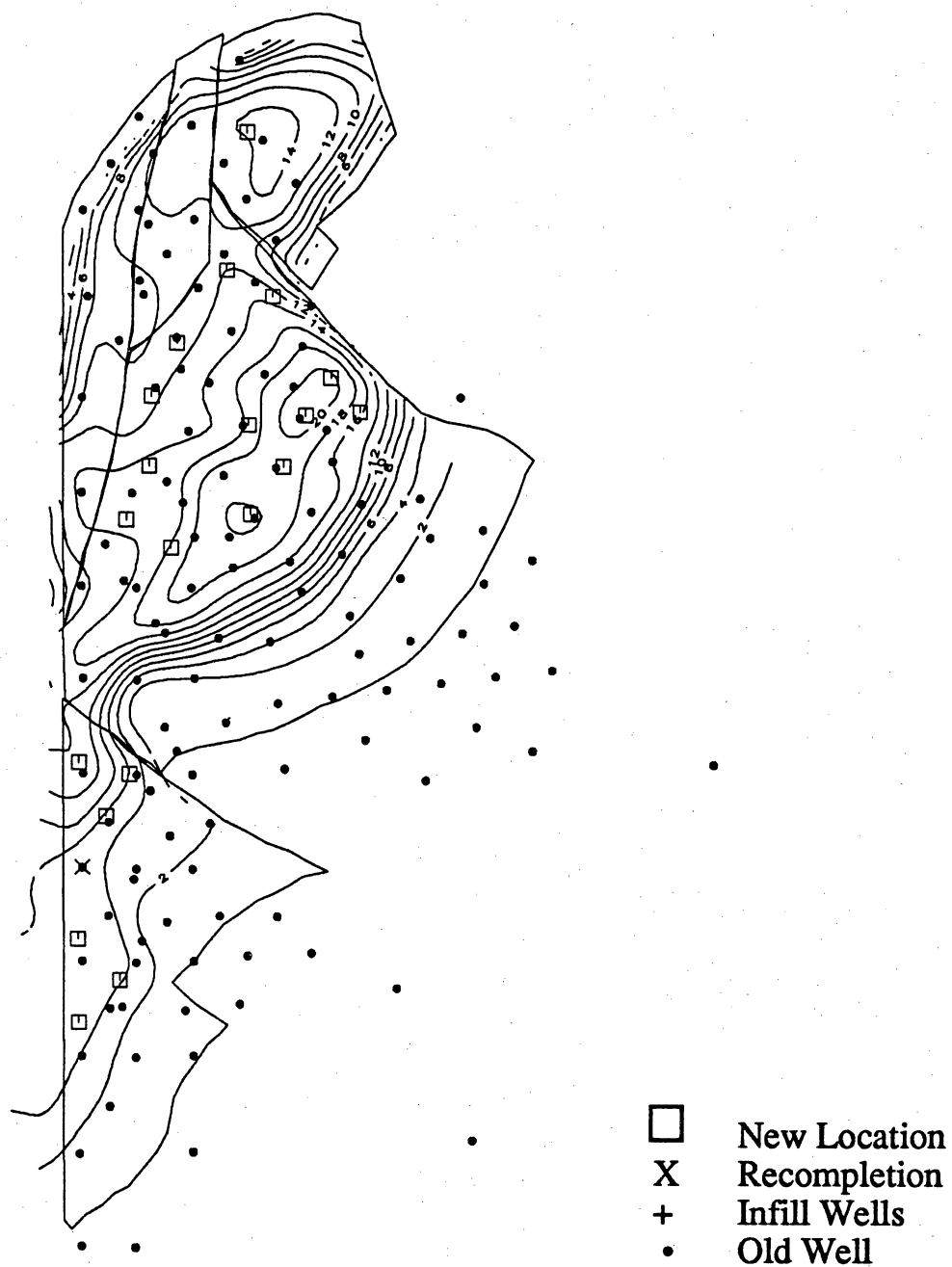


Figure XI 6. Porous hydrocarbon volume in the Upper Upper C-6-X Submember with new locations for the C-6-X Member.

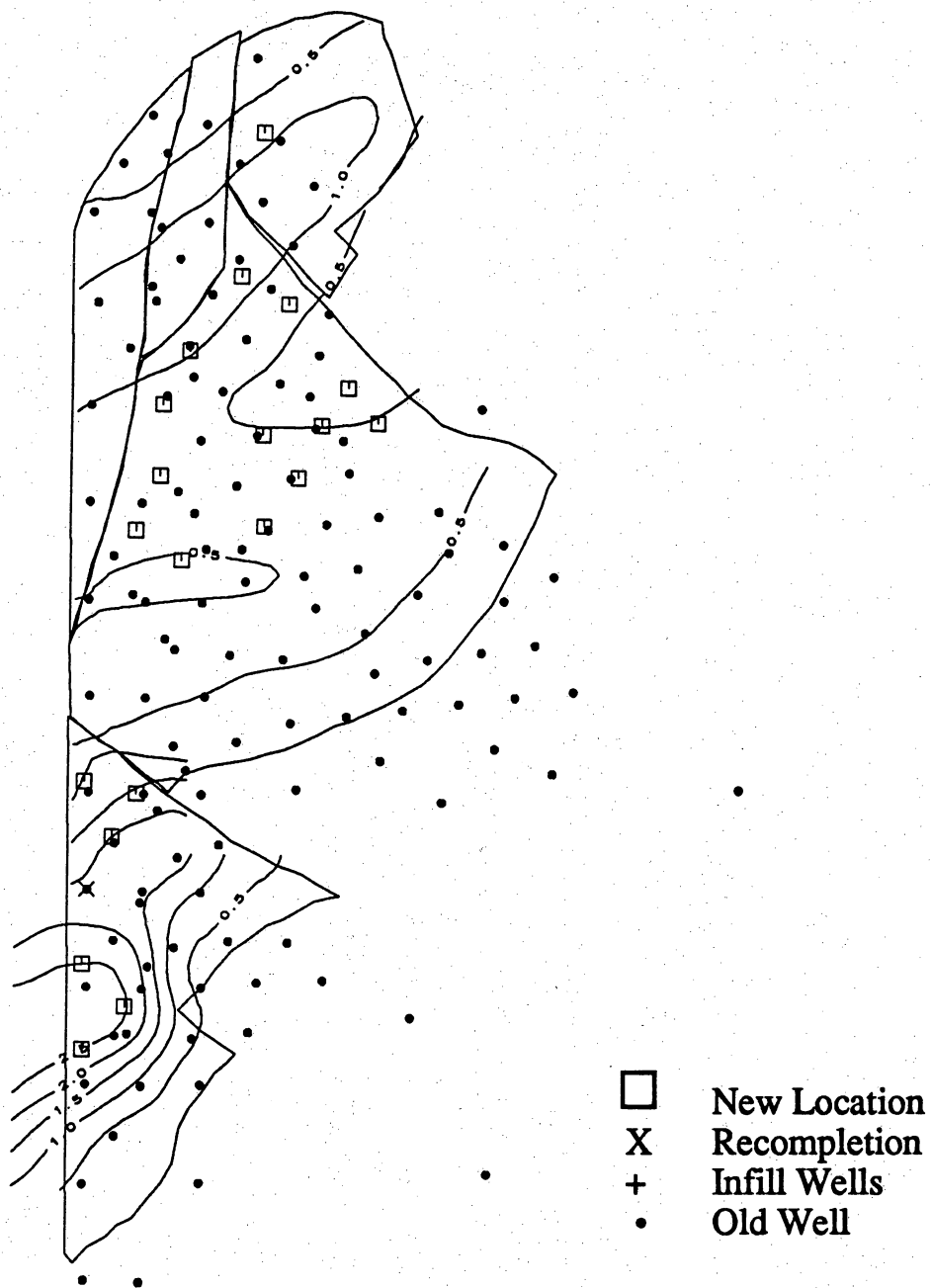


Figure XI 7. Remaining oil in the Upper Upper C-6-X Submember with new well locations for the C-6-X Member.

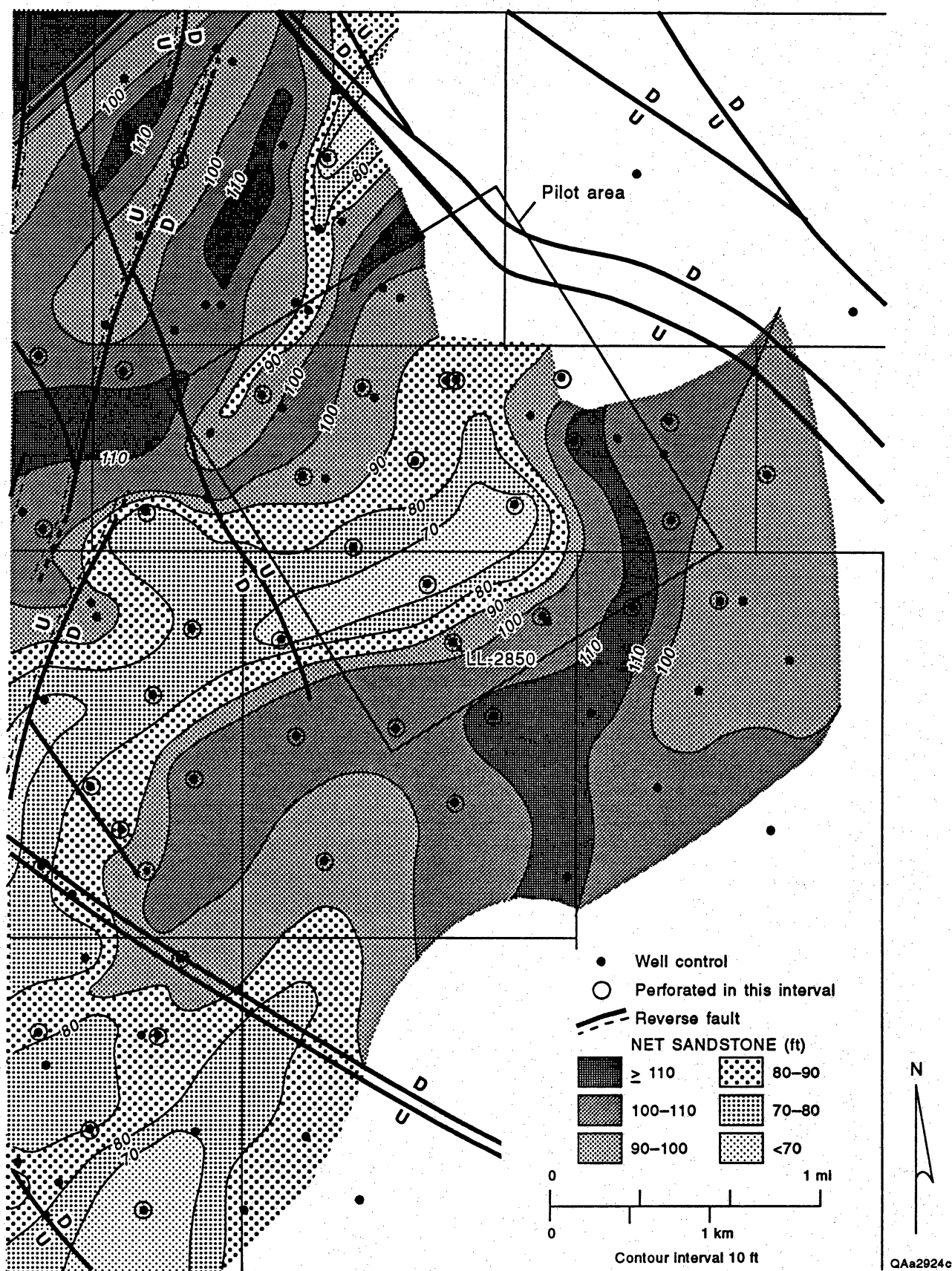


Figure XI 8. Net-sandstone thickness map of the Upper C-4-X Submember in the area of the waterflood pilot area.

Table XI 1. Summary of new well locations in the LL-652 area.

Reservoir	Total per Reservoir	Preliminary Potential (BOPD)		
		High (>250)	Moderate (250 to 150)	Low (<150)
C-4-X.01	30	6	22	2
C-4-X.New	14	8	4	2
C-4-X.03	8	3	5	-
C-5-X.02	17	3	13	1
C-5-X.16	2	2	-	-
C-5-X.New	6	4	2	-
C-6-X.01	13	4	7	2
C-6-X.New	1	-	-	-
C-6-X.08	6	4	2	-
Total area	97	34	55	8

Table XI 2. Names of new well locations in the LL-652 area.

Reservoir	Well Location	Preliminary Potential (BOPD)
C-4-X.01	LL-AD-13C5	M
C-4-X.01	LL-AD-12R10	M
C-4-X.01	LL-AF-14R9	M
C-4-X.01	LL-AH-14C5	M
C-4-X.01	LL-AI-15R11	M
C-4-X.01	LL-AJ-16R2	L
C-4-X.01	LL-AK-16R2	L
C-4-X.01	LL-AKAL-315	M
C-4-X.01	LL-ZAJ-134	M
C-4-X.01	LL-AI-13R4	M
C-4-X.01	LL-AL-13R10	M
C-4-X.01	LL-AMAN-314	M
C-4-X.01	LL-AL-12	M
C-4-X.01	LL-AI-11C6	M
C-4-X.01	LL-AI-10R9	M
C-4-X.01	LL-AF-9	M
C-4-X.01	LL-AF-8	M
C-4-X.01	LL-AG-8	H
C-4-X.01	LL-AH-8	M
C-4-X.01	LL-AI-8	M
C-4-X.01	LL-AG-07	H
C-4-X.01	LL-AF-06	H
C-4-X.01	LL-AG-04R4	M
C-4-X.01	LL-AFAG-303	M
C-4-X.01	LL-AE-03	M
C-4-X.01	LL-AD-02R6	H
C-4-X.01	LL-AA-1CR6 (1)	M
C-4-X.01	LL-ZACAD-301a	M
C-4-X.01	LL-AD-1a	L
C-4-X.01	LL-AB-1bR8 (2)	M
C-4-X New	LL-AD-7R8	L
C-4-X New	LL-ZADAE-306	M
C-4-X New	LL-ACAD-307	L
C-4-X New	LL-ACAD-306	M
C-4-X New	LL-AC-5	M
C-4-X New	LL-AC-4	H
C-4-X New	LL-AB-3	H
C-4-X New	LL-AB-2	H
C-4-X New	LL-AB-1	H
C-4-X New	LL-AC-1	H
C-4-X New	LL-AC-2	H
C-4-X New	LL-AA-1bC5	H
C-4-X New	LL-AAAB-301b	H
C-4-X New	LL-ZAA-301c (3)	M
C-4-X.03	LL-ASAT-323	M
C-4-X.03	LL-AP-21	M
C-4-X.03	LL-AQ-21R10	M

C-4-X.03	LL-AN-20	M
C-4-X.03	LL-ZAM-317	M
C-4-X.03	LL-AM-16R8	H
C-4-X.03	LL-ANAO-316	H
C-4-X.03	LL-ANAO-315	H
C-5-X.02	LL-AE-09	M
C-5-X.02	LL-AF-8	H
C-5-X.02	LL-AF-7	H
C-5-X.02	LL-AF-6	M
C-5-X.02	LL-AG-07	M
C-5-X.02	LL-AH-08	M
C-5-X.02	LL-AI-7R8	M
C-5-X.02	LL-AJ-9R10	H
C-5-X.02	LL-AI-8C3	M
C-5-X.02	LL-ZAJ-310	M
C-5-X.02	LL-AJ-10R9	M
C-5-X.02	LL-AJ-11R10	M
C-5-X.02	LL-AK-11	M
C-5-X.02	LL-AL-12	M
C-5-X.02	LL-AE-3	M
C-5-X.02	LL-AF-3R6	L
C-5-X.02	LL-ZAD-301	M
C-5-X.16	LL-AP-18R1	H
C-5-X.16	LL-AQ-19R3	M
C-5-X New	LL-AD-03	M
C-5-X New	LL-AC-03	M
C-5-X New	LL-ZAD-302	H
C-5-X New	LL-AB-2	H
C-5-X New	LL-AB-1	H
C-5-X New	LL-AC-1	H
C-6-X.01	LL-AE-8	M
C-6-X.01	LL-AE-7	M
C-6-X.01	LL-AF-8	M
C-6-X.01	LL-AG-8	H
C-6-X.01	LL-AG-9	H
C-6-X.01	LL-AH-10	M
C-6-X.01	LL-ZAJ-310	L
C-6-X.01	LL-AJ-9C6	L
C-6-X.01	LL-AI-8C6	H
C-6-X.01	LL-AH-7C2	H
C-6-X.01	LL-AG-6	M
C-6-X.01	LL-ZAE-305	M
C-6-X.01	LL-AE-4C6	M
C-6-X New	LL-AC-1R10	L
C-6-X.08	LL-AQ-20C4	H
C-6-X.08	LL-AP-19R5	M
C-6-X.08	LL-AP-18R5	H
C-6-X.08	LL-ANAO-316	H
C-6-X.08	LL-AMAN-315	M
C-6-X.08	LL-AN-14R10	H

(1) and (3) advanced locations, depending on results at the LL-AB-1bR8 and LL-AAAB-301b locations. (2) Depending on results at the LL-ZACAD-301a location.

Table XI 3. Redrilled wells, recompletions, and deepened wells targeted in the C-4-X.01, C-4-X.03, and C-5-X.16 reservoirs, LL-652 area.

Target (Reservoir)	Well	(Job)	Preliminary Potential	Comments
C-4-X.03	LL-1307	Red	H	
C-4-X.03	LL-995	D	H	
C-4-X.01	LL-2425	Red	M	
C-4-X.01	LL-2191	Red	M	
C-4-X.01	LL-3080	Rec	H	Producing 90% water from C-6-X.01 Reservoir
C-4-X.01	LL-2942	Rec	H	Producing 80% water from C-6-X.01 Reservoir
C-4-X.01	LL-997	D	M	
C-4-X.01	LL-907	D	H	
C-4-X.01	LL-857	Rec	M	
C-4-X.01	LL-1089	Rec	M	
C-4-X.01	LL-866	Red	M	
C-5-X.16	LL-992	Rec	M	Hw in C-6-X.08 reservoir
Total	12			

H=high
 M=moderate
 L=low
 Rec=Recompletion
 D=Deepening
 Red=Redrill
 w=water